OCEANOGRAPHY AND BENTHIC ECOLOGY OF PATAGONIAN FJORDS - 500 YEARS FROM THE DISCOVERY OF THE STRAIT MAGELLAN

EDITED BY: Giorgio Bavestrello and Nelson Silva

PUBLISHED IN: Frontiers in Marine Science

frontiers Research Topics

frontiers

ISSN 1664-8714
ISBN 978-2-88976-889-9
DOI 10.3389/978-2-88976-889-9

About Frontiers

Frontiers is more than just an open-access publisher of scholarly articles: it is a pioneering approach to the world of academia, radically improving the way scholarly research is managed. The grand vision of Frontiers is a world where all people have an equal opportunity to seek, share and generate knowledge. Frontiers provides immediate and permanent online open access to all its publications, but this alone is not enough to realize our grand goals.

Frontiers Journal Series

The Frontiers Journal Series is a multi-tier and interdisciplinary set of open-access, online journals, promising a paradigm shift from the current review, selection and dissemination processes in academic publishing. All Frontiers journals are driven by researchers for researchers; therefore, they constitute a service to the scholarly community. At the same time, the Frontiers Journal Series operates on a revolutionary invention, the tiered publishing system, initially addressing specific communities of scholars, and gradually climbing up to broader public understanding, thus serving the interests of the lay society, too.

Dedication to Quality

Each Frontiers article is a landmark of the highest quality, thanks to genuinely collaborative interactions between authors and review editors, who include some of the world's best academicians. Research must be certified by peers before entering a stream of knowledge that may eventually reach the public - and shape society; therefore, Frontiers only applies the most rigorous and unbiased reviews.
Frontiers revolutionizes research publishing by freely delivering the most outstanding research, evaluated with no bias from both the academic and social point of view. By applying the most advanced information technologies, Frontiers is catapulting scholarly publishing into a new generation.

What are Frontiers Research Topics?

Frontiers Research Topics are very popular trademarks of the Frontiers Journals Series: they are collections of at least ten articles, all centered on a particular subject. With their unique mix of varied contributions from Original Research to Review Articles, Frontiers Research Topics unify the most influential researchers, the latest key findings and historical advances in a hot research area! Find out more on how to host your own Frontiers Research Topic or contribute to one as an author by contacting the Frontiers Editorial Office: frontiersin.org/about/contact

OCEANOGRAPHY AND BENTHIC ECOLOGY OF PATAGONIAN FJORDS - 500 YEARS FROM THE DISCOVERY OF THE STRAIT MAGELLAN

Topic Editors:
Giorgio Bavestrello, University of Genoa, Italy
Nelson Silva, Pontificia Universidad Católica de Valparaíso, Chile

Citation: Bavestrello, G., Silva, N., eds. (2022). Oceanography and Benthic Ecology of Patagonian Fjords - 500 Years From the Discovery of the Strait Magellan. Lausanne: Frontiers Media SA. doi: 10.3389/978-2-88976-889-9

Table of Contents

frontiers in Marine Science

ORIGINAL RESEARCH
published: 23 February 2021
doi: 10.3389/fmars.2021.612195

Genetic Conservation Management of Marine Resources and Ecosystems of Patagonian Fjords

Anna Maria Addamo[1,2], Serena Zaccara[3], Günter Försterra[4], Juan Höfer[4,5], Ricardo García-Jiménez[2], Giuseppe Crosa[3] and Annie Machordom[3]*

[1] European Commission, Joint Research Centre (JRC), Ispra, Italy, [2] Departamento de Biodiversidad y Biología Evolutiva, Museo Nacional de Ciencias Naturales (MNCN-CSIC), Madrid, Spain, [3] Department of Theoretical and Applied Sciences, University of Insubria, Varese, Italy, [4] Escuela de Ciencias del Mar, Pontificia Universidad Católica de Valparaíso, Valparaíso, Chile, [5] Fundación San Ignacio del Huinay, Puerto Montt, Chile

OPEN ACCESS

Edited by:
Giorgio Bavestrello, University of Genoa, Italy

Reviewed by:
Leocadio Blanco-Bercial, Bermuda Institute of Ocean Sciences, Bermuda
Federica Costantini, University of Bologna, Italy

***Correspondence:**
Anna Maria Addamo
am.addamo@gmail.com;
anna.addamo@ec.europa.eu

Specialty section:
This article was submitted to Marine Ecosystem Ecology, a section of the journal Frontiers in Marine Science

Received: *30 September 2020*
Accepted: *26 January 2021*
Published: *23 February 2021*

Citation:
Addamo AM, Zaccara S, Försterra G, Höfer J, García-Jiménez R, Crosa G and Machordom A (2021) Genetic Conservation Management of Marine Resources and Ecosystems of Patagonian Fjords. Front. Mar. Sci. 8:612195. doi: 10.3389/fmars.2021.612195

The Chilean fjord region includes many remote and poorly known areas where management plans for the marine living resources and conservation strategies are urgently needed. Few data are available about the spatial distribution of its marine invertebrate fauna, prevalently influenced by complex interactions between biotic and abiotic factors, animal behavior and human activities. Patagonian fjords are a hotspot for finfish aquaculture, elevating Chile to the world's second producer of farmed salmon, after Norway, a condition that emphasizes the necessity to develop strategies for a sustainable aquaculture management. The present study focuses on the emblematic cold-water coral *Desmophyllum dianthus*, dwelling the Comau Fjord from shallow to deep waters, with the aim to illustrate population structure, demography and adaptation of the species and its potential use for the development of a sustainable conservation and management plan for human activities. The analyses of microsatellite loci of *D. dianthus* individuals from four sampling localities along horizontal and vertical gradients of Comau Fjord, lead to identify them as a panmictic population. The results also contributed to consider a careful examination of the synchrony between the temporal and spatial variations of environmental factors and the biological cycle of the species as key role player in the inference of autecology of the species. The discussion stresses the importance of molecular analyses as extremely helpful tools for studies focusing on remote areas and non-model organisms, where logistic difficulties and limited scientific knowledge hamper a better management and conservation of marine resources, and in particular the relevance of multidisciplinary approaches to reduce the extensive knowledge gap on the remote fjord ecosystems of Patagonia. This study also highlights the importance of oceanographic information in the entire process of the analyses and interpretation of genetic results.

Keywords: cold water corals, genetic structure, oceanographic conditions, conservation, aquaculture sustainability, Patagonian fjord region

INTRODUCTION

Marine biodiversity and unsustainable maritime activities cannot stand up together. Efficient management plans are urgently needed. Patagonian fjords are not only a hotspot of marine biodiversity, but also for finfish aquaculture, elevating Chile to the world's second producer of farmed salmon, after Norway (Bjørndal, 2002; FAO, 2020), a further condition that emphasizes the necessity to develop strategies for a sustainable aquaculture management. Due to its remoteness and enormous coastline, the Chilean fjord region includes many poorly known areas. Only few data are available about the spatial distribution of its marine invertebrate fauna, prevalently influenced by complex interactions between biotic and abiotic factors (Häussermann and Försterra, 2009).

Comau Fjord, located in the northern Patagonia of Chile, is one the most exploited fjords along the Patagonian coast in term of maritime activities, which are mostly characterized by artisanal fishing (18%) and aquaculture (60%), which is a large industry in Chile (Fillinger and Richter, 2013; Soto et al., 2019). An unexpected deep-water coral diversity and abundance was also described from off the Chilean coast and Central Chilean Patagonia (Bravo et al., 2005; Häussermann and Försterra, 2007, 2014; Cañete and Häussermann, 2012). Many large and dense assemblages of Cold-Water Coral (CWC) communities were recorded in shallow water of Patagonian fjords (Försterra and Häussermann, 2003; Försterra et al., 2005; Häussermann and Försterra, 2007, 2014). Among them there is the emblematic cold-water coral *Desmophyllum dianthus*, dwelling Chilean Patagonian coast and specifically the Comau Fjord from shallow to deep waters. With aquaculture and artisanal fisheries growing exponentially (see Soto et al., 2019), the Comau Fjord changed from near pristine in 2003 to heavily impacted in 2013, where abundances of benthic communities were reduced down to 25%. Similarly, several species have declined from common to very rare within the fjord (Häussermann et al., 2013). The productivity was reported to have doubled in 20 years (Mayr et al., 2014). In 2012, 99% of the *D. dianthus* specimens died along at least 15 km of the coast, probably after a large algal bloom in combination with exceptionally high efflux of harmful substances (methane and sulfide) enriched water from the cold vents due to increased salmon farming activity and volcanic activities, respectively (Försterra et al., 2014).

Strategies of marine conservation have been (and still are) based on qualitative and quantitative data describing the status of marine ecosystems, marine biodiversity, pressures and impacts of anthropogenic activities. Among all this environmental indicators, there was no room for genetic data, which on the contrary have been mostly used for taxonomic, phylogenetic and evolutionary studies in the lasts decades. However, molecular tools can be extremely helpful to determine structure, demography and environmental adaptation of marine organisms, also providing evidence especially in studies focused on remote areas and non-model organisms, where logistic difficulties and limited scientific knowledge hamper a better management and conservation of marine resources. This type of knowledge represents the baseline information necessary for the development of an effective marine conservation strategy and management plan for sustainable maritime activities.

Since not many data on the population structure of marine organisms on the Chilean fjords are available whether along horizontal or vertical distribution (see Fillinger and Richter, 2013) we hypothesize that, not excluding a horizontal gradient along the fjord (head-mouth), the steep oceanographic gradients (salinity and temperature) might have shaped the structure of its benthic communities, generating a benthic vertical zonation within the fjord.

The present study aims to assess the structure of *Desmophyllum dianthus* populations of the Comau Fjord, analyzing the genetic profile with microsatellite loci and the environmental condition of the fjord. The application of a multidisciplinary approach highlights the importance of oceanographic information in the entire process of the analyses and interpretation of genetic results, reducing the knowledge gap on the marine ecosystems in Patagonian fjords.

MATERIALS AND METHODS

Study Area and Oceanographic Description

Comau Fjord is located in Northern Patagonia, Chile (42°15′ S, 72°29′ W). It extends approx. 35 km along a north-south axis and possesses two lateral fjords, Quintupeu and Cahuelmó. At Lilihuapi Island, the Comau mouth faces west toward the Interior Sea of Chiloé. The fjord presents no sill and is characterized by a typical "U"-shape with very steep slopes, reaching a maximum depth of 497 m close to its mouth. The main freshwater inputs occur at the fjord head, where two rivers bring in average ∼6,000 mm per year of rainwater (Hromic, 2009) and tides reach up to 7.5 m (Försterra, 2009; Sobarzo, 2009). The hydrogeomorphologic features of the fjord shape an accentuated vertical variability (**Figure 1B**).

There are three main layers within Comau Fjord according to the vertical oceanographic gradients: (a) surface freshwater (0–10 m depth) that is under the direct influence of climatic events (e.g., rain and wind), and presents a strong seasonality with salinity (2-20 PSU, Practical Salinity Unit) and temperature (5–20°C), varying largely during the year; (b) a layer of brackish water (20–30 PSU) between 5 and 20 m depth that presents a sharp pycnocline mainly caused by salinity changes (halocline), except during summer months when temperature changes (from 18 to 12°C), also contributing to the stratification of the water column; (c) deep saline water (below 20 m depth), with salinity >32 (PSU) and a constant temperature (∼11°C) (Sobarzo, 2009; Sánchez et al., 2011; Fillinger and Richter, 2013). The freshwater inputs enhance the stratification of the water column within Comau, which creates a layer system with a different horizontal advection for each layer (Silva et al., 1997; Zhou et al., 2005), known as estuarine circulation. Similarly, water mass exchange with the Interior Sea of Chiloé generates a horizontal gradient across the head-mouth axis of the fjord (**Figure 1B**; Häussermann and Försterra, 2009). These changes are most likely related to the phase of the tide. The temperature

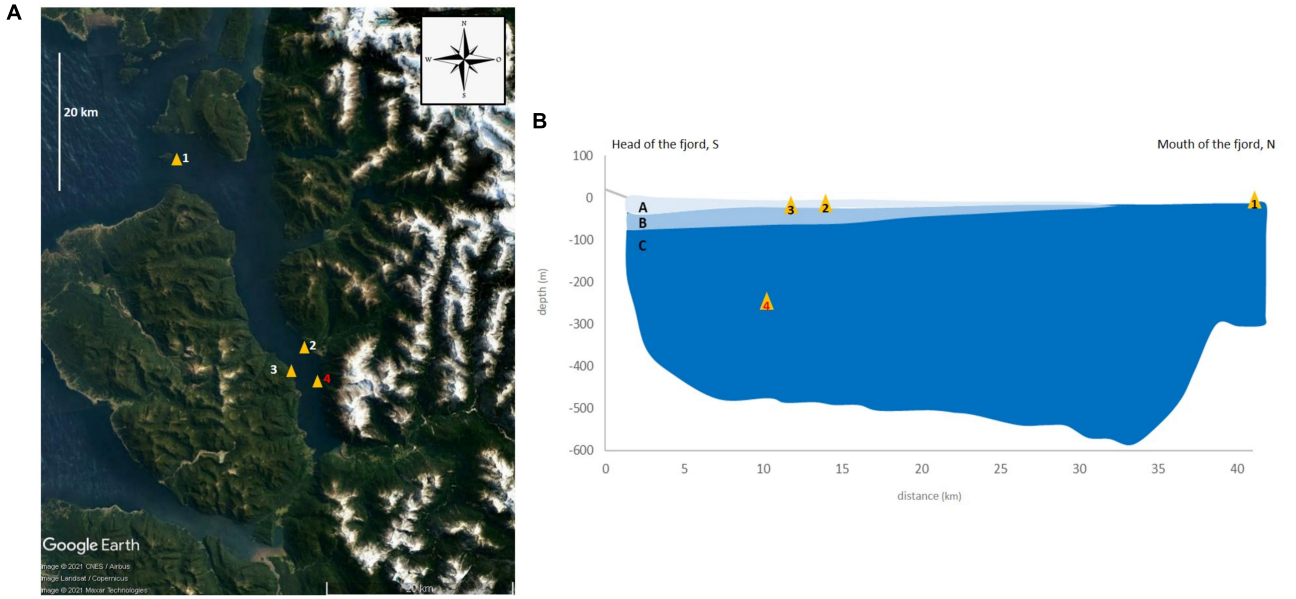

FIGURE 1 | Location and information on coral samples collected in Comau Fjord **(A)**: (1) Lilihuapi Island (ILC, 42°09′ S 72°35′ W), −20 m; (2) Punta Huinay (PHC, 42°22′ S 72°25′ W), −20 m; (3) Cross Huinay (XHC, 42°23′ 55″ S, 72°27′ 18″W), −20 m; (4) Punta Gruesa (PGC_D, 42°24′ S 72°25′ W), −250 m, D, Deep indicated in red. Simplified scheme of water layers and movement of the Comau Fjord **(B)**. A, surface freshwater layer; B, brackish water; and C, deep saline water; N, north S, south (Google Earth, Image © 2021 CNES/Airbus, Landsat/Copernicus, Maxar Technologies).

also varies along the year and moreover toward the head of the fjord, where it is increasing during some months (e.g., 0.5°C in September), decreasing in others (e.g., 0.7°C in May), or remaining stable in other months (e.g., 0.1°C in December). Important seasonal changes in salinity and temperature also occur vertically in the first 50 m of the water column, while below 50–60 m the changes are negligible (Sánchez et al., 2011; Fillinger and Richter, 2013; Höfer et al., unpublished data). Mixing water events are relevant as well. Their effects depend on wind intensity, direction, and duration of blowing under specific conditions. In the case of Huinay (i.e., sampling location no. 2, **Figure 1A**), due to the configuration of the fjord, and the presence of huge tides that produce strong currents throughout the entire water column, winds from the N or NE in combination with strong tide currents can mix the waters down to the first 100 m of the water column, introducing and removing a large amount of water from the fjord and making sessile organisms pass from one layer to another depending on the high or low tide.

Sampling Strategy

Due to the large abundance of living coral aggregations below 20 m water depths (Försterra et al., 2005), the sampling was planned to encompass the main oceanographic gradients present in the Comau Fjord: salinity (halocline, vertical, and horizontal gradient), temperature (thermocline, vertical gradient) as well as water mass exchange along a head-mouth axis. Four sampling localities across the mouth-head axis of the fjord were selected and samples were collected at different depths: Isla Lilihuapi (ILC, 42°09′ S 72°35′ W), −20 m, 25 PSU, 18°C–36 individuals; Punta Huinay (PHC, 42°22′ S 72°25′ W), −20 m, 25 PSU, 12°C–29 individuals; Cross Huinay (XHC, 42°23′ 55″ S, 72°27′ 18″W), −20 m, 25 PSU, 12°C–23 individuals; Punta Gruesa (PGC_D, 42°24′ S 72°25′ W), −250 m–37 individuals (**Figure 1**).

Biological Tissue Sampling and Molecular Analyses

Coral tissue from 125 specimens taxonomically identified as *D. dianthus* was sampled and preserved in absolute ethanol. Additional samples of *D. dianthus* from the Mediterranean Sea (Adriatic Sea, 41°30' N 17°17' E, 26 specimens) were incorporated to the Comau dataset as a sort of outgroup to support the informative capacity of microsatellites analysis.

Following the procedure described in Addamo et al. (2020), total genomic DNA was extracted from the mesenteric tissue using the QIAGEN BioSprint 15 DNA Blood Kit (Qiagen Iberia S.L., Madrid), with slight modifications, including the optional RNase treatment and an extended period of proteinase K lysis (overnight incubation at 55°C). DNA concentration was quantified using the Qubit 2.0 Fluorometer, and diluted to a final concentration of 2 ng/μl. Thirty-one microsatellite loci developed for *D. dianthus* (25 markers from Addamo et al., 2015a; six markers from Miller and Gunasekera, 2017) were organized in 1 tetraplex, 7 triplex, and 3 duplex by Multiplex Manager 1.0 (Holloley and Geerts, 2009) and analyzed in each sample. Multiplex PCRs were performed using 1X Qiagen Multiplex PCR Master Mix (Qiagen, Hilden, Germany), and following the PCR conditions described in Addamo et al. (2015a). Fluorescently labeled PCR products were run on an ABI PRISM 3730 DNA Sequencer

(Applied Biosystems), scored using the GeneScan-500 (LIZ) size standard, and analyzed with the GeneMapper software (Applied Biosystems). Estimates of null allele frequency, error scoring, and large allele dropout were calculated with the Brookfield-1 method (Brookfield, 1996) using Micro-Checker (Van Oosterhout et al., 2004) and FreeNa (Chapuis and Estoup, 2007). Due to possible asexual reproduction of colonial and free-living corals (e.g., via budding, transverse division) (Tokuda et al., 2017), which includes *D. dianthus* (Miller and Gunasekera, 2017), individuals with identical multilocus genotype were identified using the index of probability of identity (PI the probability of two individuals sharing the same genotype) calculated using GenAlEx 6.5 (Peakall and Smouse, 2012). Departures from Hardy-Weinberg Equilibrium (HWE) and genotypic linkage disequilibrium (LD) were tested using Genepop on the web version 4.7 (Raymond and Rousset, 1995; Rousset, 2008) and GenAlEx 6.5 (Peakall and Smouse, 2012). Sequential Holm-Bonferroni correction (Holm, 1979) was applied to the multiple tests. Basic information on genetic variability and diversity within and among sampling localities was estimated as allele frequency and richness, heterozygosity (Ho, He) and fixation index (F_{IS}) (**Table 1**). Computations were made using GenAlEx 6.5 and Genepop on the web version 4.7.

To investigate population structure, the number of genetic clusters (K) from multilocus genotype data was inferred with a Bayesian model-based approach implemented in Structure v2.3.4 (Falush et al., 2003). Bayesian analyses of genetic admixture model, including the information of sampling localities (LOCPRIOR) were run with settings including 50,000 MCMC interactions after a burn-in of 10,000 iterations. Ten independent chains were run to test each value of K from 1 to 5. The results from Structure were then processed in Structure Harvester (Earl and vonHoldt, 2012), Structure Selector (Li and Liu, 2018), and CLUMPAK (Kopelman et al., 2015) to detect the best-fit number of genetic clusters representing the genetic discontinuity of the data. The highest mean lnPr(X| K) (Pritchard et al., 2000), the ΔK (Evanno et al., 2005), and MedMeaK, MaxMeaK, MedMedK, MaxMedK (Puechmaille, 2016) were all considered to identify and evaluate the optimum value of K. Each cluster identified in the initial Structure run was analyzed separately using the same settings to identify potential within-cluster structure (Evanno et al., 2005). Individual/population assignment and genetic differentiation among clusters suggested by Structure, were calculated using analyses of molecular variance (AMOVA) implemented in GeneClass2 (Piry et al., 2004), Arlequin and GenAlEx 6.5, respectively. Samples were subjected to spatial genetic analysis using principal coordinate analysis (PCoA) and Isolation-by-distance Mantel test implemented in GenAlEx 6.5 and Genepop on the web version 4.7. The regression of linearized F_{ST} [i.e., $F_{ST}/(1- F_{ST})$] vs. marine geographic distance (km) was performed to assess the correlation between genetic and geographic distances. Marine geographic distances between localities were calculated using Google Earth (Google Inc, 2009) and considering the most direct marine route.

Population demography analysis was computed using Bottleneck (Cornuet and Luikart, 1997) to test a recent effective population size reduction from allele data frequencies. Detection of first-generation migrants was determined with GeneClass2 (Piry et al., 2004), setting the frequency-based method with Monte-Carlo resampling, minimum number of 10,000 simulated individuals, and 0.01 for Type I error (alpha) value.

RESULTS

After initial data check (i.e., detection and elimination of loci/sample with null allele and with 10% of missing data), the final genotype dataset includes 23 microsatellites and 118 individuals [including Mediterranean population (A)], or 99 individuals [excl. Mediterranean population (B)] (Addamo et al., 2021). Further analyses with Micro-Checker, FreeNa and GenePop confirm the absence of null alleles and linkage disequilibrium between loci in the reduced dataset (**Supplementary Table 1**). All loci were polymorphic and by locality, their allelic richness was maximum up to 34 (e.g., locus C6 in PGC_D) alleles, while the observed heterozygosity (Ho) was lowest in PGC_D (0.56 ± 0.05) and largest in PHC (0.60 ± 0.06) (**Table 1**). Analyses of populations structure indicated two main genetic clusters of *D. dianthus* ($K = 2$), corresponding to population from in the Mediterranean Sea, on one side, and the four Chilean sampling localities, on the other (**Figure 2A**). Instead, further genetic structuring was not detected between Chilean localities, which were clearly identified in a unique genetic cluster (**Figure 2B**). The optimal values of genetic clusters K representing the genetic discontinuity among *D. dianthus* individuals from the Mediterranean Sea and Chile, and the clear genetic homogeneity of the four Chilean localities in the Comau Fjord were identified by the three approaches: highest mean lnPr(X| K) (Pritchard et al., 2000), ΔK (Evanno et al., 2005), and MedMeaK, MaxMeaK, MedMedK, MaxMedK (Puechmaille, 2016; **Supplementary Figure 1**).

In concordance with the results on population differentiation, the genetic distance computed through the analysis of principal coordinates (PCoA) and the population assignment test among individuals estimated full self-population attribution (100%) for individuals from Mediterranean Sea, while most of the individuals from Chilean sites were assigned to sampling localities from Comau Fjord (84%) and only minor percentage (16%) to self-sampling localities attribution (**Figure 3**). The molecular variance (AMOVA) also indicated appreciable differences only among Mediterranean and Chilean populations group pairs (total $F_{ST} = 0.23$, $p\text{-}value = 0.000$), supporting the hypothesis of two different regions with an observed variation of 24% between both regions (**Supplementary Figure 2**).

Positive and highly significant genetic-spatial correlation was also detected from the Mantel test between Mediterranean Sea and Chile (p-value = 9.26E–15). Indeed, pairwise genetic distances between original localities increased significantly with geographic distances, showing a pattern of isolation-by-distance (IBD) on the large spatial scale (**Supplementary Figure 3A**), as also indicated by a previous study (Addamo et al., 2020).

TABLE 1 | Genetic variability and diversity by sampling locations of *Desmophyllum dianthus* in Comau Fjord.

	ILC		PHC		XHC		PGC_D	
	Mean	**SE**	**Mean**	**SE**	**Mean**	**SE**	**Mean**	**SE**
N	25.565	0.187	25.652	0.162	17.783	0.108	28.609	0.241
Na	9.348	1.355	9.522	1.285	8.261	1.043	9.870	1.509
Ne	5.008	0.940	4.776	0.823	4.864	0.769	5.218	1.059
I	1.488	0.183	1.506	0.176	1.506	0.168	1.522	0.188
Ho	0.574	0.058	0.599	0.059	0.596	0.054	0.564	0.053
He	0.618	0.063	0.621	0.062	0.639	0.059	0.623	0.063
uHe	0.630	0.064	0.634	0.063	0.657	0.061	0.634	0.064
F_{IS}	0.039	0.035	0.021	0.021	0.048	0.034	0.059	0.029
Estimates of Nm over all pops and loci								
Nm (A)	3.294	0.486	Sample set including sampled population from Mediterranean Sea (Adriatic Sea)					
Nm (B)	17.637	1.355	Sample set including only sampled populations from Chile					

*N, sample size; Na, number of alleles; Ne, number of effective alleles; I, Shannon's information index; Ho, observed heterozygosity; He, expected heterozygosity; uHe, unbiased expected heterozygosity; F_{IS}, fixation index; Nm, number of migrants. For complete locality names (see **Figure 1**). A, sample set including sampled population from Mediterranean Sea (Adriatic Sea); B, sample set including only sampled populations from Chile. For complete locality names (see **Figure 1**).*

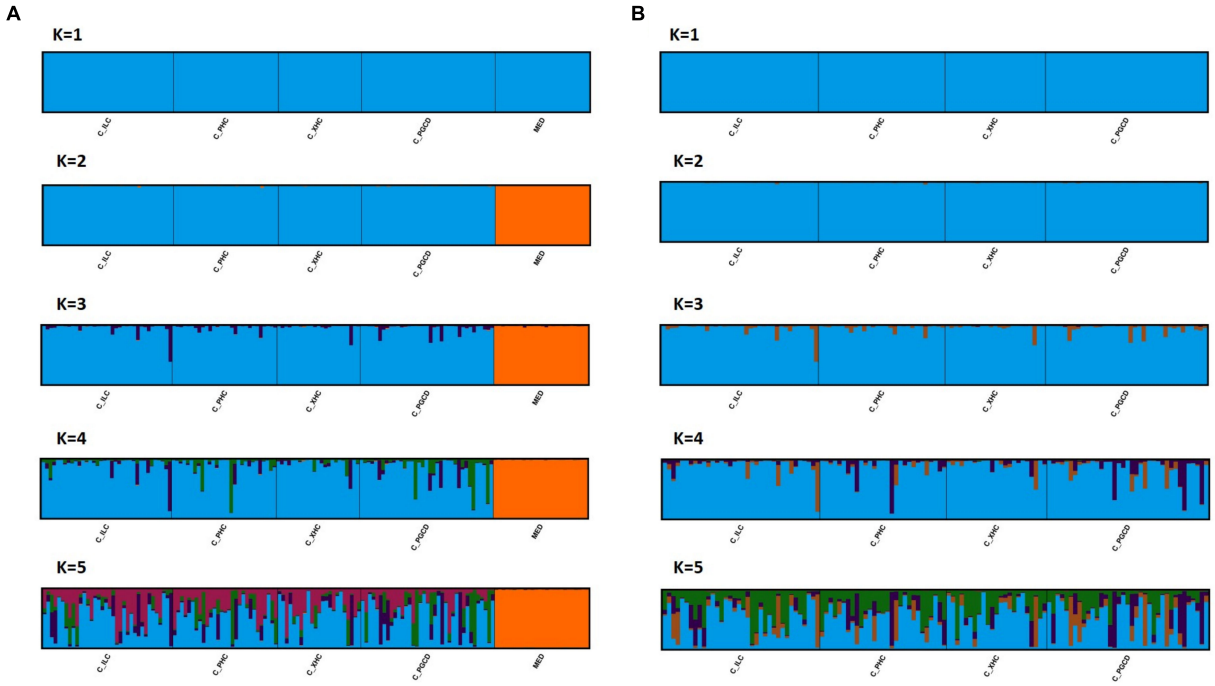

FIGURE 2 | Proportional membership of *Desmophyllum dianthus* individuals from sequential cluster analyses using STRUCTURE SELECTOR and CLUMPAK, including **(A)** or excluding **(B)** individuals from Mediterranean Sea (MED). The clusters (K = 1–5) are shown with the vertical bars representing each individual broken into colored segments based on the proportion of the genome estimated to have originated from each cluster. For complete locality names (see **Figure 1**). MED stands for Mediterranean Sea, and C_ for Chile.

Localities appeared clustered in two major genetic divergence groups: one cluster includes specimens from the Mediterranean Sea ($F_{ST} \approx 0.19$, marine distance 20,000 km), a second cluster that represents individuals from Chile ($F_{ST} \approx 0.01$, marine distance range 2–20 km). In contrast, no significant genetic-distance correlation was detected from the Mantel test for localities within Comau Fjord ($p\text{-}value = 0.826$) (**Supplementary Figure 3B**). The mean number of migrants (Nm) varied considerably whether including Mediterranean population (A) (3.3 ± 0.48) or not (B) (17.6 ± 1.35) (**Table 1**). Further tests on first generation migrant detection (short-term) revealed no migrants between Mediterranean Sea and Chile, and a significant (p = value < 0.01) exchanging volume of individuals among localities within Comau Fjord. All these results furtherly confirmed cluster K = 1 as the most probable population structure for individuals from Comau Fjord. Demographically, all populations presented a normal

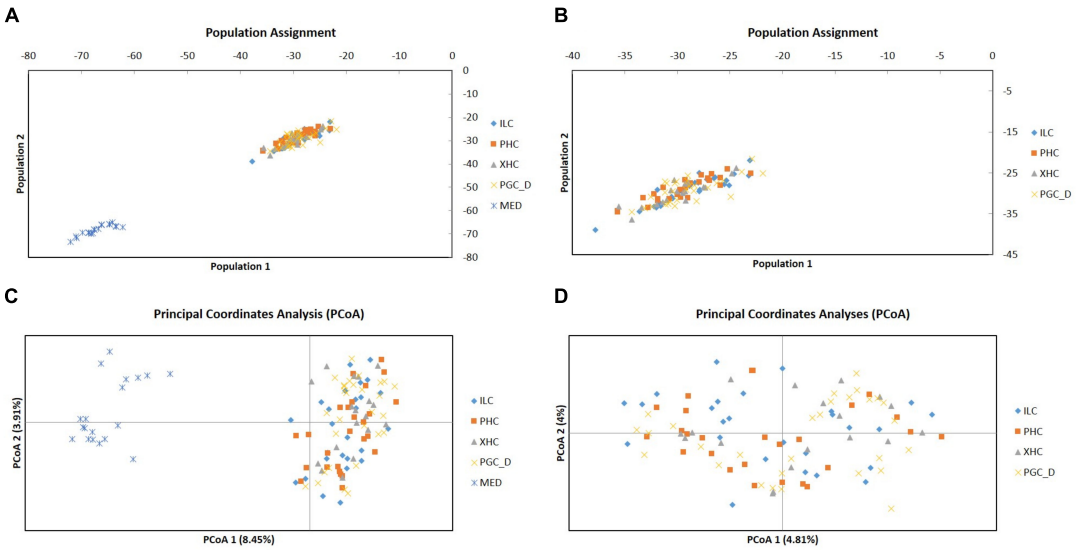

FIGURE 3 | Population assignment **(A,B)** and genetic distance **(C,D)** among *D. dianthus* individuals from each sampling locality, including **(A,C)** or excluding **(B,D)** individuals from Mediterranean Sea (MED). For complete locality names (see **Figure 1**). MED, Mediterranean.

L-shape distribution of alleles frequency, having not experienced any bottleneck event (i.e., severe reduction in population size) in recent times.

DISCUSSION

This study aimed to identify the genetic structure of *D. dianthus* populations in Comau Fjord, evaluating if the currents, water column stratification and the layer system characterizing the waters of the fjord hinder the gene flow along the fjord (head-mouth) or its vertical axis (shallow-deep). As mentioned earlier in the manuscript, the study included samples from the Mediterranean Sea into the Comau dataset as a sort of outgroup to support the informative capacity of microsatellites analysis. The genetic difference between individuals from Mediterranean Sea and Chile and the potential species misclassification have been discussed in previous studies, demonstrating the that they belong to the same species *D. dianthus* either by genetic, morphological or histological characters (Addamo et al., 2015b, 2016, 2020), confirming the widely spread distribution that denotes the species.

Although previous studies showed vertical and horizontal zonation for foraminifera communities (Hromic, 2009) within Comau Fjord, our results provide evidence of a panmictic population of *D. dianthus* within it, both along a horizontal (head-mouth) and a vertical (shallow-deep) axis. Such panmixia may be the consequence of temporal or spatial changes in the physical structure of the water column. For example, in this region the freshwater inputs toward the sea peak from June to August and then steadily decrease until March, displaying a seasonality that is going to increase due to climate change (Aguayo et al., 2019). Similarly, along the fjord the stratification caused by salinity is more intense near its head or the Cahuelmó lateral fjord (Schwabe et al., 2006), where most of the freshwater inputs arrive to the sea. Finally, surface winds and massive tides, up to 7.5 m (Försterra, 2009; Sobarzo, 2009), are able to mix the waters within Comau Fjord, weakening the water column stratification and even temporally breaking up its layer system. The strong currents throughout the entire column of water, produced by huge tides, surely favors the exchange with the Chiloe Sea and the movement of larvae and gametes along the fjord. Indeed, a combination of all these sources of spatial and temporal homogeneity in the physical structure may promote gene flow in Comau, maintaining a panmictic population spread across different locations and depths within the fjord.

The strong seasonality of the fjord system influences the highly seasonal reproduction of *D. dianthus,* which exhibits broadcast spawning around August, with the gamete production beginning in September (Feehan et al., 2019), when the freshwater inputs start declining and the spring tides are higher due to the proximity to the spring equinox. This situation enhances water column mixing around *D. dianthus* reproductive season, which in turn would increase the exchange of propagules and larvae across the fjord as supported by genetic results. All the physical processes aforementioned may be enough to promote the genetic exchange, suggesting that haloclines may not be such a strong barrier for the dispersal of *D. dianthus* propagules.

The fact that the population of *D. dianthus* in Comau Fjord extents along steep oceanographic gradients, both horizontally and with depth, resulting tolerant to a wide range of oceanographic conditions, suggests that larval dispersal along these axes is fast enough to maintain the population connected. However, it remains unknown if there is reproduction success along the entire distribution range or if we are dealing with a source/sink situation. If the latter is the case, it is important to assess which portion of the population represents the source and which the sink. In 2012 a

mayor mortality of *D. dianthus* occurred in a larger portion of the Comau Fjord with large areas showing a mortality rate close to 100% (Försterra et al., 2014). The recovery and recruitment patterns observed thereafter may help to reveal the sources and sinks of larvae, and thus mapping the gene flow within the fjord. Considering the increase in farming activities also planned in other areas of Chilean Patagonia, and their potential impact on marine biodiversity, further studies would need to reveal if for example the corals from other biogeographic areas, such as Central Patagonia, belong to the same population. This information is pivotal for managing efficiently the maritime activities and using sustainably the marine resources. The 2012 mortality event (Försterra et al., 2014) shows that despite the resilience to fluctuations in certain oceanographic conditions *D. dianthus* may be sensitive to other key parameters or that the fluctuations may occasionally exceed the ecophysiological limits of the species. This and gene flow direction are key questions that need to be addressed to install efficient conservation measures for these unique cold water coral populations. The genetic results rejected the initial hypotheses of a clear populations′ structure within the fjord, which is characterized by the vertical stratification of its water column. A carefully analysis of the biology of the species combined with the environmental and oceanographic condition, including seasonality and occasional variations that occur specifically in Comau Fjord, would help to understand why the genetic structure of *D. dianthus* population differs from other organisms, e.g., foraminifera communities (Hromic, 2009). These results highlight the importance of including detailed oceanographic information (and data based on real-time observations, when available) in the entire process of the analyses and interpretation of genetic results as extremely helpful tools for studies focusing on remote areas and non-model organisms, where logistic difficulties and limited scientific knowledge hamper a better management and conservation of marine resources.

CONCLUSION

The present study stresses the importance of multidisciplinary approach to reduce the extensive knowledge gap on the marine ecosystems in Patagonian fjords. The multidisciplinary approach, including a detailed analyses of the oceanographic characteristics of the area, molecular studies and analyses of the reproduction of the species, allowed a better understanding on the biophysical processes driving the genetic diversity of the coral population in the Comau Fjord. Although the present study establishes a useful knowledge baseline to provide guidance for ecosystem-based management and conservation, the ecological analyses and conservation implication in the Chilean Patagonia still suffer from important knowledge gaps and limitations of interdisciplinary and methodological approaches. Indeed, further studies should be carried out including other areas where smaller populations of corals have been described (Försterra et al., 2017): e.g., Reñihue Fjord, Pitipalena Fjord or the area of the mouth of the Messier Channel (48°S). In addition, other marine organisms and real-time oceanographic observations should be included to better understand the biological and ecological characteristic of marine ecosystems in Patagonia.

DATA AVAILABILITY STATEMENT

The original contributions presented in the study are included in the article/**Supplementary Material** and Zenodo doi: 10.5281/zenodo.4435966, further inquiries can be directed to the corresponding author/s.

AUTHOR CONTRIBUTIONS

This work was realized under the collaboration of all authors. AA, GF, and AM collected the samples. AA and RG-J carried out the molecular analyses and post-processing of the genotyping. AA and SZ performed the population genetic analyses. AA, SZ, GF, JH, RG-J, GC, and AM participated in the discussion of the results and in the writing of the manuscript. All authors approved the final version. The views expressed are purely those of the writers and may not in any circumstance be regarded as stating an official position of the European Commission.

FUNDING

This work was funded by the Spanish Ministry of Science and Innovation (CGL2011−23306), Fondecyt (Projects 1150843 and 1201717), and the Fundación San Ignacio del Huinay-Endesa & CSIC Projects 2011 and 2013.

ACKNOWLEDGMENTS

We would like to thank the Huinay staff for the logistical support, Jurgen Laudien (AWI) for coral samples from Lilihuapi Island, V. López Márquez (MNCN) for the collaboration in the laboratory. This was publication number 184 of Huinay Scientific Field Station. This manuscript has been finalized at the time of the COVID-19 pandemic.

SUPPLEMENTARY MATERIAL

The Supplementary Material for this article can be found online at: https://www.frontiersin.org/articles/10.3389/fmars.2021.612195/full#supplementary-material

REFERENCES

Addamo, A. M., Zaccara S., Försterra G., Höfer, J., García-Jiménez, R., Crosa, G., et al. (2021). *Data from: Microsatellites of Desmophyllum dianthus.* Comau Fjord: Zenodo. doi: 10.5281/zenodo.4435966

Addamo, A. M., García-Jiménez, R., Taviani, M., and Machordom, A. (2015a). Development of microsatellite markers in the deep-sea cup coral *Desmophyllum dianthus* by 454 sequencing and cross-species amplifications in *Scleractinia* order. *J. Hered.* 106, 322–330. doi: 10.1093/jhered/esv010

Addamo, A. M., Martínez-Baraldés, I., Vertino, A., López-González, P. J., Taviani, M., and Machordom, A. (2015b). Morphological polymorphism of *Desmophyllum dianthus* (Anthozoa: Hexacorallia) over a wide ecological and biogeographic range: stability in deep habitats? *Zool. Anz.* 259, 113–130. doi: 10.1016/j.jcz.2015.10.004

Addamo, A. M., Miller, K. J., Häussermann, V., Taviani, M., and Machordom, A. (2020). Global-scale genetic structure of a cosmopolitan cold-water coral species. *Mar. Freshwater Ecosyst.* 31, 1–14. doi: 10.1002/aqc.3421

Addamo, A. M., Vertino, A., Stolarski, J., García-Jiménez, R., Taviani, M., and Machordom, A. (2016). Merging scleractinian genera: the overwhelming genetic similarity between solitary *Desmophyllum* and colonial *Lophelia*. *BMC Evol. Biol.* 16:108. doi: 10.1186/s12862-016-0654-8

Aguayo, R., León-Muñoz, J., Vargas-Baecheler, J., Montecinos, A., Garreaud, R., Urbina, M., et al. (2019). The glass half-empty: climate change drives lower freshwater input in the coastal system of the Chilean Northern Patagonia. *Clim. Change* 155, 417–435. doi: 10.1007/s10584-019-02495-6

Bjørndal, T. (2002). The competitiveness of the Chilean salmon aquaculture industry. *Aquac. Econ. Manag.* 6, 97–116. doi: 10.1080/13657300209380306

Bravo, A., Försterra, G., and Häussermann, V. (2005). "Fishing in troubled waters – evidence for higher diversity and high abundance of cold water corals along the Chilean coast," in *Proceedings of the 3rd International Symposium on Deep-Sea Corals Science and Management*, eds R. Brock and R. Y. George (Miami, FL: Rosenstiel School of Marine and Atmospheric Science), 234.

Brookfield, J. F. Y. (1996). A simple new method for estimating null allele frequency from heterozygote deficiency. *Mol. Ecol.* 5, 453–455. doi: 10.1046/j.1365-294X.1996.00098.x

Cañete, J. I., and Häussermann, V. (2012). Colonial life under the humboldt current system: deep-sea corals from O'Higgins I seamount. *Lat. Am. J. Aquat. Res.* 40, 467–472.

Chapuis, M.-P., and Estoup, A. (2007). Microsatellite null alleles and estimation of population differentiation. *Mol. Biol. Evol.* 24, 621–631. doi: 10.1093/molbev/msl191

Cornuet, J. M., and Luikart, G. (1997). Description and power analysis of two tests for detecting recent population bottlenecks from allele frequency data. *Genetics* 144, 2001–2014. doi: 10.1093/genetics/144.4.2001

Earl, D. A., and vonHoldt, B. M. (2012). STRUCTURE HARVESTER: a website and program for visualizing STRUCTURE output and implementing the Evanno method. Conserv. Genet. Resour. 4, 359–361. doi: 10.1007/s12686-011-9548-7

Evanno, G., Regnaut, S., and Goudet, J. (2005). Detecting the number of clusters of individuals using the software STRUCTURE: a simulation study. *Mol. Ecol.* 14, 2611–2620. doi: 10.1111/j.1365-294X.2005.02553.x

Falush, D., Stephens, M., and Pritchard, J. K. (2003). Inference of population structure using multilocus genotype data: linked loci and correlated allele frequencies. *Genetics* 164, 1567–1587. doi: 10.1111/j.1471-8286.2007.01758.x

FAO (2020). *GLOBEFISH Highlights April 2020 Issue, with Annual 2019 Statistics – A Quarterly Update on World Seafood Markets.* Globefish Highlights No. 2–2020. Rome: FAO. doi: 10.4060/ca9528en

Feehan, K. A., Waller, R. G., and Häussermann, V. (2019). Highly seasonal reproduction in deep-water emergent *Desmophyllum dianthus* (Scleractinia: Caryophylliidae) from the Northern Patagonian Fjords. *Mar. Biol.* 166:52. doi: 10.1007/s00227-019-3495-3

Fillinger, L., and Richter, C. (2013). Vertical and horizontal distribution of *Desmophyllum dianthus* in Comau Fjord, Chile: a cold-water coral thriving at low pH. *PeerJ* 1:e194. doi: 10.7717/peerj.194

Försterra, G. (2009). "Ecological and biogeographical aspects of the Chilean Fjord region," in *Marine Benthic Fauna of Chilean Patagonia*, eds V. Häussermann and G. Försterra (Santiago: Nature in Focus), 61–76.

Försterra, G., Beuck, L., Häussermann, V., and Freiwald, A. (2005). "Shallow water *Desmophyllum dianthus* (Scleractinia) from Chile: characteristics of the biocenoses, the bioeroding community, heterotrophic interactions and (palaeo)-bathymetrical implications," in *Cold-Water Corals and Ecosystems*, eds A. Freiwald and J. M. Roberts (Berlin: Springer-Verlag), 937–977. doi: 10.1007/3-540-27673-4_48

Försterra, G., and Häussermann, V. (2003). First report on large scleractinian (Cnidaria: Anthozoa) accumulations in cold-temperate shallow water of south Chilean fjords. *Zool. Verh.* 345, 117–128.

Försterra, G., Häussermann, V., and Laudien, J. (2017). "Animal forests in the Chilean fiord region: discoveries and perspectives in shallow and deep waters," in *Marine Animal Forests*, eds S. Rossi, L. Bramanti, A. Gori, and C. Orejas Saco del Valle (Cham: Springer), 1–35. doi: 10.1007/978-3-319-17001-5_3-1

Försterra, G., Häussermann, V., Laudien, J., Jantzen, C., Sellanes, J., and Muñoz, P. (2014). Mass die off of the cold-water coral *Desmophyllum dianthus* in the Chilean Patagonian Fjord Region. *Bull. Mar. Sci.* 90, 895–899. doi: 10.5343/bms.2013.1064

Google Inc (2009). *Google Earth*. Available online at: https://www.google.com/earth/versions/#download-pro (accessed December 1, 2019).

Häussermann, V., and Försterra, G. (eds.) (2009). *Marine Benthic Fauna of Chilean Patagonia*. Santiago: Nature in Focus.

Häussermann, V., and Försterra, G. (2007). Extraordinary abundance of hydrocorals (Cnidaria, Hydrozoa, Stylasteridae) in shallow water of the Patagonian fjord region. *Polar Biol.* 30, 487–492. doi: 10.1007/s00300-006-0207-5

Häussermann, V., and Försterra, G. (2014). Vast reef-like accumulation of the hydrocoral *Errina antarctica* (Cnidaria, Hydrozoa) wiped out in Central Patagonia. *Coral Reefs* 33:29. doi: 10.1007/s00338-013-1088-z

Häussermann, V., Försterra, G., Melzer, R. R., and Meyer, R. (2013). Gradual changes of benthic biodiversity in Comau Fjord, Chilean Patagonia – lateral observations over a decade of taxonomic research. *Spixiana* 36, 161–171.

Holloley, C. E., and Geerts, P. G. (2009). Multiplex Manager 1.0: a cross-platform computer program that plans and optimizes multiplex PCR. *BioTechniques* 46, 511–517. doi: 10.2144/000113156

Holm, S. (1979). A simple sequentially rejective multiple test procedure. *Scand. J. Stat.* 6, 65–70.

Hromic, T. (2009). Estructura comunitaria del taxa Foraminiferida (Protozoa), según profundidad, en el fiordo Comau, Chiloé, Chile. *An. Inst. Patagon. (Chile)* 37, 39–51. doi: 10.4067/S0718-686X2009000100004

Kopelman, N. M., Mayzel, J., Jakobsson, M., Rosenberg, N. A., and Mayrose, I. (2015). CLUMPAK: a program for identifying clustering modes and packaging population structure inferences across K. *Mol. Ecol. Resour.* 15, 1179–1191. doi: 10.1111/1755-0998.12387

Li, Y.-L., and Liu, J.-X. (2018). StructureSelector: a web based software to select and visualize the optimal number of clusters using multiple methods. *Mol. Ecol. Resour.* 18, 176–177. doi: 10.1111/1755-0998.12719

Mayr, C., Rebolledo, L., Schulte, K., Schuster, A., Zolitschka, B., Försterra, G., et al. (2014). Responses of nitrogen and carbon deposition rates in Comau Fjord (42°S, Southern Chile) to natural and anthropogenic impacts during the last century. *Cont. Shelf Res.* 78, 29–38. doi: 10.1016/j.csr.2014.02.004

Miller, K. J., and Gunasekera, R. M. (2017). A comparison of genetic connectivity in two deep sea corals to examine whether seamounts are isolated islands or stepping stones for dispersal. *Sci. Rep.* 7:46103. doi: 10.1038/srep46103

Peakall, R., and Smouse, P. E. (2012). GenAlEx 6.5: genetic analysis in excel. population genetic software for teaching and research—an update. *Bioinformatics* 28, 2537–2539. doi: 10.1093/bioinformatics/bts460

Piry, S., Alapetite, A., Cornuet, J.-M., Paetkau, D., Baudouin, L., and Estoup, A. (2004). GeneClass2: a software for genetic assignment and first-generation migrant detection. *J. Hered.* 95, 536–539. doi: 10.1093/jhered/esh074

Pritchard, J. K., Stephens, M., and Donnelly, P. (2000). Inference of population structure using multilocus genotype data. *Genetics* 155, 945–959.

Puechmaille, S. J. (2016). The program structure does not reliably recover the correct population structure when sampling is uneven: subsampling and new estimators alleviate the problem. *Mol. Ecol. Resour.* 16, 608–627. doi: 10.1111/1755-0998

Raymond, M., and Rousset, F. (1995). GENEPOP version1.2: population genetics software for exact tests and ecumenicism. *J. Hered.* 86, 248–249. doi: 10.1093/oxfordjournals.jhered.a111573

Rousset, F. (2008). Genepop'007: a complete re-implementation of the genepop software for windows and linux. *Mol. Ecol. Resour.* 8, 103–106. doi: 10.1111/j.1471-8286.2007.01931.x

Sánchez, N., González, H. E., and Iriarte, J. L. (2011). Trophic interactions of pelagic crustaceans in Comau Fjord (Chile): their role in the food web structure. *J. Plankton Res.* 33, 1212–1229. doi: 10.1093/plankt/fbr022

Schwabe, E., Försterra, G., Häussermann, V., Melzer, R., and Schrödl, M. (2006). Chitons (Mollusca: Polyplacophora) from the southern Chilean Comau Fjord, with reinstatement of *Tonicia calbucensis* plate, 1897. *Zootaxa* 1341, 1–27. doi: 10.11646/zootaxa.1341.1.1

Silva, N., Calvete, C., and Sievers, H. (1997). Características oceanográficas físicas y químicas de canales australes chilenos entre Puerto Montt y Laguna San Rafael (Crucero Cimar-Fiordo 1). *Cienc. Tecnol. Mar.* 20, 23–106.

Sobarzo, M. (2009). "The fjord region of southern chile: oceanographic aspects," in *Marine Benthic Fauna of Chilean Patagonia*, eds V. Häussermann and G. Försterra (Santiago: Nature in Focus), 53–60.

Soto, M. V., Arratia, P., Cabello, M., Moreno, R., and Whyndam, K. (2019). Natural hazards and exposure of strategic connectivity in extreme territories. Comau Fjord, North Patagonia, Chile. *Rev. Geogr. Norte Gd.* 73, 57–75.

Tokuda, Y., Haraguchi, H., and Ezaki, Y. (2017). First real-time observation of transverse division in azooxanthellate scleractinian corals. *Sci. Rep.* 7:41762. doi: 10.1038/srep41762

Van Oosterhout, C., Hutchinson, W. F., Wills, D. P. M., and Shipley, P. (2004). Micro-Checker: software for identifying and correcting genotyping errors in microsatellite data. *Mol. Ecol. Notes* 4, 535–538. doi: 10.1111/j.1471-8286.2004.00684.x

Zhou, M., Zhu, Y., and Tande, K. (2005). Circulation of euphausiids in two Norwegian sub-arctic fjords. *Mar. Ecol. Prog. Ser.* 300, 159–178. doi: 10.3354/meps300159

Conflict of Interest: The authors declare that the research was conducted in the absence of any commercial or financial relationships that could be construed as a potential conflict of interest.

frontiers in Marine Science

ORIGINAL RESEARCH
published: 09 April 2021
doi: 10.3389/fmars.2021.636208

Selective Feeding by a Predatory Sea Star Across a Depth Gradient in Northern Patagonia, Chile

Ignacio Garrido[1,2,3], Luis Miguel Pardo[1,2], Ladd E. Johnson[3] and Dirk Schories[1,4]*

[1] *Laboratorio Costero de Recursos Acuáticos de Calfuco, Instituto de Ciencias Marinas y Limnológicas, Universidad Austral de Chile, Valdivia, Chile,* [2] *Centro de Investigación Dinámica de Ecosistemas Marinos de Altas Latitudes, Valdivia, Chile,* [3] *Département de Biologie and Québec-Océan, Université Laval, Quebec City, QC, Canada,* [4] *DLR Projektträger, Bonn, Germany*

Sea stars often function as keystone predators in food webs of intertidal and subtidal communities, especially in temperate and sub-polar regions. In South America the sea star *Cosmasterias lurida* is distributed along both the Atlantic and Pacific coasts of Patagonia and is one of the most conspicuous and abundant benthic predators in the shallow subtidal zone (<25 m). Its feeding strategy and prey selection are, however, still poorly known. This study describes the feeding behavior of *C. lurida* at a site in the Seno del Reloncaví (Chile), assessing its abundance, size and prey selection in the field relative to observed prey abundance and size along a bathymetric gradient. We hypothesized that *C. lurida* is a generalist predator, feeding on suitable prey according to their availability. However, we found that this predator only consumed a limited number (7 of 48) of potential prey species, primarily the slipper limpets *Crepipatella* spp. and the mussels *Aulacomya ater* and *Mytilus chilensis*. Electivity analysis revealed a clear preference for one mussel (*A. ater*) but not the other (*M. chilensis*) as well as depth-dependent selectivity for the slipper limpets, which changed from avoidance to preference with increasing depth. Sea star densities varied with depth, peaking between depths of 5 and 10 m, but the size of sea stars and the size of their prey did not vary significantly along a depth gradient. No significant correlations were found with the most commonly selected prey. These results would indicate that while this predator may be a generalist–opportunist, its feeding behavior is context-dependent and its high selectivity for certain species suggests that this sea star plays a key role structuring subtidal benthic communities in Patagonia.

Keywords: ***Cosmasterias lurida*, benthic ecology, feeding behavior, starfish, predation, dietary preference**

OPEN ACCESS

Edited by:
Eduardo Joel Quiroga Jamett, Pontifical Catholic University of Valparaíso, Chile

Reviewed by:
Benny K. K. Chan, Academia Sinica, Taiwan
Aldo S. Pacheco, National University of San Marcos, Peru

****Correspondence:***
Ignacio Garrido
ignacio.garrido@uach.cl;
ignacio.garrido-iriondo.1@ulaval.ca

Specialty section:
This article was submitted to Marine Ecosystem Ecology, a section of the journal Frontiers in Marine Science

Received: *01 December 2020*
Accepted: *19 March 2021*
Published: *09 April 2021*

Citation:
Garrido I, Pardo LM, Johnson LE and Schories D (2021) Selective Feeding by a Predatory Sea Star Across a Depth Gradient in Northern Patagonia, Chile. Front. Mar. Sci. 8:636208. doi: 10.3389/fmars.2021.636208

INTRODUCTION

Predators strongly affect populations of their prey, but in turn, the availability of prey also regulates the behavior of predators (Sih et al., 1985; Gaymer and Himmelman, 2002; Ross et al., 2003; Navarrete and Manzur, 2008; Skein et al., 2018). In benthic marine communities, sea stars are one of the most active predators and control both directly and indirectly the abundance and distribution of numerous species (Paine, 1966; McClintock, 1994; Saier, 2001; Manzur and Navarrete, 2011; Calderwood et al., 2016; Gianguzza et al., 2016). They have thus been recognized as important

components of intertidal and subtidal communities, at times even being considered keystone species (Paine, 1966; Dayton, 1985; Gaymer and Himmelman, 2008; Menge and Sanford, 2013).

The effect of sea stars on benthic communities depends on their feeding strategy and the trophic level of their prey in the community (Ross et al., 2003; Menge and Sanford, 2013; Motti et al., 2018). Many sea stars are opportunistic omnivores [e.g., *Oreaster reticulatus* (Linnaeus, 1758), Martín et al. (2001)], but some species are specialized predators [e.g., *Heliaster helianthus* (Lamarck, 1816), *Meyenaster gelatinosus* (Meyen, 1834), Urriago et al. (2011)], herbivores [e.g., *Phataria unifascialis* (Gray, 1840), *Pharia pyramidatus* (Gray, 1840), Salguero and Bonilla (2010)], or detritus feeders [e.g., *Pentaceraster cumingi* (Gray, 1840), Salguero and Bonilla (2010) and *Hyphalaster inermis* (Sladen, 1883), Mironov et al. (2016)]. The prey of sea stars consist of a wide range of organisms including sponges, sea anemones, mollusks, polychaetes, crustaceans, and even other echinoderms (Mutschke and Mah, 2009). Further, cannibalism as well as ontogenetic changes in diet can occur (Verling et al., 2003; Urriago et al., 2012; Baeta and Ramon, 2013; Fernandez et al., 2017; Deaker et al., 2020). For example, *Heliaster helianthus* (Lamarck, 1822) a keystone predator in rocky intertidal habitats of central Chile, showed ontogenetic changes in habitat and diet composition of prey as it grew. That is, when individuals were recruits inhabit boulders and crevices in the high or mid-high intertidal zones preying on small species, mostly on the periwinkle *Austrolittorina araucana* (d'Orbigny, 1840) while adults prey on more species including mussels and limpets in the lower intertidal zone (Manzur et al., 2010).

In southern South America, the sea star *Cosmasterias lurida* (Philippi 1858) is one of the most abundant benthic predators in shallow subtidal habitats and can be found on both soft sediments and rocky bottoms (**Figure 1**). *C. lurida* is widely distributed along the temperate shores of South America, ranging from La Serena (29° 56′ S) on the Pacific coast of Chile to Golfo de San Matias (38° 00′ S) on the Atlantic coast of Argentina (Madsen, 1956; Hernández and Tablado, 1985; Clark and Downey, 1992) as well as around the Falkland (Malvinas) Islands, Burdwood Bank, and South Georgia (Vásquez and Castilla, 1984; Hernández and Tablado, 1985; Fraysse et al., 2018). Although its bathymetric distribution is large, ranging between the lower intertidal zone and 650 m in depth (Madsen, 1956; Clark and Downey, 1992), highest abundances have been recorded in shallow water habitats (Vásquez and Castilla, 1984; Pastor-de-Ward et al., 2007). Despite its wide geographic and bathymetric distribution, previous work on this species has focused mainly on its reproductive biology (Pastor-de-Ward et al., 2007; Cossi et al., 2015, 2017; Fraysse et al., 2020) and biochemistry (Seldes and Gros, 1985; Maier et al., 1993, 1998; Roccatagliata et al., 1994). However, a wide range of prey items in its diet has been also recorded (Castilla and Moreno, 1982; Vásquez and Castilla, 1984; Pastor-de-Ward et al., 2007; Gordillo and Archuby, 2012), and *C. lurida* is thought to be an important consumer in the shallow benthic food webs along the Patagonian coast (Adami and Gordillo, 1999; Schejter et al., 2008; Gordillo and Archuby, 2012; Amsler et al., 2014; Cossi et al., 2015; Fraysse et al., 2018). For example, *C. lurida* within kelp beds [*Macrocystis pyrifera* (L.) C. Agardh, 1820] in Tierra del Fuego (Chile) mainly preyed on barnacles [*Balanus* spp. (Costa, 1778)] and slipper limpets [*Crepipatella dilatata* (Lamarck, 1822)] but also consumed 25 other species, including other gastropods, other crustaceans, bivalves, ascidians, brachiopods, fish, priapulids, sea urchins, and carrion (Vásquez and Castilla, 1984). In contrast, the main prey items of *C. lurida* in the shallow soft sediment environments of the Magellan Strait (Chile) were endobenthic bivalves, primarily *Ameghinomya antiqua* (P. P. King, 1832) (Garrido, unpublished data). These differences in diet suggest that this species behaves as a generalist-opportunist, being able to use different resources depending on the prey availability in the habitat (Ross et al., 2003). However, understanding trophic relationships between predators and prey requires information on both the availability of prey and the preference of the predator. Although spatial associations between predators and prey have been interpreted as preferences, true preference requires an explicit behavior (Singer, 2000; Underwood et al., 2004) where the predator selects a particular prey over others. A proxy of preference, known as electivity, can be estimated as the difference of the relative proportion of prey in the diet compared to the available relative proportion in the local environment (Singer, 2000; Underwood et al., 2004).

Although previous studies (Madsen, 1956; Vásquez and Castilla, 1984; Gordillo and Archuby, 2012) have observed *C. lurida* feeding on different prey items, Vásquez and Castilla (1984) suggested that this predator is an opportunistic-generalist with little selectivity of prey. In the northern Patagonian zone of Chile, *C. lurida,* like many higher trophic level sea stars, feeds on a wide range of prey in shallow rocky environments. In this study we test the hypothesis that the diet of *C. lurida* would reflect prey availability in the environment, i.e., no selectivity of prey. We tested this hypothesis by quantifying sea star abundance, prey abundance, and prey electivity across a depth gradient where pronounced changes in the prey availability.

MATERIALS AND METHODS

Study Site

Field observations using SCUBA were conducted in 2010 from May to July (austral winter) at Yerbas Buenas Bay (41° 40′ 20″ S; 72° 39′ 25″ W), a cove located in Seno del Reloncaví, a large bay extending 34 km south from Puerto Montt, Chile (**Figure 2**). Seno del Reloncaví geographically marks the end of Chile's central valley and the beginning of the Patagonian region and is the first of several large extensions of channels and fjords of the Golfo de Ancud (Soto-Mardones et al., 2009). During our research, tidal level was measured continuously every 10 min at depths of 5 and 20 m with SOLINST pressure sensors, where maximum measured difference between low and high tide was approximately 7 m. All reported depths were corrected to the level of the annual mean tide to be able to compare data taken by SCUBA divers during different tide levels.

Predator and Prey Abundance

To quantify sea star densities and assess prey availability at this site, we selected five transects perpendicular to the coastline from

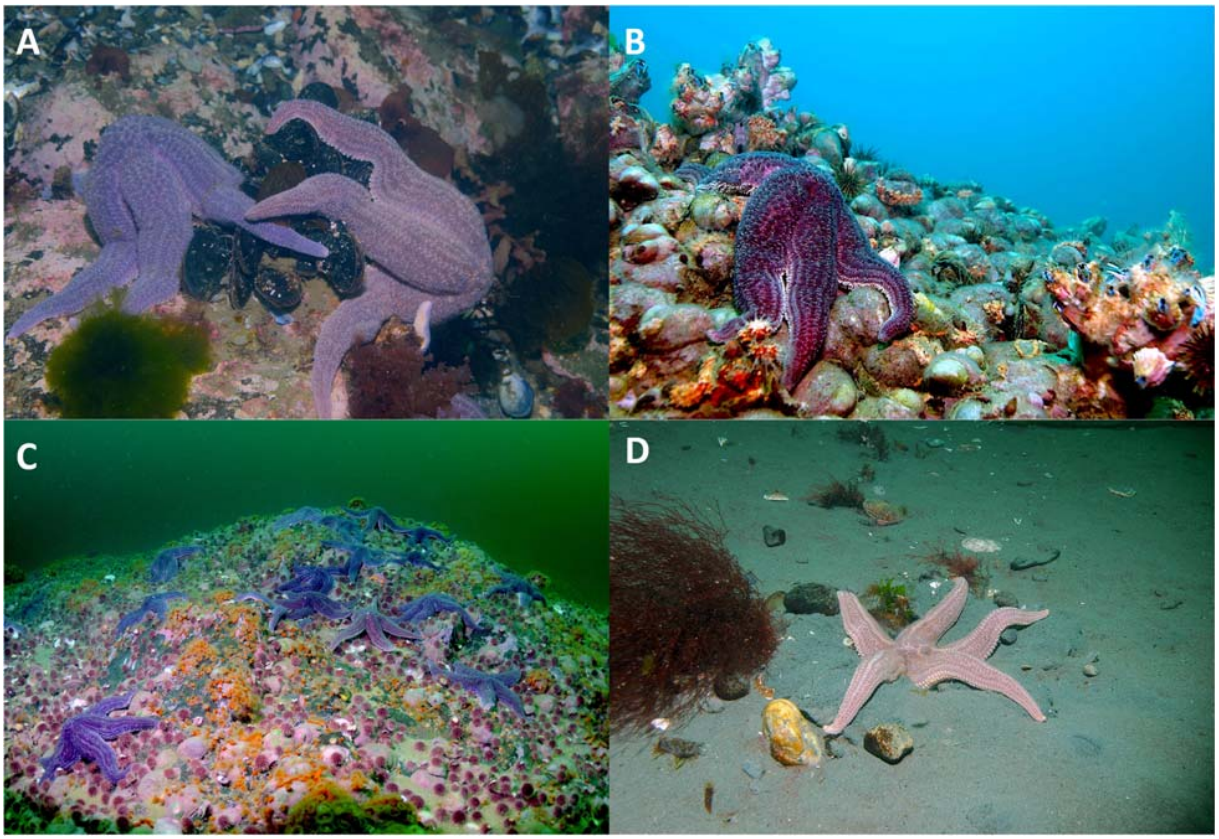

FIGURE 1 | The sea star *Cosmasterias lurida* on different substrata in southern Chile. **(A)** Feeding on mussels on a rocky bottom at 7-m depth; **(B)** feeding on *Crepipatella* spp. on a rocky bottom at 8-m depth; **(C)** occurring at high densities on a rocky bottom at 10-m depth; **(D)** foraging on a sandy bottom at 9-m depth (**A–C** – Yerbas Buenas Bay, Seno del Reloncaví; **(D)** – Faro San Isidro, Magellan Strait, Chile).

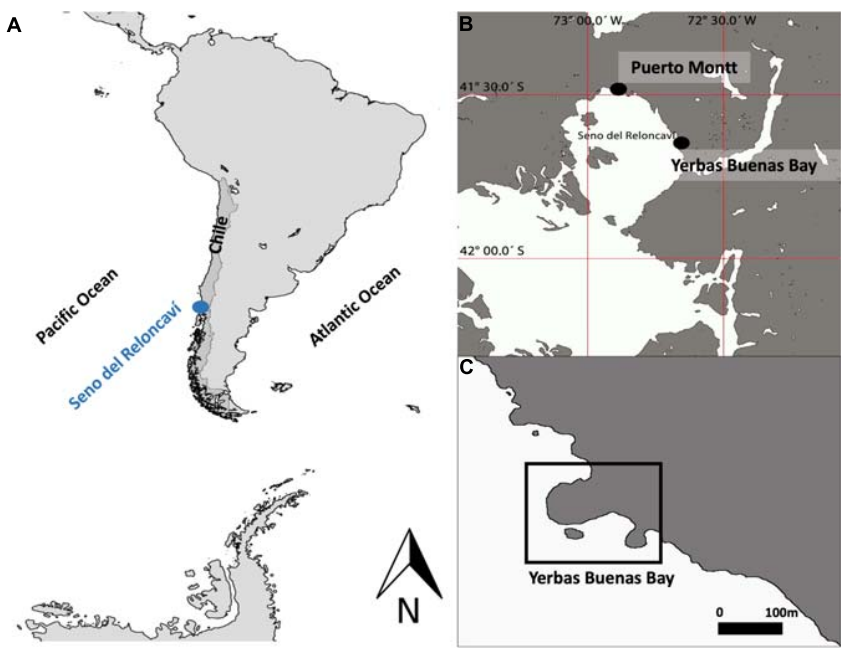

FIGURE 2 | South America **(A)** Seno del Reloncaví and **(B)** the study site at Yerbas Buenas Bay **(C)**.

the lowest intertidal level to a depth of 30 m and separated from one another by 10 m. Using a subaquatic GPS connected to a surface buoy with a GPS antenna (Schories and Niedzwiedz, 2012), we georeferenced these transects, allowing future studies to precisely relocate the study area without the need for physical markers in the field. For this study, transects were censused only once, each on a different day between May 1 and June 29 with two objectives: (1) determine the density of *C. lurida* and (2) assess the availability of potential prey (see details below). For each transect, two divers connected by a rope of 3-m length worked in parallel. While one diver handled the subaquatic GPS and measured depths, the other diver counted all *C. lurida* between them and recorded photo-quadrats (0.12 m^2) using an underwater camera (Nikon D300 inside a Sea and Sea underwater housing) mounted over an aluminum frame that assured that all photo-quadrats were taken from the same distance and were perpendicular to the bottom.

Cosmasterias lurida Density in Relation to Depth

As described above, *C. lurida* were counted by one of the divers along each transect within the area separating the divers for the length of the transect within each 5-m depth intervals, starting from the surface down to 30 m (i.e., six depth intervals in total: 0–5, >5–10, >10–15, >15–20, >20–25, >25–30 m). The actual area surveyed within each depth range depended on the bottom slope and was calculated using the starting and ending points of the GPS positions at depths of 0, 5, 10, 15, 20, 25, and 30 m and the difference in depths between each interval. In this way following the Pythagorean theorem we calculated the total distance traveled for each depth interval and multiplied it by the transect width (3 m). The density of *C. lurida* was then calculated as the number of individuals per m^2 (ind./m^2).

Prey Availability in Relation to Depth

Along each transect, three photo-quadrants of the bottom (see above), separated by at least 2 m from each other, were taken at each 1 m depth interval along the transects to estimate the prey field (i.e., the relative abundances of epibenthic invertebrates considered to be potential prey items of *C. lurida*). A total 360 photo-quadrats were thus recorded along the five transects. Photographs were analyzed using the software Coral Point Count with Excel extensions [CPCe 3.6; (Kohler and Gill, 2006)] to superimpose a uniform 10 × 10 grid of points on each image after which the benthic component (algae, sessile and mobile invertebrates, bare substratum) under each point was determined (**Figure 3**). Nearly all organisms were able to be identified at the species level, and only a few images of poor quality (due to shade, excess particles in the water column or distortion) could not be identified either at the species level or the taxonomic group. In these cases, they were classified as unknown. Any organisms that were identifiable in the photo were also noted. Empty shells of the most abundant mollusks [the mussels *Aulacomya atra* (Molina, 1782) and *Mytilus chilensis* (Hupe, 1854) and the slipper limpets *Crepipatella* spp.] could be easily identified in the images. They were not included in estimates of the relative abundances of epibenthic invertebrates but gave additional evidence of possible important prey items for *C. lurida*. *Crepipatella* spp. included two cryptic species, *Crepipatella peruviana* (Lamarck, 1822) and *C. dilatata* that could not be distinguished in the field.

In situ Feeding of *Cosmasterias lurida*

Four transects running perpendicular from the shore to a depth of 30 m were also surveyed to observe *in situ* feeding behavior of *C. lurida* and determine if there were differences in the prey consumption across this depth gradient. Each transect was again divided into five intervals of 5 m of depth (see above). Within each depth interval we turned over every *C. lurida* encountered and recorded if the sea star was feeding and if so, what prey was being consumed. Observations were divided into five behavioral classes: (1) feeding on mussels (*Aulacomya ater* or *Mytilus chilensis*); (2) feeding on the slipper limpets *Crepipatella* spp.; (3) feeding on other species; (4) stomach extended but without any retained prey (with activity – "W/activity"); and (5) no activity (no feeding – "N/activity"). As the number of observations was not identical between each transect and depth interval, it was standardized as a percentage. In addition, the first 20 sea stars that were observed feeding (i.e., with stomach everted and a prey trapped within) within each depth interval of a given transect were collected and placed in separate mesh bags together with the prey item. The wet weight and disk diameter were measured for each sea star and body length for the associated prey item.

Statistical Analysis

Cosmasterias lurida Density in Relation to Depth

Differences in density of sea stars among depth intervals were analyzed with the non-parametric Kruskal–Wallis test and pair-wise comparisons by a Dunn test, because the data did not comply with the assumptions of normality and homogeneity of the variances, even after testing various transformations.

In situ Feeding of *Cosmasterias lurida*

Feeding activity data of *C. lurida* fulfilled the assumption of normality (Shapiro Wilk) and homogeneity of variance (Levene's test). Thus, a two-way ANOVA was used to compare differences in feeding activity with depth interval. We performed *a posteriori* test (Tukey HSD) for cases that were significant ($p < 0.05$). The proportion of the species preyed upon by sea stars among depth intervals was visually examined using a Principal Coordinate Analysis (PCO) performed on a Bray-Curtis dissimilarity index matrix estimated from the relative abundance (%) of prey item at each depth. Then, we use a One-way PERMANOVA to test differences in prey proportions along the depth gradient. The data were not transformed to calculate the resemblance matrix. A Pearson correlation was used to determine the relationship between length of the predator and the three most frequently observed prey species consumed by the sea star. Univariate analyses were performed on R software (version 4.0.2; R Development Core Team, 2020) and multivariate analyses were performed on PRIMER software (Version 7.0).

The Dietary Electivity of *Cosmasterias lurida*

The dietary electivity analysis was performed using a selection index of relative prey availability (Pearre, 1982). The coefficient "C" [which is a correction of V coefficient of Yule (X^2)]

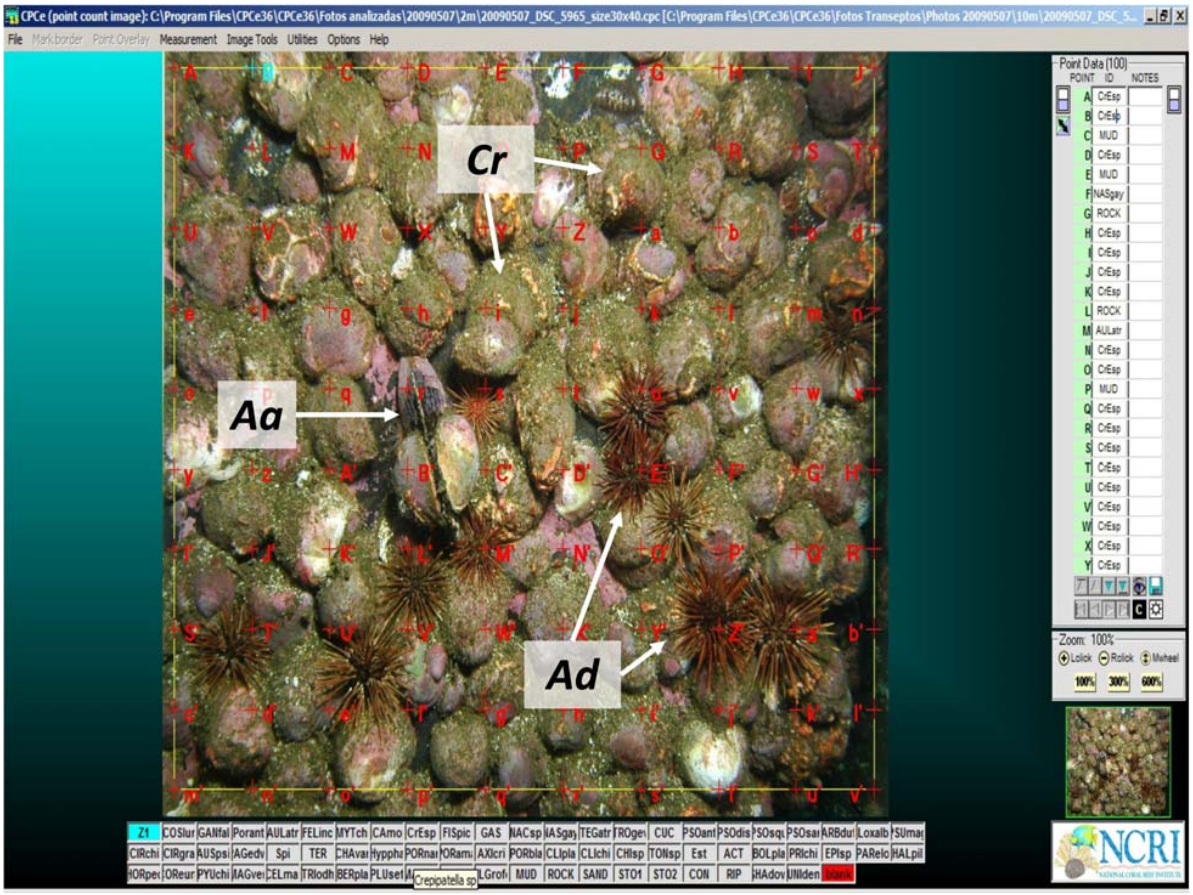

FIGURE 3 | Image analysis of photo-quadrats (example from 10-m depth) with red crosses indicating the matrix of uniform 10 × 10 points used to assess potential prey abundance. The mussel *Aulacomya atra* (*Aa*), the sea urchin, *Arbacia dufresnii (Ad),* and the slipper limpets *Crepipatella* spp. (*Cr*) are easily identified in the image.

(Kendall, 1952; Kendall and Stuart, 1973) was calculated for each item by depth interval using the following formulae:

$$C = \left(\frac{x_y^2}{n}\right)^{1/2} \qquad x^2 = \frac{n\,(|a_d b_e - b_d a_e| - n/2)^2}{a\ b\ d\ e}$$

where:

n: Number of total individuals feeding,

a_d: Number of a given prey item in the diet,

b_e: Available number of the other prey items in the environment,

b_d: Number of other prey items in the diet,

a_e: Available number of a particular prey item in the environment,

a: Sum of a_d and a_e,

b: Sum of b_d and b_e,

d: Sum of a_d and b_d,

c: Sum of a_e and b_e.

The C index ranges from −1 to +1 with the value 0 indicating no selection, i.e., the prey was consumed according to its availability. A value of 1 is absolute preference (maximum electivity), whereas a value of −1 indicates that the predator avoids the prey completely. Those extreme values are called absolute associations (Kendall, 1952). The significance of prey selectivity index C was tested using a Chi-square test (Pearre, 1982).

RESULTS

Distribution and Density of *Cosmasterias lurida*

Cosmasterias lurida was restricted from 2 to 25 m of depth at Yerbas Buenas Bay (**Figure 4**) and was not observed deeper even though rocky substratum continued to a depth of 35 m. Densities reached peak abundance in the >5–10-m interval (0.93 ± 0.56 ind/m^2) where they were over twice the levels observed in any other interval. In contrast, densities were very low in the >20–25-m interval, less than 10% observed overall. Sea star abundance was significantly different among depth intervals [Kruskal–Wallis, H (5, n = 140) = 39.4; $p < 0.001$; Dunn method].

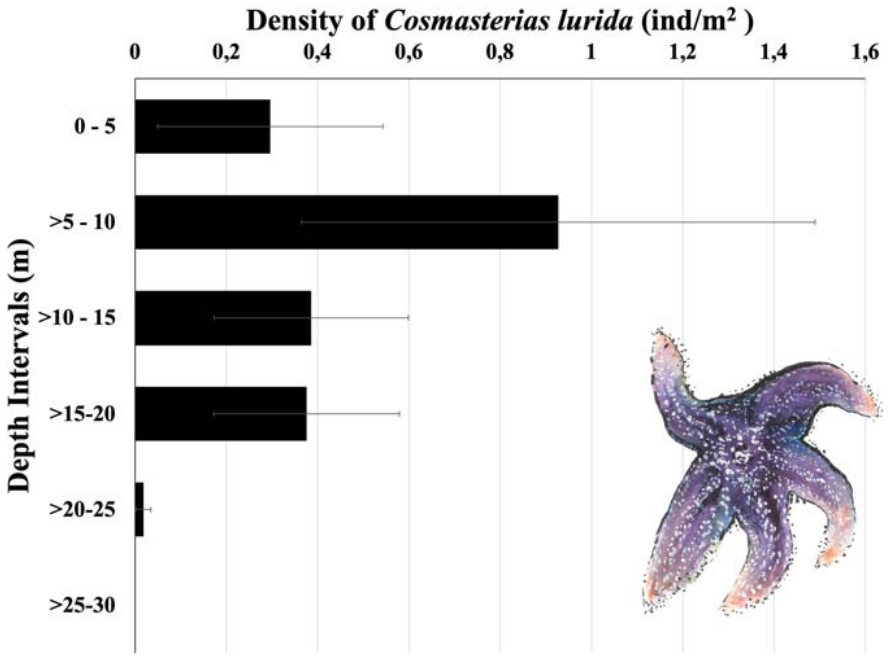

FIGURE 4 | Densities [mean (ind/m^2), SE] of the sea star *Cosmasterias lurida* at different depth intervals. The shallowest depth at which an individual was found 2.4 m (illustration of *C. lurida* by Fernanda Pardo).

Bathymetric Distribution of Potential Prey Species

Forty-eight species of benthic invertebrates considered as potential prey items were identified in the survey (**Supplementary Material**) and covered 56% of the bottom at this site with the remaining surface being shell fragments and sand (31%), bare rock (10%, including bedrock and cobbles), and mud (4%). The percent covers of the general taxa were 16% sessile gastropods, 15% echinoids, 11% algae, 3% bivalves, 3% holothuroids, 3% crustaceans, 2% anthozoa, 1% polychaetes, 1% porifera, <1% polyplacophores, <1% ascidians, <1% brachiopods, <1% bryozoans, <1% hydrozoans, and <1% asteroids.

The most abundant potential prey species at the site were the slipper limpets *Crepipatella* spp., the mussels *Aulacomya ater* and *Mytilus chilensis*, the barnacles *Notobalanus flosculus* (Darwin, 1854), *Elminius kingii* (Gray, 1831), *Balanus laevis* (Bruguière, 1789), and *Austromegabalanus psittacus* (Molina 1788), and the sea urchins *Pseudechinus magellanicus* (Philippi, 1857), *Arbacia dufresnii* (Blainville, 1825), and *Loxechinus albus* (Molina, 1782).

Unlike most gastropods, *Crepipatella* spp. are sessile. They were most abundant between depths of 0 and 10 m (18–20% cover) but decreased thereafter, falling to 3% within the deepest interval where sea stars occurred (>20–25 m; **Figure 5**). Other sessile species were mussels and barnacles. They were also more abundant in shallow depth intervals and, indeed, were not observed below 15 m, except for the barnacle *A. psittacus*, which was recorded only in some transects below the 15 m but in low abundance. The two mussel species, *A. ater* and *M. chilensis*, were less abundant than *Crepipatella* spp., reaching only 1% and 11% cover, respectively, in the shallowest depth interval (**Figure 5**). Barnacles were relatively abundant (13% in this same depth interval) but mainly consisted of small individuals (<1-cm diameter). Among mobile animals, the sea urchins *P. magellanicus, A. dufresnii,* and *L. albus* were the most abundant and were recorded in all depth intervals (**Figure 5**). *P. magellanicus* was the most abundant sea urchin species and occurred primarily in depths from 10 to 15 m. A diverse group of mobile small gastropods (<1 cm) was observed at the site but even collectively they were not abundant (**Figure 5**, **Supplementary Material**, and **Table 1**).

In situ Feeding Activity of *Cosmasterias lurida*

Regarding the feeding activity survey of *C. lurida*, significant differences were found in the interaction between the prey items and the depth intervals (F = 8.512; df = 9, 48; P < 0.001) (**Table 2**). Regardless of the depth interval, approximately half the sea stars sampled were not feeding, and no individuals of *C. lurida* were found feeding at depths below 20 m (0–5 m = 55%; >5–10 m = 46%; >10–15 m = 43%; >15–20 m = 57%; >20–25 = 0%; **Figure 6**). Among those that were feeding (0–5 m = 42%; >5–10 m = 45%; >10–15 m = 52%; >15–20 m = 31%; **Figure 6**), only seven species of the 48 taxonomic groups recorded in the photo-quadrats were observed as prey (**Supplementary Material**). Moreover, the principal prey observed were limited to just four species [the two species of *Crepipatella* (51%), *Aulacomya ater* (36%), and *Mytilus chilensis* (8%)] with three other taxa making up the balance (holothuroid, crustacean, gastropod – each <2%; **Figure 6**). Regarding the proportion of

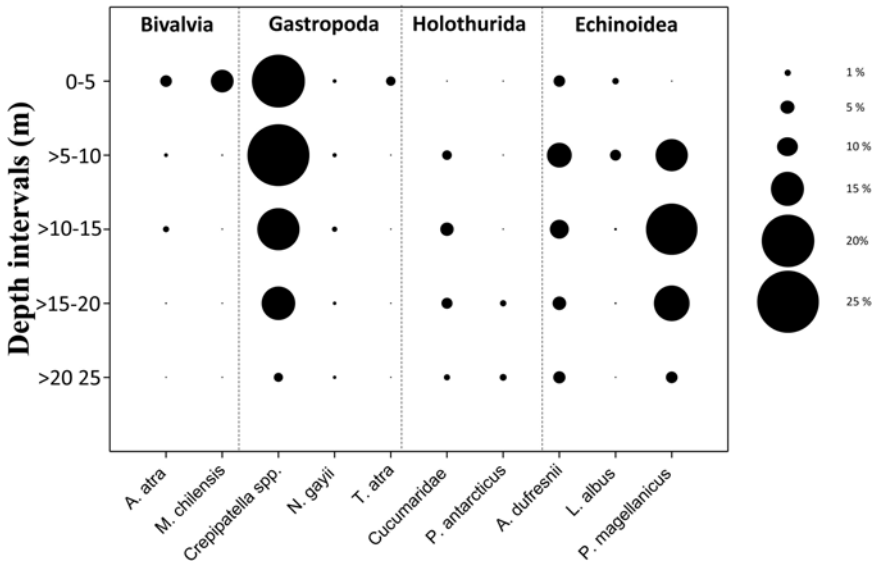

FIGURE 5 | Prey availability – Abundance (percent cover) at different depth intervals of common invertebrates that are potential prey of the sea star *Cosmasterias lurida* in Yerbas Buenas Bay.

TABLE 1 | Abundance (percent cover) of the potential prey of the sea star *Cosmasterias lurida* in photo-quadrats at depths down to 25 m (no sea stars were observed below this depth).

Taxa/Depth (m)	0–5		5–10		10–15		15–20		20–25	
	%E	%P	%E	%P	%E	%P	%E	%P	%E	%P
Asteroidea	0.30	–	0.46	–	0.79	–	0.22	–	0.24	–
Bivalvia	11.05	75.73	1.16	64.10	1.70	25.00	0.19	1.73	0.02	–
Gastropoda	23.88	12.86	23.40	30.77	15.78	73.33	12.23	96.55	3.66	–
Holothuroidea	0.07	–	2.93	–	4.28	1.67	5.22	1.72	3.79	–
Echinoidea	5.42	–	22.32	–	24.06	–	16.52	–	7.55	–
Crustacea	13.15	1.41	0.02	1.28	0.05	–	1.07	–	0.26	–
Polychaeta	0.65	–	0.12	–	0.12	–	0.51	–	3.04	–
Porifera	–	–	0.07	–	0.73	–	1.28	–	1.41	–
Polyplacophora	0.67	–	0.32	–	0.14	–	0.11	–	0.02	–
Anthozoa	–	–	0.09	–	0.98	–	3.31	–	2.96	–
Ascidiacea	–	–	–	–	0.20	–	0.01	–	–	–
Brachiopoda	–	–	–	–	–	–	–	–	–	–
Bryozoa	–	–	–	–	–	–	0.09	–	0.12	–
Opisthobranchia	–	–	0.03	–	–	–	0.07	–	0.06	–
Hydrozoa	–	–	–	–	–	–	–	–	–	–
Ochrophyta	2.70	–	–	–	–	–	–	–	0.02	–
Rhodophyta	6.98	–	9.55	–	4.72	–	9.40	–	21.36	–
Mud, Sand, Rock, Shell, Cobble/Pebble	33.24	–	38.72	–	46.15	–	49.35	–	54.98	–
Shadow	1.59	–	0.58	–	0.21	–	0.20	–	0.13	–
Unidentified	0.30	10.00	0.23	3.85	0.09	–	0.22	–	0.38	–

%E, Percent cover of potential prey; %P, Percentage of each taxa in diet of C. lurida; "–," Percentage <1%.

the species preyed upon by *C. lurida* PERMANOVA showed significant differences among depth intervals (**Table 3**). The posteriori Pair-wise test indicated that the most similar depth intervals were >10–15 and >15–20 dissimilar depth intervals were 0–5 and >15–20 m (**Table 3**). Those differences are better visualized in the PCO analysis, where the shift in the importance of the major prey items (*A. ater* and *Crepipatella* spp.) shift with depth can be seen (upper panels of **Figure 7**) as well as the lack of importance of the other mussel (*M. chilensis*) and other prey items (lower panels of **Figure 7**). With regards to the size of sea stars [mean disk diameter ± SD: 31.0 ± 4.5 mm and the size of prey sizes (mean length ± SD: 57.0 ± 26.0 mm)] that

TABLE 2 | Results of two-way ANOVA with item prey and depth interval as fixed factors.

Source	DF	SS	MS	*F*	*P*
Prey item	3	604.547	201.516	23.664	<0.001
Depth interval	3	12.797	4.266	0.501	0.683
Prey item × depth interval	9	652.391	72.488	8.512	<0.001
Residuals	48	408.75	8.516		
Total	63	1678.484	26.643		

TABLE 3 | PERMANOVA partitioning and analysis of prey item per depth intervals (4) from Yerbas Buenas Bay, based Bray–Curtis dissimilarities.

Source	df	*SS*	MS	Pseudo-*F*	*P*(perm)
Depth interval	3	16415.4	5471.8	7.6	0.001
Residual	12	8688	724	–	–
Total	15	25103.4	–	–	–
Pair-Wise Test		***t***		***P*(perm)**	**Similarities (%)**
Depth					
0–5 vs. >5–10		0.9		0.572	59.7
0–5 vs. >10–15		2.1		0.049	35.4
0–5 vs. >15–20		4.2		0.028	12.9
>5–10 vs. >10–15		1.9		0.087	55.9
>5–10 vs. >15–20		6.9		0.033	33.1
>10–15 vs. >15–20		1.6		0.15	68.3

Pseudo F statistics were calculated for each term using direct analogs to univariate expectations of mean squares (EMS); p-values were obtained using 9999 permutations under a reduced model. Each term is identified as contributing either a fixed or random component to the overall model. The Pair-Wise Test below indicating similarities (%) among depth intervals.

they consumed, neither varied significantly with depth, and there were no significant correlations between predator and prey size for the three most commonly selected prey: *A. ater* [Pearson (r) = 0.238, n = 99, $p > 0.05$]; *M. chilensis* [Pearson (r) = −0.383, n = 25, $p > 0.05$]; *Crepipatella* spp. [Pearson (r) = 0.207, n = 134, $p > 0.05$].

Prey Electivity

The electivity (C) of different prey types changed by depth interval (**Table 4** and **Figure 8**). In shallower depth intervals, the sea star had a high positive electivity for the mussel *A. ater* in depths of 0–15 m, especially in the >5–10-m depth interval (C = 0.72). It also had a slight but not significant positive electivity for the other mussel, *M. chilensis*, but only in the >5–10-m depth interval. Electivity changed dramatically below 10 m where there was a moderately high electivity for *Crepipatella* spp., which increased with depth (C = 0.28 and 0.44 in the >10–15-m and >15–20-m depth intervals, respectively). This contrasts sharply with the shallowest depth intervals with the significantly negative electivity value (C = −0.33) in the 0–5-m interval, which indicated that *Crepipatella* spp. was avoided there, and C = 0.062 for the >5–10-m depth interval, where this gastropod was not selected by the sea star. With regard to other prey, the index was close to 0 in the shallowest depth interval, indicating that they were consumed to the degree of their availability in the environment, but in all other depth intervals, the indices were negative as these other prey were avoided to

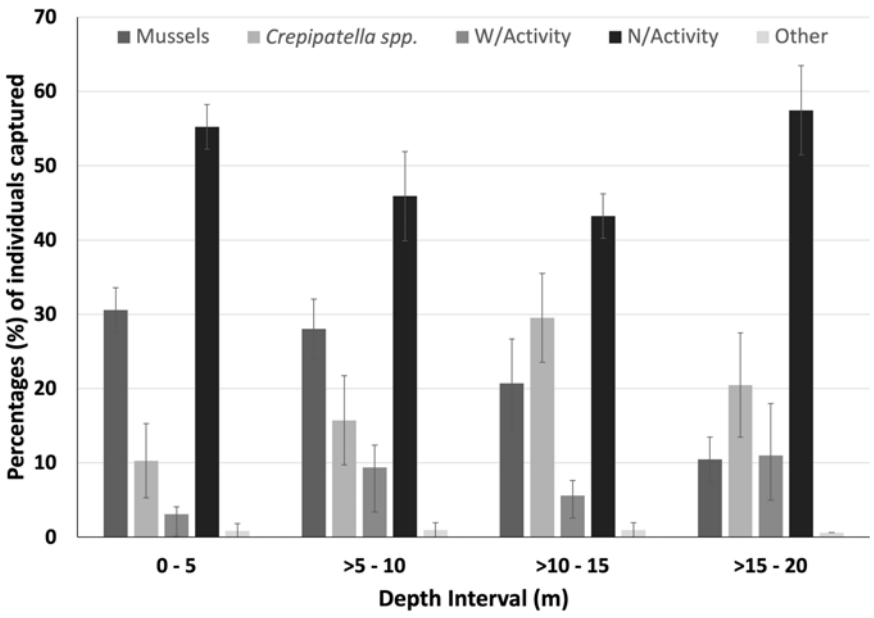

FIGURE 6 | Five categories of feeding activity of the sea star *Cosmasterias lurida* in Yerbas Buenas Bay: 1, feeding on mussels; 2, feeding on *Crepipatella* spp.; 3, with activity (W/activity; stomachs out but no associated prey); 4, no activity (N/activity); and 5, feeding on other prey species. No sea stars were observed feeding below 20 m in depth. Bars represent standard errors.

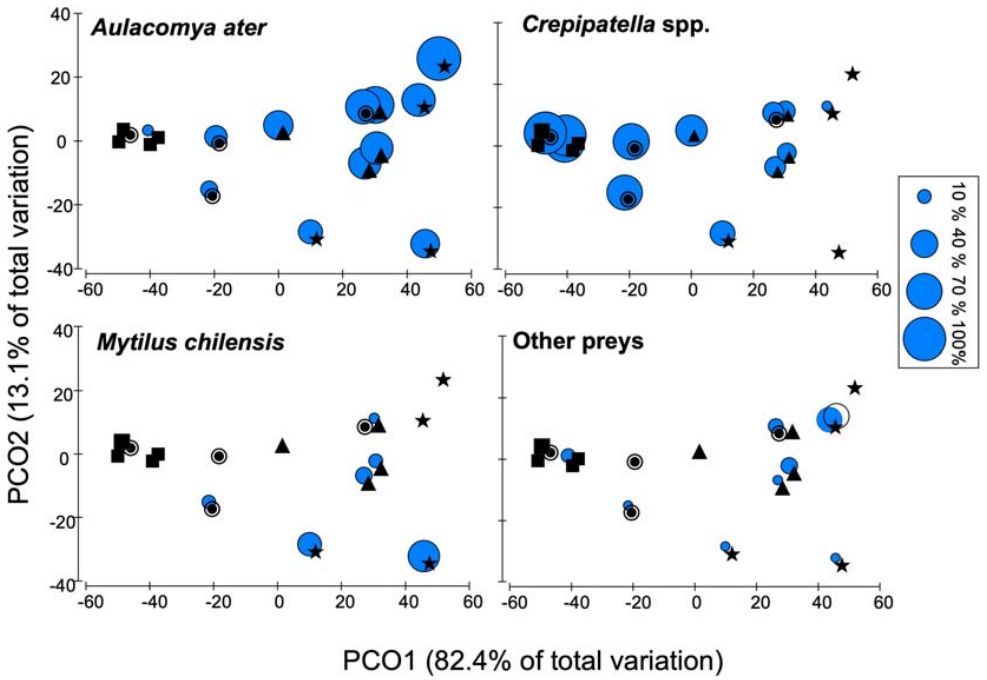

FIGURE 7 | Principal Coordinates Analysis (PCO) showing prey distinctly selected according to depth. Symbols represent different depth intervals (m); ★ = 0–5, ▲ = >5–10, ◉ = >10–15, ■ = >15–20. The size of the circles represent the proportion of the main species preyed upon by *Cosmasterias lurida*.

a moderate degree (**Table 4** and **Figure 8**). If we compare the most common prey with their availability in the environment (**Figure 8**), there is a dramatic shift in prey choice from mussels in shallow depths (where they are rare relative to all other potential prey) to *Crepipatella* spp. in deeper depth intervals. *Crepipatella* spp. was abundant in the 0–5-m depth interval (19%) but made up only 10% of prey consumed in this interval. In the next deeper interval (>5–10-m) the cover was similar (22% cover), but consumption increased to 31%. In the deeper intervals of >10–15 m and >15–20 m, *Crepipatella* spp. were less abundant (14% and 12% cover, respectively) but were observed as prey items 67% and 96% of the time, respectively. In the 0–5-m depth interval, *M. chilensis* and *A. ater* occurred at low percent cover (8% and 3%, respectively) but were frequently consumed (21% and 58%, respectively). In the >5–10-m depth interval, abundance of both species decreased dramatically (0.17% and 1%, respectively), but 8% and 57% of the sea star diet was *M. chilensis* and *A. ater*, respectively. In the deeper intervals of >10–15 m and >15–20 m, *M. chilensis* and *A. ater* were present at very low cover, so not part of the main diet of *C. lurida*. Other prey items collectively occurred at high cover in all depth intervals studied with 26% (0–5 m), 29% (>5–10 m), 36% (>10–15 m), 29% (>15–20 m), and 18% (>20–25 m). They were, however, less commonly observed as prey [11% (0–5 m), 5% (>5–10 m), 4% (>10–15 m), 3% (>15–20 m), and 0% (>20–25)].

TABLE 4 | Electivity values (C index) for feeding in the sea star *Cosmasterias lurida*.

Depth interval (m)	Prey item	C index	Chi-square value
0–5	*Crepipatella* spp.	−0.33***	0.0016
	Aulacomya ater	0.439***	0
	Mytilus chilensis	0.003	0.7515
	Other prey*	−0.013	0.6228
>5–10	*Crepipatella* spp.	0.062	0.3663
	Aulacomya ater	0.72***	0
	Mytilus chilensis	0.165**	0.0125
	Other prey*	−0.338***	0.0002
>10–15	*Crepipatella* spp.	0.28***	0.0026
	Aulacomya ater	0.258***	0.0012
	Mytilus chilensis	0.034	0.193
	Other prey*	−0.437***	0
>15–20	*Crepipatella* spp.	0.44***	0.0001
	Aulacomya ater	0.009	0.3537
	Mytilus chilensis	–	–
	Other prey*	−0.474***	0

*Values near 0 indicating no selectivity and values of +1 and −1 indicating absolute preference and avoidance, respectively. No values could be calculated for the depths below 20 m as no sea stars were observed feeding there. * Other prey included all prey observed as the diet of Cosmasterias lurida.***P < 0.01, **P < 0.05.*

DISCUSSION

The impact of any predator on community structure and organization depends on multiple factors, for example, the degree of selectivity (generalist vs. selective predators) when choosing their prey, prey diversity, trophic level of the prey together

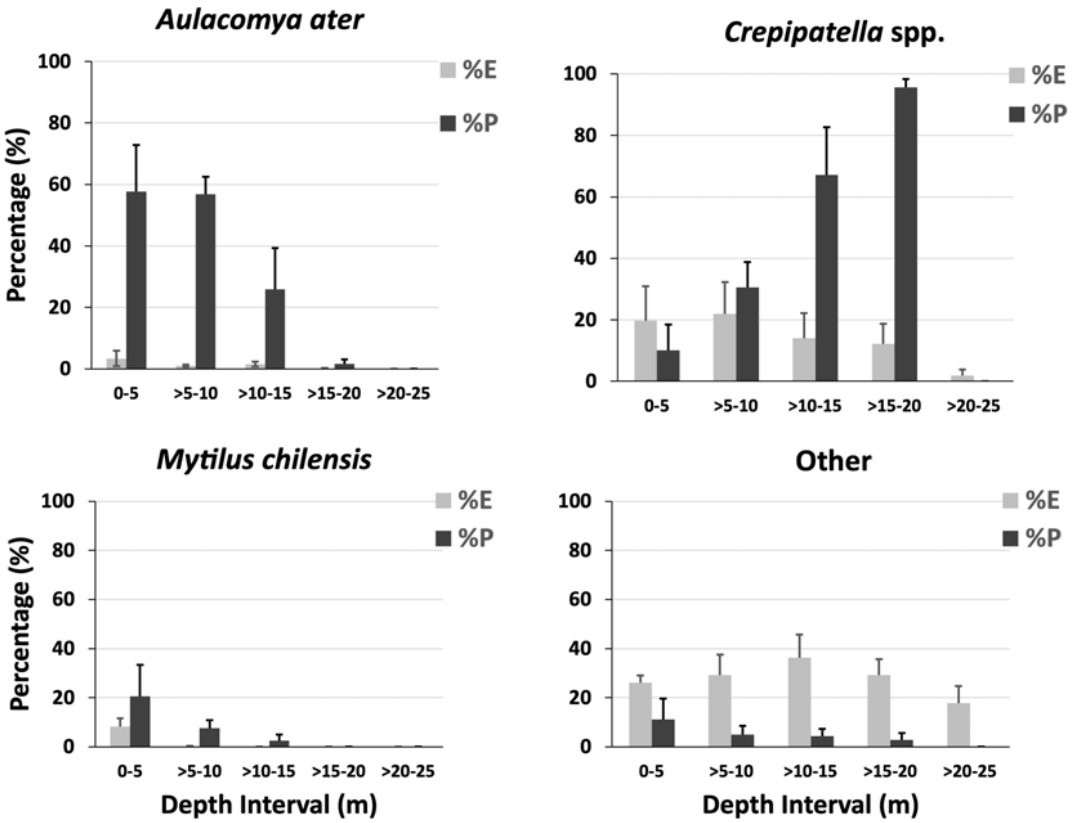

FIGURE 8 | Availability of potential prey (percent cover) in the environment compared to their occurrence in the diet (percentage) of the sea star *Cosmasterias lurida* in Yerbas Buenas Bay.

with their defense mechanisms or prey recruitment dynamics. Predator behavior is especially relevant because selective predators can have strong indirect effects on competition among prey, producing drastic changes in community structure, especially when having preferences for competitive dominants (Paine et al., 1985; Castilla, 1999; Rettig and Smith, 2021). In many marine ecosystems sea stars are considered to be keystone species (Paine, 1966, 1969; McClintock and Lawrence, 1985; Menge and Sanford, 2013), and indeed, this general ecological concept arose from early studies on sea star ecology (Paine, 1966, 1969). However, this original concept has evolved into a holistic vision and is now used in a more complex conceptual framework to be able to define an entire ecosystem as a "keystone species complex" (Hermosillo-Nunez et al., 2018). In many cases, prey diversity (species and size), system productivity, prey recruitment dynamics, and predator preferences have all been important factors determining their impacts (Menge and Sanford, 2013). Because sea stars prey strongly on bivalves, mussels are often a principal component of the diet of many asteroids, especially in shallow waters (Castilla and Crisp, 1970; Tokeshi, 1991; Tokeshi and Romero, 1995; Gaymer et al., 2001a,b; Gaymer and Himmelman, 2002; Gil and Zaixso, 2008; Lamare et al., 2009). For example, *Heliaster helianthus*, described as a keystone predator in intertidal communities along the central coast of Chile, limits the lower distribution of the mussel *Perumytilus purpuratus* (Lamarck, 1819), which can monopolize the rocky surface when *H. helianthus* is absent (Paine et al., 1985). The dominance of filter-feeding gastropods, the slipper limpets *Crepipatella* spp. (52% of all feeding observations), in the diet would then seem, at first glance, to go against this trend, suggesting that *C. lurida* does not appear to be a predator that specializes on mussels but is instead a generalist. However, the electivity analysis across depth showed clearly that one of the mussel species, *Aulacomya ater*, was preferred in shallower zones. Strikingly, the other mussel species, *Mytilus chilensis*, was never preferentially consumed by this sea star, and this difference could possibly explain why this mussel occurred in higher abundance than the preferred species. Regardless, this pattern goes against the generalization that sea stars invariably prefer feeding on mussels. The subtle differences that might drive the distinction between these two very similar species remain unknown and worthy of future investigation.

The large proportion of gastropod prey in the diet of *C. lurida* was, however, not surprising for several reasons. First, unlike most gastropods, slipper limpets are sessile and thus cannot move to escape predators as observed in many other systems where mobile gastropods are common (McClintock, 1985; Bryan et al., 1997; San-Martin et al., 2009). Second, it was the most abundant substratum occupier at this site and thus was the most available item in the prey field. Therefore, there was a high overall electivity index for this group, especially at greater depths (5–20 m) where

alternative invertebrate prey were either scarce (e.g., mussels) or highly mobile (e.g., sea urchins).

Selective removal of species by sea stars can structure benthic communities (Paine, 1966; Gaymer and Himmelman, 2008; Manzur et al., 2010), and *C. lurida* may be acting as a keystone predator in Patagonian rocky subtidal ecosystems. Indeed, the dominance of the slipper limpets *Crepipatella* spp. at our study site (reaching 100% in some photo-quadrats) may rely on the selective predation of *C. lurida* on the mussel *A. atra*, a potential competitor for space. Manipulative experiments would be needed to establish any such role of this predator. For example, the very low abundance of mussels below depths of 5 m could be due simply to competitive displacement by *Crepipatella* spp. or by predation from *C. lurida*, which occurred at its highest local densities at depths between 5 and 15 m. Either mechanism could allow the slipper limpets to monopolize the substratum. Alternatively, physiological restrictions could limit mussels to inhabit shallower subtidal environments. However, both *A. ater* and *M. chilensis* have been recorded at depths up to 25 m in other localities (Solís and Lozada, 1971; Lorenzen et al., 1979; Cazzaniga, 1990; Zagal et al., 2001), making this latter possibility unlikely.

The decrease in abundance of *Crepipatella* spp. below a depth of 20 m corresponded to the low abundance of sea stars also observed at these depths, suggesting that it is not predation that is determining the lower limit of these species. However, the spatial distribution and abundance of asteroids often tracks that of their prey (Gaymer and Himmelman, 2002; Himmelman et al., 2005), and the low abundance of all invertebrates indicates that other ecological processes (e.g., low recruitment) are structuring benthic assemblages at deeper depths, which were dominated primarily by octocorals, mainly *Primnoella* sp. (Garrido, unpublished data), and another calyptraeid gastropod, *Calyptraea aurita* (Reeve, 1859) (Holtheuer et al., 2018), below depths of 20 m.

The depth-dependent selectivity that we observed in our study contrasts strikingly with the only other detailed study of the feeding ecology of this species (Vásquez and Castilla, 1984). That study, conducted in southern Patagonia, concluded that *C. lurida* was a generalist, consuming prey species according to their availability in the environment. Their assessment of selectivity was, however, based on a much simpler, non-parametric analysis, which may have been unable to resolve smaller differences. For example, consistent with our results, *A. ater*, the preferred prey in our study, was ranked higher as a prey species (#3) than its availability (#5) at their study site, but their selectivity analysis only assessed the ensemble of the prey available and not individual species. In addition, they did not stratify their sampling by depth [likely because of the limited bathymetric distribution (2–12 m) of *C. lurida* at their site], which again may have limited resolution. A major ecological difference was, however, that barnacles were both the most abundant prey species at their site and the most common prey species (27%). In contrast, we saw almost no predation on barnacles even though they represented 13% of the available prey in the shallowest depth interval. Interestingly, they also recorded many more prey species (27) than we did (7), in spite of similar sampling efforts (132 vs. 136 observations of feeding associated with a prey species, respectively) and the high diversity of potential prey species at our study site (48 species). One consistency between the two studies was the high percentage of sea stars not associated with any prey (both approximately 50%). The underlying causes in both cases remains unknown, but it is surprising to see almost half the population of this predator was not feeding even when potential prey (e.g., slipper limpets) were readily available (e.g., shallow depth intervals).

An additional explanation for the differences between our results and those of Vásquez and Castilla (1984) is the difference in the timing of sampling which was done in the austral summer in their study (January and April) but in the austral winter in our study (May to July). Species can exhibit seasonal changes in their feeding behavior in response to temporal variation in biotic parameters (e.g., density, energy content of prey) and abiotic factors (e.g., substratum, temperature) (Christensen, 1970; Kreiling et al., 2020). Such changes in diet, feeding preferences and foraging behavior have been reported for other sea stars [e.g., *Asterias rubens* (Castilla, 1972); *Luidia clathrate* (McClintock and Lawrence, 1985); *Astropecten marginatus* (Guilherme and Rosa, 2014)], due possibly to seasonal variations in the nutritional value of prey (e.g., reproductive condition) that might lead to prey switching by predators (Krebs et al., 1977; Ostfeld, 1982) or seasonal changes in energetic requirements of sea star predators (Aguera et al., 2012). Such possibilities certainly exist, but both studies were only conducted over 4-month periods, and thus temporal variability in the diet could not be assessed. Regardless, the differences between the two studies caution against making generalizations from studies restricted to one place and one time. Spatial and temporal variation in patterns and processes are, of course, the norm for ecological studies, even when involving the same suite of species, but the contrasting results from these two studies emphasize the need for greater spatiotemporal sampling to better understand the feeding behavior of *C. lurida*. Another limitation of our study is that *in situ* observations of the feeding behavior only provide a "snapshot" of an individual's diet and cannot determine if individuals are specialists or generalists. In contrast, stable isotope analysis (Wang et al., 2014; Zenteno et al., 2019) does integrate past feeding activity and could be used as a complementary approach to confirm and extend the patterns observed in this study. Finally, as all our observations were made during daylight hours, we also do not know if these sea stars were feeding differently at night although given that they are not visual predators, this possibility is unlikely. Regardless, these questions can and should be addressed in future studies on the feeding behavior of this and other predatory sea stars.

Overall, we found that *C. lurida* does not feed on prey in direct proportion to their availability in the habitat, showing selectivity of certain prey species (in particular, the mussel *A. ater*). Thus, our original hypothesis that this species is an opportunist-generalist is not supported as *C. lurida* appears to be a flexible specialist, one with strong preferences but also an ability to change its prey selection according to the environmental context. However, it appears to limit its prey selection mostly to sessile species because the sea urchins *Loxechinus albus*, *Arbacia dufresnii,* and *Pseudechinus magellanicus* were never recorded in

the diet of *C. lurida* even though they occurred in relatively high abundance at our study site. One explanation is that sea urchins, including one of the species in our study (*Loxechinus albus*), can have effective risk-avoidance behaviors to sea star attacks (Urriago et al., 2011, 2012).

Prey electivity could also change depending on the size of predators and prey (Paine, 1976; Barbeau and Scheibling, 1994). However, we did not find a predator–prey size relationship between *C. lurida* and any of its three primary prey species. Similarly, observations on feeding behavior in another Chilean sea star, *Meyenaster gelatinosus*, did not indicate preferences for any particular size of the sea urchin *L. albus*, the dominant invertebrate species at that study site (Dayton et al., 1977). In contrast, *Leptasterias polaris* (Müller and Troschel, 1842) and *Asterias vulgaris* (Packard, 1863), two common subtidal sea stars in eastern Canada, had differences in their use of prey (species and size of bivalves) that may facilitate their coexistence (Gaymer et al., 2001a). On the Pacific coast of North America, the selection of different sizes of prey (mussels) appears to maximize the energy intake in the competing sea stars *Leptasterias hexactis* (Stimpson, 1862) and *Pisaster ochraceus* (Brandt, 1835) (Menge and Menge, 1974). Thus, the presence of competitors might select for intraspecific differences in size to partition the trophic niche. This is not the case, however, for our study system, because no other predatory sea stars co-occur with *C. lurida* (Garrido, unpublished data).

This study shows the importance of assessing the environmental context to describe the trophic behavior of predators. Laboratory studies about dietary preference indicate that asteroids show preferences for some prey offered, but they did not consider the relative abundance of prey in the environment (Castilla and Crisp, 1970; Castilla, 1972; Rochette et al., 1994; Pratchett, 2007). On the other hand, field studies usually show generalist behaviors regardless of environmental variability. Species that have been considered as generalists are frequently much more selective when the environmental offer is evaluated (Gaymer and Himmelman, 2008). Detailed and realistic knowledge of the trophic habits of species is a critical element for constructing food webs (Martinez, 1993), which, in turn, help to predict effects of perturbations on communities (Pérez-Matuz et al., 2017). In addition, anthropogenic activity, such as coastal urbanization that results in the destruction of habitats, needs to be considered as it can significantly affect sea star populations and their impact on the trophic structure and function of subtidal communities (Chan et al., 2018). In this sense, this study is a key contribution to understanding food web dynamics of the benthic marine communities of northern Patagonia.

DATA AVAILABILITY STATEMENT

The original contributions presented in the study are included in the article/**Supplementary Material**, further inquiries can be directed to the corresponding author.

AUTHOR CONTRIBUTIONS

IG: conceptualization, validation, formal analysis, writing, and visualization. LP: conceptualization, investigation, and writing – review and editing. LJ: conceptualization, validation, and writing – review and editing. DS: conceptualization, investigation, validation, formal analysis, and writing. All authors contributed to the article and approved the submitted version.

FUNDING

This work was supported by the International Bureau, Bonn, Federal Republic of Germany (FRG) (project #CHL 07/001 and CHL 07/007), the Direction of Investigation and Development of the Universidad Austral de Chile, Valdivia, Chile (S-2008-14), and FONDAP-IDEAL Center (Program 15150003).

ACKNOWLEDGMENTS

We are grateful for the assistance of the Scientific Diving Group of the Universidad Austral de Chile in the field, especially to Jose Luis Kappes, Maria José Díaz, Isabel del Moral, and Jorge Holtheuer.

SUPPLEMENTARY MATERIAL

The Supplementary Material for this article can be found online at: https://www.frontiersin.org/articles/10.3389/fmars.2021.636208/full#supplementary-material

REFERENCES

Adami, M. L., and Gordillo, S. (1999). Structure and dynamics of the biota associated with *Macrocystis pyrifera* (Phaeophyta) from the Beagle Channel, Tierra del Fuego. *Sci. Mar.* 63, 183–191. doi: 10.3989/scimar.1999.63s1183

Aguera, A., Trommelen, M., Burrows, F., Jansen, J. M., Schellekens, T., and Smaal, A. (2012). Winter feeding activity of the common starfish (*Asterias rubens* L.): the role of temperature and shading. *Journal of Sea Research* 72, 106–112. doi: 10.1016/j.seares.2012.01.006

Amsler, C. D., McClintock, J. B., and Baker, B. J. (2014). Chemical mediation of mutualistic interactions between macroalgae and mesograzers structure unique coastal communities along the Western Antarctic Peninsula. *J. Phycol.* 50, 1–10. doi: 10.1111/jpy.12137

Baeta, M., and Ramon, M. (2013). Feeding ecology of three species of Astropecten (Asteroidea) coexisting on shallow sandy bottoms of the northwestern Mediterranean Sea. *Mar. Biol.* 160, 2781–2795. doi: 10.1007/s00227-013-2270-0

Barbeau, M. A., and Scheibling, R. E. (1994). Procedural effects of prey tethering experiments: predation of juvenile scallops by crabs and sea stars. *Mar. Ecol. Prog. Ser.* 111, 305–310. doi: 10.3354/meps111305

Bryan, P. J., McClintock, J. B., and Hamann, M. (1997). Behavioral and chemical defenses of marine prosobranch gastropod Calliostoma canaliculatum in response to sympatric seastars. *J. Chem. Ecol.* 23, 645–658. doi: 10.1023/b:joec.0000006401.97339.b9

Calderwood, J., O'connor, N. E., and Roberts, D. (2016). Efficiency of starfish mopping in reducing predation on cultivated benthic mussels (*Mytilus edulis* Linnaeus). *Aquaculture* 452, 88–96. doi: 10.1016/j.aquaculture.2015.10.024

Castilla, J. C. (1972). Responses of *Asterias rubens* to bivalve prey in a Y-maze. *Mar. Biol.* 12, 222–228. doi: 10.1007/bf00346770

Castilla, J. C. (1999). Coastal marine communities: trends and perspectives from human exclusion experiments. *Trends Ecol. Evol.* 14, 280–283. doi: 10.1016/s0169-5347(99)01602-x

Castilla, J. C., and Crisp, D. J. (1970). Responses of *Asterias rubens* to olfactory stimuli. *J. Mar. Biol. Assoc. U.K.* 50, 829–847.

Castilla, J. C., and Moreno, C. A. (1982). "Sea urchins and *Macrocystis pyrifera*: experimental test of their ecological relations in southern Chile," in *Echinoderms*, ed. J. M. Lawrence (Rotterdam: Balkema), 257–263.

Cazzaniga, N. J. (1990). A concern for grammar: the name of the *Magellanic mussel* (Bivalvia: Mytilidae). *Malacol. Rev.* 27:110.

Chan, Y. K. S., Toh, T. C., and Huang, D. (2018). Distinct size and distribution patterns of the sand-sifting sea star, archaster typicus, in an urbanised marine environment. *Zool. Stud.* 57:11.

Christensen, A. M. (1970). Feeding biology of the sea-star Astropecten irregularis Pennant. *Ophelia* 8, 1–134.

Clark, A. M., and Downey, M. E. (1992). *Starfishes of the Atlantic*. London: Chapman Hall.

Cossi, P. F., Boy, C. C., Gimenez, J., and Perez, A. F. (2015). Reproductive biology and energy allocation of the sea star *Cosmasterias lurida* (Echinodermata: Asteroidea) from the Beagle Channel, Tierra del Fuego, Argentina. *Polar Biol.* 38, 1321–1333. doi: 10.1007/s00300-015-1696-x

Cossi, P. F., Boy, C. C., and Perez, A. F. (2017). Pattern of energy allocation during the gametogenesis of the asteroid *Cosmasterias lurida* (Forcipulatida: Stichasteridae) from the Beagle Channel, Ushuaia, ArgentinaPaula. *Rev. Biol. Trop.* 65, S197–S206.

Dayton, P. K. (1985). The structure and regulation of some south american kelp communities. *Ecol. Monogr.* 55, 447–468. doi: 10.2307/2937131

Dayton, P. K., Rosental, R. J., Mahen, L. C., and Antezana, T. (1977). Population structure and foraging biology of the predaceus chilean asteroid *Meyenaster gelatinosus* and the escape biology of its prey. *Mar. Biol.* 39, 361–370. doi: 10.1007/bf00391939

Deaker, D. J., Aguera, A., Lin, H.-A., Lawson, C., Budden, C., Dworjanyn, S. A., et al. (2020). The hidden army: corallivorous crown-of-thorns seastars can spend years as herbivorous juveniles. *Biol. Lett.* 16:20190849. doi: 10.1098/rsbl.2019.0849

Fernandez, W. S., Dias, G. M., Majer, A. P., Delboni, C. G., Denadai, M. R., and Turra, A. (2017). Resource partitioning between sympatric starfish from tropical unconsolidated substrate: implications for coexistence and top-down control on benthic prey. *Estuar. Coast. Shelf Sci.* 196, 141–149. doi: 10.1016/j.ecss.2017.06.039

Fraysse, C., Calcagno, J., and Perez, A. F. (2018). Asteroidea of the southern tip of South America, including Namuncura Marine Protected Area at Burdwood Bank and Tierra del Fuego Province, Argentina. *Polar Biol.* 41, 2423–2433. doi: 10.1007/s00300-018-2377-3

Fraysse, C. P., Perez, A. F., Calcagno, J. A., and Boy, C. C. (2020). Energetics and development modes of Asteroidea (Echinodermata) from the Southwestern Atlantic Ocean including Burdwood Bank/MPA Namuncura. *Polar Biol.* 43, 175–186. doi: 10.1007/s00300-020-02621-6

Gaymer, C., and Himmelman, J. (2002). Mussel beds in deeper water provide an unusual situation for competitve interactions between the seastars *Leptasterias polaris* and *Asterias vulgaris*. *J. Exp. Mar. Biol. Ecol.* 277, 13–24. doi: 10.1016/s0022-0981(02)00234-4

Gaymer, C. F., and Himmelman, J. H. (2008). A keystone predatory sea star in the intertidal zone is controlled by a higher-order predatory sea star in the subtidal zone. *Mar. Ecol. Prog. Ser.* 370, 143–153. doi: 10.3354/meps07663

Gaymer, C. F., Himmelman, J. H., and Johnson, L. E. (2001a). Distribution and feeding ecology of the seastars *Leptasterias polaris* and *Asterias vulgaris* in the northern Gulf of St Lawrence, Canada. *J. Mar. Biol. Assoc. U.K.* 81, 827–843. doi: 10.1017/s0025315401004660

Gaymer, C. F., Himmelman, J. H., and Johnson, L. E. (2001b). Use of prey resources by the seastars *Leptasterias polaris* and *Asterias vulgaris*: a comparison between field observations and laboratory experiments. *J. Exp. Mar. Biol. Ecol.* 262, 13–30. doi: 10.1016/s0022-0981(01)00264-7

Gianguzza, P., Di Trapani, F., Bonaviri, C., Agnetta, D., Vizzini, S., and Badalamenti, F. (2016). Size-dependent predation of the mesopredator *Marthasterias glacialis* (L.) (Asteroidea). *Mar. Biol.* 163:65.

Gil, D. G., and Zaixso, H. E. (2008). Feeding ecology of subantarctic sea star *Anasterias minuta* within tide pools in Patagonia, Argentina. *Biol. Trop.* 56, 311–328.

Gordillo, S., and Archuby, F. (2012). Predation by drilling gastropods and asteroids upon mussels in rocky shallow shores of southernmost South America: paleontological implications. *Acta Palaeontol. Polon.* 57, 633–646. doi: 10.4202/app.2010.0116

Guilherme, P. D. B., and Rosa, L. C. (2014). Seasonal variation in body size and diet of the sea star *Astropecten marginatus* (Paxillosida, Astropectinidae) off coast of Parana, Southern Brazil. *Rev. Biol. Trop.* 62, 59–68. doi: 10.15517/rbt.v62i1.7888

Hermosillo-Nunez, B. B., Ortiz, M., and Rodriguez-Zaragoza, F. A. (2018). Keystone species complexes in kelp forest ecosystems along the northern Chilean coast (SE Pacific): improving multispecies management strategies. *Ecol. Indic.* 93, 1101–1111. doi: 10.1016/j.ecolind.2018.06.014

Hernández, D. A., and Tablado, A. (1985). *Asteroidea de Puerto Deseado (Santa Cruz, Argentina)*. Argentina: Centro Nacional Patagónico.

Himmelman, J. H., Dutil, C., and Gaymer, C. F. (2005). Foraging behavior and activity budgets of sea stars on a subtidal sediment bottom community. *J. Exp. Mar. Biol. Ecol.* 322, 153–165. doi: 10.1016/j.jembe.2005.02.014

Holtheuer, J., Aldea, C., Schories, D., and Gallardo, C. S. (2018). The natural history of *Calyptraea aurita* (Reeve, 1859) from Southern Chile (Gastropoda, Calyptraeidae). *Zookeys* 798, 1–22. doi: 10.3897/zookeys.798.25736

Kendall, M. G. (1952). *The Advanced Theory of Statistics*, 5th Edn. New York, NY: Hafner.

Kendall, M. G., and Stuart, A. (1973). *The Advanced Theory of Statistics. Vol 2. Inference and Relationship*, 3rd Edn. New York, NY: Hafner.

Kohler, K. E., and Gill, S. M. (2006). Coral point count with excel extensions (CPCe): a visual basic program for the determination of coral and substrate coverage using random point count methodology. *Comput. Geosci.* 32, 1259–1269. doi: 10.1016/j.cageo.2005.11.009

Krebs, J. R., Erichsen, J. T., Webber, M. I., and Charnov, E. L. (1977). Optimal prey selection in the great tit (*Parus major*). *Anim. Behav.* 25, 30–38. doi: 10.1016/0003-3472(77)90064-1

Kreiling, A. K., O'gorman, E. J., Palsson, S., Benhaim, D., Leblanc, C. A., Olafsson, J. S., et al. (2020). Seasonal variation in the invertebrate community and diet of a top fish predator in a thermally stable spring. *Hydrobiologia* 848, 531–545. doi: 10.1007/s10750-020-04409-5

Lamare, M. D., Channon, T., Cornelisen, C., and Clarke, M. (2009). Archival electronic tagging of a predatory sea star: testing a new technique to study movement at the individual level. *J. Exp. Mar. Biol. Ecol.* 373, 1–10. doi: 10.1016/j.jembe.2009.02.010

Lorenzen, S., Gallardo, C., Jara, C., Clasing, E., Pequeño, G., and Moreno, C. A. (1979). *Mariscos y Peces de Importancia Comercial en el SUR DE CHILE*. Valdivia: Universidad Austral de Chile.

Madsen, J. (1956). Asteroidea with a survey of the asteroidea of the Chilean Shelf. *Lunds Univ. Arsskrift. N. F. Avd.* 52, 1–53.

Maier, M. S., Kuriss, A., and Seldes, A. M. (1998). Isolation and structure of glucosylceramides from the starfish *Cosmasterias lurida*. *Lipids* 33, 825–827. doi: 10.1007/s11745-998-0277-8

Maier, M. S., Roccatagliata, A., and Seldes, A. M. (1993). 2 Novel steroidal glycoside sulfates from the starfish *Cosmasterias lurida*. *J. Nat. Prod.* 56, 939–942. doi: 10.1021/np50096a020

Manzur, T., Barahona, M., and Navarrete, S. A. (2010). Ontogenetic changes in habitat use and diet of the sea star Heliasther helianthus on the coast of central Chile. *J. Mar. Biol. Assoc. U.K.* 90, 537–546. doi: 10.1017/s0025315409990786

Manzur, T., and Navarrete, S. A. (2011). Scales of detection and escape of the sea urchin *Tetrapygus niger* in interactions with the predatory sun star *Heliaster helianthus*. *J. Exp. Mar. Biol. Ecol.* 407, 302–308. doi: 10.1016/j.jembe.2011.06.025

Martín, A., Penchaszadeh, P., and Atienza, D. (2001). Densidad y hábitos alimentarios de *Oreaster reticulatus* (Linnaeus, 1758) (Echinodermata,

Asteroidea) en praderas de fanerógamas marinas de Venezuela. *Bol. Instit. Español Oceanogr.* 17, 203–208.

Martinez, N. D. (1993). Effect of scale on food web structure. *Science* 260, 242–243. doi: 10.1126/science.260.5105.242

McClintock, J. B. (1985). Avoidance and escape responses of the Sub-Antarctic limpet *Nacella edgari* (powell) (mollusca, gastropoda) to the sea star *Anasterias perrieri* (smith) (echinodermata, asteroidea). *Polar Biol.* 4, 95–98. doi: 10.1007/bf00442906

McClintock, J. B. (1994). Trophic biology of Antarctic shallow-water echinoderms. *Mar. Ecol. Prog. Ser.* 111, 191–202. doi: 10.3354/meps111191

McClintock, J. B., and Lawrence, J. M. (1985). Characteristics of foraging in the soft bottom benthic starfish *Luidia clathrata* (echinodermata: Asteroidea): prey selectivity, switching behavior, functional responses and movement patterns. *Oecologia* 66, 291–298. doi: 10.1007/bf00379867

Menge, B. A., and Sanford, E. (2013). "Ecological role of sea stars from populations to meta-ecosystems," in *Starfish: Biology and Ecology of the Asteroidea*, ed. J. M. Lawrence (Baltimore: Johns Hopkins University Press), 67–80.

Menge, J. L., and Menge, B. A. (1974). Role of resource allocation, aggression and spatial heterogeneity in coexistence of two competing intertidal starfish. *Ecol. Monogr.* 44, 189–209. doi: 10.2307/1942311

Mironov, A. N., Dilman, A. B., Vladychenskaya, I. P., and Petrov, N. B. (2016). Adaptive strategy of the Porcellanasterid sea stars. *Biol. Bull.* 43, 503–516. doi: 10.1134/s106235901606011x

Motti, C. A., Bose, U., Roberts, R. E., Mcdougall, C., Smith, M. K., Hall, M. R., et al. (2018). Chemical ecology of chemosensation in asteroidea: insights towards management strategies of pest species. *J. Chem. Ecol.* 44, 147–177. doi: 10.1007/s10886-018-0926-4

Mutschke, E., and Mah, C. (2009). "Asteroidea-starfish," in *Marine Benthic Fauna of Chilean Patagonia. Santiago*, eds V. Häussermann and G. Fösterra (Cham: Springer), 802–830.

Navarrete, S. A., and Manzur, T. (2008). Individual and population level responses of a keystone predator to geographic variation in prey. *Ecology* 89, 2005–2018. doi: 10.1890/07-1231.1

Ostfeld, R. S. (1982). Foraging strategies and prey switching in the California sea otter. *Oecologia* 53, 170–178. doi: 10.1007/bf00545660

Paine, R. T. (1966). Food web complexity and species diversity. *Am. Nat.* 100, 65–87. doi: 10.1086/282400

Paine, R. T. (1969). A note on trophic complexity and community stability. *Am. Nat.* 103, 91–104. doi: 10.1086/282586

Paine, R. T. (1976). Size-limited predation: an observational and experimental approach with the mytilus-pisaster interaction. *Ecology* 57, 858–873. doi: 10.2307/1941053

Paine, R. T., Castilla, J. C., and Cancino, J. (1985). Perturbation and recovery patterns of starfish dominated intertidal assemblages in Chile, New Zealand and Washington State. *Am. Nat.* 125, 679–691. doi: 10.1086/284371

Pastor-de-Ward, C. T., Rubilar, T., Díaz-De-Vivar, M. E., Gonzalez-Pisani, X., Zarate, E., Kroeck, M., et al. (2007). Reproductive biology of *Cosmasterias lurida* (Echinodermata: Asteroidea) an anthropogenically influenced substratum from Golfo Nuevo, Northern Patagonia (Argentina). *Mar. Biol.* 151, 205–217. doi: 10.1007/s00227-006-0479-x

Pearre, S. (1982). Estimating prey preference by predators: uses of various indices, and a proposal of another based on X2. *Can. J. Fish. Aquat. Sci.* 39, 914–923. doi: 10.1139/f82-122

Pérez-Matuz, A., Ospina-Alvarez, A., Camus, P. A., Carrasco, S. A., Fernandez, M., Gelcich, S., et al. (2017). Temperate rocky subtidal reef community reveals human impacts across the entire food web. *Mar. Ecol. Prog. Ser.* 567, 1–16. doi: 10.3354/meps12057

Pratchett, M. S. (2007). Feeding preferences of *Acanthaster planci* (Echinodermata: Asteroidea) under controlled conditions of food availability. *Pac. Sci.* 61, 113–120. doi: 10.1353/psc.2007.0011

R Development Core Team (2020). *R: A Language and Environment for Statistical Computing*. Vienna: R Foundation for Statistical Computing.

Rettig, J. E., and Smith, G. R. (2021). Relative strength of top-down effects of an invasive fish and bottom-up effects of nutrient addition in a simple aquatic food web. *Environ. Sci. Pollut. Res. Int.* 28, 5845–5853. doi: 10.1007/s11356-020-10933-7

Roccatagliata, A. J., Maier, M. S., Seldes, A. M., Iorizzi, M., and Minale, L. (1994). Starfish saponins .2. Steroidal oligoglycosides from the starfish *Cosmasterias lurida*. *J. Nat. Product.* 57, 747–754. doi: 10.1021/np50108a010

Rochette, R., Hamel, J.-F., and Himmelman, J. H. (1994). Foraging strategy of the asteroid *Leptasterias polaris*: role of prey odors, current and feeding status. *Mar. Ecol. Prog. Ser.* 106, 93–100. doi: 10.3354/meps106093

Ross, D. J., Johnson, C. R., and Hewitt, C. L. (2003). Variability in the impact of an introduced predator (*Asterias amurensis* : Asteroidea) on soft-sediment assemblages. *J. Exp. Mar. Biol. Ecol.* 288, 257–278. doi: 10.1016/s0022-0981(03)00022-4

Saier, B. (2001). Direct and indirect effects of seastars *Asterias rubens* on mussel beds (*Mytilus edulis*) in the Wadden Sea. *J. Sea Res.* 46, 29–42. doi: 10.1016/s1385-1101(01)00067-3

Salguero, B. M. L., and Bonilla, H. R. (2010). Estructura comunitaria y trófica de las estrellas de mar (Echinodermata; Asteroidea) en arrecifes rocosos de Loreto, Golfo de California, México. *Hidrobiológica* 20, 127–134.

San-Martin, A., Rovirosa, J., Gaete, K., Olea, A., and Ampuero, J. (2009). Mantle defensive response of marine pulmonate *Trimusculus peruvianus*. *J. Exp. Mar. Biol. Ecol.* 376, 43–47. doi: 10.1016/j.jembe.2009.06.005

Schejter, L., Bremec, C. S., and Hernandez, D. (2008). Comparison between disturbed and undisturbed areas of the Patagonian scallop (*Zygochlamys patagonica*) fishing ground "Reclutas" in the Argentine Sea. *J. Sea Res.* 60, 193–200. doi: 10.1016/j.seares.2008.04.007

Schories, D., and Niedzwiedz, G. (2012). Precision, accuracy, and application of diver-towed underwater GPS receivers. *Environ. Monit. Assess.* 184, 2359–2372. doi: 10.1007/s10661-011-2122-7

Seldes, A. M., and Gros, E. G. (1985). Main sterols from the starfish *Comasterias lurida*. *Comp. Biochem. Physiol. Part B Comp. Biochem.* 80, 337–339. doi: 10.1016/0305-0491(85)90215-9

Sih, A., Crowley, P., Mcpeek, M., Petranka, J., and Strohmeier, K. (1985). Predation, competition and prey communities: a review of field experiments. *Annu. Rev. Ecol. Syst.* 16, 269–311. doi: 10.1146/annurev.es.16.110185.001413

Singer, M. C. (2000). Reducing ambiguity in describing plant - insect interactions: "Preference", "acceptability" and "electivity". *Ecol. Lett.* 3, 159–162. doi: 10.1046/j.1461-0248.2000.00136.x

Skein, L., Robinson, T. B., and Alexander, M. E. (2018). Impacts of mussel invasions on the prey preference of two native predators. *Behav. Ecol.* 29, 353–359. doi: 10.1093/beheco/arx172

Solís, I. U., and Lozada, E. L. (1971). Algunos aspectos biológicos de la cholga de Magallanes Aulacomya ater Molina. *Biol. Pesquera* 5, 109–144.

Soto-Mardones, L., Letelier, J., Salinas, S., Pinillas, E., and Belmar, J. P. (2009). Analysis of oceanographic and atmospheric parameters of Seno de Reloncaví. *Gayana* 73, 141–155.

Tokeshi, M. (1991). Extraoral and intraoral feeding: flexible foraging tactics in South American sun-star, *Heliaster helianthus*. *J. Zool.* 225, 439–447. doi: 10.1111/j.1469-7998.1991.tb03827.x

Tokeshi, M., and Romero, L. (1995). Quantitative analysis of foraging behaviour in a field popolation of the South American sun-star *Heliaster helianthus*. *Mar. Biol.* 122, 297–303.

Underwood, A. J., Chapman, M. G., and Crowe, T. P. (2004). Identifying and understanding ecological preferences for habitat or prey. *J. Exp. Mar. Biol. Ecol.* 300, 161–187. doi: 10.1016/j.jembe.2003.12.006

Urriago, J. D., Himmelman, J. H., and Gaymer, C. F. (2011). Responses of the black sea urchin *Tetrapygus niger* to its sea star predators *Heliaster helianthus* and *Meyenaster gelatinosus* under field conditions. *J. Exp. Mar. Biol. Ecol.* 399, 17–24. doi: 10.1016/j.jembe.2011.01.004

Urriago, J. D., Himmelman, J. H., and Gaymer, C. F. (2012). Sea urchin *Tetrapygus niger* distribution on elevated surfaces represents a strategy for avoiding predatory sea stars. *Mar. Ecol. Prog. Ser.* 444, 85–95. doi: 10.3354/meps09396

Vásquez, J. A., and Castilla, J. C. (1984). Some aspects of the biology and trophic range of *Cosmasterias lurida* (Asteroidea, Asteriinae) in belts of *Macrocystis pyrifera* at Puerto Toro, Chile. *Ambientes Acuaticos* 7, 47–51.

Verling, E., Crook, A. C., Barnes, D. K. A., and Harrison, S. S. C. (2003). Structural dynamics of a sea star (*Marthasterias glacialis*) population. *J. Mar. Biol. Assoc. U.K.* 83, 583–592. doi: 10.1017/s0025315403007513h

Wang, T. W., Chan, T. Y., and Chan, B. K. K. (2014). Trophic relationships of hydrothermal vent and non-vent communities in the upper sublittoral and upper bathyal zones off Kueishan Island, Taiwan: a combined morphological, gut content analysis and stable isotope approach. *Mar. Biol.* 161, 2447–2463. doi: 10.1007/s00227-014-2479-6

Zagal, C., Hermosilla, C., and Riedemann, A. (2001). *Guía de Invertebrados Marinos del Litoral Valdiviano*. Chile: Santiago de Chile.

Zenteno, L., Cardenas, L., Valdivia, N., Gomez, I., Hofer, J., Garrido, I., et al. (2019). Unraveling the multiple bottom-up supplies of an Antarctic nearshore benthic community. *Prog. Oceanogr.* 174, 55–63. doi: 10.1016/j.pocean.2018.10.016

Conflict of Interest: DS was employed by the Universidad Austral de Chile during the time the field data for this research was collected. DS is employed by DLR Project Management Agency.

The remaining authors declare that the research was conducted in the absence of any commercial or financial relationships that could be construed as a potential conflict of interest.

frontiers in Marine Science

ORIGINAL RESEARCH
published: 09 April 2021
doi: 10.3389/fmars.2021.612386

Seasonal Changes in Dissolved Organic Matter Composition in a Patagonian Fjord Affected by Glacier Melt Inputs

Matthew G. Marshall[1], Anne M. Kellerman[2], Jemma L. Wadham[1,3], Jon R. Hawkings[2,4], Giovanni Daneri[5], Rodrigo Torres[5], Helena V. Pryer[1], Alexander Beaton[6], Hong Chin Ng[7], Alejandra Urra[8], Laura F. Robinson[7] and Robert G. M. Spencer[2]*

[1] Bristol Glaciology Centre, School of Geographical Sciences, University of Bristol, Bristol, United Kingdom, [2] Geochemistry Group, National High Magnetic Field Laboratory, Department of Earth, Ocean and Atmospheric Science, Florida State University, Tallahassee, FL, United States, [3] Centre for Arctic Gas Hydrate, Environment and Climate, Department of Geosciences, UiT The Arctic University of Norway, Tromsø, Norway, [4] German Research Centre for Geosciences GFZ, Potsdam, Germany, [5] Centro de Investigación en Ecosistemas de la Patagonia, Coyhaique, Chile, [6] Ocean Technology and Engineering Group, National Oceanography Centre, Southampton, United Kingdom, [7] School of Earth Sciences, University of Bristol, Bristol, United Kingdom, [8] Centro de Estudios Científicos, Valdivia, Chile

OPEN ACCESS

Edited by:
Angel Borja, Technological Center Expert in Marine and Food Innovation (AZTI), Spain

Reviewed by:
Tzong-Yueh Chen, National Taiwan Ocean University, Taiwan
J. German Rodriguez, Technological Center Expert in Marine and Food Innovation (AZTI), Spain

***Correspondence:**
Matthew G. Marshall
mm5876@bristol.ac.uk

Specialty section:
This article was submitted to Marine Ecosystem Ecology, a section of the journal Frontiers in Marine Science

Received: *30 September 2020*
Accepted: *04 March 2021*
Published: *09 April 2021*

Citation:
Marshall MG, Kellerman AM, Wadham JL, Hawkings JR, Daneri G, Torres R, Pryer HV, Beaton A, Ng HC, Urra A, Robinson LF and Spencer RGM (2021) Seasonal Changes in Dissolved Organic Matter Composition in a Patagonian Fjord Affected by Glacier Melt Inputs. Front. Mar. Sci. 8:612386. doi: 10.3389/fmars.2021.612386

Biogeochemical processes in fjords are likely affected by changes in surrounding glacier cover but very little is known about how meltwater directly influences dissolved organic matter (DOM) in fjords. Moreover, the data available are restricted to a handful of northern hemisphere sites. Here we analyze seasonal and spatial variation in dissolved organic carbon (DOC) concentration and DOM composition (spectrofluorescence, ultrahigh resolution mass spectrometry) in Baker-Martinez Fjord, Chilean Patagonia (48°S), to infer the impacts of rapid regional deglaciation on fjord DOM. We show that surface layer DOC concentrations do not vary significantly between seasons, but DOM composition is sensitive to differences in riverine inputs. In summer, higher protein-like fluorescence reflects increased glacial meltwater inputs, whilst molecular level data show weaker influence from marine DOM due to more intense stratification. We postulate that the shifting seasonal balance of riverine and marine waters affects the supply of biolabile peptides and organic nitrogen cycling in the surface layer. Trends in DOM composition with increasing salinity are consistent with patterns in estuaries (i.e. preferential removal of aromatic compounds and increasing relative contribution of unsaturated and heteroatom-rich DOM from marine sources). Preliminary estimates also suggest that at least 10% of the annual organic carbon stock in this fjord is supplied by the four largest, glacially fed rivers and that these inputs are dominated by dissolved (84%) over particulate organic carbon. Riverine DOC may therefore be an important carbon subsidy to bacterial communities in the inner fjord. The overall findings highlight the biogeochemical sensitivity of a Patagonian fjord to changes in glacier melt input, which likely has relevance for other glaciated fjords in a warming climate.

Keywords: dissolved organic matter, Chilean Patagonia, FT-ICR MS, glacier melt, fjord biogeochemistry

INTRODUCTION

Fjords are critical zones of fresh and marine water interaction (e.g., Bianchi et al., 2020), which support hotspots of ecological productivity (e.g., Iriarte et al., 2007) and important carbon sinks (e.g., Smith et al., 2015) in the mid- to high-latitudes. The biogeochemistry of fjords is thought sensitive to the effects of climate change, especially where the enhanced melting and long-term retreat of glaciers will lead to changes in the timing, magnitude and composition of freshwater inputs (Cuevas et al., 2019; Saldías et al., 2019). The impact of glacial meltwaters on fjord nutrient cycles has attracted much interest in recent years (Hawkings et al., 2014, 2016; Hopwood et al., 2020). However, we know very little about the direct influence of glaciers on dissolved organic matter (DOM) in fjords, especially beyond the effects on overall biolability and the fluorescent fraction (Paulsen et al., 2017, 2018). Focused analysis of the wider DOM pool via molecular methods, as offered by this study, can help to improve our understanding of how carbon cycling in fjords might be affected by accelerated glacier melting and eventual landscape deglaciation.

Dissolved organic matter is an important phase in the aquatic biogeochemical cycles of carbon and major nutrients (e.g., Burd et al., 2016) and its overall reactivity is strongly linked to its composition (Amon and Benner, 1994; Sun et al., 1997; Hopkinson et al., 1998; Mostovaya et al., 2017). In coastal waters, DOM comprises a complex mixture of material from marine and terrestrial sources, modified through biological and photochemical degradation (Hernes and Benner, 2003; Spencer et al., 2009; Ward et al., 2017) and physico-chemical removal mechanisms (Sholkovitz, 1976; Eisma, 1986; Keil et al., 1994; Aufdenkampe et al., 2001). Changes in the source and supply of DOM will have a profound effect on its composition, its role as an energy source to heterotrophic bacteria and its pathway through aquatic ecosystems (Pace et al., 2004; Welti et al., 2017). DOM cycling in fjords is therefore sensitive to major changes in the upstream landscape (Asmala et al., 2016; Ward et al., 2017), which is primarily driven by rapid rates of glacier retreat in large regions of the higher latitudes (Zemp et al., 2015).

Enhanced glacier melting will likely increase the supply of reactive DOM to fjords in the short term (Milner et al., 2017). This hypothesis rests upon evidence from bioincubation studies which show that DOM in glacial meltwaters is protein-rich, highly bioavailable and easily respired by downstream heterotrophs (Hood et al., 2009; Fellman et al., 2010; Singer et al., 2012; Lawson et al., 2014; Hemingway et al., 2019). Although few studies have directly assessed the impact in fjords, data from Young Sound, Greenland, suggest that glacial DOM may support offshore bacteria even when other sources of organic matter are more plentiful (Paulsen et al., 2017, 2018). Moreover, the incorporation of glacial organic carbon into the biomass of higher organisms in land-based systems highlights a potential to support complex food webs in fjords (Hågvar and Ohlson, 2013; Fellman et al., 2015). The supply of biolabile DOM in meltwaters will decline as glaciers recede in the long term and more stable terrestrial organic matter is mobilized from expanding proglacial zones (Milner et al., 2017; Paulsen et al., 2017; Hemingway et al., 2019). However, more detailed analysis of DOM composition in glacially influenced fjords is needed to better understand its sensitivity to predicted changes in meltwater supply and the overall impact on fjord biogeochemistry.

The formation of DOM by primary production in fjords is also sensitive to changing glacier influences. For example, marine-terminating glaciers can sustain highly productive ecosystems via hydrodynamic controls on nutrient supply (Meire et al., 2017). Upwellings of deeper nutrient-rich waters, which stimulate primary productivity at the surface, might shut down when submarine meltwater discharge ceases as glaciers retreat onto land (Hopwood et al., 2018). Primary productivity is limited further by reduced light transmission through the water column as turbid meltwaters get redirected to the fjord surface (Aracena et al., 2011). Under such conditions, DOM derived from glacial and terrestrial sources may play a greater role in carbon cycling by microbial food webs at the heads of the fjords (González et al., 2013).

Chilean Patagonia contains an extensive network of fjords that are fed by rivers draining near-pristine catchments with variable glacier cover (Pantoja et al., 2011). The region contains the largest volume of land ice in the southern hemisphere outside Antarctica (Millan et al., 2019), concentrated in two major icefields which are melting rapidly (Glasser et al., 2011; Foresta et al., 2018). Accelerated melting is increasing freshwater flux to the coast in this region (Dussaillant et al., 2019), with implications for fjord hydrodynamics and the supply of organic matter (Iriarte et al., 2014). Freshwater flux is driven primarily by summertime melting but, in contrast to fjords in polar regions, heavy precipitation sustains year-round freshwater inputs and above-freezing sea level temperatures support a more limited amount of glacial melting in winter (Rebolledo et al., 2019). Understanding how fjord DOM composition responds to seasonal changes in freshwater source (intense glacial melting in summer and heavier precipitation in winter) is relevant for glacially influenced fjords in other wet, maritime locations, such as New Zealand and the Gulf of Alaska, contrasting with polar fjords where freshwater inputs are driven almost exclusively by melt cycles.

Here we present DOC concentration and detailed DOM composition data (determined via fluorescence analysis and ultrahigh resolution mass spectrometry) from the heavily glaciated Baker-Martinez Fjord (BMF) in Chilean Patagonia. We compare summer and winter DOM composition in the surface layer to subsurface conditions across seasons within a single year to infer changes in DOM source and in-fjord processing within the context of changing glacier melt inputs. We apply molecular level techniques that have advanced understanding of DOM in temperate estuarine settings (Osterholz et al., 2016; Seidel et al., 2017) to enhance the interpretation of fjord DOM beyond the relatively small fluorescent fraction, which has been the focus of the few studies in glaciated fjords so far (Paulsen et al., 2018). We aim to: (i) assess the impact of glacier melt inputs on fjord DOM composition by comparing summer (high melt) and winter (low melt) conditions; (ii) examine variations in DOM molecular composition along the salinity gradient to elucidate

environmental controls and infer biogeochemical processes; and (iii) conduct a preliminary assessment of the relative importance of riverine inputs to the organic matter pool in the BMF.

MATERIALS AND METHODS

Study Region

The BMF is situated between the Northern and Southern Patagonian Icefields (NPI, SPI) at ∼48°S (**Figure 1**) and consists of two largely disconnected sub-basins: the northerly Martinez Channel (typically < 500 m deep) and the deeper (up to ∼1075 m) Baker Channel to the south (Piret et al., 2019). Strong freshwater inputs from several glacier-fed rivers and high annual rainfall maintain a stratified water column typical of fjords, with a freshwater lens sitting above higher salinity waters (Rebolledo et al., 2019). Vertical exchange between the two layers is largely controlled by semidiurnal tides (Ross et al., 2014), whilst the prevailing westerly winds drive the general circulation patterns in the fjord (Aiken, 2012), such as subsurface warm water intrusions from Baker Channel into Jorge Montt Fjord (Moffat, 2014). Freshwater inputs peak with river discharge in the austral summer (December-March) due to seasonal glacier melting rather than with maximum rainfall in the austral winter (May-August) (Rebolledo et al., 2019). The regimes of the largest rivers, the Baker and Pascua, are dominated by melting of the NPI and SPI, respectively (Dirección General de Aguas, 2019). Discharge from the Huemules River, driven primarily by melting of Steffen Glacier, NPI, and direct meltwater inputs from Jorge Montt Glacier, SPI, are not well quantified at present. The Bravo River, at the head of Mitchell Fjord, is less influenced by meltwaters from smaller mountain glaciers. Strong turbid meltwater inputs lead to light limitation and relatively low levels of primary productivity in BMF (49–840 mg C m^{-2} d^{-1}), when compared to Chilean fjords between 44 and 47°S (1667–2616 mg C m^{-2} d^{-1}), where glacial cover and meltwater inputs are much lower (Aracena et al., 2011; González et al., 2011; Jacob et al., 2014).

Sampling

Fjord water samples were collected during research cruises in the austral summer (16–23 February) and winter (4–9 July) of 2017. A RBRmaestro or RBRconcerto CTD was deployed from the *RV Sur Austral* to obtain water column profiles of temperature, salinity, turbidity and chlorophyll fluorescence at each station (**Figure 1**). Water was sampled from selected depths (approximately 1, 5, 50, 150, and 250 m as water depth and conditions allowed) using a standard 10 L Niskin bottle or a 10 L Go-Flo bottle (General Oceanics). Where logistically possible, the same stations were revisited in winter to capture seasonal differences. Exceptions include the summer stations in Jorge Montt Fjord (S12 and S13) where floating ice mélange restricted access in winter to one alternative site (S20), and an additional winter station near the mouth of the Baker Channel (S21) which could not be accessed in summer due to rough conditions. An underway sampling system, comprising a Teflon diaphragm pump and custom-made epoxy coated "torpedo" (towfish) that extended 2 m from the side of the ship was deployed during passage between stations to capture variations in the surface layer (∼1.5 m depth) at higher spatial resolution.

River samples were collected from the Baker River (in summer; **Figure 1** site D) and rivers in the Huemules valley (both seasons; **Figure 1** sites A-C) during complementary land-based sampling campaigns. Samples were collected from the mouth of the Baker in winter (**Figure 1**, site D) and the Bravo (**Figure 1**, site E) and Pascua (**Figure 1**, site F) rivers in both seasons during the fjord surveys. Although the Baker, Bravo and Pascua rivers were sampled only once per season, collectively these samples establish a baseline of DOM composition from the major rivers emptying into the BMF.

Analytical Methods

Dissolved Organic Carbon (DOC) and Nutrient Concentrations

Samples for DOC measurement were filtered to 0.45 μm using either Whatman® Polycap GW PES filter capsules (fjord surface samples), Geotech Versapor filter capsules (fjord subsurface samples) or Whatman® Puradisc AQUA syringe filters (river samples) and stored frozen in acid-clean HDPE bottles (Nalgene®). DOC concentrations were determined for all fresh and marine water samples on a Shimadzu TOC-L_{CHN} analyzer equipped with the saline sample kit (e.g., Kellerman et al., 2020). The limits of detection (LoD = LoB + [1.645 × SD of low concentration sample]; where LoB = limit of blank) and quantification (LoQ = LoB + [5 × SD of low concentration sample]) were calculated as 2.7 μM and 3.7 μM, respectively (Armbruster and Pry, 2008). Repeat measurement of a 40 μM standard varied by <±5%.

Samples for dissolved nutrient analysis were filtered to 0.45 μm using either Whatman® Polycap GW PES filter capsules (fjord surface sample) or Whatman® GD/XP dpPP syringe filters (river samples/fjord samples at depth) and stored frozen in acid-clean HDPE bottles (Nalgene®). Concentrations of ammonium (NH_4^+), nitrate (NO_3^-), nitrite (NO_2^-), total dissolved nitrogen (TDN), dissolved organic nitrogen (DON), and soluble reactive phosphorus (SRP; PO_4^{3-}) were measured on a LaChat QuikChem® 8500 series 2 flow injection analyzer using established colorimetric methods, with matrix matched standards (e.g., Hawkings et al., 2015). DON concentrations were taken as the difference between TDN, measured following an alkaline persulfate/UV digestion at 120°C to convert all DON to NO_3^- (Hosomi and Sudo, 1986) with alterations for saline samples, and the sum of inorganic nitrogen forms (NH_4^+ + NO_3^- + NO_2^-) measured prior to digestion. Digest efficiency was checked with organic N spiked samples and standards. LoDs were 0.10 μM, 0.07 μM, and 0.03 μM for DON, NO_3 and SRP, respectively, with a precision <±5% for NO_3 and SRP and <±15% for DON.

DOM Fluorescence Analysis

Dissolved organic matter samples for fluorescence analysis were collected in the same way as for DOC concentration. Excitation-emission matrices (EEMs) were collected on an Agilent Cary Eclipse Fluorescence Spectrophotometer with xenon flash bulb. Scans were conducted in 10 mm quartz cuvettes over excitation wavelengths 240–450 nm at 5 nm intervals and emission

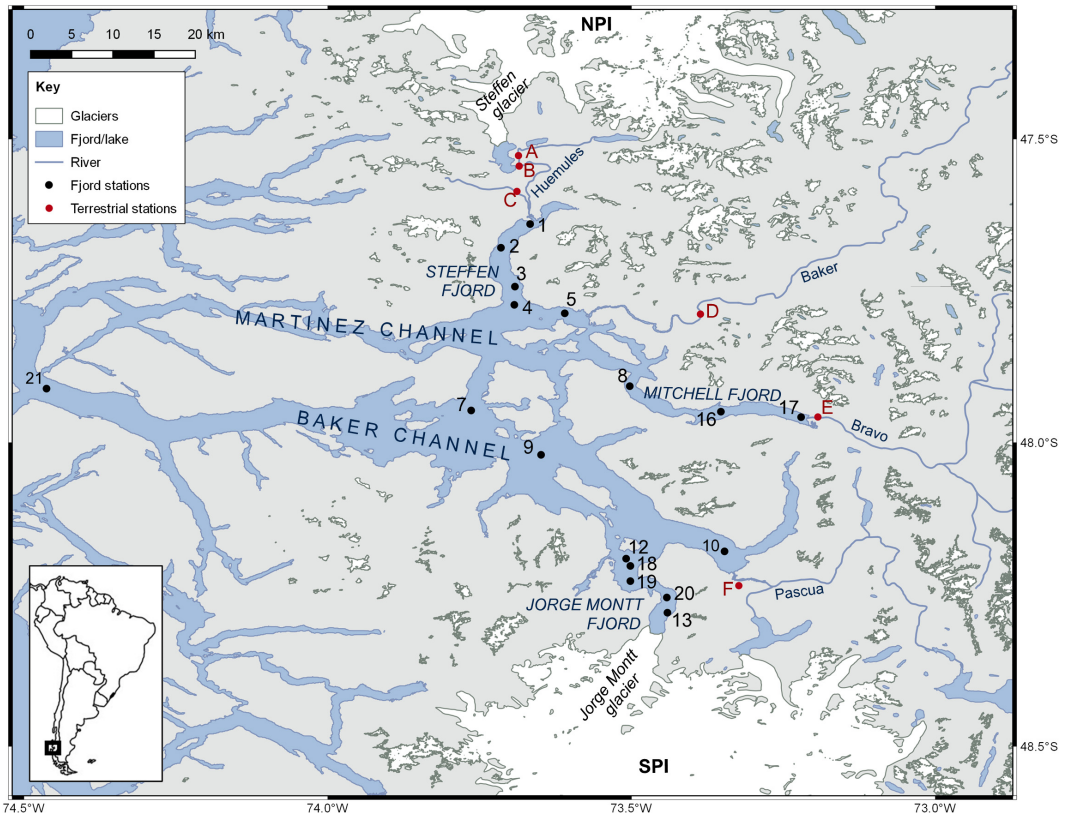

FIGURE 1 | Location of sampling stations (1–21) in Baker-Martinez Fjord and on the tributary rivers (A–F).

wavelengths 300–600 nm at 2 nm intervals, using 5 nm monochromator slit widths and 0.1 s integrations. All EEMs were corrected for instrumental biases and Raman/Rayleigh scatter prior to subsequent analysis (Murphy et al., 2013).

Ultrahigh Resolution Mass Spectrometry

Large volume (1 L) samples were filtered through either PES capsule filters (0.45 μm; as above for fjord surface samples) or pre-combusted (450°C, 5 h) GF/Fs (nominally 0.7 μm; all Steffen valley, summer Baker River and fjord water column samples) into pre-cleaned polycarbonate bottles (10% HCl for 24 h followed by copious rinsing with 18.2 MΩ cm^{-1} ultra-pure water) and acidified to pH ∼2 with analytical grade HCl. Filtered samples were solid phase extracted (SPE) onto 200 mg Varian Bond Elut PPL cartridges following established protocols (Dittmar et al., 2008). Based on DOC measurements for each sample, the SPE-DOM was eluted with methanol to obtain a target concentration of ∼60 μg C ml^{-1}.

Analyses were conducted on a custom built 21 tesla Fourier transform ion cyclotron resonance mass spectrometer (FT-ICR MS) at the National High Magnetic Field Laboratory (NHMFL) (Smith et al., 2018). Samples were introduced via electrospray ionization (2.6–3.2 kV) at a rate of 600 nl min^{-1} and analyzed in negative ion mode. Mass spectra for each sample were derived from 100 coadded scans and calibrated against known *m/z* values using Predator software (NHMFL). Formulae were assigned to all peaks with mass calibration errors < 500 ppb and intensities 6 times greater than the RMS signal to noise ratio plus baseline (PetroOrg software, Florida State University) using stoichiometric combinations within the range of $C_{1-45}H_{1-92}N_{0-4}O_{1-25}S_{0-2}$. All assigned formulae were categorized into compound groups based on elemental ratios and values of the modified aromaticity index (AI_{mod}; Koch and Dittmar, 2006) using the following classification scheme: condensed aromatics (CA; $AI_{mod} > 0.66$); polyphenolics (PP; $0.66 \geq AI_{mod} > 0.5$); highly unsaturated and phenolic (HUP; $AI_{mod} \leq 0.5$; H/C < 1.5); aliphatic ($2 \geq H/C \geq 1.5$; $N = 0$); peptide-like ($2 \geq H/C \geq 1.5$; $N > 0$) and sugar-like (H/C > 1.5; O/C > 0.9) (Kellerman et al., 2018). Further subdivisions include low and high O/C ratios (<0.5 or >0.5) for HUPs and aliphatics.

Particulate Organic Carbon Concentrations

Particulate organic carbon (POC) concentrations were measured from large volume (1–3 L) grab samples collected from each of the four largest tributary rivers entering the BMF. POC samples were not collected at fjord stations. Particles were retained on pre-combusted (450°C, 5 h) GF/F filters (Whatman®), which were then dried and analyzed directly through high temperature (1000°C) catalytic combustion on a Thermo Electron Flash Elemental Analyzer 1110. Organic carbon (OC) content was determined following removal of inorganic carbon by acidification (Hedges and Stern, 1984). All samples

were corrected for the filter blank, assessed as 0.03 ± 0.01% for total carbon (TC) and 0.02 ± 0.01% for OC (n = 10). The % OC content was converted to POC concentration using the suspended sediment concentration (SSC), which was determined as the mass of dry sediment retained on pre-weighed membrane filters from a known volume of water (∼300 ml).

Flux Calculations

We estimate the magnitudes of DOC and POC fluxes from the four principal rivers as cumulative annual discharge multiplied by mean DOC or POC concentrations. Annual discharge for the Baker and Pascua rivers is well constrained by long-term records from the Chilean Water Authority (Dirección General de Aguas, 2019). We also make use of the first discharge data for the Huemules River, derived from a stage-discharge rating curve (r^2 = 0.97; RMSE < ±9%) based on pressure sensor readings from a stable bedrock position within the river and 14 Rhodamine wt dye injection traces over the austral summer and winter in 2017 (Bartholomew et al., 2011). Only an estimate of the average annual discharge of the Bravo River was available (Aracena et al., 2011).

Statistical Methods

Multi-way DOM fluorescence data was decomposed into separate components using parallel factor (PARAFAC) analysis with the drEEM Toolbox for MATLAB (Murphy et al., 2013). The dataset contained 407 EEMs, including samples from the BMF (n = 129), its tributary rivers (n = 102) and additional freshwater and marine bodies (n = 176) from the broader study region (42–48°S). A seven-component PARAFAC model, which explained >98.6% of variance across all samples, was found to fit the data best following inspection of residuals and use of split-half validation. All model components matched components in the OpenFluor database (Murphy et al., 2014).

All other statistical tests were performed in R (R Core Team, 2015). Non-parametric Mann Whitney tests (for unpaired, non-normally distributed data) were used to assess the significance of seasonal differences in water column structure, bulk geochemistry and FT-ICR MS data at the compound category level. Mann Whitney tests were also used to test differences between the fjord surface and subsurface layers. Molecular level relationships with water column properties and season were tested using Spearman rank correlations between the relative intensities of individual formulae present in all fjord samples and CTD data; correlations with season were tested by means of a dummy variable (i.e., summer = 0; winter = 1). Raw p-values < 0.028 for these correlations were deemed significant at the 95% confidence interval following a false discovery rate correction (Benjamini and Hochberg, 1995), which minimizes the number of false positive (Type I) errors arising from the large number of tests for ∼18,000 formulae. The relationships between salinity variations and FT-ICR MS relative intensities for major compound categories were also assessed using Spearman rank correlation tests.

Principal Components Analysis (PCA) was applied to a dataset comprising normalized FT-ICR MS compound category relative intensities (%) and PARAFAC fluorescence loadings (%) for each fjord sample, to assess variation in DOM composition across the fjord samples. All variables were first standardized between 0 and 1 using the *decostand* function in the R vegan package (Oksanen et al., 2016). Multivariate correlations between the ordination (PCA) results and water column properties were assessed by permutation (n = 999) using the *envfit* function (Oksanen et al., 2016).

RESULTS

Seasonality in Fjord Water Column Properties and Chemical Composition

The physical properties of the BMF water column display marked seasonality, with significantly lower salinities (Mann Whitney; $p < 0.001$) and higher turbidity ($p < 0.05$) linked to a thicker ($p < 0.01$) freshwater layer in summer. Surface temperatures are higher in summer ($p < 0.01$) despite strong meltwater input, except near the head of Steffen Fjord (S1 and S2) where winter warming coincides with the largest increase in surface salinity across the study area (**Table 1**).

The chemical composition of the surface layer also varies seasonally. Dissolved nutrients (NO_3, SRP) mostly fall below the analytical LoD in summer but reach detectable concentrations in winter (**Table 1**). This coincides with increased surface chlorophyll concentrations in winter ($p < 0.01$). Nutrient concentrations show limited variability in the surface layer but increase exponentially with salinity, reaching maximum subsurface concentrations of ∼25 μM and ∼2 μM for NO_3 and SRP, respectively. However, nutrient concentrations are highly variable at salinities >25 (**Supplementary Figure 1**).

Surface DOC concentrations are highly variable across the BMF (∼20–200 μM) and seasonal differences (summer = 85.7 ± 41.1 μM; winter = 72.1 ± 33.1 μM; mean ± SD) are not statistically significant (**Figure 2A**). Subsurface DOC is generally less variable (summer = 56.5 ± 8.5 μM; winter = 41.7 ± 4.3 μM) but the seasonal difference is significant ($p < 0.001$). Spatial variations in surface DOC are largely controlled by differences in river inputs (**Supplementary Figures 2a,b**), with the highest concentrations in Mitchell Fjord linked to outflow from the organic-rich Bravo River. The lowest surface DOC concentrations are in Steffen Fjord near the mouth of the Huemules River (**Figure 1** and **Table 1**), which is dominated by glacial meltwater inputs.

Surface DON concentrations are generally low in summer and increase in winter (**Figure 2B**). The difference is only statistically significant ($p < 0.05$) when the Baker and Pascua River plumes (S5 and S10, respectively), which show little seasonal change (**Table 1**), are excluded from the analysis. This suggests that the wintertime increase in fjord surface DON concentrations is not linked to changes in the major rivers. Patterns in Jorge Montt Fjord deviate from the general trend, as surface DON concentrations are higher in summer (3.6 μM at S13, vs. 2.4 μM at S20 in winter; **Table 1**). DON concentrations are highly variable but, in general, are lower at lower salinity (**Figure 2B**). Variation in DON largely controls the N/C molar ratio, which generally increases with salinity, with two high

TABLE 1 | Physical and chemical properties of surface layer and selected subsurface depths at survey stations in Baker-Martinez Fjord in austral summer (February) and austral winter (July) 2017.

Station		Sample depth (m)	Freshwater depth (m)		Salinity		Temperature (°C)		Turbidity (NTU)		Chlorophyll (μg/L)		DOC (μM)		DON (μM)		N/C (molar ratio)		NO_3 (μM)		SRP (μM)	
			Feb	Jul	Feb	Jul	Feb	Jul	Feb	Jul	Feb	Jul	Feb	Jul	Feb	Jul	Feb	Jul	Feb	Jul	Feb	Jul
Surface Lens																						
Martinez Channel & Inlets																						
Steffen Fjord	S1	1	4.2	0.7	1.6	16.4	4.9	6.8	60.0	9.7	0.192	0.975	36.6	21.2	1.1	3.4	0.030	0.161	0.34	3.04	< 0.03	0.39
	S2	1	6.5	4.7	1.3	13.1	4.7	6.2	63.7	11.2	0.235	0.683	49.0	64.8	1.1	5.1	0.023	0.079	0.33	0.57	< 0.03	0.37
	S3	1	7.7	–	1.2	–	7.4	–	59.5	–	0.215	–										
	S4	1	7.6	3.4	1.2	5.6	10.4	5.8	29.1	15.6	0.312	1.066	39.3	64.8	2.4	3.5	0.061	0.054	0.08	1.18	< 0.03	0.12
Baker plume	S5	1	5.0	3.0	0.5	0.7	11.6	5.9	93.5	32.9	0.226	0.484	44.1	61.9	1.9	1.7	0.043	0.028	< 0.07	0.50	< 0.03	0.27
Mitchell Fjord	S17	1	6.0	5.3	0.4	1.9	9.3	3.7	32.0	9.9	0.500	1.005	199.7	188.3	2.9	3.7	0.014	0.020	0.21	0.89	< 0.03	0.03
	S16	1	8.6	5.7	0.6	3.3	12.4	4.0	15.7	12.9	0.567	1.144	130.8	110.1	2.0	3.2	0.015	0.029	< 0.07	1.18	< 0.03	0.26
	S8	1	7.7	4.4	0.9	4.7	13.0	4.4	20.1	10.3	0.394	1.032	128.3	166.8	3.6	5.1	0.028	0.030	< 0.07	0.84	< 0.03	0.10
Baker Channel & Inlets																						
Jorge Montt Fjord	S13	1	8.2	–	2.1	–	4.9	–	3.0	–	0.966	–	60.0	–	3.6	–	0.063	–	< 0.07	–	<0.03	–
	S20	1	–	8.6	–	6.7	–	2.1	–	4.2	–	1.140	–	52.7	–	2.4	–	0.046	–	1.18	–	0.10
	S12	1	8.2	–	2.0	–	7.1	–	4.4	–	0.963	–	60.6	–	3.8	–	0.060	–	< 0.07	–	<0.03	–
Pascua plume	S10	1	5.0	5.5	1.1	5.9	8.8	4.9	30.4	7.4	0.296	0.892	46.0	58.0	2.3	2.2	0.049	0.038	0.53	1.30	0.04	0.20
Central fjord	S7	1	6.8	3.8	0.8	7.2	11.6	5.8	51.2	12.1	0.385	0.795	60.9	95.6	1.9	3.2	0.031	0.033	0.07	1.96	< 0.03	0.30
	S9	1	7.8	6.2	2.5	13.2	11.0	6.3	8.8	2.3	0.652	0.897	77.3	65.3	2.0	2.7	0.026	0.041	< 0.07	2.91	< 0.03	0.28
Outer fjord	S21	1	–	3.1	–	16.0	–	6.4	–	1.1	–	0.972	–	67.2	–	6.9	–	0.103	–	0.83	–	0.44
Subsurface																						
Steffen Fjord	S1	40	–	–	–	31.9	–	11.4	–	0.4	–	0.053	–	41.9	–	7.6	–	0.182	–	8.78	–	1.06
	S4	270	–	–	–	33.9	–	8.2	–	0.5	–	0.035	–	36.7	–	7.5	–	0.204	–	19.06	–	1.92
Baker plume	S5	140	–	–	–	33.7	–	8.9	–	0.7	–	0.044	–	45.9	–	1.6	–	0.036	–	21.13	–	1.72
Mitchell Fjord	S17	130	–	–	–	33.7	–	8.8	–	0.4	–	0.087	–	74.9	–	7.4	–	0.098	–	17.78	–	1.35
Jorge Montt Fjord	S20	30	–	–	–	30.7	–	8.9	–	49.9	–	0.073	–	43.1	–	5.3	–	0.123	–	8.28	–	0.90
	S20	180	–	–	–	31.5	–	10.8	–	0.9	–	0.048	–	47.5	–	7.0	–	0.147	–	5.35	–	0.96
Baker Channel	S9	180	–	–	–	33.8	–	8.4	–	0.2	–	0.021	–	38.8	–	9.0	–	0.233	–	20.56	–	1.76

Subsurface data presented only for depths from which samples were collected for FT-ICR MS analysis in winter.

anomalies at intermediate salinities (~16) in winter samples from near the mouth of the Baker Channel (S21) (**Figure 2C** and **Supplementary Figure 2f**).

Trends in DOM Composition

DOM Fluorescence

The PARAFAC model identified three terrestrial humic-like (C_{498}, C_{452}, C_{446}), one marine humic-like (C_{390}) and three protein-like fluorophores (C_{304}, C_{328}, C_{354} – the latter being tryptophan-like) (**Supplementary Table 1**). Humic-like fluorescence intensity is directly correlated with DOC concentrations but inversely correlated with salinity and N/C ratios (**Figure 3**). The same relationships exist for two protein-like fluorophores (C_{328}, C_{354}) but with weaker correlations (**Figure 3**). The other protein-like component (C_{304}) does not vary systematically with any of these variables (**Figure 3**).

Surface layer fluorescence intensities are similar in both seasons for most PARAFAC components, except for protein-like C_{328} and C_{304}, which are found at significantly lower intensities in winter (Mann Whitney, $p < 0.001$). Generally, fluorescence intensities in the fjord surface layer are similar to the rivers for all components, except C_{304} which has significantly lower intensity in the fjord in winter ($p < 0.05$). Spatial variations in surface layer humic-like fluorescence correspond to DOC concentration patterns and largely reflect compositional variability of riverine inputs (**Supplementary Figures 2a,b**, **3a,b**). Protein-like fluorescence intensity is generally lower but local spikes, which are mostly driven by increases in C_{354} (up to 1.2 R.U.), occur at intermediate salinities (~13) near the mouth of Jorge Montt Fjord, in the upper Martinez Channel and (where data are available in winter only) the mid-Baker Channel (**Supplementary Figures 3c–f**). This suggests potential sources of C_{354} in the fjord. However, summertime intensities of C_{354} are 0.03–0.09 R.U. in the rivers (mean ± SD = 0.05 ± 0.03 R.U., $n = 6$) but this drops to zero in the surface layer of Steffen Fjord (S1, S2, and S4), near the head of Martinez Channel (S5), and in Baker Channel (S7, S9, and S10), suggesting possible consumption of this component.

Molecular Composition

A total of 18,383 unique formulae in the mass range of 175–1000 Da were identified in 26 fjord and 8 river samples of SPE-DOM. Of these, 5,321 (28.9%) were common to all fjord samples and 2,870 (15.6%) were exclusive to the fjord. Only 976 formulae (5.3%) were found exclusively in river samples and these were mostly aliphatic or HUPs. HUPs comprise the bulk of all formulae (72.1 ± 3.1%) and sample intensities (83.7 ± 5.5%), including in the N-containing fraction (78.9 ± 4.5% of formulae and 84.5 ± 6.4% of intensity). The mean relative intensities of other major compound groups listed in descending order were PP (9.6 ± 4.4%), aliphatic (3.6 ± 0.8%), CA (2.5 ± 1.2%), sugar-like (0.3 ± 0.2%), and peptide-like (0.3 ± 0.2%). There were no significant differences between the rivers and the fjord surface layer when comparing formulae counts or relative intensities for each compound category. However, the subsurface waters had higher relative intensities of HUP ($p = 0.001$) and peptide-like ($p < 0.05$) formulae, but lower relative intensities of PP ($p = 0.001$), CA ($p < 0.01$), and sugar-like ($p < 0.01$) formulae than surface waters. The fjord surface layer exhibited an increase in HUP ($p < 0.05$) and decrease in PP ($p < 0.05$) relative intensities from summer to winter.

The molecular composition of fjord DOM displays a marked transition with salinity, reflecting differences in compound group relative intensities between seasons in the surface layer and the subsurface (**Figure 4**). The general relationship shows a decline in more aromatic compounds (PP, CA) and an increase in HUPs with increasing salinity. Aliphatics show no discernible trend with salinity, whereas peptide-like compounds increase with salinity. Correlations between individual formulae and environmental variables confirm that PP and CA compounds are associated with less saline and more turbid conditions — characteristic of the surface layer, where they are relatively more enriched in summer (**Table 2**). The HUP and aliphatic fractions in the surface layer display a shift from more O-rich formulae in summer to more O-poor formulae in winter, with the O-poor formulae more strongly associated with more saline, higher chlorophyll, and less turbid conditions (**Table 2**).

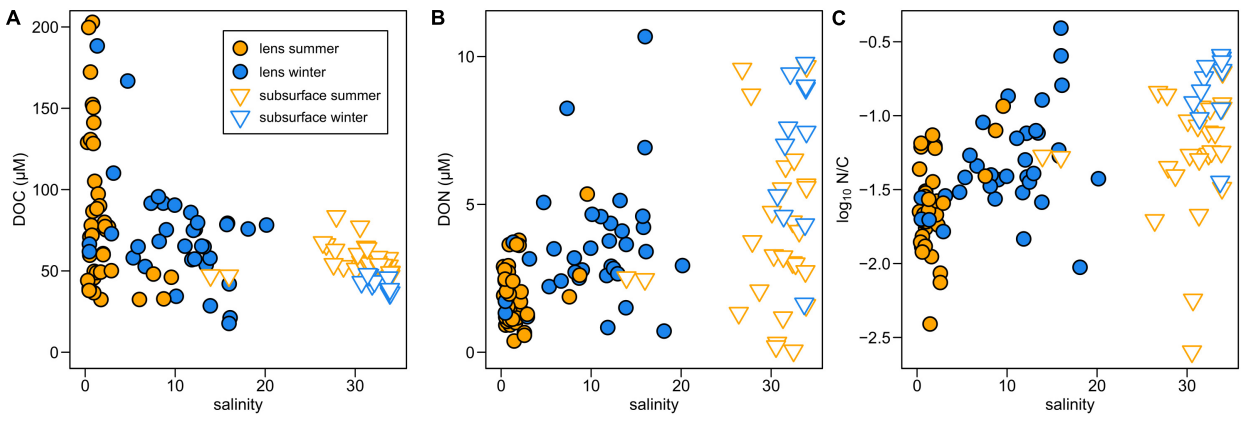

FIGURE 2 | Variations in concentrations of **(A)** DOC, **(B)** DON, and **(C)** the molar N/C ratio (log scale) with salinity in Baker-Martinez Fjord.

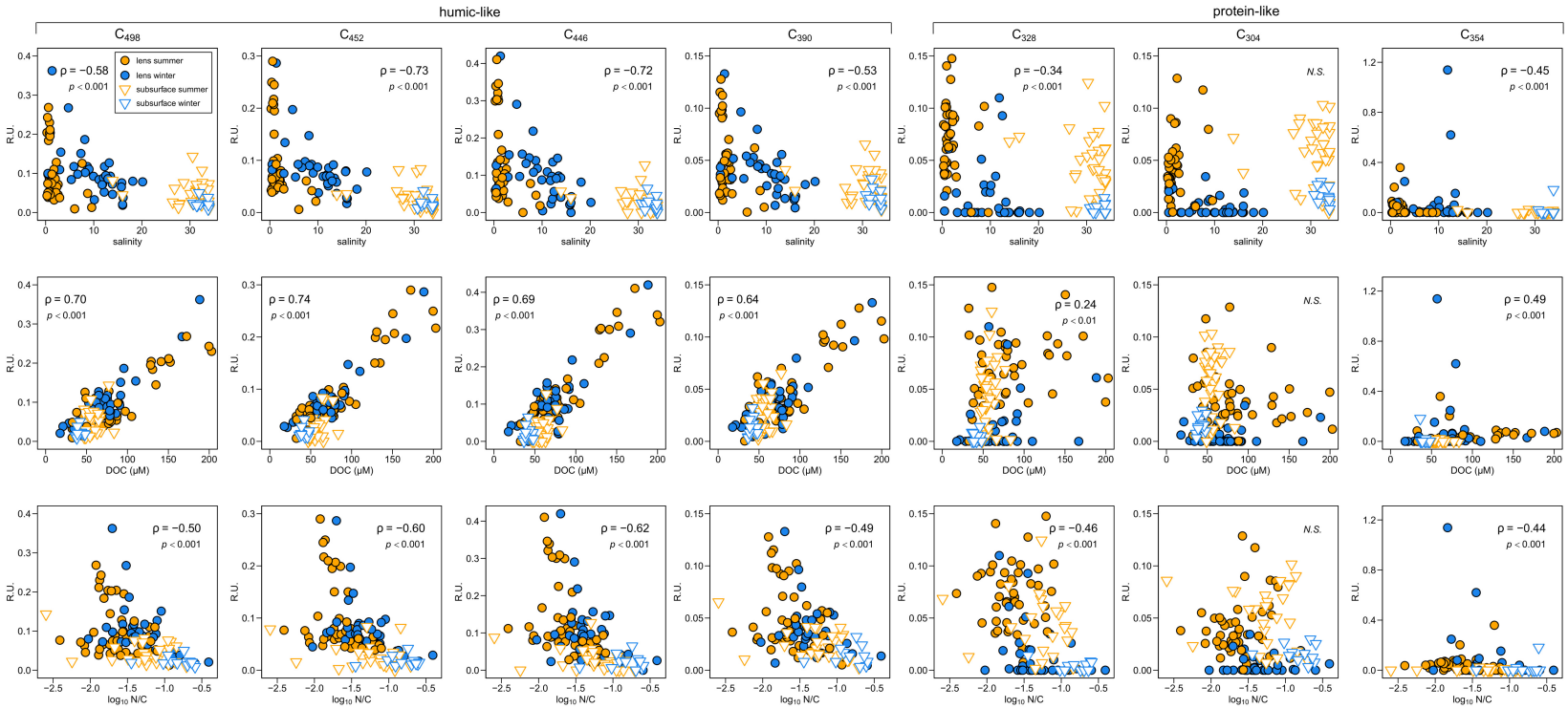

FIGURE 3 | Dissolved organic matter fluorescence intensity variations with respect to salinity (top row), DOC concentration (middle row) and molar N/C ratios (log scale, bottom row) in Baker-Martinez Fjord. Different *y*-axis scales (fluorescence intensity; Raman units) used for each PARAFAC component. Symbol shapes and colors indicate surface/subsurface samples and sampling season, respectively; key in upper left panel. Each sub-panel is annotated with non-parametric correlation coefficient (Spearman's ρ) and *p*-value or "*N.S.*" for non-significant ($p > 0.05$) relationships.

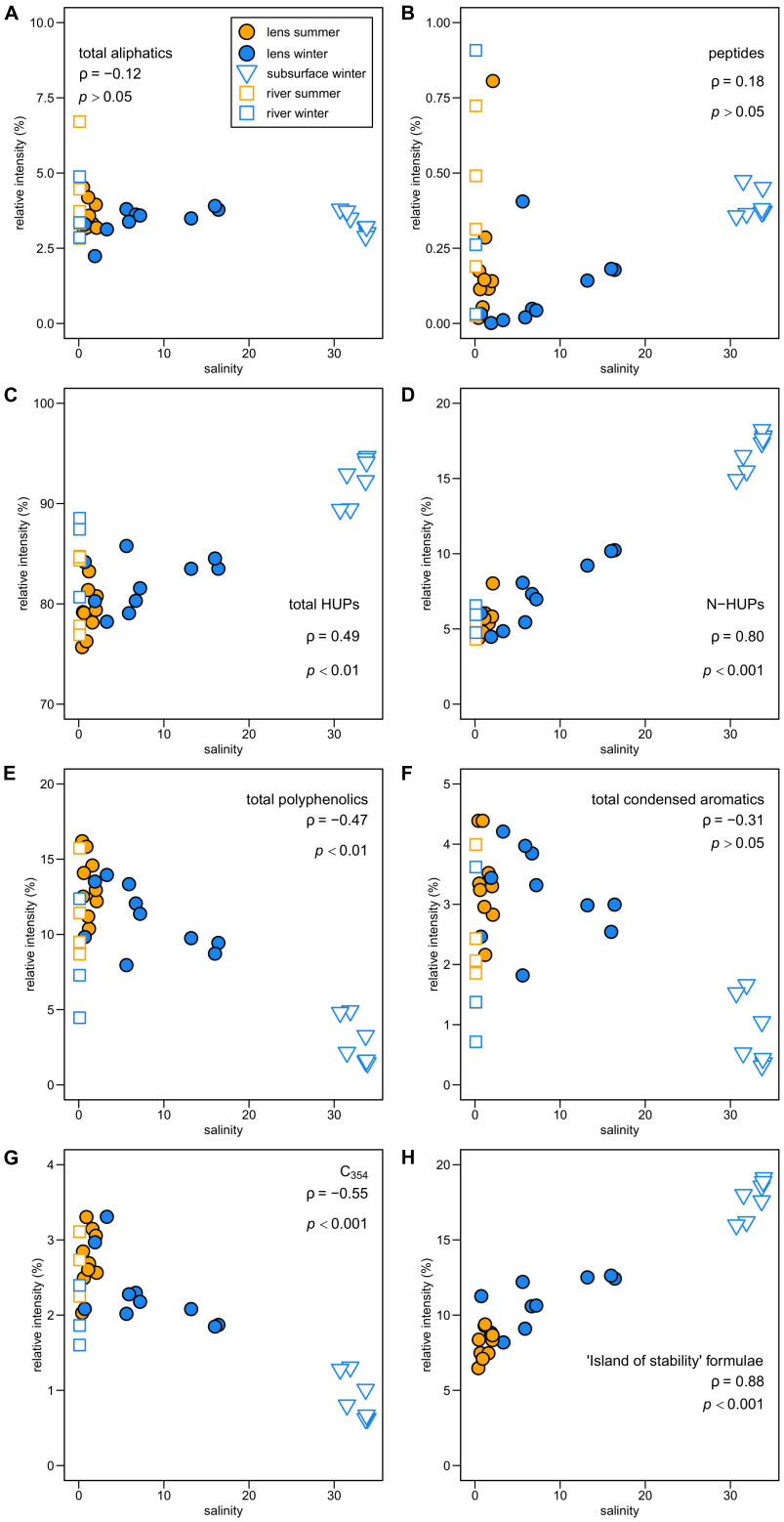

FIGURE 4 | Relationship between FT-ICR MS compound category relative intensities and salinity in Baker-Martinez Fjord for **(A)** aliphatic, **(B)** peptide-like, **(C)** all HUPs, **(D)** N-HUPs, **(E)** polyphenolic and **(F)** condensed aromatic formulae. Sub-panel **(G)** shows variations in formulae correlated with tryptophan-like (C_{354}) fluorescence in river samples across the broader region; and **(H)** shows variations in formulae from a stable pool of marine DOM, termed the "island of stability" (Lechtenfeld et al., 2014). Sub-panels annotated with non-parametric correlation coefficient (Spearman's ρ) and *p*-value where $p > 0.05$ is not deemed significant. River samples excluded from correlations but shown for reference.

TABLE 2 | Characteristics of FT-ICR MS-derived formulae that are significantly correlated (Spearman rank, p-value < 0.028) with season and water column properties in Baker-Martinez Fjord.

		Season		Salinity		Chlorophyll		Turbidity	
		Summer	**Winter**	**Higher salinity**	**Lower salinity**	**Higher chlorophyll**	**Lower chlorophyll**	**Higher turbidity**	**Lower turbidity**
Number of correlated formulae		1770 ± 27	2075 ± 45	2942 ± 196	4334 ± 118	4075 ± 105	2453 ± 185	3624 ± 89	2445 ± 169
Intenity-weighted molecular properties of correlated formulae	mass	476.6 ± 2.3	464.4 ± 1.0	451.0 ± 0.6	498.9 ± 2.7	521.1 ± 2.1	446.6 ± 0.7	492.4 ± 3.0	448.4 ± 0.6
	C	20.8 ± 0.1	22.8 ± 0.1	20.9 ± 0.0	22.4 ± 0.1	24.9 ± 0.1	19.9 ± 0.0	22.0 ± 0.1	20.7 ± 0.0
	H	20.1 ± 0.1	28.3 ± 0.1	26.0 ± 0.0	20.3 ± 0.1	25.1 ± 0.3	24.9 ± 0.0	19.8 ± 0.1	25.8 ± 0.0
	O	13.0 ± 0.1	10.0 ± 0.0	10.6 ± 0.0	13.1 ± 0.1	12.3 ± 0.1	11.1 ± 0.0	13.0 ± 0.1	10.6 ± 0.0
	N	0.03 ± 0.00	0.12 ± 0.01	0.21 ± 0.01	0.05 ± 0.00	0.05 ± 0.00	0.25 ± 0.02	0.05 ± 0.00	0.23 ± 0.02
	S	0.01 ± 0.00	0.06 ± 0.00	0.08 ± 0.00	0.01 ± 0.00	0.02 ± 0.00	0.08 ± 0.00	0.02 ± 0.00	0.08 ± 0.00
	H/C	0.97 ± 0.01	1.24 ± 0.00	1.25 ± 0.00	0.91 ± 0.01	0.99 ± 0.01	1.25 ± 0.00	0.91 ± 0.01	1.25 ± 0.00
	O/C	0.63 ± 0.00	0.44 ± 0.00	0.51 ± 0.00	0.59 ± 0.00	0.50 ± 0.01	0.56 ± 0.00	0.60 ± 0.00	0.51 ± 0.00
	N/C	0.00 ± 0.00	0.01 ± 0.00	0.01 ± 0.00	0.00 ± 0.00	0.00 ± 0.00	0.01 ± 0.00	0.00 ± 0.00	0.01 ± 0.00
	Almod	0.36 ± 0.00	0.26 ± 0.00	0.22 ± 0.00	0.42 ± 0.00	0.40 ± 0.01	0.20 ± 0.00	0.42 ± 0.00	0.22 ± 0.00
Relative intensities of correlated formulae by compound category (%)	Aliph. O-rich	0.22 ± 0.02	0.00 ± 0.00	0.65 ± 0.04	0.13 ± 0.01	0.00 ± 0.00	0.83 ± 0.04	0.15 ± 0.01	0.39 ± 0.03
	Aliph. O-poor	0.16 ± 0.02	0.19 ± 0.01	0.30 ± 0.01	0.80 ± 0.05	1.17 ± 0.06	0.23 ± 0.01	0.65 ± 0.05	0.19 ± 0.01
	Peptide	0.06 ± 0.01	0.01 ± 0.00	0.10 ± 0.02	0.00 ± 0.00	0.00 ± 0.00	0.15 ± 0.02	0.00 ± 0.00	0.09 ± 0.02
	HUP O-rich	20.33 ± 1.14	10.53 ± 0.72	24.43 ± 1.66	22.43 ± 1.47	8.40 ± 0.68	23.86 ± 1.59	21.39 ± 1.44	21.96 ± 1.59
	HUP O-poor	0.53 ± 0.03	22.95 ± 0.85	16.21 ± 0.94	3.92 ± 0.19	12.34 ± 0.57	4.90 ± 0.47	2.96 ± 0.14	13.58 ± 0.88
	HUP with N	0.02 ± 0.00	1.20 ± 0.17	2.44 ± 0.38	0.14 ± 0.01	0.12 ± 0.00	2.16 ± 0.36	0.11 ± 0.01	2.37 ± 0.37
	PP O-rich	3.20 ± 0.26	0.00 ± 0.00	0.00 ± 0.00	7.28 ± 0.61	5.07 ± 0.45	0.00 ± 0.00	7.02 ± 0.59	0.00 ± 0.00
	PP O-poor	0.76 ± 0.05	0.02 ± 0.00	0.04 ± 0.01	2.16 ± 0.15	1.73 ± 0.12	0.02 ± 0.00	2.07 ± 0.14	0.03 ± 0.00
	PP with N	0.01 ± 0.00	0.01 ± 0.00	0.02 ± 0.00	0.07 ± 0.00	0.06 ± 0.00	0.01 ± 0.00	0.07 ± 0.00	0.01 ± 0.00
	CA O-rich	0.27 ± 0.03	0.01 ± 0.00	0.00 ± 0.00	2.27 ± 0.19	2.18 ± 0.19	0.00 ± 0.00	1.62 ± 0.13	0.00 ± 0.00
	CA O-poor	0.01 ± 0.00	0.00 ± 0.00	0.00 ± 0.00	0.11 ± 0.01	0.10 ± 0.01	0.00 ± 0.00	0.07 ± 0.00	0.00 ± 0.00
	CA with N	0.00 ± 0.00	0.00 ± 0.00	0.00 ± 0.00	0.00 ± 0.00	0.00 ± 0.00	0.00 ± 0.00	0.00 ± 0.00	0.00 ± 0.00
	Sugars	0.02 ± 0.00	0.00 ± 0.00	0.04 ± 0.01	0.17 ± 0.02	0.14 ± 0.02	0.04 ± 0.01	0.16 ± 0.02	0.01 ± 0.00

The characteristics of directly and inversely correlated formulae are split across the two columns per variable (corresponding to summer/winter for season, or higher/lower values for other variables). Results are reported as the mean ± 1 SE across all samples (n = 26, except for "season" correlations where only surface layer samples were included and n = 19) for the number of correlated formulae, their (intensity-weighted) molecular properties and percentage relative intensities of specific compound categories (Aliph., aliphatics; HUP, highly unsaturated and phenolic; PP, polyphenolic; CA, condensed aromatics). Very small standard errors are reported as zero when mean values are also close to zero.

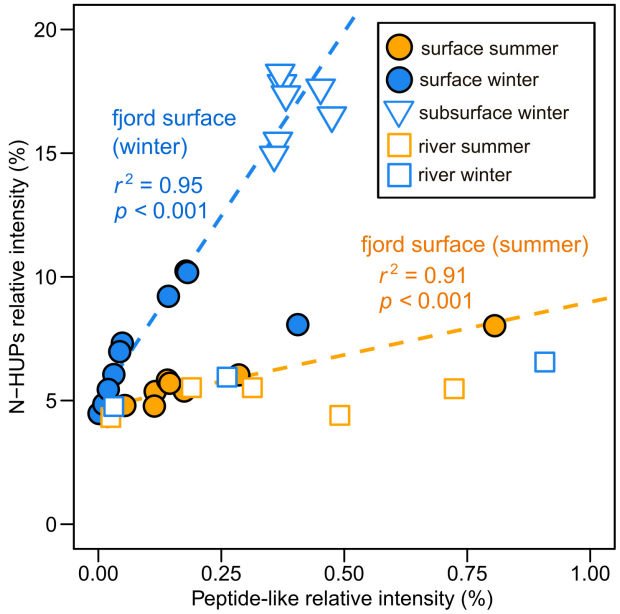

FIGURE 5 | Relationship between FT-ICR MS relative intensities of nitrogen-containing highly unsaturated and phenolic compounds (N-HUPs) and peptide-like formulae in the surface layer and subsurface waters of Baker-Martinez Fjord and its tributary rivers. Separate linear regression lines (n = 9 with normally distributed residuals) used to illustrate the difference in the relationship between seasons for fjord surface layer samples (winter regression excludes the one outlier sample).

N-containing formulae in fjord DOM comprise a greater share of surface layer sample intensity in winter and are correlated directly with salinity but inversely with chlorophyll and turbidity (**Table 2**). This pattern is driven primarily by changes in N-HUPs. The relative intensities of all N-containing formulae, and N-HUPs exclusively, are directly correlated with DON concentrations (both give Pearson's r = 0.89; p < 0.001) when excluding one outlier sample (S5, depth 140 m, winter) from the analysis. Peptide-like formulae are a comparatively minor constituent of DON and display a weaker correlation with DON concentrations (r = 0.55; p < 0.01). Overall, surface layer peptide-like formulae intensities increase in summer, whereas N-HUPs intensities decrease (**Table 2**).

The relationship between peptide-like and N-HUP relative intensities differs between the seasons, with surface layer conditions more closely resembling the rivers in summer and the fjord subsurface in winter (**Figure 5**). The molecular properties of peptide-like formulae also differ significantly between rivers and the fjord surface layer over the seasons with respect to the fjord subsurface, as shown by a one-way multivariate analysis of variance (MANOVA; Pillai's trace = 0.19; F-test = 60.2; and p < 0.001) of the molecular properties (continuous dependent variables) across sample types (independent factor variable) in **Table 3**. Higher relative intensities of peptide-like formulae in the fjord surface layer in summer (**Figure 5**) and overall association of peptide-like formulae with more saline/less turbid conditions (**Table 2**) that characterize winter, suggest multiple controls over peptide-like material in the fjord.

Multivariate Relationships

Multivariate (PCA) analysis reveals relative variations in fjord DOM composition that are linked to the season and water depth (**Figure 6**). The first three PCA components explain 72.7% of the variance in the dataset. PC1 distinguishes surface layer DOM (richer in CAs and PPs and correlated with higher DOC concentrations) from subsurface DOM (characterized by higher relative intensities of O-rich HUPs and correlated with higher salinities, DON and nutrient concentrations). Subsurface samples (positive PC1 scores) are also associated with higher C_{304} (protein-like) and C_{390} (marine humic-like) fluorescence loadings.

PC2 reflects seasonal differences in surface layer DOM. Positive PC2 scores are associated with summer samples, characterized by higher protein-like fluorescence loadings, higher relative intensities of O-rich aliphatics and peptide-like compounds and directly correlated with turbidity and water temperature. Negative PC2 scores associated with winter samples reflect higher humic-like fluorescence loadings, higher relative intensities of O-poor HUPs and O-poor aliphatics and strong direct correlation with chlorophyll.

The relationship between PC2 and PC3 suggests a convergence in DOM composition across much of the fjord surface in winter, characterized by higher C_{390} fluorescence and O-poor HUPs/aliphatics (**Figure 6B**). In contrast, surface samples span greater compositional space in summer, with samples from Jorge Montt Fjord, and the Baker and Pascua plumes relatively enriched in protein-like fluorescence, O-rich aliphatics and peptides, whereas Steffen and Mitchell Fjords are enriched in O-rich HUPs (**Figure 6B**).

Estimating River Fluxes

We estimate that the four principal rivers draining into BMF supply > 42 Gg of organic carbon each year, with >84% as DOC and <16% as POC (**Table 4**). Despite turbid inputs, the low organic content (<0.4%) of suspended sediments means that POC comprises a smaller share (2–32%) of total OC export than DOC (68–98%) in all rivers. The Baker River is the biggest single input of freshwater and OC, accounting for approximately half of the total annual flux. The next largest input from the Pascua River provides 38% of the freshwater and 26% of the OC from rivers each year. The Bravo River's OC flux is disproportionately high for its size due to high DOC concentrations; its annual DOC flux is similar to the Pascua River, which has an annual discharge at least six times larger. The dilute and predominantly NPI-fed Huemules River provides modest shares of the total freshwater (6%) and OC (2%) fluxes.

DISCUSSION

Seasonality in DOM Composition in Fjord Surface Layer

Seasonal changes in the fjord surface layer reflect a shifting balance between marine and freshwater influences that are linked to variations in river discharge and glacier melt cycles. The overall freshening, higher turbidity and low nutrient content in summer (**Table 1**) is consistent with strong meltwater input

TABLE 3 | Comparison of properties of peptide-like formulae detected in FT-ICR MS spectra from river, fjord surface and fjord subsurface water samples in Baker-Martinez Fjord.

Properties of peptide-like formulae	Rivers		Fjord surface layer		Fjord subsurface
	Summer *(n = 5)*	Winter *(n = 3)*	Summer *(n = 9)*	Winter *(n = 10)*	Winter *(n = 7)*
No. of formulae	157 ± 38	180 ± 96	118 ± 27	76 ± 25	314 ± 20
Rel. intensity (%)	0.34 ± 0.12	0.40 ± 0.26	0.21 ± 0.08	0.11 ± 0.04	0.40 ± 0.02
Mass (Da)	499.4 ± 4.8	500.2 ± 4.6	493.8 ± 4.5	468.2 ± 4.5	464.1 ± 3.7
H/C	1.60 ± 0.01	1.61 ± 0.00	1.60 ± 0.00	1.57 ± 0.00	1.58 ± 0.00
O/C	0.61 ± 0.01	0.61 ± 0.01	0.59 ± 0.01	0.55 ± 0.01	0.57 ± 0.01
N	1.64 ± 0.05	1.56 ± 0.04	1.24 ± 0.03	1.20 ± 0.03	1.37 ± 0.03
S	0.06 ± 0.01	0.00 ± 0.00	0.06 ± 0.01	0.24 ± 0.02	0.31 ± 0.02

Values are means ± 1 SE for samples of the same type, showing the number of peptide-like formulae, their share of sample relative intensity (%), formula mass (Da), H/C, O/C, and numbers of N and S atoms in each peptide-like formula.

from glaciers (Marín et al., 2013; Aracena et al., 2015; Hawkings et al., 2015). Weaker glacial melting in winter leads to increased surface salinities and nutrient concentrations (**Table 1**) as marine influences strengthen in the upper fjord layers, potentially enhanced by greater mixing with subsurface waters during winter storms (Montero et al., 2017). Seasonal cycles in freshwater input also control changes in the composition of surface layer DOM, with implications for its overall reactivity and biogeochemical fate. We discuss, in turn, three mechanisms relating to changes in freshwater input that affect DOM composition in BMF.

First, seasonal changes in freshwater DOM composition are transferred directly into the fjord surface layer. For example, higher protein-like fluorescence in summer (**Figure 3**) is consistent with strong meltwater inputs supplying DOM from glacial sources (Barker et al., 2006; Dubnick et al., 2010; Fellman et al., 2010; Kellerman et al., 2020). This is particularly evident downstream of Jorge Montt Glacier and near the mouths of the Baker and Pascua Rivers (**Figure 6B**), where summer discharge is driven by melting of the NPI and SPI, respectively (Dussaillant et al., 2012; Rebolledo et al., 2019). Protein-like fluorescence intensity decreases as meltwater inputs decline in winter (**Figure 3**). Higher surface layer humic-like fluorescence loadings in winter (**Figure 6A**) are consistent with more dominant non-glacial inputs, likely driven by heavier rainfall and increased flushing of vegetated terrain, soils and wetlands (Koch et al., 2005; Fellman et al., 2008, 2014; Ohno et al., 2010). Such DOM sources may dominate the River Bravo year round, as it is a less glacially influenced catchment. The year-round presence of humic-like fluorescence, PPs and CAs and their associations with higher DOC concentrations (**Figures 3**, **6A**), suggest continuous inputs of terrestrial DOM via rivers and runoff from the highly vegetated banks of BMF.

Second, river discharge magnitude regulates the degree of mixing between fresh and marine waters in the surface layer. High discharge in summer accounts for higher protein-like fluorescence (**Figure 3**) from glacial meltwaters and increased relative intensities of PPs, which are derived from vascular plants and indicative of stronger terrestrial inputs (Riedel et al., 2016). Reduced glacial melting, weaker river discharge and greater turbulence in the fjord results in a thinner freshwater lens in winter, leading to higher surface salinities (**Table 1**) and increased relative intensities of HUPs (**Figure 4**). In particular, greater N-HUP relative intensities in winter are consistent with the higher heteroatom (i.e., N) content of marine DOM (Sleighter and Hatcher, 2008; Osterholz et al., 2016). Moreover, the coincident increases in surface nutrient concentrations (**Table 1**) and inverse correlation between N-HUPs and chlorophyll (**Table 2**) indicate that these N-HUPs are likely sourced from subsurface waters rather than recently produced DOM near the surface, which is consistent with reduced stratification of the water column in winter.

Third, changes in the turbidity of freshwater inputs regulate primary production and the formation of autochthonous DOM in the fjord surface layer. Higher turbidity levels and greater stratification associated with strong glacial melt inputs suppress summertime primary production in BMF (Aracena et al., 2011). As meltwater inputs decline and turbidity levels fall in winter (**Table 1**), light is less limiting to the fjord ecosystem and primary production becomes a more important source of DOM. This accounts for the stronger association of O-poor aliphatics and HUPs with the winter surface layer (**Figure 6A** and **Table 2**) and, combined with the direct correlation of these compounds with chlorophyll (**Table 2**), is consistent with DOM derived from recent production by phytoplankton (Sleighter and Hatcher, 2008; Kujawinski et al., 2009; Landa et al., 2014). This molecular pool contrasts with the O-rich aliphatics and HUPs that are more strongly associated with the summer surface layer (**Figure 6A** and **Table 2**), and suggestive of stronger terrestrial influences when primary production is suppressed.

These seasonal shifts in surface layer DOM composition could affect how organic matter is processed by bacterial communities in BMF throughout the year. In summer, meltwater inputs likely support the bacterial cycling of biolabile, protein-rich DOM from glacial sources (Hood et al., 2009; Fellman et al., 2014). This may be the dominant pathway for bacterial carbon cycling, especially where autochthonous DOM production is limited by high turbidity at the fjord heads (González et al., 2013) and where cold, low salinity conditions offer a competitive advantage to bacteria that are better adapted to glacial DOM (Gutiérrez et al., 2015; Paulsen et al., 2018). In contrast, bacterial activity may become increasingly coupled to autochthonous DOM sources as light becomes less limiting with decreased

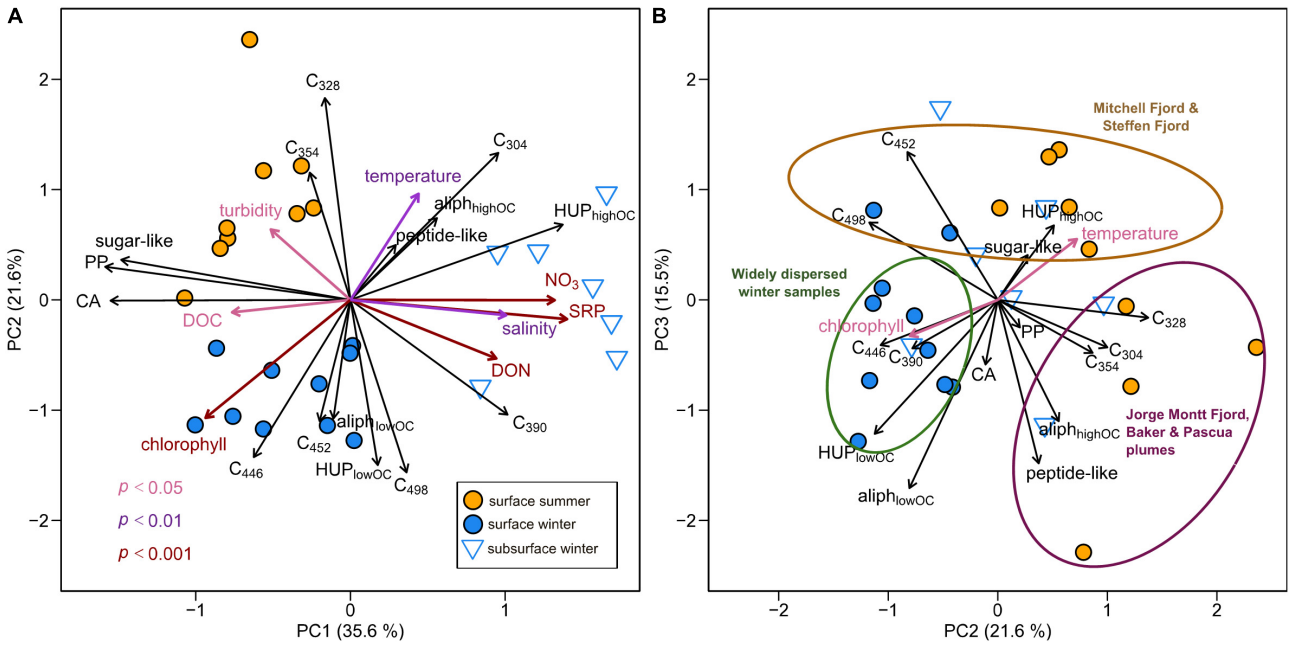

FIGURE 6 | Principal components analysis (PCA) of DOM composition in Baker-Martinez Fjord showing variations with respect to the **(A)** first and second, and **(B)** second and third principal components. PCA based on relative variations in fluorescence (PARAFAC loadings;%) and molecular composition (FT-ICR MS compound category relative intensities;%) across surface layer samples in summer and winter and subsurface waters in winter. Black arrows show loadings of variables used in PCA (refer to main text for explanation of abbreviations). Colored arrows show correlated environmental variables fit by permutation (color denotes significance level; see key on sub-panel **A**).

discharge (Montero et al., 2011). However, the increased supply of relatively unreactive HUPs from subsurface waters may constrain the overall reactivity of surface layer DOM in winter (Mostovaya et al., 2017).

Seasonality in N-Containing DOM

Dissolved organic matter biolability in the fjord may be most sensitive to changes in the N-containing fraction (i.e., DON). The strong correlation between DON concentrations and N-HUPs, which comprise the majority of all N-containing formulae and have higher intensities in the winter surface layer (**Figure 4** and **Table 1**), suggests that the DON pool is dominated by refractory compounds from subsurface waters. The availability of peptide material, a small but biolabile fraction of DON (Aluwihare et al., 2005; Mulholland and Lee, 2009), may therefore exert a critical control over the reactivity of N-containing DOM in the fjord surface layer. The reduced number and lower N-content of peptide-like formulae in the fjord surface layer with respect to both riverine and subsurface sources (**Table 3**), suggest possible consumption of the most N-rich peptides. This effect is stronger in winter when there may be greater uptake by phytoplankton as increased light availability stimulates productivity (Mulholland and Lee, 2009).

Significant differences in peptide-like formulae across water sources (MANOVA, $p < 0.001$; **Table 3**) suggest that biolabile nitrogen sources in the fjord surface layer could be sensitive to changes in the balance of marine and freshwater influences. Similarities between peptide-like formulae in the rivers and surface layer in summer support a dominance of freshwater-derived peptide material (**Table 3**), with glaciers and proglacial lakes likely to be major sources (Spencer et al., 2014). Seasonal shifts in the composition of surface layer peptide-like formulae and their relationship with N-HUPs intensity (**Figure 5** and **Table 3**) suggest an increased supply of peptide material from subsurface waters in winter, although rivers may continue to be an important local control in the near-shore zone (e.g., **Supplementary Figure 5**). The impacts of these changes in the supply of peptide material should, however, be viewed within the context of overall ecosystem productivity. When productivity is low in summer, organic N consumption might be limited to the bacterial uptake of biolabile, freshwater peptide material (González et al., 2013). Higher productivity in winter could lead to a greater total uptake by phytoplankton and bacteria, potentially supporting the co-metabolism of more stable subsurface peptide material alongside recent material from *in situ* production (Aluwihare et al., 2005; Aluwihare and Meador, 2008).

Our data contrast with previous studies of estuarine and marine DOM that identify proteins as a key component of the DON pool and an important source of biolability (Fellman et al., 2010; Lønborg et al., 2015; Yamashita et al., 2015). The inverse correlations between protein-like fluorescence and N/C ratios across seasons and sampling depths (**Figure 3**) suggest that proteins are generally not a major component of DON in BMF. We also observe only tentative evidence for protein consumption where surface layer tryptophan-like

TABLE 4 | Annual freshwater and organic carbon (OC) fluxes from the four principal rivers entering Baker-Martinez Fjord.

	Baker	Pascua	Bravo	Huemules	Total
Catchment properties[a]					
Total area (km^2)	29,107	15,079	1,062	671	45,919
Glacial cover (%)	8	19	15	71	–
Forest cover (%)	20	12	23	4	–
Wetland cover excluding lakes (%)	4	4	4	4	–
Total lake volume ($\times 10^6$ m^3)	754,002	79,782	67	1,355	–
Discharge[b]					
Mean summer (m^3 s^{-1})	1,268	835	–	218	–
Mean winter (m^3 s^{-1})	754	617	–	51	–
Mean annual (m^3 s^{-1})	932	714	112	121	–
Cumulative annual (km^3 a^{-1})	29.4	22.5	3.5	3.8	59.2
Share of annual freshwater input (%)	50	38	6	6	
Concentration data[c]					
SSC summer (mg L^{-1})	60.2	35.7	18.1	87.5	–
Sediment OC content (%)	0.19	0.38	0.25	0.09	–
POC summer (mg C L^{-1})	0.114	0.136	0.045	0.079	–
DOC summer (mg C L^{-1})	0.644	0.454	2.518	0.153	–
DOC winter (mg C L^{-1})	0.643	0.273	1.997	0.236	–
DOC annual mean (mg C L^{-1})	0.644	0.364	2.258	0.171	–
Annual fluxes					
SSC (Gg a^{-1})	1,769	804	64	334	2,971
POC (Mg C a^{-1})	3,360	3,056	160	301	6,877
DOC (Mg C a^{-1})	18,920	8,201	7,975	653	35,749
TOTAL OC flux (Mg C a^{-1})	22,280	11,257	8,135	954	42,626
POC (%)	15	27	2	32	16
DOC (%)	85	73	98	68	84
Share of annual OC input by rivers (%)	52	26	19	2	100

[a] *Catchment areas calculated from a high resolution digital elevation model (Farr et al., 2007) using the Whitebox-GAT geospatial processing package (Lindsay, 2016). Catchment properties calculated from superimposed datasets including the Randolph Glacier Inventory (RGI Consortium, 2017), the National Mapping Organization's Global Land Cover raster (Tateishi et al., 2014), the SWAMP raster (Gumbricht et al., 2019) and the HydroLAKES database (Messager et al., 2016).*

[b] *Discharge data sources as described in main text (Section "Flux Calculations").*

[c] *SSC and POC concentrations measured in summer only (n = 1 for Baker, Pascua and Bravo; n = 25 for Huemules). DOC concentrations measured in both summer (n = 1 for Baker, Pascua and Bravo; n = 46 for Huemules) and winter (n = 1 for Baker, Pascua and Bravo; n = 15 for Huemules). Concentrations expressed in units of mass per liter rather than molar units (used elsewhere) as more appropriate for flux calculations.*

(C_{354}) fluorescence falls to zero (**Supplmentary Figure 3**) but this is not detectable in the molecular formulae associated with C_{354} (**Figure 4G**). Moreover, consumption effects may be masked by autochthonous production in the fjord (**Supplementary Figure 3**).

Changes in DOM Composition Along the Salinity Gradient

We use a correlative approach to track changes in DOM composition with salinity, similar to other coastal studies (Osterholz et al., 2016; Seidel et al., 2017). However, we are unable to assess mixing processes along a single axial transect as our samples are dispersed across a complex fjord system, capturing freshwater influences from multiple rivers and the Jorge Montt Glacier and marine water influences from two discrete entry routes at the mouths of the Baker and Martinez channels. These multiple end-members confound simple mixing analyses (Asmala et al., 2016). Instead, we interpret changes in DOM composition along a salinity gradient that cuts across spatial, seasonal and depth variations, which reflect the overall shifting balance of marine and freshwater influences in the fjord.

The overall transition in the BMF from aromatic-rich DOM at low salinity to more saturated DOM at higher salinity (**Figure 4**) is typical of estuarine systems (Medeiros et al., 2015; Osterholz et al., 2016; Seidel et al., 2017). This is consistent with freshwater inputs from rivers as the major source of aromatic compounds (i.e., PPs and CAs) derived from degraded and leached vascular plants and soils (Ohno et al., 2010). The strong correlation between HUPs, especially N-HUPs, and salinity (**Figures 4C,D**) supports marine waters as a source of unsaturated and heteroatom-rich DOM (Medeiros et al., 2015; Osterholz et al., 2016). The similar trend for the 'island of stability' group (**Figure 4H**), a pool of stable molecular formulae that persist in the deep ocean (Lechtenfeld et al., 2014), suggests that subsurface waters in the BMF are likely to be a key source of these compounds and HUPs.

There is, however, considerable variability in the molecular composition of low salinity samples (**Figures 4E,F**), which makes

it difficult to reliably determine any non-conservative mixing patterns. For example, elevated relative intensities of PPs and CAs in the fjord surface layer with respect to some river samples (**Figures 4E,F**) could indicate substantial contributions of aromatic DOM from smaller streams and diffuse overland flow. However, the similar numbers of PP and CA formulae in rivers and fjord surface layer samples suggest that these downstream changes in relative intensity could just reflect an adjustment in internal composition as other DOM is added and other components possibly removed within the fjord.

The changes in molecular composition with salinity in BMF are consistent with the overall removal of aromatic DOM from surface waters by adsorption and flocculation processes (Sholkovitz, 1976). Photochemical degradation can also remove a wide range of compounds (HUPs, PPs, CAs) from surface waters (Spencer et al., 2009; Stubbins et al., 2010) but these processes will be limited by turbid conditions in BMF (Aracena et al., 2011; Marín et al., 2013). Bacterial degradation is also an effective removal mechanism for a wide range of phenolic and aromatic compounds (Stubbins et al., 2010; Medeiros et al., 2015; Mostovaya et al., 2017). Such processes might degrade terrestrial organic material and reinforce the inverse correlation between humic-like fluorescence and salinity (**Figure 3**). Alternatively, some bacteria might also convert reactive humic substances into more stable compounds (Shimotori et al., 2010; Romera-Castillo et al., 2011).

Trends in molecular composition with salinity do not necessarily capture changes in all DOM fractions. We speculate that complex patterns in protein-like fluorescence (**Figure 3**) arise from multiple sources and possible consumption processes affecting a small but reactive DOM fraction (Paulsen et al., 2018). Spikes in protein-like fluorescence (especially tryptophan-like, C_{354}) in winter suggest a possible contribution from by-products of primary production (Murphy et al., 2008; Romera-Castillo et al., 2010; Lønborg et al., 2015), facilitated by reduced turbidity and less light limitation in the fjord. However, rapid utilization of autochthonous proteins by bacteria could maintain low protein-like fluorescence intensities at the surface in winter (Determann et al., 1998; Yamashita et al., 2008). Moderate protein-like fluorescence in some subsurface samples suggests that sinking organic matter may undergo bacterial degradation or sloppy feeding by grazers (Poulet et al., 1991; Urban-Rich et al., 2004; Møller, 2007). Higher subsurface protein-like fluorescence in summer could indicate that large seasonal inputs of terrestrial organic matter are processed by fjord ecosystems (Meerhoff et al., 2019) and undergo bacterial degradation at depth (Nagata et al., 2000; Fox et al., 2017).

Assessing the Importance of Riverine OC Fluxes to Baker-Martinez Fjord

Due to scarcity in biogeochemical data from this region, our estimate of > 42 Gg C a^{-1} is the first attempt to calculate the combined annual OC flux of the four main rivers draining into BMF (**Table 4**). This value likely underestimates the total flux into the BMF as we were unable to constrain inputs from the marine-terminating Jorge Montt Glacier. The estimate is also based on a limited sample set but the data used in our calculations are broadly consistent with previously reported POC concentrations (0.074–0.158 mg C L^{-1}; Vargas et al., 2011), although there are no published DOC concentrations to compare to our measurements. Nevertheless, we contend that our calculations provide a useful, conservative baseline for monitoring future changes in OC export in response to upstream landscape change linked to glacier retreat (Milner et al., 2017).

Our OC flux estimate ($\sim$40 Gg C a^{-1}) is relatively modest in global terms, even for glacially influenced regions. For example, the estimated annual export of carbon from the Greenland Ice Sheet is two orders of magnitude larger ($\sim$1500 Gg C a^{-1}; Lawson et al., 2014; Hood et al., 2015) and those from the Himalayas ($\sim$100 Gg C a^{-1}; Hemingway et al., 2019) and Gulf of Alaska ($\sim$130 Gg C a^{-1}; Hood et al., 2009) are over twice the size. However, area-normalized fluxes (or yields) demonstrate that OC export from our study catchments is consistent with the range of estimates for other glaciated regions. We calculate a combined annual OC yield of 0.93 Mg C km^{-2} a^{-1} for the four main river basins draining into the BMF, assuming a combined catchment area of $\sim 46 \times 10^3$ km^2. This compares with an estimated yield for the Greenland Ice Sheet of 0.88 Mg C km^{-2} a^{-1}, assuming an area of $\sim 1{,}700 \times 10^3$ km^2 (Hawkings et al., 2016), and lies within the range of reported yields for the Himalayas, 0.50 Mg C km^{-2} a^{-1} (Hemingway et al., 2019), and the Gulf of Alaska, 1.65 Mg C km^{-2} a^{-1} (Hood et al., 2009).

Comparing our riverine OC flux to crude estimates of carbon fixation by primary production suggests that rivers supply a substantial proportion (10–64%) of the total annual OC input to BMF (**Supplementary Table 2**). Even the lower range of our estimates (10%) supports rivers being an important source of carbon to the fjord heads, where primary production is most limited (Vargas et al., 2011; González et al., 2013). In general, primary production rates are lower in BMF than in other Chilean fjords with weaker glacial influences (Aracena et al., 2011) but spatiotemporal variabilities make it difficult to constrain annual carbon fixation across the fjord (**Supplementary Table 2**). Overall, we regard our calculations as conservative in favor of autochthonous production due to the use of springtime primary production rates, which reflect peak productivity (Aracena et al., 2011; González et al., 2013; Jacob et al., 2014), and an underestimation of allochthonous inputs. For example, freshwater fluxes from Jorge Montt Glacier are substantial (1.9–4.5 km^3 a^{-1}, 2012–2017; Bown et al., 2019) but we cannot constrain OC export from this glacier as the OC concentration of its meltwaters is unknown.

The bulk composition of riverine OC shows a dominance of DOC over POC that is in line with the broad range of conditions in fjords across Chilean Patagonia and the Arctic (**Table 5**) but is atypical of glacial rivers where POC may comprise 50–90% of the total OC load (Lawson et al., 2014; Hood et al., 2015). This suggests that proglacial lakes are a major upstream sink for particulates, including biolabile POC (Meyers et al., 1984; Carrivick and Tweed, 2013). Although SSCs are low (<0.1 g L^{-1}) compared to typical glacial rivers (0.5–10 g L^{-1}) (Knudsen et al., 2007; Lawson et al., 2014), we

TABLE 5 | Dissolved organic carbon: POC ratios for major input rivers of the Baker-Martinez Fjord compared to published data for water masses in other fjords and channels in Chilean Patagonia and the Arctic.

Location and sample	Sample type	DOC (mg L^{-1})	POC (mg L^{-1})	DOC:POC	Study
CHILEAN PATAGONIA					
Baker-Martinez Fjord					
Baker River[a]	River	0.644	0.114	5.6	*This study*
Pascua River[a]	River	0.364	0.136	2.7	*This study*
Huemules River[a]	River	0.153	0.079	1.9	*This study*
Bravo River[a]	River	2.518	0.045	56.0	*This study*
Martinez Channel[b]	Surface fjord	1.320	0.140	9.4	1
Inner Sea of Chiloé					
Mean for inner sea area[b]	Surface marine	0.910	0.256	3.6	2
Reloncavi Fjord[c]	Surface fjord	0.740	0.325	2.3	2
Magellan Strait					
Magellan Strait[b]	Surface marine	1.720	0.392	4.4	3
Beagle Magellan Water	Subsurface marine	0.815	0.234	3.5	4
Sub-Antarctic Shelf Water	Subsurface marine	0.700	0.129	5.4	4
Sub-Antarctic Water	Subsurface marine	0.640	0.077	8.3	4
ARCTIC					
Young Sound, Greenland[d]	Surface fjord	1.285	0.024	53.5	5
	Subsurface fjord	1.261	0.026	48.5	5
	Shelf water	1.068	0.025	42.7	5
	River	0.504	0.056	9.0	5
Kongsfjorden, Svalbard					
October	Surface fjord	1.158	0.189	6.1	6
April	Surface fjord	0.713	0.283	2.5	6
August	Surface fjord	1.091	0.276	4.0	7
August	Subsurface fjord	1.309	0.068	19.3	7
August	River	0.877	0.673	1.3	7
Norway					
Ballsfjord	Surface fjord	1.500	0.748	2.0	8
Ullsfjord	Surface fjord	1.370	0.325	4.2	8

[a] *Annual mean concentrations reported in* ***Table 4****.*
[b] *DOC:POC calculated from concentrations converted from depth-integrated concentrations reported in study.*
[c] *As b. but concentrations read off from graph in study and expressed as mean for all stations within Reloncavi Fjord.*
[d] *Mean concentrations for summer (July) study period; molar DOC concentrations converted into mg* L^{-1}.
(1) González et al., 2013; (2) González et al., 2019; (3) González et al., 2016; (4) Barrera et al., 2017; (5) Paulsen et al., 2017; (6) Brogi et al., 2019; (7) Zhu et al., 2016; (8) Gašparović et al., 2005.

may overestimate annual POC fluxes by using summer SSCs, which can be double winter values in the Baker River (Quiroga et al., 2012). Our results therefore provide a conservative estimate for the importance of riverine DOC as a carbon subsidy to the fjord.

Bulk composition is an important factor affecting the fate of riverine OC in BMF. Strong inputs of terrestrial POC drive high rates of carbon burial at the fjord heads (Rebolledo et al., 2019) and supplement available food sources for zooplankton (Meerhoff et al., 2019). However, the larger and more biolabile DOC flux is likely to be critical for bacterial carbon cycling in the fjord (Vargas et al., 2011; Brett et al., 2017). Riverine DOC may be especially important for bacteria in the near-shore zone in summer (González et al., 2013), when discharge is highest and autochthonous substrates are lacking (Aracena et al., 2011). We would therefore expect carbon cycling in BMF to be sensitive to changes in the supply of biolabile OC from rivers as a result of accelerated glacier melting and retreat (Foresta et al., 2018).

Biogeochemical Impacts of Changing Glacier Melt Inputs on Baker-Martinez Fjord

Seasonal and spatial variation in DOM composition, coupled to the relative importance of riverine OC inputs, suggest that glaciers exert an important control over the biogeochemistry of BMF. We hypothesize the following biogeochemical impacts of enhanced glacier melting on BMF, which highlight potential sensitivities in other glaciated fjords, especially those in wet maritime regions.

1. **Reduced efficiency of the fjord as a carbon sink.** The strongest molecular signatures of recent primary production in BMF occur in the surface layer DOM pool in winter (**Figure 6**). This is consistent with strong turbid meltwater inputs in summer suppressing the fixation of new carbon by primary production. In the short-term, these effects could intensify through enhanced melting

of the NPI and SPI and the production of deeper and longer lasting turbid meltwater plumes (Foresta et al., 2018). Higher sedimentation rates and the binding of organic matter to sediment surfaces (Sholkovitz, 1976) could increase carbon burial efficiency in inner fjord areas but these processes are likely to be dominated by older, terrestrial carbon sources (Rebolledo et al., 2019). Although fjords are globally important carbon sinks (Smith et al., 2015), the probable decline in fjord primary production (Aracena et al., 2011; Włodarska-Kowalczuk et al., 2019) may mean that Patagonian fjords play a reduced role in new carbon sequestration.

2. **Carbon cycling will be increasingly influenced by allochthonous DOM.** The sensitivity of surface layer DOM composition to changes in river inputs, coupled to the widespread and year-round presence of aromatic and humic-rich DOM reported here shows that terrestrial inputs are a significant source of organic matter for the ecosystem in BMF. In the short term, allochthonous DOM from enhanced meltwater discharge may become an increasingly important resource for heterotrophic bacteria in the fjord (González et al., 2013), especially if inputs of glacial DOM are highly labile (Hood et al., 2009; Fellman et al., 2010). In the long term, glacier retreat may lead to reduced DOC export in summer and allow rain-driven export of aromatic and humic-rich DOM from soils and wetlands in winter to dominate annual fluxes (Fellman et al., 2010; Milner et al., 2017). In the absence of more readily labile material, these terrestrial DOM sources could become the most important substrate for fjord bacteria (Mostovaya et al., 2017).

3 **Changes in organic nitrogen substrates available to fjord communities.** Seasonal changes in peptide-like formulae in the BMF (**Figure 5** and **Table 3**) suggest that the composition of biolabile components of the DON pool are sensitive to changes in the strength of freshwater (and hence meltwater) inputs. Changes in water and DON supply could affect plankton community structure and nitrogen cycling processes, given the selective consumption of biolabile N-compounds by phytoplankton and heterotrophic bacteria (Liu et al., 2017). This may have particular relevance where DON is an important source of biolabile N for planktonic communities in N-limited fjords (Bronk et al., 2007; González et al., 2011; Iriarte et al., 2014).

4 **Expansion of the above conditions as marine-terminating glaciers retreat onto land.** The limited observational data from Jorge Montt Fjord suggest that conditions in this inlet differ slightly from the rest of BMF, with higher surface DON in summer accompanied by lower turbidity and higher chlorophyll levels (**Table 1**). However, the rapid, ongoing retreat of Jorge Montt Glacier may eventually produce a new land-terminating glacier and redirect the present submarine discharge of meltwaters to the surface layer (Rivera et al., 2012). This will likely lead to reduced downstream primary productivity as turbidity levels in this sector of the fjord become more similar to those in Steffen Fjord and the heads of the Baker and Martinez channels. Such hypothesized changes are also applicable to the fjords on the western side of the SPI where other marine-terminating glaciers are retreating (Foresta et al., 2018).

CONCLUSION

We have presented the first detailed analysis of DOM composition in a Chilean Patagonian fjord, using molecular level techniques that have improved understanding of DOM cycling in other aquatic environments. Our results suggest that significant seasonal differences in DOM composition in the surface waters of BMF are controlled by variations in river discharge linked to glacier melt cycles. The changes in fjord surface layer DOM may reflect a combination of seasonal changes in riverine DOM composition, differences in the degree of mixing of subsurface and surface DOM sources, and the regulation of primary production and new DOM formation by turbid river plumes. The composition of peptide-like formulae in the surface waters may be particularly sensitive to these seasonal controls on DOM composition, with implications for the cycling of biolabile DON. Trends in DOM composition with increasing salinity observed here are typical of estuarine systems and suggest preferential removal of terrestrial aromatic compounds and increased influence of unsaturated and heteroatom-rich compounds from marine sources. Our results also demonstrate that glacially fed rivers could provide a major supply of DOC to the BMF and influence carbon cycling processes. Overall, these findings indicate that the composition and processing of DOM in BMF will be affected by the accelerated melting of the NPI and SPI, which suggests biogeochemical sensitivity for other glaciated fjords in a warming climate.

DATA AVAILABILITY STATEMENT

Publicly available datasets were analyzed in this study. This data can be found here: https://zenodo.org/record/4603220#.YEz-EOj7SUk.

AUTHOR CONTRIBUTIONS

MM and AK developed the study from the aims of the NERC/CONICYT-funded PISCES research project, which was conceived by JW and LR. MM conducted all analyses with significant assistance from AK in FT-ICR MS analysis and JH in macronutrient analyses. MM wrote the manuscript, with contributions from AK, JW, JH, and RS. All authors contributed to fieldwork operations and data collection.

FUNDING

This work was part of the NERC/CONICYT-funded PISCES project (NE/P003133/1 – PII20150106). MM was funded by a

Ph.D. studentship through the NERC GW4+ Doctoral Training Partnership (NE/L002434/1). The National High Magnetic Field Laboratory, Tallahassee, FL, United States, provided instrument time and a travel bursary to MM to conduct FT-ICR MS analysis. JH was supported by a European Commission Horizon 2020 Marie Skłodowska-Curie Actions fellowship ICICLES (Grant Agreement #793962). JW also acknowledges a Royal Society Wolfson Merit Award and a Leverhulme Trust Senior Research Fellowship.

ACKNOWLEDGMENTS

We sincerely thank everyone who assisted with fieldwork in Chile, including the crew of the *R.V. Sur Austral* (COPAS, Tortel, Chile), the team at the Centro de Investigación en Ecosistemas de la Patagonia (CIEP, Coyhaique, Chile), and Dr. Sebastien Bertrand and team (University of Ghent, Belgium). Special thanks to Dr. Kate Hendry (co-investigator on PISCES project, University of Bristol) for assistance in boat survey planning. We wish to thank the National High Magnetic Field Laboratory, Tallahassee, FL, United States, for providing instrument time and Dr. Lissa Anderson, in particular, for technical support. We thank Dr. Fotis Sgouridis and James Williams for laboratory support at LOWTEX (University of Bristol, United Kingdom).

SUPPLEMENTARY MATERIAL

The Supplementary Material for this article can be found online at: https://www.frontiersin.org/articles/10.3389/fmars.2021.612386/full#supplementary-material

REFERENCES

Aiken, C. M. (2012). Seasonal thermal structure and exchange in Baker Channel, Chile. *Dyn. Atmos. Oceans* 58, 1–19. doi: 10.1016/J.DYNATMOCE.2012.07.001

Aluwihare, L. I., and Meador, T. (2008). "Chemical composition of marine dissolved organic nitrogen," in *Nitrogen in the Marine Environment*, eds D. G. Capone, D. A. Bronk, M. R. Mulholland, and E. J. Carpenter (Cambridge, MA: Academic Press). doi: 10.1016/B978-0-12-372522-6.00003-7

Aluwihare, L. I., Repeta, D. J., Pantoja, S., and Johnson, C. G. (2005). Two chemically distinct pools of organic nitrogen accumulate in the ocean. *Science* 308, 1007–1010. doi: 10.1126/science.1108925

Amon, R. M. W., and Benner, R. (1994). Rapid cycling of high-molecular-weight dissolved organic matter in the ocean. *Nature* 369, 549–552. doi: 10.1038/369549a0

Aracena, C., Kilian, R., Lange, C. B., Bertrand, S., Lamy, F., Arz, H. W., et al. (2015). Holocene variations in productivity associated with changes in glacier activity and freshwater flux in the central basin of the Strait of Magellan. *Palaeogeogr. Palaeoclimatol. Palaeoecol.* 436, 112–122. doi: 10.1016/J.PALAEO.2015.06.023

Aracena, C., Lange, C. B., Rebolledo, L., Iriarte, J. L., Rebolledo, L., and Pantoja, S. (2011). Latitudinal patterns of export production recorded in surface sediments of the Chilean Patagonian fjords (41–55°S) as a response to water column productivity. *Continental Shelf Res.* 31, 340–355. doi: 10.1016/j.csr.2010.08.008

Armbruster, D. A., and Pry, T. (2008). Limit of blank, limit of detection and limit of quantitation. *Clin. Biochem. Rev.* 29(Suppl. 1), S49–S52.

Asmala, E., Kaartokallio, H., Carstensen, J., and Thomas, D. N. (2016). Variation in riverine inputs affect dissolved organic matter characteristics throughout the estuarine gradient. *Front. Mar. Sci.* 2:125. doi: 10.3389/fmars.2015.00125

Aufdenkampe, A. K., Hedges, J. I., Richey, J. E., Krusche, A. V., and Llerena, C. A. (2001). Sorptive fractionation of dissolved organic nitrogen and amino acids onto fine sediments within the Amazon Basin. *Limnol. Oceanogr.* 46, 1921–1935. doi: 10.4319/lo.2001.46.8.1921

Barker, J. D., Sharp, M. J., Fitzsimons, S. J., and Turner, R. J. (2006). Abundance and dynamics of dissolved organic carbon in glacier systems. *Arctic Antarctic Alpine Res.* 38, 163–172.

Barrera, F., Lara, R. J., Krock, B., Garzón-Cardona, J. E., Fabro, E., and Koch, B. P. (2017). Factors influencing the characteristics and distribution or surface organic matter in the Pacific-Atlantic connection. *J. Mar. Syst.* 175, 36–45. doi: 10.1016/j.jmarsys.2017.07.004

Bartholomew, I., Nienow, P., Sole, A., Mair, D., Cowton, T., Palmer, S., et al. (2011). Supraglacial forcing of subglacial drainage in the ablation zone of the Greenland ice sheet. *Geophys. Res. Lett.* 38:L08502. doi: 10.1029/2011GL047063

Benjamini, Y., and Hochberg, Y. (1995). Controlling the false discovery rate: A practical and powerful approach to multiple testing. *J. R. Stat. Soc. Ser. B (Methodological)* 57, 289–300. doi: 10.1111/j.2517-6161.1995.tb02031.x

Bianchi, T. S., Arndt, S., Austin, W. E. N., Benn, D. I., Bertrand, S., Cui, X., et al. (2020). Fjords as Aquatic Critical Zones (ACZs). *Earth Sci. Rev.* 203:103145. doi: 10.1016/j.earscirev.2020.103145

Bown, F., Rivera, A., Pętlicki, M., Bravo, C., Oberreuter, J., and Moffat, C. (2019). Recent ice dynamics and mass balance of Jorge Montt Glacier, Southern Patagonia Icefield. *J. Glaciol.* 65, 732–744. doi: 10.1017/jog.2019.47

Brett, M. T., Bunn, S. E., Chandra, S., Galloway, A. W. E., Guo, F., Kainz, M. J., et al. (2017). How important are terrestrial organic carbon inputs for secondary production in freshwater ecosystems? *Freshw. Biol.* 62, 833–853. doi: 10.1111/fwb.12909

Brogi, S. R., Jung, J. Y., Ha, S. Y., and Hur, J. (2019). Seasonal differences in dissolved organic matter properties and sources in an Arctic fjord: implications for future conditions. *Sci. Total Environ.* 694:133740. doi: 10.1016/j.scitotenv.2019.133740

Bronk, D. A., See, J. H., Bradley, P., and Killberg, L. (2007). DON as a source of bioavailable nitrogen for phytoplankton. *Biogeosciences* 4, 283–296. doi: 10.5194/bg-4-283-2007

Burd, A. B., Frey, S., Cabre, A., Ito, T., Levine, N. M., Lønborg, C., et al. (2016). Terrestrial and marine perspectives on modeling organic matter degradation pathways. *Glob. Change Biol.* 22, 121–136. doi: 10.1111/gcb.12987

Carrivick, J. L., and Tweed, F. S. (2013). Proglacial lakes: character, behaviour and geological importance. *Quaternary Sci. Rev.* 78, 34–52. doi: 10.1016/j.quascirev.2013.07.028

Cuevas, L. A., Tapia, F. J., Iriarte, J. L., González, H. E., Silva, N., and Vargas, C. A. (2019). Interplay between freshwater discharge and oceanic waters modulates phytoplankton size-structure in fjords and channel systems of the Chilean Patagonia. *Prog. Oceanogr.* 173, 103–113. doi: 10.1016/j.pocean.2019.02.012

Determann, S., Lobbes, J. M., Reuter, R., and Rullkötter, J. (1998). Ultraviolet fluorescence excitation and emission spectroscopy of marine algae and bacteria. *Mar. Chem.* 62, 137–156. doi: 10.1016/S0304-4203(98)00026-7

Dirección General de Aguas (2019). *Hydrometeorological Service: DGA Stations Statistics*. Santiago, CA: Dirección General de Aguas.

Dittmar, T., Koch, B., Hertkorn, N., and Kattner, G. (2008). A simple and efficient method for the solid-phase extraction of dissolved organic matter (SPE-DOM) from seawater. *Limnol. Oceanogr. Methods* 6, 230–235. doi: 10.4319/lom.2008.6.230

Dubnick, A., Barker, J., Sharp, M., Wadham, J., Lis, G., Telling, J., et al. (2010). Characterization of dissolved organic matter (DOM) from glacial environments using total fluorescence spectroscopy and parallel factor analysis. *Anal. Glaciol.* 51, 111–122.

Dussaillant, A. J., Buytaert, W., Meier, C., and Espinoza, F. (2012). Hydrological regime of remote catchments with extreme gradients under accelerated change: the Baker basin in Patagonia. *Hydrol. Sci. J.* 57, 1530–1542. doi: 10.1080/02626667.2012.726993

Dussaillant, I., Berthier, E., Brun, F., Masiokas, M., Hugonnet, R., Favier, V., et al. (2019). Two decades of glacier mass loss along the Andes. *Nat. Geosci.* 12, 802–808. doi: 10.1038/s41561-019-0432-5

Eisma, D. (1986). Flocculation and de-flocculation of suspended matter in estuaries. *Netherlands J. Sea Res.* 20, 183–199. doi: 10.1016/0077-7579(86)90041-4

Farr, T. G., Rosen, P. A., Caro, E., Crippen, R., Duren, R., Hensley, S., et al. (2007). The shuttle radar topography mission. *Rev. Geophys.* 45:RG2004. doi: 10.1029/2005RG000183

Fellman, J. B., D'Amore, D. V., Hood, E., and Boone, R. D. (2008). Fluorescence characteristics and biodegradability of dissolved organic matter in forest and wetland soils from coastal temperate watersheds in southeast Alaska. *Biogeochemistry* 88, 169–184. doi: 10.1007/s10533-008-9203-x

Fellman, J. B., Hood, E., Raymond, P. A., Hudson, J., Bozeman, M., and Arimitsu, M. (2015). Evidence for the assimilation of ancient glacier organic carbon in a proglacial stream food web. *Limnol. Oceanogr.* 60, 1118–1128. doi: 10.1002/lno.10088

Fellman, J. B., Hood, E., Spencer, R. G. M., Stubbins, A., and Raymond, P. A. (2014). Watershed glacier coverage influences dissolved organic matter biogeochemistry in coastal watersheds of southeast Alaska. *Ecosystems* 17, 1014–1025. doi: 10.1007/s10021-014-9777-1

Fellman, J. B., Spencer, R. G. M., Hernes, P. J., Edwards, R. T., D'Amore, D. V., and Hood, E. (2010). The impact of glacier runoff on the biodegradability and biochemical composition of terrigenous dissolved organic matter in near-shore marine ecosystems. *Mar. Chem.* 121, 112–122. doi: 10.1016/j.marchem.2010.03.009

Foresta, L., Gourmelen, N., Weissgerber, F., Nienow, P., Williams, J. J., Shepherd, A., et al. (2018). Heterogeneous and rapid ice loss over the Patagonian Ice Fields revealed by CryoSat-2 swath radar altimetry. *Remote Sensing Environ.* 211, 441–455. doi: 10.1016/J.RSE.2018.03.041

Fox, B. G., Thorn, R. M. S., Anesio, A. M., and Reynolds, D. M. (2017). The in situ bacterial production of fluorescent organic matter; an investigation at a species level. *Water Res.* 125, 350–359. doi: 10.1016/j.watres.2017.08.040

Gašparović, B., Plavšić, M., Ćosović, B., and Reigstad, M. (2005). Organic matter characterization and fate in the sub-arctic Norwegian fjords during the late spring/summer period. *Estuarine Coastal Shelf Sci.* 62, 95–107. doi: 10.1016/j.ecss.2004.08.008

Glasser, N. F., Harrison, S., Jansson, K. N., Anderson, K., and Cowley, A. (2011). Global sea-level contribution from the Patagonian Icefields since the Little Ice Age maximum. *Nat. Geosci.* 4, 303–307. doi: 10.1038/ngeo1122

González, H. E., Castro, L., Daneri, G., Iriarte, J. L., Silva, N., Vargas, C. A., et al. (2011). Seasonal plankton variability in Chilean Patagonia fjords: carbon flow through the pelagic food web of Aysen Fjord and plankton dynamics in the Moraleda Channel basin. *Continental Shelf Res.* 31, 225–243. doi: 10.1016/J.CSR.2010.08.010

González, H. E., Castro, L. R., Daneri, G., Iriarte, J. L., Silva, N., Tapia, F., et al. (2013). Land–ocean gradient in haline stratification and its effects on plankton dynamics and trophic carbon fluxes in Chilean Patagonian fjords (47–50°S). *Prog. Oceanogr.* 119, 32–47. doi: 10.1016/J.POCEAN.2013.06.003

González, H. E., Graeve, M., Kattner, G., Silva, N., Castro, L., Iriarte, J. L., et al. (2016). Carbon flow through the pelagic food web in southern Chilean Patagonia: Relevance of Euphausia vallentini as a key species. *Mar. Ecol. Prog. Ser.* 557, 91–110. doi: 10.3354/meps11826

González, H. E., Nimptsch, J., Giesecke, R., and Silva, N. (2019). Organic matter distribution, composition and its possible fate in the Chilean North-Patagonian estuarine system. *Sci. Total Environ.* 657, 1419–1431. doi: 10.1016/j.scitotenv.2018.11.445

Gumbricht, T., Román-Cuesta, R. M., Verchot, L. V., Herold, M., Wittmann, F., Householder, E., et al. (2019). *Tropical and Subtropical Wetlands Distribution Version 2*. Bogor: Center for International Forestry Research. doi: 10.17528/CIFOR/DATA.00058

Gutiérrez, M. H., Galand, P. E., Moffat, C., and Pantoja, S. (2015). Melting glacier impacts community structure of Bacteria, Archaea and Fungi in a Chilean Patagonia fjord. *Environ. Microbiol.* 17, 3882–3897. doi: 10.1111/1462-2920.12872

Hågvar, S., and Ohlson, M. (2013). Ancient carbon from a melting glacier gives high ^{14}C age in living pioneer invertebrates. *Sci. Rep.* 3:2820. doi: 10.1038/srep02820

Hawkings, J., Wadham, J., Tranter, M., Telling, J., Bagshaw, E., Beaton, A., et al. (2016). The Greenland Ice Sheet as a hot spot of phosphorus weathering and export in the Arctic. *Glob. Biogeochem. Cycles* 30, 191–210. doi: 10.1002/2015GB005237

Hawkings, J. R., Wadham, J. L., Tranter, M., Lawson, E., Sole, A., Cowton, T., et al. (2015). The effect of warming climate on nutrient and solute export from the Greenland Ice Sheet. *Geochem. Perspect. Lett.* 1, 94–104. doi: 10.7185/geochemlet.1510

Hawkings, J. R., Wadham, J. L., Tranter, M., Raiswell, R., Benning, L. G., Statham, P. J., et al. (2014). Ice sheets as a significant source of highly reactive nanoparticulate iron to the oceans. *Nat. Commun.0* 5:3929. doi: 10.1038/ncomms4929

Hedges, J. I., and Stern, J. H. (1984). Carbon and nitrogen determinations of carbonate-containing solids. *Limnol. Oceanogr.* 29, 657–663. doi: 10.4319/lo.1984.29.3.0657

Hemingway, J. D., Spencer, R. G. M., Podgorski, D. C., Zito, P., Sen, I. S., and Galy, V. V. (2019). Glacier meltwater and monsoon precipitation drive Upper Ganges Basin dissolved organic matter composition. *Geochim. Cosmochim. Acta* 244, 216–228. doi: 10.1016/J.GCA.2018.10.012

Hernes, P. J., and Benner, R. (2003). Photochemical and microbial degradation of dissolved lignin phenols: implications for the fate of terrigenous dissolved organic matter in marine environments. *J. Geophys. Res. C Oceans* 108:3291.

Hood, E., Battin, T. J., Fellman, J., Neel, S. O., Spencer, R. G. M., O'Neel, S., et al. (2015). Storage and release of organic carbon from glaciers and ice sheets. *Nat. Geosci.* 8, 91–96. doi: 10.1038/ngeo2331

Hood, E., Fellman, J., Spencer, R. G. M., Hernes, P. J., Edwards, R., D'Amore, D., et al. (2009). Glaciers as a source of ancient and labile organic matter to the marine environment. *Nature* 462, 1044–1047. doi: 10.1038/nature08580

Hopkinson, C. S., Buffam, I., Hobbie, J., Vallino, J., Perdue, M., Eversmeyer, B., et al. (1998). Terrestrial inputs of organic matter to coastal ecosystems: an intercomparison of chemical characteristics and bioavailability. *Biogeochemistry* 43, 211–234. doi: 10.1023/A:1006016030299

Hopwood, M. J., Carroll, D., Browning, T. J., Meire, L., Mortensen, J., Krisch, S., et al. (2018). Non-linear response of summertime marine productivity to increased meltwater discharge around Greenland. *Nat. Commun.* 9:3256. doi: 10.1038/s41467-018-05488-8

Hopwood, M. J., Carroll, D., Dunse, T., Hodson, A., Holding, J. M., Iriarte, J. L., et al. (2020). Review article: how does glacier discharge affect marine biogeochemistry and primary production in the Arctic? *Cryosphere* 14, 1347–1383. doi: 10.5194/tc-14-1347-2020

Hosomi, M., and Sudo, R. (1986). Simultaneous determination of total nitrogen and total phosphorus in freshwater samples using persulfate digestion. *Int. J. Environ. Stud.* 27, 267–275. doi: 10.1080/00207238608710296

Iriarte, J. L., González, H. E., Liu, K. K., Rivas, C., and Valenzuela, C. (2007). Spatial and temporal variability of chlorophyll and primary productivity in surface waters of southern Chile (41.5-43° S). *Estuarine Coastal Shelf Sci.* 74, 471–480. doi: 10.1016/j.ecss.2007.05.015

Iriarte, J. L., Pantoja, S., and Daneri, G. (2014). Oceanographic processes in Chilean fjords of Patagonia: from small to large-scale studies. *Prog. Oceanogr.* 129, 1–7. doi: 10.1016/j.pocean.2014.10.004

Jacob, B. G., Tapia, F. J., Daneri, G., Iriarte, J. L., Montero, P., Sobarzo, M., et al. (2014). Springtime size-fractionated primary production across hydrographic and PAR-light gradients in Chilean Patagonia (41-50°S). *Prog. Oceanogr.* 129, 75–84. doi: 10.1016/j.pocean.2014.08.003

Keil, R. G., Montluçon, D. B., Prahl, F. G., and Hedges, J. I. (1994). Sorptive preservation of labile organic matter in marine sediments. *Nature* 370, 549–552. doi: 10.1038/370549a0

Kellerman, A. M., Guillemette, F., Podgorski, D. C., Aiken, G. R., Butler, K. D., and Spencer, R. G. M. (2018). Unifying concepts linking dissolved organic matter composition to persistence in aquatic ecosystems. *Environ. Sci. Technol.* 52, 2538–2548. doi: 10.1021/acs.est.7b05513

Kellerman, A. M., Hawkings, J. R., Wadham, J. L., Kohler, T. J., Stibal, M., Grater, E., et al. (2020). Glacier outflow dissolved organic matter as a window into seasonally changing carbon sources: Leverett Glacier, Greenland. *J. Geophys. Res. Biogeosci.* 125:e2019JG005161. doi: 10.1029/2019jg005161

Knudsen, N. T., Yde, J. C., and Gasser, G. (2007). Suspended sediment transport in glacial meltwater during the initial quiescent phase after a major surge event at Kuannersuit Glacier, Greenland. *Geografisk Tidsskrift*. 107, 1–7. doi: 10.1080/00167223.2007.10801370

Koch, B. P., and Dittmar, T. (2006). From mass to structure: an aromaticity index for high-resolution mass data of natural organic matter. *Rapid Commun. Mass Spectrom.* 20, 926–932. doi: 10.1002/rcm.2386

Koch, B. P., Witt, M., Engbrodt, R., Dittmar, T., and Kattner, G. (2005). Molecular formulae of marine and terrigenous dissolved organic matter detected by electrospray ionization Fourier transform ion cyclotron resonance mass spectrometry. *Geochim. Cosmochim. Acta* 69, 3299–3308. doi: 10.1016/j.gca.2005.02.027

Kujawinski, E. B., Longnecker, K., Blough, N. V., Vecchio, R., Del Finlay, L., Kitner, J. B., et al. (2009). Identification of possible source markers in marine dissolved organic matter using ultrahigh resolution mass spectrometry. *Geochim. Cosmochim. Acta* 73, 4384–4399. doi: 10.1016/j.gca.2009.04.033

Landa, M., Cottrell, M. T., Kirchman, D. L., Kaiser, K., Medeiros, P. M., Tremblay, L., et al. (2014). Phylogenetic and structural response of heterotrophic bacteria to dissolved organic matter of different chemical composition in a continuous culture study. *Environ. Microbiol.* 16, 1668–1681. doi: 10.1111/1462-2920.12242

Lawson, E. C., Wadham, J. L., Tranter, M., Stibal, M., Lis, G. P., Butler, C. E. H., et al. (2014). Greenland ice sheet exports labile organic carbon to the arctic oceans. *Biogeosciences* 11, 4015–4028. doi: 10.5194/bg-11-4015-2014

Lechtenfeld, O. J., Kattner, G., Flerus, R., McCallister, S. L., Schmitt-Kopplin, P., and Koch, B. P. (2014). Molecular transformation and degradation of refractory dissolved organic matter in the Atlantic and Southern Ocean. *Geochim. Cosmochim. Acta* 126, 321–337. doi: 10.1016/j.gca.2013.11.009

Lindsay, J. B. (2016). Whitebox GAT: a case study in geomorphometric analysis. *Comput. Geosci.* 95, 75–84. doi: 10.1016/j.cageo.2016.07.003

Liu, S., Wawrik, B., and Liu, Z. (2017). Different bacterial communities involved in peptide decomposition between normoxic and hypoxic coastal waters. *Front. Microbiol.* 8:353. doi: 10.3389/fmicb.2017.00353

Lønborg, C., Yokokawa, T., Herndl, G. J., and Antón Álvarez-Salgado, X. (2015). Production and degradation of fluorescent dissolved organic matter in surface waters of the eastern north Atlantic ocean. *Deep Sea Res. Part I Oceanogr. Res. Papers* 96, 28–37. doi: 10.1016/j.dsr.2014.11.001

Marín, V. H., Tironi, A., Paredes, M. A., and Contreras, M. (2013). Modeling suspended solids in a Northern Chilean Patagonia glacier-fed fjord: GLOF scenarios under climate change conditions. *Ecol. Model.* 264, 7–16. doi: 10.1016/j.ecolmodel.2012.06.017

Medeiros, P. M., Seidel, M., Ward, N. D., Carpenter, E. J., Gomes, H. R., Niggemann, J., et al. (2015). Fate of the Amazon River dissolved organic matter in the tropical Atlantic Ocean. *Glob. Biogeochem. Cycles* 29, 677–690. doi: 10.1002/2015GB005115

Meerhoff, E., Castro, L. R., Tapia, F. J., and Pérez-Santos, I. (2019). Hydrographic and Biological Impacts of a Glacial Lake Outburst Flood (GLOF) in a Patagonian Fjord. *Estuaries Coasts* 42, 132–143. doi: 10.1007/s12237-018-0449-9

Meire, L., Mortensen, J., Meire, P., Juul-Pedersen, T., Sejr, M. K., Rysgaard, S., et al. (2017). Marine-terminating glaciers sustain high productivity in Greenland fjords. *Glob. Change Biol.* 23, 5344–5357. doi: 10.1111/gcb.13801

Messager, M. L., Lehner, B., Grill, G., Nedeva, I., and Schmitt, O. (2016). Estimating the volume and age of water stored in global lakes using a geo-statistical approach. *Nat. Commun.* 7:13603. doi: 10.1038/ncomms13603

Meyers, P. A., Leenheer, M. J., Eaoie, B. J., and Maule, S. J. (1984). Organic geochemistry of suspended and settling particulate matter in Lake Michigan. *Geochim. Cosmochim. Acta* 48, 443–452. doi: 10.1016/0016-7037(84)90273-4

Millan, R., Rignot, E., Rivera, A., Martineau, V., Mouginot, J., Zamora, R., et al. (2019). Ice thickness and bed elevation of the Northern and Southern Patagonian Icefields. *Geophys. Res. Lett.* 46, 6626–6635. doi: 10.1029/2019GL082485

Milner, A. M., Khamis, K., Battin, T. J., Brittain, J. E., Barrand, N. E., Füreder, L., et al. (2017). Glacier shrinkage driving global changes in downstream systems. *Proc. Natl. Acad. Sci. U.S.A.* 114, 9770–9778. doi: 10.1073/pnas.1619807114

Moffat, C. (2014). Wind-driven modulation of warm water supply to a proglacial fjord, Jorge Montt Glacier, Patagonia. *Geophys. Res. Lett.* 41, 3943–3950. doi: 10.1002/2014GL060071

Møller, E. F. (2007). Production of dissolved organic carbon by sloppy feeding in the copepods Acartia tonsa, Centropages typicus, and Temora longicornis. *Limnol. Oceanogr.* 52, 79–84. doi: 10.4319/lo.2007.52.1.0079

Montero, P., Daneri, G., González, H. E., Iriarte, J. L., Tapia, F. J., Lizárraga, L., et al. (2011). Seasonal variability of primary production in a fjord ecosystem of the Chilean Patagonia: implications for the transfer of carbon within pelagic food webs. *Continental Shelf Res.* 31, 202–215. doi: 10.1016/j.csr.2010.09.003

Montero, P., Pérez-Santos, I., Daneri, G., Gutiérrez, M. H., Igor, G., Seguel, R., et al. (2017). A winter dinoflagellate bloom drives high rates of primary production in a Patagonian fjord ecosystem. *Estuarine Coastal Shelf Sci.* 199, 105–116. doi: 10.1016/j.ecss.2017.09.027

Mostovaya, A., Hawkes, J. A., Dittmar, T., and Tranvik, L. J. (2017). Molecular determinants of dissolved organic matter reactivity in lake water. *Front. Earth Sci.* 5:106. doi: 10.3389/feart.2017.00106

Mulholland, M. R., and Lee, C. (2009). Peptide hydrolysis and the uptake of dipeptides by phytoplankton. *Limnol. Oceanogr.* 54, 856–868. doi: 10.4319/lo.2009.54.3.0856

Murphy, K. R., Stedmon, C. A., Graeber, D., and Bro, R. (2013). Fluorescence spectroscopy and multi-way techniques. PARAFAC. *Anal. Methods* 5:6557. doi: 10.1039/c3ay41160e

Murphy, K. R., Stedmon, C. A., Waite, T. D., and Ruiz, G. M. (2008). Distinguishing between terrestrial and autochthonous organic matter sources in marine environments using fluorescence spectroscopy. *Mar. Chem.* 108, 40–58.

Murphy, K. R., Stedmon, C. A., Wenig, P., and Bro, R. (2014). OpenFluor–an online spectral library of auto-fluorescence by organic compounds in the environment. *Anal. Methods* 6, 658–661. doi: 10.1039/C3AY41935E

Nagata, T., Fukuda, H., Fukuda, R., and Koike, I. (2000). Bacterioplankton distribution and production in deep Pacific waters: large-scale geographic variations and possible coupling with sinking particle fluxes. *Limnol. Oceanogr.* 45, 426–435. doi: 10.4319/lo.2000.45.2.0426

Ohno, T., He, Z., Sleighter, R. L., Honeycutt, C. W., and Hatcher, P. G. (2010). Ultrahigh resolution mass spectrometry and indicator species analysis to identify marker components of soil- and plant biomass-derived organic matter fractions. *Environ. Sci. Technol.* 44, 8594–8600. doi: 10.1021/es101089t

Oksanen, J., Blanchet, F. G., Kindt, R., Legendre, P., Minchin, P. R., O'Hara, R. B., et al. (2016). *Vegan: Community Ecology Package. R Package Version 2.2–1. 2015*.

Osterholz, H., Kirchman, D. L., Niggemann, J., and Dittmar, T. (2016). Environmental drivers of dissolved organic matter molecular composition in the Delaware Estuary. *Front. Earth Sci.* 4:95. doi: 10.3389/feart.2016.00095

Pace, M. L., Cole, J. J., Carpenter, S. R., Kitchell, J. F., Hodgson, J. R., Van De Bogert, M. C., et al. (2004). Whole-lake carbon-13 additions reveal terrestrial support of aquatic food webs. *Nature* 427, 240–243. doi: 10.1038/nature02227

Pantoja, S., Luis Iriarte, J., and Daneri, G. (2011). Oceanography of the Chilean Patagonia. *Continental Shelf Res.* 31, 149–153. doi: 10.1016/j.csr.2010.10.013

Paulsen, M. L., Müller, O., Larsen, A., Møller, E. F., Middelboe, M., Sejr, M. K., et al. (2018). Biological transformation of Arctic dissolved organic matter in a NE Greenland fjord. *Limnol. Oceanogr.* 64, 1014–1033. doi: 10.1002/lno.11091

Paulsen, M. L., Nielsen, S. E. B., Müller, O., Møller, E. F., Stedmon, C. A., Juul-Pedersen, T., et al. (2017). Carbon bioavailability in a high Arctic fjord influenced by glacial meltwater, NE Greenland. *Front. Mar. Sci.* 4:176. doi: 10.3389/fmars.2017.00176

Piret, L., Troch, M., Vandekerkhove, E., Harada, N., Moffat, C., Rivera, A., et al. (2019). *Gridded Bathymetry (KMZ format) of the Baker-Martinez fjord complex (Chile, 48°S) v2*. Palisades, NY: Interdisciplinary Earth Data Alliance (IEDA). doi: 10.1594/IEDA/324869

Poulet, S. A., Williams, R., Conway, D. V. P., and Videau, C. (1991). Co-occurrence of copepods and dissolved free amino acids in shelf sea waters. *Mar. Biol.* 108, 373–385. doi: 10.1007/BF01313646

Quiroga, E., Ortiz, P., Gerdes, D., Reid, B., Villagran, S., and Quiñones, R. (2012). Organic enrichment and structure of macrobenthic communities in the glacial Baker Fjord, Northern Patagonia, Chile. *J. Mar. Biol. Assoc. U.K.* 92, 73–83. doi: 10.1017/S0025315411000385

R Core Team (2015). *R: A Language and Environment for Statistical Computing*. Vienna: R Foundation for Statistical Computing.

Rebolledo, L., Bertrand, S., Lange, C. B., Tapia, F. J., Quiroga, E., Troch, M., et al. (2019). Compositional and biogeochemical variations of sediments across the terrestrial-marine continuum of the Baker-Martínez fjord system (Chile, 48°S). *Prog. Oceanogr.* 174, 89–104. doi: 10.1016/J.POCEAN.2018.12.004

RGI Consortium (2017). *Randolph Glacier Inventory – A Dataset of Global Glacier Outlines: Version 6.0. Technical Report, Global Land Ice Measurements from Space*. Denver, CO: Digital Media. doi: 10.7265/N5-RGI-60

Riedel, T., Zark, M., Vähätalo, A. V., Niggemann, J., Spencer, R. G. M., Hernes, P. J., et al. (2016). Molecular signatures of biogeochemical transformations in dissolved organic matter from ten world rivers. *Front. Earth Sci.* 4:85. doi: 10.3389/feart.2016.00085

Rivera, A., Corripio, J., Bravo, C., and Cisternas, S. (2012). Glaciar Jorge Montt (Chilean Patagonia) dynamics derived from photos obtained by fixed cameras and satellite image feature tracking. *Ann. Glaciol.* 53, 147–155. doi: 10.3189/2012AoG60A152

Romera-Castillo, C., Sarmento, H., Álvarez-Salgado, X. A., Gasol, J. M., and Marrasé, C. (2010). Production of chromophoric dissolved organic matter by marine phytoplankton. *Limnol. Oceanogr.* 55, 446–454. doi: 10.4319/lo.2010.55.1.0446

Romera-Castillo, C., Sarmento, H., Alvarez-Salgado, X. A. Á, Gasol, J. M., and Marrasé, C. (2011). Net production and consumption of fluorescent colored dissolved organic matter by natural bacterial assemblages growing on marine phytoplankton exudates. *Appl. Environ. Microbiol.* 77, 7490–7498. doi: 10.1128/AEM.00200-11

Ross, L., Pérez-Santos, I., Valle-Levinson, A., and Schneider, W. (2014). Semidiurnal internal tides in a Patagonian fjord. *Prog. Oceanogr.* 129, 19–34. doi: 10.1016/j.pocean.2014.03.006

Saldías, G. S., Sobarzo, M., and Quiñones, R. (2019). Freshwater structure and its seasonal variability off western Patagonia. *Prog. Oceanogr.* 174, 143–153. doi: 10.1016/j.pocean.2018.10.014

Seidel, M., Manecki, M., Herlemann, D. P. R., Deutsch, B., Schulz-Bull, D., Jürgens, K., et al. (2017). Composition and transformation of dissolved organic matter in the Baltic Sea. *Front. Earth Sci.* 5:31. doi: 10.3389/feart.2017.00031

Shimotori, K., Omori, Y., and Hama, T. (2010). Bacterial production of marine humic-like fluorescent dissolved organic matter and its biogeochemical importance. *Aquatic Microb. Ecol.* 58, 55–66. doi: 10.3354/ame01350

Sholkovitz, E. R. (1976). Flocculation of dissolved organic and inorganic matter during the mixing of river water and seawater. *Geochim. Cosmochim. Acta* 40, 831–845. doi: 10.1016/0016-7037(76)90035-1

Singer, G. A., Fasching, C., Wilhelm, L., Niggemann, J., Steier, P., Dittmar, T., et al. (2012). Biogeochemically diverse organic matter in Alpine glaciers and its downstream fate. *Nat. Geosci.* 5, 710–714. doi: 10.1038/ngeo1581

Sleighter, R. L., and Hatcher, P. G. (2008). Molecular characterization of dissolved organic matter (DOM) along a river to ocean transect of the lower Chesapeake Bay by ultrahigh resolution electrospray ionization Fourier transform ion cyclotron resonance mass spectrometry. *Mar. Chem.* 110, 140–152. doi: 10.1016/j.marchem.2008.04.008

Smith, D. F., Podgorski, D. C., Rodgers, R. P., Blakney, G. T., and Hendrickson, C. L. (2018). 21 tesla FT-ICR mass spectrometer for ultrahigh-resolution analysis of complex organic mixtures. *Anal. Chem.* 90, 2041–2047. doi: 10.1021/acs.analchem.7b04159

Smith, R. W., Bianchi, T. S., Allison, M., Savage, C., and Galy, V. (2015). High rates of organic carbon burial in fjord sediments globally. *Nat. Geosci.* 8, 450–453. doi: 10.1038/ngeo2421

Spencer, R. G. M., Stubbins, A., Hernes, P. J., Baker, A., Mopper, K., Aufdenkampe, A. K., et al. (2009). Photochemical degradation of dissolved organic matter and dissolved lignin phenols from the Congo River. *J. Geophys. Res. Biogeosci.* 114:G03010. doi: 10.1029/2009JG000968

Spencer, R. G. M. M., Guo, W., Raymond, P. A., Dittmar, T., Hood, E., Fellman, J., et al. (2014). Source and biolability of ancient dissolved organic matter in glacier and lake ecosystems on the tibetan plateau. *Geochim. Cosmochim. Acta* 142, 64–74. doi: 10.1016/j.gca.2014.08.006

Stubbins, A., Spencer, R. G. M., Chen, H., Hatcher, P. G., Mopper, K., Hernes, P. J., et al. (2010). Illuminated darkness: molecular signatures of Congo River dissolved organic matter and its photochemical alteration as revealed by ultrahigh precision mass spectrometry. *Limnol. Oceanogr.* 55, 1467–1477. doi: 10.4319/lo.2010.55.4.1467

Sun, L., Perdue, E. M., Meyer, J. L., and Weis, J. (1997). Use of elemental composition to predict bioavailability of dissolved organic matter in a Georgia river. *Limnol. Oceanogr.* 42, 714–721. doi: 10.4319/lo.1997.42.4.0714

Tateishi, R., Hoan, N. T., Kobayashi, T., Alsaaideh, B., Tana, G., and Phong, D. X. (2014). Production of Global Land Cover Data – GLCNMO2008. *J. Geogr. Geol.* 6, 99-122. doi: 10.5539/jgg.v6n3p99

Urban-Rich, J., McCarty, J. T., and Shailer, M. (2004). Effects of food concentration and diet on chromophoric dissolved organic matter accumulation and fluorescent composition during grazing experiments with the copepod Calanus finmarchicus. *ICES J. Mar. Sci.* 61, 542–551. doi: 10.1016/j.icesjms.2004.03.024

Vargas, C. A., Martinez, R. A., San Martin, V., Aguayo, M., Silva, N., and Torres, R. (2011). Allochthonous subsidies of organic matter across a lake–river–fjord landscape in the Chilean Patagonia: implications for marine zooplankton in inner fjord areas. *Continental Shelf Res.* 31, 187–201. doi: 10.1016/J.CSR.2010.06.016

Ward, N. D., Bianchi, T. S., Medeiros, P. M., Seidel, M., Richey, J. E., Keil, R. G., et al. (2017). Where carbon goes when water flows: carbon cycling across the aquatic continuum. *Front. Mar. Sci.* 4:7. doi: 10.3389/fmars.2017.00007

Welti, N., Striebel, M., Ulseth, A. J., Cross, W. F., DeVilbiss, S., Glibert, P. M., et al. (2017). Bridging food webs, ecosystem metabolism, and biogeochemistry using ecological stoichiometry theory. *Front. Microbiol.* 8:1298. doi: 10.3389/fmicb.2017.01298

Włodarska-Kowalczuk, M., Mazurkiewicz, M., Górska, B., Michel, L. N., Jankowska, E., and Zaborska, A. (2019). Organic carbon origin, benthic faunal consumption, and burial in sediments of Northern Atlantic and Arctic Fjords (60–81°N). *J. Geophys. Res. Biogeosci.* 124, 3737–3751. doi: 10.1029/2019JG005140

Yamashita, Y., Fichot, C. G., Shen, Y., Jaffé, R., and Benner, R. (2015). Linkages among fluorescent dissolved organic matter, dissolved amino acids and lignin-derived phenols in a river-influenced ocean margin. *Front. Mar. Sci.* 2:92. doi: 10.3389/fmars.2015.00092

Yamashita, Y., Jaffé, R., Maie, N., and Tanoue, E. (2008). Assessing the dynamics of dissolved organic matter (DOM) in coastal environments by excitation emission matrix fluorescence and parallel factor analysis (EEM-PARAFAC). *Limnol. Oceanogr.* 53, 1900–1908. doi: 10.4319/lo.2008.53.5.1900

Zemp, M., Frey, H., Gärtner-Roer, I., Nussbaumer, S. U., Hoelzle, M., Paul, F., et al. (2015). Historically unprecedented global glacier decline in the early 21st century. *J. Glaciol.* 61, 745–762. doi: 10.3189/2015JoG15J017

Zhu, Z. Y., Wu, Y., Liu, S. M., Wenger, F., Hu, J., Zhang, J., et al. (2016). Organic carbon flux and particulate organic matter composition in Arctic valley glaciers: examples from the Bayelva River and adjacent Kongsfjorden. *Biogeosciences* 13, 975–987. doi: 10.5194/bg-13-975-2016

Conflict of Interest: The authors declare that the research was conducted in the absence of any commercial or financial relationships that could be construed as a potential conflict of interest.

frontiers in Marine Science

REVIEW
published: 20 April 2021
doi: 10.3389/fmars.2021.612628

Blooms of *Alexandrium catenella* in Coastal Waters of Chilean Patagonia: Is Subantarctic Surface Water Involved?

*David W. Crawford, Paulina Montero and Giovanni Daneri**

Centro de Investigación en Ecosistemas de la Patagonia (CIEP), COPAS Sur Austral, Universidad de Concepción, Coyhaique, Chile

At the southern tip of South America, evidence of shellfish toxicity has been recorded in the accounts of early explorers and shipwreck survivors since the late 16th Century. Blooms of the toxic dinoflagellate *Alexandrium catenella* were described in the western Magellan Strait in the early 1970s and have since shown a northward progression through Chilean Patagonia, culminating in a catastrophic toxic event around Chiloé Island in 2016. This shift has taken place through coastal areas of extremely sparse human population density, and anthropogenically driven eutrophication is therefore unlikely to be significantly involved, at least in the south. However, human activities – such as salmon cultivation – may play a role in the intensification of blooms in the more densely populated areas of northern Patagonia. In the fjords and channels of Chilean Patagonia, phytoplankton assemblages are shaped by complex interactions between freshwater (FW) run-off and intrusions of subantarctic surface water (SASW). In the context of blooms of *A. catenella*, we review the properties of SASW – transformed in coastal waters into modified subantarctic water (MSAW). FW input is characterized by very low concentrations of dissolved inorganic nitrogen (DIN) and phosphorus (DIP), but relatively high concentrations of silicic acid (DSi); DIN and DIP are instead supplied predominantly by SASW which is severely deficient in DSi. These waters therefore show strong vertical gradients in DIN, DIP and DSi, but also potentially in dissolved trace metals and CO_2. Large scale shifts in the relative inputs of SASW or FW can modify these vertical gradients, potentially forcing competitive changes in phytoplankton assemblages with latitude, with implications for growth and toxicity of *A. catenella* and other harmful species. The northward shift of blooms of *A. catenella* could be associated with anomalies in the Southern Annular Mode (SAM) that modify the influence of MSAW through variations in FW input to coastal waters. The historical presence of blooms in southern Patagonia and Tierra del Fuego, combined with the strongly contrasting conditions with latitude and depth, mean that southern Chile represents an ideal natural laboratory to study climatic and oceanographic influences on dynamics of *A. catenella* populations.

Keywords: Chile, Pacific Ocean, phytoplankton "bloom", *Alexandrium catenella*, HAB (harmful algal blooms), fjords and channels, Patagonia, subantarctic water (SAW)

OPEN ACCESS

Edited by:
Stelios Katsanevakis, University of the Aegean, Greece

Reviewed by:
Suzanne Jane Painting, Centre for Environment, Fisheries and Aquaculture Science (CEFAS), United Kingdom
Jorge I. Mardones, Instituto de Fomento Pesquero (IFOP), Chile

***Correspondence:**
Giovanni Daneri
gdaneri@ciep.cl

Specialty section:
This article was submitted to Marine Ecosystem Ecology, a section of the journal Frontiers in Marine Science

Received: *30 September 2020*
Accepted: *15 March 2021*
Published: *20 April 2021*

Citation:
Crawford DW, Montero P and Daneri G (2021) Blooms of Alexandrium catenella in Coastal Waters of Chilean Patagonia: Is Subantarctic Surface Water Involved? Front. Mar. Sci. 8:612628. doi: 10.3389/fmars.2021.612628

HISTORICAL BACKGROUND

In their search for a passage to the ocean that they would later name the "Pacific," Ferdinand Magellan's ships arrived on the 21st October, 1520 at a cape alongside a promising looking entrance. Here, according to Antonio Pigafetta, who accompanied Magellan, they named this the "Cape of the Eleven Thousand Virgins" (now Cape of the Virgins, or Cabo Vírgenes, **Figure 1**) before entering the strait (Pigafetta, 1874). After passing through the first and second narrows, the ships entered a wider body of water and rounded a cape before heading north west and naming Cabo Deseado (close to present day Cape Pilar, **Figure 1**) as they entered the Pacific Ocean on 28th November, 1520 (Pigafetta, 1874).

At the cape approximately halfway through the strait, Magellan was still some 160 miles from Cabo Deseado, and unaware that Pacific water lay less than 100 feet beneath his ship, overlain by a layer of water derived principally from the surrounding mountains, streams and glaciers. Over 60 years later, this most southerly cape on the Patagonian mainland was named "Cape Froward" (**Figure 1**) by the English explorer Thomas Cavendish during his 1586–1588 circumnavigation of the globe. In 1587, just north of Cape Froward, Cavendish encountered many corpses in the remains of Rey Don Felipe, a settlement established by Pedro Sarmiento de Gamboa in 1584. . .

> "It seemed unto us, that their whole living for a great space was altogether on muscles [mussels] and limpets; for there was not anything else to be had" (Henry, 1875).

With the population of Rey Don Felipe apparently decimated by starvation, Cavendish renamed the town as Port Famine (Puerto del Hambre, **Figure 1**). However, the settlement had survived more than two years, and it has also been proposed that the residents may have been poisoned through eating shellfish contaminated by a harmful algal bloom (HAB) (Espinoza and Espinoza, 2010). Although speculative, this suggestion is supported by an account only twelve years later during the voyage of the Dutch explorer Sebald de Weert. In May 1599 in Great Bay[1] (**Figure 1**) to the west of Cape Froward, the following reaction to eating mussels was noted. . .

> "…and afterwards satisfied their hunger with raw muscles and green herbs, which occasioned them to fall into dropsies[2] and other lingering sickness, of which several died…" (Kerr, 1824).

In April 1767, during the voyage around the world by Samuel Wallis aboard the Dolphin, similar observations were noted in the vicinity of Cape Providence (**Figure 1**), further west in the Magellan Strait. . .

> "We continued daily to gather muscles till the 5th, when several of the people being seized with fluxes[3], the surgeon desired that no more muscles might be brought into the ship" (Hawkesworth, 1773).

During the first voyage of the Beagle in May 1829 near Englefield Island in Seno Otway (**Figure 1**), to the west of Cape Froward, Captain Fitzroy's journal noted. . .

> "One of my boat's crew was ill this day; the first man that had been seriously so, although several had been slightly affected by the muscles and limpets; and one had fits" (Fitzroy, 1839).

By the late 1800s, the potential toxicity of shellfish in this region was clearly evident in an account of a survivor from a vessel foundered in the middle (**Figure 1**) of the Strait of Magellan[4]. . .

> "The mussels, which covered the rocks in great profusion, were useless for purposes of food: all of our party who partook of them became violently ill with symptoms of irritant poisoning, and quickly developed a crimson, papular rash from head to foot, accompanied by a dreadful thirst and a maddening itching. These very mussels constitute, strange to say, the staple diet of the natives, who consume them in enormous quantities and, apparently, without suffering any ill effects…" (O'Sullivan, 1893, see also, Anonymous, 1893).

Regarding the diet of indigenous people, there seems little available evidence for toxicity in shellfish (Guzmán et al., 2002), but it is noteworthy that in a Yaghan Dictionary – cited in Bruce Chatwin's famous travelog *In Patagonia* – a list of synonyms includes. . .

> "Mussels out of season – Shriveled skin – Old age" (Chatwin, 1977).

Indigenous peoples such as the Yaghan might have recognized seasonality in shellfish toxicity and could perhaps mitigate the effects, as has been noted for the Tinglit people of the Pacific coast of North America (Moss, 1993). However, there is evidence in 1891 that indigenous peoples could at times be susceptible to shellfish poisoning further south (**Figure 1**) in the Beagle Channel (Segers, 1891; Lagos, 1998).

In November 1972, a toxic phytoplankton bloom caused by the dinoflagellate *Alexandrium catenella*[5] (Guzmán et al., 1975a; Guzmán and Lembeye, 1975; Lembeye et al., 1975) occurred in the Magellan Strait, slightly to the west of Cape Froward. Cell abundance and paralytic shellfish poison (PSP)

[1]Or Green Bay, which the Dutch named Bay of de Cordes (Kerr, 1824), or Cordes Bay.

[2]Dropsy is also now known as oedema, or edema. Victims of PSP poisoning also exhibited symptoms of edema off Augusta Island, western Patagonia (García et al., 2004a) and in the Magallanes region (Montebruno, 1993).

[3]Not clear whether "seized" refers to PSP poisoning, but "fluxes" could indicate diarrhetic shellfish poisoning (DSP). It is however worth noting here that PSP and DSP toxins can co-occur in Patagonian coastal waters (García et al., 2004b).

[4]The survivor's encampment was 12 miles directly across the strait from Port Famine (O'Sullivan, 1893).

[5]For simplicity we have retained the *Alexandrium catenella* name commonly used in reports in this region, but some earlier reports used the name *Gonyaulax catenella*. We acknowledge that there has been considerable recent taxonomic debate regarding *A. catenella* in particular (John et al., 2014a; Fraga et al., 2015) and the *Alexandrium tamarense* species complex generally (John et al., 2014b).

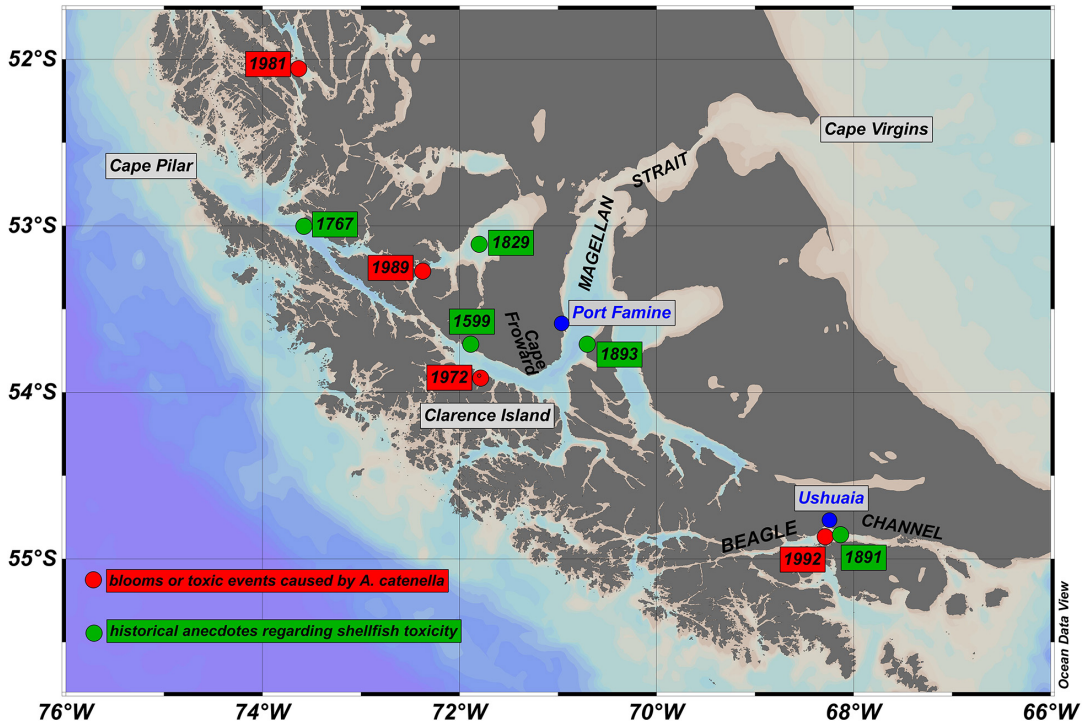

FIGURE 1 | Map of Magallanes and Tierra del Fuego regions of southern Chile and Argentina. The Magellan Strait and Beagle Channel directly connect the southern Pacific and Atlantic Oceans. Green dots show the approximate position of anecdotal reports of shellfish toxicity from pre-1900 historical sources. Accounts are reported (see text for details) for Cordes Bay, 1599 (Kerr, 1824), Cape Providence, 1767 (Hawkesworth, 1773), Englefield Island, 1829 (Fitzroy, 1839), Beagle Channel, 1891 (Segers, 1891), and Fuegian shore opposite Port Famine (O'Sullivan, 1893). Also shown in red are the approximate positions of the focal points of blooms of *A. catenella* and/or associated events of shellfish poisoning between the early 1970s and early 1990s. Events were centered on Bahia Bell, Clarence Island, 1972 (Guzmán et al., 1975a,b; Guzmán and Lembeye, 1975; Lembeye et al., 1975), Seno Union, 1981 (Lembeye, 1981a,b), Estero Núñez, 1989 (Uribe, 1988; Cited reference is given as 1988, even though the event was given as 1989), Beagle Channel, 1992 (Lembeye, 1992; Carreto and Benavides, 1993; Benavides et al., 1995). In all cases, blooms or shellfish toxicity were spread across a much wider area than indicated by the red dots (see also **Figure 2**).

were concentrated around Bahía Bell, Isla Clarence on the north shore of the Tierra del Fuego archipelago (**Figure 1**), although toxins in shellfish were noted over a much wider area (Guzmán et al., 1975b).

In February 1981, a second toxic event caused by *A. catenella* was recorded around Seno Unión (Canal Union, **Figure 1**), north of the Magellan Strait (Lembeye, 1981a,b). Here, abundance was relatively low, but ecdisic cysts of *A. catenella* were found in the digestive system of shellfish (Lembeye, 1981b) resulting in massive intoxication of the mussel *Aulacomya ater* over a wide area (Lembeye, 1981a). A further toxic event was recorded in the vicinity of Estero Núñez in April 1989 (**Figure 1**); again, cysts of *A. catenella* were detected in the digestive tract of *A. ater* and PSP toxins were found at lower concentrations across a much wider area (Uribe, 1988). Toxins were also detected in the Magellan Strait and Beagle Channel starting in October and November 1991 (Lembeye, 1992), with a bloom of *A. catenella* subsequently recorded in January–February 1992 (**Figure 1**) centered around Ushuaia in the Beagle Channel (Carreto and Benavides, 1993; Benavides et al., 1995). Although toxins initially appeared around the western entrance to the Magellan Strait, the event spread to all southern channels from approximately 49° 20′ S to 54° 55′ S (Lembeye, 1992; Benavides et al., 1995).

NORTHWARD PROGRESSION OF BLOOMS

Fewer blooms have been reported in Magellan and Fuegian regions since the 1990s, although *A. catenella* is still present at lower abundances (Guzmán et al., 2013; Pizarro et al., 2011). However, blooms and/or toxic episodes have apparently expanded northward (**Table 1** and **Figure 2**), with *A. catenella* initially detected in the early 1990s in the Aysén Region (Muñoz et al., 1992; Guzmán et al., 2002), and now routinely detected at lower abundances even in winter (Pizarro et al., 2018). Monitoring programs were initiated in 1995, and blooms expanded northwards from 45°47′ S in 1996 to the Los Lagos region around 42°S at Chiloé in 2002 (Clément et al., 2002; Molinet et al., 2003). Mardones et al. (2010) reported an outbreak in 2009 in the Aysén region that later expanded into the Inland Sea of Chiloé and, for the first time, the oceanic waters off Chiloé. This expansion reached the northern end of the Inland Sea of Chiloé following an exceptional bloom of the Dictyochophyte[6] *Pseudochattonella verruculosa* that killed many farmed salmon

[6] *Pseudochattonella verruculosa* was formerly classified in raphidophyceae but has now been ascribed to the Dictyochophycean class (Eckford-Soper and Daugbjerg, 2016). Identification of Chilean *P. verruculosa* was confirmed using the large subunit (LSU) of the nuclear ribosomal RNA gene (Mardones et al., 2019).

TABLE 1 | Approximate location and timing of the peak of major blooms or toxic events caused by *A. catenella* in Patagonian and Fuegian coastal waters. Approximate date and position of the focal point of each major event is given, although these blooms and toxic events often extended over much greater areas and periods than indicated below (see individual studies for details).

				Maximum Reported Toxicity			
Approx. Date	**Approx. Location**	**Approx. Latitude**	**Max. Reported Abundance (10^3 cells l^{-1})**	**(MU)[a]**	**μg STX eq 100 g^{-1}**	**Species most affected**	**References**
Nov 1972	Bahía Bell, Isla Clarence; Magallanes	53.88°S	600	96,000	17,280[b]	Ribbed Mussel (*Aulacomya ater*) and Chilean Mussel (*Mytilus chilensis*)	Guzmán et al. (1975a,b), Guzmán and Lembeye (1975); Lembeye et al. (1975)
Feb 1981	Seno Unión, Ultima Esperanza Province; Magallanes	52.05°S	1.7	6,730	1,211[b]	Ribbed Mussel (*Aulacomya ater*)	Lembeye (1981a,b)
Apr 1989	Estero Núñez, Seno Otway; Magallanes	53.30°S	–	11,560	2,081[b]	Ribbed Mussel (*Aulacomya ater*)	Uribe (1988)
Jan–Feb 1992	Lapataia Bay, Beagle Channel; Argentina	54.89°S	821		127,200	Chilean Mussel (*Mytilus chilensis*)	Benavides et al. (1995)
Mar 1996	Islas Huichas; Aysén	45.25°S	31[c]		107,129	Chilean Mussel (*Mytilus chilensis*)	Molinet et al. (2003)
Mar 1998	Quitralco; Aysén	45.78°S	22[c] (354[d])		99,742	Chilean Mussel (*Mytilus chilensis*)	Molinet et al. (2003)
Jan 2000	Quitralco; Aysén	45.78°S	5[c]		22,170	Ribbed Mussel (*Aulacomya ater*)	Molinet et al. (2003)
Feb–Mar 2002	Isla Gala; Aysén	44.17°S	<5[c]		22,000	Clam ("Almeja", species not given)	Molinet et al. (2003)
Mar 2002	Faro Mauchil, Quellón, Chiloé; Los Lagos	43.26°S	789		29,520	Chilean Mussel (*Mytilus chilensis*)	Clément et al. (2002), Aguilera et al. (2004)
Jul 2002	Augusta Island, San Blas Channel; Magallanes	51.25°S	–		8,575	Chilean Mussel (*Mytilus chilensis*)	García et al. (2004a)
Jan 2006	East Moraledo Channel; Aysén	44.30°S	961		9,215	Ribbed Mussel (*Aulacomya ater*)	Fuentes et al. (2008)
Feb–Mar 2009	Areas of Cuptana, Canalad, Angostura, Ester, Allan; Aysén	45.75°S	6,000		–	Reported elsewhere	Mardones et al. (2010)
Apr 2016	Chacao Channel, Chiloé; Los Lagos	41.75°S	250		5,000	Pacific Clams (*Gari solida*)	Hernández et al. (2016)
May 2016	Cucao Bay, Chiloé; Los Lagos	42.60°S	–		9,059	Surf Clams (*Mesodesma donacium*)	Álvarez et al. (2019)

[a] *Mouse units.*
[b] *Assuming approximate conversion factor of 0.18 from mouse units (FAO, 2004).*
[c] *Net samples integrated between 0 and 30 m. Abundances in Molinet et al. (2003) are difficult to decipher but counts from net samples were much lower than counts from bottles.*
[d] *Maximum count from bottle sample.*

through gill tissue damage in February 2016 (Buschmann et al., 2016; Clément et al., 2016; León-Muñoz et al., 2018; Mardones et al., 2021). This event was closely followed in April 2016 by extensive PSP poisoning of marine organisms caused by an exceptional bloom of *A. catenella* (Buschmann et al., 2016; Hernández et al., 2016). These were the worst mass mortality events caused by phytoplankton in the country's history, with major impacts on the fishing industry and the economy of the region. Media reports immediately implicated a variety of potential causative factors for the *A. catenella* bloom such as (1) the dumping 130 km offshore of rotting salmon killed by the *P. verruculosa* bloom (2) the sharp recent increase in aquaculture activities in the region (3) the coinciding of the bloom with the 2016 El Niño. Although the role of disposed salmon was later dismissed (Buschmann et al., 2016), it has been suggested that this dumping may have been related to a secondary peak in *A. catenella* (Armijo et al., 2020). The complexity of factors involved mean that we remain unable to rationalize the specific factors behind either this specific catastrophic event, or the general trends of bloom formation and toxicity of *A. catenella* throughout southern Chile.

Blooms of *Alexandrium* spp. and other HABs appear to be increasing in intensity and proliferating globally, with most research focusing on the role of eutrophication (e.g., Nixon, 1995). However, evidence for the role of increased anthropogenic nutrients in promoting HABs can be equivocal, and site-specific

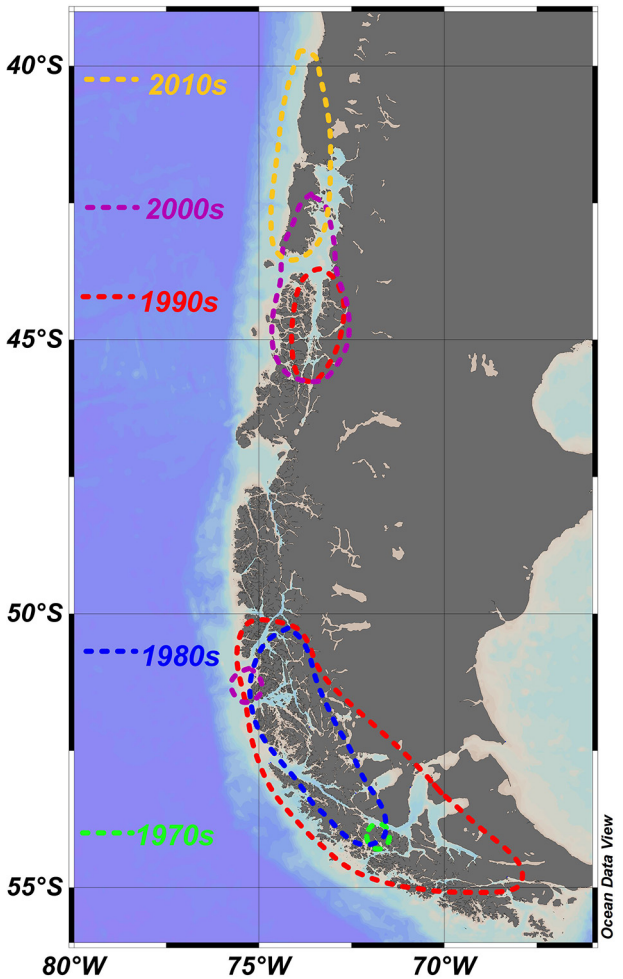

FIGURE 2 | Apparent northward shift of blooms and/or toxic episodes caused by *A. catenella*; dotted lines show approximate spread of reports for each decade. Focal points of each of the southerly blooms is also shown in **Figure 1**. Associated details are shown in **Table 1**. 1970s (Guzmán et al., 1975a,b; Guzmán and Lembeye, 1975; Lembeye et al., 1975). 1980s (Lembeye, 1981a,b; Uribe, 1988). 1990s (Lembeye, 1992; Muñoz et al., 1992; Only mentioned the presence of *A. catenella* at the mouth of Aysén Fjord: first recording in Aysén region; Carreto and Benavides, 1993; Benavides et al., 1995; Molinet et al., 2003). 2000s (Clément et al., 2002; Molinet et al., 2003; García et al., 2004a; Mardones et al., 2010). 2010s (Hernández et al., 2016).

(Davidson et al., 2014). In the fjords and channels of Patagonia, surface freshwater (FW) input is almost devoid of dissolved inorganic nitrogen (DIN) and phosphorus (DIP) but enriched in dissolved Si (DSi) (Silva, 2008), suggesting that anthropogenically driven eutrophication may not be a significant factor, at least in the sparsely populated south. With few large ports, the role of discharge of ships ballast waters (e.g., Hallegraeff, 1998), would also appear to be minimal. However, increased aquaculture activities, particularly in the Los Lagos region, may have had a regional influence on HABs in northern Patagonia. The genetic diversity of populations of *A. catenella* in southern Chile indicates that populations were not recently established as a result of human introduction (Varela et al., 2012). Recent genetic analyses have confirmed that *A. catenella* was the species responsible for the 2016 bloom, but that the genetic patterns consistent with range expansion were not evident (Paredes et al., 2019).

Toxic events have focused considerable research effort on *A. catenella* in southern Chile. This dinoflagellate has a complex life cycle with a biannual occurrence (Molinet et al., 2003), and alternation between vegetative planktonic cells and benthic resting cysts. In Patagonian waters, the role of cyst reservoirs and encystment/excystment cycles can seed recurrence of blooms within a given area (Uribe et al., 2010; Díaz et al., 2014). However, low abundance and fast depletion of cysts within sediments (<3 months, Díaz et al., 2014) has indicated a relatively minor role for cysts in bloom development (Guzmán et al., 2002; Díaz et al., 2014), although high cyst abundance was in fact observed in certain fjords following the 2009 bloom (Mardones et al., 2016a). Major blooms and their geographical expansion in Chilean waters do not appear to be the result of massive *in situ* gemination (Hernández et al., 2016), but cysts probably do play a more important role than previously thought (Mardones et al., 2016a). Indeed, studies of *A. catenella* on the eastern coast of North America have suggested a greater conversion of vegetative cells to resting cysts than previously documented and have emphasized the potential role of cyst precursors (planozygotes) in bloom dynamics (Brosnahan et al., 2017).

OCEANIC AND CLIMATIC INFLUENCE?

Temperature is known to play a significant role in blooms of *A. catenella* (e.g., Fu et al., 2012), with a critical temperature of 13°C apparently required for blooms to develop off northwest North America (Moore et al., 2008). In Chilean Patagonia, the situation appears to be more complex, with no significant relationship noted between temperature and abundance of *A. catenella* (Molinet et al., 2003), but with elevated temperatures sometimes cited as an important factor in bloom development (Guzmán et al., 2002). However, frequency of *A. catenella* blooms in the northwestern Chilean Inland Sea was weakly associated with lower temperatures but not with salinity (Díaz et al., 2014). Cultures of *A. catenella* isolated from Patagonian waters and maintained under controlled conditions have also shown complex relationships between temperature/salinity, growth rate and cell yields (Uribe et al., 2010; Aguilera-Belmonte et al., 2013; Avila et al., 2015). The optimal growth of Chilean strains of *A. catenella* (i.e., highest growth rate and highest maximal cell density) was reached within a narrow thermal range (12–15°C), while optimal growth salinity (20–30) showed a broader range (Paredes-Mella et al., 2020). Lower temperatures of ∼10°C have been shown to increase the excystment and shorten the dormancy of resting cysts (Mardones et al., 2016a) and to increase the toxin content of *A. catenella* (Aguilera-Belmonte et al., 2013; Navarro et al., 2006). The response of *A. catenella* to temperature and salinity changes shows a considerable plasticity that appears to be partially dependent on individual strains (Paredes-Mella et al., 2020).

Despite research on life cycle and physiology, the temporal and spatial variations in abundance and toxicity of *A. catenella* in

southern Chile is not well understood. Given the geographically extensive nature of toxic episodes (**Figure 2**), and the circumstantial evidence of their long term presence, at least in Magellan and Fuegian regions (**Figure 1**), it is likely that larger scale influences are involved, as speculated by many authors (**Table 2**). It is also clear that in the Magellan Strait and Beagle Channel that directly connect Pacific and Atlantic oceans, elevated abundances are more prevalent on the western side, more influenced by Pacific water (**Figure 2**, see also Lembeye, 1992; Benavides et al., 1995).

The water column of the fjords and channels of Chilean Patagonia is shaped by complex interactions between FW run-off and intrusions of oceanic water (**Figure 3**), but few detailed *in situ* hydrographic data has been published for blooms of *A. catenella* in these waters, particularly in the vertical dimension. Because of the widely differing properties of continentally derived FW and oceanic waters, caution is required in the interpretation of simple growth rate versus temperature (T) and salinity (S) experiments conducted under controlled conditions. Using raw data from the first two blooms in 1972 and 1981 (Guzmán et al., 1975a; Guzmán and Lembeye, 1975; Lembeye et al., 1975; Lembeye, 1981b), a TS plot suggests that in contrast to the diatom *Skeletonema costatum*, higher abundances of *A. catenella* were more closely associated with the low temperature and higher salinity (and density) that characterize subsurface oceanic waters (**Figure 4**). Moreover, the higher abundances of *A. catenella* were more associated with depths of 5 m and greater, in contrast to the elevated abundances of *S. costatum* associated with estuarine water (EW) at depths of 5 m and shallower (**Figure 5**). Using a larger data set, a similar response has been shown for field populations of *A. catenella* in the Magellan region (Paredes-Mella et al., 2020). An association with higher temperatures was evident in the Aysén and Los Lagos regions (Paredes-Mella et al., 2020), but it is notable that the elevated abundances of *A. catenella* were still associated with the temperature and salinity characteristic of oceanic waters at these latitudes (Sievers and Silva, 2008).

In the context of blooms of *A. catenella*, this region presents a paradox: despite extremely poor weather conditions, and almost pristine coastal environments with low human population density, the southern tip of South America suffers from some of the highest levels of natural bioaccumulation of PSP toxins by shellfish in the world (HAEDAT, webpage; Carreto and Benavides, 1993; Benavides et al., 1995; Lagos, 1998). Here we now examine features of Patagonian coastal waters that might be pertinent to blooms of *A. catenella*, with particular focus on oceanic waters.

PROPERTIES OF SUBANTARCTIC SURFACE WATER

South America is the only land mass to interrupt the subtropical front (STF) (Orsi et al., 1995) that defines the northern extent of subantarctic surface water (SASW). The coast of Chilean Patagonia is therefore in a unique oceanographic position, being strongly influenced by the presence of SASW (**Figure 3**), which shares properties with subantarctic mode water (SAMW) formed north of the polar frontal zone (Sarmiento et al., 2004; Schneider and Bravo, 2006). SAMW forms at the base of deep winter mixed layers in a circumpolar belt in the Southern Ocean, and is defined by specific oceanographic properties, with density (σ_t) in the range 26.5–27.1 kg m^{-3} (Sarmiento et al., 2004). In the

TABLE 2 | Summary of comments regarding potential larger-scale oceanic/climatic influences on blooms of *A. catenella* in Patagonian and Fuegian regions of southern Chile.

Comment	References
"The periodicity and geographic extension of the phenomenon also suggests the existence of some low frequency (ca. 10 years) climatic-hydrographic interaction underlying the high toxicity outbreaks in the region."	Uribe (1988)
"It seemed to be associated with a mesoscale phenomenon combining some complex climatic and hydrographic conditions, as suggested by its duration and geographic extent."	Benavides et al. (1995)
"The duration and geographic coverage of blooms of *A. catenella* and the presence of PSP cannot be explained by local factors. . ."	Guzmán et al. (2002)[a]
"Expanding spatial distribution of *A. catenella* blooms seems to be strongly related to surface water drift driven by wind forcing as well as by circulation features of inland seas in northwest Patagonia in southern Chile."	Molinet et al. (2003)
"Within the Chilean fjords, the extensive geographic coverage of *A. catenella* blooms associated to PSP outbreaks suggests that climatic oceanographic factors are responsible for the initiation of these phenomena."	Guzmán et al. (2013)
"Likewise, the presence of *A. catenella* in two of the stations in the Gulf of Peñas show an oceanic influence on the distribution of this species in the interior channels in the southern area..."	Pizarro et al. (2011)[a]
"Thus, other mechanisms likely account for the development and recurrence of blooms in this area, for example, the entrance of offshore planktonic populations or cysts."	Díaz et al. (2014)
"Our results suggest that large-scale atmospheric and oceanographic processes (climatic anomalies) modulated the late summer *A. catenella* bloom observed in southern Chile."	Hernández et al. (2016)

[a] *Translated from Spanish.*

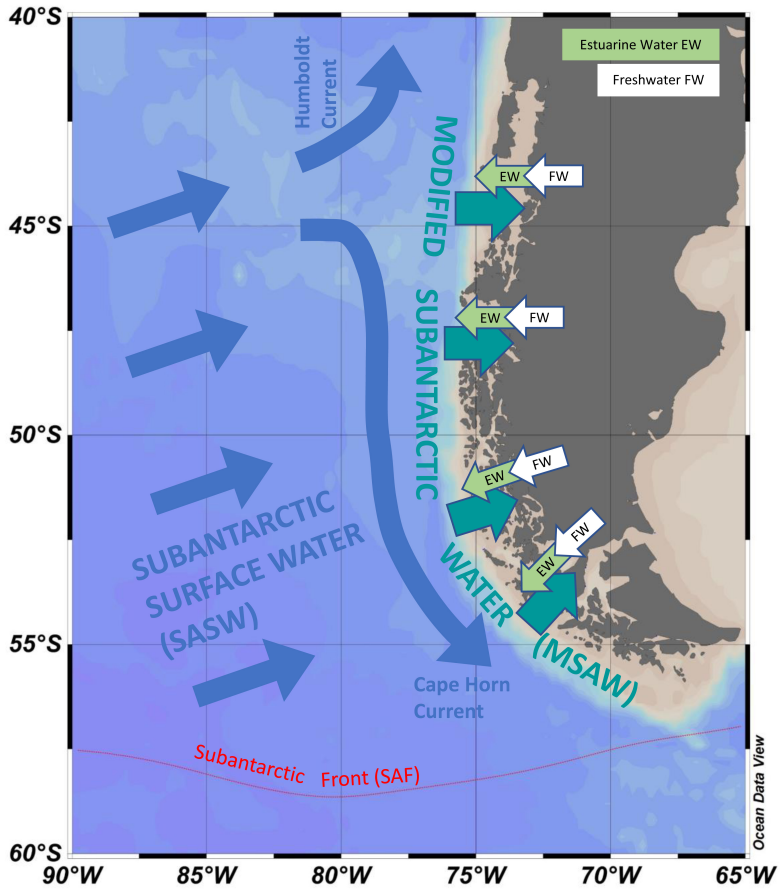

FIGURE 3 | Approximate schematic representation of how the southern Pacific Ocean influences fjords and channels of Patagonia and Tierra del Fuego. Subantarctic surface water (SASW) approaches the coast and interacts with continental run-off to form modified subantarctic water (MSAW) along the coast. MSAW enters the fjords and channels under a surface layer of estuarine water (EW) formed from freshwater flow (FW) derived from rainfall, rivers and glacial melt. Red dotted line gives approximate position of the Subantarctic Front (SAF). Position of currents and water masses are not drawn to scale.

south-eastern Pacific off the south-western coast of Patagonia (70–92°W), SAMW forms south of 56°S, varying spatially and seasonally between temperature of ca. 6–8°C, salinity of ca. 34.1–34.4, and σ_t of 26.5–27.1 (Schneider and Bravo, 2006). Immediately to the north of 56°S, surface waters have a temperature of 7–8°C and salinity of 33.9–34.1 (Schneider and Bravo, 2006), and further north off central Chile, SASW warms to 11.5–12°C and slightly freshens to 33.8–33.9 (Silva et al., 2009) due to continental run-off from northern Patagonia and the associated tongue of lower salinity water extending offshore (Orsi et al., 1995).

Another important characteristic of SAMW is a severe deficiency in silicic acid ($Si(OH)_4$ or DSi) (Sarmiento et al., 2004), a property also notable in SASW. Whereas concentrations of nitrate (NO_3^-) in SASW vary from ∼3 to ∼20 μM, depending upon latitude and season, concentrations of $Si(OH)_4$ vary from undetectable to only 2–3 μM (Odate and Fukuchi, 1995; Timmermans et al., 1998; Sedwick et al., 1999; Hiscock et al., 2003; Boyd et al., 2008), and are of the order (or less than) of measured half-saturation constants for growth of Antarctic diatoms on Si (e.g., Nelson and Tréguer, 1992). These observed nutrient concentrations lead to a negative Si* ($Si-NO_3$) of −10 to −15 μmol kg^{-1} in SAMW, which are the lowest Si* values observed anywhere in the surface of the ocean (Sarmiento et al., 2004). Negative Si* results from iron (Fe) limitation in the Southern Ocean, which increases the ratio of biogenic silica to particulate organic nitrogen (Si:N) of diatoms and exported biogenic particles, thus decreasing the dissolved $Si(OH)_4$ to NO_3^- ratio in the upper water column. Negative Si* is an important feature of SAMW, which, as the primary conduit of nutrients for the thermocline throughout the southern hemisphere and North Atlantic (Sarmiento et al., 2004), has a significant impact upon global productivity of diatoms (Sarmiento et al., 2004). Similarly, the strongly negative Si* of SASW must in some circumstances constrain the growth of diatoms in the coastal waters of Chilean Patagonia, making this region potentially sensitive to biogeochemical processes occurring in the Southern Ocean. However, modeling suggests little evidence for short term changes in properties of SASW related to recent climate change (e.g., Boyd et al., 2008).

Trace metals have received little attention in terms of their potential role in the dynamics of HABs in this region. As well

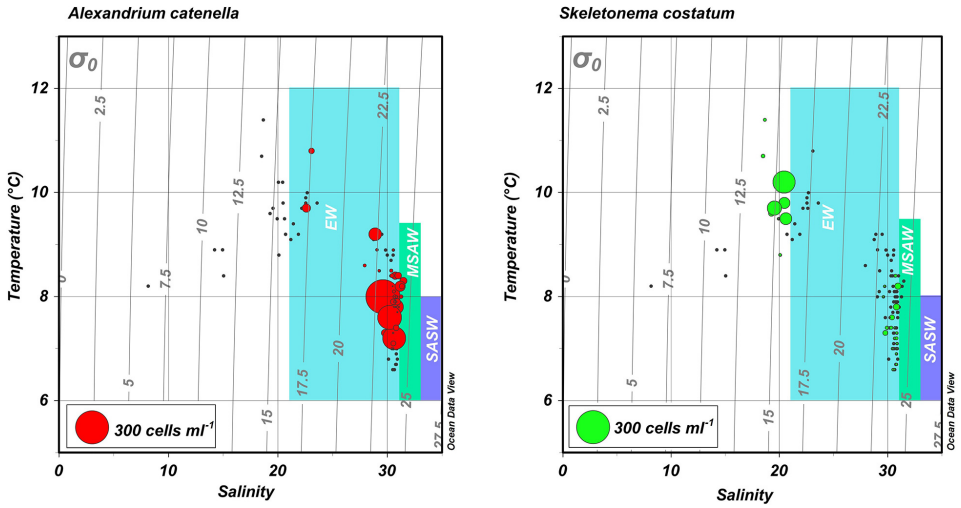

FIGURE 4 | Temperature-salinity (TS) diagrams for blooms of *A. catenella* in Magallanes and Tierra del Fuego regions in 1972 and 1981. Hydrographic and cell abundance data were taken from the area (**Figures 1**, **2**) centering on Bahia Bell, Clarence Island in 1972 (Guzmán et al., 1975a; Guzmán and Lembeye, 1975; Lembeye et al., 1975) and Seno Union, 1981 (Lembeye, 1981a,b). Circles represent abundance of the dinoflagellate *A. catenella* (left) and the diatom *S. costatum* (right). Gray lines represent contours of constant density (σ_0). Shaded areas are a schematic representation of the approximate salinity ranges of subantartic surface water (SASW; ∼33–34.6), modified subantarctic water (MSAW; ∼31–33), and estuarine water (EW; ∼21–31) according to Sievers and Silva (2008).

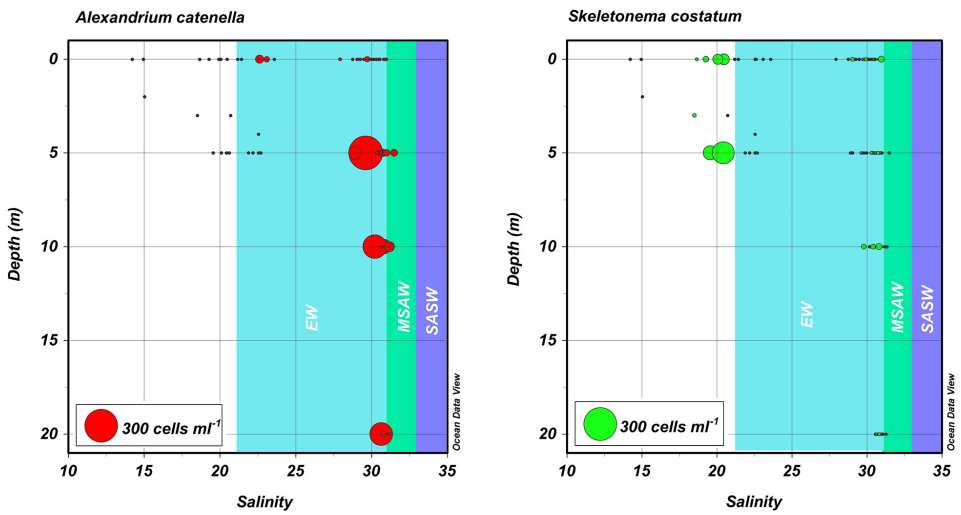

FIGURE 5 | Depth, salinity, abundance plots for blooms of *A. catenella* in Magallanes and Tierra del Fuego regions in 1972 and 1981. Hydrographic and cell abundance data were taken from the area (**Figures 1**, **2**) centering on Bahia Bell, Clarence Island in 1972 (Guzmán et al., 1975a; Guzmán and Lembeye, 1975; Lembeye et al., 1975) and from Seno Union, 1981 (Lembeye, 1981a,b). Circles represent abundance of the dinoflagellate *A. catenella* (left) and the diatom *S. costatum* (right). Shaded areas are a schematic representation of the approximate salinity ranges of subantartic surface water (SASW; ∼33–34.6), modified subantarctic water (MSAW; ∼31–33), and estuarine water (EW; ∼21–31) according to Sievers and Silva (2008).

as having a strongly negative Si*, SASW is strongly deficient in Fe, with total concentrations of dissolved Fe typically of the order ∼0.03–0.1 nM (Sedwick et al., 1999; Hutchins et al., 2001; Leblanc et al., 2005; Boyd et al., 2008). SASW approaching the coast of Chile is therefore likely to have total Fe concentrations low enough to limit the growth of diatoms and possibly other phytoplankton. A strong linear relationship between DSi and zinc (Zn) has been noted for both the South Atlantic (Wyatt et al., 2014) and the Southern Ocean (Ellwood, 2008; Croot et al., 2011), suggesting that SASW with negative Si* could also be strongly deficient in dissolved Zn. Concentrations of total dissolved Zn of 0.2 to 0.3 nM have been measured in SASW both in the Australian region (Ellwood, 2008) and the northern Drake Passage (Croot et al., 2011). In New Zealand subantarctic waters, levels of total dissolved Zn as low as 6 pM have been reported, concentrations which are the lowest documented so far for any open ocean region (Leblanc et al., 2005). Given that Zn availability can significantly alter silicification in diatoms

(De La Rocha et al., 2000), the combination of Si, Fe, and Zn deficiency in SASW could have a significant impact on growth of diatoms, and potentially other phytoplankton. Although the evidence for growth limitation of phytoplankton by Zn can be equivocal in some high-nitrate low-chlorophyll (HNLC) ocean areas, Zn could be a potentially limiting micronutrient where SASW meets the more productive coastal waters of Patagonia. Other trace elements could be significant, with the lowest global concentrations of manganese (Mn) also reported in the Drake Passage (Browning et al., 2014).

Within and north of the subantarctic front, SASW is generally relatively rich in dinoflagellates (Kopczynska et al., 2001; Wolf et al., 2014), albeit at much lower abundances than in coastal waters. In contrast, the relative abundance of diatoms increases from the polar frontal zone southwards (Wolf et al., 2014) presumably because of Si limitation north of the polar front. In enrichment studies in subantarctic waters, where Fe was added without Si, growth of dinoflagellates and other flagellated cells were stimulated, whereas growth of diatoms was limited by availability of $Si(OH)_4$ (Coale et al., 2004). In the Drake Passage, *A. tamarense* has been shown to be present at concentrations of 5–20 cells L^{-1} north of the polar front, but rarely encountered to the south of the front (Ho et al., 2003); this Antarctic strain of *A. tamarense* has been isolated and shown to be toxic (Lee et al., 2012). Routine phytoplankton counts may miss dinoflagellates present at these low abundances, which represent only 0.5–2 cells in a 100 ml sedimented sample under an inverted microscope. We have no specific information on the presence of *A. catenella* itself in SASW, but the concept of offshore low density "seed" populations advected into the coastal region (Hernández et al., 2016) cannot be ruled out.

CONTINENTAL FRESHWATER AND MODIFIED SUBANTARCTIC WATER

Continental Patagonia is subject to high levels of precipitation and glacier melt, resulting in an enormous estuarine zone with one of the greatest influences of FW on the planet (Calvete and Sobarzo, 2011). The intricate network of fjords and channels are typically characterized by a two-layer system, where continental run-off delivers DSi into near surface low salinity waters that overly oceanic water richer in DIN and DIP (Sievers and Silva, 2008). Further from shore, physical mixing and high levels of production, sinking and remineralization of biogenic particles produce what is known as modified subantarctic water (MSAW) from SASW. The properties of MSAW are therefore driven by differential inputs of both SASW and FW, with Si* more positive with proximity to FW source, and varying with latitude, from positive in the north to negative in southern Patagonia and Fuegian coastal waters (Torres et al., 2014). Average $Si(OH)_4$ concentrations in the surface waters in spring vary from ∼19 μM in northern Patagonian waters down to only ∼2 μM in southern waters (Torres et al., 2014), values similar to those of ∼3 μM at two stations north of the subantarctic front, off the tip of south-western South America (Timmermans et al., 1998). This Si deficit has been proposed as a factor in shaping phytoplankton assemblages in southern waters, where dinoflagellates dominate chlorophyll in NO_3^- rich (5–10 μM), $Si(OH)_4$ poor (<2 μM) waters of an inner-fjord in the Strait of Magellan (Torres et al., 2011a) and where concentrations of Si are lower than, or similar to, half saturation constants for growth of Antarctic diatoms (Nelson and Tréguer, 1992). In contrast, northern Patagonian coastal waters, having higher concentrations of $Si(OH)_4$, have been characterized by high rates of diatom productivity in austral spring (e.g., Montero et al., 2017). Although Si* in MSAW tends to be positive in the north, diatoms acclimated to these high levels of Si could have relatively higher half saturation constants for growth on Si, making them particularly susceptible to limitation during conditions of reduced Si. There is clear potential for the negative Si* in southern coastal waters to spread northwards because of spatial and temporal variations in continental run-off (Torres et al., 2014) or from large scale circulation changes that affect the relative input of SASW into MSAW (see later section on Latitudinal Shifts in Water Column Properties). However, to date there has been little specific attention given to the role of such variations of Si* in driving competition between toxic dinoflagellates and diatoms in this area. The ratio of concentrations of DIN and DIP have also been shown to be important in driving variations in toxicity of *Alexandrium* spp. (e.g., Lee et al., 2012), although Si* itself should have no direct bearing upon toxicity because N:P ratios are likely to be relatively constant within SASW. However, vertical gradients of DIN and DIP resulting from variations in relative inputs of SASW and freshwater could have some impact on toxicity. Optimum growth of *A. catenella* in cultures has been shown to occur at unbalanced (elevated) N:P ratios (Paredes-Mella et al., 2020), however, these experiments were conducted by varying P concentrations at very high saturating concentrations of N.

Oceanographic studies clearly focus on NO_3^- as the principal source of DIN, but any impact of increased relative presence of SASW upon the competition between diatoms and dinoflagellates could be compounded by additional sources of dissolved nitrogen. Preference for ammonium (NH_4^+) is an important functional trait potentially driving competition within phytoplankton assemblages (Glibert, 2016). NH_4^+ has been shown to be utilized by another bloom forming dinoflagellate in Patagonian coastal waters (Iriarte et al., 2005), and NH_4^+, urea and dissolved organic nitrogen (DON) are known to be utilized by some species of *Alexandrium* (Anderson et al., 2012; Dagenais-Bellefeuille and Morse, 2013). The presence of these alternative forms of dissolved N could drive the "effective" Si* to be even more negative, further favoring non-siliceous phytoplankton, of clear significance in areas such as the Inner Sea of Chiloé, where anthropogenic influences and aquaculture activities are higher, and where resulting variations in dissolved N:P ratio could also impact on toxicity of dinoflagellates. In controlled cultures, slightly higher growth rates on reduced forms of N have been shown for Chilean strains of *A. catenella* (Paredes-Mella et al., 2020). However, these experiments were conducted under highly saturating (>100 μM) concentrations of NO_3^-, NH_4^+ and urea that are not representative of Patagonian fjords (e.g., Silva, 2008); the implications of these recent data are therefore yet be resolved.

The exceptionally low concentrations of trace elements in SASW suggest that their availability to phytoplankton will be largely driven by supply from continental run-off into surface coastal waters, and so complex vertical interactions are likely between surface FW and EW, recycling within the water column, and intrusions of SASW and MSAW. Potentially limiting concentrations of Si, Fe, Zn, and other elements could not only force competitive shifts in phytoplankton but could also influence toxicity of dinoflagellates, although few data are presently available. Stratification of trace metal availability in MSAW could favor those taxa with vertical migration behaviors and the ability to feed on other cells. Indeed, mixotrophy is increasingly thought to be an important factor in nutrition of dinoflagellates and potentially in HAB formation (e.g., Jeong et al., 2015; Glibert, 2016). *Alexandrium catenella* is not only phototrophic but can also feed on *Skeletonema* (Yoo et al., 2009), a common diatom in Patagonian coastal waters (Montero et al., 2017).

Ocean "acidification" from increasing atmospheric CO_2 has been responsible for relatively small changes in pH of surface oceanic waters to date. However, Patagonian coastal waters are not only subject to this acidification, but also to much greater dynamic vertical changes in the carbonate system caused by variability in the interaction between SASW, MSAW and continentally derived FW. The dissolved concentration of free CO_2 (or its partial pressure, pCO_2) and pH are driven by complex physico-chemical and biological influences on total CO_2 (C_T) and total alkalinity (A_T), with C_T in SASW likely to be ∼2.1 mM (e.g., Boyd et al., 2008), but only <0.2 mM in melting glacial freshwater (Vargas et al., 2018). A strong linear relationship is generally observed between A_T and salinity in Patagonian waters (Torres et al., 2011b), although this relationship can also be influenced by non-carbonate sources of A_T, or variability in the FW end-members (Vargas et al., 2018). The strong vertical gradients in C_T, A_T, and pCO_2 (Torres et al., 2011b) have potential implications for HAB dynamics, with members of the *A. tamarense* species complex showing increased growth and toxicity under conditions of high pCO_2 (Fu et al., 2012; Hattenrath-Lehmann et al., 2015), a response apparently exacerbated by N limitation (Eberlein et al., 2016). Mardones et al. (2016b) have also described morphological variations and non-linear growth responses of *A. catenella* to pH/pCO_2 carbonate changes. Latitudinal gradients in the interaction between FW, SASW and MSAW could have an impact on CO_2 induced growth and toxicity of dinoflagellates such as *Alexandrium,* and further study is clearly required.

STRATIFICATION AND VERTICAL DISTRIBUTION

Despite variable wind forcing, the fjords and channels of Chilean Patagonia are generally subject to weakened vertical mixing resulting both from topographical protection, and, from the interaction between MSAW, EW, and FW. The resulting gradients in temperature, salinity and density have consequences for availability of nutrients and the light field experienced by phytoplankton, although Smayda (2002) has questioned whether the stratification that accompanies flagellate blooms is a significant trigger factor. Nonetheless, stratification of the water column regulates competition between different functional forms of phytoplankton, with vertically migrating red-tide dinoflagellates thriving under conditions of low turbulence (e.g., Margalef, 1978; Glibert, 2016). Turbulence directly inhibits the growth of some dinoflagellates (Berdalet and Estrada, 1993) and is known to reduce growth rate and chain length in cultures of *A. catenella* (Sullivan et al., 2003). In the field, subsurface populations of *A. catenella* have been observed to concentrate within a narrow depth interval (∼2 m) where both current shear and turbulence intensity were at a minimum (Sullivan et al., 2003).

In the two-layered system characteristic of Magellan and Fuegian coastal waters, the inflow of MSAW beneath a seaward flow of EW allows motile dinoflagellates such as *A. catenella* to maintain an optimum position in the water column. Some dense blooms of *A. catenella* have been noted to occur during periods of increased water column stability (e.g., Guzmán and Lembeye, 1975; Benavides et al., 1995), although it is not clear whether reduced turbulence, improved irradiance, or access to nutrients in a stratified water column were the most significant factors. Few data are available on vertical distribution of *A. catenella* in Chilean waters, but aggregation of *A. catenella* cells in the upper water column has been noted during blooms in Aysén (Molinet et al., 2003), and in the Magellan Strait (**Figure 5**). Strong stratification of PSP toxins (**Figure 6**) has also been noted in mussels held at fixed depths near Cailín Island, off Chiloé Island (García et al., 2004b), with maxima of toxins occurring at ∼5–7 m depth. This suggests an average position of *A. catenella* cells approximately at the depth of a weak pycnocline (σ_t ∼25.20) described in Quellón Bay (Cáceres et al., 2008). However, during a dense bloom in an inlet in the eastern Moraledo Channel, *A. catenella* aggregated at shallower depths of 1–3 m, in lower salinity water (Fuentes et al., 2008).

These contrasting vertical distributions could be consistent with observations on the east coast of North America that emphasized the combined role of vertical migration patterns and life cycle events in bloom dynamics of *A. catenella* (Brosnahan et al., 2017). A diel pattern of vertical migration of vegetative cells was observed, with migration to a fixed daytime light intensity (30–40% of maximum surface irradiance) during bloom development (Brosnahan et al., 2017). However, planozygotes (cyst precursors) seemed to abandon this light threshold and aggregate closer to the surface, thus potentially increasing dispersal (Brosnahan et al., 2017). Should this pattern be replicated in Patagonian waters, vegetative cells could be retained by the two-layer flow within fjords and channels, with planozygotes being dispersed by the near surface flow of low salinity EW.

LATITUDINAL SHIFTS IN WATER COLUMN PROPERTIES

Clearly some features of Patagonian and Fuegian coastal waters provide favorable conditions for growth or accumulation of

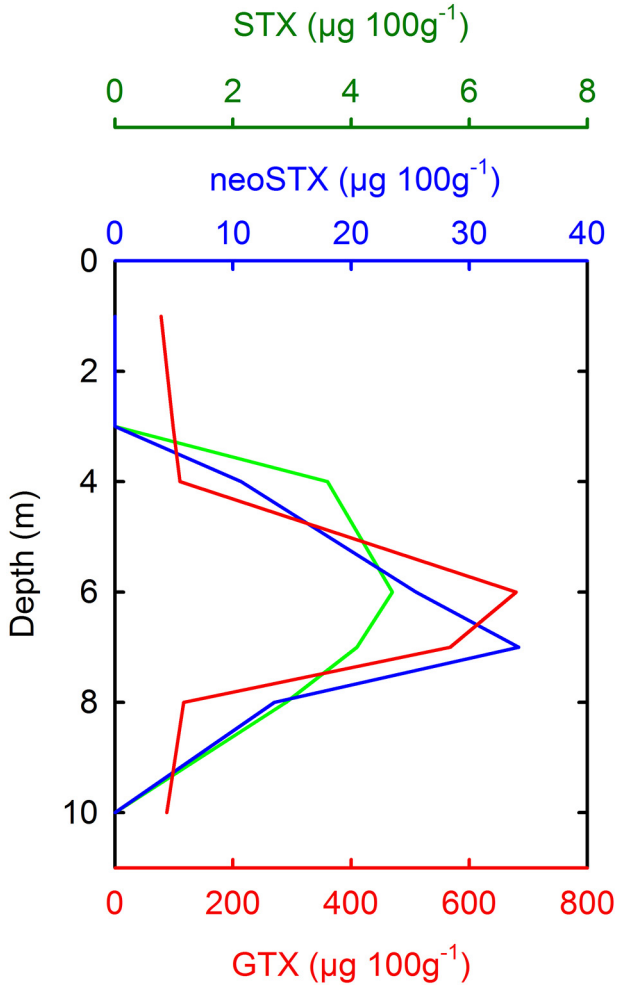

FIGURE 6 | Vertical stratification of PSP toxins in samples of mussel (*Mytilus chilensis*) tissue from Cailín Island, off Chiloé Island on April 24, 2002 (Data taken from García et al., 2004b). PSP toxins were associated with the presence of *A. catenella* (García et al., 2004b). *M. chilensis* were suspended from an aquaculture shellfish lantern at various depths, and the toxin contents therefore reflect the average position and toxicity of *A. catenella* cells in the water column. GTXs, Gonyautoxins; neoSTX, neoSaxitoxin; STX = Saxitoxin.

A. catenella. **Figure 7** provides a generalized schematic overview of the principal properties of the upper water column in these waters, as outlined in previous sections. The figure also indicates how vertical distribution and patterns of vertical migration might influence growth and retention of *A. catenella*.

The first recorded bloom in 1972 (Guzmán et al., 1975a) – and several of the major blooms that followed – occurred in El Niño years, and it has been suggested that development of *A. catenella* blooms may be influenced by ENSO variability (Guzmán et al., 2002). The exceptional 2016 bloom also coincided with positive El-Nino and Southern Annular Mode (SAM) anomalies (Hernández et al., 2016; Trainer et al., 2020), although the timing of major events over the past 50 years (from **Table 1**) has not consistently corresponded with fluctuations in the Niño 3.4 index (**Figure 8A**; see also Trainer et al., 2020). The raw monthly index for the SAM also suggests no consistent long-term relationship with bloom events (Trainer et al., 2020). However, the major bloom peaks in southern Patagonia and Tierra del Fuego between the 1970s and early 1990s seem to be associated with negative SAM anomalies when using a 12-month trailing mean (**Figure 8B**). The northward shift of blooms was then gradually associated with positive SAM anomalies (**Figure 8B**) resulting in a highly significant relationship between SAM index (12-month trailing mean) and approximate latitude (**Table 1**) of major bloom events (**Figure 8C**). The relationship was significant using SAM trailing means of 6–12 months (see legend **Figure 8C**), but not significant using either raw SAM index or a 3-month trailing mean (see legend **Figure 8C**). With flushing times in some fjords of the order of several months (Mardones et al., 2021), and long timescales involved in development and persistence of *A. catenella* blooms (Guzmán et al., 2002), a long lag period between climatic effects and bloom events would appear to be realistic.

The Southern Annular Mode is an indicator of the relative position of the belt of westerly winds prevailing over southern South America. A positive phase of SAM indicates a southerly shift in westerlies, with negative SAM anomalies associated with a northward shift of the wind belt. The timing and latitude of exceptional *A. catenella* events suggests a complicated relationship with these SAM anomalies (**Figures 8B,C**), and the mechanisms involved are as yet unclear. Water column properties (**Figure 7**) vary with latitude, and with composition of MSAW, which is potentially driven by intrusions of SASW, input of FW, variations in wind mixing and vertical stratification, or combinations of these processes.

Regarding the relative input of SASW, the ocean offshore of northern Patagonia is sensitive to the latitudinal position of the bifurcation of the west wind drift (WWD) which can be a macro scale indicator of oceanographic and meteorological variability (Gatica et al., 2009). There is also evidence for episodic decreases in sea surface temperature in the Inner Sea of Chiloé associated with a shift of sea surface currents to a zonal direction and the entry of large "parcels" of subantarctic water (Giesecke et al., 2014) which have been responsible for mass occurrence of salps, decreases in chlorophyll-*a*, and changes in phytoplankton community structure (Giesecke et al., 2014). A weakening in the annual cycle of chlorophyll-*a* concentration and abnormally cold sea surface temperature in the Inner Sea of Chiloé during 2009–2010 has also been linked to transient large-scale climate forcing (Lara et al., 2016). Intrusions of SASW into coastal waters clearly have potential biological implications, but more information is required on any direct role of SASW on dynamics of *A. catenella*.

Regarding variations in FW input into EW and MSAW, latitudinal gradients in continental precipitation can impact the Si* ratio in Patagonian coastal waters (Torres et al., 2014) with consequences for competition between siliceous and non-siliceous phytoplankton (Torres et al., 2011a, 2014). The exceptional *A. catenella* blooms of 2009 and 2016 were the first to be observed in coastal oceanic waters off Chiloé Island (Mardones et al., 2010; Buschmann et al., 2016) with the latter associated with one the driest Patagonian summers on record

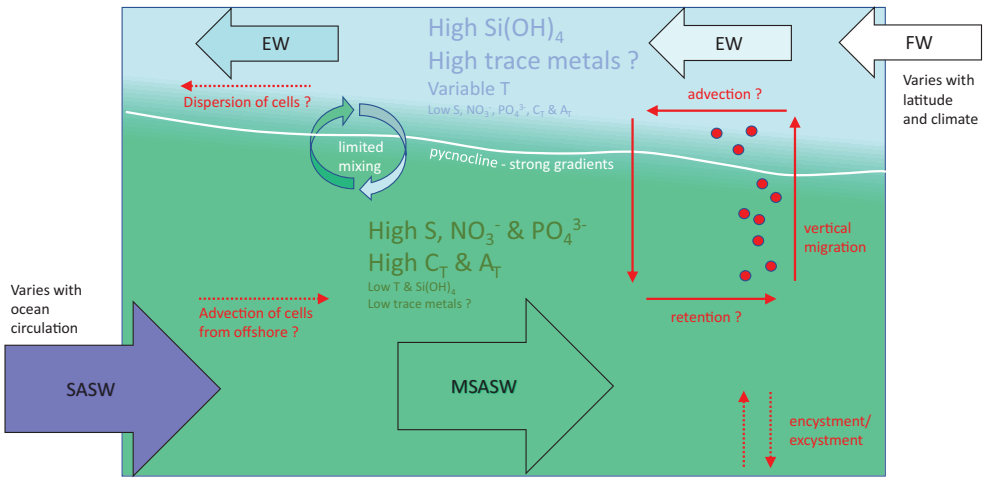

FIGURE 7 | Schematic diagram of the generalized structure of the water column in the fjords and channels of Chilean Patagonia and Tierra del Fuego, indicating the principal processes that potentially influence populations of the dinoflagellate *A. catenella*. Subantarctic surface water (SASW) flows into coastal waters and forms modified subantarctic water (MSAW) through the interaction with estuarine water (EW). MSAW is overlain by a near-surface layer of EW fed by input of continental freshwater (FW) derived from precipitation, streamflow and glacier melt; the resulting pycnocline reduces mixing between the two layers. Temperature (T) is variable in FW and EW, which are high in silicic acid ($Si(OH)_4$) and potentially in dissolved trace metals (few data available), but low in salinity (S), nitrate and phosphate (NO_3^- and PO_4^{3-}), total CO_2 (C_T) and total alkalinity (A_T). SASW and MSAW are high in S, NO_3^-, PO_4^{3-}, C_T and A_T, but low in T, $Si(OH)_4$, and dissolved trace metals. Vertical distribution is not well described for these waters, but *A. catenella* is thought to aggregate close to the pycnocline where it can optimize vertical position within strong gradients of T, S, irradiance, macro- and micro-nutrients, dissolved CO_2, and potentially turbulence. Gradients of pH and pCO_2 (not indicated) within the pycnocline – and in the surface layer – will be driven by the strong gradients in C_T and A_T, and by air-sea exchange of gaseous CO_2. Physical retention of *A. catenella* within certain fjords and channels could be promoted by vertical migration patterns within the two-layered flow. Encystment and excystment processes ensure recurrence of *A. catenella* under favorable conditions. Advection of *A. catenella* into coastal waters and dispersal of cells within the upper EW layer are major unknowns in Chilean waters. The above diagram represents a broad schematic description that depends on relative inputs of SASW and FW and associated properties; local patterns vary with ocean circulation, latitude, and climate changes.

(Clément et al., 2016; Hernández et al., 2016; León-Muñoz et al., 2018). The reduced input of FW into coastal waters apparently increased the relative supply of subsurface SASW into near surface waters (Buschmann et al., 2016; León-Muñoz et al., 2018).

The Southern Annular Mode is a weak but significant predictor of Andean streamflow south of 43°S (Masiokas et al., 2019). Over the past few decades, as positive SAM anomalies become more frequent, precipitation (Garreaud et al., 2013) and streamflow (Masiokas et al., 2019) have been significantly lower in north and central Patagonia. In contrast, precipitation and streamflow in recent years have been significantly higher south of 50°S (Garreaud et al., 2013; Masiokas et al., 2019), with dryer conditions more frequent during negative SAM phases in the far south of Patagonia (Weidemann et al., 2018).

The slightly counter-intuitive differential influences of SAM anomalies in the north and south of Patagonia could explain the northward shift in distribution of blooms. The events caused by *A. catenella* in the 1970s–1990s in southern Patagonia and Tierra del Fuego occurred during significantly drier conditions than the long-term average (Masiokas et al., 2019), whereas the region has experienced significantly wetter conditions in recent years (Masiokas et al., 2019). These observations could help to explain the lower frequency of exceptional blooms in the far south in recent years. North and central Patagonia has seen a significant reduction in streamflow from conditions that were previously wetter (Masiokas et al., 2019), potentially explaining the increased frequency of blooms in recent years.

The changing position of the westerly wind belt seems to play some long-term role in distribution and intensity of blooms, and the influence of these climatic shifts on FW flow into coastal waters appears to be significant. Variations in streamflow with latitude and consequential changes in availability of DSi, DIN and DIP could have been involved in observed shifts in distribution of *A. catenella* blooms, but other properties of a stratified water column could also be involved, such as trace metals and CO_2 (**Figure 7**). A shallower surface EW layer driven by reductions in FW would also have implications for the vertical distribution of *A. catenella* regarding optimization of irradiance and availability of DIN and DIP. SAM anomalies not only influence FW input into coastal waters but will also be associated with latitudinal variations in wind forcing and cloud cover; vertical mixing and incident irradiance are both likely drivers of the vertical position of *A. catenella* in the water column. Further research is clearly required on the detailed vertical dynamics of *A. catenella* populations and how these are influenced by oceanic and climatic forcing.

OTHER HAB SPECIES

Because of the records extending over several decades, the present review has focused upon blooms of *A. catenella*. However, variations in DSi, DIN and other key properties driven by relative inputs of SASW and FW could also impact other HAB species

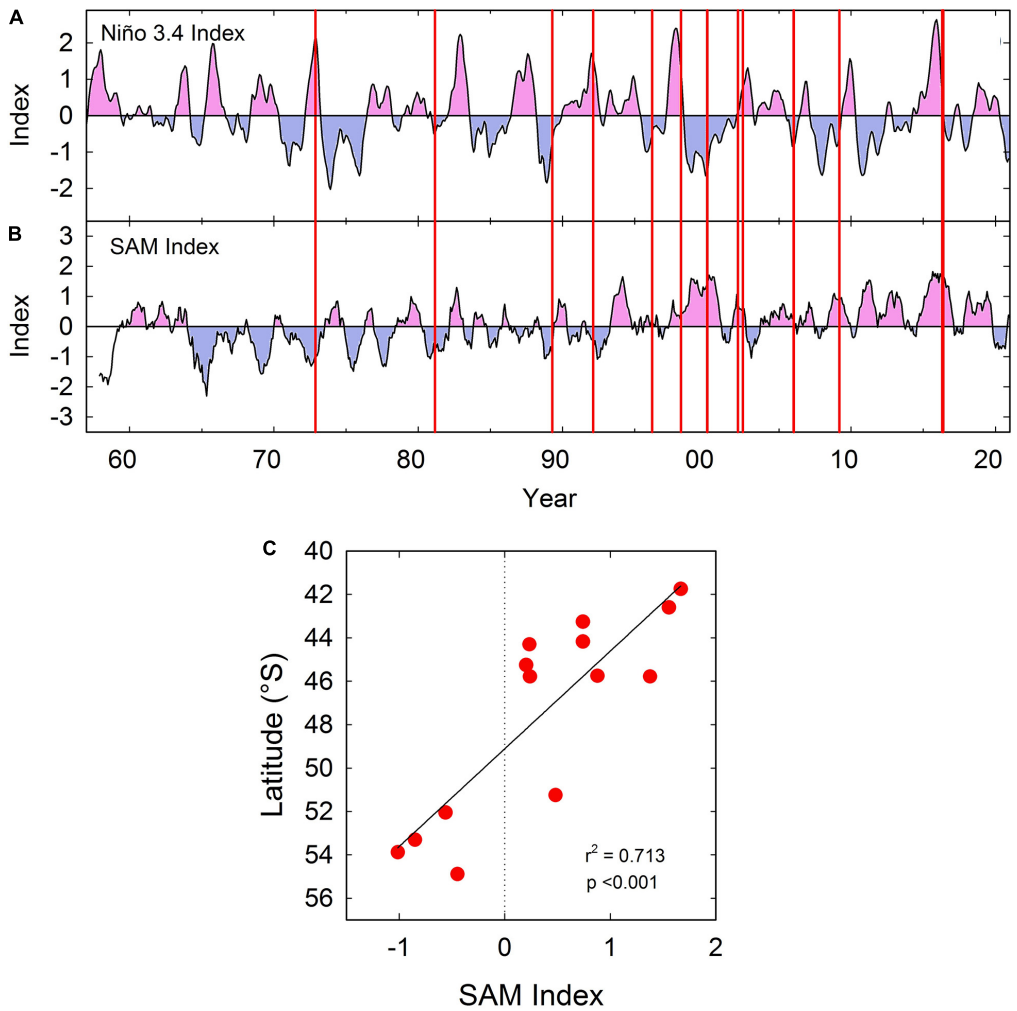

FIGURE 8 | (A) Variation in monthly Niño 3.4 index between 1957 and 2020 (3-month running mean). Data provided by Climate Prediction Center, NOAA (http://www.cpc.ncep.noaa.gov/data/indices/oni.ascii.txt). Positive anomalies shaded in pink, negative shaded in blue. Vertical red lines indicate the approximate time of peak events caused by *A. catenella* in Patagonian and Fuegian coastal waters (taken from **Table 1**). **(B)** Variation in monthly Southern Annular Mode (SAM) index (12-month trailing mean) between 1957 and 2020. Data provided by (http://www.nerc-bas.ac.uk/icd/gjma/sam.html). Vertical red lines as described in **(A)**. **(C)** Significant relationship between monthly SAM index shown in **(B)** and latitude of peak events caused by *A. catenella* (taken from **Table 1**). Linear regression is also significant with a 9 month ($r^2 = 0.601$, $p < 0.01$) or a 6 month ($r^2 = 0.428$, $p < 0.05$) trailing mean for SAM index, but is not significant with a 3-month trailing mean, or with the raw monthly index.

that have been recorded in Chilean coastal waters (e.g., Lagos, 1998; Lembeye, 2008; Díaz et al., 2019).

Several dinoflagellates produce lipophilic toxins, such as *Dinophysis* spp., responsible for DSP toxins, and *Protoceratium reticulatum,* which produces yessotoxins (YTX) (Díaz et al., 2019). Blooms of *P. reticulatum* occur off the northern Chilean coast (Díaz et al., 2019) but also occur in the fjords and channels of southern Chile (Alves-de-Souza et al., 2014, 2019). Thin layers of *P. reticulatum* and *Dinophysis acuminata* are present in Reloncaví Fjord (Alves-de-Souza et al., 2014), with blooms apparently linked to shallowing of the salinity driven pycnocline and intrusion of MSAW (Alves-de-Souza et al., 2019) presumably rich in DIN and DIP. The preference of *P. reticulatum* for low streamflow and positive SAM (Alves-de-Souza et al., 2019) may indicate a similar niche to *A. catenella,* although blooms of *P. reticulatum* are not thought to be highly toxic to humans (Díaz et al., 2019).

The catastrophic mass mortality event in northern Patagonia in early 2016 was the result of a convergence of a southerly expansion of *P. verruculosa* with the northerly expansion of *A. catenella* (Trainer et al., 2020) that coincided with positive anomalies of both El-Niño and SAM (Trainer et al., 2020). High cell densities of *P. verruculosa* were noted at relatively high temperatures (>15°C) during previous bloom episodes (Trainer et al., 2020), but in culture, growth rates and maximum cell densities do not vary strongly between temperatures of 12–18°C (Mardones et al., 2021). Cell growth of Chilean *P. verruculosa* is enhanced under moderate-high salinity conditions

(Mardones et al., 2019), and cells aggregate into thin layers within the halocline in Reloncaví Sound (Mardones et al., 2021) with a vertical migration behavior that might allow access to DIN and DIP in MSAW (León-Muñoz et al., 2018) and promote retention in a fjord with low flushing rates (Mardones et al., 2021). The apparent convergence of blooms of *P. verruculosa* and *A. catenella* in 2016 from opposite latitudes suggests a possible overlap of differential preferences along the MSAW-EW spectrum.

Dinoflagellates of the genus *Karenia* are known to produce ichthyotoxins in Chilean waters (Mardones, 2020; Mardones et al., 2020). Extensive blooms of various species of *Karenia* have been observed in Magellanic fjords (Uribe and Ruiz, 2001), around Chiloé Island (Clément et al., 2001; Mardones, 2020), off the Aysén coast (Villanueva et al., 2017), and off the Chilean coast further north ∼37–44°S (Mardones et al., 2020). In March–April 1999, an extensive bloom of *Karenia* sp. originated off the coast of Patagonia between 42° and 54°S, with toxicity extending into inshore waters around Chiloé Island (Clément et al., 2001). In the Gulf of Peñas in 2017 (Villanueva et al., 2017), high abundance of several species of *Karenia* were associated with a frontal zone between MSAW and upwelling of SASW (Villanueva et al., 2017). This association of blooms of *Karenia* spp. with offshore waters (Villanueva et al., 2017; Mardones, 2020) is supported by culture studies showing optimal growth of *K. selliformis* at temperatures and salinities between those of MSAW and SASW (Mardones et al., 2020). Extensive blooms of *Karenia* spp. in inshore waters seem to be associated with periods of low precipitation (Clément et al., 2001), indicating that offshore fronts between MSAW and SASW could shift during climate anomalies thus promoting ichthyotoxin problems closer to shore (Mardones, 2020).

Regarding siliceous species, diatoms of the genus *Pseudo-nitzschia* have been associated with amnesic shellfish poisoning (ASP) on the northern and southern coasts of Chile (Díaz et al., 2019). Other diatoms such as *Leptocylindrus* spp. and *Chaetoceros* spp. cause respiratory dysfunction in fish through mechanical gill damage (Díaz et al., 2019; Mardones, 2020). An interesting corollary to the apparent increases in non-siliceous HAB blooms would be whether blooms of HAB diatoms decrease in response to reduced availability of DSi under conditions of low FW inputs into MSAW.

The sporadic nature of blooms means that we have insufficient data on the role of large-scale oceanographic processes on growth of HAB species in Patagonian and Fuegian waters, particularly with reference to eco-physiological niches, and how competitive shifts may be driven by changing water column properties.

IMPLICATIONS AND CONCLUSIONS

The Magellan and Fuegian regions are extremely sparsely populated, and many events of water discoloration and toxicity of shellfish will have gone either unnoticed, or unrecorded. Our historical understanding of the spatial and temporal distribution of these events is therefore limited by the availability of relevant records of indigenous peoples and early explorers. Toxic episodes have been reported in the south over several centuries, but over more recent years, a northward expansion of exceptional *A. catenella* blooms has occurred. It is not known whether this represents a novel spread or is part of a longer-term cycle in distribution.

We have briefly reviewed evidence for an oceanic influence on these blooms, but there is a sparsity of available associated data on physical and chemical properties of the water column on which to speculate on detailed mechanisms. However, we have highlighted notable properties of SASW that have received little research attention. When interacting with coastal waters, properties of SASW and MSAW can potentially impact on the growth, retention, toxicity and encystment/excystment cycles of dinoflagellates such as *A. catenella* and other HAB species, and on competitive interactions between species. Variation of input of continental FW into coastal waters seems to be a major factor shaping the influence of MSAW on HAB bloom dynamics. In an enhanced dinoflagellate setting potentially driven by low DSi in SASW and MSAW, other factors could also be significant in bloom dynamics, such as dissolved trace metals and CO_2, and allelopathic interactions between species (e.g., Granéli et al., 2008).

Larger scale studies are required that extend from the fjords into the ocean, employing high resolution vertical and horizontal sampling of water column properties and life cycle stages of *A. catenella*. Elucidation of the factors involved with triggering blooms may depend on our ability to conduct studies at temporal and spatial scales appropriate for examining the interactions between FW and oceanic waters in these complex coastal areas. Chilean Patagonia represents an expansive natural mesocosm where blooms of *A. catenella* occur over an extensive latitudinal range encompassing contrasting anthropogenic influences. Even without a significant role for eutrophication, these blooms could nevertheless be influenced by large scale anthropogenically driven ocean/atmosphere interactions.

AUTHOR CONTRIBUTIONS

DC wrote the text and prepared figures. PM and GD provided reviews of available information from the literature in Chile. All authors contributed to the article and approved the submitted version.

FUNDING

This work was funded in part by Programa Regional CONICYT R17A10002, and COPAS Sur-Austral ANID PIA APOYO CCTE AFB 170006.

ACKNOWLEDGMENTS

We greatly appreciate comments from referees on an earlier draft of the manuscript. We thank Nancy Hamilton for helpful discussions on historical sources. Data and map plotting were conducted using Ocean Data View (ODV) software.

REFERENCES

Aguilera, A., Arriagada, G., Caniggia, M., Clément, A., Contreras, V., Córdova, M., et al. (2004). "Distribution of toxic algae blooms of *Alexandrium catenella* and their impact upon the Chiloé Archipelago," in *GeoHab, Global Ecology and Oceanography of Harmful Algal Blooms. Open Science Meeting, Viña del Mar, Chile, April 2004*, Chile, 24.

Aguilera-Belmonte, A., Inostroza, I., Sáez Carrillo, K., Franco, J. M., Riobó, P., and Gómez, P. I. (2013). The combined effect of salinity and temperature on the growth and toxin content of four Chilean strains of *Alexandrium catenella* (Whedon and Kofoid) Balech 1985 (Dinophyceae) isolated from an outbreak occurring in southern Chile in 2009. *Harmful Algae* 23, 55–59. doi: 10.1016/j.hal.2012.12.006

Álvarez, A., Díaz, P. A., Godoy, M., Araya, M., Ganuza, I., Pino, R., et al. (2019). Paralytic shellfish toxins in Surf Clams *Mesodesma donacium* during a large bloom of *Alexandrium catenella* dinoflagellates associated to an intense shellfish mass mortality. *Toxins* 11:188. doi: 10.3390/toxins11040188

Alves-de-Souza, C., Varela, D., Contreras, C., de La Iglesia, P., Fernández, P., Hipp, B., et al. (2014). Seasonal variability of *Dinophysis* spp. and *Protoceratium reticulatum* associated to lipophilic shellfish toxins in a strongly stratified Chilean fjord. *Deep Sea Res. II* 101, 152–162. doi: 10.1016/j.dsr2.2013.01.014

Alves-de-Souza, C., Iriarte, J. L., and Mardones, J. I. (2019). Interannual variability of *Dinophysis acuminata* and *Protoceratium reticulatum* in a Chilean Fjord: insights from the realized niche analysis. *Toxins* 11:19. doi: 10.3390/toxins11010019

Anderson, D. M., Alpermann, T. J., Cembella, A. D., Collos, Y., Masseret, E., and Montresor, M. (2012). The globally distributed genus *Alexandrium*: multifaceted roles in marine ecosystems and impacts on human health. *Harmful Algae* 14, 10–35. doi: 10.1016/j.hal.2011.10.012

Anonymous (1893). *Pater's Chats With the Boys. Tierra del Fuego*. Magellan Strait: Otago Witness (NZ).

Armijo, J., Oerder, V., Auger, P.-A., Bravo, A., and Molina, E. (2020). The 2016 red tide crisis in southern Chile: possible influence of the mass oceanic dumping of dead salmons. *Mar. Pollut. Bull.* 150:110603. doi: 10.1016/j.marpolbul.2019.110603

Avila, M., De Zarate, C., Clément, A., Carbonell, P., and Pérez, F. (2015). Efecto de factores abióticos en el crecimiento vegetative de *Alexandrium catenella* proveniente de quistes en laboratorio. *Revista de Biología Marina y Oceanografía* 50(S1), 177–185. doi: 10.4067/S0718-19572015000200004

Benavides, H., Prado, L., Díaz, S., and Carreto, J. I. (1995). "An exceptional bloom of *Alexandrium catenella* in the Beagle Channel, Argentina," in *Harmful Marine Algal Blooms. Proceedings of the Sixth Intemational Conference on Toxic Marine Phytoplankton, October 1993, Nantes, France*, eds P. Lassus, G. Arzul, E. Erard, P. Gentien, and C. Marcaillou (Nantes: Lavoisier Publishing and Intercept Ltd), 113–119. doi: 10.13140/2.1.4195.1683

Berdalet, E., and Estrada, M. (1993). "Effects of turbulence on several dinoflagellate species," in *Toxic Phytoplankton in the Sea*, eds T. J. Smayda and Y. Shimizu (Amsterdam: Elsevier), 737–741.

Brosnahan, M. L., Ralston, D. K., Fischer, A. D., Solow, A. R., and Anderson, D. M. (2017). Bloom termination of the toxic dinoflagellate *Alexandrium catenella*: vertical migration behavior, sediment infiltration, and benthic cyst yield. *Limnol. Oceanogr.* 62, 2829–2849. doi: 10.1002/lno.10664

Browning, T. J., Bouman, H. A., Henderson, G. M., Mather, T. A., Pyle, D. M., Schlosser, C., et al. (2014). Strong responses of Southern Ocean phytoplankton communities to volcanic ash. *Geophys. Res. Lett.* 41, 2851–2857. doi: 10.1002/2014GL059364

Boyd, P. W., Doney, S. C., Strzepek, R., Dusenberry, J., Lindsay, K., and Fung, I. (2008). Climate-mediated changes to mixed-layer properties in the Southern Ocean: assessing the phytoplankton response. *Biogeosciences* 5, 847–864. doi: 10.5194/bg-5-847-2008

Buschmann, A., Farías, F., Tapia, F., Varela, D., and Vásquez, M. (2016). *Comisión Marea Roja: Informe Final*. Osorno: Universidad de Los Lagos, 2016.

Cáceres, M., Valle-Levinson, A., and Bello, M. (2008). Residual flow over a bump in Quellón Bay. *Revista de Biología Marina y Oceanografía* 43, 629–639. doi: 10.4067/S0718-19572008000300022

Calvete, C., and Sobarzo, M. (2011). Quantification of the surface brackish water layer and frontal zones in southern Chilean fjords between Boca del Guafo (43° 30'S) and Estero Elefantes (46° 30'S). *Continental Shelf Res.* 31, 162–171. doi: 10.1016/j.csr.2010.09.013

Carreto, J. I., and Benavides, H. R. (1993). World record of PSP in Southern Argentina. *Harmful Algae News* 5:2.

Chatwin, B. (1977). *In Patagonia*. London: Jonathan Cape.

Clément, A., Seguel, M., Arzul, G., Guzmán, L., and Alarcón, C. (2001). "Widespread outbreak of hemolytic, ichthyotoxic *Gymnodinium* sp. in southern Chile," in *Harmful Algal Blooms 2000*, eds G. M. Hallegraeff, S. I. Blackburn, C. J. Bolch, and R. J. Lewis (Paris: Intergovernmental Oceanographic Commission of UNESCO), 66–69.

Clément, A., Aguilera, A., and Fuentes, C. (2002). "Análisis de marea roja en archipiélago de Chiloé, contingencia verano 2002," in *XXII Congreso de Ciencias del Mar. Resumenes*, (Valdivia), 124.

Clément, A., Lincoqueo, L., Saldivia, M., Brito, C. G., Muñoz, F., Fernández, C., et al. (2016). Exceptional summer conditions and HABs of *Pseudochattonella* in southern Chile create record impacts on salmon farms. *Harmful Algae News* 53, 1–3.

Coale, K. H., Johnson, K. S., Chavez, F. P., Buesseler, K. O., Barber, R. T., Brzezinski, M. A., et al. (2004). Southern Ocean iron enrichment experiment: carbon cycling in high- and low-Si waters. *Science* 304, 408–414. doi: 10.1126/science.1089778

Croot, P. L., Baars, O., and Streu, P. (2011). The distribution of dissolved zinc in the Atlantic sector of the Southern Ocean. *Deep Sea Res. II* 58, 2707–2719. doi: 10.1016/j.dsr2.2010.10.041

Dagenais-Bellefeuille, S., and Morse, D. (2013). Putting the N in dinoflagellates. *Front. Microbiol.* 4:369. doi: 10.3389/fmicb.2013.00369

Davidson, K., Gowen, R. J., Harrison, P. J., Fleming, L. E., Hoagland, P., and Moschonas, G. (2014). Anthropogenic nutrients and harmful algae in coastal waters. *J. Environ. Manage.* 146, 206–216. doi: 10.1016/j.jenvman.2014.07.002

De La Rocha, C. L., Hutchins, D. A., Brzezinski, M. A., and Zhang, Y. (2000). Effects of iron and zinc deficiency on elemental composition and silica production by diatoms. *Mar. Ecol. Prog. Ser.* 195, 71–79.

Díaz, P. A., Molinet, C., Seguel, M., Díaz, M., Labra, G., and Figueroa, R. I. (2014). Coupling planktonic and benthic shifts during a bloom of *Alexandrium catenella* in southern Chile: implications for bloom dynamics and recurrence. *Harmful Algae* 40, 9–22. doi: 10.1016/j.hal.2014.10.001

Díaz, P. A., Álvarez, G., Varela, D., Pérez-Santos, I., Díaz, M., Molinet, C., et al. (2019). Impacts of harmful algal blooms on the aquaculture industry: Chile as a case study. *Perspect. Phycol.* 6, 39–50. doi: 10.1127/pip/2019/0081

Eberlein, T., Van de Waal, D. B., Brandenburg, K. M., John, U., Voss, M., Achterberg, E. P., et al. (2016). Interactive effects of ocean acidification and nitrogen limitation on two bloom-forming dinoflagellate species. *Mar. Ecol. Prog. Ser.* 543, 127–140. doi: 10.3354/meps11568

Eckford-Soper, L., and Daugbjerg, N. (2016). The ichthyotoxic genus Pseudochattonella (Dictyochophyceae): distribution, toxicity, enumeration, ecological impact, succession and life history – a review. *Harmful Algae* 58, 51–58. doi: 10.1016/j.hal.2016.08.002

Ellwood, M. J. (2008). Wintertime trace metal (Zn, Cu, Ni, Cd, Pb and Co) and nutrient distributions in the Subantarctic Zone between 40–52°S; 155–160°E. *Mar. Chem.* 112, 107–117. doi: 10.1016/j.marchem.2008.07.008

Espinoza, J. B., and Espinoza, R. (2010). La increíble empresa de Sarmiento de Gamboa y su triste fin: Posibles causas de la tragedia en el Estrecho de Magallanes en el siglo XVI. The possible causes of the tragedy of "Port Famine" in the Strait of Magellan. *Revista Médica Chile* 138, 1456–1460.

FAO (2004). *Marine Biotoxins, FAO Food and Nutrition Paper 80*. Rome: Food and Agriculture Organization of the United Nations, 278.

Fitzroy, R. (1839). "Narrative of the surveying voyages of His Majesty's ships Adventure and Beagle between the years 1826 and 1836," in *Proceedings of the First Expedition, 1826–1830*, Vol. 1, (London: Henry Colburn).

Fraga, S., Sampedro, N., Larsen, J., Moestrup, Ø, and Calado, A. J. (2015). Arguments against the proposal 2302 by John & al. to reject the name *Gonyaulax catenella* (*Alexandrium catenella*). *Taxon* 64, 634–635. doi: 10.12705/643.15

Fu, F. X., Tatters, A. O., and Hutchins, D. A. (2012). Global change and the future of harmful algal blooms in the ocean. *Mar. Ecol. Prog. Ser.* 470, 207–233. doi: 10.3354/meps10047

Fuentes, C., Clément, A., and Aguilera, A. (2008). "Summer *Alexandrium catenella* bloom and the impact on fish farming, in the XI Aysén region, Chile," in

Proceedings of the 12th International Conference on Harmful Algae, Copenhagen, Denmark, 4–8 September, 2006, ed. Ø Moestrup (Paris: Intergovernmental Oceanographic Commission of UNESCO), 183–186.

García, C., del Carmen Bravo, M., Lagos, M., and Lagos, N. (2004a). Paralytic shellfish poisoning: post-mortem analysis of tissue and body fluid samples from human victims in the Patagonia fjords. *Toxicon* 43, 149–158. doi: 10.1016/j.toxicon.2003.11.018

García, C., Mardones, P., Sfeir, A., and Lagos, N. (2004b). Simultaneous presence of paralytic and diarrheic shellfish poisoning toxins in *Mytilus chilensis* samples collected in the Chiloe Island, Austral Chilean Fjords. *Biol. Res.* 37, 721–731.

Garreaud, R., Lopez, P., Minvielle, M., and Rojas, M. (2013). Large-scale control on the Patagonian climate. *J. Clim.* 26, 215–230. doi: 10.1175/JCLI-D-12-00001.1

Gatica, C., Quiñones, R. A., Figueroa, D., Wiff, R., Navarro, E., and Donoso, M. (2009). Asociación entre la Corriente de Deriva de los Vientos del Oeste y la abundancia relativa del pez espada (*Xiphias gladius*) frente a la costa de Chile. *Lat. Am. J. Aquat. Res.* 37, 97–105. doi: 10.3856/vol37-issue1-fulltext-8

Giesecke, R., Clément, A., Garcés-Vargas, J., Mardones, J. I., González, H. E., Caputo, L., et al. (2014). Massive salp outbreaks in the inner sea of Chiloé Island (Southern Chile): possible causes and ecological consequences. *Lat. Am. J. Aquat. Res.* 42, 604–621. doi: 103856/vol42-issue3-fulltext-18

Glibert, P. M. (2016). Margalef revisited: a new phytoplankton mandala incorporating twelve dimensions, including nutritional physiology. *Harmful Algae* 55, 25–30. doi: 10.1016/j.hal.2016.01.008

Granéli, E., Weberg, M., and Salomon, P. S. (2008). Harmful algal blooms of allelopathic microalgal species: the role of eutrophication. *Harmful Algae* 8, 94–102. doi: 10.1016/j.hal.2008.08.011

Guzmán, L., Campodonico, I., and Hermosilla, J. (1975a). Estudios sobre un florecimiento tóxico causado por *Gonyaulax catenella* en Magallanes. I.—Distribución espacial y temporal de *G. catenella*. *Ans. Inst. Pat.* VI, 173–183.

Guzmán, L., Campodonico, I., and Antunovic, M. (1975b). Estudios sobre un florecimiento tóxico causado por *Gonyaulax catenella* en Magallanes. IV.—Distribución y niveles de toxicidad del Veneno Paralítico de los Mariscos (Noviembre de 1972 - Noviembre de 1973). *Ans. Inst. Pat.* VI, 209–223.

Guzmán, L., and Lembeye, G. (1975). Estudios sobre un florecimiento tóxico causado por *Gonyaulax catenella* en Magallanes. II. – Algunas condiciones hidrográficas asociadas. *Ans. Inst. Pat.* VI, 185–195.

Guzmán, L., Pacheco, H., Pizarro, G., and Alarcón, C. (2002). "*Alexandrium catenella* y veneno paralizante de los mariscos en Chile," in *Floraciones Algales Nocivas En el Cono Sur Americano*, eds E. A. Sar, M. E. Ferrario, and B. Reguera (Madrid: Instituto Español de Oceanografía), 237–255.

Guzmán, L., Vivanco, X., Vidal, G., Pizarro, G., Hernández, C., Tocornal, M. A., et al. (2013). "Spatial and temporal variability of *Alexandrium catenella* and PSP in southern Chile (43° — 55° S) (May 2006 – July 2010)," in *Proceedings 14th International Conference on Harmful Algae, Hersonissos-Crete* (Greece), 69–71.

HAEDAT *Harmful Algal Event Database*. Available online at: http://haedat.iode.org/

Hallegraeff, G. M. (1998). Transport of toxic dinoflagellates via ships' ballast water: bioeconomic risk assessment and efficacy of possible ballast water management strategies. *Mar. Ecol. Prog. Ser.* 168, 297–309.

Hattenrath-Lehmann, T. K., Smith, J. L., Wallace, R. B., Merlo, L. R., Koch, F., Mittelsdorf, H., et al. (2015). The effects of elevated CO_2 on the growth and toxicity of field populations and cultures of the saxitoxin-producing dinoflagellate, *Alexandrium fundyense*. *Limnol. Oceanogr.* 60, 198–214. doi: 10.1002/lno.10012

Hawkesworth, J. (1773). *An Account of the Voyages Undertaken by the Order of his Present Majesty for Making Discoveries in the Southern Hemisphere, and Successively Performed by Commodore Byron, Captain Carteret, Captain Wallis, and Captain Cook, in the Dolphin, the Swallow, and the Endeavour*. London: W. Strahan & T. Cadell.

Henry, D. (ed.) (1875). *An Historical Account of all the Voyages Round the World, Performed by English Navigators; Including those Lately Undertaken by Order of his Present Majesty. The whole Faithfully Extracted from the Journals of the Voyagers. In Four Volumes*. London: Printed for F. Newbery.

Hernández, C., Díaz, P. A., Molinet, C., and Seguel, M. (2016). Exceptional climate anomalies and northwards expansion of Paralytic Shellfish Poisoning outbreaks in Southern Chile. *Harmful Algae News* 54, 1–2.

Hiscock, M. R., Marra, J., Smith, W. O., Goericke, R., Measures, C., Vink, S., et al. (2003). Primary productivity and its regulation in the Pacific Sector of the Southern Ocean. *Deep Sea Res. II* 50, 533–558. doi: 10.1016/S0967-0645(02)00583-0

Ho, K.-C., Kang, S.-H., Lam, I. H. Y., and Hodgkiss, I. J. (2003). Distribution of *Alexandrium tamarense* in Drake Passage and the threat of harmful algal blooms in the Antarctic Ocean. *Ocean Polar Res.* 25, 625–631.

Hutchins, D. A., Sedwick, P. N., DiTullio, G. R., Boyd, P. W., Quéguiner, B., Griffiths, F. B., et al. (2001). Control of phytoplankton growth by iron and silicic acid availability in the subantarctic Southern Ocean: experimental results from the SAZ Project. *J. Geophys. Res.* 106, 31559–31572. doi: 10.1029/2000JC000333

Iriarte, J. L., Quiñones, R. A., and Gonzáles, R. R. (2005). Relationship between biomass and enzymatic activity of a bloom-forming dinoflagellate (Dinophyceae) in southern Chile (41°S): a field approach. *J. Plankton Res.* 27, 159–166. doi: 10.1093/plankt/fbh167

Jeong, H. J., Lim, A. S., Franks, P. J. S., Lee, K. H., Kim, J. H., Kang, N. S., et al. (2015). A hierarchy of conceptual models of red-tide generation: Nutrition, behavior, and biological interactions. *Harmful Algae* 47, 97–115. doi: 10.1016/j.hal.2015.06.004

John, U., Litaker, W., Montresor, M., Murray, S., Brosnahan, M. L., and Anderson, D. M. (2014a). (2302) Proposal to reject the name *Gonyaulax catenella* (*Alexandrium catenella*) (Dinophyceae). *Taxon* 63, 932–933. doi: 10.12705/634.21

John, U., Litaker, R. W., Montresor, M., Murray, S., Brosnahan, M. L., and Anderson, D. M. (2014b). Formal revision of the *Alexandrium tamarense* species complex (Dinophyceae) taxonomy: the introduction of five species with emphasis on molecular-based (rDNA) classification. *Protist* 165, 779–804. doi: 10.1016/j.protis.2014.10.001

Kerr, R. (1824). *A General History and Collection of Voyages and Travels, Arranged in Systematic Order: Forming a Complete History of the Origin and Progress of Navigation, Discovery, and Commerce, by Sea and Land, from the Earliest Ages to the Present Time*, Vol. 10. Edinburgh & London: William Blackwood & T. Cadell.

Kopczynska, E. E., Dehairs, F., Elskens, M., and Wright, S. (2001). Phytoplankton and microzooplankton variability between the Subtropical and Polar Fronts south of Australia: thriving under regenerative and new production in late summer. *J. Geophys. Res.* 106, 31597–31609.

Lagos, N. (1998). Microalgal blooms: a global issue with negative impact in Chile. *Biol. Res.* 31, 375–386.

Lara, C., Saldías, G. S., Tapia, F. J., Iriarte, J. L., and Broitman, B. R. (2016). Interannual variability in temporal patterns of Chlorophyll-a and their potential influence on the supply of mussel larvae to inner waters in northern Patagonia (41–44°S). *J. Mar. Syst.* 155, 11–18. doi: 10.1016/j.jmarsys.2015.10.010

Leblanc, K., Hare, C. E., Boyd, P. W., Bruland, K. W., Sohst, B., Pickmere, S., et al. (2005). Fe and Zn effects on the Si cycle and diatom community structure in two contrasting high and low-silicate HNLC areas. *Deep Sea Res. I* 52, 1842–1864. doi: 10.1016/j.dsr.2005.06.005

Lee, T. C.-H., Kwok, O.-T., Ho, K.-C., and Lee, F. W.-F. (2012). Effects of different nitrate and phosphate concentrations on the growth and toxin production of an *Alexandrium tamarense* strain collected from Drake Passage. *Mar. Environ. Res.* 81, 62–69. doi: 10.1016/j.marenvres.2012.08.009

Lembeye, G. (1981a). Segunda aparición del veneno paralitico de los mariscos (VPM) asociado a *Gonyaulax catenella*, en Magallanes (Chile), 1981. *Ans. Inst. Pat.* 12, 273–276.

Lembeye, G. (1981b). Estructura del fitoplancton asociado a la presencia del veneno paralitico de los mariscos en Seno Union y áreas adyacentes (Magallanes, Chile), 1981. *Ans. Inst. Pat.* 12, 277–289.

Lembeye, G. (1992). Major PSP outbreak in Chile, 1991–1992. *Harmful Algae News* 2, 1–2.

Lembeye, G. (2008). "Harmful algal blooms in the austral Chilean channels and fjords," in *Progress in the Oceanographic Knowledge of Chilean Interior Waters, from Puerto Montt to Cape Horn*, eds N. Silva and S. Palma (Valparaíso: Comité Oceanográfico Nacional - Pontificia Universidad Católica de Valparaíso), 99–103.

Lembeye, G., Guzmán, L., and Campodónico, I. (1975). Estudios sobre un florecimiento tóxico causado por *Gonyaulax catenella* en Magallanes. III. – Fitoplancton asociado. *Ans. Inst. Pat.* VI, 197–208.

León-Muñoz, J., Urbina, M. A., Garreaud, R., and Iriarte, J. L. (2018). Hydroclimatic conditions trigger record harmful algal bloom in western Patagonia (summer 2016). *Sci. Rep.* 8:1330. doi: 10.1038/s41598-018-19461-4

Mardones, J., Clément, A., Rojas, X., and Aparicio, C. (2010). *Alexandrium catenella* during 2009 in Chilean waters, and recent expansion to coastal ocean. *Harmful Algae News* 41, 8–9.

Mardones, J. I., Bolch, C., Guzmán, L., Paredes, J., Varela, D., and Hallegraeff, G. M. (2016a). Role of resting cysts in Chilean *Alexandrium catenella* dinoflagellate blooms revisited. *Harmful Algae* 55, 238–249. doi: 10.1016/j.hal.2016.03.020

Mardones, J. I., Müller, M. N., and Hallegraeff, G. M. (2016b). Toxic dinoflagellate blooms of *Alexandrium catenella* in Chilean fjords: a resilient winner from climate change. *ICES J. Mar. Sci.* 74, 988–995. doi: 10.1093/icesjms/fsw164

Mardones, J. I., Fuenzalida, G., Zenteno, K., Alves-de-Souza, C., Astuya, A., and Dorantes-Aranda, J. J. (2019). Salinity-growth response and ichthyotoxic potency of the Chilean *Pseudochattonella verruculosa*. *Front. Mar. Sci.* 6:24. doi: 10.3389/fmars.2019.00024

Mardones, J. I. (2020). Screening of Chilean fish-killing microalgae using a gill cell-based assay. *Latin Am. J. Aquatic Res.* 48, 329–335. doi: 10.3856/vol48-issue2-fulltext-2400

Mardones, J. I., Norambuena, L., Paredes, J., Fuenzalida, G., Dorantes-Aranda, J. J., Lee Chang, K. J., et al. (2020). Unraveling the *Karenia selliformis* complex with the description of a non-gymnodimine producing Patagonian phylotype. *Harmful Algae* 98:101892. doi: 10.1016/j.hal.2020.101892

Mardones, J. I., Paredes, J., Godoy, M., Suarez, R., Norambuena, L., Vargas, V., et al. (2021). Disentangling the environmental processes responsible for the world's largest farmed fish-killing harmful algal bloom: Chile, 2016. *Sci. Total Environ.* 766:144383. doi: 10.1016/j.scitotenv.2020.144383

Margalef, R. (1978). Life forms of phytoplankton as survival alternatives in an unstable environment. *Oceanol. Acta* 1, 493–509.

Masiokas, M. H., Cara, L., Villalba, R., Pitte, P., Luckman, B. H., Toum, E., et al. (2019). Streamflow variations across the Andes (18°–55°S) during the instrumental era. *Sci. Rep.* 9:17879. doi: 10.1038/s41598-019-53981-x

Molinet, C., Lafon, A., Lembeye, G., and Moreno, C. A. (2003). Patrones de distribución espacial y temporal de floraciones de *Alexandrium catenella* (Whedon & Kofoid) Balech 1985, en aguas interiores de la Patagonia noroccidental de Chile. *Revista Chilena de Historia Natural* 76, 681–698.

Montebruno, D. (1993). Paralytic shellfish poisoning in Chile. *Med. Sci. Law* 33, 243–246.

Montero, P., Daneri, G., Tapia, F., Iriarte, J. L., and Crawford, D. (2017). Diatom blooms and primary production in a channel ecosystem of central Patagonia. *Latin Am. J. Aquatic Res.* 45, 999–1016. doi: 10.3856/vol45-issue5-fulltext-16

Moore, S. K., Trainer, V. L., Mantua, N. J., Parker, M. S., Laws, E. A., Backer, L. C., et al. (2008). Impacts of climate variability and future climate change on harmful algal blooms and human health. *Environ. Health* 7 (Suppl. 2):S4. doi: 10.1186/1476-069X-7-S2-S4

Moss, M. (1993). Shellfish, gender, and status on the Northwest Coast: reconciling archeological, ethnographic, and ethnohistorical records of the Tlingit. *Am. Anthropol.* 95, 631–652.

Muñoz, P., Avaria, S., Sievers, H., and Prado, R. (1992). Presencia de dinoflagelados toxicos del genero en el Seno Aysen, Chile. *Revista de Biología Marina Valparaíso* 27, 187–212.

Navarro, J. M., Muñoz, M. G., and Contreras, A. M. (2006). Temperature as a factor regulating growth and toxin content in the dinoflagellate *Alexandrium catenella*. *Harmful Algae* 5, 762–769. doi: 10.1016/j.hal.2006.04.001

Nelson, D. M., and Tréguer, P. (1992). Role of silicon as a limiting nutrient to Antarctic diatoms: evidence from kinetic studies in the Ross Sea ice-edge zone. *Mar. Ecol. Prog. Ser.* 80, 255–264.

Nixon, S. W. (1995). Coastal marine eutrophication: a definition, social causes, and future concerns. *Ophelia* 41, 199–219.

Odate, T., and Fukuchi, T. (1995). Physical and chemical properties of surface water in the Southern Ocean in summer 1991/92. *Proc. NIPR Symp. Polar Biol.* 8, 77–85.

Orsi, A. H., Whitworth, T., and Nowlin, W. D. (1995). On the meridional extent and fronts of the Antarctic Circumpolar Current. *Deep Sea Res. I* 42, 641–673.

O'Sullivan, D. R. (1893). *Tierra del Fuego. The Fortnightly Review. Old Series LIX (New Series LIII).* London: Chapman & Hall, 36–53.

Pigafetta, A. (1874). *The First Voyage Around the World by Magellan, Translated from the Accounts of Pigafetta and Other Contemporary Writers. Accompanied by Original Documents, with Notes and an Introduction by Lord Stanley of Alderley*. London: Hakluyt Society.

Paredes, J., Varela, D., Martínez, C., Zúñiga, A., Correa, K., Villarroel, A., et al. (2019). Population genetic structure at the northern edge of the distribution of *Alexandrium catenella* in the Patagonian fjords and its expansion along the open Pacific Ocean coast. *Front. Mar. Sci.* 5:532. doi: 10.3389/fmars.2018.00532

Paredes-Mella, J., Varela, D., Fernández, P., and Espinoza-González, O. (2020). Growth performance of *Alexandrium catenella* from the Chilean fjords under environmental drivers: plasticity as a response to a highly variable environment. *J. Plankton Res.* 42, 119–134. doi: 10.1093/plankt/fbaa011

Pizarro, G., Garrido, C., Cárdenas, C., Frangópulos, M., Alarcón, C., Guzmán, L., et al. (2011). Distribución espacial de *Alexandrium catenella* y de toxinas paralizantes en el plancton y mariscos entre el Golfo de Penas y Canal Trinidad (Primavera 2008). *Ciencia y Tecnología del Mar* 34, 19–30.

Pizarro, G., Paz, P., Alarcón, C., Toro, C., Frangópulos, M., Salgado, P., et al. (2018). Winter distribution of toxic, potentially toxic phytoplankton, and shellfish toxins in fjords and channels of the Aysén region, Chile. *Lat. Am. J. Aquat. Res.* 46, 120–139. doi: 10.3856/vol46-issue1-fulltext-13

Sarmiento, J. L., Gruber, N., Brzezinski, M. A., and Dunne, J. P. (2004). High-latitude controls of thermocline nutrients and low latitude biological productivity. *Nature* 427, 56–60.

Schneider, W., and Bravo, L. (2006). Argo profiling floats document Subantarctic Mode Water formation west of Drake Passage. *Geophys. Res. Lett.* 33:L16609. doi: 10.1029/2006GL026463

Sedwick, P. N., DiTullio, G. R., Hutchins, D. A., Boyd, P. W., Griffiths, F. B., Crossley, A. C., et al. (1999). Limitation of algal growth by iron deficiency in the Australian Subantarctic region. *Geophys. Res. Lett.* 26, 2865–2868. doi: 10.1029/1998GL002284

Segers, P. A. (1891). Chronic mussel poisoning. *Br. Med. J. (suppl.)* 1891, 169–170.

Sievers, H. A., and Silva, N. (2008). "Water masses and circulation in austral Chilean channels and fjords," in *Progress in the Oceanographic Knowledge of Chilean Interior Waters, from Puerto Montt to Cape Horn*, eds N. Silva and S. Palma (Valparaíso: Comité Oceanográfico Nacional - Pontificia Universidad Católica de Valparaíso), 53–58.

Silva, N. (2008). "Dissolved oxygen, pH, and nutrients in the austral Chilean channels and fjords," in *Progress in the Oceanographic Knowledge of Chilean Interior Waters, from Puerto Montt to Cape Horn*, eds N. Silva and S. Palma (Valparaíso: Comité Oceanográfico Nacional - Pontificia Universidad Católica de Valparaíso), 37–43.

Silva, N., Rojas, N., and Fedel, A. (2009). Water masses in the Humboldt Current System: properties, distribution, and the nitrate deficit as a chemical water mass tracer for Equatorial Subsurface Water off Chile. *Deep Sea Res. II* 56, 1004–1020. doi: 10.1016/j.dsr2.2008.12.013

Smayda, T. J. (2002). Turbulence, water mass stratification and harmful algal blooms: an alternative view and frontal zones as "pelagic seed banks". *Harmful Algae* 1, 95–112.

Sullivan, J. M., Swift, E., Donaghay, P. L., and Rines, J. E. B. (2003). Small-scale turbulence affects the division rate and morphology of two red-tide dinoflagellates. *Harmful Algae* 2, 183–199. doi: 10.1016/S1568-9883(03)00039-8

Timmermans, K. R., van Leeuwe, M. A., de Jong, J. T. M., McKay, R. M. L., Nolting, R. F., Witte, H. J., et al. (1998). Iron stress in the Pacific region of the Southern Ocean: evidence from enrichment bioassays. *Mar. Ecol. Prog. Ser.* 166, 27–41.

Torres, R., Frangópulos, M., Hamamé, M., Montecino, V., Maureira, C., Pizarro, G., et al. (2011a). Nitrate to silicate ratio variability and the composition of micro-phytoplankton blooms in the inner-fjord of Seno Ballena (Strait of Magellan, 54°S). *Continental Shelf Res.* 31, 244–253. doi: 10.1016/j.csr.2010.07.014

Torres, R., Pantoja, S., Harada, N., González, H. E., Daneri, G., Frangópulos, M., et al. (2011b). Air-sea CO_2 fluxes along the coast of Chile: From CO_2 outgassing in central northern upwelling waters to CO_2 uptake in southern Patagonian fjords. *J. Geophys. Res.* 116:C09006. doi: 10.1029/2010JC006344

Torres, R., Silva, N., Reid, B., and Frangópulos, M. (2014). Silicic acid enrichment of subantarctic surface water from continental inputs along the Patagonian archipelago interior sea (41–56°S). *Prog. Oceanogr.* 129, 50–61. doi: 10.1016/j.pocean.2014.09.008

Trainer, V. L., Moore, S. K., Hallegraeff, G., Kudela, R. M., Clement, A., Mardones, J. I., et al. (2020). Pelagic harmful algal blooms and climate change: lessons from nature's experiments with extremes. *Harmful Algae* 91:101591. doi: 10.1016/j.hal.2019.03.009

Uribe, J. C. (1988). Antecedentes sobre un tercer brote de veneno paralizante de moluscos (VPM), en la región de Magallanes. *Ans. Inst. Pat. Ser. Cs. Nts., Punta Arenas (Chile)* 18, 97–101.

Uribe, J. C., and Ruiz, M. (2001). *Gymnodinium* brown tide in the Magellanic fjords, Southern Chile. *Revista de Biología Marina y Oceanografía* 36, 155–164.

Uribe, J. C., Oyarzún, S., and Latorre, V. (2010). *Alexandrium catenella* (Whedon & Kofoid) Balech, 1985, in Magellan waters, Chile. *Anales Instituto Patagonia (Chile)* 38, 103–110.

Varela, D., Paredes, J., Alves-de-Souza, C., Seguel, M., Sfeir, A., and Frangópulos, M. (2012). Intraregional variation among *Alexandrium catenella* (Dinophyceae) strains from southern Chile: Morphological, toxicological and genetic diversity. *Harmful Algae* 15, 8–18. doi: 10.1016/j.hal.2011.10.029

Vargas, C. A., Cuevas, L. A., Silva, N., González, H. E., De Pol-Holz, R., and Narváez, D. A. (2018). Influence of glacier melting and river discharges on the nutrient distribution and DIC recycling in the Southern Chilean Patagonia. *J. Geophys. Res. Biogeosci.* 123, 256–270. doi: 10.1002/2017JG003907

Villanueva, F., Cortez, H., Uribe, C., Peña, P., and Cassis, D. (2017). Mortality of Chilean farmed salmon in wellboats in transit through a *Karenia* bloom. *Harmful Algae News* 57, 4–5.

Weidemann, S. S., Sauter, T., Kilian, R., Steger, D., Butorovic, N., and Schneider, C. (2018). A 17-year record of meteorological observations across the Gran Campo Nevado Ice Cap in Southern Patagonia, Chile, related to synoptic weather types and climate modes. *Front. Earth Sci.* 6:53. doi: 10.3389/feart.2018.00053

Wolf, C., Frickenhaus, S., Kilias, E. S., Peeken, I., and Metfies, K. (2014). Protist community composition in the Pacific sector of the Southern Ocean during austral summer 2010. *Polar Biol.* 37, 375–389. doi: 10.1007/s00300-013-1438-x

Wyatt, N. J., Milne, A., Woodward, E. M. S., Rees, A. P., Browning, T. J., Bouman, H. A., et al. (2014). Biogeochemical cycling of dissolved zinc along the GEOTRACES South Atlantic transect GA10 at 40°S. *Global Biogeochem. Cycles* 28, 44–56. doi: 10.1002/2013GB004637

Yoo, Y. D., Jeong, H. J., Kim, M. S., Kang, N. S., Song, J. Y., Shin, W., et al. (2009). Feeding by phototrophic red-tide dinoflagellates on the ubiquitous marine diatom *Skeletonema costatum*. *J. Eukaryotic Microbiol.* 56, 413–420. doi: 10.1111/j.1550-7408.2009.00421.x

Conflict of Interest: The authors declare that the research was conducted in the absence of any commercial or financial relationships that could be construed as a potential conflict of interest.

frontiers in Marine Science

ORIGINAL RESEARCH
published: 04 May 2021
doi: 10.3389/fmars.2021.635855

Depth-Dependent Diversity Patterns of Rocky Subtidal Macrobenthic Communities Along a Temperate Fjord in Northern Chilean Patagonia

Vicente I. Villalobos[1], Nelson Valdivia[1,2], Günter Försterra[3], Stacy Ballyram[4,5], Juan Pablo Espinoza[4,5], Jemma L. Wadham[6], Katherine Burgos-Andrade[1] and Vreni Häussermann[7]*

[1] Instituto de Ciencias Marinas y Limnológicas, Facultad de Ciencias, Universidad Austral de Chile, Valdivia, Chile, [2] Centro FONDAP de Investigación de Dinámicas de Ecosistemas Marinos de Altas Latitudes (IDEAL), Universidad de Concepción, Concepción, Chile, [3] Escuela de Ciencias del Mar, Facultad de Recursos Naturales, Pontificia Universidad Católica de Valparaíso, Valparaíso, Chile, [4] Huinay Scientific Field Station, Puerto Montt, Chile, [5] Programa de Magíster en Oceanografía, Escuela de Ciencias del Mar, Facultad de Recursos Naturales, Pontificia Universidad Católica de Valparaíso, Valparaíso, Chile, [6] Department of Geographical Sciences, Bristol Glaciology Centre, University of Bristol, Bristol, United Kingdom, [7] Facultad de Economía y Negocios, Universidad San Sebastián, Puerto Montt, Chile

OPEN ACCESS

Edited by:
Giorgio Bavestrello, University of Genoa, Italy

Reviewed by:
Ricardo A. Scrosati, St. Francis Xavier University, Canada
Cesar A. Cardenas, Instituto Antártico Chileno (INACH), Chile

****Correspondence:***
Vicente I. Villalobos
vicente.villalobos@alumnos.uach.cl

Specialty section:
This article was submitted to Marine Ecosystem Ecology, a section of the journal Frontiers in Marine Science

Received: *30 November 2020*
Accepted: *01 April 2021*
Published: *04 May 2021*

Citation:
Villalobos VI, Valdivia N, Försterra G, Ballyram S, Espinoza JP, Wadham JL, Burgos-Andrade K and Häussermann V (2021) Depth-Dependent Diversity Patterns of Rocky Subtidal Macrobenthic Communities Along a Temperate Fjord in Northern Chilean Patagonia. Front. Mar. Sci. 8:635855. doi: 10.3389/fmars.2021.635855

Understanding the distribution of biodiversity along environmental gradients allows us to predict how communities respond to natural and anthropogenic impacts. In fjord ecosystems, the overlap of strong salinity and temperature gradients provides us with the opportunity to assess the spatial variation of biodiversity along abiotic environmental gradients. However, in Northern Chilean Patagonia (NCP), a unique and at the same time threatened fjord system, the variation of macrobenthic communities along abiotic environmental gradients is still poorly known. Here, we tested whether macrobenthic species diversity and community structure followed systematic patterns of variation according to the spatial variation in salinity and temperature in Comau Fjord, NCP. A spatially extensive nested sampling design was used to quantify the abundance of subtidal macrobenthic species along the fjord axis (fjord sections: head, middle, and mouth) and a depth gradient (0–21 m). The vertical structure of the water column was strongly stratified at the head of the fjord, characterized by a superficial (depth to ca. 5 m) low-salinity and relatively colder layer that shallowed and decayed toward the mouth of the fjord. The biotic variation followed, in part, this abiotic spatial pattern. Species richness peaked at high salinities (>27 psu) between 5 and 10 m in the head section and between 15 and 21 m in the middle and mouth sections. Diversity and evenness were also highest at these salinities and depth ranges in the head and middle sections, but at shallower depth ranges in the mouth. Information theory-based model selection provided a strong empirical support to the depth- and section-dependent salinity, but not temperature, effects on the three biodiversity metrics. Erect algae and the edible mussel *Aulacomya atra* numerically dominated in shallow water (0–3 m) at the head and the middle of the fjord, coinciding with the horizontal extension of the low-density water layer—these taxa were further replaced by the crustose algae *Lithothamnion* sp. and deep-dwelling suspension filters (e.g., corals, polychaetes, and sponges) along depth

gradient. Macrobenthic biodiversity correlated, therefore, with the influence of freshwater inputs and the density-driven stratification of the water column in this ecosystem. The spatially variable (across both, horizontal and vertical fjord axes) thresholds observed in our study question the widely accepted pattern of increasing biodiversity with increasing distance from the head of estuarine ecosystems. Finally, non-linear environmental stress models provide us a strong predictive power to understand the responses of these unique ecosystems to natural and anthropogenic environmental changes.

Keywords: patagonian fjord system, environmental drivers, biodiversity hotspot, marine animal forests, salinity-driven system

INTRODUCTION

Biodiversity plays a central role in maintaining the functioning and the goods and services that ecosystems provide to human society (Cardinale et al., 2012). Predicting changes in community measures such as species diversity and composition along environmental gradients is, thus, one of the main objectives of ecology (Hutchinson, 1953; Paine et al., 2018). Therefore, defining the relationships between abiotic environmental factors and the spatial patterns of biodiversity, particularly in ecosystems characterized by pronounced environmental gradients, is relevant for fundamental ecology and helps to inform ecosystem management and conservation strategies (e.g., Dayton, 1971; Underwood et al., 2000; Palacios et al., 2021).

Fjords are ideal natural laboratories to study the effect of abiotic environmental variations on the distribution of benthic communities (Brattegard, 1980; McGovern et al., 2020). The characteristic U-shape of a fjord (Howe et al., 2010) provides deep, large, and almost-vertical rock walls that sustain dense and diverse assemblages of marine invertebrates (Gasbarro et al., 2018). Some studies demonstrate the associations between community proxies and environmental factors along southern fjords (e.g., sediment properties: Gutt et al., 1999; salinity and predation: Smith and Witman, 1999; surface inclination; Cárdenas and Montiel, 2015; terrestrial organic matter inputs: Quiroga et al., 2016). However, most studies that treat quantitative aspects of fjord benthic biodiversity have been conducted in the northern hemisphere, and the study of southern fjord benthic communities (except for several emergent studies on Antarctic systems) has been focused mostly on species inventories and the description of distribution patterns (e.g., Häussermann et al., 2013; Betti et al., 2017).

The coastline of Chilean Patagonia extends 1,500 km from 41° to 56° S, with a total of ca. 100,000 km of coastline; it represents one of the longest fjord regions in the world and is characterized by a high hydrographic and geomorphological complexity (Pantoja et al., 2011). The Patagonian fjord region sustains important supporting ecosystem services, such as clean and cold water for aquaculture, fast currents for hydroelectric energy, cultural services such as tourist destinations, and supporting services such as biodiversity and primary productivity (Iriarte et al., 2010; González et al., 2013; Outeiro et al., 2015). This region is a biodiversity hotspot (Fernandez et al., 2000; Gutt et al., 2003) that harbors unique assemblages of marine invertebrates (Försterra et al., 2017).

Along the Chilean Patagonian fjords, the freshwater input into the fjord produces strong vertical and horizontal gradients in density (Dávila et al., 2002). The hydrography of this system is characterized by a highly stratified water column with two layers of different salinities: a shallow low-salinity layer (ca. 2–20 psu) and the deeper high-salinity layer (ca. 30 psu), which limit at 5–10 m depth—this border tends to shallow from the head of the fjord toward the ocean (Valle-Levinson et al., 2007; Castillo et al., 2016). Besides, the upper 30–50 m are influenced by seasonal variability in solar radiation, freshwater inputs, and mixing induced by wind and tides (Sobarzo Bustamante, 2009; Pérez-Santos et al., 2014). In this way, the diversity and structure (i.e., the combination of species incidences and abundances) of benthic communities would be expected to show non-linear patterns of variation along the different sections of the fjord (i.e., from the head to the mouth), depth, and salinity. This prediction is based on the premise that subtidal fjord communities are composed mostly by marine organisms (Dahl, 1956; Bulger et al., 1993), which can be physiologically sensitive to variations in water salinity (Smyth et al., 2014). According to early and recent environmental stress models, the interaction between physiological constrains imposed by abiotic factors, dispersal limitations, and density-dependent biotic interactions have been shown to lead to non-linear diversity-environment relationships in different marine ecosystems (e.g., Menge and Sutherland, 1987; Scrosati and Heaven, 2007; Thompson et al., 2020). In rocky intertidal habitats, for example, the overlap between species adapted to the physiologically demanding conditions of the supralittoral and those adapted to the infralitoral generates unimodal patterns of species richness, diversity, and evenness, in addition to a significant variation in community structure along the vertical intertidal stress gradient (e.g., Menge and Sutherland, 1987; Scrosati and Heaven, 2007; Heaven and Scrosati, 2008). In subtidal fjord habitats, however, local adaptation could lead to environmentally decoupled community patterns (Basset et al., 2013; Elliott and Quintino, 2019). For Chilean Patagonian fjords, therefore, the association between vertical and horizontal abiotic gradients and ecological communities still needs to be determined.

Here, we use a spatially extensive sampling program to examine the relationships between abiotic environmental gradients and the distribution of macrobenthic species in a

Northern Chilean Patagonian fjord (NCP). Three hypotheses were tested:

H1) Since the influence of freshwater inputs decreases from the head to the mouth of the fjord and the fjord benthos is colonized mostly by marine species (Bulger et al., 1993), we predict an increase in macrobenthic species richness, diversity, and evenness, and a major change in community structure, from the head to the mouth of the fjord and with increasing salinity.

H2) The sharp vertical (along depth) variation in salinity, which shows a threshold at 5–10 m depth, should have non-linear effects on the diversity and structure of fjord macrobenthic communities: species richness, diversity, and evenness should peak between 5 and 10 m depth because of the overlap between species occurring at shallow (above 5–10 m) and deep (below 5–10 m) substrata, leading to a unimodal environmental-diversity relationship. In addition, and assuming the existence of strong abiotic environmental filtering in these ecosystems (Smyth et al., 2014), then we predict a notable change in community structure between the shallow and deep strata.

H3) Since the vertical structure of salinity varies horizontally from the head to the mouth of the fjord, we expect that richness, diversity, and evenness will peak—and community structure will change—at different depths along the fjord sections. This pattern would be represented by a strong empirical evidence supporting an interactive effect of fjord section, depth, and salinity on univariate and multivariate community metrics.

To test these hypotheses, we analyzed the horizontal (along the fjord) and vertical (along increasing depth) variation of species abundances and salinity of the water column in Comau Fjord, NCP. In addition, we analyzed the spatial variation in water temperature as a potentially relevant environmental covariable in these ecosystems. This fjord harbors a unique subtidal ecosystem, inhabited by speciose communities of deep-water organisms, like corals, that thrive below 20 m depth (e.g., Häussermann and Försterra, 2009; Häussermann et al., 2013). However, rampant anthropogenic direct and indirect pressures, such as the multiple impacts derived from aquaculture activities, industrial and artisanal fisheries, and climate change, pose severe threats to this exceptional and complex ecological system (Försterra et al., 2017; Iriarte, 2018; Soto et al., 2019).

MATERIALS AND METHODS

Study Site

The study was conducted in the Comau fjord, located in NCP (ca. 42°S; **Figure 1**). The fjord is 34.3 km long, its widest part is at the mouth (ca. 10 km), and the narrowest (ca. 2 km) is near the head. The geomorphology of the fjord creates an almost north-south axis (along ca. 72.47°W) of environmental variation, oriented toward 346° in relation to the geographical north (Häussermann and Försterra, 2009). The main freshwater inputs are located on the eastern side (Quintupeu and Cahuelmó fjords) and at the head (Vodudahue and Leptepu rivers) of the fjord. The Comau fjord has an over-deepened sill, which could lead to shorter bottom water residence times relative to southernmost fjords (Häussermann and Försterra, 2009). The mouth connects the fjord with the Ancud Gulf, across the Marilmó and Comau passes, and to the Hornopirén channel, across the Cholgo channel. The fjord depths are around 500 m along the entire fjord, to <50 m very close to the head, due to the estuary proximity (Häussermann and Försterra, 2009).

The Comau fjord follows an estuarine circulation with a marked vertical stratified structure of the column water mainly determined according to the salinity and temperature regimes. This accentuated structure fluctuates annually in position and intensity mainly influenced by the annual cycles of solar radiation, precipitation, and tides mixing (Försterra, 2009; Sobarzo Bustamante, 2009). The surface layer is very variable: thicker, colder, and lower salinity in winter; warmer, and relatively higher salinity in summer. The main water body below this superficial layer has a relatively constant salinity and temperature throughout the year. On average, the surface low-salinity layer varies between 2 and 20 psu and has temperatures that range between 7 and 20°C; the deep sea-influenced water layer has a salinity > 32.5 psu and a temperature of ca. 11°C. Both layers converge vertically at ca. 10 m (Häussermann and Försterra, 2009). However, anomalous atmospheric events, such as the transition to a positive phase of the Southern Annular Mode and the intensification of the positive phase of the El Niño Southern Oscillation, have been shown to account for the recent decay in freshwater inputs in northern Patagonia (Boisier et al., 2018; Aguayo et al., 2019) and the concomitant weakening of the haline stratification of NCP fjords (León-Muñoz et al., 2018).

Environmental Gradients

The physicochemical characteristics of the Comau Fjord were measured at 64 stations across the fjord during February 19–21, 2020. At each station and between 0 and 100 m depth, temperature (° C) and salinity (psu) were recorded at intervals of 0.5 m with a CTD AML Plus X oceanographic probe. Then, an Inverse Distance Weighting and Nearest Neighbor interpolation was made to extract values at 0, 1, 3, 6, 10, 15, and 21 m at each ecological sample sites. The vertical profiles were carried out. The Brunt-Väisälä frequency or "buoyancy frequency" was calculated from the temperature and salinity values. This parameter was used to determine the vertical stratification of the water column, according to Stewart (2008):

$$N^2 = -gE,$$

where N is the buoyant frequency, g is gravity and E is the stability of the water column, which was calculated according to the expression:

$$E = -\frac{1}{\rho}\frac{\delta\rho}{\delta z},$$

where ρ is the water density (1.025 kg m^{-3}) and z is the depth. Positive values of $\mathbf{N^2}$ represents water column stratification (i.e., a low-density layer located above a high-density layer). Therefore, when the values of $\mathbf{N^2}$ are high, the water column is highly stratified and vice versa. On the other hand, negative values of $\mathbf{N^2}$ represents water column mixing (Garcés-Vargas et al., 2013). Surface and vertical distributions of environmental

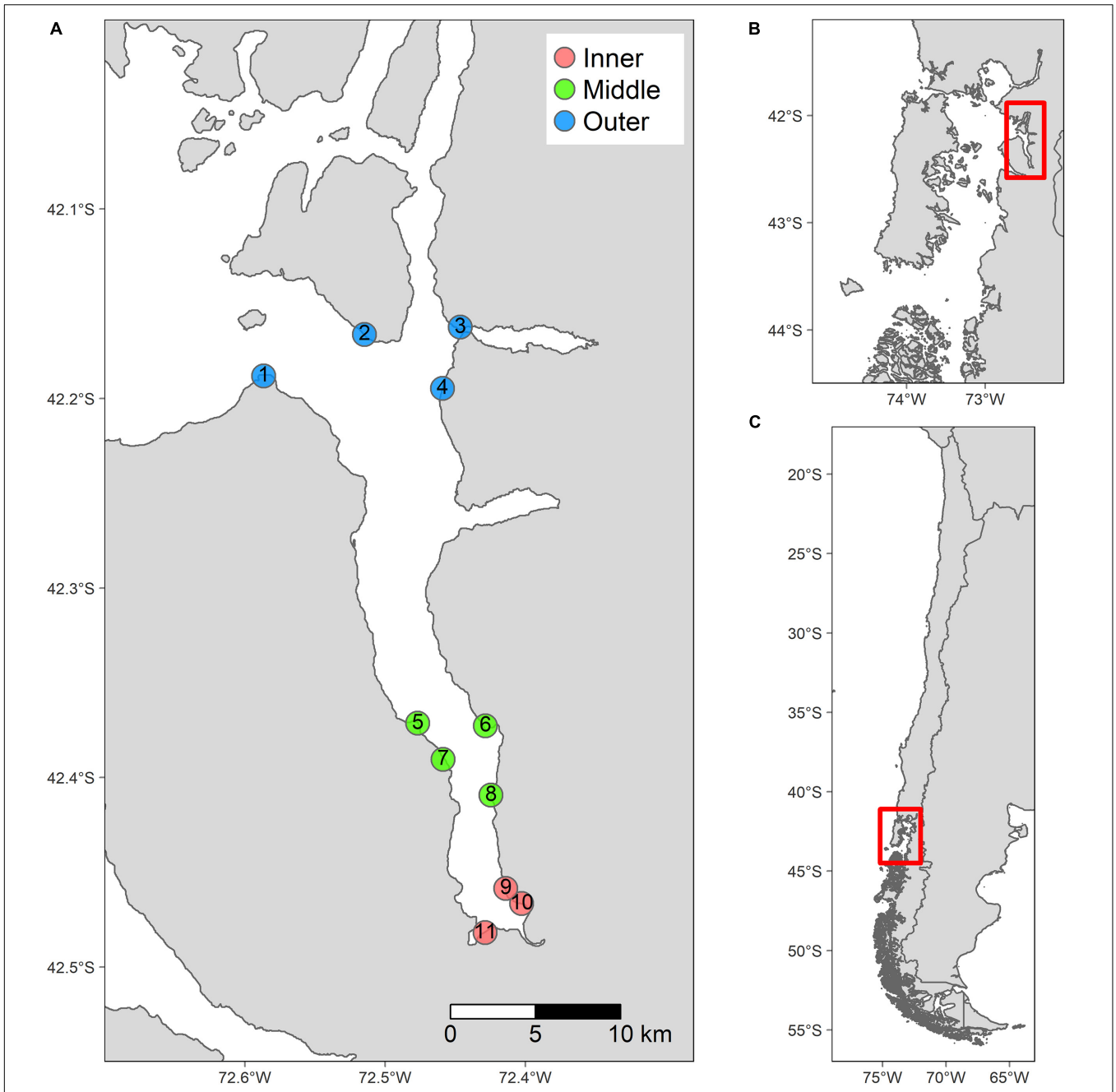

FIGURE 1 | Study site and experimental design. **(A)** Map of the Comau Fjord with the sampling sites (circles) nested within the head, middle and mouth sections of the fjord (colors). **(B)** Northern Patagonia with Comau fjord highlighted by a red square. **(C)** Section of the Southern Cone of South America with the Northern Patagonia highlighted by a red square.

variables were plotted using Ocean Data View 5.2.0 software (ODV; Schlitzer, 2020).

Ecological Sampling Design

To test our predictions, we used a nested sampling design composed of three 10-km^2 sections (head, middle, and mouth) located along the fjord and separated by ca. 10–30 km (**Figure 1**). In each section, four coastal sites, separated between 1 and 5 km, were randomly chosen, except for the head section where only three sites were located due to logistical limitations. At each site, a 26-m alongshore transect consisting of ten rectangular 0.28-m^2 (62 × 45 cm) observational units (OUs), was positioned at seven depth strata (0, 1, 3, 6, 10, 15, and 21 m). The experimental units were equidistantly distributed within each transect. This design yielded a total of 741 OUs. To survey exclusively within the subtidal range, the 0 m depth was set at

the lowest tide mark relative to the historical zero. All transects consisted of almost vertical hard rocky substrates with some small patches of soft sediments. The design was orthogonal, considering the effect of depth and sections (both crossed), and at the same time hierarchical, by considering the effect of sites (nested in sections) as explanatory variables. The study was conducted during two field campaigns in November–December 2017 and July 2018.

Species Abundance Estimations and Diversity Measures

The abundances of sessile and mobile macrobenthic species (>0.5 mm) were measured in each OU by means of underwater photographs (photo-quadrats) taken by the team of SCUBA divers of the Huinay Scientific Field Station. A frame with graduated strips of 62 × 45 cm was placed over each OU. This plot size was chosen to maximize the image quality associated with the camera's optimal size resolution. The area covered by the frame was photographed with a still Olympus E-m5 OMD camera, equipped with an Olympus M. Zuiko 9–18 mm F4-5.6 lens and a Nautikam NA-EM5 housing. The camera was mounted on a tripod with two Inon D2000x2 strobe lights.

To quantify the percentage cover of each macrobenthic species on each photo-quadrat, we focused on the primary-space holders (i.e., basal species). However, when superposition of organisms occurred, we included secondary-space holders (sessile species attached to the primary-space holders) and the associated mobile species. The images were processed with the Coral Point Count with Excel extensions (CPCe) v4.1 freeware (Kohler and Gill, 2006) at the Laboratory of Coastal Ecology of the Universidad Austral de Chile (UACh). For each image, the quadrant area was first delimited with a digital border, and then a squared grid of 100 equidistant points was established. Each readily visible element found at each point was identified either as species (invertebrates or algae) or characteristic of the benthos (e.g., substrate type). The number of points associated with each species was used as a measure of relative abundance of species (i.e., percentage cover). Points that intersected elements such as shadows or the frame were excluded from the calculations.

All organisms were identified at the finest possible taxonomic resolution with aid of specialized taxonomic guides (Häussermann and Försterra, 2009; WoRMS, 2020). The main criterion for determining species identity was to achieve at least one morphological feature characteristic of the species.

Species richness (S) was expressed as the total number of taxa in each OU. The Shannon diversity (H'; Shannon, 1948) was expressed as $-\sum_{i=1}^{S}(p_i \times \log_2 p_i)$, where p_i is the proportional abundance of species i and combines both species richness and relative abundances. The Pielou evenness (J'; Pielou, 1969) was expressed as $\frac{H'}{\log_e S}$, where $log_e S$ is the maximum diversity (H'_{max}). J' summarize the dominance structure of the community and ranges from 0 to 1 (Magurran, 1988). The Bray-Curtis coefficient (BC; Bray and Curtis, 1957) was expressed as $\frac{\sum_{i=1}^{S}|y_{ij}-y_{ik}|}{\sum_{i=1}^{S}(y_{ij}y_{ik})}$, where y_{ij} and y_{ik} are the abundances of species i for the observation units j and k, respectively. BC combines species occurrences and relative abundances and is used as a measure of dissimilarity (or distance) between pairs of OUs. BC ranges from 0 (same species and abundances in both objects, i.e., maximum similarity) to 1 (no species with abundance > 0 in common, i.e., maximum dissimilarity).

TABLE 1 | Description of the models constructed for the information-criteria-based model selection.

Model ID	Description	Notation
G_1	Section + Section : Depth + Site	$\beta_0\beta_1 X_1 f_{X_1}(X_2) Zb$
G_2	Section + Section : Salinity + Site	$\beta_0\beta_1 X_1 f_{X_1}(X_3) Zb$
G_3	Section + Section : Temperature + Site	$\beta_0\beta_1 X_1 f_{X_1}(X_4) Zb$
G_4	Section + Section : (Depth + Salinity) + Site	$\beta_0\beta_1 X_1 f_{X_1}(X_2) f_{X_1}(X_3) Zb$
G_5	Section + Section : (Salinity + Temperature) + Site	$\beta_0\beta_1 X_1 f_{X_1}(X_3) f_{X_1}(X_4) Zb$
G_6	Section + Section : (Depth * Salinity) + Site	$\beta_0\beta_1 X_1 f_{X_1}(X_3.X_4) Zb$
G_7	Section + Section : (Salinity * Temperature) + Site	$\beta_0\beta_1 X_1 f_{X_1}(X_3.X_4) Zb$
G_8	Intercept only	β_0

The mathematical notation is shown.

Statistical Analysis

Data were analyzed with generalized additive mixed-effect models (GAMM or also Hierarchical GAM; Wood, 2017; Pedersen et al., 2019). These models incorporate smooth functions of one or more covariates and can analyze non-linear relationships between covariates and the response variable including random effects. Each diversity measure (S, H', and J') was analyzed in individual models. The effect of temperature (°C), salinity (psu), depth (m), and fjord section were inferred in an information theoretic approach for model selection (Burnham and Anderson, 2002). The focus of these analysis was to assess the inter-dependent (i.e., interactive) effect of temperature, salinity, and depth combinations on each diversity measure across the fjord sections. Thus, we followed a parsimonious approach and constructed a family of GAMMs that included the main effect of fjord section, the interactive effect of temperature, salinity, and depth combinations across fjord sections, and the random effect of fjord sites for each diversity measure (**Table 1**).

To avoid problems of overfitting and increased residual variation derived from collinearity between continuous variables (Dormann et al., 2013), the Pearson correlation coefficient was calculated for depth, salinity, and temperature combinations (**Supplementary Figure 1**). Temperature-depth correlation was high (r = 0.84). Therefore, the models that included temperature and depth combinations were excluded from the analysis, since depth often corresponds with driving temperature gradients and can be used as their proxy in statistical models (McArthur et al., 2010).

Graphical inspections of the residuals suggested that the Poisson (log link) and Gaussian (identity link) structure of errors were appropriate for species richness (S) and for Shannon diversity (H') and Pielou evenness (J'), respectively.

The smooth functions for depth, temperature, and salinity were fitted using thin plate regression splines and the maximum number of basis functions was set to seven. Model parameters were estimated through maximum likelihood. Bias-corrected Akaike Information Criteria (AICc) was used to select the top model accounting for the data (Akaike, 1973). Model selection was based on Δ_i, expressed a $AICc_i – AICc_{min}$, Akaike weight, which represents the probability of each model as $w_i = Prob\{model\, g_i \mid data\} = \frac{l_i}{\sum_{j=1}^{R} l_j}$, where $l_i = L(g_i \mid data) = e^{-0.5_i}$, and the evidence ratio of the top model, calculated as w_{top} / w_j (Burnham et al., 2011).

Permutational multivariate analysis of variance was used to analyze community structure (PERMANOVA; Anderson, 2001; Anderson and Braak, 2003). We used the best model selected in univariate analysis. Therefore, the model included the effect of depth ranges, salinity, fjord section, their interactions, and fjord sites (as a permutation constrain) on the variations in community structure (see section "Model Selection" below). The Bray-Curtis coefficient was used as a measure of dissimilarity with 999 random permutations. The patterns of variation in community structure were examined using a non-metric multidimensional scaling chart (NMDS) based on Bray-Curtis dissimilarities. In addition, the percentage contribution of each taxon to the between-group variation in community structure was calculated with a (di)similarity percentage analysis (SIMPER) based on Bray-Curtis dissimilarities. For all multivariate analyses, the depths were grouped into four depth ranges (0–1 3–6, 10–15, and 21 m).

All statistical analyses and plots were performed in the R software, version 4.0.3 (R Core Team, 2021). The "raster" package was used for the Inverse Distance Weighting and Nearest Neighbor interpolation (Hijmans, 2020); "vegan" for the calculation of S and H', MDS, PERMANOVA, and SIMPER analyses (Oksanen et al., 2019); "car" for the correlation scatterplot (Fox and Weisberg, 2018); "mgcViz" for the GAMM visualization (Fasiolo et al., 2018); and "mgcv" for the GAMMs (Wood, 2011).

RESULTS

Summer Environmental Conditions of Comau Fjord

Surface salinity varied from 5 psu at the head to 25 psu at the mouth of the fjord (**Figure 2A**). The vertical distribution of salinity showed a superficial freshwater-influenced layer (ca. 20 psu; < 5 m) placed above a homogeneous ca. 32-psu layer along the fjord (**Figure 2B**). At the head, lowest salinity values were registered (ca. 5–17 psu) in the first 3 m, followed by a strong halocline at 4–5 m (ca. 19–30 psu), which gradually shallowed along the middle section until almost disappearing at the mouth (**Figure 2B**). The surface temperature varied from 13°C at the head to ca. 16 at the mouth of the fjord (**Figure 2C**). The vertical distribution of temperature showed a warmer layer (ca. 14–17°C; < ca. 15 m) placed above a colder layer along the central part of the fjord (ca. 11–13°C; **Figure 2D**). However, the head section registered a superficial cold-water influence from the riverine input (ca. 13°C; < 3 m) and the head section showed a homothermic- ocean-influenced layer (14–13°C) along the column water (**Figure 2D**).

The Brunt-Väisälä frequency distribution exhibited a highly stratified water column (75–125 cycl/h) at the first ca. 3 m along the fjord (**Figure 2E**). However, a considerable but minor difference in the vertical water density was still observed at 5 and 10 m (50 and 25 cycl/h, respectively) along the head and middle sections (**Figure 2E**).

Cumulative Diversity Along the Comau Fjord

A total of 130 taxa were identified in the Comau fjord (among which 49.2% identified at species, 31.5% at genus, 0.1% at family, and 18.4% at class level). One-hundred and fourteen taxa of sessile and mobile macroinvertebrates and 18 taxa of macroalgae were identified (**Supplementary Table 1**). The cumulative richness was higher at the middle and the mouth of the fjord than in the head section (**Figure 3A**), which partially support our prediction about the horizontal gradient. In the case of depth strata, the higher values of species richness were registered at 10 and 15 m and the minima at 0 and 1 m (**Figure 3B**).

The sites that showed the lowest species richness and diversity (i.e., sites 9 and 11 at 21 m at the head section; **Supplementary Figure 2**) were visually related to a substrate with "poor" quality sediment conditions, such as high homogeneity and grayish or blackish sediments (**Supplementary Figure 3**). Both sites also coincided with the location of a salmon (cage raft type) and mussel (longline type) farm, respectively. On the other hand, the third and last site of the head section, which did not show that a dramatic decrease in richness and diversity (**Supplementary Figure 2**), was related to a more hard, vertical, and clean substrate.

Model Selection

For species richness (S'), Shannon diversity (H'), and Pielou evenness (J'), the model with the lowest AICc was that included the separate and interactive effects of depth and salinity for each fjord section, and the random effect of sites nested in fjord sections (g_6 in **Table 1** and **Supplementary Table 2**). The probability of g_6 of being the best model given the data (Akaike weight, w_6) was ca. 0.9999 for the three diversity measures. Thus, the empirical support for model g_6 was more than one million times that of the closest competing model at each set of models (S': evidence ratio, ER_4 = 1422582; H': $ER_5 = 1.5 * 10^8$; and J': $ER_7 = 2.0 * 10^8$). Importantly, g_6 was $1.3 * 10^{130}$, $6.6 * 10^{64}$, and $3.2 * 10^{39}$ for S, H', and J', respectively, more likely than the null model (g_8 in **Tables 2–4**, respectively); this provides a very strong empirical support to the effect of the depth, salinity, and fjord section on S', H', and J'. Model g_6 accounted for a 46, 38, and 26% of the variation in S', H', and J', respectively (r^2_8 in **Tables 2–4**, respectively).

Species richness (S) increased with increasing depth and peaked at 5–10 m (27–30 psu) in the head section and at 15–21 m (27–30 psu) in the middle and mouth

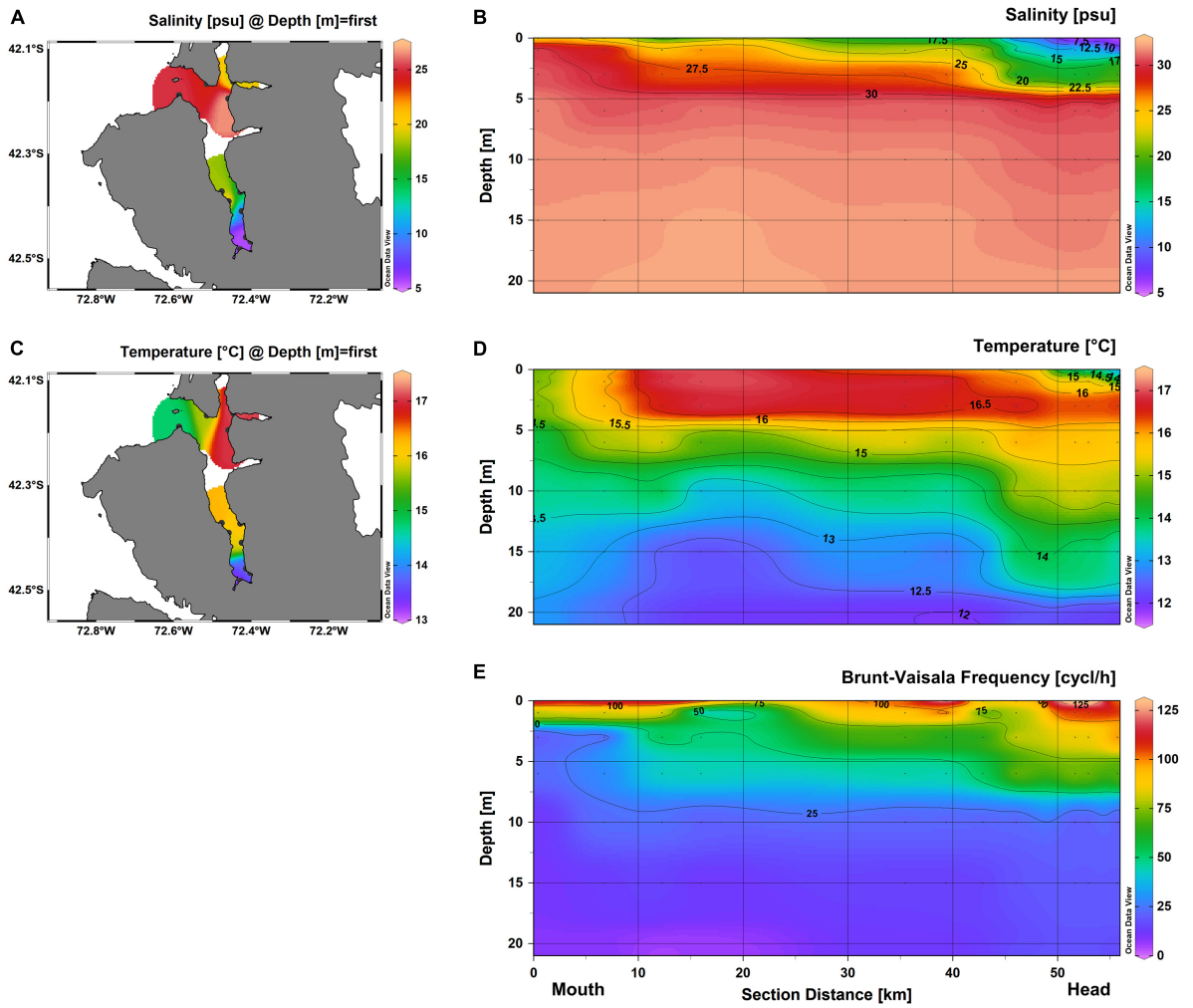

FIGURE 2 | Environmental variables distribution along Comau Fjord. CTD castings data showing **(A)** superficial and **(B)** longitudinal profile of temperature, **(C)** superficial and **(D)** longitudinal profile of salinity, and **(E)** longitudinal profile of Brunt-Väisälä frequency. All the physicochemical characteristics were measured during February 2020.

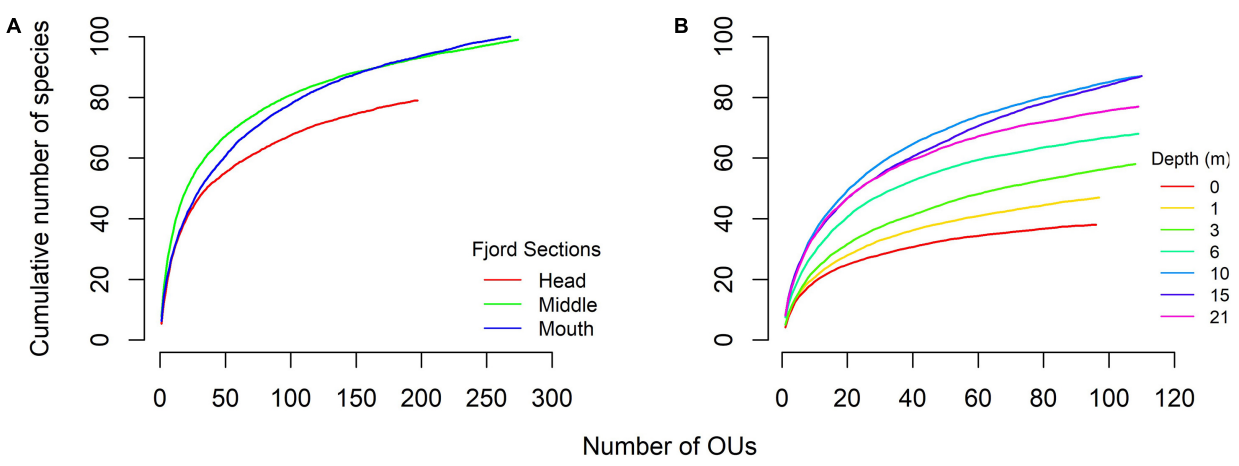

FIGURE 3 | Species-accumulation curves (SACs) of macrobenthic communities of Comau fjord. Separates SACs were performed for each **(A)** fjord sections and **(B)** depth strata. Cumulative number of species is shown as mean from each random combination of OUs (0.28 m^2).

TABLE 2 | Summary of information-criteria-based model selection for the species richness (S).

Mod	Se	Se:De	Se:Sa	Se:Te	De:Sa	Sa:Te	r^2	edf	AICc	Δ	*w*	*ER*
G_6	+	+	+		+		0.46	40	3.558	0	0.9999	1
G_4	+	+	+				0.42	26	3,586	28	$7 * 10^{-7}$	1,422,582
G_7	+	+	+			+	0.42	32	3,593	35	$2.4 * 10^{-8}$	41,222,176
G_1	+	+					0.42	23	3,593	35	$2 * 10^{-8}$	50,100,817
G_5	+		+	+			0.40	23	3,605	47	$6.2 * 10^{-11}$	$1.6 * 10^{10}$
G_3	+			+			0.34	21	3,687	129	$1 * 10^{-28}$	$1 * 10^{28}$
G_2	+		+				0.34	16	3,687	130	$6.7 * 10^{-29}$	$1.5 * 10^{28}$
G_8							0	0	4,157	599	$7.6 * 10^{-131}$	$1.3 * 10^{130}$

Mod, models included in the selection process; Se, fjord section; De, depth; Sa, Salinity; and Te, Temperature. The ":" symbol represents a statistical interaction between factors. r^2, r-squared adjusted; edf, estimated degrees of freedom; AICc, bias-corrected Akaike Information Criteria; Δ, the difference between AICc's calculated; w, Akaike weights; ER, evidence ratio of the top model. For the calculations see "Materials and Methods" section.

TABLE 3 | Summary of information-criteria-based model selection for the Shannon diversity (H').

Mod	Se	Se:De	Se:Sa	Se:Te	De:Sa	Sa:Te	r^2	edf	AICc	Δ	*w*	*ER*
G_6	+	+	+		+		0.38	36	954	0	0.9999	1
G_5	+		+	+			0.32	25	992	38	$6.7 * 10^{-9}$	$1.5 * 10^{8}$
G_7	+	+	+			+	0.33	34	1,000	45	$1.4 * 10^{-12}$	$7.3 * 10^{9}$
G_4	+	+	+				0.31	24	1,007	53	$3.3 * 10^{-12}$	$3 * 10^{11}$
G_1	+	+					0.30	24	1,016	62	$4.0 * 10^{-14}$	$2.5 * 10^{13}$
G_3	+			+			0.25	19	1,064	109	$1.8 * 10^{-24}$	$5.4 * 10^{23}$
G_2	+		+				0.24	14	1,066	112	$5.1 * 10^{-25}$	$1.9 * 10^{24}$
G_8							0	1	1,253	299	$1.5 * 10^{-65}$	$6.6 * 10^{64}$

*Parameter codes as in **Table 2**.*

TABLE 4 | Summary of information-criteria-based model selection for the Pielou evenness (J').

Mod	Se	Se:De	Se:Sa	Se:Te	De:Sa	Sa:Te	r^2	edf	AICc	Δ	*w*	*ER*
G_6	+	+	+		+		0.26	35	–389	0	0.9999	1
G_7	+	+	+			+	0.21	29	–350	39	$2.7 * 10^{-9}$	$2.0 * 10^{8}$
G_5	+		+	+			0.19	24	–330	59	$1.3 * 10^{-13}$	$2.0 * 10^{12}$
G_4	+	+	+				0.18	24	–328	61	$6 * 10^{-14}$	$4.5 * 10^{13}$
G_1	+	+					0.16	19	–312	77	$1.6 * 10^{-17}$	$1.7 * 10^{16}$
G_3	+			+			0.16	19	–312	77	$1.5 * 10^{-17}$	$1.8 * 10^{16}$
G_2	+		+				0.13	16	–295	94	$3.6 * 10^{-21}$	$7.3 * 10^{16}$
G_8							0	2	–209	180	$8.4 * 10^{-40}$	$3.2 * 10^{39}$

*Parameter codes as in **Table 2**.*

sections (**Figures 4A–C**). Yet, the environmental effects on S' were strongest in the head (compare effect magnitudes in **Figures 4A–C**). Diversity (H') and evenness (J') followed a similar pattern for the head and middle fjord sections (**Figures 4D,E,G,H**). On the other hand, at the mouth section, H' and J' presented an increase at the first three meters and highest salinities, and reduced values along higher depths (**Figures 4F,I**). These results support the hypothesis of interdependent effects of spatial and environmental factors on biodiversity (H3).

Patterns of Community Structure

The analysis of permutational multivariate variance (PERMANOVA) supported the hypothesis of significant interactive effects of depth, fjord sections, and salinity ($p < 0.001$) on community structure (H3; **Supplementary Table 3**). Non-metric multidimensional scaling ordination (NMDS) for the community structure showed that at the head section of the fjord a vertical pattern with a "shallow" group (0–1 m) differed from a "deeper" group (21 m), and an intermediate group (3–15 m) covering the almost complete gradient (**Figure 5A**). On the other hand, at the middle and mouth sections, a more homogeneous vertical pattern was observed between 3 and 21 m with only the 0–1 stratum differing from the rest of the depth ranges (**Figures 5B,C**). The same method of ordination showed that within the 0–1 stratum each fjord section presented a group of quadrats that differ between them and a shared group (**Figure 6**).

In general, the most dominant taxa in Comau Fjord were the crustose algae *Lithothamnion* sp. and the mussel *Aulacomya*

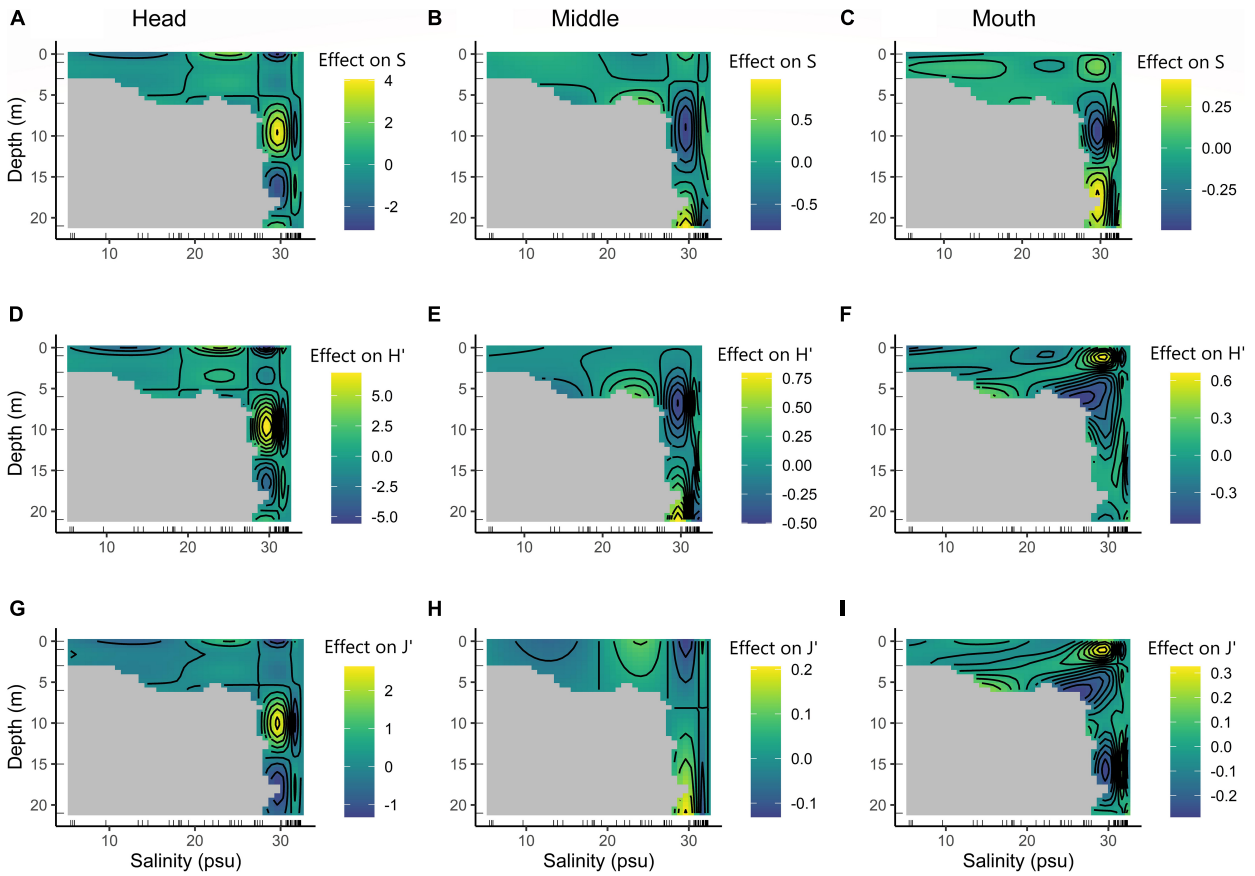

FIGURE 4 | Estimated smooth interactive effect of depth and salinity on diversity measures (species richness, Shannon diversity, and Pielou evenness's) as a function of the generalized additive mixed model (GAMM) output. **(A–C)** Estimated interactive effect of depth and salinity on species richness. **(D–F)** Estimated interactive effect of depth and salinity on Shannon diversity. **(G–I)** Estimated interactive effect of depth and salinity on Pielou evenness. The gray zones represent absent depth-by-salinity combinations.

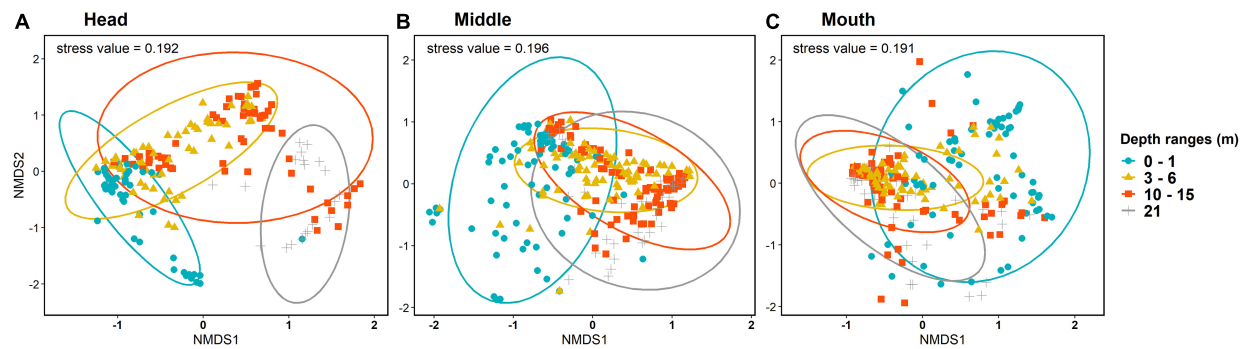

FIGURE 5 | Non-metric Multidimensional Scaling (NMDS) ordination plots of the observational units based on Bray-Curtis dissimilarities between depth ranges at **(A)** head, **(B)** middle, and **(C)** mouth sections of Comau fjord.

atra, contributing ca. 50% to the dissimilarity between sections and depths (**Table 5A**). The relative abundances of both species appeared to have inverse relationships with depth and fjord sections, where *A. atra* dominated the first 3 m with the highest abundances at the head section, while *Lithothamnion* sp. dominated below 6 m with the highest abundances at the mouth section (**Figure 7**). Subdominant taxa like the limpet *Crepipatella* sp., the brown macroalgae *Macrocystis pyrifera*, the filamentous macroalgae *Ectocarpus* sp. and *Acrosiphonia* sp., and the foliose macroalga *Ulva* sp. dominated at 0–1 m. The encrusting anemone *Epizoanthus fiordicus*, the soft coral *Clavulariidae* spp., and the polychaetes *Spiochaetopterus* sp. and

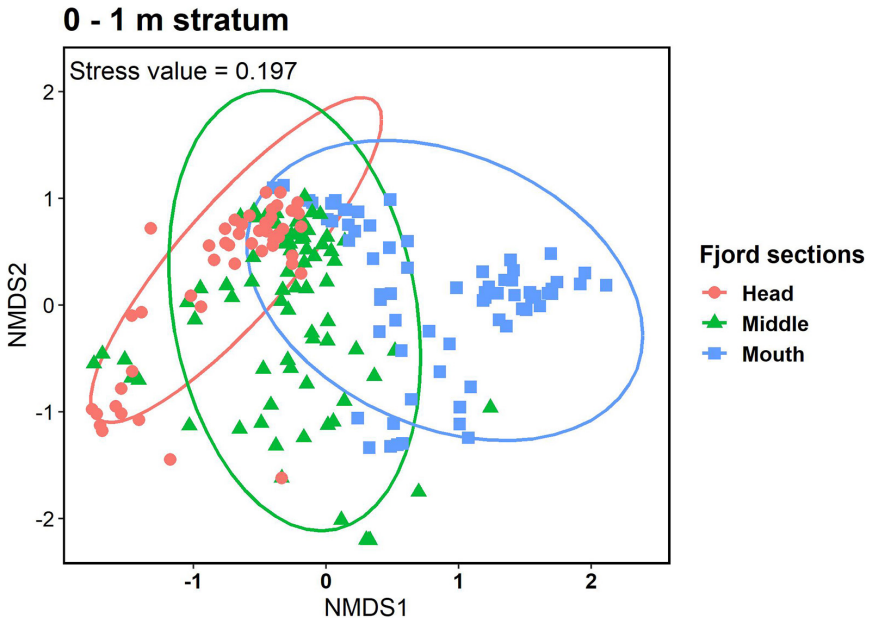

FIGURE 6 | Non-metric Multidimensional Scaling (NMDS) ordination plot of the observational units based on Bray-Curtis dissimilarities between fjord sections at 0–1 column water stratum of Comau fjord.

Chaetopterus variopedatus dominated below the 10–15 strata, following an intermediate zone (3–6 m) mostly dominated by *Lithothamnion* sp. (**Table 5B**). Within the head, *Lithothamnion* sp. was the main contributor to the dissimilarities between intermediate depths (3–15 m) but with significant decreases in abundance at 0–1 and 21 m depths (**Table 6**). However, *A. atra* and a group of green (*Ulva* sp. and *Acrosiphonia* sp.) and brown (*Ectocarpus* sp. *Ceramiales* sp.) macroalgae dominated above the 3 m stratum, while the anthzoans *Calvulariidae* sp. and *E. fiordicus* and the holoturid *P. disciformis* was characteristic for the benthic community below the 10–15 m stratum (**Table 6**). See **Supplementary Figure 4** for a graphical representation of the subdominant taxa along depth and sections of Comau fjord.

DISCUSSION

This study revealed that diversity and structure of the macrobenthic subtidal rocky bottom communities of the Comau Fjord are significantly associated with both horizontal and vertical abiotic environmental gradients, particularly salinity, emphasizing their interdependent relationship. A double-layer structure of the water column (0–21 m) was observed along the fjord: A colder freshwater-influenced layer located above a homogeneous salty layer produced a strong density stratified parcel of water at ca. 5 m in the head that shallowed toward the mouth. Our analyses showed a depth-dependent increase of species richness toward high salinities (>27 psu) along the fjord axis. This corroborates the positive relationship of salinity and the number of species along estuarine environments (Whitfield et al., 2012). Peaks of richness were observed at different depths for the head (5–10 m) and middle and mouth (15–21 m) sections. Diversity and evenness followed the trends of richness along depth and salinities at the head and middle sections, but both metrics peaked at shallow depths in the mouth. Community structure changed from macroalgae in shallow depths (0–1 m) to crustose algae in intermediate depths (3–6), to deep-dwelling suspension feeders below 10–15 m at the head and the middle sections. In contrast, the mouth section maintained a community dominated by mobile predators and crustose algae down to 15 m. At 21 m, the mouth was numerically dominated by dense patches of suspension feeders, mainly Anthozoa. These complex non-linear patterns of variation could be accounted for by the overlap of species with different environmental tolerances (i.e., freshwater and oceanic) and the decay of the low-salinity layer toward the mouth of the fjord. In a broader context, our results could be related to the first half of a unimodal pattern of an environmental stress gradient (e.g., Scrosati and Heaven, 2007; Zwerschke et al., 2013), where, in this case, low salinities (at shallow depths and close to the head) represent the upper stress boundary, and high salinities (at deep depths and close to the mouth) represent the middle to lower stress boundary.

Spatial Patterns of Species Richness and Diversity

The vertical patterns of the three diversity measures were dependent of the fjord sections, with maxima observed at different depths along the fjord sections. Generally, this suggests a non-linear, depth-dependent pattern that can be compared with the well-described pattern of decreasing diversity from the head to the mouth of estuarine ecosystems (e.g., Ysebaert et al., 2003; Meire et al., 2005; Beuchel et al., 2006). Our results contradict therefore previous work in other temperate

TABLE 5 | Summary of SIMPER results for sections and depth ranges of Comau fjord.

(A) Fjord sections	Abundance		Contribution (± SD)	Cumulative contribution
	Head	Middle		
Aulacomya atra	21.40	19.31	24.38 ± 18	24.38
Lithothamnion sp.	13.97	21.45	23.29 ± 18	47.67
Unid. coralline (morpho 1)	4.03	4.11	5.94 ± 7	53.61
Ectocarpus sp.	4.49	0.91	4.37 ± 7	57.98
Acrosiphonia sp.	2.97	2.17	4.17 ± 10	62.15
Macrocystis pyrifera	0.74	4.03	4.09 ± 11	66.23
Ulva sp.	3.55	1.48	3.89 ± 7	70.13
Crepipatella sp.	1.83	2.05	3.11 ± 5	73.24
Clavulariidae spp.	1.23	1.44	2.05 ± 3	75.29
Epizoanthus fiordicus	0.96	1.19	2.02 ± 4	77.31
Psolidium disciformis	0.97	0.54	1.42 ± 3	78.73
Ceramiales sp.	1.13	0.16	1.10 ± 4	79.83
Spiochaetopterus patagonicus	0.86	0.08	1.07 ± 3	80.90
	Head	**Mouth**		
Lithothamnion sp.	13.97	31.69	29.51 ± 20	29.51
Aulacomya atra	21.40	9.79	20.61 ± 18	50.12
Crepipatella sp.	1.83	10.07	9.03 ± 14	59.15
Unid. coralline (morpho 1)	4.03	3.62	5.28 ± 7	64.43
Ectocarpus sp.	4.49	0.48	3.95 ± 7	68.38
Ulva sp.	3.55	0.00	2.79 ± 6	71.17
Acrosiphonia sp.	2.97	.02	2.22 ± 8	73.39
Spiochaetopterus patagonicus	0.86	1.13	1.89 ± 4	75.28
Cosmasterias lurida	0.19	1.85	1.84 ± 3	77.12
Clavulariidae spp.	1.23	.70	1.48 ± 3	78.60
Macrocystis pyrifera	0.74	0.61	1.27 ± 5	79.87
Epizoanthus fiordicus	0.96	0.40	1.26 ± 3	81.13
	Middle	**Mouth**		
Lithothamnion sp.	21.45	31.69	27.71 ± 17	27.71
Aulacomya atra	19.31	9.79	20.42 ± 16	48.13
Crepipatella sp.	2.05	10.07	9.50 ± 13	57.63
Unid. coralline (morpho 1)	4.11	3.62	5.68 ± 7	63.31
Macrocystis pyrifera	4.03	0.61	4.06 ± 10	67.36
Cosmasterias lurida	0.64	1.85	2.15 ± 3	69.51
Acrosiphonia sp.	2.17	0.02	2.03 ± 6	71.54
Clavulariidae spp.	1.44	0.70	1.65 ± 2	73.19
Corynactis sp.	0.67	1.21	1.61 ± 3	74.80
Epizoanthus fiordicus	1.19	0.40	1.46 ± 2	76.26
Ectocarpus sp.	0.91	0.48	1.32 ± 3	77.59
Hydrolithon sp.	0.82	0.74	1.29 ± 2	78.87
Ulva sp.	1.48	0.00	1.28 ± 4	80.16
(B) Depth ranges	**0–1**	**3–6**		
Aulacomya atra	27.02	17.65	24.09 ± 16	24.09
Lithothamnion sp.	5.01	30.03	23.83 ± 16	47.91
Crepipatella sp.	9.85	4.14	10.02 ± 14	57.93
Macrocystis pyrifera	6.42	0.74	5.86 ± 13	63.79
Ectocarpus sp.	5.84	0.58	5.17 ± 8	68.97
Acrosiphonia sp.	5.50	0.54	4.77 ± 10	73.74
Ulva sp.	4.38	0.86	3.93 ± 8	77.67
Unid. coralline (morpho 1)	2.85	2.46	3.71 ± 5	81.37

(Continued)

TABLE 5 | Continued

(B) Depth ranges	Abundance		Contribution (± SD)	Cumulative contribution
	3–6	10–15		
Lithothamnion sp.	30.03	32.52	31.62 ± 17	31.62
Aulacomya atra	17.65	11.18	21.32 ± 15	52.94
Crepipatella sp.	4.14	3.37	6.18 ± 7	59.12
Unid. coralline (morpho 1)	2.46	4.58	5.72 ± 6	64.84
Clavulariidae spp.	0.57	2.62	2.78 ± 3	67.62
Cosmasterias lurida	1.63	0.52	2.11 ± 3	69.73
Corynactis sp.	1.28	0.79	1.93 ± 4	71.66
Epizoanthus fiordicus	0.00	1.61	1.70 ± 3	73.36
Hydrolithon sp.	0.43	1.33	1.59 ± 2	74.95
Spiochaetopterus patagonicus	0.07	1.20	1.45 ± 3	76.40
Anthothoe chilensis	1.27	.22	1.37 ± 3	77.77
Chaetopterus variopedatus	0.17	0.87	1.24 ± 4	79.01
Ulva sp.	0.86	0.23	1.11 ± 3	80.12
	10–15	**21**		
Lithothamnion sp.	32.52	22.61	34.48 ± 22	34.48
Aulacomya atra	11.18	5.90	14.55 ± 16	49.03
Unid. coralline (morpho 1)	4.58	7.32	8.83 ± 8	57.86
Crepipatella sp.	3.37	0.74	3.77 ± 6	61.63
Epizoanthus fiordicus	1.61	2.48	3.73 ± 5	65.36
Spiochaetopterus patagonicus	1.20	1.94	3.24 ± 5	68.59
Clavulariidae spp.	2.62	1.12	2.99 ± 4	71.58
Psolidium disciformis	1.01	1.17	2.19 ± 3	73.77
Chaetopterus variopedatus	0.87	1.00	2.02 ± 5	75.79
Hydrolithon sp.	1.33	.73	1.86 ± 9	77.65
Unid. sponge (morpho 5)	0.56	1.00	1.29 ± 2	78.94
Desmophyllum dianthus	0.06	1.45	1.26 ± 3	80.21

The average abundances (% cover) of relevant taxa in each section group, their contribution (% ± standard deviation) to the within-group dissimilitude, and cumulative total (%) of contributions (80% cut-off) are shown.

fjords: for instance, Kuklinski (2013) attributes the absence of horizontal trends in temperate fjord benthic communities to a scarcity of environmental gradients in this axis. In this sense, horizontal patterns of fjord epibenthic organisms can be strongly context- and taxonomic group-dependent (Brattegard, 1966; Rosenberg and Möller, 1979; Hansen and Ingólfsson, 1993). In a more general context, our results agree with a recent model of biogeography, the sub-habitat dependence hypothesis (Scrosati et al., 2020), which predicts that a geographical biodiversity pattern within a given region will differ between different sub-habitats (depths and fjord sections in our case). This model assumes that the main abiotic drivers of sessile species distributions varies across the sub-habitat types.

A low-salinity water layer was clearly associated with the zones of low benthic diversity, mainly at the upper ca. 10 m of the column water. In estuaries, a salinity between 24 and 30 psu has been considered as the physiological limit that distinguishes between marine and "brackish" species (Dahl, 1956; Bulger et al., 1993). An average salinity of ca. 10 psu has been suggested to present the minimum diversity of species (Attrill and Rundle, 2002) and the range between 30 and 40 psu the maximum diversity of species (mostly marine species; Whitfield et al., 2012). The tolerance of marine organisms to

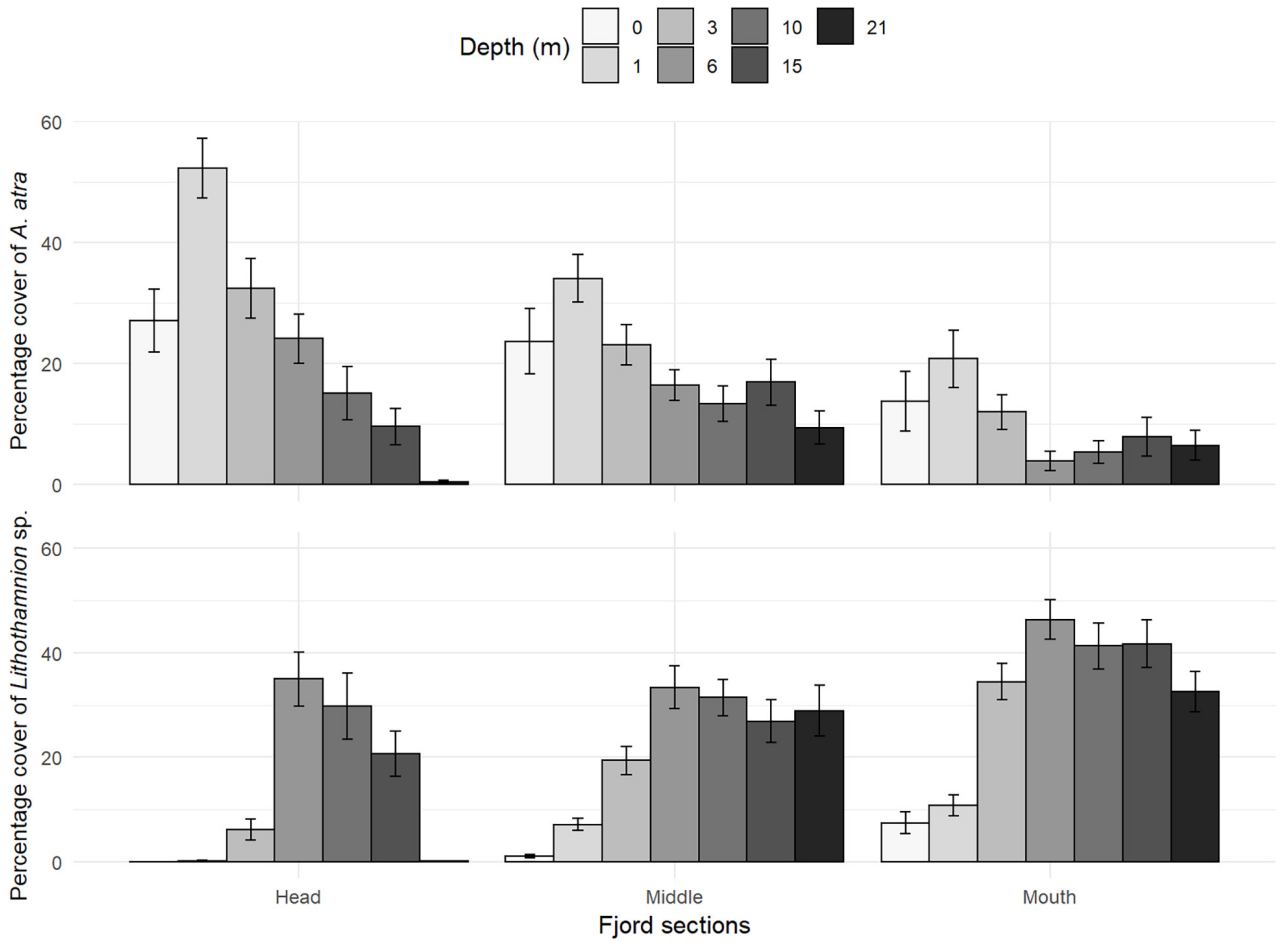

FIGURE 7 | Mean relative abundances (percentage cover) of the most abundant species on Comau fjord along fjord sections and depth: (upper panel) the edible mussel *Aulacomya atra* and (lower panel) the crustose algae *Lithothamnion* sp. Vertical lines represent the standard errors (± SE).

variations in salinity can be also temperature-dependent, due to the negative effect of the latter on osmoregulatory capacities (e.g., Navarro et al., 2019; Vargas-Chacoff et al., 2019). In our study, however, the empirical evidence supporting the effects of salinity on the diversity measures was much stronger than that of temperature and the interaction of both variables. Nevertheless, the role of temperature as part of the environmental filters and drivers of population dynamics could well be stronger at different moments of the year. For example, salinity tolerance may vary seasonally according to the annual temperature regime (Smyth and Elliott, 2016). Unfortunately, we were unable to analyze the temporal variation in environmental conditions. In addition, the high temperature-depth correlation indicates that part of the vertical patterns in the diversity proxies would well be accounted for by variations in temperature. Further long-term observational studies—coupled with well-designed manipulative experiments—are needed to fully disentangle the effects of salinity and temperature on these communities.

At the mouth of the fjord, the spatial patterns of species richness differed from those of Shannon diversity and Pielou evenness. This could be attributed to differential environmental effects on species incidences (related to abiotic environmental filtering) and species abundances (related to population dynamics). The outer sections of a NCP fjord are characterized by a relatively homogeneous water column with more oceanic, high-salinity environmental conditions (Castillo et al., 2016). Therefore, other factors, besides salinity, are likely driving the assembly and population dynamics at the fjord's mouth. In this section, for example, milder abiotic environmental conditions could be associated with a stronger influence of density-dependent biotic interactions, as predicted by early and recent environmental stress models tested elsewhere (Menge and Sutherland, 1987; Scrosati and Heaven, 2007).

Community Structure and Environmental Variability in Shallow Waters

At the head of the fjord, the edible mussel *Aulacomya atra* peaked in abundance at shallow waters (0–3 m depth; **Figure 7**). This peak coincided with the absence of carnivorous predators. On the other hand, the mouth was characterized by minimum abundances of *A. atra* and maximum abundances of predators

TABLE 6 | Summary of SIMPER results for depth ranges at the head of Comau fjord.

Depth ranges (m)	Abundances		Contribution (± SD)	Cumulative contribution
	0–1	3–6		
Aulacomya atra	36.83	28.16	26.95 ± 14	26.95
Lithothamnion sp.	0.07	20.81	16.97 ± 15	43.93
Ectocarpus sp.	15.64	1.89	12.98 ± 11	56.91
Acrosiphonia sp.	11.76	0.07	9.47 ± 15	66.38
Ulva sp.	10.51	257	9.32 ± 10	75.70
Unid. coralline (morpho 1)	1.43	4.31	4.07 ± 6	79.77
Ceramiales sp.	2.84	1.37	3.35 ± 6	83.12
	3–6	**10–15**		
Lithothamnion sp.	20.81	25.26	26.82 ± 18	26.82
Aulacomya atra	28.16	12.30	26.63 ± 17	53.45
Unid. coralline (morpho 1)	4.31	5.40	6.25 ± 6	59.70
Crepipatella sp.	3.00	3.04	4.45 ± 5	64.15
Clavulariidae spp.	0.03	3.84	3.26 ± 4	67.41
Ulva sp.	2.57	0.42	2.88 ± 5	70.30
Actinothoe sp.	2.84	0.16	2.66 ± 4	72.95
Chaetopterus variopedatus	0.03	1.74	2.23 ± 6	75.18
Psolidium disciformis	0.02	2.31	2.16 ± 3	77.35
Ectocarpus sp.	1.89	0.11	2.11 ± 3	79.46
Macrocystis pyrifera	2.05	0.12	2.10 ± 5	81.55
	10–15	**21**		
Lithothamnion sp.	25.26	0.18	28.65 ± 30	28.65
Aulacomya atra	12.30	0.40	15.44 ± 22	44.09
Unid. coralline (morpho 1)	5.40	5.02	9.03 ± 9	53.12
Spiochaetopterus patagonicus	1.54	2.32	5.37 ± 8	58.48
Epizoanthus fiordicus	1.86	2.68	4.76 ± 8	63.24
Chaetopterus variopedatus	1.74	0.14	4.65 ± 15	67.89
Clavulariidae spp.	3.84	0.37	4.45 ± 7	72.34
Psolidium disciformis	2.31	1.76	4.26 ± 6	76.60
Crepipatella sp.	3.04	0.00	3.32 ± 7	79.92
Megallania venosa	0.40	0.63	1.59 ± 4	81.51

See details in ***Table 5****.*

such as *Cosmasterias lurida*. Low-salinity waters in the head of the fjord may act as a refuge area for prey like mussels (Witman and Grange, 1998; Wing and Leichter, 2011; Sjøtun et al., 2015). For instance, Wing and Leichter (2011) show that, despite the negative consequences caused by reduced salinities on mussel growth (e.g., Navarro, 1988), these organisms can develop dense patches of individuals within the low-salinity layer at the head of a temperate fjord, where salinity is low enough to restrict the access to predators (e.g., *Cosmasterias* sp.). Furthermore, in a New Zealand temperate fjord, Witman and Grange (1998) determined that predation success in low-salinity stressful habitats strongly depends on the time before predation is interrupted by vertical fluctuations in the low-salinity layer caused by changes in freshwater discharges.

Similarly, the low or null abundance of foliose macroalgae found at shallow depths (0–1 m) at the mouth of the fjord could well be associated with a negative consumptive effect of the sea urchins *Loxechinus albus* and *Arbacia dufresnii* in this section. The almost total decrease of these herbivores toward the middle and head sections of the fjord coincided with a significant increase in the abundance of the large, perennial brown algae *Macrocystis pyrifera* together with the appearance of small, ephemeral algae (i.e., *Ectocarpus* sp., *Acrosiphonia* sp., and *Ulva* sp.). The latter increased significantly in abundance toward the head, co-dominating the substrate next to *A. atra*. The exclusion of grazers from the low-salinity fjord sections can allow the development of seaweed-dominated communities (e.g., Ayling, 1981; Husa et al., 2014). As with the invertebrate case, the low-salinity layer observed in this study could also be providing an important refuge for macroalgae in the first few meters of the water column.

At the middle and the mouth of the fjord, the red crustose algae *Lithothamnion* sp. dominated the community. Species in this genus are very well adapted to low light and temperature regimes (Johansen, 2018), which could result in competitive advantage over other algae and in the ability to thrive at greater depths. The penetration of light into the water column in NCP is strongly limited by the presence of particulate material of terrestrial origin in the head zone (Huovinen et al., 2016), which will define the lower limit of distribution of foliose algae in sites where discharges are high (e.g., Barrett and Edgar, 2010). Indeed, the variation of substrate inclination, which influences the degree of sedimentation and light regimes, has been suggested to influence the co-occurrence patterns of macroalgae elsewhere (e.g., South Patagonia, Cárdenas and Montiel, 2015). In addition, salinity can determine the proportion of red and brown algae in the first few meters of the estuaries (e.g., Munda, 1978; Schubert et al., 2011). Red algae appear to be more sensitive to variations in salinity than brown algae (Cole and Sheath, 1990) and it is suggested that salinity of 20 psu or less is the critical lower limit of tolerance for several red algae (Johansen, 2018). This could explain the reduced abundance of *Lithothamnion* sp. in the first meters of the head and the subsequent increase (up to 90%) of its abundance toward greater depths (see **Figure 7**).

Habitat-Forming Species and the Marine Animal Forests

The macrobenthic communities observed below 6 m stood out with a high level of clustering, or "patchiness", composed of groups of multiple invertebrate species associated with an increase in local diversity. Generally, these patches were found to be surrounded by low diversity areas dominated by the crustose algae *Lithothamnion* sp. These observations coincide with the shallow rocky bottom communities described by Grange et al. (1981) in the New Zealand temperate fjords, Betti et al. (2017) in a fjord in Southern Patagonia, and Cárdenas and Montiel (2015) in the Strait of Magellan, Chile. Sessile suspension feeders like bivalves, sponges, and corals play a role as ecosystem engineers (sensu Jones et al., 1994) and can maintain complex three-dimensional structures that provide habitats and refuges for other species—these associations have been named as "Marine Animal Forests", because of their structural and functional similarity to terrestrial forests (Rossi et al., 2017). These communities occur widely around the world, from the tropics (e.g., Soares et al.,

2017) to the poles (e.g., Arntz and Gallardo, 1994; Cárdenas and Montiel, 2017) and are characteristic of the rocky walls of the Comau Fjord (Försterra et al., 2017).

This study highlights the occurrence of several habitat-forming species such as mussels (e.g., *A. atra*), brachiopods (e.g., *Magellania venosa*), polychaetes (e.g., *Chaetopterus variopedatus*), sponges (e.g., *Scopalina* sp.), and cold-water coral forests (e.g., *Desmophylum dianthus;* Försterra et al., 2017). An increase in structural complexity induced by these habitat-forming organisms may be contributing to the maintenance of the observed diversity thresholds. This idea is supported by Smith and Witman (1999) who observed elsewhere that highly diverse benthic patches are maintained by increased habitat biogenic complexity that enhances larval recruitment. Försterra (2009) describes the extraordinary occurrence of "deep-sea species" in the shallow depths of the fjords of Patagonia (e.g., Comau Fjord), a phenomenon that has also been reported in similar fjords in New Zealand (e.g., Grange et al., 1981) and Australia (Barrett and Edgar, 2010). Overall, the facilitative effects of habitat-forming species could be contributing to the maintenance of the diversity found 10–15 m depth in the Comau Fjord (Reise, 2002; Gili et al., 2006).

Natural and Anthropogenic Sedimentation and Their Impacts on Suspension Feeders' Communities

The richness and abundance of species below 15 meters decreased notably at the head of the Comau fjord, which coincided with a high quantity of low-quality sediments accumulated on the bottom (**Supplementary Figure 3**). Here, two of the three sites were located adjacent to the outlet of a tributary rivers. The two sites with the highest levels of accumulated sediments also showed the lowest diversity and abundance of benthic species (**Supplementary Figure 2**). In pristine non-glacial fjords, freshwater discharges in the form of rivers and inland runoff are usually the most important factors in affecting total sedimentation rates and the proportions of organic (<10%) and inorganic (>90%) particles in the sediments (Pearson, 1980; Syvitski et al., 2012). Epibenthic sessile suspension filter communities are highly susceptible to sediment discharges (Evans et al., 1980; Farrow et al., 1983), because of the obstruction of the filtering organs (e.g., Bell et al., 2015) and enhanced substrate instability (Gili et al., 2006). This could explain the decrease in richness and abundance of species found at the head, in addition to the large variation in the diversity proxies accounted for by the differences among sites. A similar pattern has been described for glacial fjords, where the sedimentation from glacial discharges usually leads to a dominance by buried worms and mollusks (e.g., Wlodarska-Kowalczuk et al., 2005; Voronkov et al., 2013; Valdivia et al., 2020).

An alternative and non-exclusive explanation to the punctual low diversity found below 15 m in the head section would stem from negative effects of salmon and mussel farms operating in the fjord. Our observation of low-quality sediments in the nearby of marine farms (see **Supplementary Figure 3**) suggests the occurrence of a degraded habitat due to an excess accumulation of organic matter and a possible eutrophication event. Benthic communities react according to the deficiencies in oxygen concentration caused by organic enrichment (Hargrave, 2010). In the fjords of Northern Patagonia (e.g., Comau fjord), the input of organic material of terrestrial origin through the multiple freshwater discharges (Villagrán, 1988; Bustamante, 2009) and the efficient export of algal biomass to sediments in productive times (e.g., González et al., 2010) enhance organic matter flows to the benthic system in the head, increasing the possibility of a eutrophication event. Generally speaking, the frequency of hypoxic conditions in estuarine environments has increased significantly, strongly accelerated by human activity (Diaz and Rosenberg, 1995; Breitburg et al., 2018) and negatively affecting the benthic fauna of fjords (Soto and Norambuena, 2004; Hargrave, 2010). The rapid expansion of the aquaculture industry in Chilean Patagonia represents an environmental risk with important associated regional impacts. For example, the overload of ecosystem-level carrying capacity is currently degrading the endemic fjord communities in Chilean Patagonia (Buschmann et al., 2006; Niklitschek et al., 2013; Soto et al., 2019).

CONCLUSION

The diversity and structure of the benthic community in the Comau Fjord were significantly associated with both horizontal and vertical abiotic environmental gradients, determined by the influence of freshwater discharges. Species richness, diversity, and evenness peaked under high-salinity conditions, whose positions in depth varied across the horizonal axis of the fjord. Community structure was associated with a superficial water layer of low salinity. Dense patches of suspension feeders, or marine animal forests, may be contributing to the maintenance of diversity through facilitative interactions. Understanding the long-term impact of climate change-induced changes in salinity on the diversity and structure of fjord communities is necessary to generate sustainable management strategies for these ecosystems. Finally, an empirical and permanent assessment of the ecological impacts of anthropogenic sources of sedimentation is necessary to protect current communities and prevent future losses in ecosystem functioning.

DATA AVAILABILITY STATEMENT

The raw data supporting the conclusions of this article will be made available by the authors, without undue reservation.

AUTHOR CONTRIBUTIONS

VH and GF conceived and designed the study. JW provided the samples. SB and JE collected the samples. VV, KB-A, and SB processed the samples. VV and NV analyzed, interpreted data, and wrote the first draft. All authors reviewed and approved the text.

FUNDING

The study was financially supported by the FONDECYT #1190529 (NV), FONDECYT #1161699 (VH), and CONICYT/ANID #20150106 (VH and JW). NV was financially supported by FONDAP grant #15150003 (IDEAL). This work is part of VV Honors thesis, submitted to the Universidad Austral de Chile.

ACKNOWLEDGMENTS

We thank all the members of the Huinay Field and Research team and PISCES project team who realized the sampling and fieldwork, and to all the members of the Coastal Ecology Lab (Lafkenchelab, UACH) who provided considerable help during the processing and analyzing period. José Garcés-Vargas was fundamental to complete the environmental analysis and visualization. Constructive criticism by Luis Miguel Pardo and Humberto González greatly improved the early research. This is publication #187 of Huinay Scientific Field Station.

SUPPLEMENTARY MATERIAL

The Supplementary Material for this article can be found online at: https://www.frontiersin.org/articles/10.3389/fmars.2021.635855/full#supplementary-material

REFERENCES

Aguayo, R., León-Muñoz, J., Vargas-Baecheler, J., Montecinos, A., Garreaud, R., Urbina, M., et al. (2019). The glass half-empty: climate change drives lower freshwater input in the coastal system of the Chilean Northern Patagonia. *Clim. Change* 155, 417–435. doi: 10.1007/s10584-019-02495-6

Akaike, H. (1973). A new look at the statistical model identification. *IEEE Trans. Automat. Contr.* 19, 716–723. doi: 10.1109/TAC.1974.1100705

Anderson, M., and Braak, C. T. (2003). Permutation tests for multi-factorial analysis of variance. *J. Stat. Comput. Simul.* 73, 85–113. doi: 10.1080/00949650215733

Anderson, M. J. (2001). Permutation tests for univariate or multivariate analysis of variance and regression. *Can. J. Fish. Aquat. Sci.* 58, 626–639. doi: 10.1139/f01-004

Arntz, W. E., and Gallardo, V. A. (1994). "Antarctic benthos: present position and future prospects," in *Antarctic Science: Global Concerns*, ed. G. Hempel (Berlin: Springer), 243–277. doi: 10.1007/978-3-642-78711-9_16

Attrill, M. J., and Rundle, S. D. (2002). Ecotone or ecocline: ecological boundaries in estuaries. *Estuar. Coast. Shelf Sci.* 55, 929–936. doi: 10.1006/ecss.2002.1036

Ayling, A. M. (1981). The role of biological disturbance in temperate subtidal encrusting communities. *Ecology* 62, 830–847. doi: 10.2307/1937749

Barrett, N. S., and Edgar, G. J. (2010). Distribution of benthic communities in the fjord-like Bathurst Channel ecosystem, south-western Tasmania, a globally anomalous estuarine protected area. *Aquat. Conserv.* 20, 397–406. doi: 10.1002/aqc.1085

Basset, A., Barbone, E., Elliott, M., Li, B.-L., Jorgensen, S. E., Lucena-Moya, P., et al. (2013). A unifying approach to understanding transitional waters: fundamental properties emerging from ecotone ecosystems. *Estuar. Coast. Shelf Sci.* 132, 5–16. doi: 10.1016/j.ecss.2012.04.012

Bell, J. J., McGrath, E., Biggerstaff, A., Bates, T., Bennett, H., Marlow, J., et al. (2015). Sediment impacts on marine sponges. *Mar. Pollut. Bull.* 94, 5–13. doi: 10.1016/j.marpolbul.2015.03.030

Betti, F., Bavestrello, G., Bo, M., Enrichetti, F., Loi, A., Wanderlingh, A., et al. (2017). Benthic biodiversity and ecological gradients in the Seno Magdalena (Puyuhuapi Fjord, Chile). *Estuar. Coast. Shelf Sci.* 198, 269–278. doi: 10.1016/j.ecss.2017.09.018

Beuchel, F., Gulliksen, B., and Carroll, M. L. (2006). Long-term patterns of rocky bottom macrobenthic community structure in an Arctic fjord (Kongsfjorden, Svalbard) in relation to climate variability (1980–2003). *J. Mar. Syst.* 63, 35–48. doi: 10.1016/j.jmarsys.2006.05.002

Boisier, J. P., Alvarez-Garreton, C., Cordero, R. R., Damiani, A., Gallardo, L., Garreaud, R. D., et al. (2018). Anthropogenic drying in central-southern Chile evidenced by long-term observations and climate model simulations. *Elementa Sci. Anthrop.* 6:74. doi: 10.1525/elementa.328

Brattegard, T. (1966). The natural history of the Hardangerfjord 7. Horizontal distribution of the fauna of rocky shores. *Sarsia* 22, 1–54. doi: 10.1080/00364827.1966.10409561

Brattegard, T. (1980). "Why biologists are interested in fjords," in *Fjord Oceanography*, eds H. J. Freeland, D. M. Farmer, and C. D. Levings (Boston, MA: Springer US), 53–66. doi: 10.1007/978-1-4613-3105-6_2

Bray, J. R., and Curtis, J. T. (1957). An ordination of the upland forest communities of Southern Wisconsin. *Ecol. Monogr.* 27, 326–349. doi: 10.2307/1942268

Breitburg, D., Levin, L. A., Oschlies, A., Grégoire, M., Chavez, F. P., Conley, D. J., et al. (2018). Declining oxygen in the global ocean and coastal waters. *Science* 359:eaam7240. doi: 10.1126/science.aam7240

Bulger, A. J., Hayden, B. P., Monaco, M. E., Nelson, D. M., and McCormick-Ray, M. G. (1993). Biologically-based estuarine salinity zones derived from a multivariate analysis. *Estuaries* 16, 311–322. doi: 10.2307/1352504

Burnham, K. P., and Anderson, D. R. (2002). "Information and likelihood theory: a basis for model selection and inference," in *Model Selection and Multimodel Inference: A Practical Information-Theoretic Approach*, eds K. P. Burnham and D. R. Anderson (New York, NY: Springer), 49–97. doi: 10.1007/978-0-387-22456-5_2

Burnham, K. P., Anderson, D. R., and Huyvaert, K. P. (2011). AIC model selection and multimodel inference in behavioral ecology: some background, observations, and comparisons. *Behav. Ecol. Sociobiol.* 65, 23–35. doi: 10.1007/s00265-010-1029-6

Buschmann, A. H., Riquelme, V. A., Hernández-González, M. C., Varela, D., Jiménez, J. E., Henríquez, L. A., et al. (2006). A review of the impacts of salmonid farming on marine coastal ecosystems in the southeast Pacific. *ICES J. Mar. Sci.* 63, 1338–1345. doi: 10.1016/j.icesjms.2006.04.021

Bustamante, M. S. (2009). "The southern Chilean fjord region: oceanographic aspects," in *Marine Benthic Fauna of Chilean Patagonia*, eds V. Häussermann and G. Försterra (Santiago: Nature In focus), 53–60.

Cárdenas, C. A., and Montiel, A. (2015). The influence of depth and substrate inclination on sessile assemblages in subantarctic rocky reefs (Magellan region). *Polar Biol* 38, 1631–1644. doi: 10.1007/s00300-015-1729-5

Cárdenas, C. A., and Montiel, A. (2017). "Coexistence in cold waters: animal forests in seaweed-dominated habitats in southern high-latitudes," in *Marine Animal Forests: The Ecology of Benthic Biodiversity Hotspots*, eds S. Rossi, L. Bramanti, A. Gori, and C. Orejas (Cham: Springer International Publishing), 257–276. doi: 10.1007/978-3-319-21012-4_50

Cardinale, B. J., Duffy, J. E., Gonzalez, A., Hooper, D. U., Perrings, C., Venail, P., et al. (2012). Biodiversity loss and its impact on humanity. *Nature* 486, 59–67. doi: 10.1038/nature11148

Castillo, M. I., Cifuentes, U., Pizarro, O., Djurfeldt, L., and Caceres, M. (2016). Seasonal hydrography and surface outflow in a fjord with a deep sill: the Reloncaví fjord, Chile. *Ocean Sci.* 12, 533–544. doi: 10.5194/os-12-533-2016

Cole, K. M., and Sheath, R. G. (1990). *Biology of the Red Algae*. Cambridge: Cambridge University Press.

Dahl, E. (1956). Ecological salinity boundaries in Poikilohaline waters. *Oikos* 7, 1–21. doi: 10.2307/3564981

Dávila, P. M., Figueroa, D., and Müller, E. (2002). Freshwater input into the coastal ocean and its relation with the salinity distribution off austral Chile (35–55°S). *Cont. Shelf Res.* 22, 521–534. doi: 10.1016/S0278-4343(01)00072-3

Dayton, P. K. (1971). Competition, disturbance, and community organization: the provision and subsequent utilization of space in a rocky intertidal community. *Ecol. Monogr.* 41, 351–389. doi: 10.2307/1948498

Diaz, R., and Rosenberg, R. (1995). Marine benthic hypoxia: a review of its ecological effects and the behavioural response of benthic macrofauna. *Oceanogr. Mar. Biol. Annu. Rev.* 33, 245–303.

Dormann, C. F., Elith, J., Bacher, S., Buchmann, C., Carl, G., Carré, G., et al. (2013). Collinearity: a review of methods to deal with it and a simulation study evaluating their performance. *Ecography* 36, 27–46. doi: 10.1111/j.1600-0587.2012.07348.x

Elliott, M., and Quintino, V. (2019). "The estuarine quality paradox concept?," in *Encyclopedia of Ecology (Second Edition)*, ed. B. Fath (Oxford: Elsevier), 78–85. doi: 10.1016/B978-0-12-409548-9.11054-1

Evans, R. A., Gulliksen, B., and Sandnes, O. K. (1980). "The effect of sedimentation on rocky bottom organisms in Balsfjord, Northern Norway," in *Fjord Oceanography NATO Conference Series*, eds H. J. Freeland, D. M. Farmer, and C. D. Levings (Boston, MA: Springer US), 603–607. doi: 10.1007/978-1-4613-3105-6_54

Farrow, G. E., Syvitski, J. P. M., and Tunnicliffe, V. (1983). Suspended particulate loading on the macrobenthos in a highly Turbid Fjord: knight inlet, British Columbia. *Can. J. Fish. Aquat. Sci.* 40, s273–s288. doi: 10.1139/f83-289

Fasiolo, M., Nedellec, R., Goude, Y., and Wood, S. N. (2018). Scalable visualisation methods for modern Generalized Additive Models. *arXiv* [Preprint] arXiv:1809.10632,

Fernandez, M., Jaramillo, E., Marquet, P. A., Moreno, C. A., Navarrete, S. A., Ojeda, F. P., et al. (2000). Diversity, dynamics and biogeography of Chilean benthic nearshore ecosystems: an overview and guidelines for conservation. *Rev. Chil. Hist. Nat.* 73, 797–830. doi: 10.4067/S0716-078X2000000400021

Försterra, G. (2009). "Ecological and biogeographical aspects of the Chilean fjord region," in *Marine Benthic Fauna of Chilean Patagonia*, eds V. Häussermann and G. Försterra (Santiago: Nature In focus), 61–76.

Försterra, G., Häussermann, V., and Laudien, J. (2017). "Animal forests in the Chilean fjords: discoveries, perspectives, and threats in shallow and deep waters," in *Marine Animal Forests: The Ecology of Benthic Biodiversity Hotspots*, eds S. Rossi, L. Bramanti, A. Gori, and C. Orejas (Cham: Springer International Publishing), 277–313. doi: 10.1007/978-3-319-21012-4_3

Fox, J., and Weisberg, S. (2018). *An R Companion to Applied Regression*. Thousand Oaks, CA: SAGE Publications.

Garcés-Vargas, J., Ruiz, M., Pardo, L. M., Nuñez, S., and Pérez-Santos, I. (2013). Caracterización hidrográfica del estuario del río Valdivia, centro-sur de Chile. *Lat. Am. J. Aquat. Res.* 41, 113–125. doi: 10.3856/vol41-issue1-fulltext-9

Gasbarro, R., Wan, D., and Tunnicliffe, V. (2018). Composition and functional diversity of macrofaunal assemblages on vertical walls of a deep northeast Pacific fjord. *Mar. Ecol. Prog. Ser.* 597, 47–64. doi: 10.3354/meps12599

Gili, J.-M., Rossi, S., Pagès, F., Orejas, C., Teixidó, N., López-González, P. J., et al. (2006). A new trophic link between the pelagic and benthic systems on the Antarctic shelf. *Mar. Ecol. Prog. Ser.* 322, 43–49. doi: 10.3354/meps322043

González, H. E., Calderón, M. J., Castro, L., Clement, A., Cuevas, L. A., Daneri, G., et al. (2010). Primary production and plankton dynamics in the Reloncaví Fjord and the Interior Sea of Chiloé, Northern Patagonia, Chile. *Mar. Ecol. Prog. Ser.* 402, 13–30. doi: 10.3354/meps08360

González, H. E., Castro, L. R., Daneri, G., Iriarte, J. L., Silva, N., Tapia, F., et al. (2013). Land–ocean gradient in haline stratification and its effects on plankton dynamics and trophic carbon fluxes in Chilean Patagonian fjords (47–50°S). *Prog. Oceanogr.* 119, 32–47. doi: 10.1016/j.pocean.2013.06.003

Grange, K. R., Singleton, R. I., Richardson, J. R., Hill, P. J., and Main, W. (1981). Shallow rock-wall biological associations of some southern fiords of New Zealand. *N. Z. J. Zool* 8, 209–227. doi: 10.1080/03014223.1981.10427963

Gutt, J., Arntz, W. E., Balguerias, E., Brandt, A., Gerdes, D., Gorny, M., et al. (2003). Distintos enfoques sobre preguntas acerca de la Biodiversidad: contribuciones Alemanas a los estudios Bentonicos en America del Sur y la Antartida. *Gayana (Concepción)* 67, 177–189. doi: 10.4067/S0717-65382003000200007

Gutt, J., Helsen, E., Arntz, W., and Buschmann, A. (1999). Biodiversity and community structure of the mega-epibenthos in the Magellan region (South America). *Sci. Mar.* 63, 155–170. doi: 10.3989/scimar.1999.63s1155

Hansen, J. R., and Ingólfsson, A. (1993). Patterns in species composition of rocky shore communities in sub-arctic fjords of eastern Iceland. *Mar. Biol.* 117, 469–481. doi: 10.1007/BF00349323

Hargrave, B. (2010). Empirical relationships describing benthic impacts of salmon aquaculture. *Aquacult. Environ. Interact.* 1, 33–46. doi: 10.3354/aei00005

Häussermann, V., and Försterra, G. (2009). *Marine Benthic Fauna of Chilean Patagonia: Illustrated Identification Guide*. Santiago: Nature in Focus.

Häussermann, V., Försterra, G., Melzer, R., and Meyer, R. (2013). Gradual changes of benthic biodiversity in Comau fjord, Chilean Patagonia – Lateral observations over a decade of taxonomic research. *Spixiana* 36, 161–171.

Heaven, C. S., and Scrosati, R. A. (2008). Benthic community composition across gradients of intertidal elevation, wave exposure, and ice scour in Atlantic Canada. *Mar. Ecol. Prog. Ser.* 369, 13–23. doi: 10.3354/meps07655

Hijmans, R. J. (2020). *raster: Geographic Data Analysis and Modeling. R package version 3.4-5*.

Howe, J. A., Austin, W., Forwick, M., Paetzel, M., Harland, R., and Cage, A. (2010). Fjord systems and archives: a review. *Geol. Soc. Spec. Publ.* 344, 5–15. doi: 10.1144/SP344.2

Huovinen, P., Ramírez, J., and Gómez, I. (2016). Underwater Optics in Sub-Antarctic and Antarctic coastal ecosystems. *PLoS One* 11:e0154887. doi: 10.1371/journal.pone.0154887

Husa, V., Steen, H., and Sjøtun, K. (2014). Historical changes in macroalgal communities in Hardangerfjord (Norway). *Mar. Biol. Res.* 10, 226–240. doi: 10.1080/17451000.2013.810751

Hutchinson, G. E. (1953). The concept of pattern in ecology. *Proc. Acad. Nat. Sci. Phila.* 105, 1–12. doi: 10.1017/cbo9780511608537.002

Iriarte, J. L. (2018). Natural and human influences on marine processes in Patagonian subantarctic coastal waters. *Front. Mar. Sci.* 5:360. doi: 10.3389/fmars.2018.00360

Iriarte, J. L., González, H. E., and Nahuelhual, L. (2010). Patagonian fjord ecosystems in southern Chile as a highly vulnerable region: problems and needs. *Ambio* 39, 463–466. doi: 10.1007/s13280-010-0049-9

Johansen, H. W. (2018). *Coralline Algae: A First Synthesis*. Boca Raton, FL: CRC Press, doi: 10.1201/9781351070928

Jones, C. G., Lawton, J. H., and Shachak, M. (1994). Organisms as ecosystem engineers. *Oikos* 69, 373–386. doi: 10.2307/3545850

Kohler, K. E., and Gill, S. M. (2006). Coral point count with excel extensions (CPCe): a visual basic program for the determination of coral and substrate coverage using random point count methodology. *Comput. Geosci.* 32, 1259–1269. doi: 10.1016/j.cageo.2005.11.009

Kuklinski, P. (2013). Biodiversity and abundance patterns of rock encrusting fauna in a temperate fjord. *Mar. Environ. Res.* 87–88, 61–72. doi: 10.1016/j.marenvres.2013.03.005

León-Muñoz, J., Urbina, M. A., Garreaud, R., and Iriarte, J. L. (2018). Hydroclimatic conditions trigger record harmful algal bloom in western Patagonia (summer 2016). *Sci. Rep.* 8:1330. doi: 10.1038/s41598-018-19461-4

Magurran, A. E. (1988). *Ecological Diversity and Its Measurement*. Princeton, NJ: Princeton University Press.

McArthur, M. A., Brooke, B. P., Przeslawski, R., Ryan, D. A., Lucieer, V. L., Nichol, S., et al. (2010). On the use of abiotic surrogates to describe marine benthic biodiversity. *Estuar. Coast. Shelf Sci.* 88, 21–32. doi: 10.1016/j.ecss.2010.03.003

McGovern, M., Poste, A. E., Oug, E., Renaud, P. E., and Trannum, H. C. (2020). Riverine impacts on benthic biodiversity and functional traits: A comparison of two sub-Arctic fjords. *Estuar. Coast. Shelf Sci.* 240:106774. doi: 10.1016/j.ecss.2020.106774

Meire, P., Ysebaert, T., Damme, S. V., den Bergh, E. V., Maris, T., and Struyf, E. (2005). The Scheldt estuary: a description of a changing ecosystem. *Hydrobiologia* 540, 1–11. doi: 10.1007/s10750-005-0896-8

Menge, B. A., and Sutherland, J. P. (1987). Community regulation: variation in disturbance, competition, and predation in relation to environmental stress and recruitment. *Am. Nat.* 130, 730–757. doi: 10.1086/284741

Munda, I. M. (1978). Salinity dependent distribution of benthic algae in estuarine areas of Icelandic fjords. *Bot. Mar.* 21, 451–468. doi: 10.1515/botm.1978.21.7.451

Navarro, J. M. (1988). The effects of salinity on the physiological ecology of Choromytilus chorus (Molina, 1782) (Bivalvia: Mytilidae). *J. Exp. Mar. Bio. Ecol.* 122, 19–33. doi: 10.1016/0022-0981(88)90209-2

Navarro, J. M., Paschke, K., Ortiz, A., Vargas-Chacoff, L., Pardo, L. M., and Valdivia, N. (2019). The Antarctic fish Harpagifer antarcticus under current temperatures and salinities and future scenarios of climate change. *Prog. Oceanogr.* 174, 37–43. doi: 10.1016/j.pocean.2018.09.001

Niklitschek, E. J., Soto, D., Lafon, A., Molinet, C., and Toledo, P. (2013). Southward expansion of the Chilean salmon industry in the Patagonian Fjords: main environmental challenges. *Rev. Aquac.* 5, 172–195. doi: 10.1111/raq.12012

Oksanen, J., Blanchet, F. G., Friendly, M., Kindt, R., Legendre, P., McGlinn, D., et al. (2019). *vegan: Community Ecology Package*. Available online at: https://CRAN.R-project.org/package=vegan (accessed October 6, 2020).

Outeiro, L., Häussermann, V., Viddi, F., Hucke-Gaete, R., Försterra, G., Oyarzo, H., et al. (2015). Using ecosystem services mapping for marine spatial planning in southern Chile under scenario assessment. *Ecosyst. Serv.* 16, 341–353. doi: 10.1016/j.ecoser.2015.03.004

Paine, C. E. T., Deasey, A., and Duthie, A. B. (2018). Towards the general mechanistic prediction of community dynamics. *Funct. Ecol.* 32, 1681–1692. doi: 10.1111/1365-2435.13096

Palacios, M., Osman, D., Ramirez, J., Huovinen, P., and Gomez, I. (2021). Photobiology of the giant kelp Macrocystis pyrifera in the land-terminating glacier fjord Yendegaia (Tierra del Fuego): a look into the future? *Sci. Total Environ.* 751:141810. doi: 10.1016/j.scitotenv.2020.141810

Pantoja, S., Luis Iriarte, J., and Daneri, G. (2011). Oceanography of the Chilean Patagonia. *Cont. Shelf Res.* 31, 149–153. doi: 10.1016/j.csr.2010.10.013

Pearson, T. H. (1980). "Macrobenthos of Fjords," in *Fjord Oceanography*, eds H. J. Freeland, D. M. Farmer, and C. D. Levings (Boston, MA: Springer US), 569–602. doi: 10.1007/978-1-4613-3105-6_53

Pedersen, E. J., Miller, D. L., Simpson, G. L., and Ross, N. (2019). Hierarchical generalized additive models in ecology: an introduction with mgcv. *PeerJ* 7:e6876. doi: 10.7717/peerj.6876

Pérez-Santos, I., Garcés-Vargas, J., Schneider, W., Ross, L., Parra, S., and Valle-Levinson, A. (2014). Double-diffusive layering and mixing in Patagonian fjords. *Prog. Oceanogr.* 129, 35–49. doi: 10.1016/j.pocean.2014.03.012

Pielou, E. C. (1969). *An introduction to Mathematical Ecology*. New York, NY: Wiley-Interscience.

Quiroga, E., Ortiz, P., González-Saldías, R., Reid, B., Tapia, F. J., Pérez-Santos, I., et al. (2016). Seasonal benthic patterns in a glacial Patagonian fjord: the role of suspended sediment and terrestrial organic matter. *Mar. Ecol. Prog. Ser.* 561, 31–50. doi: 10.3354/meps11903

R Core Team (2021). *R: A Language and Environment for Statistical Computing*. Vienna: R Foundation for Statistical Computing.

Reise, K. (2002). Sediment mediated species interactions in coastal waters. *J. Sea Res.* 48, 127–141. doi: 10.1016/S1385-1101(02)00150-8

Rosenberg, R., and Möller, P. (1979). Salinity stratified benthic macrofaunal communities and long-term monitoring along the west coast of Sweden. *J. Exp. Mar. Biol. Ecol.* 37, 175–203. doi: 10.1016/0022-0981(79)90094-7

Rossi, S., Bramanti, L., Gori, A., and Orejas, C. (2017). *Marine Animal Forests: The Ecology of Benthic Biodiversity Hotspots*. Cham: Springer International Publishing.

Schlitzer, R. (2020). *Ocean Data View*. Available online at: https://odv.awi.de (accessed April 12, 2021).

Schubert, H., Feuerpfeil, P., Marquardt, R., Telesh, I., and Skarlato, S. (2011). Macroalgal diversity along the Baltic Sea salinity gradient challenges Remane's species-minimum concept. *Mar. Pollut. Bull.* 62, 1948–1956. doi: 10.1016/j.marpolbul.2011.06.033

Scrosati, R., and Heaven, C. (2007). Spatial trends in community richness, diversity, and evenness across rocky intertidal environmental stress gradients in eastern Canada. *Mar. Ecol. Prog. Ser.* 342, 1–14. doi: 10.3354/meps342001

Scrosati, R. A., Freeman, M. J., and Ellrich, J. A. (2020). The subhabitat dependence of biogeographic pattern. *Front. Ecol. Evol.* 8:550612. doi: 10.3389/fevo.2020.550612

Shannon, C. E. (1948). A mathematical theory of communication. *Bell Syst. Tech. J.* 27, 379–423.

Sjøtun, K., Husa, V., Asplin, L., and Sandvik, A. D. (2015). Climatic and environmental factors influencing occurrence and distribution of macroalgae – a fjord gradient revisited. *Mar. Ecol. Prog. Ser.* 532, 73–88. doi: 10.3354/meps11341

Smith, F., and Witman, J. D. (1999). Species diversity in subtidal landscapes: maintenance by physical processes and larval recruitment. *Ecology* 80, 51–69. doi: 10.1890/0012-9658(1999)080[0051:sdislm]2.0.co;2

Smyth, K., and Elliott, M. (2016). "Effects of changing salinity on the ecology of the marine environment," in *Stressors in the Marine Environment: Physiological and Ecological Responses; Societal Implications*, eds M. Solan and N. Whiteley (Oxford: University Press), 161–174. doi: 10.1093/acprof:oso/9780198718826.003.0009

Smyth, K., Mazik, K., and Elliott, M. (2014). Behavioural effects of hypersaline exposure on the lobster *Homarus gammarus* (L) and the crab Cancer pagurus (L). *J. Exp. Mar. Biol. Ecol.* 457, 208–214. doi: 10.1016/j.jembe.2014.04.016

Soares, M. D. O., Rossi, S., Martins, F. A. S., and Carneiro, P. B. D. M. (2017). The forgotten reefs: benthic assemblage coverage on a sandstone reef (Tropical South-western Atlantic). *J. Mar. Biolog. Assoc.* 97, 1585–1592. doi: 10.1017/S0025315416000965

Sobarzo Bustamante, M. (2009). "The Southern Chilean fjord region: oceanographic aspects," in *Marine Benthic Fauna of Chilean Patagonia*, eds V. Häussermann and G. Försterra (Santiago: Nature In focus), 53–60.

Soto, D., and Norambuena, F. (2004). Evaluation of salmon farming effects on marine systems in the inner seas of southern Chile: a large-scale mensurative experiment. *J. Appl. Ichthyol.* 20, 493–501. doi: 10.1111/j.1439-0426.2004.00602.x

Soto, M. V., Arratia, P., Cabello, M., Moreno, R., Whyndam, K., Soto, M. V., et al. (2019). Amenazas de origen natural y exposición de obras de conectividad estratégica en territorios extremos. Fiordo Comau, Norpatagonia de Chile. *Revist. Geogr. Norte Grande* 73, 57–75. doi: 10.4067/S0718-34022019000202.x00057

Stewart, R. H. (2008). *Introduction to Physical Oceanography*. Texas, TX: Texas A & M University. Available online at: https://open.umn.edu/opentextbooks/textbooks/introduction-to-physical-oceanography

Syvitski, J. P. M., Burrell, D. C., and Skei, J. M. (2012). *Fjords: Processes and Products*. New York, NY: Springer Science & Business Media.

Thompson, P. L., Guzman, L. M., De Meester, L., Horvath, Z., Ptacnik, R., Vanschoenwinkel, B., et al. (2020). A process-based metacommunity framework linking local and regional scale community ecology. *Ecol. Lett.* 23, 1314–1329. doi: 10.1111/ele.13568

Underwood, A. J., Chapman, M. G., and Connell, S. D. (2000). Observations in ecology: you can't make progress on processes without understanding the patterns. *J. Exp. Mar. Biol. Ecol.* 250, 97–115. doi: 10.1016/S0022-0981(00)00181-7

Valdivia, N., Garrido, I., Bruning, P., Piñones, A., and Pardo, L. M. (2020). Biodiversity of an Antarctic rocky subtidal community and its relationship with glacier meltdown processes. *Mar. Environ. Res.* 159:104991. doi: 10.1016/j.marenvres.2020.104991

Valle-Levinson, A., Sarkar, N., Sanay, R., Soto, D., and León, J. (2007). Spatial structure of hydrography and flow in a Chilean fjord, Estuario Reloncaví. *Estuar. Coasts* 30, 113–126. doi: 10.1007/BF02782972

Vargas-Chacoff, L., Muñoz, J. L. P., Ocampo, D., Paschke, K., and Navarro, J. M. (2019). The effect of alterations in salinity and temperature on neuroendocrine responses of the Antarctic fish Harpagifer antarcticus. *Comp. Biochem. Physiol. Part A Mol. Integr. Physiol.* 235, 131–137. doi: 10.1016/j.cbpa.2019.05.029

Villagrán, C. (1988). Expansion of Magellanic Moorland during the late Pleistocene: palynological evidence from northern Isla de Chiloé, Chile. *Quat. Res.* 30, 304–314. doi: 10.1016/0033-5894(88)90006-3

Voronkov, A., Hop, H., and Gulliksen, B. (2013). Diversity of hard-bottom fauna relative to environmental gradients in Kongsfjorden, Svalbard. *Polar Res.* 32:11208. doi: 10.3402/polar.v32i0.11208

Whitfield, A. K., Elliott, M., Basset, A., Blaber, S. J. M., and West, R. J. (2012). Paradigms in estuarine ecology – A review of the Remane diagram with a suggested revised model for estuaries. *Estuar. Coast. Shelf Sci.* 97, 78–90. doi: 10.1016/j.ecss.2011.11.026

Wing, S. R., and Leichter, J. J. (2011). Variation in environmental conditions in a subtidal prey refuge: effects of salinity stress, food availability and predation on mussels in a fjord system. *Mar. Ecol. Prog. Ser.* 422, 201–210. doi: 10.3354/meps08911

Witman, J. D., and Grange, K. R. (1998). Links between rain, salinity, and predation in a Rocky Subtidal community. *Ecology* 79, 2429–2447. doi: 10.1890/0012-9658(1998)079[2429:lbrsap]2.0.co;2

Wlodarska-Kowalczuk, M., Pearson, T. H., and Kendall, M. A. (2005). Benthic response to chronic natural physical disturbance by glacial sedimentation in an Arctic fjord. *Mar. Ecol. Prog. Ser.* 303, 31–41. doi: 10.3354/meps303031

Wood, S. N. (2011). Fast stable restricted maximum likelihood and marginal likelihood estimation of semiparametric generalized linear models. *J. R. Stat. Soc. Ser. B Stat. Methodol.* 73, 3–36. doi: 10.1111/j.1467-9868.2010.00749.x

Wood, S. N. (2017). *Generalized Additive Models: An Introduction with R*, 2 Edn. Boca Raton, FL: Chapman and Hall, doi: 10.1201/9781315370279

WoRMS (2020). *World Register of Marine Species*. Available online at: http://www.marinespecies.org/ (accessed October 6, 2020).

Ysebaert, T., Herman, P. M. J., Meire, P., Craeymeersch, J., Verbeek, H., and Heip, C. H. R. (2003). Large-scale spatial patterns in estuaries: estuarine macrobenthic communities in the Schelde estuary, NW Europe. *Estuar. Coast. Shelf Sci.* 57, 335–355. doi: 10.1016/S0272-7714(02)00359-1

Zwerschke, N., Bollen, M., Molis, M., and Scrosati, R. A. (2013). An environmental stress model correctly predicts unimodal trends in overall species richness and diversity along intertidal elevation gradients. *Helgol. Mar. Res.* 67, 663–674. doi: 10.1007/s10152-013-0352-5

Conflict of Interest: The authors declare that the research was conducted in the absence of any commercial or financial relationships that could be construed as a potential conflict of interest.

frontiers in Marine Science

ORIGINAL RESEARCH
published: 13 May 2021
doi: 10.3389/fmars.2021.612309

Sediment Provenance in the Baker-Martínez Fjord System (Chile, 48°S) Indicated by Magnetic Susceptibility and Inorganic Geochemistry

Matthias Troch[1], Sebastien Bertrand[1], Benjamin Amann[1], Dawei Liu[1], Juan A. Placencia[2] and Carina B. Lange[3,4,5]*

[1] Renard Centre of Marine Geology, Department of Geology, Ghent University, Ghent, Belgium, [2] Departamento de Química Ambiental, Facultad de Ciencias, Universidad Católica de la Santísima Concepción, Concepción, Chile, [3] Centro de Investigación Oceanográfica COPAS Sur-Austral and Departamento de Oceanografía, Universidad de Concepción, Concepción, Chile, [4] Centro de Investigación Dinámica de Ecosistemas Marinos de Altas Latitudes (IDEAL), Universidad Austral de Chile, Valdivia, Chile, [5] Scripps Institution of Oceanography, University of California, San Diego, La Jolla, United States

OPEN ACCESS

Edited by:
Selvaraj Kandasamy, Xiamen University, China

Reviewed by:
Yuan-Pin Chang, National Sun Yat-sen University, Taiwan
Madhavaraju Jayagopal, Universidad Nacional Autonoma de Mexico, Mexico
Prakash Babu Chakka, Council of Scientific and Industrial Research (CSIR), India

****Correspondence:***
Matthias Troch
matthias.troch@ugent.be

Specialty section:
This article was submitted to Marine Biogeochemistry, a section of the journal Frontiers in Marine Science

Received: *20 January 2021*
Accepted: *12 April 2021*
Published: *13 May 2021*

Citation:
Troch M, Bertrand S, Amann B, Liu D, Placencia JA and Lange CB (2021) Sediment Provenance in the Baker-Martínez Fjord System (Chile, 48°S) Indicated by Magnetic Susceptibility and Inorganic Geochemistry. Front. Mar. Sci. 8:612309. doi: 10.3389/fmars.2021.612309

Fjord sediments are increasingly used as high-resolution archives of climate and environmental change, including variations in glacier mass balance and terrestrial hydrology. To accurately interpret such sediment records, it is crucial to comprehend sediment transport processes and determine sediment provenance. With this in mind, our main objective is to identify cost-effective parameters that can be used to reconstruct relative variations in the origin of sediments deposited in the Baker-Martínez fjord system, which is located between the Northern (NPI) and Southern (SPI) Patagonian Icefields. We focus on estimating the proportions of sediment derived from each icefield, taking advantage of the clearly distinct lithologies that underlie NPI (Patagonian Batholith) and SPI (Eastern Andean Metamorphic Complex) glaciers. The magnetic susceptibility and inorganic geochemistry of 21 surface sediment samples collected along the fjord system and that of suspended sediment samples from the four main rivers that discharge at its heads were investigated. Results indicate that sediments derived from the NPI are characterized by higher magnetic susceptibility and log(Ti/Al) values than those from the SPI, reflecting the mafic nature of the batholith. In fjords that receive contributions from both the NPI and SPI, magnetic susceptibility and log(Ti/Al) primarily reflect sediment provenance. In fjords receiving sediment from only one icefield, however, these parameters are positively correlated with grain size and reflect the progressive settling of particles from the surficial plume. Our results suggest that magnetic susceptibility and log(Ti/Al) can be used to reconstruct sediment provenance within the Baker-Martínez fjord system, but that only log(Ti/Al) can provide quantitative estimates of the proportions of sediment derived from each icefield. Ultimately, applying these provenance indicators to long sediment cores from the Baker-Martínez fjord system could allow reconstructing relative variations in sediment input from each icefield, which may in turn be interpreted as changes in river discharge and/or glacier mass balance.

Keywords: grain size, river suspended sediment, Patagonia, fjord sediment, Northern Patagonian Icefield, Southern Patagonian Icefield

INTRODUCTION

Fjord sediments constitute valuable and high-resolution paleoenvironmental archives due to high accumulation rates of particles of glacial and fluvial origin (Syvitski and Shaw, 1995; Bianchi et al., 2020). Patagonian fjord sediments in particular are increasingly recognized as high-resolution archives of past climate and environmental changes (Lamy et al., 2010; Caniupán et al., 2014; Bertrand et al., 2017; Ríos et al., 2020). During the last decade, these archives have been extensively used to reconstruct changes in seismic activity (St-Onge et al., 2012; Van Daele et al., 2013; Piret et al., 2018; Wils et al., 2020), volcanic activity (Fontijn et al., 2014; Wils et al., 2018), precipitation (Lamy et al., 2010; Bertrand et al., 2014) and glacier variability (Bertrand et al., 2012a, 2017; Kilian and Lamy, 2012). However, accurately interpreting such sediment records requires a comprehensive understanding of terrestrial sediment transport processes and of the provenance of the sediments deposited in these fjords.

In fjords, terrestrial sediment transport is directly linked to river and/or glacier dynamics (Syvitski and Shaw, 1995; Bianchi et al., 2020; Hogan et al., 2020). When sediment-laden freshwater is discharged into a saline fjord, the freshwater mass forms a buoyant, hypopycnal plume that transports most of the fine-grained suspended sediments seaward. On the contrary, the coarse bedload sediments settle relatively quickly near the river mouth or glacier front (Syvitski and Shaw, 1995). Settling of the suspended sediments from the hypopycnal plume occurs in response to a decreasing flow velocity and increasing salinity, which enhances flocculation, palletization and/or agglomeration (Syvitski and Shaw, 1995). Variations in this hydrodynamic system, due to e.g., seasonal variations in meltwater discharge, affect the flow velocity of the hypopycnal plume and its ability to transport suspended sediment, resulting in temporal changes in sediment grain size throughout the fjord system (Powell and Molnia, 1989; Cowan and Powell, 1990; Syvitski and Shaw, 1995; Bianchi et al., 2020).

Identifying sediment provenance is often an essential prerequisite for paleoclimate and paleoenvironmental reconstructions, since most fjords contain terrigenous sediments supplied by multiple sources. However, studies that evaluate the effectiveness of provenance tracers in Patagonian fjords are currently lacking. Recently, Liu et al. (2020) showed that bulk mineralogy and major and rare earth element geochemistry could be used to qualitatively reconstruct the provenance of Patagonian river sediments, whereas Nd and Sr isotopes allowed for quantitative provenance analysis. Likewise, Villaseñor et al. (2019) successfully used Nd and Sr isotopes to reconstruct Pleistocene glacial silt provenance to the continental slope at 46°S. Measuring Nd and Sr isotopes is, however, time-consuming and expensive, which limits its application on fjord sediment cores to a handful of pre-selected samples. A much more cost-effective provenance indicator that has shown promising results along the Chilean continental margin is bulk inorganic geochemistry. Some elemental ratios, such as Fe/Al, Mg/Zr, Ti/K, and Ba/Al for instance, have proven to be reliable provenance indicators of sediments derived from different sources along the southern Andes (Klump et al., 2000; Lamy et al., 2001; Stuut et al., 2007; Siani et al., 2010). Whether these indicators are also applicable to Patagonian fjord sediments has, however, not yet been evaluated. In proximal environments, some of these elements are known to be closely related to grain size (Bertrand et al., 2012b; Liu et al., 2019), which may limit their use as provenance tracers (Weltje, 2012).

With this in mind, the research objective of this paper is to identify cost-effective physical and geochemical parameters that can be used to reconstruct relative variations in the origin of sediments deposited in the Baker-Martínez fjord system (Chilean Patagonia, 48°S). This fjord system is particularly promising to reconstruct past glacier variability, as it is located between the Northern (NPI) and Southern Patagonian Icefields (SPI). In addition, the distinct lithologies underlying both icefields, i.e., the Patagonian Batholith (NPI) and the Eastern Andean Metamorphic complex (SPI), suggest that compositional tracers could permit telling apart sediments derived from these two icefields. Previous studies highlighted the magnetic (Michelena and Kilian, 2015) and geochemical (Pankhurst et al., 1999; Faúndez et al., 2002; Augustsson and Bahlburg, 2003; Liu et al., 2020) differences that exist between the Patagonian Batholith and Eastern Andean Metamorphic Complex. Therefore, we focus on magnetic susceptibility and inorganic geochemistry, as these parameters are widely applicable and relatively easy to measure on both discrete samples (e.g., handheld magnetic sensors and ICP or XRF-based techniques) and on sediment cores (e.g., core logging and XRF core scanning). Both parameters are also relatively cheap to analyze and could thus complement lower-resolution isotope-based reconstructions (Revel-Rolland et al., 2005; Meyer et al., 2011; Bonneau et al., 2017).

SETTING

The ∼150 km long, W-E oriented Baker-Martínez fjord system is located between the NPI and the SPI, and it is subdivided into two parallel channels: Martínez in the north and Baker in the south (**Figure 1**). Both channels are interconnected near their heads via Troya Channel, and distally via Sierralta Channel. Each also has a series of tributary fjords, i.e., Steffen and Mitchell for Martínez, and Jorge Montt and Steele for Baker (**Figure 1**).

The Baker-Martínez fjord system has a hyperhumid maritime climate with a steep west–to–east precipitation gradient, due to the interaction of the southern westerlies with the Andes orographic high (Garreaud et al., 2013). Annual precipitation decreases from >2,000 mm/year over the icefields to <500 mm/year at the Chile–Argentina border (**Figure 1**; Fick and Hijmans, 2017). The mean air temperature of *ca.* 8°C remains relatively stable with longitude, but decreases with latitude (Sagredo and Lowell, 2012; Garreaud et al., 2013). Due to the cold climate and to the relatively recent deglaciation, physical weathering dominates and chemical weathering is relatively negligible (Kaiser et al., 2005; Bertrand et al., 2012b).

Freshwater enters the Baker-Martínez fjord system from four glacier-fed rivers, i.e., Baker, Pascua, Huemules and

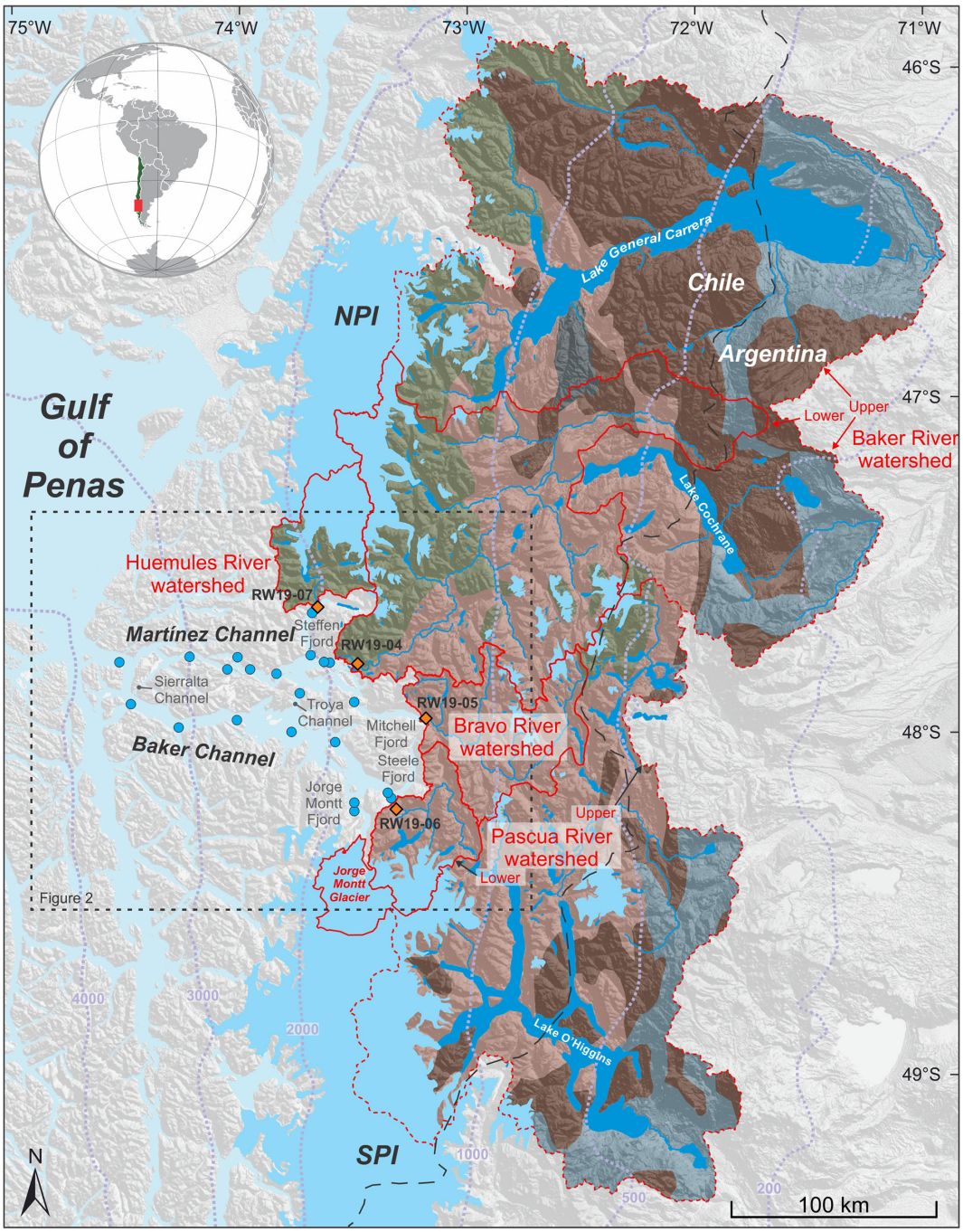

FIGURE 1 | Location of the Baker-Martínez fjord system in Chilean Patagonia with indication of the main geological units of the studied watersheds (Segemar, 2003; Sernageomin, 2003; Gómez et al., 2019), icefields (NPI and SPI; Northern and Southern Patagonian Icefield), mountain glaciers, and main rivers discharging in the fjord system. The mean annual precipitation (in mm) gradient is represented by purple dashed isohyets (Fick and Hijmans, 2017).

Bravo, and from Jorge Montt Glacier (**Figure 1**). Baker and Huemules rivers receive meltwater from NPI outlet glaciers, whereas Pascua River is mostly fed by the SPI. Bravo River is not connected to any icefield but it receives meltwater from isolated mountain glaciers. Baker, Pascua, and Bravo rivers have a nivo-glacial regime with glacial contributions during summer, whereas Huemules River is strictly proglacial (Aiken, 2012; González et al., 2013; Lara et al., 2015). Mean annual discharge varies by one order of magnitude across the four river watersheds: 1,133 m^3/s (Baker), 753 m^3/s (Pascua), 121 m^3/s (Huemules), and 112 m^3/s (Bravo) (Pantoja et al., 2011; Dussaillant et al., 2012; Pryer et al., 2020). Jorge Montt Glacier has an estimated mean annual discharge of *ca.* 129 m^3/s, based on a negative mass balance of -2.20 ± 0.38 Gt/year (Foresta et al., 2018) and a mean annual precipitation of 3,752 mm (Boisier et al., 2018). This estimate is in agreement with those from Mernild et al. (2017) (*ca.* 100 m^3/s) and Moffat et al. (2018) (25–150 m^3/s).

The hypopycnal plumes corresponding to the main freshwater sources flow in a westward direction through the Baker-Martínez fjord system toward the Gulf of Penas (Pérez-Santos et al., 2014; Ross et al., 2014). Consequently, the heads of Martínez and Baker channels receive meltwater and sediment from the NPI and SPI, respectively, before merging in the Troya Channel (**Figure 2**). Average spring-summer suspended sediment distributions quantified by MERIS-ENVISAT (2005–2011; González et al., 2013) and Landsat 8 (2016; International Initiative on Water Quality, 2019) satellite data reveal that NPI-derived meltwater and sediment can reach the distal part of Baker Channel through Troya and Sierralta channels (**Figure 2**). Water and sediments from the head of Baker

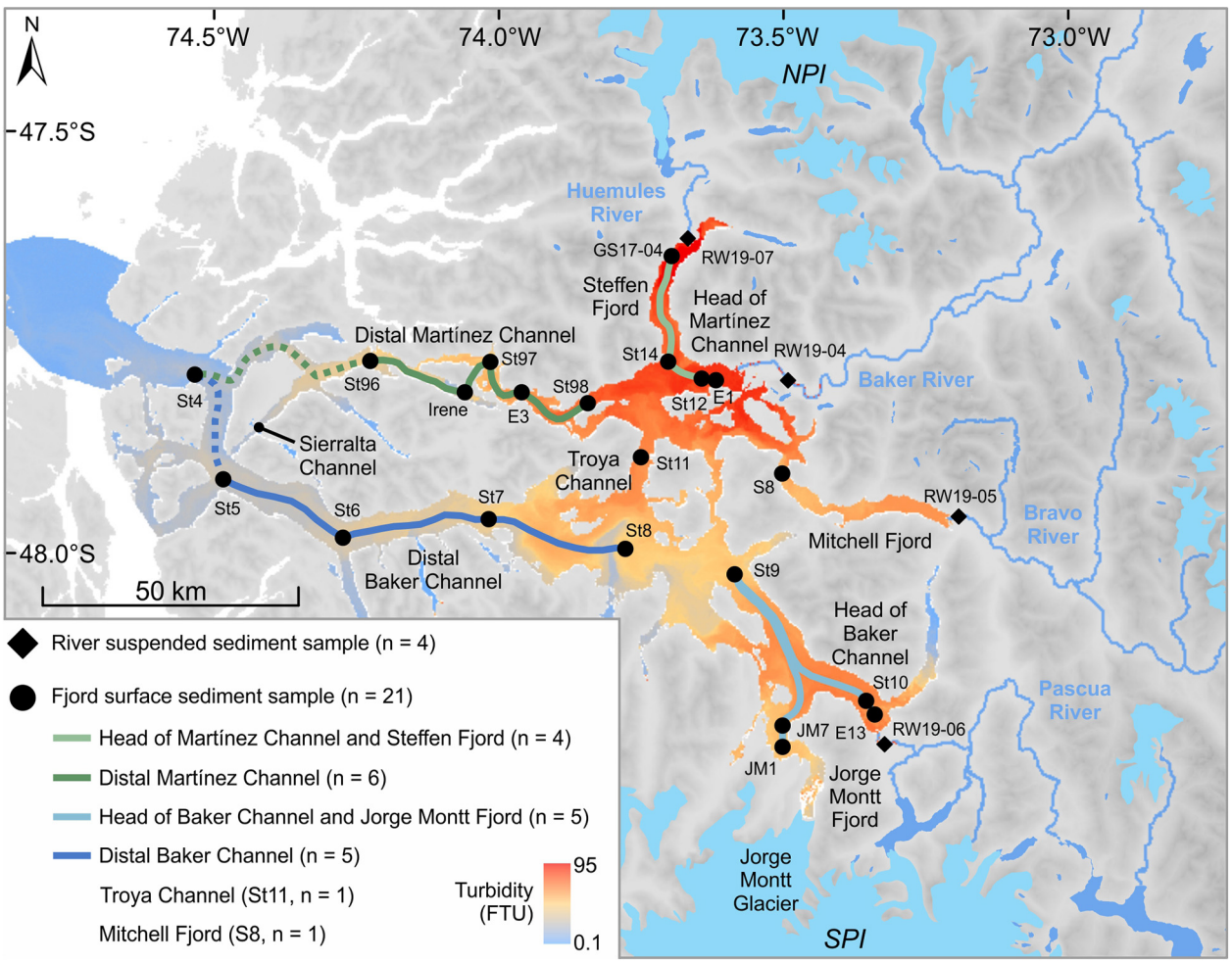

FIGURE 2 | Location of the fjord surface sediment samples in the Baker-Martínez fjord system and of the river suspended sediment samples collected in the four main rivers that discharge into the fjord system. The fjord surface sediment dataset ($n = 21$) is split into six subsets based on sample location. The colored lines connecting the fjord samples represent the four subsets of the fjord sample dataset with $n > 1$. Note that sample St4 is located downstream of the confluence of Baker and Martínez channels, and thus belongs to both the distal Baker Channel and distal Martínez Channel datasets (stippled lines). The background turbidity data is derived from Landsat 8 satellite images from 08-01-2016 and 31-01-2016 (satellite data source: USGS) by the International Initiative on Water Quality (2019). See **Table 2** for the exact location of the sampling sites.

Channel, on the other hand, do not seem to cross over to the Martínez Channel.

Lithogenic particles constitute the majority (84.8–97.2 wt%) of the sediments deposited in the Baker-Martínez fjord system. The rest is composed of organic matter (0.4–3.8 wt%), biogenic opal (1.1–10.2 wt%) and calcium carbonate (0–2.5 wt%) (Rebolledo et al., 2019). Most of the lithogenic particles are derived from bedrock erosion by NPI and SPI glaciers, and are transported to the Baker-Martínez fjord system by the aforementioned glacier-river systems. Although some of the watersheds are <10% glaciated, e.g., the Baker River watershed, the glacier-covered areas contribute significantly more water and sediments to the fjords than the drier regions (**Figure 1**; Dussaillant et al., 2012; Liu et al., 2020). In addition, suspended sediment data from the outflow of lakes General Carrera, Cochrane, and O'Higgins indicate that these lakes act as efficient sediment traps (HidroAysén, 2010; Vandekerkhove et al., 2020). Consequently, sediments from the upper Baker and upper Pascua river watersheds rarely reach the Baker-Martínez fjord system (**Figure 1**).

The regional geology mainly consists of two lithological units (**Figure 1** and **Table 1**; Gómez et al., 2019): the Patagonian Batholith, which is mainly composed of granite, granodiorite, diorite, tonalite, and gabbro, under and around the NPI (Pankhurst et al., 1999; Hervé et al., 2007; Michelena and Kilian, 2015) and the Eastern Andean Metamorphic Complex, which is mainly composed of metamorphosed sandstone and mudstone, under and around the SPI (Faúndez et al., 2002; Augustsson and Bahlburg, 2003; Hervé et al., 2008). The relative proportions of these two lithologies vary considerably across the four watersheds (**Table 1**). The Eastern Andean Metamorphic Complex varies from ∼100% in the Bravo and lower Pascua river watersheds to 50% in the lower Baker River watershed, and the Patagonian Batholith varies from 100% in the Huemules River watershed to 36% in the lower Baker River watershed (**Figure 1** and **Table 1**). Three additional lithologies occur in the easternmost reaches of our study region, i.e., Mesozoic and Cenozoic volcanic rocks, Miocene sedimentary rocks, and fluvioglacial deposits derived from Quaternary glacier advances (Kaplan et al., 2005; Boex et al., 2013; Davies et al., 2020).

TABLE 1 | Surface area of the four studied river watersheds and Jorge Montt Glacier, and areal proportions of the corresponding bedrock lithologies (Gómez et al., 2019).

Watershed	Surface area (km^2)	Bedrock lithology		
		PB (%)	EAMC (%)	Other* (%)
Lower Baker River	8,425	36	50	14
Bravo River	1,894	1	99	0
Lower Pascua River	1,125	0	100	0
Huemules River	1,102	100	0	0
Jorge Montt Glacier	500	0	100	0

*All parameters were calculated using ArcMap and the UTM18S projection. The Patagonian Batholith (PB) and Eastern Andean Metamorphic Complex (EAMC) are assumed to be the bedrock underlying the NPI and SPI, respectively (**Figure 1**; Gómez et al., 2019). *Other lithologies include Mesozoic and Cenozoic volcanic rocks, Miocene sedimentary rocks and fluvioglacial deposits (**Figure 1**; Segemar, 2003; Sernageomin, 2003; Gómez et al., 2019).*

MATERIALS AND METHODS

This study makes use of fjord surface sediment samples to evaluate the applicability of magnetic susceptibility and inorganic geochemistry as tracers of sediment provenance within the Baker-Martínez fjord system (**Figure 1**). Sediment grain size was also analyzed to estimate the influence of differential sediment settling from the hypopycnal plume on magnetic susceptibility and inorganic geochemistry (Snowball et al., 1999; Sandgren and Snowball, 2001; Bertrand et al., 2012b; Bloemsma et al., 2012; Lipp et al., 2020). In addition, suspended sediments from the four main rivers flowing into the Baker-Martínez fjord system were sampled at the river mouths to characterize the physical and geochemical properties of the sediments reaching the fjord system (**Figure 1**). River sediments are preferred over bedrock samples since they integrate all the lithologies available within their respective watersheds.

Sampling

Twenty-one fjord surface sediment samples (**Figure 1** and **Table 2**) were collected during five different campaigns carried out in the Baker-Martínez fjord system between 2013 and 2017: (1) CIMAR 20 Fiordos (November 2014), (2) COPAS Sur-Austral 2014 (October 2014; Rebolledo et al., 2019), (3) University of Washington field expedition to Jorge Montt Fjord (March 2013; Boldt, 2014), (4) PISCES 17 (February 2017), and (5) Ghent University field expedition to the Baker-Martínez fjord system (February 2017). These sediment samples were obtained using grab samplers or by sub-sampling the upper 1–2 cm of Rumhor, gravity, or Kasten cores.

River Water samples (RW19, **Table 2**) were collected in February 2019 (austral summer) at the mouths of the Baker, Pascua, Huemules and Bravo rivers (**Figure 1**). The upper 20 cm of the water column was sampled using a bucket from a boat. Between 100 and 155 L of water was collected per site, stored in pre-rinsed LDPE cubitainers (10 or 20 L), and filtered using a 90 mm diameter PES membrane (pore size 0.22 μm) within 48 hours of collection. The volume (weight of water) of filtered water was recorded to calculate the suspended sediment concentration of each sample.

Magnetic Susceptibility

Volume-specific magnetic susceptibility was measured on all samples using a Bartington MS2G single-frequency (1.3 kHz) sensor connected to a Bartington MS3 meter. Samples were packed into 1 mL plastic vials and the volume-specific values were divided by sample weight measured with a Mettler Toledo ME104T (0.1 mg) balance to calculate mass-specific

TABLE 2 | Location of the fjord and river sediment sampling sites.

Fjord/river	Station	Campaign*	Latitude	Longitude
Fjord surface sediment samples				
Martínez Channel	St96	CF20	−47.773	−74.226
	Irene	CO14	−47.811	−74.063
	St97	CF20	−47.774	−74.015
	E3	CO14	−47.813	−73.956
	St98	CF20	−47.823	−73.844
	St12	CF20	−47.788	−73.635
	E1	CO14	−47.785	−73.610
Steffen Fjord	St14	CF20	−47.768	−73.694
	GS17-04	UGent17	−47.643	−73.688
Troya Channel	St11	CF20	−47.881	−73.742
Baker Channel	St4	CF20	−47.789	−74.534
	St5	CF20	−47.913	−74.484
	St6	CF20	−47.982	−74.274
	St7	CF20	−47.960	−74.018
	St8	CF20	−47.995	−73.778
	St9	CF20	−48.025	−73.586
	St10	CF20	−48.174	−73.355
	E13	CO14	−48.195	−73.337
Jorge Montt Fjord	JM7	UW13	−48.203	−73.502
	JM1	UW13	−48.228	−73.502
Mitchell Fjord	S8	PI17	−47.907	−73.503
River suspended sediment samples				
Baker River	RW19-04	UGent19	−47.796	−73.492
Bravo River	RW19-05	UGent19	−47.957	−73.193
Pascua River	RW19-06	UGent19	−48.225	−73.323
Huemules River	RW19-07	UGent19	−47.628	−73.668

**CF20: CIMAR 20 Fiordos (November 2014).*
CO14: COPAS Sur-Austral 2014 (October 2014, Rebolledo et al., 2019).
PI17: PISCES 17 (February 2017).
UGent17: Ghent University field expedition to the Baker-Martínez fjord system (February 2017).
UGent19: Ghent University field expedition (February 2019).
UW13: University of Washington field expedition to Jorge Montt Fjord (March 2013; Boldt, 2014).

magnetic susceptibility values (Sandgren and Snowball, 2001). All magnetic susceptibility measurements reported in this article are mass-specific.

Inorganic Geochemistry

Major (Al, Ca, Fe, K, Mg, Mn, Na, P, Si, and Ti) and trace (Ba, Sr, and Zr) element concentrations were measured on the fjord surface and river suspended sediment samples by Inductively Coupled Plasma-Atomic Emission Spectrometry (ICP-AES). Here, we evaluate the ability of the lithogenic elements Al, Fe, K, Mn, Ti, and Zr to reconstruct sediment provenance. The other elements were not considered as provenance indicators as their concentrations within fjord sediments are affected by variations in productivity (Ca, Mg, P, Si, Ba, and Sr) or salinity (Na) (Boyle, 2001; Raitzsch et al., 2010; Bertrand et al., 2012b; Faust et al., 2014; Liguori et al., 2016; Liu et al., 2020). All samples were prepared using the Li Metaborate fusion technique to ensure the complete dissolution of sediment, including refractory minerals such as zircon (Murray et al., 2000). ICP-AES analysis was performed at Ghent University (Varian 720-ES) and Université Libre de Bruxelles (Thermo Scientific iCAP^{TM} 7000). Sample preparation consisted in mixing 200 ± 0.5 mg of Li-metaborate/Li-tetraborate (80:20 wt%) or Li-metaborate/Li-bromide (98.50:1.50 wt%) with 50 ± 0.5 mg of sediment in a Pt:Au crucible. To fuse the mixture, the crucible was placed in a muffle furnace for 12 min at 1,050°C. The resulting glass bead was allowed to cool down for 2 min. It was then transferred into a 50 mL beaker containing 25 mL of ultrapure HNO_3 (5%). This solution was magnetically stirred for 60 to 90 min to dissolve the glass bead. Afterward, the solution was filtered (0.45 μm GHP membrane) and 5 mL was pipetted into a centrifuge tube containing 35 mL of ultrapure HNO_3 (5%). The dilution factor (∼4,000×) was calculated from the precise weight of sediment used for fusion. The inorganic geochemical data is presented as **Supplementary Material** (**Supplementary Table 1**).

Element concentrations were analyzed in terms of Al-based log-ratios (Weltje and Tjallingii, 2008; Bertrand et al., 2012b; Weltje, 2012). Al is useful as a normalizer since it occurs in comparable concentrations in most plutonic and metamorphic rocks (Calvert et al., 2001; McLennan et al., 2003), and is relatively independent of grain size and provenance (Bertrand et al., 2012b). This is confirmed for Patagonian bedrock and river sediments by Liu et al. (2019, 2020). The precision on all elemental ratios was better than 1%, except for K/Al (better than 2%), and Zr/Al (better than 4%) (Bertrand et al., 2012b).

Grain Size

Grain size was determined on the terrigenous fraction of the sediment using a Malvern Mastersizer 3000 laser diffraction particle size analyzer. To isolate the terrigenous fraction, samples were treated with boiling H_2O_2 (2 mL, 30%), HCl (1 mL, 10%) and NaOH (1 mL, 2 N), to remove organic matter, carbonates and biogenic silica. The samples were then boiled with $(NaPO_3)_6$ (1 mL, 2%) to prevent flocculation and continuous ultrasounds (10%) were used during analysis. A stirrer (2,500 rpm) kept the samples in suspension. The grain-size distributions were measured three times during 12 s per sample. The mode of the distributions was calculated using the Mastersizer 3000 v3.62 software. The grain size of sample RW19-05 (Bravo River) could not be analyzed due to a limited sample amount.

Statistical Analysis

Principal component analysis was carried out using XLSTAT 2016 after log-transforming the variables. Magnetic susceptibility and inorganic geochemistry were used as active variables, and the fjord surface sediment samples as active observations, to construct the principal component model. The grain-size mode was then projected as a supplementary variable, and the river suspended sediment samples as supplementary observations, in the principal component biplot.

To facilitate data interpretation, the fjord surface sediment dataset (n = 21) was split into six subsets based on sample location: (1) head of Martínez Channel and Steffen Fjord (n = 4), (2) head of Baker Channel and Jorge Montt Fjord (n = 5), (3) distal part of Martínez Channel (n = 6), (4) distal part of Baker Channel (n = 5), (5)

Troya Channel (n = 1), and (6) Mitchell Fjord (n = 1) (**Figure 2**). Note that sample St4 is located downstream of the confluence of Baker and Martínez channels, and thus belongs to both the distal Baker Channel and distal Martínez Channel datasets.

RESULTS

River Suspended Sediment Concentrations

Suspended sediment concentrations measured in summer 2019 vary by a magnitude of ∼50 over the four studied rivers. Huemules (57.2 mg/L) and Baker (35.8 mg/L) rivers have significantly higher suspended sediment concentrations than Pascua (5.2 mg/L) and Bravo (1.1 mg/L) rivers.

Magnetic Susceptibility

Magnetic susceptibility varies by a factor of ∼seven between the four river suspended sediment samples (**Figure 3**). Suspended sediments from NPI-fed rivers, i.e., Huemules and Baker, have distinctly higher values (508 and 609 . 10^{-6} m^3/kg, respectively) than those from the SPI-fed Pascua River (294 . 10^{-6} m^3/kg). On the extreme end of the spectrum, suspended sediments from Bravo River have a magnetic susceptibility of 2,137 . 10^{-6} m^3/kg (**Figure 3**).

A similar contrast in magnetic susceptibility is discernible between samples from the heads of the Baker-Martínez fjord system. Fjord surface sediment samples from the head of Martínez Channel and Steffen Fjord have relatively high values between 603 and 990 . 10^{-6} m^3/kg, whereas samples from the head of Baker Channel and Jorge Montt Fjord have significantly lower values varying between 249 and 284 . 10^{-6} m^3/kg

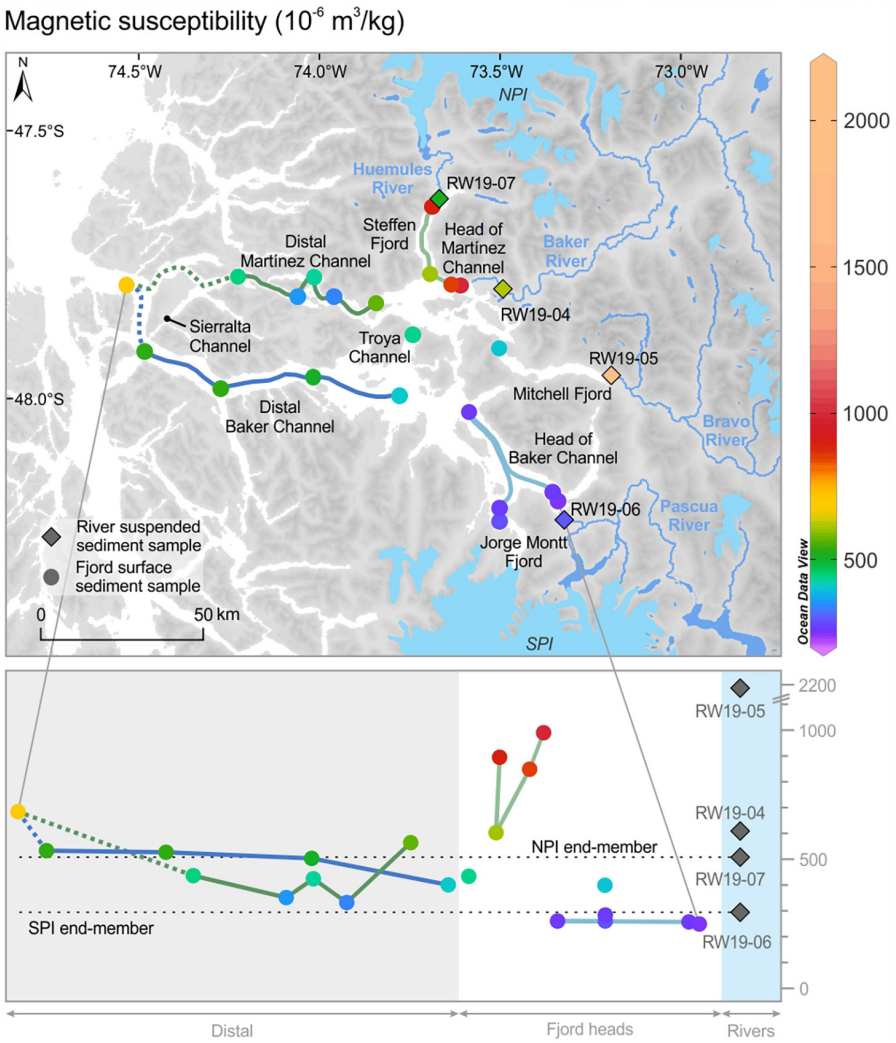

FIGURE 3 | Spatial variability in the magnetic susceptibility of the fjord and river sediment samples. The colored lines between the fjord samples represent the four subsets with n > 1 (**Figure 2**). In the bottom panel, the fjord samples are plotted according to longitude. The provenance end-members are defined by the RW19-07 (NPI) and RW19-06 (SPI) river sediment samples.

(**Figure 3**). In Mitchell Fjord, the surface sediment sample has a significantly lower magnetic susceptibility (399 . 10^{-6} m^3/kg) compared to the suspended sediment sample from the river that flows into it (Bravo River; RW19-05; 2,137 . 10^{-6} m^3/kg; **Figure 3**).

The relation between magnetic susceptibility and distance differs between channels (**Figure 3**). Whereas the magnetic susceptibility of the surface sediment samples is highly variable and does not have a clear trend with distance in Martínez Channel, it consistently increases westward in Baker Channel.

Inorganic Geochemistry

The principal component analysis of the fjord surface sediment samples (**Figure 4**) shows two principal components explaining 85% of the variance (PC1: 52%, and PC2: 33%). The first principal component mostly reflects the compositional difference between proximal (negative loadings) and distal (positive loadings) samples. The second principal component, on which magnetic susceptibility and log(Ti/Al) have the highest loadings, mostly separates the Martínez Channel samples (top two quadrants), from those from Baker Channel (bottom quadrants).

The river suspended sediment sample from Pascua River (RW19-06) has a geochemical composition similar to the fjord samples from the head of Baker Channel, and those from Huemules and Bravo rivers (RW19-07 and RW19-05) to the fjord samples from the head of Martínez Channel. The sample from Baker River (RW19-04) is similar to the fjord samples from the distal part of Martínez Channel (**Figure 4**).

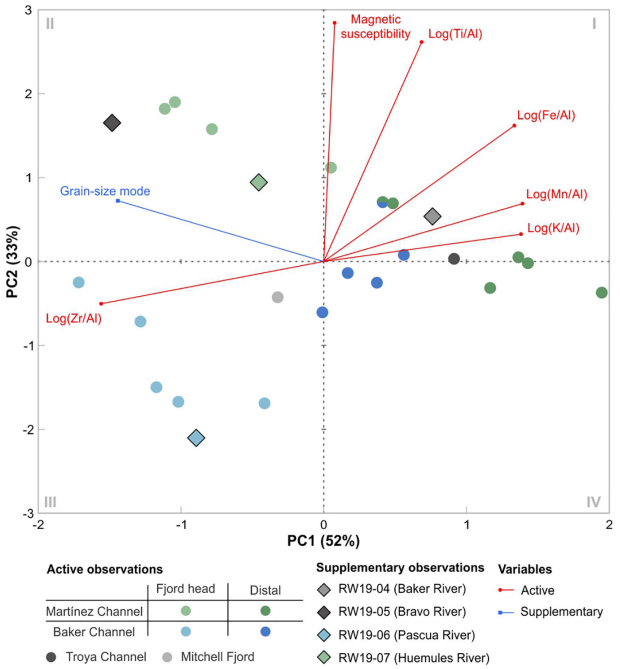

FIGURE 4 | Principal component biplot of the magnetic susceptibility and geochemical composition (active variables) of the fjord surface sediment samples (active observations) and projected river suspended sediment samples (supplementary observations). The grain-size mode is projected in the biplot (supplementary variable).

Grain Size

The river suspended sediment samples have a unimodal grain-size distribution with a mode that is consistently between 3.60 to 3.64 μm (**Figures 5A**, **6**). The proximal fjord surface sediment samples (<5 km from the river mouth) also display a fine silt mode but its exact value (4–7 μm) is consistently higher than that of the river suspended sediment samples (**Figures 5B**, **6**). In addition, most of the proximal fjord surface sediment samples have a second mode in the medium silt to fine sand fraction (15–100 μm; **Figure 5B**). The distal fjord surface sediment samples (>5 km from the river mouth) have a grain-size mode and distribution that are comparable to those of the river suspended sediment samples, with a mode averaging at 3.73 ± 0.48 μm (**Figures 5C**, **6**). In the distal sections of both the Martínez and Baker channels, the grain-size mode decreases toward the Pacific Ocean, however, the grain-size mode of the most westward sample deviates from this trend (**Figure 6**).

DISCUSSION

Magnetic Susceptibility and Inorganic Geochemistry as Provenance Tracers

This section evaluates whether magnetic susceptibility and/or inorganic geochemistry can be used to trace sediment provenance, i.e., to distinguish between sediments derived from the NPI and from the SPI. In addition to analyzing the fjord surface sediment samples, the four river suspended sediment samples are considered as potential provenance end-members, hereafter referred to as "NPI end-member" and "SPI end-member."

The first requirement for inorganic geochemical elements to work as reliable provenance indicators is the absence of biological control on their concentrations. For the surface sediment samples from the Baker-Martínez fjord system, this lack of biological control is shown by the lack of significant correlation between the Al-based log ratios of Fe, K, Mn, Ti, and Zr and organic carbon, biogenic opal and $CaCO_3$ contents (**Supplementary Table 2**).

In the principal component biplot of the fjord surface sediment samples (**Figure 4**), the first principal component (PC1, 52%) seems to reflect variations in distance within the fjords, to which grain size is associated. The second principal component (PC2, 33%) differentiates the sediments at the head of Martínez Channel and Steffen Fjord from those at the head of Baker Channel and Jorge Montt Fjord. This suggests that PC2 is able to differentiate sediments of NPI origin (PC2 > 0) from sediments derived from the lithologies underlying the SPI (PC2 < 0). The PC2 scores of the Huemules (RW19-07) and Pascua (RW19-06) river suspended sediment samples, which represent rivers entirely fed by the NPI and SPI, respectively, confirm this differentiation (**Figure 4**). Therefore, we suggest

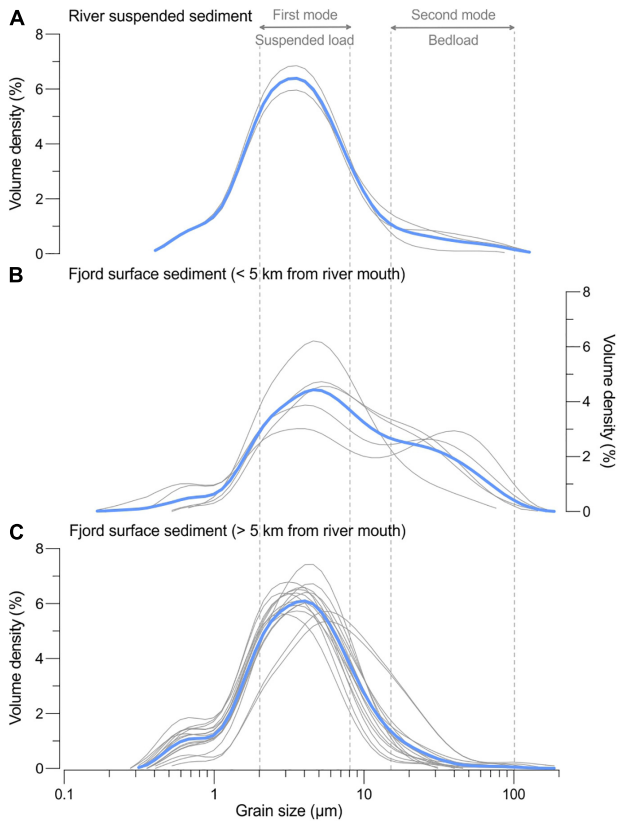

FIGURE 5 | Grain-size distributions of **(A)** the river suspended sediment samples, **(B)** the fjord surface sediment samples located less than 5 km from a river mouth, and **(C)** the fjord surface sediment samples located more than 5 km from a river mouth. The distributions shown in blue represent the average grain-size distribution of each group.

that PC2 reflects sediment provenance. The observation that magnetic susceptibility and log(Ti/Al) both have high PC2 loadings (≥0.86) and low PC1 loadings (≤0.41) (**Figure 4**) additionally suggests that these two variables can serve as provenance tracers.

The contrast in magnetic susceptibility between sediments derived from the lithologies underlying the NPI and SPI is clearly visible in the values measured on the river suspended sediment samples and on the fjord surface sediment samples from the heads of Martínez and Baker channels (**Figure 3**). Samples from the rivers originating from NPI outlet glaciers (Baker River; RW19-04, and Huemules River; RW19-07) and those from the fjords in which these rivers discharge (head of Martínez Channel and Steffen Fjord) have consistently higher values than their SPI counterparts (**Figure 3**). This difference in magnetic susceptibility reflects the igneous nature of the bedrock underling the NPI (Patagonian Batholith) compared to that of the metamorphic basement under the SPI (Eastern Andean Metamorphic Complex). This is supported by (a) the generally higher abundance of magnetic minerals in magmatic rocks compared to metamorphosed sedimentary rocks (McEnroe et al., 2004; Direen et al., 2008), and (b) their distinct magnetic signatures on lithospheric magnetic anomaly maps (Maus et al., 2008; Michelena and Kilian, 2015). Although titanomagnetite, pyrrhotite, and ilmenite are generally considered as the main magnetic carriers in the Patagonian Batholith plutonic suite (Michelena and Kilian, 2015), it is unlikely that these dense and refractory minerals are transported in suspension in the regional rivers and fjords (Bertrand et al., 2012b). These minerals may, however, also occur as inclusions in fine-grained plagioclase (Scofield and Roggenthen, 1986; Andrews, 2008; Andrews et al., 2010), which can then be transported in suspension, as previously suggested for northern Patagonian fjord sediments (Ghazoui, 2011; Bertrand et al., 2012b). Alternatively, hornblende and biotite, which are relatively abundant in the Patagonian Batholith (Pankhurst et al., 1999; Sernageomin, 2003; Hervé et al., 2007) could also contribute to the high magnetic susceptibility of suspended sediments derived from the NPI.

As suggested by the principal component analysis results (**Figure 4**), log(Ti/Al) is one of the most powerful variables to differentiate between sediments derived from the NPI and SPI. The higher log(Ti/Al) signature of NPI-derived sediments is clearly supported by the composition of the Huemules (RW19-07) and Baker (RW19-04) river suspended sediments samples, and by that of surface sediment samples from the head of Martínez Channel and Steffen Fjord (**Figure 7**). Sediments derived from the SPI (RW19-06; Pascua River, and surface sediment samples from the head of Baker Channel and Jorge Montt Fjord) have consistently lower log(Ti/Al) values (**Figure 7**).

The geochemical distinction between sediments derived from the NPI and SPI is most probably related to the geochemical composition of the Patagonian Batholith and Eastern Andean Metamorphic Complex lithologies that are effectively eroded to produce the river sediments transported in suspension and eventually deposited into the fjords (**Figure 1** and **Table 1**; Liu et al., 2020). Although the Patagonian Batholith contains granite, granodiorite, diorite, tonalite, and gabbro, the geochemistry of RW19-07 (Huemules River) suggests that the composition of the Patagonian Batholith-derived sediment that reaches the Baker-Martínez fjord system is best represented by diorite and tonalite (**Supplementary Figure 1A**), in agreement with the occurrence of diorite and tonalite in the Baker and Huemules river watersheds (Parada et al., 1997; Pankhurst et al., 1999). This is supported by the composition of RW19-04 (Baker River), which also plots among the diorite and tonalite samples (**Supplementary Figure 1A**). Likewise, the Eastern Andean Metamorphic Complex consists of meta-sandstone and -mudstone, and the geochemistry of RW19-05 (Bravo River) and RW19-06 (Pascua River) suggests that the metamorphosed mudstones best represent the Eastern Andean Metamorphic Complex-derived sediment reaching the Baker-Martínez fjord system (**Supplementary Figure 1B**). This observation likely results from the grain size of the sediment produced by erosion of metamorphosed mudstone (fine) vs. sandstone (coarse), resulting in a higher contribution of sediment of meta-mudstone origin. Hence, we suggest that the NPI end-member is best represented by diorite and tonalite

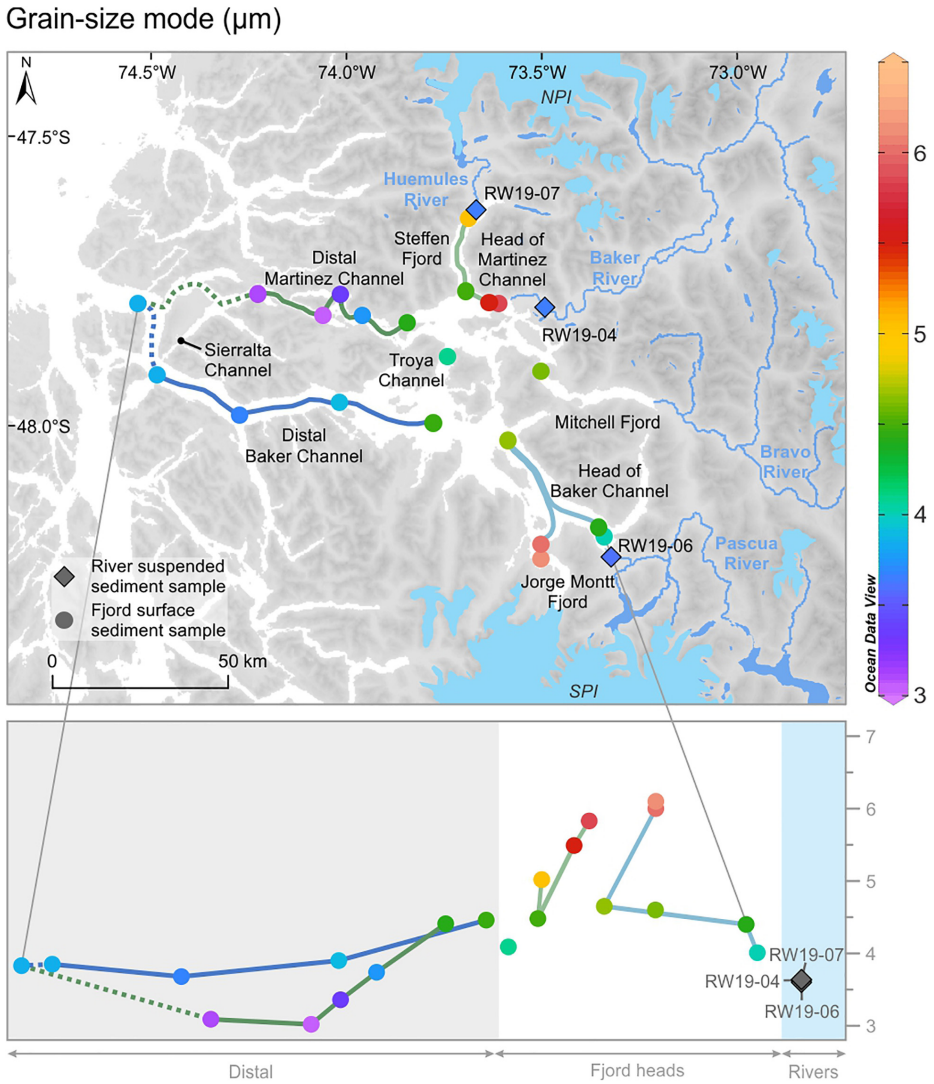

FIGURE 6 | Spatial variability in the grain-size mode of the fjord and river sediment samples. The colored lines between the fjord samples represent the four subsets with $n > 1$ (**Figure 2**). In the bottom panel, the fjord samples are plotted according to longitude.

from the Patagonian Batholith, and the SPI end-member by metamorphosed mudstones from the Eastern Andean Metamorphic Complex.

Our results suggest that the sediment derived from the NPI is more magnetic and richer in Ti than the sediment from the SPI (**Figure 8**). These differences result from the nature of the bedrock effectively eroded by NPI vs. SPI glaciers (**Figure 1**). Since the Huemules River directly originates from the NPI, sample RW19-07 was used to define the NPI end-member. Likewise, sample RW19-06 from Pascua River was used to define the SPI end-member. Sample RW19-04 from Baker River was not used to define the NPI end-member since Baker River also drains the Eastern Andean Metamorphic Complex in the eastern non-glaciated part of the watershed (**Figure 1** and **Table 1**; Liu et al., 2020), and is therefore not entirely representative of the NPI. Sample RW19-05 was not considered as a provenance end-member since the suspended sediment concentration in Bravo River (1.1 mg/L) is too low to accurately represent sediment transport toward the Baker-Martínez fjord system.

Spatial Variations in Grain Size and Its Influence on the Provenance Tracers

In this section, we evaluate whether grain size variations limit the ability of magnetic susceptibility and inorganic geochemistry, i.e., log(Ti/Al), to track sediment provenance throughout the Baker-Martínez fjord system. To serve this purpose, the grain-size mode was projected in the principal component biplot of the fjord surface sediment samples (**Figure 4**). The results clearly show that grain-size mode has a strong loading on PC1 (loading = −0.87) but not on PC2 (loading = 0.24), suggesting that sediment provenance across the Baker-Martínez fjord system is relatively independent of grain size variations.

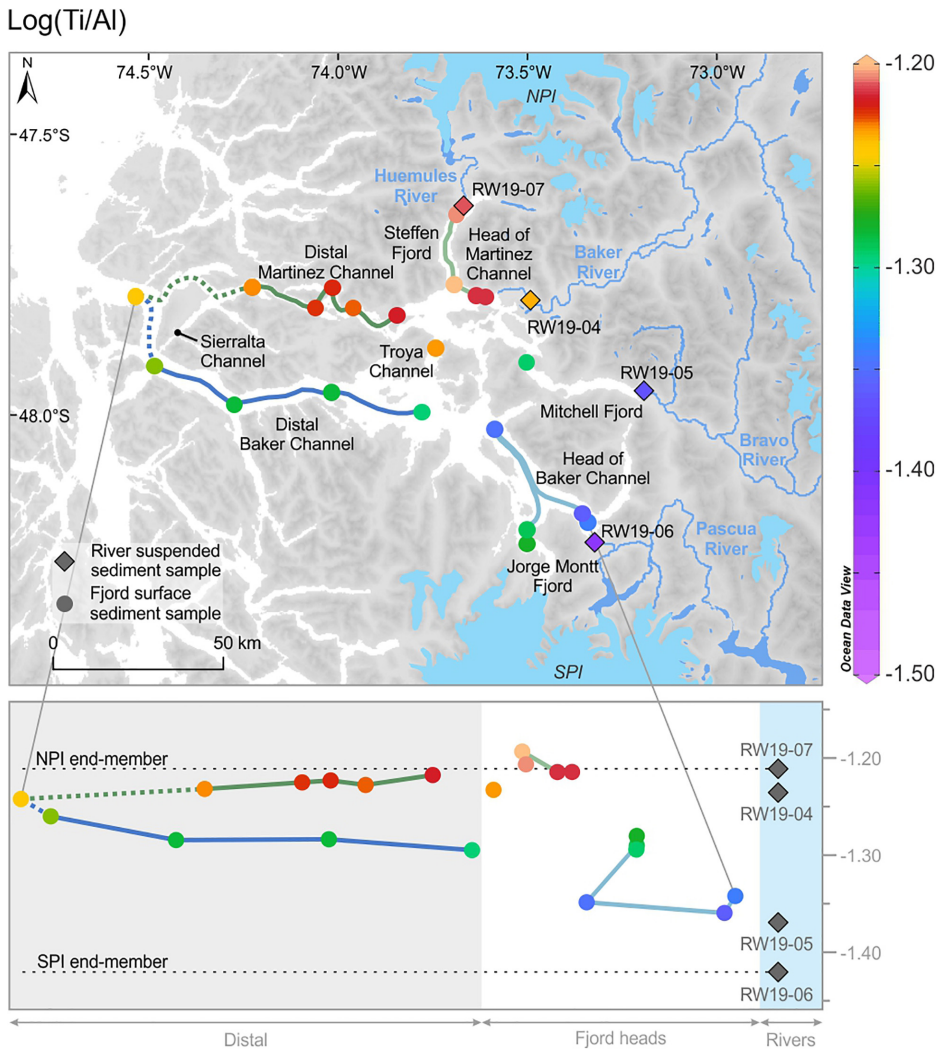

FIGURE 7 | Spatial variability in log(Ti/Al) of the fjord and river sediment samples. The colored lines between the fjord samples represent the four subsets with $n > 1$ (**Figure 2**). In the bottom panel, the fjord samples are plotted according to longitude. Error bars are smaller than the size of the symbols. The provenance end-members are defined by the RW19-07 (NPI) and RW19-06 (SPI) river sediment samples.

Although variations in magnetic susceptibility and log(Ti/Al) across the entire Baker-Martínez fjord system seem to reflect sediment provenance (section "Magnetic Susceptibility and Inorganic Geochemistry as Provenance Tracers"), variations in these two indicators within specific fjords appear influenced by grain size, as suggested by the spread of these samples along PC1 (**Figure 4**). The positive within-fjord relations between magnetic susceptibility and grain-size mode are confirmed for Martínez Channel and Steffen Fjord ($r = 0.91$; $p < 0.01$; $n = 10$) and for the head of Baker Channel and Jorge Montt Fjord ($r = 0.79$; $p = 0.11$; $n = 5$). In these two cases, coarser samples are more magnetic and grain size seems to be the primary factor controlling their magnetic susceptibility values, in agreement with the findings of Snowball et al. (1999), Sandgren and Snowball (2001), Bertrand et al. (2012b), Shin et al. (2020), and Piret et al. (2021). In the distal part of Baker Channel, however, the relation between magnetic susceptibility and grain-size mode is negative and insignificant ($r = -0.68$; $p = 0.21$; $n = 5$), which suggests that, for these samples, provenance plays a more important role in determining magnetic susceptibility than grain size.

A similar influence of grain size on log(Ti/Al) can be observed in Martínez Channel and Steffen Fjord ($r = 0.62$; $p = 0.05$; $n = 10$) and for the head of Baker Channel and Jorge Montt Fjord ($r = 0.92$; $p < 0.05$; $n = 5$). In these two cases, log(Ti/Al) is positively correlated with grain-size mode, in agreement with the results of Bertrand et al. (2012b) who suggest that Ti/Al in Patagonian fjord sediments is primarily controlled by grain size and hydrodynamic sorting of minerals. As with magnetic susceptibility, the relation between log(Ti/Al) and grain-size mode is weakly negative and insignificant in the distal part of Baker Channel ($r = -0.48$, $p = 0.41$; $n = 5$), where grain size is relatively stable (**Figure 6**). This again suggests that, in the distal

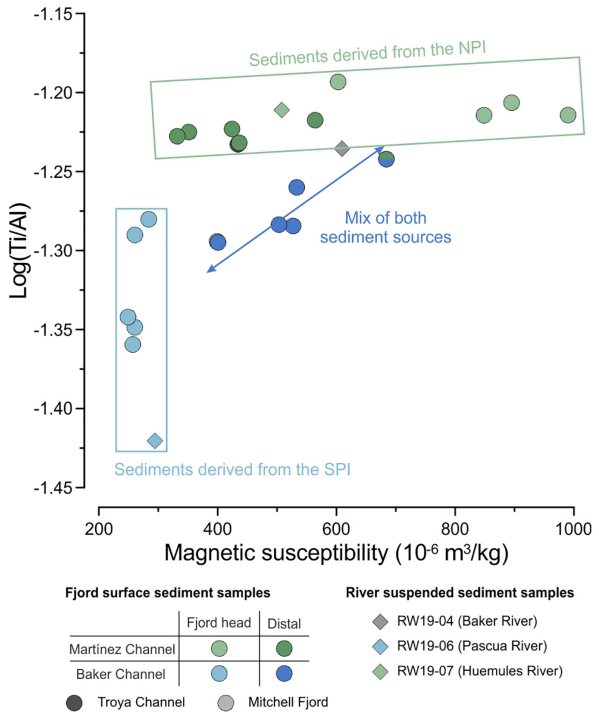

FIGURE 8 | Log(Ti/Al) vs. magnetic susceptibility of the fjord and river sediment samples. The green and blue rectangles represent sediments derived from the Northern (NPI) and Southern (SPI) Patagonian Icefields, respectively. RW19-05 is considered as an outlier (RESULTS section "Magnetic Susceptibility") and was thus not included. Error bars are smaller than the size of the symbols.

part of Baker Channel, provenance plays a more important role than grain size in controlling log(Ti/Al).

To summarize, within fjords fed by meltwater from one icefield, such as Martínez Channel, the head of Baker Channel and Steffen and Jorge Montt fjords, magnetic susceptibility and log(Ti/Al) are controlled by grain size. However, in fjords where sediments are derived from both icefields, i.e., the distal part of Baker Channel, magnetic susceptibility and log(Ti/Al) are primarily driven by sediment provenance.

Sediment Provenance Quantification

Throughout the distal part of Baker Channel, magnetic susceptibility and log(Ti/Al) of the fjord surface sediment samples increase westward (**Figures 3**, **7**), from values roughly halfway between the end-members toward values similar to the NPI end-member, whereas the grain-size mode decreases by ∼1 μm (**Figure 6**). These increasing trends can only be explained by the mixing, in different proportions, of sediments derived from the NPI and SPI.

A linear mixing model based on log(Ti/Al), with RW19-07 (Huemules River) and RW19-06 (Pascua River) as NPI and SPI end-members, was applied to quantitatively estimate the NPI vs. SPI sediment contributions to the distal part of Baker Channel (**Figure 9**). Magnetic susceptibility was not included in the model since the samples in the distal part of Baker Channel exceed the end-member limits (**Figure 3**), suggesting that factors other than provenance influence the exact magnetic susceptibility values. Therefore, the ability of magnetic susceptibility to differentiate between sediments derived from the NPI and SPI remains qualitative.

The provenance quantification results suggest that the fjord sediment samples from the distal part of Baker Channel derive from both the NPI and SPI, and that the NPI is the dominant source (60–85%) throughout the fjord (**Figure 9**). The higher relative input of NPI-derived sediment is in agreement with (1) the larger drainage area of the Huemules and lower Baker river watersheds, which are the main contributors of NPI-related sediment to the Baker-Martínez fjord system, compared to the lower Pascua River watershed and Jorge Montt Glacier (**Table 1**), (2) the higher combined mean annual discharge of Huemules (121 m^3/s) and Baker (1,133 m^3/s) rivers vs. Pascua River (753 m^3/s) and Jorge Montt Glacier (129 m^3/s) (Pantoja et al., 2011; Pryer et al., 2020), (3) the higher suspended sediment concentrations in Huemules (57.2 mg/L) and Baker (35.8 mg/L) rivers compared to Pascua River (5.2 mg/L), and (4) the satellite-derived average spring-summer suspended sediment distribution throughout the Baker-Martínez fjord system (**Figure 2**).

The provenance quantification also suggests that the proportion of NPI-derived sediments increases westward from 60 to 85% throughout the distal part of Baker Channel (**Figure 9**). The first location at which mixing between the two sources can occur is around Troya Channel, probably slightly to the west of station St8, as suggested by the surface turbidity map (**Figure 2**). The high amount of NPI-derived sediments at St8 and St7 suggests the presence of an effective southward transport of suspended sediments from Martínez Channel to Baker Channel, especially in summer when river discharge and suspended sediment concentrations are maximum (Aiken, 2012; Amann et al., Submitted). Although the proportion of NPI vs. SPI-derived sediment does not significantly change between stations St8 and St6, the proportion of NPI-derived sediment increases to about 80% at stations St5 and St4, suggesting an additional input of NPI-derived sediment via Sierralta Channel and the western end of Martínez Channel (**Figure 9**), in agreement with variations in surface turbidity values (**Figure 2**).

It is worth mentioning that the proportions of NPI and SPI-derived sediments shown in **Figure 9** are relative, i.e., an increase in sediment input from one of the sources results in an apparent decrease in the contribution of the other source. This comment is valid for both spatial changes inferred from surface sediment samples, and for temporal changes inferred from sediment cores. Interpreting changes in sediment provenance to the distal part of Baker Channel through time therefore requires considering possible changes in the two sources. In addition, an increase in the input of sediments derived from the Eastern Andean Metamorphic Complex could also be caused by processes independent of meltwater input, such as intense precipitation in the eastern part of the lower Baker River watershed (**Figure 1**). This would complicate the interpretation of the provenance tracers in terms of variations in meltwater input since sediment derived from the eastern part of the lower Baker River watershed is compositionally similar to SPI-derived sediments.

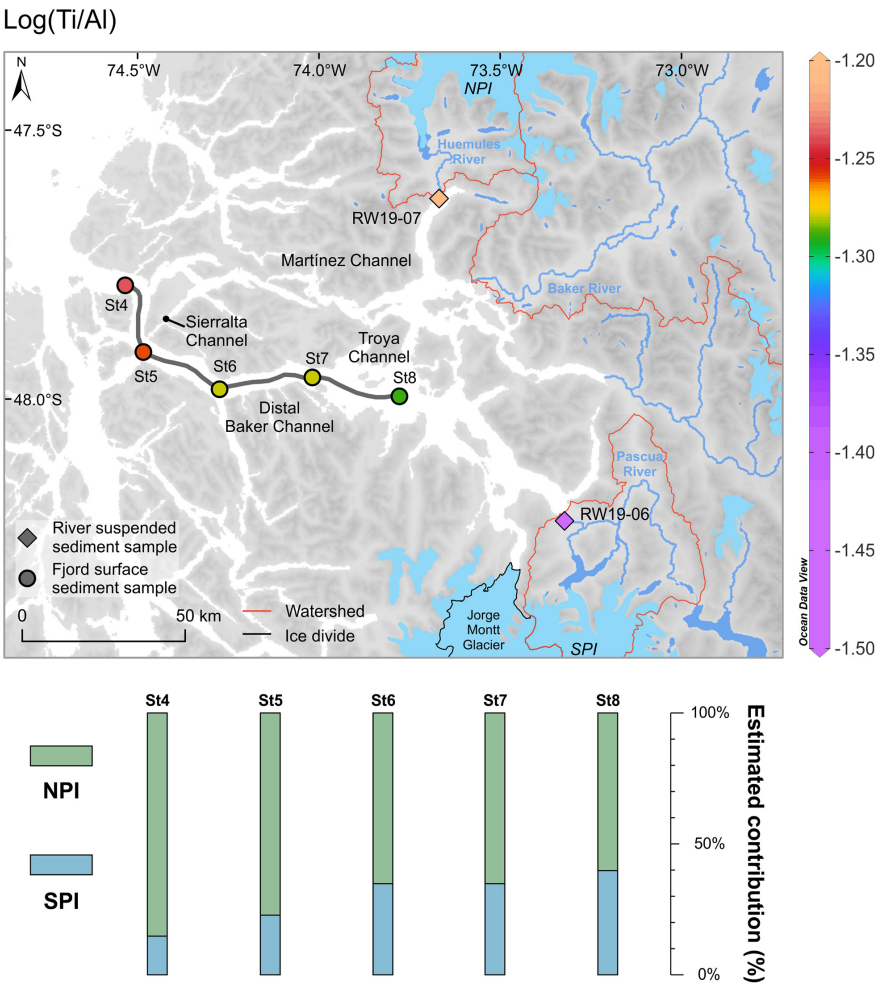

FIGURE 9 | Relative contributions of NPI- and SPI-derived sediments to the distal part of Baker Channel, as estimated by linear mixing based on log(Ti/Al). NPI sediments mostly originate from the Huemules and lower Baker River watersheds, whereas SPI sediments mostly represent sediment input from Jorge Montt Glacier and from the lower Pascua River watershed. RW19-07 and RW19-06 were used to define the NPI and SPI end-members.

A limitation of our study is that the sediment end-members were entirely defined using single river suspended sediment samples collected in summer. Although summer corresponds to the peak in meltwater contribution and sediment input (Amann et al., Submitted), this characterization of the sediment sources does not take into account the possible seasonal changes in the composition of the sediment reaching the fjords. The good agreement between the composition of the river suspended sediments and that of the fjord surface sediment samples from the heads of Martínez and Baker channels, which represent year-round sedimentation (**Figure 7**), however, suggests that seasonal variations in sediment composition are limited and/or that most of the fjord sediments are supplied during the meltwater season in summer. Collecting river suspended sediment samples during all four seasons and over multiple years could contribute to a more accurate definition of the end-members, and ultimately to a more robust quantitative mixing model. The magnetic and geochemical contrasts between the end-members, however, are unlikely to change since they reflect the clear lithological differences that characterize the NPI vs. SPI watersheds.

CONCLUSION

Our results suggest that magnetic susceptibility and log(Ti/Al) can be used as provenance tracers to differentiate NPI- from SPI-derived sediments throughout the Baker-Martínez fjord system, but that only log(Ti/Al) can provide quantitative estimates of the proportions of sediment derived from each icefield. The ability of these tracers to distinguish between sediment derived from each icefield reflects the high magnetic susceptibility and Ti content of the igneous rocks underlying the NPI, compared to the weakly magnetic and Ti-poor metamorphic bedrock that underlies the SPI. Within fjords fed by meltwater from only one icefield, e.g., Martínez Channel, the head of Baker Channel and Steffen and Jorge Montt fjords, variations in magnetic susceptibility and log(Ti/Al) are mostly driven by changes in grain size, which in turn reflect the progressive settling of sediment from the hypopycnal plume. In fjords receiving sediments from both icefields, such as the distal part of Baker Channel, magnetic susceptibility and log(Ti/Al) can serve as qualitative and quantitative tracers of sediment provenance, respectively.

We suggest that log(Ti/Al), and to a lesser extent magnetic susceptibility, can be applied to long sediment cores from the Baker-Martínez fjord system to reconstruct relative variations in sediment input from each icefield, which may in turn be interpreted as changes in river discharge and/or glacier mass balance. To do so, sediment cores must come from a fjord receiving sediment from both sources, such as the distal part of Baker Channel, and grain size must remain relatively stable. Although the results presented here are specific to the Baker-Martínez fjord system, they suggest that cost-effective parameters such as sediment inorganic geochemistry, can be used to reconstruct sediment provenance with a relatively good precision, if the main processes affecting the concentration of each element are adequately understood.

DATA AVAILABILITY STATEMENT

The original contributions presented in the study are included in the article/**Supplementary Material**, further inquiries can be directed to the corresponding author.

AUTHOR CONTRIBUTIONS

MT conducted all laboratory analyses on the fjord surface sediment samples, processed the data, interpreted the results, and wrote the manuscript. SB designed this study, obtained funding, led the field expedition during which the river suspended sediment samples were collected, coordinated the collaborative research activities, and wrote the manuscript with MT. BA and DL collected the river suspended sediment samples and measured river suspended sediment concentrations. BA analyzed the grain size, magnetic susceptibility, and inorganic geochemistry of the river suspended sediment samples together with MT. JP provided the CIMAR 20 Fiordos samples. CL co-organized the COPAS Sur-Austral 2014 cruise and provided the CO14 fjord samples. All authors contributed to the interpretation of the results and to the writing of the manuscript, and all approved the final version.

FUNDING

This research was funded by the UGent project HYDROPROX (01N02216). Some of the sediment samples used in this study were collected with funding from the Chilean National Oceanographic Committee (CONA Grant C20F1404) and from the COPAS Sur-Austral Center.

ACKNOWLEDGMENTS

We thank the captain and crew of the R/V Sur-Austral for their help during sample collection and Lorena Rebolledo for splitting the CO14 samples. We are grateful to Dr. Charles Nittrouer (University of Washington, School of Oceanography and Department of Earth and Space Sciences) and to Dr. Carlos Moffat (University of Delaware) for collecting JM1 and JM7, and to Ellen De Wilde for analyzing the grain size and magnetic susceptibility of these samples. We also thank the PISCES team from the University of Bristol for providing the PI-FC17-S8 sediment core, Loic Piret for his help during RW19 sample collection and for constructive discussions, Veerle Vandenhende for operating the ICP-AES, and Dr. Elke Vandekerkhove for providing valuable suggestions on an earlier version of this manuscript. This work was part of the first author's MSc thesis at Ghent University.

SUPPLEMENTARY MATERIAL

The Supplementary Material for this article can be found online at: https://www.frontiersin.org/articles/10.3389/fmars.2021.612309/full#supplementary-material

REFERENCES

Aiken, C. M. (2012). Seasonal thermal structure and exchange in Baker Channel. *Chile. Dynamics Atmospheres Oceans* 58, 1–19. doi: 10.1016/j.dynatmoce.2012.07.001

Amann, B., Bertrand, S., Garreton, C. A., and Reid, B. (Submitted). Seasonal variations in the origin of river sediments (Baker River, Chile, 48°S): a pre-requisite for climate and hydrological reconstructions. *J. Geophys. Res.: Earth Surface*

Andrews, J. T. (2008). The role of the Iceland Ice Sheet in the North Atlantic during the late Quaternary: a review and evidence from Denmark Strait. *J. Quaternary Sci.* 23, 3–20. doi: 10.1002/jqs.1142

Andrews, J. T., Jennings, A. E., Coleman, G. C., and Eberl, D. D. (2010). Holocene variations in mineral and grain-size composition along the East Greenland glaciated margin (ca 67°–70°N): local versus long-distance sediment transport. *Quaternary Sci. Rev.* 29, 2619–2632. doi: 10.1016/j.quascirev.2010.06.001

Augustsson, C., and Bahlburg, H. (2003). Active or passive continental margin? Geochemical and Nd isotope constraints of metasediments in the backstop of a pre-Andean accretionary wedge in southernmost Chile (46°30′–48°30′S). *Geol. Soc. Lond. Special Publications* 208, 253–268. doi: 10.1144/GSL.SP.2003.208.01.12

Bertrand, S., Hughen, K., Sepúlveda, J., and Pantoja, S. (2014). Late Holocene covariability of the southern westerlies and sea surface temperature in northern Chilean Patagonia. *Quaternary Sci. Rev.* 105, 195–208. doi: 10.1016/j.quascirev.2014.09.021

Bertrand, S., Hughen, K. A., Lamy, F., Stuut, J. B., Torrejon, F., and Lange, C. B. (2012a). Precipitation as the main driver of Neoglacial fluctuations of Gualas glacier, Northern Patagonian Icefield. *Clim. Past* 8, 519–534. doi: 10.5194/cp-8-519-2012

Bertrand, S., Hughen, K. A., Sepúlveda, J., and Pantoja, S. (2012b). Geochemistry of surface sediments from the fjords of Northern Chilean Patagonia (44–47°S): spatial variability and implications for paleoclimate reconstructions. *Geochim. Cosmochim. Acta* 76, 125–146. doi: 10.1016/j.gca.2011.10.028

Bertrand, S., Lange, C. B., Pantoja, S., Hughen, K., Van Tornhout, E., and Wellner, J. S. (2017). Postglacial fluctuations of Cordillera Darwin glaciers (southernmost Patagonia) reconstructed from Almirantazgo fjord sediments. *Quaternary Sci. Rev.* 177, 265–275. doi: 10.1016/j.quascirev.2017.10.029

Bianchi, T. S., Arndt, S., Austin, W. E. N., Benn, D. I., Bertrand, S., Cui, X., et al. (2020). Fjords as aquatic critical zones (ACZs). *Earth-Sci. Rev.* 203:103145. doi: 10.1016/j.earscirev.2020.103145

Bloemsma, M. R., Zabel, M., Stuut, J. B. W., Tjallingii, R., Collins, J. A., and Weltje, G. J. (2012). Modelling the joint variability of grain size and chemical

composition in sediments. *Sedimentary Geol.* 280, 135–148. doi: 10.1016/j.sedgeo.2012.04.009

Boex, J., Fogwill, C., Harrison, S., Glasser, N. F., Hein, A., Schnabel, C., et al. (2013). Rapid thinning of the late Pleistocene Patagonian Ice Sheet followed migration of the Southern Westerlies. *Sci. Rep.* 3:2118. doi: 10.1038/srep02118

Boisier, J. P., Alvarez-Garretón, C., Cepeda, J., Osses, A., Vásquez, N., and Rondanelli, R. (2018). CR2MET: a high-resolution precipitation and temperature dataset for hydroclimatic research in Chile. *Geophys. Res. Abstracts* 20:19739.

Boldt, K. V. (2014). *Fjord Sedimentation During the Rapid Retreat of Tidewater Glaciers: Observations and Modeling*. Ph.D. thesis, Washington, WA: University of Washington.

Bonneau, L., Toucanne, S., Bayon, G., Jorry, S. J., Emmanuel, L., and Silva Jacinto, R. (2017). Glacial erosion dynamics in a small mountainous watershed (Southern French Alps): a source-to-sink approach. *Earth Planetary Sci. Lett.* 458, 366–379. doi: 10.1016/j.epsl.2016.11.004

Boyle, J. F. (2001). "Inorganic geochemical methods in paleolimnology," in *Tracking Environmental Change Using Lake Sediments Volume 2: Physical and Geochemical Methods*, eds W. M. Last and J. P. Smol (Dordrecht: Kluwer Academic Publishers), 83–141.

Calvert, S. E., Pedersen, T. F., and Karlin, R. E. (2001). Geochemical and isotopic evidence for post-glacial palaeoceanographic changes in Saanich Inlet, British Columbia. *Mar. Geol.* 174, 287–305. doi: 10.1016/S0025-3227(00)00156-0

Caniupán, M., Lamy, F., Lange, C. B., Kaiser, J., Kilian, R., Arz, H. W., et al. (2014). Holocene sea-surface temperature variability in the Chilean fjord region. *Quaternary Res.* 82, 342–353. doi: 10.1016/j.yqres.2014.07.009

Cowan, E. A., and Powell, R. D. (1990). Suspended sediment transport and deposition of cyclically interlaminated sediment in a temperate glacial fjord, Alaska, U.S.A. *Geol. Soc. Lond. Special Publications* 53, 75–89. doi: 10.1144/GSL.SP.1990.053.01.04

Davies, B. J., Darvill, C. M., Lovell, H., Bendle, J. M., Dowdeswell, J. A., Fabel, D., et al. (2020). The evolution of the Patagonian Ice Sheet from 35 ka to the present day (PATICE). *Earth-Sci. Rev.* 204:103152. doi: 10.1016/j.earscirev.2020.103152

Direen, N. G., Pfeiffer, K. M., and Schmidt, P. W. (2008). Strong remanent magnetization in pyrrhotite: a structurally controlled example from the Paleoproterozoic Tanami orogenic gold province, northern Australia. *Precambrian Res.* 165, 96–106. doi: 10.1016/j.precamres.2008.05.007

Dussaillant, J. A., Buytaert, W., Meier, C., and Espinoza, F. (2012). Hydrological regime of remote catchments with extreme gradients under accelerated change: the Baker basin in Patagonia. *Hydrological Sci. J.* 57, 1530–1542. doi: 10.1080/02626667.2012.726993

Faúndez, V., Hervé, F., and Lacassie, J. P. (2002). Provenance and depositional setting of pre-Late Jurassic turbidite complexes in Patagonia. *Chile. N. Z. J. Geol. Geophys.* 45, 411–425. doi: 10.1080/00288306.2002.9514982

Faust, J. C., Knies, J., Slagstad, T., Vogt, C., Milzer, G., and Giraudeau, J. (2014). Geochemical composition of Trondheimsfjord surface sediments: sources and spatial variability of marine and terrigenous components. *Continental Shelf Res.* 88, 61–71. doi: 10.1016/j.csr.2014.07.008

Fick, S. E., and Hijmans, R. J. (2017). WorldClim 2: new 1-km spatial resolution climate surfaces for global land areas. *Int. J. Climatol.* 37, 4302–4315. doi: 10.1002/joc.5086

Fontijn, K., Lachowycz, S. M., Rawson, H., Pyle, D. M., Mather, T. A., Naranjo, J. A., et al. (2014). Late Quaternary tephrostratigraphy of southern Chile and Argentina. *Quaternary Sci. Rev.* 89, 70–84. doi: 10.1016/j.quascirev.2014.02.007

Foresta, L., Gourmelen, N., Weissgerber, F., Nienow, P., Williams, J. J., Shepherd, A., et al. (2018). Heterogeneous and rapid ice loss over the Patagonian Ice Fields revealed by CryoSat-2 swath radar altimetry. *Remote Sensing Environ.* 211, 441–455. doi: 10.1016/j.rse.2018.03.041

Garreaud, R., Lopez, P., Minvielle, M., and Rojas, M. (2013). Large-Scale control on the patagonian climate. *J. Clim.* 26, 215–230. doi: 10.1175/JCLI-D-12-00001.1

Ghazoui, Z. (2011). *Sédimentation Récente Dans les Fjords de Patagonie Chilienne: Caractérisation des Sources Sédimentaires et Implication Pour la Reconstitution des Changements Environnementaux au Cours de l'Holocène*. Master's thesis, Brussels, BE: Université Libre de Bruxelles.

Gómez, J., Schobbenhaus, C., and Montes, N. E. (2019). *Geological Map of South America 2019. Scale 1:5 000 000. Commission for the Geological Map of the World (CGMW), Colombian Geological Survey and Geological Survey of Brazil*. Paris: Colombian Geological Survey and Geological Survey of Brazil.

González, H. E., Castro, L. R., Daneri, G., Iriarte, J. L., Silva, N., Tapia, F., et al. (2013). Land-ocean gradient in haline stratification and its effects on plankton dynamics and trophic carbon fluxes in Chilean Patagonian fjords (47-50°S). *Prog. Oceanogr.* 119, 32–47. doi: 10.1016/j.pocean.2013.06.003

Hervé, F., Calderón, M., and Faúndez, V. (2008). The metamorphic complexes of the Patagonian and Fuegian Andes. *Geol. Acta* 6, 43–53.

Hervé, F., Pankhurst, R. J., Fanning, C. M., Calderon, M., and Yaxley, G. M. (2007). The South Patagonian batholith: 150my of granite magmatism on a plate margin. *Lithos* 97, 373–394.doi: 10.1016/j.lithos.2007.01.007

HidroAysén. (2010). *HidroAysén - Centrales Hidroeléctricas de Aysén S.A. Caracterización del Régimen Sedimentológico y Efectos de la Construcción de Centrales PHA*. HidroAysén, 687.

Hogan, K. A., Jakobsson, M., Mayer, L., Reilly, B. T., Jennings, A. E., Stoner, J. S., et al. (2020). Glacial sedimentation, fluxes and erosion rates associated with ice retreat in Petermann Fjord and Nares Strait, north-west Greenland. *Cryosphere* 14, 261–286. doi: 10.5194/tc-14-261-2020

International Initiative on Water Quality [IIWQ] (2019). *World Water Quality Information and Capacity Building Portal (Source: UNESCO, powered by EOMAP 2017–2019)*. Available online at: worldwaterquality.org.

Kaiser, J., Lamy, F., and Hebbeln, D. (2005). A 70-kyr sea surface temperature record off southern Chile (Ocean Drilling Program Site 1233). *Paleoceanography* 20, 1–15. doi: 10.1029/2005PA001146

Kaplan, M. R., Douglass, D. C., Singer, B. S., Ackert, R. P., and Caffee, M. W. (2005). Cosmogenic nuclide chronology of pre-last glacial maximum moraines at Lago Buenos Aires, 46°S. *Argentina. Quaternary Res.* 63, 301–315. doi: 10.1016/j.yqres.2004.12.003

Kilian, R., and Lamy, F. (2012). A review of Glacial and Holocene paleoclimate records from southernmost Patagonia (49-55°S). *Quaternary Sci. Rev.* 53, 1–23. doi: 10.1016/j.quascirev.2012.07.017

Klump, J., Hebbeln, D., and Wefer, G. (2000). The impact of sediment provenance on barium-based productivity estimates. *Mar. Geol.* 169, 259–271. doi: 10.1016/S0025-3227(00)00092-X

Lamy, F., Hebbeln, D., Röhl, U., and Wefer, G. (2001). Holocene rainfall variability in Southern Chile: a marine record of latitudinal shifts of the Southern Westerlies. *Earth Planetary Sci. Lett.* 185, 369–382. doi: 10.1016/S0012-821X(00)00381-2

Lamy, F., Kilian, R., Arz, H. W., Francois, J., Kaiser, J., and Prange, M. (2010). Holocene changes in the position and intensity of the southern westerly wind belt. *Nat. Geosci.* 3, 695–699. doi: 10.1038/ngeo959

Lara, A., Bahamondez, A., González-Reyes, A., Muñoz, A. A., Cuq, E., and Ruiz-Gómez, C. (2015). Reconstructing streamflow variation of the Baker River from tree-rings in Northern Patagonia since 1765. *J. Hydrol.* 529, 511–523. doi: 10.1016/j.jhydrol.2014.12.007

Liguori, B. T. P., De Almeida, M. G., and De Rezende, C. E. (2016). Barium and its importance as an indicator of (Paleo) productivity. *Anais Academia Brasileira Ciências* 88, 2093–2103. doi: 10.1590/0001-3765201620140592

Lipp, A. G., Shorttle, O., Syvret, F., and Roberts, G. G. (2020). Major-element composition of sediments in terms of weathering and provenance: implications for crustal recycling. *Geochem. Geophys. Geosyst.* 21:e2019GC008758. doi: 10.1029/2019GC008758

Liu, D., Bertrand, S., Villaseñor, T., Van Dijck, T., Fagel, N., and Mattielli, N. (2020). Provenance of northwestern Patagonian river sediments (44–48°S): a critical evaluation of mineralogical, geochemical and isotopic tracers. *Sedimentary Geol.* 408:105744. doi: 10.1016/j.sedgeo.2020.105744

Liu, D., Bertrand, S., and Weltje, G. J. (2019). An empirical method to predict sediment grain size from inorganic geochemical measurements. *Geochem. Geophys. Geosyst.* 20, 3690–3704. doi: 10.1029/2018GC008154

Maus, S., Yin, F., Lühr, H., Manoj, C., Rother, M., Rauberg, J., et al. (2008). Resolution of direction of oceanic magnetic lineations by the sixth-generation lithospheric magnetic field model from CHAMP satellite

magnetic measurements. *Geochem. Geophys. Geosyst.* 9:Q07021. doi: 10.1029/2008GC001949

McEnroe, S., Brown, L., and Robinson, P. (2004). Earth analog for Martian magnetic anomalies: remanence properties of hemo-ilmenite norites in the Bjerkreim-Sokndal intrusion. *Rogaland, Norway. J. Appl. Geophys.* 56, 195–212. doi: 10.1016/S0926-9851(04)00052-7

McLennan, S. M., Bock, B., Hemming, S. R., Hurowitz, J. A., Lev, S. M., and McDaniel, D. K. (2003). "The roles of provenance and sedimentary processes in the geochemistry of sedimentary rocks," in *Geochemistry of Sediments and Sedimentary Rocks: Evolution Considerations to Mineral Deposit-Forming Environments*, ed. D. R. Lentz (Newfoundland: Geological Association of Canada, GeoText 4, St. John's), 7–38.

Mernild, S. H., Liston, G. E., Hiemstra, C., and Wilson, R. (2017). The Andes Cordillera. Part III: glacier surface mass balance and contribution to sea level rise (1979-2014). *Int. J. Climatol.* 37, 3154–3174. doi: 10.1002/joc.4907

Meyer, I., Davies, G. R., and Stuut, J.-B. W. (2011). Grain size control on Sr-Nd isotope provenance studies and impact on paleoclimate reconstructions: an example from deep-sea sediments offshore NW Africa. *Geochem. Geophys. Geosyst.* 12:Q03005. doi: 10.1029/2010GC003355

Michelena, M. D., and Kilian, R. (2015). Magnetic signatures of the orogenic crust of the Patagonian Andes with implication for planetary exploration. *Phys. Earth Planetary Interiors* 248, 35–54. doi: 10.1016/j.pepi.2015.08.005

Moffat, C., Tapia, F. J., Nittrouer, C. A., Hallet, B., Bown, F., Boldt, K. L., et al. (2018). Seasonal evolution of ocean heat supply and freshwater discharge from a rapidly retreating tidewater glacier: jorge montt. *Patagonia. J. Geophys. Res.: Oceans* 123, 4200–4223. doi: 10.1002/2017JC013069

Murray, R. W., Miller, D. J., and Kryc, K. A. (2000). *Analysis of Major and Trace Elements in Rocks, Sediments, and Interstitial Waters by Inductively Coupled Plasma–Atomic Emission Spectrometry (ICP-AES). ODP Technical Note 29*. 27.

Pankhurst, R. J., Weaver, S. D., Hervé, F., and Larrond, P. (1999). Mesozoic-Cenozoic evolution of the North Patagonian Batholith in Aysen, southern Chile. *J. Geol. Soc.* 156, 673–694. doi: 10.1144/gsjgs.156.4.0673

Pantoja, S., Iriarte, L., and Daneri, G. (2011). Oceanography of the Chilean Patagonia. *Continental shelf Res.* 31, 149–153. doi: 10.1016/j.csr.2010.10.013

Parada, M. A., Palacios, C., and Lahsen, A. (1997). Jurassic extensional tectono-magmatism and associated mineralization of the El Faldeo polymetallic district, Chilean Patagonia: geochemical and isotopic evidence of crustal contribution. *Mineralium Deposita* 32, 547–554. doi: 10.1007/s001260050121

Pérez-Santos, I., Garcés-Vargas, J., Schneider, W., Ross, L., Parra, S., and Valle-Levinson, A. (2014). Double-diffusive layering and mixing in Patagonian fjords. *Prog. Oceanogr.* 129, 35–49. doi: 10.1016/j.pocean.2014.03.012

Piret, L., Bertrand, S., Hawkings, J., Kylander, M. E., Torrejón, F., Amann, B., et al. (2021). High-resolution fjord sediment record of a receding glacier with growing intermediate proglacial lake (Steffen Fjord, Chilean Patagonia). *Earth Surface Processes Landforms* 46, 239–251. doi: 10.1002/esp.5015

Piret, L., Bertrand, S., Kissel, C., De Pol-Holz, R., Tamayo Hernando, A., and Van Daele, M. (2018). First evidence of a mid-Holocene earthquake-triggered megaturbidite south of the Chile Triple Junction. *Sedimentary Geol.* 375, 120–133. doi: 10.1016/j.sedgeo.2018.01.002

Powell, R. D., and Molnia, B. F. (1989). Glacimarine sedimentary processes, facies and morphology of the south-southeast Alaska shelf and fjords. *Mar. Geol.* 85, 359–390. doi: 10.1016/0025-3227(89)90160-6

Pryer, H. V., Hawkings, J. R., Wadham, J. L., Robinson, L. F., Hendry, K. R., Hatton, J. E., et al. (2020). The influence of glacial cover on riverine silicon and iron exports in Chilean Patagonia. *Glob. Biogeochem. Cycles* 34:e2020GB006611. doi: 10.1029/2020GB006611

Raitzsch, M., Dueñas-Bohórquez, A., Reichart, G. J., de Nooijer, L. J., and Bickert, T. (2010). Incorporation of Mg and Sr in calcite of cultured benthic foraminifera: impact of calcium concentration and associated calcite saturation state. *Biogeosciences* 7, 869–881. doi: 10.5194/bg-7-869-2010

Rebolledo, L., Bertrand, S., Lange, C. B., Tapia, F. J., Quiroga, E., Troch, M., et al. (2019). Compositional and biogeochemical variations of sediments across the terrestrial-marine continuum of the Baker-Martínez fjord system (Chile, 48°S). *Progr. Oceanogr.* 174, 89–104. doi: 10.1016/j.pocean.2018.12.004

Revel-Rolland, M., Arnaud, F., Chapron, E., Desmet, M., Givelet, N., Alibert, C., et al. (2005). Sr and Nd isotopes as tracers of clastic sources in Lake Le Bourget sediment (NW Alps, France) during the Little Ice Age: palaeohydrology implications. *Chem. Geol.* 224, 183–200. doi: 10.1016/j.chemgeo.2005.04.014

Ríos, F., Kilian, R., Lange, C. B., Baeza-Urrea, O., Arz, H. W., Zindorf, M., et al. (2020). Environmental and coastline changes controlling Holocene carbon accumulation rates in fjords of the western Strait of Magellan region. *Continental Shelf Res.* 199:104101. doi: 10.1016/j.csr.2020.104101

Ross, L., Pérez-Santos, I., Valle-Levinson, A., and Schneider, W. (2014). Semidiurnal internal tides in a Patagonian fjord. *Progr. Oceanogr.* 129, 19–34. doi: 10.1016/j.pocean.2014.03.006

Sagredo, E. A., and Lowell, T. V. (2012). Climatology of Andean glaciers: a framework to understand glacier response to climate change. *Glob. Planetary Change* 8, 101–109. doi: 10.1016/j.gloplacha.2012.02.010

Sandgren, P., and Snowball, I. (2001). "Application of mineral magnetic techniques to paleolimnology," in *Tracking Environmental Change Using Lake Sediments Volume 2: Physical and Geochemical Methods*, eds W. M. Last and J. P. Smol (Dordrecht: Kluwer Academic Publishers), 217–237.

Scofield, N., and Roggenthen, W. M. (1986). Petrologic evolution of plagioclase-rich cumulates from the Wichita Mountains, Oklahoma: effects upon magnetic remanence properties. *Geology* 14:908. doi: 10.1130/0091-7613198614<908:PEOPCF<2.0 .CO;2

Segemar (2003). *Mapa Geológico de la Provincia de Santa Cruz, Republica Argentina*. 1:750 000

Sernageomin (2003). Mapa Geológico de Chile: versión digital. Servicio Nacional de Geología y Minería, Publicación Geológica Digital No. 4, (CD-ROM, versión1.0, 2003). Santiago: Servicio Nacional de Geología y Minería.

Shin, J. Y., Kim, S., Zhao, X., Yoo, K. C., Yu, Y., Lee, J. I., et al. (2020). Particle-size dependent magnetic properties of Scotia Sea sediments since the Last Glacial Maximum: glacial ice-sheet discharge controlling magnetic proxies. *Palaeogeogr. Palaeoclimatol. Palaeoecol.* 557:109906. doi: 10.1016/j.palaeo.2020.109906

Siani, G., Colin, C., Michel, E., Carel, M., Richter, T., Kissel, C., et al. (2010). Late Glacial to Holocene terrigenous sediment record in the Northern Patagonian margin: paleoclimate implications. *Palaeogeogr. Palaeoclimatol. Palaeoecol.* 297, 26–36. doi: 10.1016/j.palaeo.2010.07.011

Snowball, I., Sandgren, P., and Petterson, G. (1999). The mineral magnetic properties of an annually laminated Holocene lake-sediment sequence in northern Sweden. *Holocene* 9, 353–362. doi: 10.1191/095968399670520633

St-Onge, G., Chapron, E., Mulsow, S., Salas, M., Viel, M., Debret, M., et al. (2012). Comparison of earthquake-triggered turbidites from the Saguenay (Eastern Canada) and Reloncavi (Chilean margin) Fjords: implications for paleoseismicity and sedimentology. *Sedimentary Geol.* 243–244, 89–107. doi: 10.1016/j.sedgeo.2011.11.003

Stuut, J. W., Kasten, S., Lamy, F., and Hebbeln, D. (2007). Sources and modes of terrigenous sediment input to the Chilean continental slope. *Quaternary Int.* 161, 67–76. doi: 10.1016/j.quaint.2006.10.041

Syvitski, J. P., and Shaw, J. (1995). Sedimentology and Geomorphology of Fjords. *Dev. Sedimentol.* 53, 113–178. doi: 10.1016/S0070-4571(05)80025-1

Van Daele, M., Versteeg, W., Pino, M., Urrutia, R., and De Batist, M. (2013). Widespread deformation of basin-plain sediments in Aysén fjord (Chile) due to impact by earthquake-triggered, onshore-generated mass movements. *Mar. Geol.* 337, 67–79. doi: 10.1016/j.margeo.2013.01.006

Vandekerkhove, E., Bertrand, S., Mauquoy, D., McWethy, D., Reid, B., Stammen, S., et al. (2020). Neoglacial increase in high-magnitude glacial lake outburst flood frequency, upper Baker River, Chilean Patagonia (47°S). *Quaternary Sci. Rev.* 248:106572. doi: 10.1016/j.quascirev.2020.106572

Villaseñor, T., Tentori, D., Marsaglia, K. M., and Pinto, L. (2019). The changing Patagonian landscape: erosion and westward sediment transfer paths in northern Patagonia during the Middle and Late Pleistocene. *Basin Res.* 32, 1035–1053. doi: 10.1111/bre.12413

Weltje, G. J. (2012). Quantitative models of sediment generation and provenance: state of the art and future developments. *Sedimentary Geol.* 280, 4–20. doi: 10.1016/j.sedgeo.2012.03.010

Weltje, G. J., and Tjallingii, R. (2008). Calibration of XRF core scanners for quantitative geochemical logging of sediment cores: theory and

application. *Earth Planetary Sci. Lett.* 274, 423–438. doi: 10.1016/j.epsl.2008.07.054

Wils, K., Van Daele, M., Kissel, C., Moernaut, J., Schmidt, S., Siani, G., et al. (2020). Seismo-turbidites in aysén fjord (Southern Chile) reveal a complex pattern of rupture modes along the 1960 megathrust earthquake segment. *J. Geophys. Res.: Solid Earth* 125, 1–23. doi: 10.1029/2020JB019405

Wils, K., Van Daele, M., Lastras, G., Kissel, C., Lamy, F., and Siani, G. (2018). Holocene event record of aysén fjord (Chilean Patagonia): an interplay of volcanic eruptions and crustal and megathrust earthquakes. *J. Geophys. Res.: Solid Earth* 123, 324–343. doi: 10.1002/2017JB014573

Conflict of Interest: The authors declare that the research was conducted in the absence of any commercial or financial relationships that could be construed as a potential conflict of interest.

frontiers in Marine Science

ORIGINAL RESEARCH
published: 09 June 2021
doi: 10.3389/fmars.2021.635190

Separate Feeding Between the Pelagic Stage of the Squat Lobster *Munida gregaria* and the Larger Sized Zooplankton Crustacean Groups in the Beagle Channel as Revealed by Stable Isotopes

Leonardo R. Castro[1,2], Humberto E. González[2,3], José Garcés-Vargas[2,3] and Pamela Barrientos[1]*

[1] Departamento de Oceanografía and Centro de Investigación Oceanográfica COPAS Sur-Austral, Universidad de Concepción, Concepción, Chile, [2] Centro FONDAP de Investigación en Dinámica de Ecosistemas Marinos de Altas Latitudes (IDEAL), Valdivia-Punta Arenas, Chile, [3] Instituto de Ciencias Marinas y Limnológicas, Universidad Austral de Chile, Valdivia, Chile

OPEN ACCESS

Edited by:
Eduardo Joel Quiroga Jamett, Catholic University of Valparaíso, Chile

Reviewed by:
Mauricio F. Landaeta, Universidad de Valparaiso, Chile
Kusum Komal Karati, Centre for Marine Living Resources and Ecology (CMLRE), India

***Correspondence:**
Leonardo R. Castro
lecastro@oceanografia.udec.cl

Specialty section:
This article was submitted to Marine Ecosystem Ecology, a section of the journal Frontiers in Marine Science

Received: *30 November 2020*
Accepted: *10 May 2021*
Published: *09 June 2021*

Citation:
Castro LR, González HE, Garcés-Vargas J and Barrientos P (2021) Separate Feeding Between the Pelagic Stage of the Squat Lobster Munida gregaria and the Larger Sized Zooplankton Crustacean Groups in the Beagle Channel as Revealed by Stable Isotopes. Front. Mar. Sci. 8:635190. doi: 10.3389/fmars.2021.635190

In southern Patagonia, the Beagle Channel shows very low production during winter but simultaneously sustains very dense aggregations of the pelagic stage of squat lobster (*Munida gregaria*), a benthic decapod whose pelagic juveniles have the largest body size within the chitinous pelagic community. To assess the coexistence of the mesozooplankton community and the pelagic *M. gregaria* stage under the harsh feeding winter conditions, we conducted a research cruise at two locations connected to the Beagle Channel, Yendegaia Bay (land terminating-glacier) and Pia Fjord (marine-terminating glacier). Our results showed that the zooplankton communities were similar in these two fjords, that a single pelagic group dominated in terms of biomass (pelagic *Munida gregaria*), and that differences in vertical distribution existed between most of the principal crustacean zooplankton and pelagic *M. gregaria*. All groups showed consumption of terrestrially derived organic matter, as revealed by their $\delta^{13}C$ values. However, the isotopic composition, trophic positions (TP), and isotopic niche areas of the groups separated pelagic *M. gregaria*, presenting some of the lowest $\delta^{15}N$ and the highest $\delta^{13}C$ values, and the narrowest isotopic niche width. Pelagic *M. gregaria* was dominated by a single body size class along the 0–100 m water column, with no diel changes in vertical distribution, remained mostly in the upper layers (0–50 m), and benefited from the slightly higher phytoplankton concentrations at shallower depths as revealed by their higher $\delta^{13}C$ values and low trophic position. In contrast, the other groups, including zoea *M. gregaria* stages, developed changes in distribution between day and night or remained deeper in the water column. These groups showed higher $\delta^{15}N$ values, higher TP, and lower $\delta^{13}C$ values, most of which probably fed on a nanoheterotrophs and terrestrial particulate organic matter mixture at deeper layers. Thus, the different vertical distributions, different trophic level food sources, and slightly

different organic carbon sources apparently reduced any potential competence for food resources and form part of the feeding strategy that may facilitate the coexistence of the different large pelagic crustaceans under harsh feeding winter conditions in this high latitude austral region.

Keywords: Beagle channel, stable isotopes, *Munida gregaria*, *Euphausia vallentini*, zooplankton, Patagonia

INTRODUCTION

Austral Patagonia has recently received attention with regard to global climate change because it contains some of the largest freshwater reserves in continental areas (other than Antarctica) in the form of extensive ice fields and glaciers (González et al., 2016; RGI, 2017). Recent reports have documented the retrieval of these ice masses during the last two decades associated with changes in nival and rain precipitation (Climate Change, 2007, 2013; Rivera et al., 2007; Casassa et al., 2010; Marín et al., 2013). These variations, in turn, have induced changes in the amount of water received in the coastal and fjord environments and the amount of terrestrial originated debris conducted toward the adjacent marine system (Dussaillant et al., 2009; Meerhoff et al., 2019; Ross et al., 2020).

The Beagle Channel, one of the only two channels that connects the Pacific and Atlantic oceans in South America, is one of these high-latitude environments in which numerous fjords and glaciers contribute to glacier melted water and runoff, particularly in spring and summer. Because of the difficulties in oceanographic research in winter, most studies on pelagic components of the community and trophic functioning in these areas have been conducted in warmer months (spring and summer) or other seasons in the Atlantic side of the Beagle Channel (Almandoz et al., 2011; Aguirre et al., 2012; Riccialdelli et al., 2017; Diez et al., 2018). Information on the origin of the organic carbon that sustains the pelagic trophic web and how it is trespassed along the different components, thus, remains undocumented for the coldest months (winter), particularly to the Pacific Ocean branches of the Beagle Channel. Previous studies in the northern Chilean Patagonia (42–46°S) have proposed that, in contrast to the spring season, when primary production in the coastal areas is diatom-based, winter production is fueled by the microbial community (González et al., 2010, 2011). Other studies further south (Magellan Strait, 53°S) in Patagonia have documented the important role of the filter feeding euphausiid species (*Euphausia vallentini*) in channelizing a large amount of phytoplanktonic carbon production in spring, the main source of organic carbon entering the fjords and channels (González et al., 2016). Finally, most recent studies carried out in spring on the Atlantic side of the Beagle Channel (BC; 55°S) report that the carbon flux in the area is based on combined marine phytoplankton, macroalgae, and terrestrially derived plant debris with the largest fraction provided by these latter two sources that reach the higher trophic levels of the food web (Riccialdelli et al., 2017).

Because stable isotope enrichment occurs along the trophic web, stable isotope analyses are currently widely utilized to study the structure and fluxes along food webs (Vander Zanden and Rasmussen, 2001; Post, 2002). In marine ecosystems, for instance, the nitrogen stable isotope ^{15}N has been utilized to indicate the trophic position of certain species along the food web to determine whether this position is shared by other organisms in the same location or if changes occur between seasons or among environments (Lindsay et al., 1998; Tanaka et al., 2008; Malzahn and Boersma, 2009). The carbon stable isotope ^{13}C, in turn, has been utilized to identify the sources of organic carbon in coastal environments because ^{13}C values change if they proceed from terrestrial environments or from marine sources (phytoplankton or macroalgae) (Vander Zanden and Rasmussen, 1999, 2001; Vargas et al., 2011). Stable isotopes were also utilized to determine changes in feeding habits when organisms grow or changed their distribution or depths of residence to feed on prey with different isotopic content (Overman and Parrish, 2001; Laiz-Carrion et al., 2011; Montecinos et al., 2016; Bernal et al., 2020).

Given its high abundance and because its role as an important detritivore species that returns organic matter from the surface sediments to higher level marine predators, such as sea lions, seals, birds, squid, fishes and even whales, the galatheid squat lobster *Munida gregaria* is considered a key species in Patagonian channels and fjords (Tapella et al., 2002; Vinuesa and Varisco, 2007; Diez et al., 2012; Betti et al., 2020). The species has two morphs, a benthic adult morph, originally named *M. gregaria*, and a post-larval-juvenile pelagic morph, originally named *M. subrugosa,* that can reach the size of adults while still in the water column (Pérez-Barros et al., 2008, 2010, 2011). While the depth distributions of both morphs have been reported, there are insufficient studies on shorter-term (diel, seasonal) variations in distributions of different sized pelagic stages in the water column (Meerhoff et al., 2013, 2014), with most reports on the zoea stages of development (Castro et al., 2011, 2019). For these stages, ontogenetic migration from the inner channel zones of zoea release to offshore zones and back to inner areas as megalopa or juveniles, has been documented in northern Chilean Patagonian channels (León et al., 2008; Meerhoff et al., 2013, 2014; Mujica et al., 2013). Whether the juvenile stages change in vertical distribution as they grow or if they carry out shorter-term changes (seasonal, diel vertical migrations) remain to be determined.

Pelagic *M. gregaria* is a large-sized crustacean in the water column of Patagonian fjords and channels. Other large crustacean zooplankton, usually found in most high-latitude Patagonian channel areas, are euphausiids (*Euphausia vallentini*), amphipods (*Eurythemistos* sp.), some large decapods such as *Sergestes arcticus*, and some mid- to large-sized copepods, such as *Calanus australis* or *Rhincalanus* sp. Other holozooplankton groups, but small, often collected in large numbers, are ostracods,

cladocerans, and small-sized copepods (Rosenberg and Palma, 2003; Biancalana et al., 2007; Zagami et al., 2011; Aguirre et al., 2012; Giesecke et al., 2019). How these crustacean assemblages cope to survive in a common environment during the winter low production season in these high-latitude areas remains to be determined.

In the present study, we utilized stable isotope analyses and stratified plankton sampling to explore whether the most abundant and large-sized crustacean pelagic groups in the BC develop differential feeding and/or vertical distributions conducive to favor their coexistence during the austral winter. Because most crustacean zooplankton are essentially omnivorous (although some are often classified as mostly herbivores (e.g., *E. vallentini*, calanoid copepods, ostracods), carnivores, or detritivores (e.g., amphipods, *M. gregaria*, *Sergestes* sp.) and because of the scarce winter food availability, we expected most groups would probably develop an opportunistic feeding mode without a clear separation in food items ingested and thereafter, a wide overlay in isotopic trophic niches. At the same time, because of the low winter marine primary production, the different groups would either subsist feeding on microzooplankton and hence reach mid- to high trophic positions, feed on allochthonous organic matter from terrestrial origin or, finally, partition the food resources by residing in different depth layers. Accordingly, the objectives of the present study were to assess (a) whether the largest body size and more abundant zooplankton crustacean groups were the same in different fjords, (b) whether their organic carbon source was primarily of marine origin (autochthonous) or terrestrially (allochthonous) derived, (c) whether the trophic positions and isotopic niche widths differed among crustacean groups, and finally, (d) to evaluate whether potentially different feeding behavior (determined from isotopic composition) along with potential differences in vertical distributions might constitute a way of partitioning the environment to facilitate the maintenance of different groups within this low winter production high-latitude system. Particular emphasis is given to juvenile *M. gregaria* because it is a species that has been reported to expand its high abundance toward lower latitude channels and fjords (Diez et al., 2016, 2018).

MATERIALS AND METHODS

Field work. From July 19 to 26, 2017, was conducted a research cruise on board the Motorboat "Forrest" to the BC. Two locations connected to the BC were studied for three days in the austral winter: Yendegaia Bay (central BC, land-terminating-glaciers) and Pia fjord (northwestern arm BC, marine-terminating glaciers). The Yendegaia Bay, ∼10 km long, ∼2.5 km wide and with a maximum depth of ∼220 m, is connected to the Yendegaia River in its head, which incorporates melted water from the Serka (also called Stopanni) glacier located ∼11 km inland. The western arm of Pia fjord, ∼14 km long, 1.25 km wide and with a maximum depth of ∼200 m, receives freshwater directly from the Guilcher glacier in its inner flank (**Figure 1**).

At each location, a longitudinal transect was conducted, in which hydrographic profiles were obtained with a Seabird 25 CTD equipped with a fluorometer and turbidity sensor. Absolute salinity and conservative temperature were derived by applying the algorithms proposed in the Thermodynamic Equation of Seawater 2010 according to the new standards of seawater properties adopted by the Intergovernmental Oceanographic Commission (Valladares et al., 2011). Along the center of the transects, zooplankton profiles of stratified samplings were conducted at each location four times during a 24 h cycle. The profiles included stratified zooplankton samples collected with a 0.5 × 0.5 m mouth opening Tucker trawl (300 μm mesh, equipped with a GO flowmeter) at three depth strata: 0–10, 10–50, 50–100 m. The profiles were obtained during the day and at night. Once onboard, the samples were split and one fraction was preserved in 5% formalin, and the other was drained and then frozen at −20°C for later isotope ($\delta^{13}C$, $\delta^{15}N$) analyses. Additional zooplankton samples (0–50 m depth) were collected at night to increase the number of organisms for isotopic analyses. Once in the laboratory, all samples for isotope analyses were transferred to −80°C. Seawater samples along the water column were also collected using 5 L Niskin bottles from six depths (0, 5, 10, 20, 50, and 100 m) both during the day and at night. Seawater samples (0.4 L) were filtered (Whatman GF/F) for chlorophyll-a determinations and 0.5–1.0 L were also filtered (GFF 0.7 μm pore precombusted filters) for stable isotopes in particulate organic matter (POM) analyses. All samples were stored on board initially at −20°C and then transferred to −80°C in the laboratory.

Laboratory work. In the laboratory, formalin-preserved zooplankton samples were identified as functional group levels and counted. *Munida gregaria* were classified as either zoea or pelagic *M. gregaria* (megalopa, juveniles). All zooplankton groups were measured (cephalothorax length and total length). Biomass (wet weight) measurements were conducted on larger-sized zooplankton groups on a high-resolution analytical scale (±0.000001 g), and then individual wet weight (*WW*) values were transformed into dry weight (*DW*) following Wiebe (1988):

$$LOG\ (WW) = 0.975 + 0.946\ LOG\ (DW)$$

For the other smaller-sized or less abundant zooplankton groups, biomass was estimated by calculating their individual volume and then utilizing Wiebe (1988) displaced volume (*DV*) to dry weight (*DW*) relationship:

$$LOG\ (DV)\ \ 1.037 + 0.839\ LOG\ (DW)$$

From the frozen zooplankton samples, the largest crustaceans (*M. gregaria* pelagic, *E. vallentini, Sergestes arcticus*, mysid larvae) and the most abundant zooplankton groups (copepods and ostracods) were sorted for isotope analyses and for total carbon and nitrogen determinations. The number of individuals in each crustacean group used for the isotope analyses was estimated from the weight per sample as described in the Stable Isotope Facility web page at the University of California at Davis.[1] Only

[1]http://stableisotopefacility.ucdavis.edu/

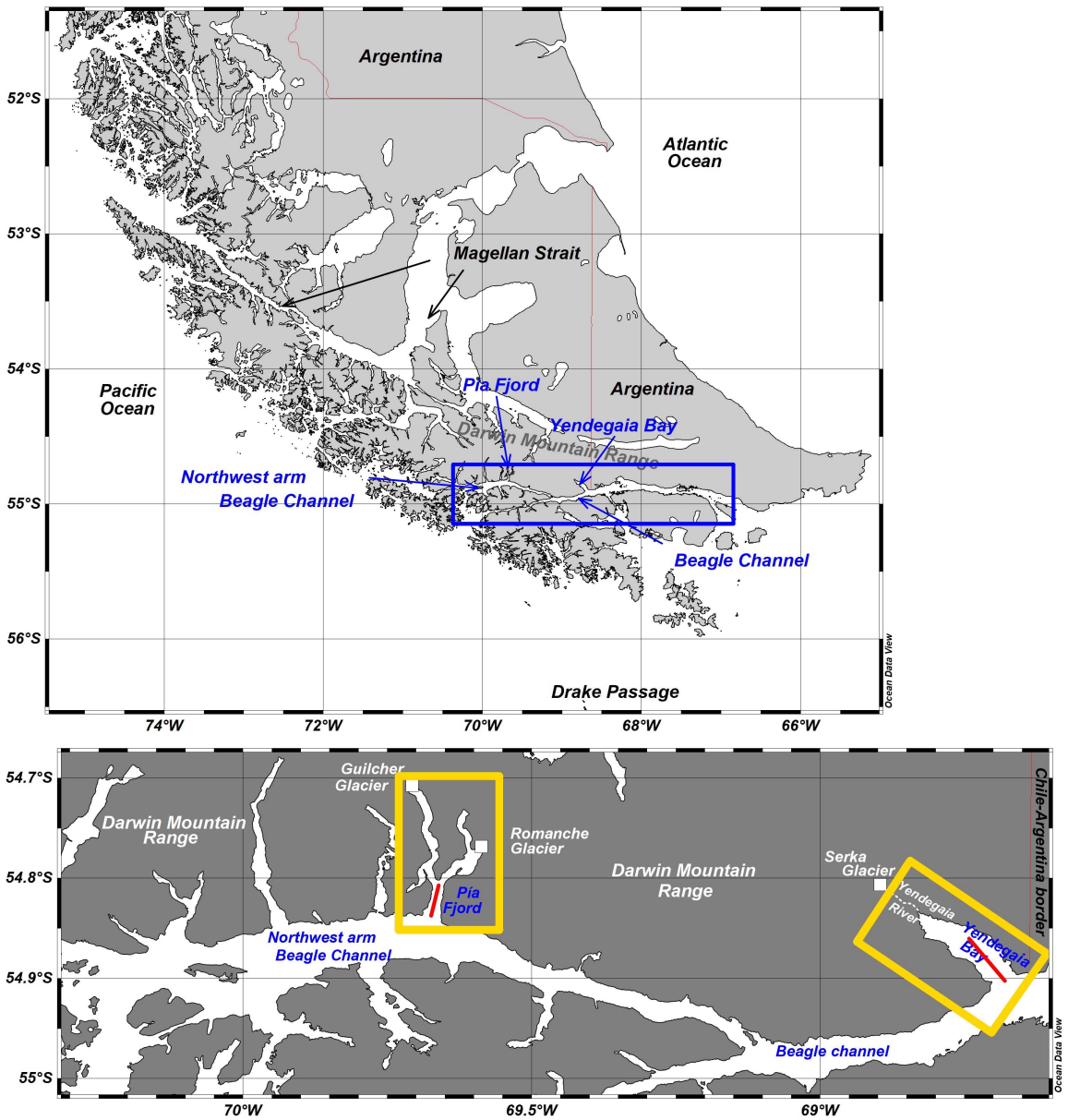

FIGURE 1 | Map of the Southern Patagonia showing the Beagle channel (upper panel) and both sampling locations: Pia fjord and Yendegaia bay (lower panel). Red lines in each location indicates the zooplankton sampling track.

the abdominal muscular tissue from *E. vallentini* and pelagic *M. gregaria* were used for isotopic analyses. The ^{13}C and ^{15}N isotopes in the samples were determined using an Elementar Vario EL Cube elemental analyzer (Elementar Analysensysteme GmbH, Hanau, Germany) interfaced with an Isoprime VisION IRMS (Elementar UK Ltd, Cheadle, United Kingdom) isotope ratio mass spectrometer, or a PDZ Europa ANCA-GSL elemental analyzer interfaced to a PDZ Europa 20-20 isotope ratio mass spectrometer (Sercon Ltd., Cheshire, United Kingdom). The final delta values are expressed relative to the international standards Vienna Pee Dee Belemnite and Air for carbon and nitrogen, respectively.

Data analyses. The trophic positions of the different groups were estimated based on isotopic ^{15}N enrichment, following Vander Zanden (1997):

$$Trophic\ Position\ (TP) = \lambda + (\delta^{15}N_{organism} - \delta^{15}N_{base})\ /3.4$$

where $\delta^{15}N_{organism}$ is the isotopic value measured, *3.4* is the average de $\delta^{15}N$ enrichment per trophic level (Post, 2002), and $\delta^{15}N_{\ base}$ is usually the $\delta^{15}N$ from organisms that show an herbivorous feeding mode. In this study, we used the same approach used by Riccialdelli et al. (2017), which is the mean $\delta^{15}N$ value reported for all benthic filter feeders (*Notochthamalus scabrosus* $\delta^{15}N$ = 12.7‰; *Aulacomya atra* $\delta^{15}N$ = 12.0‰,

Brachydontes purpuratus $\delta^{15}N$ = 11.3‰; *Mytilus chilensis* $\delta^{15}N$ = 11.9‰) from the same region (BC), assuming they were all herbivorous. λ Represents the reference value (TL = 2) in the food web.

Bayesian standard ellipse areas (SEAB) were also calculated to determine the isotopic niche width (Jackson et al., 2011) of the largest body size and most abundant crustacean groups (pelagic *Munida gregaria*, *E. vallentini adults, Sergestes arcticus*, ostracods, and copepods). To estimate niche width, we used the estimate function in the Stable Isotope Bayesian Ellipses in R (SIBER) v3.6.1. The program first estimates a Bayesian standard ellipse that describes the data in a $\delta^{13}C$–$\delta^{15}N$ space for each group and can also perform an arithmetic correction for a small number ($n < 30$) of samples (standard ellipse area corrected, SEAC) (Young et al., 2017).

We calculated the relative importance of terrestrial particulate organic carbon (POC) in the diet of all crustacean major groups by applying a two-source mixing model (Bianchi, 2007):

$$\%POC_{terrestrial} = (d^{13}C_{sample} - d^{13}C_{marine}) / (d^{13}C_{terrestrial} - d^{13}C_{marine})$$

where $\delta^{13}C$ sample is the mean isotopic composition of each crustacean group, $\delta^{13}C_{marine}$ is the marine end-member, and $\delta^{13}C_{terrestrial}$ is the terrestrial end-member. Particulate organic matter has been used as an endmember in some trophic studies (Post, 2002; Benstead et al., 2006; Vargas et al., 2011). However, POM is a mixture of terrestrial and marine organic matter in this zone (Riccialdelli et al., 2017); hence, our POM isotope values could not be used as marine end members [in fact, our ^{13}C POM = −24.51 ± 0.53‰ were very similar with C2 plants ($\delta^{13}C$ = −23.9‰) reported by Riccialdelli et al., 2017]. Accordingly, we utilized $\delta^{13}C$ values from C2 plants as terrestrial end members and macroalgae values (chlorophyta, rhodophyta, phaeophyta) as marine end members, all reported by Riccialdelli et al. (2017) for the BC.

Statistical analyses included a Kolmogorov-Smirnov test with the Lilliefors correction to explore whether the zooplankton group abundance and the $\delta^{13}C$ and $\delta^{15}N$ data series followed normal distributions. Since none of the series followed this distribution ($p < 0.05$), Mann-Whitney U-tests non-parametric tests were then utilized to look for differences in total abundance between locations in the larger crustacean groups, and median tests were utilized to determine whether statistical differences existed between day and night samples. Potential differences in vertical distributions during the day and night among sampled depths were evaluated using the interaction term (day/night × depths) in PERMANOVA. Lineal regressions were utilized to assess the potential relationships between the isotope composition and C/N with *M. gregaria* body length (cephalothorax length). The stable isotope composition in *M. gregaria* was also compared among the depths of collection using Kruskal-Wallis non-parametric tests. All analyses were carried out in R (v. 3.5.1) using the Lillie.test function (to test for normality) and lm (linear models).

RESULTS

Hydrographic Conditions

The hydrographic vertical section of Yendegaia Bay shows a well mixed 0–200 m deep water column with conservative temperature values varying between 6.5 and 7.3°C and absolute salinity values fluctuating between 31 and 32 g/kg (**Figure 2**). A very narrow surface layer (<5 m) was observed, with low salinity (30.5–31.5 g/kg), low temperature (<6.5°C), and maximum fluorescence and turbidity values (0.2 mg/m^3 fluorescence and turbidity values of approximately 1.5 NTU). The highest temperature (7–7.3°C) occurred deeper than 100 m near the bottom at the inner part of the fjord, where salinity did not reach higher than 32 g/kg.

In the Pia fjord, the water column was less mixed in terms of temperature and salinity, particularly at the outer side of the fjord (**Figure 2**). Compared with the Yendegaia bay, surface water was colder (<5°C), less saline (29.5–30.5 g/kg), and showed higher fluorescence values (>0.3 mg/m^3) down to 25 m deep toward the mouth of the fjord, and higher turbidity values (2.5 NTU) toward the head of the fjord. Deeper than 100 m, toward the entrance of the fjord, the seawater was warmer (>8°C) and saltier (>32 g/kg), evidencing a mixture with saltier water entering the BC from the oceanic area.

Zooplankton Groups Abundance and Vertical Distribution

A similar number of zooplankton functional groups were identified in the plankton samples: 20 in Yendegaia Bay and 22 in Pia Fjord (**Table 1**). The mean abundance of individuals collected in all groups were very low in both locations (mean per group: Yendegaia bay = 0.44 ± 1.37 ind./m^3; Pia fjord = 0.70 ± 2.05 ind./m^3), and the 5 numerically most abundant groups (copepods, ostracods, *E. vallentini* juveniles, *E. vallentini* adults, pelagic *M. gregaria*) were the same. Copepods and ostracods represented approximately 90% of all individuals collected in each zone (**Figure 3**), and both showed higher abundances in Pia fjord (copepods Mann-Whitney *U*: 27; $p = 0.03$; ostracods: Mann-Whitney *U*: 27; $p = 0.03$). *E. vallentini* juveniles and adults together accounted for ca. in 3.1% of all individuals in all groups in Yendegaia Bay and 1.5% Pia fjord and showed no difference in abundance between locations (*E. vallentini* juveniles: Mann-Whitney *U*: 45; $p = 0.346$; *E. vallentini* adults: Mann-Whitney *U*: 58,5; $p = 0.923$). Zoea and pelagic *M. gregaria* stage together represented ca. 1% in Yendegaia Bay and 0.2% in Pia Fjord, and both showed higher abundance in Yendegaia Bay (Zoea *M. gregaria*: Mann-Whitney *U*: 18; $p = 0.004$; juvenile *M. gregaria*: Mann-Whitney *U*: 25; $p = 0.021$), while the other comparatively large body sized zooplankton groups, *Sergestes* sp. and mysid larvae, reached low abundance representing less than 1% in each location and both showed a low frequency (≤50%) in all zooplankton profiles and no difference in abundance between locations (*Sergestes* sp.: Mann-Whitney *U*: 46; $p = 0.381$; mysis larvae: Mann-Whitney *U*: 49; $p = 0.497$).

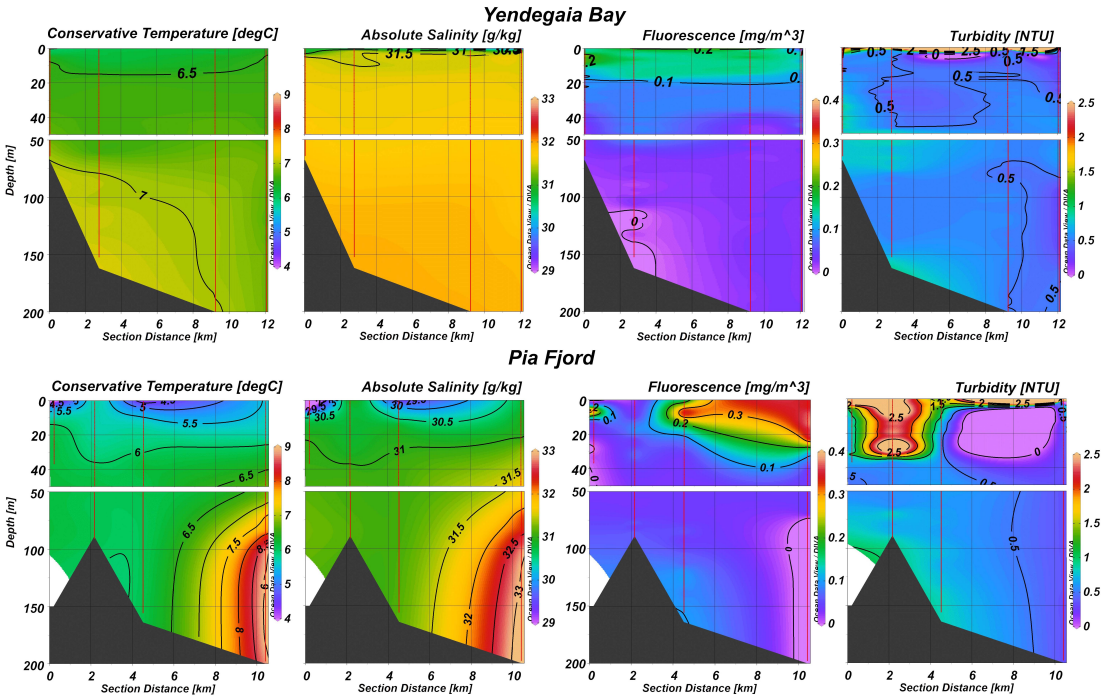

FIGURE 2 | Vertical section of hydrographic characteristics (conservative temperature, absolute salinity, fluorescence and turbidity) along the sampling track located from the center of Yendegaia bay and Pia fjord toward the Beagle channel.

Among the larger-body-sized zooplankton groups, the pelagic *M. gregaria* stage was the largest (>40 mm total length, TL) and the highest total dry weight (DW) biomass, accounting for more than 70% of the total zooplankton biomass (95% in Yendegaia Bay; 73% in Pia Fjord; **Figure 3**). In individual size basis, one 2.9 cm total length body size pelagic *M. gregaria* (0.37 g/ind DW) was equivalent to 2663 2.5-mm prosome length copepods (0.000138 g/ind.DW) (**Table 1**), with copepods being the most abundant zooplankton group and, after the pelagic *M. gregaria* stage, the following crustacean group in terms of biomass contribution.

The five more abundant zooplankton groups occurred in both the day and night samplings (**Figure 4**). Of these, the zoea and pelagic *M. gregaria* stage did not show differences in abundance between day and night (Median tests, $p > 0.05$; **Table 2**). These results contrast with the other groups (*E. vallentini* juveniles and adults, copepods, ostracods, *Sergestes* sp.), which showed higher abundance along the water column during the night than during the day (Median tests, $p < 0.05$, **Table 2**), suggesting that the incorporation of individuals from deeper layers (>100 m) at night was associated with vertical migrations.

Pelagic *M. gregaria* stage occurred mostly in the 0–50 m depth range and showed no statistical difference in vertical distribution between day and night (PERMANOVA, depths × day/night: F = 1.786; $p = 0.718$). *M. gregaria* zoea stages were more abundant at the deepest layer (50–100 m) during the day. At night, they dispersed along the water column, increasing their mean abundance tenfold in the intermediate layer (zoea $d/n_{10-50m} = 0.1$). Copepods, a group that showed a high number of individuals (>2 ind/m^3) at the three layers sampled day and at night, showed significant day-night differences in vertical distribution (PERMANOVA, depths × day/night; F = 0.128; $p = 0.048$). The other groups, with minimum abundance at the three layers sampled during the daytime, did not show statistical differences ($p > 0.05$) in day-night distributions, probably because their daytime aggregations were deeper than our samplings. At night, though, most of the large-sized crustacean groups studied here shared the 0–50 m shallower depth range at night, except for *Sergestes* sp., which occurred mostly at the deepest layer (50–100 m) at night (**Figure 4**).

Stable Isotopes, Trophic Positions, and Isotopic Niche Width in Crustacean Groups

The range of mean $\delta^{13}C$ values for all crustacean groups was narrow (1.7‰), with the highest value for adult *E. vallentini* (−19.50 ± 1.22‰) and the lowest for mysid larvae (−21.27 ± 1.07‰) (**Table 3** and **Figure 5A**). *The M. gregaria* pelagic stage showed the lowest $\delta^{15}N$ values (12.43 ± 0.74‰) and *Sergestes* sp. the highest (15.32 ± 1.11‰). The C/N ratio revealed a clear distinction between *M. gregaria* and *E. vallentini* lower values (*M. gregaria* = 4.08 ± 1.43‰; *E. vallentini* 4.73 ± 1.68‰) compared with the higher values of the other four groups (range: 7.02–9.97‰) (**Table 3**).

The Trophic positions (TP) estimated for all groups showed *that Sergestes* sp. had the highest position (TP = 3), followed by *E. vallentini* adults and copepods (TP = 2.8), mysid larvae

TABLE 1 | Abundance (ind./m^3) and biomass (g/m^3 dry weight, DW) of the different zooplankton groups collected during the winter cruise 2017 to Yendegaia bay and Pia fjord in the Beagle channel, indicating the percentage of positive stations (Posit. Stat.), mean abundance (±standard deviation), individual dry weights, total biomass (±standard deviation) and percentage of the total biomass corresponding to each group at each location.

	Yendegaia bay		Pia fjord		Yendegaia bay	Pia fjord			
	Freq. Total Posit. Stat. %	Abundance Mean (ind/m^3)	SD	Abundance Mean (ind/m^3)	SD	Ind. D.W. (ug/ind.)	Biomass Mean D.W. (ug/m^3)	% DW	Biomass Mean D.W. (ug/m^3)	% DW
Crustaceans										
Copepods	100	5.654	4.690	7.819	2.703	138.2	781.5	2.34	1080.7	9.22
Ostracods	100	3.711	3.946	6.425	3.399	66.4	246.6	0.74	426.8	3.64
Euphausia vallentini juvenile	100	0.215	0.161	0.165	0.081	41.9	9.0	0.03	6.9	0.06
Euphausia vallentini adult	88	0.099	0.173	0.070	0.068	2368.9	235.0	0.70	166.3	1.42
Munida gregaria pelagic	100	0.086	0.033	0.023	0.010	368230.5	31816.5	95.29	8569.8	73.13
Mysis larvae	50	0.052	0.098	0.001	0.001	155.2	8.0	0.02	0.2	1.35E-03
Munida gregaria Zoea	63	0.013	0.010	0.004	0.007	133.2	1.8	0.01	0.5	4.26E-03
Sergestes sp.	50	0.011	0.013	0.002	0.002	19712.5	213.7	0.64	32.1	0.27
Isopods	63	0.006	0.010	0.005	0.008	213.4	1.2	3.73E-03	1.0	0.01
Amphipods	100	0.005	0.005	0.007	0.007	426.0	2.0	0.01	3.1	0.03
Indetermined Zoea	38	0	0	0.004	0.003	73954.2	0	0	317.9	2.71
Indetermined Crustacean larvae	88	0.046	0.053	0.003	0.003	69.0	3.2	0.01	0.2	1.64E-03
Other groups										
Chaetognaths	100	0.044	0.045	1.163	0.610	496.5	22.0	0.07	577.3	4.93
Medusae	75	0.044	0.085	0.092	0.120	152.7	6.7	0.02	14.1	0.12
Briozoa	100	0.027	0.033	0.050	0.084	2.1	0.1	1.69E-04	0.1	8.73E-04
Siphonophores	88	0.024	0.019	0.241	0.146	1700.3	41.0	0.12	409.0	3.49
Gastropod larv.	63	0.009	0.009	0.006	0.010	0.2	2.0E-03	5.85E-06	1.3E-03	1.09E-05
Fish larvae	63	0.004	0.006	0.002	0.002	167.6	0.7	2.19E-03	0.3	2.54E-03
Polychaets	88	0.004	0.003	0.018	0.007	309.9	1.1	3.43E-03	5.4	4.63E-02
Fish eggs	25	0.002	0.003	1.990E-04	3.980E-04	208.2	0.4	1.06E-03	4.1E-02	3.54E-04
Pteropods	13	0.001	0.001	0	0	499.4	0.3	8.95E-04	0	0
Ctenophores	25	0	0	0.005	0.010	20424.2	0	0	107.2	0.91
Appendicularians	13	0	0	1.830E-04	3.661E-04	285.2	0	0	0.1	4.45E-04

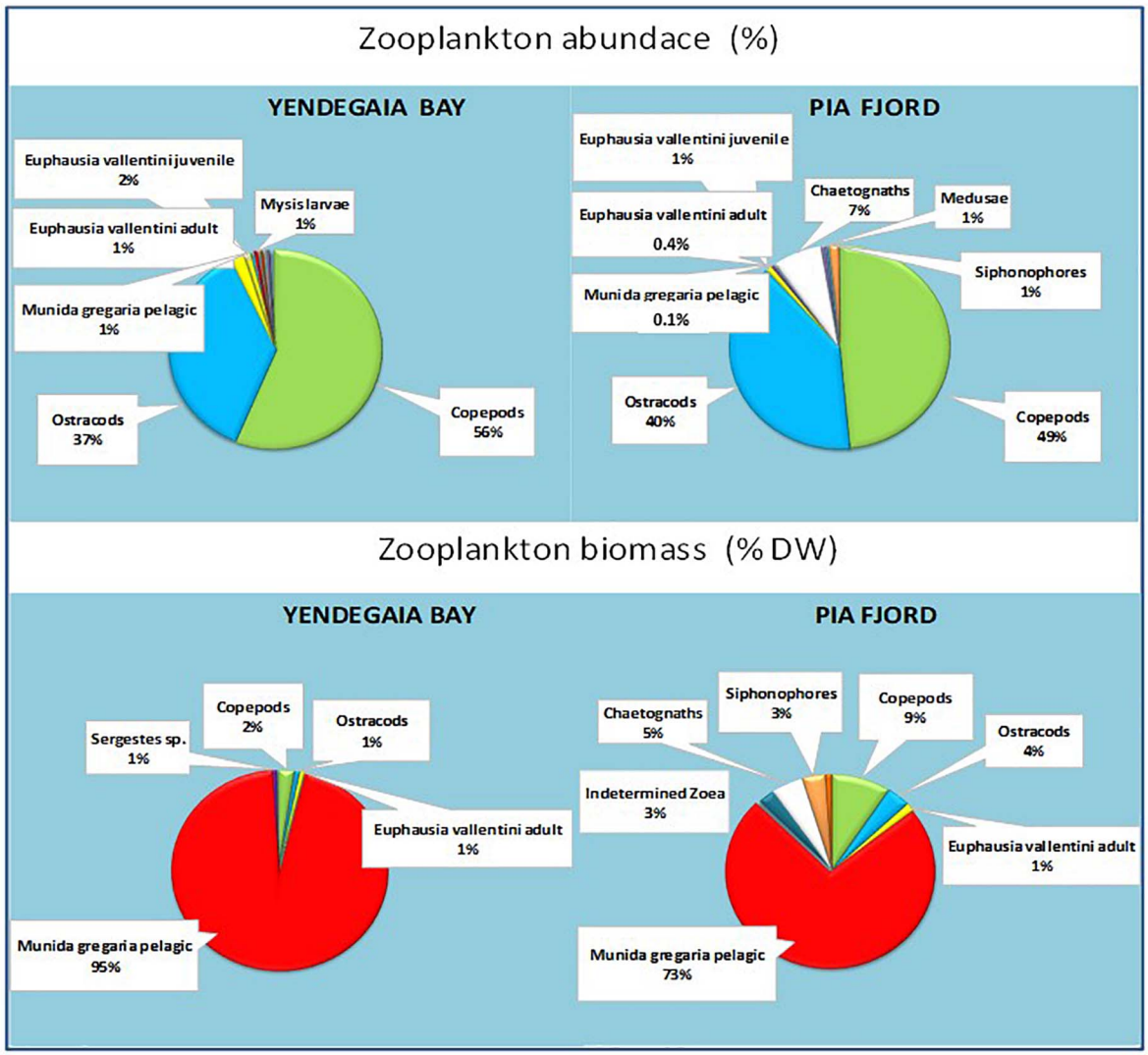

FIGURE 3 | Zooplankton abundance (%) and biomass (dry weight; %) of the most abundant groups in Yendegaia bay and Pia fjord in winter 2017. Pelagic *Munida gregaria*, copepods and ostracods are highlighted because of their relative importance both numerically and in terms of biomass.

TABLE 2 | Mean abundance (ind/10 m^3), standard deviations (SD) and medians of the main pelagic crustacean functional groups at day and night time.

	Day			Night			X^2	*df*	*p*-value	
	Mean	**SD**	**median**	**Mean**	**SD**	**median**				
Munida gregaria pelagic	0.43	0.48	0.31	0.33	0.45	0.06	0.485	1	0.486	*n.s.*
Munida gregaria Zoea	0.09	0.15	0.01	0.07	0.10	0.03	0.0001	1	0.770	*n.s.*
Euphausia vallentini Juvenile	0.42	0.67	0.04	1.94	1.98	1.66	1.721	1	0.019	*
Euphausia vallentini Adult	0.03	0.06	0.00	1.52	1.86	0.98	2.752	1	0.033	*
Copepods	30.09	30.71	13.24	101.72	45.98	84.00	4.911	1	0.024	*
Ostracods	9.53	15.89	0.00	63.38	55.73	0.00	2.801	1	0.040	*
Sergestes sp.	0.00	0.00	5.07	4.10	15.09	38.47	1.931	1	0.037	*
Mysis larvae	0.02	0.05	0.00	0.45	1.13	0.00	0.113	1	0.736	n.s.

*Mann-Whitney U tests (X^2) results between day and night abundances. n.s.: not significant; *$p < 0.05$, **$p < 0.01$.*

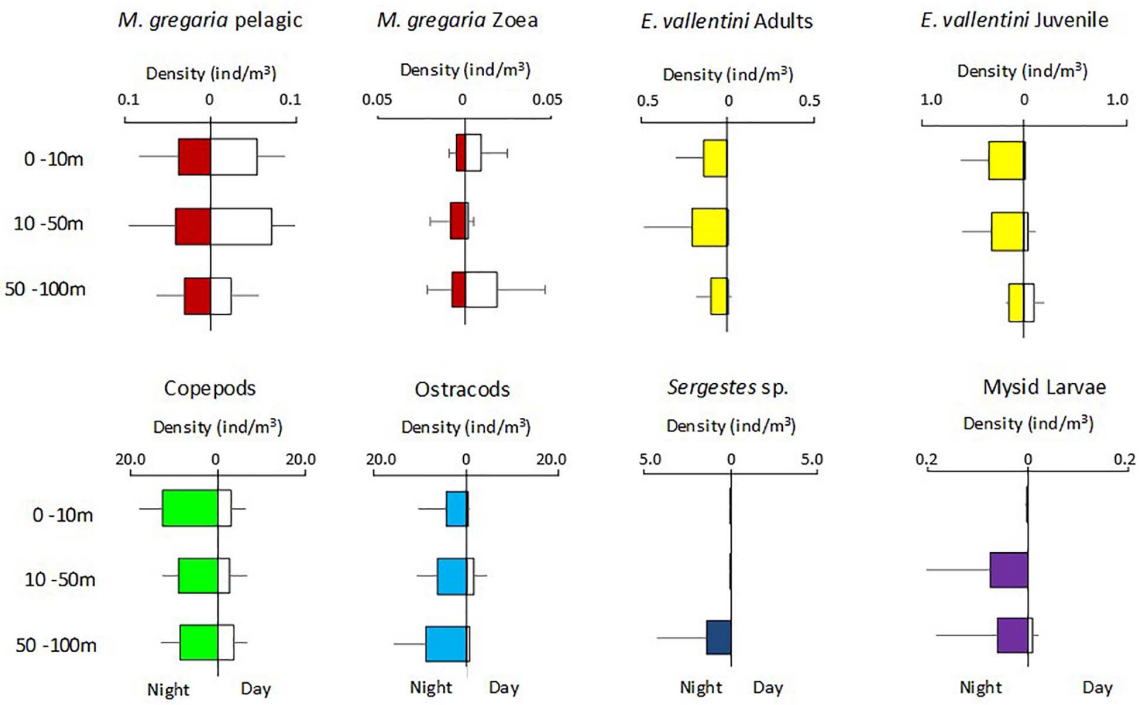

FIGURE 4 | Vertical distribution of the most abundant zooplankton crustacean groups at day (white) and night time (colored) collected at both locations (pooled data). Abundance are expressed as density of individuals at each sampled stratum (ind./m^3).

(TP = 2.7), ostracods (TP = 2.6), and the pelagic *M. gregaria* stage with the lowest trophic position (TP = 2.1). The isotopic ellipses diagram shows a great degree of overlap in isotopic niche width among most groups except pelagic *M. gregaria* that occurred at the bottom of the ellipses diagram and that overlapped only partially with the other groups (**Figure 5B**). While pelagic *M. gregaria* showed the narrowest ellipse areas, *Sergestes* sp. showed the widest area (**Figure 5C**). Adult *E. vallentini*, and copepods, in turn showed similar ellipse areas, as revealed by the mean SEAc values, and ostracods showed values between the later groups and pelagic *M. gregaria* (**Table 3**). The relative importance of terrestrial organic carbon (TOC) in the diet of all crustaceans, as depicted by the $\delta^{13}C$ content, indicates that all groups analyzed were deeply dependent on terrestrial carbon, with percentages of terrestrial contribution varying from 41% in *E. vallentini* to 54% in mysid larvae (**Table 3**). Within the crustacean assemblage, pelagic *M. gregaria* (43%) and *Sergestes* sp. (42%) showed a lower proportion of terrestrial organic carbon in their tissues, compared with ostracods and copepods (50%).

Munida gregaria Stable Isotopes at Different Body Lengths and at Different Depths

Pelagic *M. gregaria* showed a wide range of body lengths (11.9–40.8 mm total length, TL), particularly at the surface layer where the size range was wider than that at other depths (**Figure 6**). Along the water column, however, their length distribution was dominated by a narrow body size range (15–20 mm TL) at all depths.

Over the length range of pelagic *M. gregaria* utilized for isotope and C/N analyses (6.9–21.5 cephalothorax length, CL), very small isotopic changes were observed in $\delta^{13}C$ (linear model, $n = 44$, $p = 0.0104$) and $\delta^{15}N$ (lineal model, $n = 44$, $p = 0.0213$) with cephalothorax length but with very low coefficients of determination ($R^2 = 0.14$ and $R^2 = 0.12$ for $\delta^{13}C$ and $\delta^{15}N$, respectively) (**Figure 7**). No significant relationship was observed between C/N and pelagic *M. gregaria* cephalothorax length (linear model, $n = 44$, $p = 0.3408$, $R^2 = 0.02$).

Along the water column, $\delta^{13}C$ in particulate matter (POM) ranged from −25.6 to −23.6‰ and did not show increases in mean values from the surface layer ($\delta^{13}C$ $POM_{0-10\ m} = -24.8 \pm 0.4$‰) to deeper layers ($\delta^{13}C$ $POM_{100\ m} = -24.0 \pm 0.4$‰). No significant difference was observed in the mean isotopic values of $\delta^{13}C$ in pelagic *M. gregaria* (Kruskal-Wallis, $p = 0.237$), suggesting that they eat terrestrial plant carbon and phytoplankton/macroalga-derived carbon throughout the column. However, a slight increase in $\delta^{15}N$ in pelagic *M gregaria* toward higher depths was observed (**Figure 8**), which coincided with the slightly higher trophic positions toward deeper waters ($TP_{0-10m} = 2.1$, $TP_{10-50m} = 2.13$, $TP_{50-100m} = 2.17$). The $\delta^{15}N$ difference among depths was not statistically significant when the mean values were compared (Kruskal-Wallis, $p = 0.126$). Means C/N values among depths were not significantly different (Kruskal-Wallis, $p = 0.444$).

TABLE 3 | Stable isotopes in the major pelagic crustaceans collected in the winter 2017 cruise to the Beagle channel, indicating number of samples analyzed (*n*), $\delta^{13}C$ (±standard deviation), $\delta^{15}N$ (±standard deviation), C/N ratio, trophic position (TP), corrected Stable Isotope Bayesian ellipse area (niche width; SEAc) and terrestrial organic carbon content (TOC) in the different groups.

Groups	*n*	$\delta^{13}C$ (‰)	δ^{15N} (‰)	C/N	TP	SEAc	TOC (%)
Munida gregaria pelagic	131	−19.81 ± 0.93	12.43 ± 0.74	4.08 ± 1.43	2.1	2.16	43
Euphausia vallentini adult	21	−19.50 ± 1.22	14.58 ± 1.16	4.73 ± 1.68	2.8	4.66	41
Copepods	32	−20.77 ± 1.33	14.10 ± 0.94	7.26 ± 3.40	2.8	4.95	50
Ostracods	21	−20.75 ± 1.16	14.75 ± 1.06	9.97 ± 4.81	2.6	3.29	50
Sergestes sp.	13	−21.07 ± 1.29	15.34 ± 1.17	7.02 ± 3.59	3.0	5.26	42
Mysis larvae	4	−21.27 ± 1.07	14.26 ± 1.28	8.04 ± 4.79	2.7	–	54

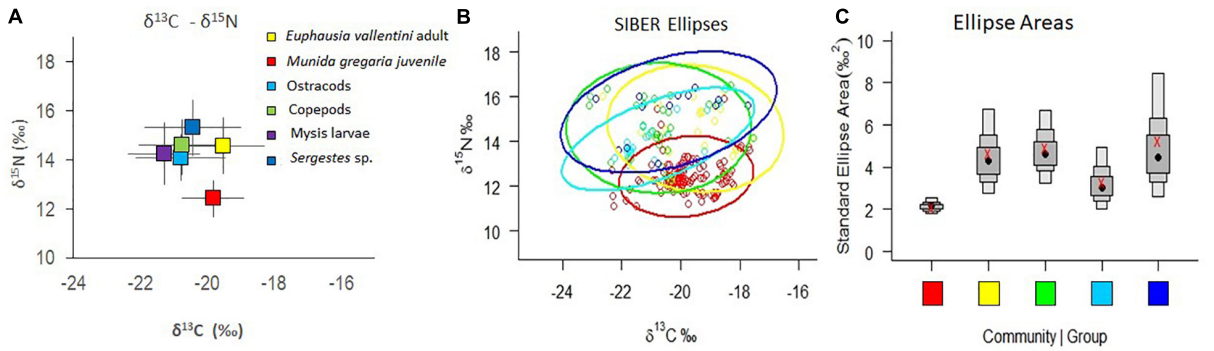

FIGURE 5 | Stable isotopes $\delta^{13}C$ and $\delta^{15}N$ values of the most abundant crustacean zooplankton groups in both locations (pooled data) sampled in winter 2017. **(A)** $\delta^{13}C$ and $\delta^{15}N$ plot of mean values (bars are standard deviations). **(B)** Stable Isotope Bayesian ellipses showing the width of the isotopic niche of each of the crustacean groups. **(C)** Box and whiskers plot of ellipse areas of each group showing the median, 50, 75, and 95% limits, and corrected mean value (x). Mysid larvae were not included in ellipses nor box and whiskers diagrams because of the low number of replicates available (<5 samples).

DISCUSSION

The general objective of this study was to assess how the dominant chitinous zooplankton groups in the BC survive during the winter low production season in this high latitude region. Our results show that the zooplankton community was similar in two fjords connected to the BC, where a single pelagic group dominated in terms of biomass (pelagic *Munida gregaria*), and that differences in vertical distribution occurred between most principal crustacean zooplankton groups and *M. gregaria*, which was partially explained by apparent shifts in vertical distribution between day and night in the former groups. All groups showed a high dependence on terrestrially derived organic matter, as revealed by their $\delta^{13}C$ values. However, the isotopic composition, TP estimates, and isotopic niche widths of the groups clearly separated pelagic *M. gregaria* from the others, presenting the lowest $\delta^{15}N$ and highest $\delta^{13}C$ values, and a narrower niche width. This group was dominated by a single body size class along the 0–100 m water column and remained during the day and at night, mostly in the upper layers (0–50 m), apparently benefiting from the higher phytoplankton concentrations (compared to deeper layers), as revealed by their higher $\delta^{13}C$ values and low TP. In contrast, the other groups changed in vertical distribution between day and night or remained deeper in the water column during the day, and showed slightly higher $\delta^{15}N$ values, higher TP, and lower $\delta^{13}C$ values, probably feeding on a microzooplankton-terrestrial POM mixture at deeper layers. Trophic flows through microbial loops from heterotrophic nanoflagellates and ciliates toward crustacean zooplankton have been reported during the winter season in Nord-Patagonian fjords (González et al., 2010).

The zooplankton community characteristics in both locations were similar despite local hydrographic differences between fjords exerted by different water exchange and freshening effects given by marine and land-terminating glaciers. The Pia fjord, closer to the Pacific Ocean connection than Yendegaia Bay, showed lower temperature and salinity at the surface, a large input of oceanic water at depth, and a more stratified water column (**Figure 2**). The chlorophyll *a* concentrations were very low (range: 0.03–0.28 mg/m^3) in both locations reaching values between one and two orders of magnitude lower than those observed in the same area in spring (Giesecke et al., 2019). The mesozooplankton community in this fjord, with abundances of organisms also one to two orders of magnitude lower than in spring (Giesecke et al., 2019), included a relatively similar number of taxa (20–22 functional groups) and a similar total number of organisms per group compared with Yendegaia Bay, but showed some gelatinous organisms not present in Yendegaia (apendicularia and ctenophores). The five numerically most abundant groups (copepods, ostracods, *E. vallentini* juveniles, *E. vallentini* adults, and pelagic *M. gregaria*) were the same in both locations, copepods and ostracods representing 90% of the zooplankton abundance in each zone, and were the most frequent and abundant mesozooplankton groups reported previously in

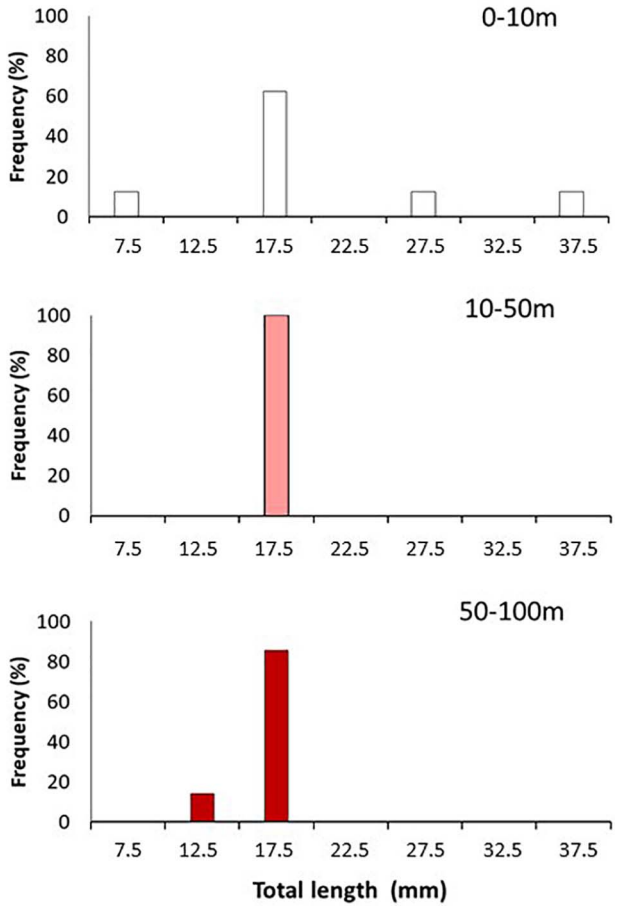

FIGURE 6 | Total length frequency distribution (%) of pelagic *Munida gregaria* collected at the three sampled strata (0–10 m, 10–50 m and 50–100 m depth) in both locations (pooled data) in winter 2017.

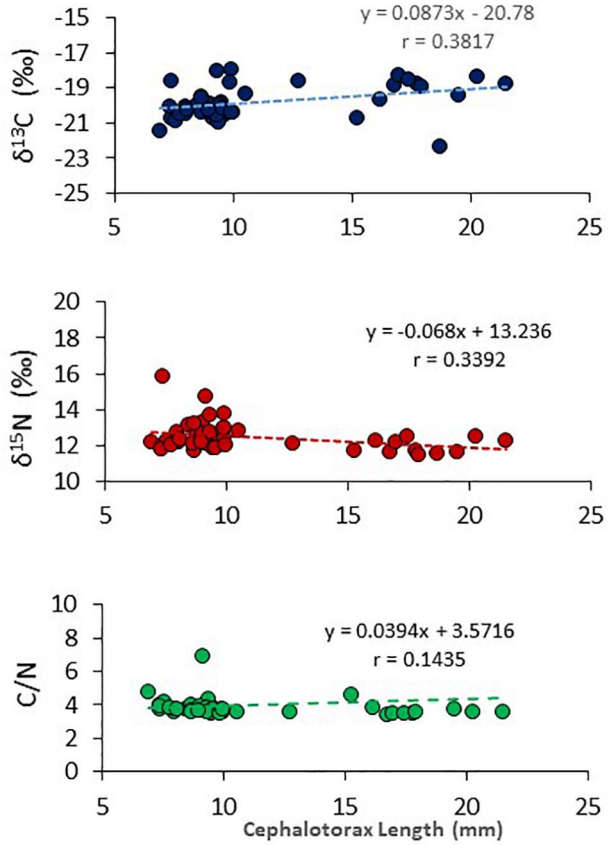

FIGURE 7 | Stable isotope values ($\delta^{13}C$, upper panel; $\delta^{15}N$, middle panel) and C/N ratio (bottom panel) in different body length (cephalothorax length, mm) pelagic *Munida gregaria* collected in winter 2107. Linear model regressions are also shown in both panels.

the BC but in other seasons (Biancalana et al., 2007; Aguirre et al., 2012; Giesecke et al., 2019). However, when transformed into biomass estimates (D/W), the relative importance of most zooplankton groups in our winter study significantly decreased, and pelagic *M. gregaria* became the most important group with biomass representing from ∼70–90% of the total zooplankton biomass in both locations (**Figure 3**).

The vertical distributions of the larger-sized crustacean groups differed between day and night, except for pelagic *M. gregaria*. While most groups showed an increase in abundance at all sampled layers during the night, apparently after a diel residence of most individuals deeper than our maximum depth sampled (e.g., *E. vallentini* 150 m diurnal mean weight depth; Hamame and Antezana, 2010), suggesting a diel vertical migration, pelagic *M. gregaria* remained mostly in the shallower 0–50 m layer in both periods. Diel vertical migration has been reported for most of these groups in other locations, including the Patagonian region, but in other seasons (Castro et al., 1993; Hamame and Antezana, 2010; Valle-Levinson et al., 2014). In *M. gregaria* zoea diel changes in vertical distribution have been documented mainly for the earlier stages in northern Patagonia and, depending on the location, in synchrony with semidiurnal tides (Castro et al., 2011, 2019). The vertical distribution of the pelagic *M. gregaria* in our study coincides with previous observations of post-larval stages in the Baker basin (47°S) or the inner sea of Chiloé (42°S), where their position has been associated with the halocline apparently to favor horizontal transport (Castro et al., 2019; Meerhoff et al., 2019). This also coincides with acoustic reports of juvenile *M. gregaria* in the BC where it reached maximum depths deeper than 80 m but that situated this species denser aggregations between 21 and 28 m depth (Diez et al., 2016, 2018). In neither of these studies in the BC further north in the northern and central Chilean Patagonian zone (Castro et al., 2019; Meerhoff et al., 2019), diel vertical migrations were documented for the post-larval (juvenile or megalopa) stages.

Stable isotope results show a narrow range in $\delta^{13}C$ (−21.2 to −19.5‰) and $\delta^{15}N$ (12.4–15.4‰) mean values across all groups. These low $\delta^{13}C$ values highlight the importance of terrestrial organic matter in sustaining the winter trophic web in the area (TOC = 41–54%). A relatively similar range of mean $\delta^{13}C$ values (−20.8 ± 3.8‰) was reported for zooplankton in spring in the

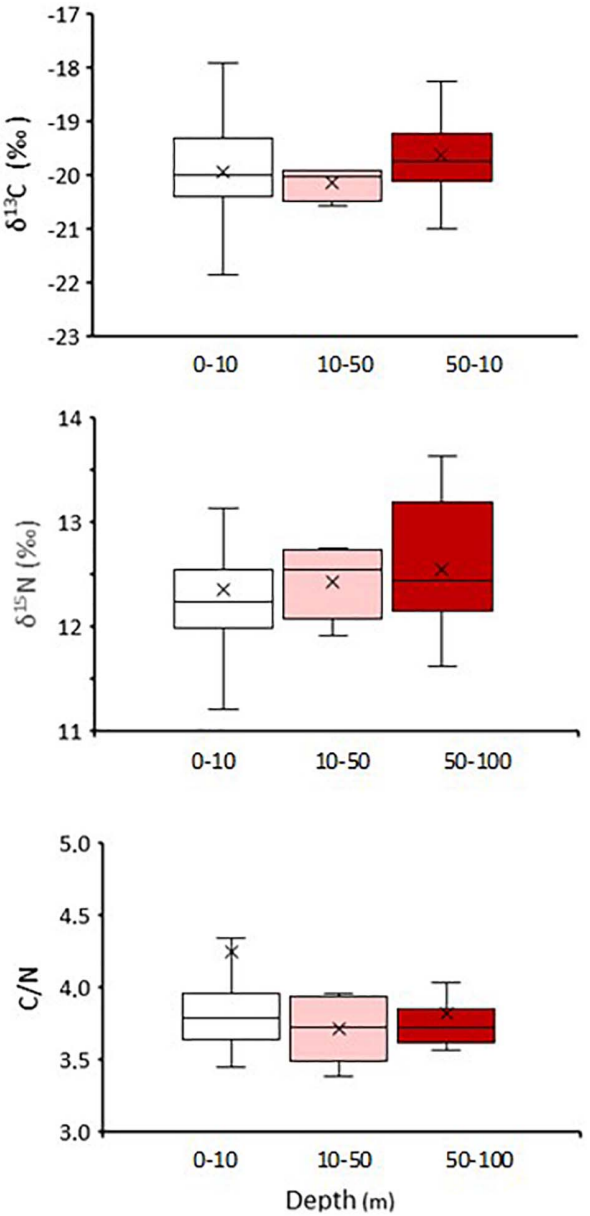

FIGURE 8 | Stable isotope (δ^{13}C, upper panel; δ^{15}N middle panel) and C/N ratio (bottom panel) in abdominal muscle of pelagic *Munida gregaria* at the three depth of collection (0–10 m, 10–50 m and 50–100 m depth).

same BC by Riccialdelli et al. (2017). However, among all groups in our study, pelagic *M. gregaria* (-19.81 ± 0.93‰) along with *E. vallentini* (-19.50 ± 1.22‰) showed the highest δ^{13}C values suggesting that marine particulate organic matter might also be an important part of their diet, at least in these two taxa. The δ^{15}N values and isotopic ellipses indicate that most groups superpose their isotopic niche, except for pelagic *M. gregaria*, which showed the lowest δ^{15}N values (12.43 ± 0.74‰) and TP (2.1) and a narrower isotopic niche, suggesting some differences in feeding resources compared to the other crustacean groups. The δ^{15}N values determined were within the range reported for this species: 10–12‰ in northern Patagonia (Meerhoff et al., 2019) and 14.1 ± 0.7‰ in the same BC in spring (Riccialdelli et al., 2017). Interestingly, δ^{13}C and δ^{15}N stable isotope values were similar at different *M. gregaria* body lengths in our study.

Slight differences in trends were observed in δ^{13}C and δ^{15}N values in pelagic *M. gregaria* toward deeper layers. In δ^{13}C, no clear differences were observed among depths, suggesting that a mixture of terrestrial and marine POM was ingested along the water column. Increasing values were observed in δ^{15}N toward higher depths, which resulted in a slightly higher TP deeper in the water column. Dissimilar trends in δ^{13}C and δ^{15}N in pelagic *M. gregaria* tissues with depth apparently resulted from a combination of processes that include, first, terrestrial organic carbon entering at the sea surface plus phytoplankton, and secondly, in addition to the sinking of organic matter from those sources in shallow waters, the potential addition of sinking fecal pellets, microzooplankton, or zooplankton debris into the pelagic *M. gregaria* diets at higher depths, which would result in similar δ^{13}C values but higher δ^{15}N and higher trophic levels deeper in the water column. Sediment trap samples deployed at 100 and 200 m depth from the study area (BC) showed a high amount of fecal material throughout the year (González, unpublished data). These sequential processes highlight the role of terrestrial and marine phytoplankton at the surface layers and of the sinking matter and microzooplankton at deeper layers, which determine a similar but significant terrestrial organic matter signal along the pelagic *M. gregaria* vertical distribution but with different trophic positions at different depths. The higher δ^{15}N and TP values of the other zooplankton or deeper resident crustacean groups coincide with the higher δ^{15}N and TP of those pelagic *M. gregaria* present in deeper waters, supporting this hypothesis, which suggests that feeding in deeper environments may modify the TP of organisms and hence induce separate feeding patterns among groups.

This study aimed to assess whether the more abundant and largest-body-sized crustacean pelagic groups in the BC develop differential feeding strategies conducive to favoring their coexistence during the austral low production winter season. Our overall results showed that two major groups could be identified in terms of feeding strategies: the first group included a mixture of some of the most abundant holoplankton organisms (>90% numerically) plus zoea *M. gregaria* stages, that reside deeper in the water column and move vertically during the day. The holoplanktonic group may feed on sinking organic matter or microzooplankton at depth and hence showed slightly higher trophic levels than the other group. The second group contained a single species (pelagic *M. gregaria*), which constitutes the dominant pelagic group in terms of biomass (>70%), resides mostly at the shallower 50 m of the water column, rich in terrestrially derived organic matter and some marine phytoplankton that constitutes its food, and which infringes them a lower trophic position and a slightly different terrestrial organic carbon signature in their tissues, compared with organisms in the other zooplankton groups. Pelagic *M. gregaria* did not change in vertical distribution during the day (at least not detected by our sampling methods) and so overlapped its distribution only with

those vertical migrating zooplankton groups at night, reducing the potential competence for food resources. The different (i) vertical distributions, (ii) trophic level food sources, and (iii) slightly different original organic carbon sources, seem to be part of the adaptive feeding strategy that facilitates the coexistence of different pelagic crustaceans under harsh feeding winter conditions at this high latitude region.

DATA AVAILABILITY STATEMENT

The original contributions presented in the study are included in the article/supplementary material, further inquiries can be directed to the corresponding author/s.

AUTHOR CONTRIBUTIONS

LC (zooplankton), HG (POM), and JG-V (hydrographic data) collaborated in the samples collection at sea and data analyses at the laboratory. PB also worked on the zooplankton analyses and stable isotope samples preparation. All authors participated in the manuscript writing.

FUNDING

This study was supported by the National Agency for Scientific Research and Development (ANID) through the project FONDAP-IDEAL Center (grant number 15150003). Additional funding was provided by the COPAS Sur Austral Center (ANID PIA APOYO CCTE AFB170006), which partially financed zooplankton analyses and LC and PB.

ACKNOWLEDGMENTS

The authors acknowledge the collaboration of E. Menschel and J. Martin and the Forrest vessel crew for their help at sea and S. Soto for assistance with statistical analyses.

REFERENCES

Aguirre, G. E., Capitanio, F. L., Lovrich, G. A., and Esnal, G. B. (2012). Seasonal variability of metazooplankton in coastal sub-Antarctic waters (Beagle Channel). *Mar. Biol. Res.* 8, 341–353. doi: 10.1080/17451000.2011.627922

Almandoz, G. O., Hernando, M. P., Ferreyra, G. A., Schloss, I. R., and Ferrario, M. E. (2011). Seasonal phytoplankton dynamics in extreme southern South America (Beagle Channel, Argentina). *J. Sea Res.* 66, 47–57. doi: 10.1016/j.seares.2011.03.005

Benstead, J. P., March, J. G., Fry, B., Ewel, K. C., and Pringle, C. M. (2006). Testing isosource: Stable isotope analysis of a tropical fishery with diverse organic matter sources. *Ecology* 87, 326–333. doi: 10.1890/05-0721

Bernal, A., Castro, L. R., and Costalago, D. (2020). Elucidating trophic pathways of the most abundant fish larvae in Northern Patagonia using $\delta^{13}C$ and $\delta^{15}N$ isotopes. *Mar. Ecol. Progr. Ser.* 650, 253–267. doi: 10.3354/meps13374

Betti, F., Castro, L. R., Bavestrello, G., Enrichetti, F., and Daneri, G. (2020). Distribution, abundance and ecological requirements of the benthic phase of *Munida gregaria* (Anomura; Munididae) in the Puyuhuapi Fjord (Chilean Patagonia). *Reg. Stud. Mar. Sci.* 40:101534. doi: 10.1016/j.rsma.2020.101534

Biancalana, F., Barría, M. S., and Hoffmeyer, M. S. (2007). Micro and mesozooplankton composition during winter in Ushuaia and Golondrina bays (Beagle channel, Argentina). *Braz. J. Oceanogr.* 55, 83–95. doi: 10.1590/s1679-87592007000200002

Bianchi, T. S. (2007). *Biogeochemistry of Estuaries*. Oxford: Oxford University Press, 706.

Casassa, G., Wendt, J., Wendt, A., Lopez, P., Schuler, T., Maas, H., et al. (2010). Outburst floods of glacial lakes in Patagonia: is there an increasing trend? *Geophys. Res. Abstr.* 12:12821.

Castro, L. R., Bernal, P. A., and Troncoso, V. A. (1993). Coastal intrusion of copepods: mechanisms and consequences in the population biology of *Rhincalanus nasutus*. . *J. Plankton Res.* 15, 501–515. doi: 10.1093/plankt/15.5.501

Castro, L. R., Cáceres, M. A., Silva, N., Muñoz, M. I., León, R., Landaeta, M. F., et al. (2011). Short-term variations in mesozooplankton, ichthyoplankton, and nutrients associated with semi-diurnal tides in a Patagonian Gulf. *Cont. Shelf Res.* 31, 282–292. doi: 10.1016/j.csr.2010.09.005

Castro, L. R., Soto, S., and González-Saldías, F. (2019). Ontogenetic and short-term fluctuations in the residence depth of young pelagic stages of *Munida gregaria* in different zones of northern Patagonia. *Progr. Oceanogr.* 174, 173–184. doi: 10.1016/j.pocean.2018.09.018

Climate Change (2007). *Synthesis Report. Contribution of Working Groups I, II and III to the Fourth Assessment Report of the Intergovernmental Panel on Climate Change*, eds Core Writing Team, R. K. Pachauri, and A. Reisinger (Geneva, Switzerland: IPCC), 104.

Climate Change (2013). *The Physical Science Basis. Contribution of Working Group I to the Fifth Assessment Report of the Intergovernmental Panel on Climate Change*, eds T. F. Stocker, D. Qin, G.-K. Plattner, M. Tignor, S. K. Allen, J. Boschung, A. Nauels, Y. Xia, V. Bex and P. M. Midgley (Cambridge, United Kingdom and New York, NY, USA: Cambridge University Press), 1535.

Diez, M. J., Cabreira, A. G., Madirolas, A., and Lovrich, G. A. (2016). Hydroacoustical evidence of the expansion of pelagic swarms of *Munida gregaria* (Decapoda, Munididae) within the Beagle Channel and the Argentine Patagonian Shelf, and its relationship with habitat features. *J. Sea Res.* 114, 1–12. doi: 10.1016/j.seares.2016.04.004

Diez, M. J., Cabreira, A. G., Madirolas, A., Martin, J. N., Scioscia, G., Schiavini, A., et al. (2018). Winter is cool: spatio-temporal patterns of squat lobster *Munida gregaria* and the Fuegian sprat *Sprattus fuegensis* in a sub-Antarctic estuarine environment. *Polar Biol.* 41, 2591–2605. doi: 10.1007/s00300-018-2394-2

Diez, M. J., Pérez-Barros, P., Romero, M. C., Scioscia, G. F., Tapella, F., Cabreira, A. G., et al. (2012). Pelagic swarms and beach strandings of the squat lobster *Munida gregaria* (Anomura: Munididae) in the Beagle Channel. Tierra del Fuego. *Polar Biol.* 35, 973–983. doi: 10.1007/s00300-011-1144-5

Dussaillant, A., Benito, G., Buytaert, W., Carling, P., Meier, C., and Espinoza, F. (2009). Repeated glacial-lake outburst floods in Patagonia: an increasing hazard? *Nat. Hazards* 54, 469–481. doi: 10.1007/s11069-009-9479-8

Giesecke, R., Höfer, J., Vallejosa, T., and González, H. E. (2019). Death in southern Patagonian fjords: copepod community structure and mortality in land- and marine-terminating glacier-fjord systems. *Progr. Oceanogr.* 174, 162–172. doi: 10.1016/j.pocean.2018.10.011

González, H. E., Calderón, M. J., Castro, L., Clement, A., Cuevas, L. A., Daneri, G., et al. (2010). Primary production and its fate in the pelagic food web of the Reloncaví Fjord and plankton dynamics of the Interior Sea of Chiloé, Northern Patagonia, Chile. *Mar. Ecol. Progr. Ser.* 402, 13–30. doi: 10.3354/meps08360

González, H. E., Castro, L., Daneri, G., Iriarte, J. L., Silva, N., Vargas, C. A., et al. (2011). Seasonal plankton variability in Chilean Patagonia Fjords: carbon flow through the pelagic food web of the Aysen Fjord and plankton dynamics in the Moraleda Channel basin. *Cont. Shelf Res.* 31, 225–243. doi: 10.1016/j.csr.2010.08.010

González, H. E., Graeve, M., Kattner, G., Silva, N., Castro, L., Iriarte, J. L., et al. (2016). Carbon flow through the pelagic food web in southern Chilean Patagonia: relevance of *Euphausia vallentini* as key species. *Mar. Ecol. Progr. Ser.* 557, 91–110. doi: 10.3354/meps11826

Hamame, M., and Antezana, T. (2010). Migración vertical diurno-nocturna y alimentación de *Euphausia vallentini* en los fiordos del sur de Chile. *Deep Sea Res. II* 57, 642–650.

Jackson, A., Inger, R., Parnell, A. C., and Bearshop, S. (2011). Comparing isotopic niche widths among and within communities: SIBER–Stable Isotope Bayesian ellipses in R. *J. Anim. Ecol.* 80, 595–602. doi: 10.1111/j.1365-2656.2011.01806.x

Laiz-Carrion, R., Quintanilla, J. M., Mercado, J. M., and García, A. (2011). Combined study of daily growth variability and nitrogen-carbon isotopic signature analysis of schooling *Sardina pilchardus* larvae. *J. Fish Biol.* 79, 896–914. doi: 10.1111/j.1095-8649.2011.03048.x

León, R., Castro, L. R., and Cáceres, M. (2008). Dispersal of *Munida gregaria* (Decapoda: Galatheidae) larvae in Patagonian channels of southern Chile. *ICES J. Mar. Sci.* 65, 1131–1143. doi: 10.1093/icesjms/fsn093

Lindsay, D. J., Minagawa, M., Mitani, I., and Kawaguchi, K. (1998). Trophic shift in the Japanese anchovy *Engraulis japonicus* in its early life history stages as detected by stable isotope ratios in Sagami Bay, Central Japan. *Fish. Sci.* 64, 403–410. doi: 10.2331/fishsci.64.403

Malzahn, A. M., and Boersma, M. (2009). Trophic flexibility in larvae of two fish species (lesser sand eel, *Ammodites marinus* and dab, *Limanda limanda*) Advances in the early life history study of fish. *Sci. Mar.* 73, 131–139. doi: 10.3989/scimar.2009.73s1131

Marín, V. H., Tironi, A., Parades, M. A., and Contreras, M. (2013). Modeling suspended solids in a Northern Chilean Patagonia glacier-fed fjord: GLOF scenarios under climate change conditions. *Ecol. Model.* 264, 7–16. doi: 10.1016/j.ecolmodel.2012.06.017

Meerhoff, E., Castro, L., and Tapia, F. (2013). Influence of freshwater discharges and tides on the abundance and distribution of larval and juvenile *Munida gregaria* in the Baker river estuary, Chilean Patagonia. *Cont. Shelf Res.* 61, 1–11. doi: 10.1016/j.csr.2013.04.025

Meerhoff, E., Castro, L. R., Tapia, F. J., and Pérez-Santos, I. (2019). Hydrographic and biological impacts of a Glacial Lake Outburst Flood (GLOF) in a Patagonian Fjord. *Estuaries Coasts* 42, 132–143. doi: 10.1007/s12237-018-0449-9

Meerhoff, E., Tapia, F., and Castro, L. R. (2014). Spatial structure of the meroplankton community along a Patagonian fjord – the role of changing freshwater inputs. *Prog. Oceanogr.* 129, 125–135. doi: 10.1016/j.pocean.2014.05.015 x

Montecinos, S., Castro, L. R., and Neira, S. (2016). Stable isotope (δ^{13}C and δ^{15}N) and trophic position of Patagonian sprat (*Sprattus fuegensis*) from the Northern Chilean Patagonia. *Fish. Res.* 179, 139–147. doi: 10.1016/j.fishres.2016.02.014

Mujica, A., Nava, M. L., Saavedra, M., Pereira, J., and Vargas, A. (2013). Distribution and abundance of larvae of *Munida gregaria* (Fabricius, 1793), *Sergestes arcticus* Kroyer, 1855 and *Neotrypea uncinata* (H. Milne-Edwards, 1837) between Puerto Montt (41°30'S) and Laguna San Rafael (46°30'S), southern Chile. *Lat. Am. J. Aquat. Res.* 41, 828–838. doi: 10.3856/vol41-issue5-fulltext-3

Overman, N. C., and Parrish, D. L. (2001). Stable isotope composition of walleye: δ^{15}N accumulation with age and area-specific differences in δ^{13}C. *Can. J. Fish. Aquat. Sci.* 58, 1253–1260. doi: 10.1139/f01-072

Pérez-Barros, P., Romero, M. C., Calcagno, J. A., and Lovrich, G. A. (2010). Similar feeding habits of two morphs of *Munida gregaria* (Decapoda) evidence the lack of trophic polymorphism. *Rev. Biol. Mar. Oceanog.* 45, 461–470. doi: 10.4067/s0718-19572010000300011

Pérez-Barros, P., Calcagno, J. A., and Lovrich, G. A. (2011). Absence of a prezygotic behavioral barrier to gene flow between the two sympatric morphs of the squat lobster *Munida gregaria* (Fabricius, 1793) (Decapoda: Anomura: Galatheidae). *Helgoland Mar. Res.* 65, 513–523. doi: 10.1007/s10152-010-0240-1

Pérez-Barros, P., D'Amato, M. E., Guzman, N. V., and Lovrich, G. A. (2008). Taxonomic status of two South American sympatric squat lobsters, *Munida gregaria* and *Munida subrugosa* (Crustacea: Decapoda: Galatheidae), challenged by DNA sequence information. *Biol. J. Linn. Soc. Lond.* 94, 421–434. doi: 10.1111/j.1095-8312.2008.00987.x

Post, D. M. (2002). Using stable isotopes to estimate trophic position: models, methods and assumptions. *Ecology* 83, 703–718. doi: 10.1890/0012-9658(2002)083[0703:usitet]2.0.co;2

RGI (2017). *Randolph Glacier Inventory–A Dataset of Global Glacier Outlines: Version 6.0: Technical Report*. Boulder, CO: Global Land Ice Measurements from Space, doi: 10.7265/N5-RGI-60

Riccialdelli, L., Newsome, S. D., Fogel, M. L., and Fernández, D. A. (2017). Trophic interactions and food web structure of a sub Antarctic marine food web in the beagle channel: Bahía Lapataia, Argentina. *Polar Biol.* 40, 807–821. doi: 10.1007/s00300-016-2007-x

Rivera, A., Benham, T., Casassa, G., Bamber, J., and Dowdeswell, A. J. (2007). Ice elevation and areal changes of glaciers from the Northern Patagonia Ice field, Chile. *Glob. Planet. Chang.* 59, 126–137. doi: 10.1016/j.gloplacha.2006.11.037

Rosenberg, P., and Palma, S. (2003). Cladocerans in Patagonian fjords and channels, between the Penas Gulf and Strait of Magellan. *Invest. Mar. Valparaíso* 31, 15–24.

Ross, L., Pérez-Santos, I., Parady, B., Castro, L., Valle-Levinson, A., and Schneider, W. (2020). Glacial lake outburst flood (GLOF) events and water response in a Patagonian fjord. Water Quality and Ecosystems. *Water* 12:248. doi: 10.3390/w12010248

Tanaka, H., Takasuka, A., Aoki, I., and Ohshimo, S. (2008). Geographical variations in the trophic ecology of Japanese anchovy, *Engraulis japonicus*, inferred from carbon and nitrogen stable isotope ratios. *Mar. Biol.* 154, 557–568. doi: 10.1007/s00227-008-0949-4

Tapella, F., Romero, M. C., Lovrich, G. A., and Chizzini, A. (2002). "Life history of the galatheid crab *Munida subrugosa* in sub Antarctic waters of the Beagle Channel, Argentina," in *Crabs in Cold Water Regions: Biology, Management and Economics*, eds A. J. Paul, E. G. Dawe, R. Elner, G. S. Jamieson, G. H. Kruse, R. S. Otto, et al. (Fairbanks, AK: University of Alaska Sea Grant), 115–133.

Valladares, J., Fennel, W., and Morozov, E. G. (2011). Announcement: replacement of EOS-80 with the International Thermodynamic Equation of Seawater—2010 (TEOS-10). *Deep Sea Res.* 58:978. doi: 10.1016/j.dsr.2011.07.005

Valle-Levinson, A., Castro, L. R., Pizarro, O., and Cáceres, M. (2014). Twilight vertical migrations of zooplankton in a Chilean fjord. *Progr. Oceanogr.* 129, 114–124. doi: 10.1016/j.pocean.2014.03.008

Vander Zanden, M. J., and Rasmussen, J. B. (1999). Primary consumer delta C-13 and delta N-15 and the trophic position of aquatic consumers. *Ecology* 80, 1395–1404. doi: 10.1890/0012-9658(1999)080[1395:pccana]2.0.co;2

Vander Zanden, M. J., and Rasmussen, J. B. (2001). Variation in delta N-15 and delta C-13 trophic fractionation: implications for aquatic food web studies. *Limnol. Oceanogr.* 46, 2061–2066. doi: 10.4319/lo.2001.46.8.2061

Vander Zanden, M. J. (1997). Comparing trophic position of freshwater fish calculated using stable nitrogen ratios (δ^{15}N) and literature dietary data. *Can. J. Fish. Aquat. Sci.* 54, 1142–1158. doi: 10.1139/f97-016

Vargas, C. A., Martínez, R. A., San Martin, V., Aguayo, M., Silva, N., and Torres, R. (2011). Allochthonous subsidies of organic matter across a lake-river-fjord landscape in the Chilean Patagonia: implications for marine zooplankton in inner fjord areas. *Cont. Shelf Res.* 31, 187–201. doi: 10.1016/j.csr.2010.06.016

Vinuesa, J. H., and Varisco, M. (2007). Trophic ecology of the lobster krill *Munida gregaria* in San Jorge Gulf, Argentina. *Investig. Mar.* 35, 25–34.

Wiebe, P. H. (1988). Functional regression equations for zooplankton displacement volume, wet weight, dry weight, and carbon: a correction. *Fish. Bull. (U. S.)* 86, 833–835.

Young, H., Nigro, K., Mccauley, D. J., Ballance, L. T., Oleson, E. M., and Baumann-Pickering, S. (2017). Limited trophic partitioning among sympatric delphinids off a tropical oceanic atoll. *Plos One* 12:e0181526. doi: 10.1371/journal.pone.0181526

Zagami, G., Antezana, T., Ferrari, I., Granata, A., Sitran, R., Minutoli, R., et al. (2011). Species diversity, spatial distribution, and assemblages of zooplankton within the Strait of Magellan in austral summer. *Polar Biol.* 34, 1319–1333. doi: 10.1007/s00300-011-0962-9

Conflict of Interest: The authors declare that the research was conducted in the absence of any commercial or financial relationships that could be construed as a potential conflict of interest.

frontiers in Marine Science

BRIEF RESEARCH REPORT
published: 09 July 2021
doi: 10.3389/fmars.2021.613265

Argo Float Reveals Biogeochemical Characteristics Along the Freshwater Gradient Off Western Patagonia

Alexander Galán[1], Gonzalo S. Saldías[2,3], Andrea Corredor-Acosta[3], Richard Muñoz[2], Carlos Lara[4,5] and José Luis Iriarte[3,6,7]*

[1] Centro de Investigación de Estudios Avanzados del Maule (CIEAM), Vicerrectoría de Investigación y Postgrado & Departamento de Obras Civiles, Facultad de Ciencias de la Ingeniería, Universidad Católica del Maule, Talca, Chile, [2] Departamento de Física, Facultad de Ciencias, Universidad del Bío-Bío, Concepción, Chile, [3] Centro FONDAP de Investigación en Dinámica de Ecosistemas Marinos de Altas Latitudes (IDEAL), Valdivia, Chile, [4] Departamento de Ecología, Facultad de Ciencias, Universidad Católica de la Santísima Concepción, Concepción, Chile, [5] Centro de Investigación en Recursos Naturales y Sustentabilidad (CIRENYS), Universidad Bernardo O'Higgins, Santiago, Chile, [6] Instituto de Acuicultura, Universidad Austral de Chile, Puerto Montt, Chile, [7] Centro de Investigación Oceanográfica COPAS Sur-Austral, Universidad de Concepción, Concepción, Chile

The coastal region off Chilean Patagonia has been poorly studied due to the lack of available observations. Here we analyzed, by the very first time, biogeochemical (BGC) data to elucidate the role that biological and physical processes play on nitrate, oxygen, pH and hydrographic variables, along a salinity gradient off central Patagonia. Argo float profiles covering the upper ocean from December 2015 to July 2019 reveal that offshore waters are characterized by low temperatures and high salinities related to high oxygen and medium-high values of pH and nitrate. As the Argo float drifted onshore, freshwater influences the upper 50–100 m with low salinity and high temperature. Waters under the influence of the continental runoff were characterized by medium-to-high oxygen and pH levels, and the lowest nitrate concentrations. Interestingly, oxygen-deficient waters located beneath the freshwater-modified layer showed the lowest pH and highest nitrate. A comprehensive analysis of the temporal and vertical variability of the oxygen:nitrate ratio, in conjunction with biological-related and physical parameters, indicates that the BGC variability seems to be the result of a synergistic interaction between physical and biological processes, where the stratification sets up the environment and promotes the biological response that, in turn, is auto-regulated by modifying the chemical composition in the freshwater-influenced zone. The arrival of future floats with additional sensors (Chlorophyll/Fluorescence, Photosynthetically Active Radiation, Backscatter, etc.) will add new BGC properties that improve our understanding of the coastal marine response to the increasing freshwater input off western Patagonia in the context of climate change.

Keywords: stratification, Patagonian ice fields, Argo floats, HYCOM, freshening, biogeochemical processes, Redfield ratio

OPEN ACCESS

Edited by:
Eduardo Joel Quiroga Jamett, Pontifical Catholic University of Valparaíso, Chile

Reviewed by:
Fabrizio D'Ortenzio, Centre National de la Recherche Scientifique (CNRS), France
Stephen C. Riser, University of Washington, United States

****Correspondence:***
Gonzalo S. Saldías
gsaldias@ubiobio.cl

Specialty section:
This article was submitted to Marine Biogeochemistry, a section of the journal Frontiers in Marine Science

Received: *01 October 2020*
Accepted: *01 June 2021*
Published: *09 July 2021*

Citation:
Galán A, Saldías GS, Corredor-Acosta A, Muñoz R, Lara C and Iriarte JL (2021) Argo Float Reveals Biogeochemical Characteristics Along the Freshwater Gradient Off Western Patagonia. Front. Mar. Sci. 8:613265. doi: 10.3389/fmars.2021.613265

1. INTRODUCTION

Ocean biogeochemistry (BGC) has been frequently studied in particular regions, commonly associated with long-term monitoring programs. The lack of a global observational array of BGC parameters has led to the recent development of autonomous platforms, such as Argo floats, to measure nutrients, dissolved oxygen, and bio-optical properties

(Gould et al., 2004; Claustre et al., 2020). The Argo network comprises a global array of more than 4,000 free-drifting and battery-powered profiling floats measuring temperature, salinity, oxygen, nitrate, and pH from the surface to about 2,000 m depth (Riser et al., 2016; Claustre et al., 2020). However, only <10% of the floats are equipped with sensors other than temperature and salinity. The BGC-Argo program is transforming our understanding of ocean variability over regional (e.g., Mediterranean Sea) and basin-scale efforts (e.g., SOCCOM; Southern Ocean Carbon and Climate Observations and Modeling) relying heavily on BGC-Argo measurements (Roemmich et al., 2019). The use of BGC-Argo floats has helped to increase the understanding of key bio-physical processes in the upper ocean, including (i) the initiation of spring phytoplankton blooms occurring prior to a significant shoaling of the mixed layer in the western North Atlantic (Boss and Behrenfeld, 2010), (ii) the development of new parameterizations to monitoring CO_2 in the subarctic North Pacific (Li et al., 2019), (iii) the temporal coupling between physical and biological properties with the development of the seasonal pycnocline in the western North Pacific (Sukigara et al., 2011), and (iv) a significant CO_2 outgassing in the high-latitude Southern Ocean linked to the upwelling of deep water (Gray et al., 2018), among others.

The freshwater input into the coastal ocean is one of the leading causes of sea-level rise and coastal stratification (Munk, 2003). In general, the melting of Greenland and Antarctic ice sheets is the primary source of freshwater impacting significantly sea-level rise (Vizcaíno et al., 2008; Nerem et al., 2018; Adusumilli et al., 2020). Off western Patagonia, the Subantarctic Water (SAAW) is mixed with freshwater from river outflows, rain, and ice melting, generating Modified Subantarctic Waters (MSAAW) (Sievers and Silva, 2008; Saldías et al., 2019). Recently, the first study analyzing the freshwater structure and seasonal variability off western Patagonia showed that the largest freshwater content is centered off central Patagonia next to the Gulf of Penas, where the low-salinity surface layer dominates the stratification of the upper ocean. In contrast, the freshwater content plays a minor role in setting up the stratification off northern and southern Patagonia (Saldías et al., 2019). The BGC properties of the coastal ocean off western Patagonia has been largely overlooked due to the lack of continuous field campaigns. In comparison, most efforts have been focused in fjords and channels along the entire Chilean Patagonia (Pantoja et al., 2011; Iriarte et al., 2014, and references therein). To the best of our knowledge, this is the first study reporting BGC variability in the coastal ocean off the Gulf of Penas in central Patagonia, a region influenced by freshwater from rivers and melting from the two major Patagonian icefields.

The local stratification, product of a strong thermohaline interaction between the runoff of continental waters with the SAAW at the Chilean Patagonia fjords (41–53°S) (Dávila et al., 2002; Iriarte et al., 2014; Saldías et al., 2019), has an important effect on the phytoplankton dynamics (i.e., distribution and activity) (González et al., 2013; Iriarte et al., 2014; Jacob et al., 2014; León-Muñoz et al., 2018) since stratification keeps phytoplankton cells within the euphotic zone by limiting the depth of turbulent mixing. Nevertheless, stratification also leads to the eventual cessation of primary production after phytoplankton blooms, owing to the reduction in the vertical supply of macronutrients from subsurface waters (Iriarte et al., 2007, 2014). However, little is known about the phytoplankton response to freshwater-influenced stratification in the coastal region, further considering that inorganic nutrients availability should present a marked seasonality related mainly with the intrusion of nutrient-poor waters (except for silicic acid); modulated mainly by the pluvial (autumn-winter) and snowmelt (spring) Patagonian seasonal regimes (Iriarte et al., 2017, and references therein). In this intricate scenario, we study the spatiotemporal BGC variability to understand the role of biological (e.g., primary production or respiration) and physical (e.g., water column stratification or air-sea interaction) processes on the recorded BGC measurements, and propose that stratification triggers the biological response, which, in turn, modulates the elemental variability (i.e., consume vs. production) of the coastal system off central Patagonia.

2. MATERIALS AND METHODS

We used profiles of temperature, salinity, pressure, oxygen, pH, and nitrate from a BGC Argo profiling float (5904663) during December 2015–July 2019 (see **Figure 1**). Only good quality-controlled data were used, and thus, pH data from December 2019 were not considered (see **Figure 2d**) since their values increased sharply to ranges over 25. We have only used flag $n = 1$ "Good Data" according to the section 3.2 Reference table 2: Argo quality control flag scale (Argo user's manual). Unfortunately, the 5904663 float did not have PAR (Photosynthetic Active Radiation), chlorophyll, and backscatter sensors to complement the BGC measurements. Argo floats are programmed to descend to a parking depth ranging from 1,000 to 2,000 m. At this depth they drift with the flow field for ∼10 days, after which they ascend to the surface recording the specified variables in a continuous profile (Roemmich et al., 2009; Wong et al., 2020). The 5904663 float recorded data to a depth of 2,000 m. However, a low-resolution sampling interval of ∼100 m was programmed below 1,000 m. The higher vertical resolution is ∼1 m in the top 100 m. Here, our focus is on the BGC variability in the upper ocean by which the top 500 m are analyzed.

Maps of surface salinity were obtained from the HYbrid Coordinate Ocean Model (HYCOM) with a spatial resolution of 1/12° (https://www.hycom.org/dataserver/gofs-3pt0/analysis/) for two contrasting freshwater conditions on March 25 and August 16, 2018 (see **Figure 1**). HYCOM uses isopycnal coordinates in the open ocean, terrain-following coordinates in shallow coastal regions, and z-level coordinates in the mixed layer, thus being optimal for large domains with variable topography and ocean conditions (Bleck and Boudra, 1981; Bleck, 2002). A T-S diagram and time series of concomitant surface temperature and salinity data reveal a high correlation in temperature ($R = 0.97$) and a fairly acceptable correlation in salinity ($R = 0.65$) between the surface HYCOM and Argo float data (**Supplementary Figure 1**).

A time series of surface total Chlorophyll-a (Chl-a) was obtained from monthly satellite data from version 4.2 of the

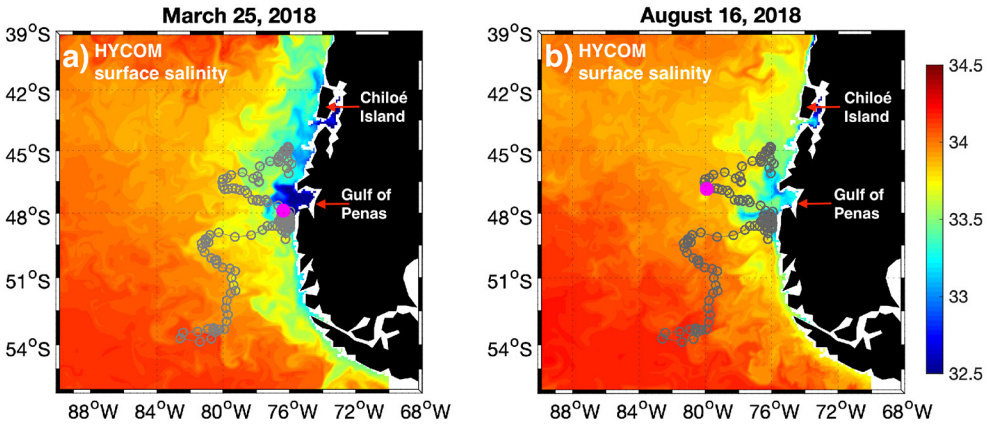

FIGURE 1 | Maps of surface salinity from HYCOM global model on **(a)** March 25, 2018, and **(b)** August 16, 2018. The gray circles denote the trajectory of BGC Argo float 5904663 from December 8, 2015 (offshore, southwest limit) to July 3, 2019 (nearshore, north of Gulf of Penas). The magenta dot shows the location of the float on the same date of the corresponding HYCOM salinity field.

Ocean Color Climate Change Initiative (OC-CCI, a merged product available at http://www.oceancolour.org/), at processing level 3 and spatial resolution of 4 km. To obtain the Chl-a values around the location of the BGC-Argo float, a nine-pixel window centered in the location of the BGC-Argo float was used at each time step. Only match-ups with a coefficient of variation <0.15 and 50% of valid data in the window were considered. Then, the median Chl-a concentration of these pixels was taken as the total Chl-a estimate (Corredor-Acosta et al., 2018). The blank spaces in the Chl-a time series correspond to missing data (i.e., months in which the criteria were not met).

The stability of the water column, was quantified through the Potential Energy Anomaly (PEA) following Saldías et al. (2019). The PEA is the amount of mechanical energy required to instantaneously mix the water column (Simpson et al., 1981). Therefore, a highly stratified water column would require more energy to become homogenized. To characterize the stratification of the water column across the zonal gradient (offshore-onshore) along the trajectory of the BGC-Argo float, the PEA was evaluated for the entire upper ocean (500 m depth) and for the first 250 m of depth, where the greatest changes in physical and chemical properties were observed.

3. RESULTS

The coastal ocean off western Patagonia has a low-salinity band along its entire latitudinal extension. The major freshwater content comes from the Gulf of Penas in central Patagonia (**Figures 1a,b**). The BGC Argo float 5904663 was deployed on the southwestern tip of its trajectory (∼54°S–83°W) on December 2015 and drifted in the north and northeast direction. By about April 2017 the float reached the coastal region south of the Gulf of Penas and stayed looping around until April 2018, before continuing farther north (**Figure 1**; gray trajectory). The contrast in freshwater conditions between the examples of March 25 and August 16, 2018 is remarkable, with the float being profiling the region next to the mouth of the Gulf of Penas (a magenta dot in **Figure 1** denotes the position of the float) during a high freshwater outflow event (**Figure 1a**), and being drifted farther offshore when the freshwater content was considerably reduced in winter (**Figure 1b**).

The vertical structure of the upper 500 m along the path of sampling is shown in **Figure 2**. During most of 2016 the float measured the vertical structure and BGC variability in offshore waters. Low temperatures (<8°C), high salinity (generally >34), high oxygen (>250 μmol kg^{-1}), and medium-to-high values of pH (about 7.9–8.1) and Nitrate (about 20–25 μmol kg^{-1}) characterized the upper ocean of offshore waters (**Figures 2a–e**). A low-salinity buoyant layer frequently influenced the profiles near the Guf of Penas in the top 50–100 m during most of 2017 and early 2018 (**Figure 2b**). This freshwater layer was characterized, relative to periods with higher surface salinity such as June-December 2018, by high temperature (>11°C), high oxygen (>250 μmol kg^{-1}) and pH (>8), and low nitrate (<15 μmol kg^{-1}) concentrations (**Figures 2a–e**). This pattern was repeated during the following freshening event in spring-summer 2018–2019. A sharp vertical gradient in BGC properties was found below the surface low-salinity layer with low-oxygen, low-pH, and high-nitrate waters. Note that the depth of the base of this subsurface layer fluctuated around 200–450 m (**Figures 2a–e**), and that low-pH (<7.8) and high-nitrate (>28 μmol kg^{-1}) intermediate waters were restricted to the pools of low oxygen (<180 μmol kg^{-1}).

Vertical profiles of hydrographic (temperature, salinity, and potential density) and BGC (oxygen, pH, and nitrate) variables during contrasting freshwater conditions (same as in **Figure 1**) are presented in **Figure 3**. Elevated freshwater conditions with a low salinity layer occupied the top 50 m of the water column (**Figure 3B**). Low salinity and high temperature contributed to a low-density buoyant upper layer that only reached a higher density as in the farther offshore profile at 100 m

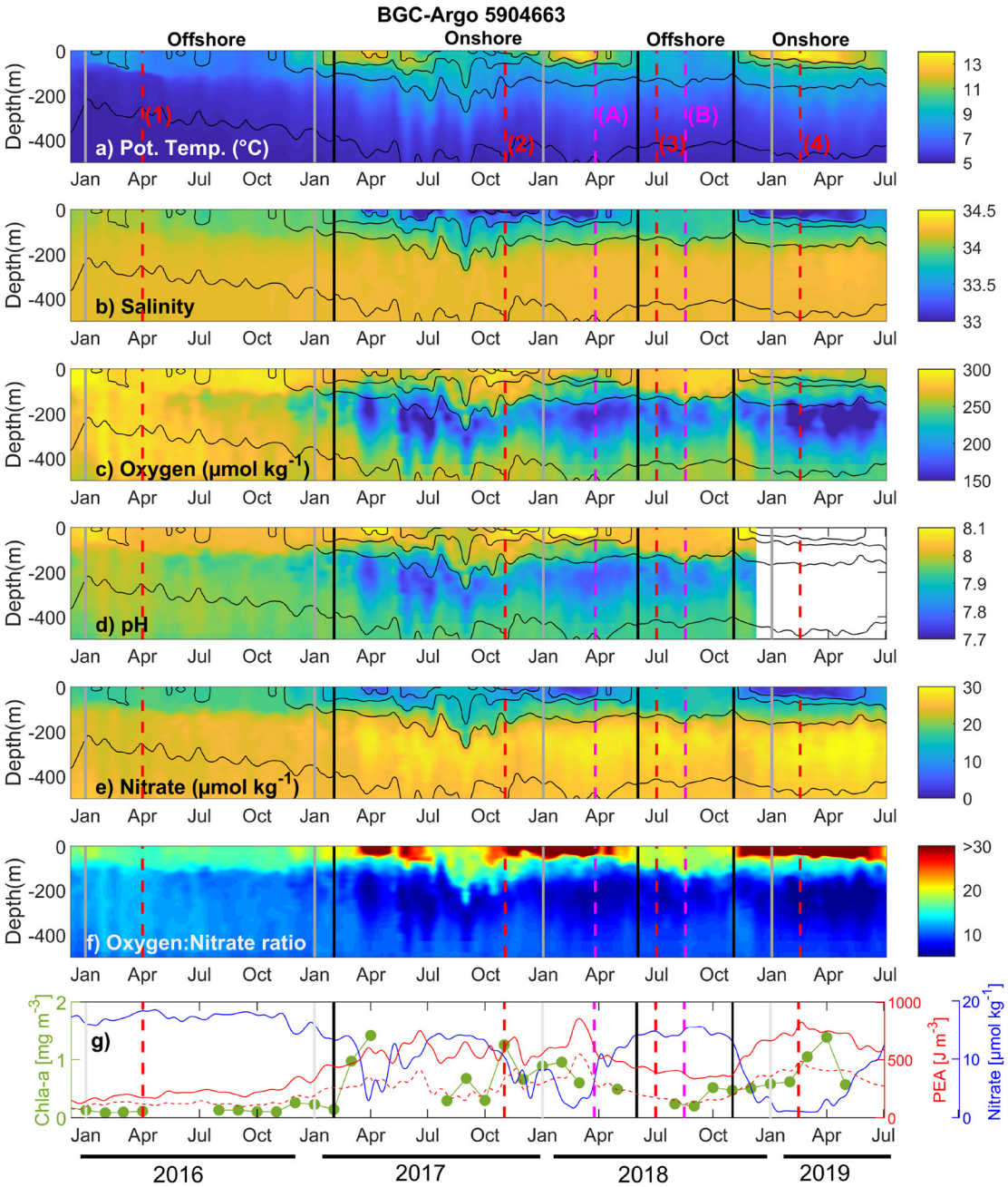

FIGURE 2 | Evolution of the upper ocean (top 500 m) **(a)** potential temperature, **(b)** salinity, **(c)** oxygen, **(d)** pH, **(e)** Nitrate, **(f)** Oxygen:Nitrate ratio, **(g)** surface Chlorophyll-a (Chl-a; green line), Potential Energy Anomaly (PEA) for the upper 250 m (solid red line) and 500 m (dashed red line), and surface nitrate (1 m depth; blue line), along the trajectory of BGC-Argo float 5904663 from December 2015 to July 2019. Black contours denote isopycnals. Vertical red lines indicate the dates of selected T-S diagrams shown in **Figure 4**. Vertical magenta lines correspond to the dates of the two HYCOM salinity maps shown in **Figure 1a** (March 25, 2018) and **Figure 1b** (August 16, 2018). Vertical black lines indicate the transition from offshore to onshore (and vice versa) and gray lines denote the beginning of each year. The Oxygen:Nitrate ratio is shown between 5 and 30 (range that contain the 96.9% of the data) to facilitate the interpretation. The ratio is presented in positive values (it has been multiplied by −1 with respect to the Redfield ratio).

depth (**Figure 3C**)—the density structure of both profiles were practically identical below 100 m. BGC properties were very different on both dates, not only in the top layer but also at deeper levels. In general, oxygen and pH (nitrate) concentrations were considerably (slightly) lower (higher) on March 25 than August 16, 2018 when high freshwater conditions existed off the Gulf of Penas (**Figures 3D–F**). However, pH increased whereas nitrate concentration decreased in the low-salinity (top 50 m) upper

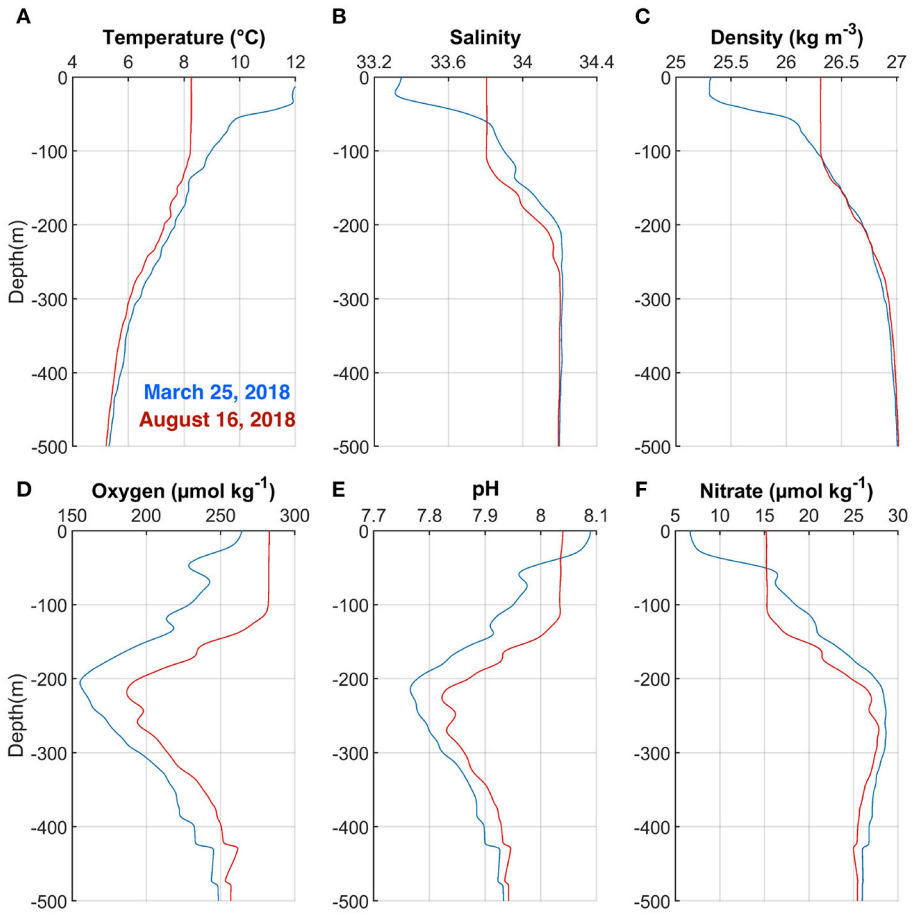

FIGURE 3 | Vertical profiles of **(A)** Temperature, **(B)** Salinity, **(C)** Potential density, **(D)** Oxygen, **(E)** pH, and **(F)** Nitrate on March 25 (blue curves) and August 16 (red curves), 2018 (see **Figure 1**).

layer (**Figures 3E,F**; blue curves), which is coherent with the BGC characteristics of meltwater from nearby glaciers.

The stoichiometric ratio proposed by Redfield (1934) established that, in average, marine organic matter and the required oxygen consumption keeps the following elemental proportion: 106C : 16N : 1P : $-138O_2$. Taking into account the variability of the Readfield ratio in the global ocean (Anderson, 1995; Lenton and Watson, 2000; Karl et al., 2001; Klausmeier et al., 2004), the stoichiometric proportion regarding to oxygen and nitrate should fluctuate between 8.6 and 10.6, considering that the oxygen coefficient could oscillate between −138 and −170 (Anderson, 1995; Johnson, 2010). The spatiotemporal variability of the oxygen and nitrate (O_2:NO_3^-) ratio (**Figure 2f**) was used to assess the linkages between the cycling of these elements relative to the Redfield proportion and to elucidate which processes, biological (i.e., primary production or respiration) or physical (i.e., water column stratification, horizontal transport, and/or air-sea interaction), are the main modulators of the elemental signal registered. Much of the vertical variability in the O_2:NO_3^- ratio occurred onshore, with maximum values (>30) coinciding with events of high Chl-a (**Figure 2g**), and conditions of marked water column stratification (evidenced by elevated PEA; **Figure 2g**) associated to the high freshwater content off Gulf of Penas. This freshwater runoff produces sharp horizontal and vertical salinity gradients (**Figures 1**, **2b**) in the coastal zone. In contrast, subsurface waters beneath this freshwater layer, particularly between 150 and 300 m depth, showed the lower O_2:NO_3^- ratio (∼5.0) throughout the float path and relative to the expected Redfield stoichiometry (8.6–10.6). Farther offshore, away from the freshwater influence, differences in O_2:NO_3^- ratio between surface (∼15) and subsurface waters (∼10) are less pronounced and, below the mixed layer, somewhat closer to the expected Redfield model.

4. DISCUSSION

BGC-Argo floats are key platforms for the study of coastal systems characterized by high terrestrial input of carbon and nutrients, which could promote short-term fluctuations in primary productivity and oxygen levels, changes in pH,

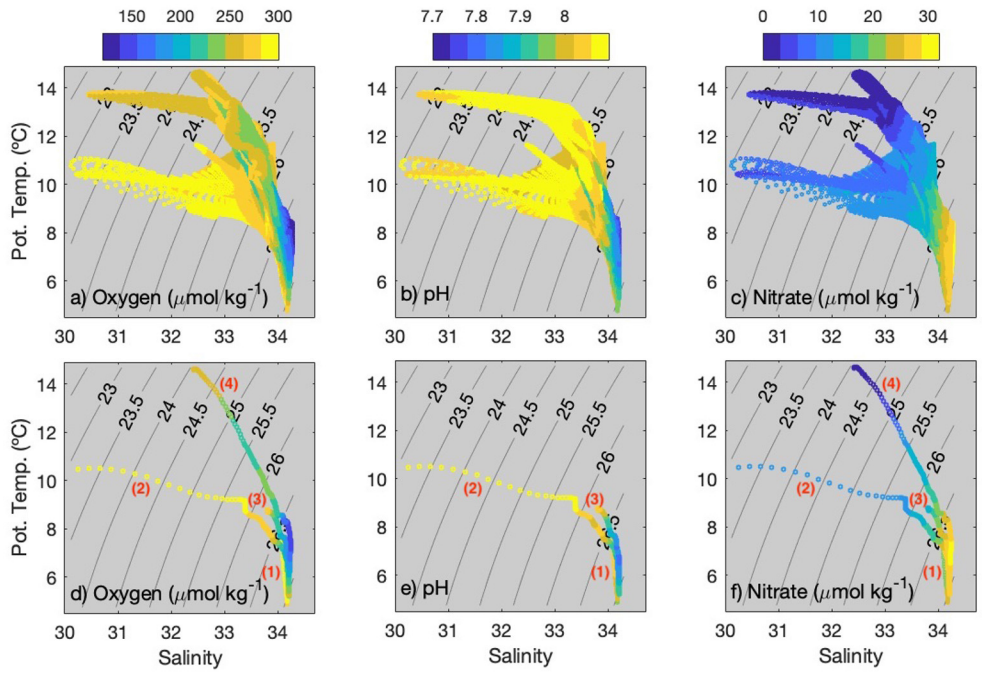

FIGURE 4 | T-S diagrams with values of **(a,d)** oxygen, **(b,e)** pH, and **(c,f)** Nitrate in color. All data are included in top panels, whereas selected dates with contrasting freshwater conditions are shown in bottom panels—the dates are (1) April 01, 2016, (2) November 01, 2017, (3) July 01, 2018, and (4) February 15, 2019.

and coastal ocean acidification (Wallace et al., 2014; Gledhill et al., 2015). In similar high-latitude regions, such as the west coast of Norway, the highest transports of dissolved organic carbon and nutrients occur during periods of high freshwater outflows (Frigstad et al., 2020). The subsurface layer of this system has been characterized with high salinity, low O_2, and high ammonium values suggesting that processes such as organic matter remineralization (e.g., nitrate/nitrite reduction and/or dissimilatory nitrate reduction to ammonium) could be occurring below the upper fresher layer (Frigstad et al., 2020). Similar BGC processes are suggested in southeastern Greenland where high nutrient content and particulate organic carbon fluxes below the euphotic (and fresher) layer imply significant remineralization (Seifert et al., 2019). Our results regarding high (low) oxygen and low (high) nitrate concentrations at surface (subsurface) levels during the recorded pulses of freshwater suggest that autotrophic (remineralization) processes would dominate above (below) the pycnocline.

The largest freshwater inputs into the coastal ocean are linked to polar and subpolar regions, such as the coastal oceans of Alaska (Royer, 1982; Johnson et al., 1988), Greenland (Jones et al., 2008), and Norway (Mork, 1981). Little is known about buoyancy-driven currents and BGC variability associated with the freshwater influence off western Patagonia where river outflows provides about 27,800–33,500 $m^3\ s^{-1}$ of freshwater into the coastal ocean (from ∼40 to 56°S), forming an extensive low-salinity tongue (Neshyba and Fonseca, 1980; Dávila et al., 2002; Saldías et al., 2019). The high freshwater outflows in the region modify the properties of subantarctic water (SAAW) in the surface layer (**Figure 1**), generating the Modified Subantarctic Water (MSAAW) (Silva et al., 1995; Sievers and Silva, 2008). T-S diagrams are presented in **Figure 4** to clarify the BGC characteristics of the water masses. Thus, freshwater events with MSAAW off western Patagonia would be primarily characterized by medium-to-high oxygen (>250 μmol kg^{-1}), high pH (> 8), and low-to-medium nitrate (<10–15 μmol kg^{-1}) concentrations (**Figures 4a–c**). Note that warmer freshwater events present even lower nitrate (<5 μmol kg^{-1}; **Figure 4c**). The presence of Equatorial Subsurface Water (ESSW), with high (low) salinity and nitrate (oxygen) [**Figures 4d,f**; profile (4)], can also be identified from the T-S diagrams but mainly during 2019 when the float drifted slightly north of Gulf of Penas (**Figure 1**). The high subsurface salinity pool was evident from January to July 2019, occupying a depth range of about 200–400 m (**Figure 2b**). This finding is consistent with previous information suggesting the region around the Gulf of Penas as the southern limit of the spreading of ESSW (Silva et al., 2009), which could penetrate partially into nearby channels and fjords, as suggested by Sievers and Silva (2008).

There are strong land-ocean hydrographic and BGC gradients in fjords and channels of the Chilean Patagonia—inorganic nutrient concentrations present large spatial variability with nitrate (silicic acid) increasing (decreasing) from inland waters toward the Gulf of Penas (González et al., 2013). However, high vertical carbon flux and elevated sinking would avoid exporting a large fraction of materials into the coastal ocean (González et al., 2013). The freshwater outflows from nearby fjords and channels modify coastal waters' physicochemical

characteristics off central Patagonia in approximately the top 50 m (see **Figures 3E,F**). These low-salinity nitrate-deficient waters would affect this coastal system's primary productivity in a large coastal extension (**Figure 1**). The relatively higher surface pH conditions during freshwater events should also modify the rates of the biologically-modulated chemical processes. This limiting condition is exacerbated by the entry of warm brackish waters due to the effect of a sharp pycnocline hindering the upwelling of nutrient-rich waters. Nitrate has been recognized as a limiting nutrient in the surface waters of northern Patagonia (Iriarte et al., 2007). On the other hand, periods of low freshwater conditions would favor the upwelling of subsurface nutrient-rich waters promoting phytoplankton blooms, sometimes of anomalous species as observed off Chiloé Island in summer 2016 (León-Muñoz et al., 2018). Although the freshwater tongues are less likely to influence the BGC properties of the upper boundary of the Antarctic Intermediate Waters (AAIW), which are located below SAAW at around 150–200 m depth off the Gulf of Penas (Silva et al., 2009), they undoubtedly represent a buoyant boundary decreasing air-sea fluxes to reach down in the water column.

Spatiotemporal variability of the O_2:NO_3^- ratio seems to be mainly modulated by both changes in the primary production at the surface (∼100 m depth)—using Chl-a as a proxy of photosynthetic activity, and organic matter respiration below the mixed layer at the coast, and by physical mechanisms (e.g., horizontal transport and/or air-sea interaction) occurring offshore. The higher values of the O_2:NO_3^- ratio registered at the surface (>30.0; **Figure 2f**) during periods of maximum Chl-a availability and higher water column stratification (**Figure 2g**), appears to be the result of *in situ* nitrate consumption and oxygen production by photosynthetic organisms when the float reached the area of freshwater influence. The tight coupling between nitrate consumption and chlorophyll increase at the surface is denoted in **Figure 2g**. This photoautotrophic activity is also evidenced by a marked increase in the pH (**Figure 2d**), caused by the assimilation of inorganic carbon. In contrast, the lower O_2:NO_3^- ratio (∼5.0) observed onshore below the mixed layer (**Figure 2f**), seems to be the result of local organic matter remineralization, characterized by the return of inorganic nitrogen to the system while oxygen is consumed (**Figures 2e,c**). The expected input of CO_2, as a result of this respiration process, reduces, in consequence, the pH (**Figure 2d**). Relative to the coastal zone, oceanic waters were characterized to be less productive, with reduced biologically-mediated oxygen-consuming processes at depth owing the more limited organic matter load. The slightly high O_2:NO_3^- values (over the expected Redfield ratio), registered at surface in this oceanic waters with minimal phototrophic activity, can probably be explained by the effect of air-sea gas exchange, which, in turn, is modulated by the degree of oxygen saturation of the seawater (Johnson, 2010). In this sense, coastal surface (subsurface) waters were oversaturated (undersaturated) in oxygen, as a clear signal of *in situ* oxygen produced (consumed) by photosynthesis (respiration); whereas offshore waters were closer to the equilibrium with the atmosphere (**Supplementary Figure 2**). Thus, the O_2:NO_3^- ratio observed offshore, suggests that the cycling of these elements, far from the freshwater influence, is less biologically controlled, and that their availability is principally modulated by the circulation and by the chemical characteristics of the SAAW and AAIW at surface and subsurface levels, respectively (Silva et al., 2009, and references therein).

Throughout the BGC-Argo float trajectory, there is a seasonal change in the trophic status as the float reached the freshwater-influenced coastal area. Relative to the time series analyzed, the first phytoplankton bloom (up to 1.5 mg Chl-a m^{-3}) occurred during austral fall (March-April 2017), supported likely by nutrients remineralized from the organic matter produced and accumulated during summer time. After an evident diminished autotrophic activity in winter (∼0.2 mg Chl-a m^{-3}) as response to the surface depletion of nutrients in the coastal zone (see Nitrate in **Figure 2e**), photosynthesis is reactivated in spring, and reached a second Chl-a peak (∼1.3 mg Chl-a m^{-3}) in summer (November 2017) when light availability is greater in near-surface waters. This productive season is probably supported by the injection of subsurface nutrients that reach the upper layer by the end of winter, when the stratification is considerably reduced (**Figures 2a–f**). By the end of 2018, when the float returned onshore, the productive response of the system seems to be repeated: phototrophic activity began in spring (Chl-a slightly higher than 0.5 mg m^{-3}), and was maximum by the end of summer (∼1.3 mg Chl-a m^{-3}; April 2019). Interestingly, the BGC signal denotes the close coupling between surface and subsurface waters, considering that the biological material produced at the surface settles down and is respired at greater depths. Thus, the BGC variability off central Patagonia seems to be the result of a synergistic interaction between physical and biological processes, where stratification sets up the environment and facilitates the biological response that, in turn, is autoregulated by modifying the chemical composition and the availability of elemental components in the freshwater-influenced coastal area.

The arrival of new BGC Argo floats fully equipped (additional sensors of Chlorophyll, PAR, backscatter) to the region will provide new insights about the influence of freshening and freshwater stratification on BGC properties and their variability (e.g., chlorophyll fluctuations and trends, nitrogen and carbon cycling, and carbon sequestration, among others). Satellite fields of surface chlorophyll show that high phytoplankton biomass occurs mainly in spring-summer when the freshwater content off central Patagonia is the largest of its annual cycle (Saldías et al., 2019). However, the vertical structure and the depth of chlorophyll peaks related to the freshwater events are poorly understood. More extended time series will also add essential information on the freshening's interannual variability and its role in BGC processes considering the significant melting of Patagonian ice fields since 1968–1975 (Rignot et al., 2003). Finally, it is important to highlight that there may be deviations in BGC readings due to sensor drift (Johnson et al., 2017). Unfortunately, we do not have *in situ* measurements to evaluate how much variability could be due to a natural trend or a technical artifact. Johnson et al. (2017) found that sensor drift was constant throughout the water column. Hence, the potential impact of sensor drift in our measurements does

not change our conclusions as, for example, the observed trend of nitrate at depth (500 m) is much lower than the variability of the upper layer where large BGC fluctuations occur (**Supplementary Figure 3**).

DATA AVAILABILITY STATEMENT

Publicly available datasets were analyzed in this study. The datasets analyzed for this study can be found in the Biogeochemical Argo Float website https://biogeochemical-argo.org/# and HYCOM website https://www.hycom.org/dataserver/gofs-3pt0/analysis/.

AUTHOR CONTRIBUTIONS

AG, GS, CL, and AC-A wrote the manuscript. RM and JI participated in discussions about the manuscript. JI revised the manuscript. GS, AC-A, and RM analyzed the data sets. All authors contributed to the article and approved the submitted version.

FUNDING

The primary funding source of this study was provided by FONDAP Research Center on Dynamics of High Latitude Marine Ecosystems (IDEAL; Program 15150003). FONDAP IDEAL has fully supported AC-A. CL has been partially funded by FONDECYT 11090209 and the Millenium Nucleus Understanding Past coastal upWelling system and Environmental Local and Lasting impacts (UPWELL; NCN19_153). GS has been partially funded by ANID—Millennium Science Initiative Program—Code ICN2019_015 (Coastal Social-Ecological Millennium Institute, SECOS) and FONDECYT grant 1190805. AG has been funded by Vicerrectoría de Investigación y Postgrado, Universidad Católica del Maule.

ACKNOWLEDGMENTS

These data were collected and made freely available by the Coriolis project and programmes that contribute to it (http://www.coriolis.eu.org). We thank to two reviewers for providing constructive comments that improved the original version of the manuscript.

SUPPLEMENTARY MATERIAL

The Supplementary Material for this article can be found online at: https://www.frontiersin.org/articles/10.3389/fmars.2021.613265/full#supplementary-material

REFERENCES

Adusumilli, S., Fricker, H. A., Medley, B., Padman, L., and Siegfried, M. R. (2020). Interannual variations in meltwater input to the Southern Ocean from Antarctic ice shelves. *Nat. Geosci.* 13, 616–620. doi: 10.1038/s41561-020-0616-z

Anderson, L. A. (1995). On the hydrogen and oxygen content of marine phytoplankton. *Deep Sea Res. Part I: Oceanogr. Res. Pap.* 42, 1675–1680. doi: 10.1016/0967-0637(95)00072-E

Bleck, R. (2002). An oceanic general circulation model framed in hybrid isopycnic-Cartesian coordinates. *Ocean Model.* 4, 55–88. doi: 10.1016/S1463-5003(01)00012-9

Bleck, R., and Boudra, D. B. (1981). Initial testing of a numerical ocean circulation model using a hybrid (quasi-isopycnic) vertical coordinate. *J. Phys. Oceanogr.* 11, 755–770. doi: 10.1175/1520-0485(1981)011<0755:ITOANO>2.0.CO;2

Boss, E., and Behrenfeld, M. (2010). *In situ* evaluation of the initiation of the North Atlantic phytoplankton bloom. *Geophys. Res. Lett.* 37, 1–5. doi: 10.1029/2010gl044174

Claustre, H., Johnson, K. S., and Takeshita, Y. (2020). Observing the global ocean with biogeochemical-argo. *Annu. Rev. Mar. Sci.* 12, 23–48. doi: 10.1146/annurev-marine-010419-010956

Corredor-Acosta, A., Morales, C. E., Brewin, R. J., Auger, P.-A., Pizarro, O., Hormazabal, S., et al. (2018). Phytoplankton size structure in association with mesoscale eddies off central-southern Chile: the satellite application of a phytoplankton size-class model. *Remote Sens.* 10:834. doi: 10.3390/rs10060834

Dávila, P. M., Figueroa, D., and Müller, E. (2002). Freshwater input into the coastal ocean and its relation with the salinity distribution off austral Chile (35–55°S). *Contin. Shelf Res.* 22, 521–534. doi: 10.1016/S0278-4343(01)00072-3

Frigstad, H., Kaste, Ø., Deininger, A., Kvalsund, K., Christensen, G., Bellerby, R. G., et al. (2020). Influence of riverine input on Norwegian coastal systems. *Front. Mar. Sci.* 7:332. doi: 10.3389/fmars.2020.00332

Gledhill, D. K., White, M. M., Salisbury, J., Thomas, H., Mlsna, I., Liebman, M., et al. (2015). Ocean and coastal acidification off New England and Nova Scotia. *Oceanography* 28, 182–197. doi: 10.5670/oceanog.2015.41

González, H. E., Castro, L. R., Daneri, G., Iriarte, J. L., Silva, N., Tapia, F. J., et al. (2013). Land-ocean gradient in haline stratification and its effects on plankton dynamics and trophic carbon fluxes in Chilean Patagonian fjords (47–50°S). *Prog. Oceanogr.* 119, 32–47. doi: 10.1016/j.pocean.2013.06.003

Gould, J., Roemmich, D., Wijffels, S., Freeland, H., Ignaszewsky, M., Jianping, X., et al. (2004). Argo profiling floats bring new era of *in situ* ocean observations. *Eos Trans. Am. Geophys. Union* 85, 185–191. doi: 10.1029/2004EO190002

Gray, A. R., Johnson, K. S., Bushinsky, S. M., Riser, S. C., Russell, J. L., Talley, L. D., et al. (2018). Autonomous biogeochemical floats detect significant carbon dioxide outgassing in the high-latitude southern ocean. *Geophys. Res. Lett.* 45, 9049–9057. doi: 10.1029/2018GL078013

Iriarte, J., León-Mu noz, J., Marcé, R., Clément, A., and Lara, C. (2017). Influence of seasonal freshwater streamflow regimes on phytoplankton blooms in a patagonian fjord. *N. Z. J. Mar. Freshw. Res.* 51, 304–315. doi: 10.1080/00288330.2016.1220955

Iriarte, J. L., González, H. E., Liu, K. K., Rivas, C., and Valenzuela, C. (2007). Spatial and temporal variability of chlorophyll and primary productivity in surface waters of southern Chile (41.5-43°S). *Estuar. Coast. Shelf Sci.* 74, 471–480. doi: 10.1016/j.ecss.2007.05.015

Iriarte, J. L., Pantoja, S., and Daneri, G. (2014). Oceanographic processes in Chilean Fjords of Patagonia: from small to large-scale studies. *Prog. Oceanogr.* 129, 1–7. doi: 10.1016/j.pocean.2014.10.004

Jacob, B., Tapia, F. J., Daneri, G., Iriarte, J. L., Montero, P., Sobarzo, M. A., et al. (2014). Springtime size-fractionated primary production across hydrographic and PAR-light gradients in Chilean Patagonia (41–50S). *Prog. Oceanogr.* 129, 75–84. doi: 10.1016/j.pocean.2014.08.003

Johnson, K. S. (2010). Simultaneous measurements of nitrate, oxygen, and carbon dioxide on oceanographic moorings: observing the redfield ratio in real time. *Limnol. Oceanogr.* 55, 615–627. doi: 10.4319/lo.2010.55.2.0615

Johnson, K. S., Plant, J. N., Coletti, L. J., Jannasch, H. W., Sakamoto, C. M., Riser, S. C., et al. (2017). Biogeochemical sensor performance in the SOCCOM profiling float array. *J. Geophys. Res.* 122, 6416–6436. doi: 10.1002/2017JC012838

Johnson, W. R., Royer, T. C., and Luick, J. L. (1988). On the seasonal variability of the Alaska Coastal Current. *J. Geophys. Res*. 93, 12423–12437. doi: 10.1029/JC093iC10p12423

Jones, E., Anderson, L., Jutterström, S., and Swift, J. (2008). Sources and distribution of fresh water in the East Greenland Current. *Prog. Oceanogr*. 78, 37–44. doi: 10.1016/j.pocean.2007.06.003

Karl, D. M., Björkman, K. M., Dore, J. E., Fujieki, L., Hebel, D. V., Houlihan, T., et al. (2001). Ecological nitrogen-to-phosphorus stoichiometry at station aloha. *Deep Sea Res. Part II Top. Stud. Oceanogr*. 48, 1529–1566. doi: 10.1016/S0967-0645(00)00152-1

Klausmeier, C. A., Litchman, E., Daufresne, T., and Levin, S. A. (2004). Optimal nitrogen-to-phosphorus stoichiometry of phytoplankton. *Nature* 429, 171–174. doi: 10.1038/nature02454

Lenton, T. M., and Watson, A. J. (2000). Redfield revisited: 1. regulation of nitrate, phosphate, and oxygen in the ocean. *Glob. Biogeochem. Cycles* 14, 225–248. doi: 10.1029/1999GB900065

León-Mu noz, J., Urbina, M. A., Garreaud, R., and Iriarte, J. L. (2018). Hydroclimatic conditions trigger record harmful algal bloom in western Patagonia (summer 2016). *Sci. Rep*. 8:1330. doi: 10.1038/s41598-018-19461-4

Li, B., Watanabe, Y., Hosoda, S., Sato, K., and Nakano, Y. (2019). Quasi-real-time and high-resolution spatiotemporal distribution of ocean anthropogenic CO_2. *Geophys. Res. Lett*. 46, 4836–4843. doi: 10.1029/2018GL081639

Mork, M. (1981). Circulation phenomena and frontal dynamics of the Norwegian Coastal Current. *Philos. Trans. R. Soc. Lond. Ser. A Math. Phys. Sci*. 635–647. doi: 10.1098/rsta.1981.0188

Munk, W. (2003). Ocean freshening, sea level rising. *Science* 300, 2041–2043. doi: 10.1126/science.1085534

Nerem, R. S., Beckley, B. D., Fasullo, J. T., Hamlington, B. D., Masters, D., and Mitchum, G. T. (2018). Climate-change-driven accelerated sea-level rise detected in the altimeter era. *Proc. Natl. Acad. Sci. U.S.A*. 115, 2022–2025. doi: 10.1073/pnas.1717312115

Neshyba, S., and Fonseca, T. R. (1980). Evidence for counterflow to the west wind drift off South America. *J. Geophys. Res*. 85, 4888–4892. doi: 10.1029/JC085iC09p04888

Pantoja, S., Iriarte, J. L., and Daneri, G. (2011). Oceanography of the Chilean Patagonia. *Contin. Shelf Res*. 31, 149–153. doi: 10.1016/j.csr.2010.10.013

Rignot, E., Rivera, A., and Casassa, G. (2003). Contribution of the Patagonia Icefields of South America to sea level rise. *Science* 302, 434–437. doi: 10.1126/science.1087393

Riser, S. C., Freeland, H. J., Roemmich, D., Wijffels, S., Troisi, A., Belbéoch, M., et al. (2016). Fifteen years of ocean observations with the global Argo array. *Nat. Clim. Change* 6, 145–153. doi: 10.1038/nclimate2872

Roemmich, D., Alford, M. H., Claustre, H., Johnson, K. S., King, B., Moum, J., et al. (2019). On the future of Argo: a global, full-depth, multi-disciplinary array. *Front. Mar. Sci*. 6:439. doi: 10.3389/fmars.2019.00439

Roemmich, D., Johnson, G. C., Riser, S., Davis, R., Gilson, J., Owens, W. B., et al. (2009). The argo program: observing the global ocean with profiling floats. *Oceanography* 22, 34–43. doi: 10.5670/oceanog.2009.36

Royer, T. C. (1982). Coastal fresh water discharge in the northeast Pacific. *J. Geophys. Res*. 87, 2017–2021. doi: 10.1029/JC087iC03p02017

Saldías, G. S., Sobarzo, M., and Qui nones, R. (2019). Freshwater structure and its seasonal variability off western Patagonia. *Prog. Oceanogr*. 174, 143–153. doi: 10.1016/j.pocean.2018.10.014

Seifert, M., Hoppema, M., Burau, C., Elmer, C., Friedrichs, A., Geuer, J. K., et al. (2019). Influence of glacial meltwater on summer biogeochemical cycles in Scoresby Sund, East Greenland. *Front. Mar. Sci*. 6:412. doi: 10.3389/fmars.2019.00412

Sievers, H., and Silva, N. (2008). "Water masses and circulation in austral Chilean channels and fjords," in *Progress in the Oceanographic Knowledge of Chilean Interior Waters, From Puerto Montt to Cape Horn*, eds N. Silva and S. Palma (Valparaíso: Comité Oceanográfico Nacional - Pontificia Universidad Católica de Valparaíso), 53–58.

Silva, N., Rojas, N., and Fedele, A. (2009). Water masses in the Humboldt Current System: properties, distribution, and the nitrate deficit as a chemical water mass tracer for Equatorial Subsurface Water off Chile. *Deep Sea Res. Part II* 56, 1004–1020. doi: 10.1016/j.dsr2.2008.12.013

Silva, N., Sievers, H., and Prado, R. (1995). Características oceanográficas y una proposición de circulación para algunos canales Australes de Chile entre 41°20′S y 46°40′S. *Rev. Biol. Mar*. 30, 207–254.

Simpson, J., Crisp, D., and Hearn, C. (1981). The shelf-sea fronts: implications of their existence and behaviour. *Philos. Trans. R. Soc. Lond. Ser. A* 302, 531–546. doi: 10.1098/rsta.1981.0181

Sukigara, C., Suga, T., Saino, T., Toyama, K., Yanagimoto, D., Hanawa, K., et al. (2011). Biogeochemical evidence of large diapycnal diffusivity associated with the subtropical mode water of the North Pacific. *J. Oceanogr*. 67, 77–85. doi: 10.1007/s10872-011-0008-5

Vizcaíno, M., Mikolajewicz, U., Gröger, M., Maier-Reimer, E., Schurgers, G., and Winguth, A. M. (2008). Long-term ice sheet-climate interactions under anthropogenic greenhouse forcing simulated with a complex Earth System Model. *Clim. Dyn*. 31, 665–690. doi: 10.1007/s00382-008-0369-7

Wallace, R. B., Baumann, H., Grear, J. S., Aller, R. C., and Gobler, C. J. (2014). Coastal ocean acidification: The other eutrophication problem. *Estuar. Coast. Shelf Sci*. 148, 1–13. doi: 10.1016/j.ecss.2014.05.027

Wong, A., Wijffels, S. E., Riser, S. C., Pouliquen, S., Hosoda, S., Roemmich, D., et al. (2020). Argo data 1999-2019: two million temperature-salinity profiles and subsurface velocity observations from a global array of profiling floats. *Front. Mar. Sci*. 7:700. doi: 10.3389/fmars.2020.00700

Conflict of Interest: The authors declare that the research was conducted in the absence of any commercial or financial relationships that could be construed as a potential conflict of interest.

frontiers in Marine Science

ORIGINAL RESEARCH
published: 20 July 2021
doi: 10.3389/fmars.2021.628454

Climate and Land Cover Trends Affecting Freshwater Inputs to a Fjord in Northwestern Patagonia

Jorge León-Muñoz[1,2], Rodrigo Aguayo[3], Rafael Marcé[4,5], Núria Catalán[5,6,7], Stefan Woelfl[8], Jorge Nimptsch[8], Ivan Arismendi[9], Camila Contreras[10], Doris Soto[2] and Alejandro Miranda[11,12]*

[1] Departamento de Química Ambiental, Facultad de Ciencias, Universidad Católica de la Santísima Concepción, Concepción, Chile, [2] Centro Interdisciplinario para la Investigación Acuícola (INCAR), Concepción, Chile, [3] Facultad de Ciencias Ambientales, Centro EULA, Universidad de Concepción, Concepción, Chile, [4] Catalan Institute for Water Research (ICRA), Scientific and Technological Park of the University of Girona, Girona, Spain, [5] Universitat de Girona, Giona, Spain, [6] United States Geological Survey, Boulder, CO, United States, [7] Laboratoire des Sciences du Climat et de l'Environnement, LSCE, CEA, CNRS, UVSQ, Gif-sur-Yvette, France, [8] Facultad de Ciencias, Instituto de Ciencias Marinas y Limnológicas, Universidad Austral de Chile, Valdivia, Chile, [9] Department of Fisheries, Wildlife and Conservation Sciences, Oregon State University, Corvallis, OR, United States, [10] Departamento de Ingeniería Civil y Ambiental, Facultad de Ingeniería, Universidad del Bío-Bío, Concepción, Chile, [11] Laboratorio de Ecología del Paisaje y Conservación, Departamento de Ciencias Forestales, Universidad de La Frontera, Temuco, Chile, [12] Center for Climate and Resilience Research (CR2), Santiago, Chile

OPEN ACCESS

Edited by:
Brian Reid, Patagonian Ecosystems Investigation Research Center (CIEP), Chile

Reviewed by:
Vanesa Magar, Center for Scientific Research and Higher Education in Ensenada (CICESE), Mexico
Facundo Scordo, University of Nevada, Reno, United States

***Correspondence:**
Jorge León-Muñoz
jleon@ucsc.cl

Specialty section:
This article was submitted to Coastal Ocean Processes, a section of the journal Frontiers in Marine Science

Received: *12 November 2020*
Accepted: *28 June 2021*
Published: *20 July 2021*

Citation:
León-Muñoz J, Aguayo R, Marcé R, Catalán N, Woelfl S, Nimptsch J, Arismendi I, Contreras C, Soto D and Miranda A (2021) Climate and Land Cover Trends Affecting Freshwater Inputs to a Fjord in Northwestern Patagonia. Front. Mar. Sci. 8:628454. doi: 10.3389/fmars.2021.628454

Freshwater inputs strongly influence oceanographic conditions in coastal systems of northwestern Patagonia (41–45°S). Nevertheless, the influence of freshwater on these systems has weakened in recent decades due to a marked decrease in precipitation. Here we evaluate potential influences of climate and land cover trends on the Puelo River (640 m^3s^{-1}), the main source of freshwater input of the Reloncaví Fjord (41.5°S). Water quality was analyzed along the Puelo River basin (six sampling points) and at the discharge site in the Reloncaví Fjord (1, 8, and 25 m depth), through six field campaigns carried out under contrasting streamflow scenarios. We also used several indicators of hydrological alteration, and cross-wavelet transform and coherence analyses to evaluate the association between the Puelo River streamflow and precipitation (1950–2019). Lastly, using the WEAP hydrological model, land cover maps (2001–2016) and burned area reconstructions (1985–2019), we simulated future land cover impacts (2030) on the hydrological processes of the Puelo River. Total Nitrogen and total phosphorus, dissolved carbon, and dissolved iron concentrations measured in the river were 3–15 times lower than those in the fjord. Multivariate analyses showed that streamflow drives the carbon composition in the river. High streamflow conditions contribute with humic and colored materials, while low streamflow conditions corresponded to higher arrival of protein-like materials from the basin. The Puelo River streamflow showed significant trends in magnitude (lower streamflow in summer and autumn), duration (minimum annual streamflow), timing (more floods in spring), and frequency (fewer prolonged floods). The land cover change (LCC) analysis indicated that more than 90% of the basin area maintained its land cover, and that the main changes were attributed to recent large wildfires. Considering these land cover trends, the hydrological simulations

project a slight increase in the Puelo River streamflow mainly due to a decrease in evapotranspiration. According to previous simulations, these projections present a direction opposite to the trends forced by climate change. The combined effect of reduction in freshwater input to fiords and potential decline in water quality highlights the need for more robust data and robust analysis of the influence of climate and LCC on this river-fjord complex of northwestern Patagonia.

Keywords: Patagonia, climate change, hydrological modeling, water quality, land-ocean interface, land cover change

INTRODUCTION

The land-ocean interface in river deltas and fjords is the natural bridge between terrestrial and marine systems. In these areas, nutrients, organic matter and sediments transported by rivers meet with those coming from the coastal and open ocean. Globally, oceans receive more than 36,000 km^3 of freshwater and about 20 billion tons of sediments (Milliman and Farnsworth, 2011). About 95% of this volume enters through the rivers. The freshwater input represents important regulating and provisioning ecosystem services, influencing the coastal system's physical-chemical characteristics, supporting the reproduction of numerous species, many of which sustain important fisheries and subsistence activities (Nixon and Buckley, 2002; Barbier et al., 2011).

The coastal system of Northwestern Patagonia (41–45°S) is comprised by extensive and interconnected fjords, bays and channels that receive important freshwater inputs from the southern Andes Range (Milliman and Farnsworth, 2011; Pantoja et al., 2011; Iriarte et al., 2014). Most of the freshwater inputs come from numerous rivers that are fed by rainfall runoff, snow melt and glacier melt from relatively small basins ($<$ 10,000 km^2). Freshwater inputs influence the coastal dynamics at different spatial and temporal scales, producing marked density gradients in the seawater column (Dávila et al., 2002; Saldías et al., 2019), changing nutrient ratios, and bringing high concentrations of organic matter (dissolved and particulate) and silicic acid (Silva et al., 2011; Vargas et al., 2011; Torres et al., 2020). Inorganic nutrients and solar radiation are strongly seasonal, limiting the relatively high primary productivity of estuarine systems in western Patagonia (0.5–3.0 g C m^{-2} d^{-1}) dominated mainly by diatoms (90%) (Iriarte et al., 2007; Jacob et al., 2014; Raymond and Spencer, 2015). Changes in freshwater input could have negative implications on oceanographic processes to fjords in the inner seas of Chilean Patagonia. The ecosystem services that these systems provide depend on the interplay of different water masses, especially including the upper estuarine layer (Sievers and Silva, 2008), which strongly depends on the magnitude, timing, and duration of freshwater input. The depth, extent and chemistry of this layer/water mass also depends on the complexity of processes occurring at the climate-dependent river-ocean interface.

The influence of rivers on the coastal systems in this region has weakened during the last decades (León-Muñoz et al., 2018; Aguayo et al., 2019, 2021) due to a marked decrease in precipitation during summer and autumn (Boisier et al., 2018). The precipitation decline has been attributed to the positive trend of the Southern Annular Mode (SAM), an index that describes the movement of the low-pressure belt that generates westerly winds. The SAM trend has been attributed to stratospheric ozone depletion and increased greenhouse gases concentration, which suggests the effects of a global anthropogenic forcing on the local precipitation regime (Arblaster and Meehl, 2006; Eyring et al., 2013; Boisier et al., 2018). This trend has increased the climate synergy with El Niño-Southern Oscillation (ENSO), promoting severe droughts during austral summers (Garreaud, 2018). Climate projections for the next decades (2020–2070) follow this trend. Recent studies have evaluated the hydrological impacts of climate projections in the region (Puelo River; 41°S) predicting a prolongation of warm and dry conditions, seasonal changes in hydrological regimes and an increase in severe drought frequency (Aguayo et al., 2019, 2021; Pessacg et al., 2020).

Apart from shifts in climate conditions, the magnitude and spatial expansion of land cover changes (LCC) may strongly alter river hydrology (Ellison et al., 2017) and biogeochemistry (Cuevas et al., 2006; Raymond et al., 2008; Aufdenkampe et al., 2011), and thus their influence on the coastal systems. A large proportion of native forest cover has been identified as a factor providing resilience to coastal systems strongly influenced by freshwater against climate change (Desmit et al., 2018; Khoury and Coomes, 2020). Native forest substitution by exotic tree plantations in south-central Chile (34–41°S; Miranda et al., 2017; Uribe et al., 2020) has been identified as one of the causes of lower streamflow during summer (Little et al., 2009; Iroumé and Palacios, 2013; Alvarez-Garreton et al., 2019). Climate change has also increased the recurrence of wildfires in this region (Urrutia-Jalabert et al., 2018), which could potentially alter hydrological processes (Rulli and Rosso, 2007; Boisramé et al., 2019). The impact of LCC on riverine biogeochemistry can affect nutrients and carbon cycling. Dissolved organic matter (DOM) composition is strongly influenced by land cover. For example, different types of vegetation reflected as divergent biomarkers in coastal waters (Hernes and Benner, 2003; Raymond and Spencer, 2015).

Anthropogenic alterations of the natural streamflow regime by way of LCCs make isolating the impacts of climate change on hydrology a daunting task (Yang et al., 2017; Chanapathi and Thatikonda, 2020). In Chile the hydrological impacts of LCCs have been evaluated mainly in south-central Chile ($<$ 41°S; Stehr et al., 2010; Aguayo et al., 2016; Martínez-Retureta et al., 2020;

Barría et al., 2021; Galleguillos et al., 2021) and not in tributary basins to the coastal system of northwestern Patagonia. Nevertheless, using rivers like Puelo River as sentinels, several studies have reported anomalous events in fjords of northwestern Patagonia (e.g., surface hypoxia events, harmful algal blooms), mainly during severe droughts (Valle-Levinson et al., 2007; León-Muñoz et al., 2013, 2018; Iriarte et al., 2017; Díaz et al., 2021). Although northern Patagonian basins have not yet been modified by irrigation channels or reservoirs and still maintain extensive little-degraded native forest cover (CONAF and UACH, 2014; Astorga et al., 2018), recent threats such as increased wildfires and their joint effect with climate change have not been evaluated hydrologically to date. Considering this context, here we evaluate the influence of climate and land cover trends on the freshwater inputs of the Puelo River Basin to the Reloncaví Fjord (41.5°S; **Figure 1**). Specifically, we aim to 1) characterize the water quality of freshwater inputs along the Puelo River network and the Reloncaví Fjord (2018–2019), 2) evaluate trends in natural flow regime (1950–2019), precipitation-streamflow associations (1950–2019), and land cover (2001–2016) for the Puelo River Basin, and 3) estimate the potential future impacts of LCC (2030), mainly caused by forest fires, on the hydrological processes of the Puelo River.

MATERIALS AND METHODS

Study Area

The study area comprises the Puelo River Basin and the Reloncaví Fjord (**Figure 1**). The basin (∼9,000 km^2; 66% of its drainage area in Argentina and 34% in Chile) is located in the central latitudes covered by the Valdivian Rainforest ecoregion. An important part of the basin is covered by native forest (CONAF and UACH, 2014), with minimal anthropogenic interventions (24% of the basin is located in protected areas). According to Köppen-Geiser's classification, the basin has temperate and polar climates with tundra characteristics (Beck et al., 2018). The precipitation range follows a strong longitudinal gradient that can vary between 500 mm and 4700 mm per year (Lara et al., 2008; Aguayo et al., 2019). Half of annual precipitation is concentrated during the austral winter. Recently, Aguayo et al. (2021) determined that the Puelo River Basin has a low aridity index (< 1), suggesting that it is energy-limited. The same basin showed, on average, an evaporation index close to 0 during all seasons except in summer, where evapotranspiration represents 37% of precipitation.

The Puelo River has a mean streamflow of 640 m^3 s^{-1} (2400 mm yr^{-1}) with a pluvial-nival hydrological regime in the proximity of its mouth, with a maximum peak in winter and a second and lower peak during spring (León-Muñoz et al., 2013). In contrast, the sub-basins located at higher elevations have a nival-pluvial hydrological regime. Puelo River is classified as a high-runoff river (>750 mm yr^{-1}); it has one of the highest runoff levels in mesoscale basins (Milliman and Farnsworth, 2011). During austral summer and autumn (low-flow season), the streamflow of the Puelo River is significantly correlated with the streamflow of other rivers of northwestern Patagonia ($r > 0.4$; Lara et al., 2008).

The Puelo River is the main source of freshwater input of the Reloncaví Fjord, the northernmost fjord on Chile's coast and one of the coastal systems most intensively used for aquaculture in the last decades. Chile is one of the world's 10 top aquaculture producers, the second-largest exporter of salmon and trout, and the largest exporter of mussel (*Mytilus chilensis*). The Reloncaví Fjord has historically been used for smoltification and growth of salmonids by industrial salmon farming (Quiñones et al., 2019; Soto et al., 2019). This fjord is also essential for the seed production of Chilean mussel farming (Molinet et al., 2015). The fjord has a J-shape; it is 55 km long and less than 3 km near the head. The bathymetry of the Reloncaví Fjord shows depths >400 m in the area close to the mouth with a deep sill (∼ 150 m depth) located 15 km inland (Valle-Levinson et al., 2007). This fjord has a three-layer circulation pattern with an upper brackish layer flowing into the mouth and is strongly associated with freshwater inputs from the Puelo River and other tributaries (Cochamoì River Q = 100 m^3 s^{-1}; Petrohueì River Q = 250 m^3 s^{-1}). The system's stratification varies along the fjord and between seasons, decreasing toward the mouth and being maximum in winter. The Reloncaví Fjord has been extensively studied by several research projects, mainly oceanographic, including paleoclimate (Rebolledo et al., 2015), fjord hydrodynamics (Valle-Levinson et al., 2014; Castillo et al., 2016), fjord biogeochemistry (Farías et al., 2017; González et al., 2019; Vergara-Jara et al., 2019; Yevenes et al., 2019) and plankton biology (González et al., 2013; Iriarte et al., 2017).

Data

Hydrology and Climate

Daily instrumental data of precipitation, air temperature, and streamflow were obtained from the Dirección General de Aguas de Chile, Dirección Meteorológica de Chile, Subsecretaría de Recursos Hídricos de Argentina and the Servicio Meteorológico Nacional de Argentina. According to these records, the Puelo River Basin contains one of the largest and most extensive networks of stations in western Patagonia. However, the location of the stations is spatially heterogeneous (**Figure 1**). Given this limitation, precipitation and temperature monthly data were complemented with CHIRPSv2 (2000–2019; 0.05°; Funk et al., 2015) and MODIS MOD11C3 (2000–2019; 0.05°; Wan et al., 2015) products, respectively. The associated biases between instrumental data and gridded products were corrected with different methodologies detailed in Aguayo et al. (2019). Wind and relative humidity monthly data were directly obtained from the ERA5 atmospheric reanalysis (2000–2019; 0.25°; Hersbach et al., 2020).

Water Quality

Six sampling sites were chosen within the drainage network to characterize the water quality of the Puelo River (**Figure 1** and **Table 1**). Sampling sites were located downstream of Lake Inferior (P1), before and after (P2, P3) the confluences with its main tributaries, the Ventisquero (V1) and Manso (M1) rivers, and downstream of Lake Tagua-Tagua (P4) before its discharge in the Reloncaví Fjord (**Figure 1**). One additional sampling site was established in the Reloncaví Fjord near the Puelo River

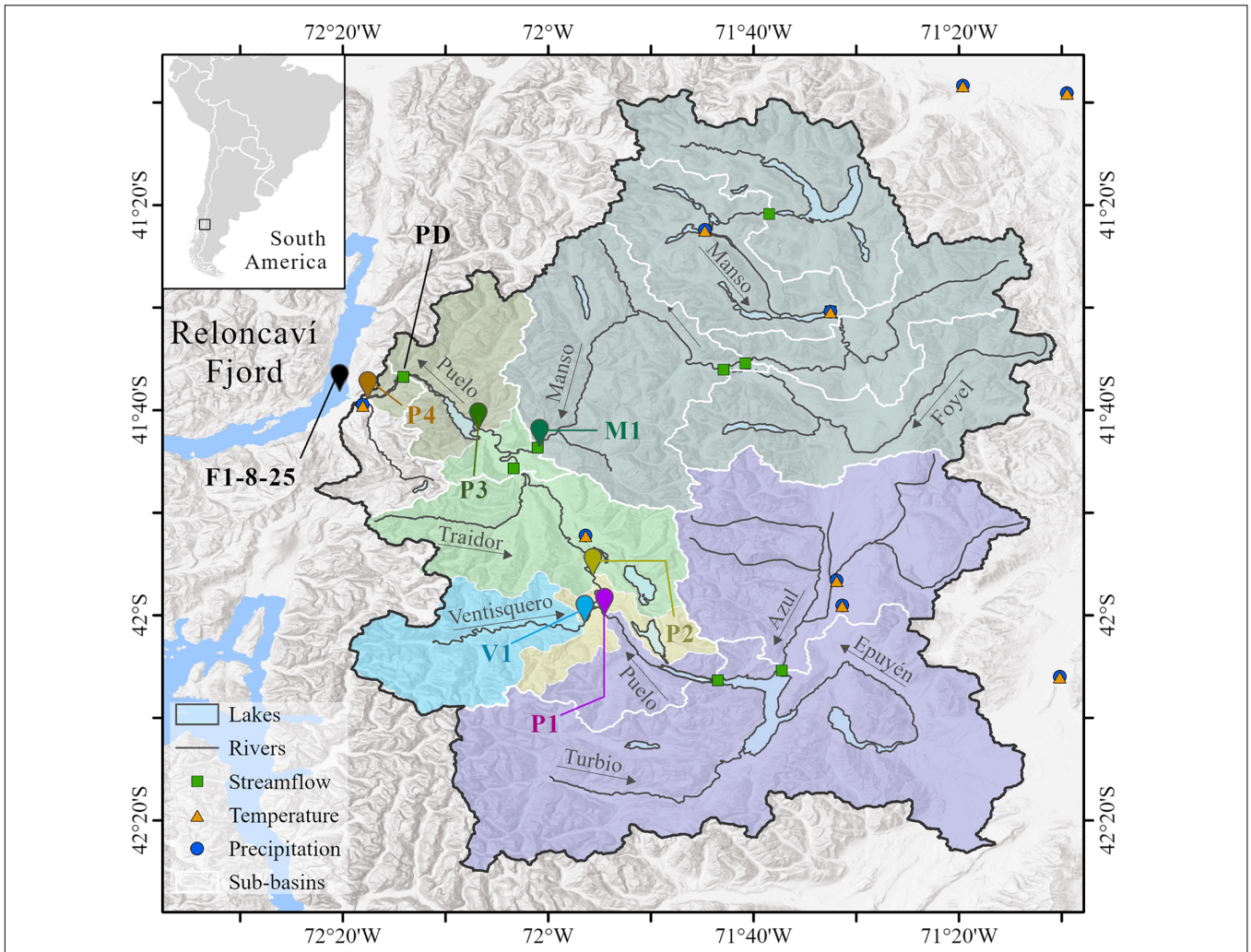

FIGURE 1 | Study area composed of the Puelo River Basin and the Reloncaví Fjord. Within the basin, the names and arrows indicate the principal rivers of the Puelo River drainage network. Geometric symbols indicate the fluviometric and meteorological stations used in the study. Vignettes indicate the sampling points in the Puelo River drainage network (P1, P2, P3, P4, V1 and M1) and Reloncaví Fjord (F; depths 1, 8, and 25 m). The colored polygons represent the sub-basins for each sampling point. The white lines indicate the sub-basins used in the hydrological modeling (section "Hydrologic Modeling of LCC").

mouth (**Figure 1** and **Table 1**). At this site the samples were extracted at 1, 8, and 25 m depth. The 1 m depth sample was intended to represent the upper brackish layer of the fjord (strong freshwater influence). The 25 m depth sample was designed to represent the fjord's middle layer (below the pycnocline). Finally, the 8 m depth sample aims to reflect the seasonal changes in the system stratification, which, as mentioned, is highly dependent on freshwater inputs and other forcing factors such as tides and wind (Valle-Levinson et al., 2014; Castillo et al., 2016). According to continuous measurements carried out between May and September, 2018 these depths presented mean salinity values of 7, 28 and 30, respectively. Each sampling site was visited six times between 2018 and 2019 (42 site-date combinations). The timing of each field campaign was determined based on the monthly Flow Duration Curve (FDC) of the Puelo River during the period 1990–2019 (**Figure 2**). Considering the distance between sampling sites and the characteristics of the study area (**Figure 1**), each campaign was sampled within 3 days, which allowed capturing the variability of short-term events such as floods (**Figure 2**).

The water samples collected in field campaigns were used to analyze nutrients ($N\text{-}NH_4$, $N\text{-}NO_3$, $N\text{-}NO_2$, N-TOTAL, $P\text{-}PO_4$, P-TOTAL), dissolved organic and inorganic carbon concentration (i.e., DOC and DIC), DOM optical spectroscopy, and dissolved iron. For nutrient analysis, the water samples were collected (0.25 L) and stored at −18°C for further analysis according to standard methods established by American Public Health Association, 2005 in the Institute of Marine and Limnological Sciences, Faculty of Sciences, Universidad Austral de Chile.

$N\text{-}NO_3$ was determined by the cadmium reduction method (APHA 4500-E), whereas $N\text{-}NO_2$ by diazotizing with sulfanilamide and coupling with N-(1-naphthyl)-ethylenediamine dihydrochloride (APHA 4500-NO_2 – B).

TABLE 1 | Biophysical attributes of each sub-basin delimited by the sampling points within the Puelo River Basin (**Figure 1**).

		P1	P2	P3	P4	M1	V1
General attributes	Area (km^2)	3,455	4,116	8,497	8,936	3,591	460
	Mean elevation (m)	1,022	1,029	1,078	1,067	1,186	1,149
	Mean slope (deg)	21.8	22.6	22.8	23.1	22.3	29.2
	Mean snow cover extent (%)	36%	38%	36%	36%	34%	54%
	Lakes (km^2)	79.3	96.9	212.7	230.6	91.4	4.3
	Mean annual precipitation (mm)	1,890	2,280	2,400	2,550	2,070	4,800
	Mean annual air temperature (°C)	6.4	6.3	5.8	5.8	4.9	4.8
Burned area (km^2)	Total area	485.9	497.7	592.0	630.0	48.8	11.0
	1990–1999	100.2	111.2	187.1	224.9	38.6	11.0
	2000–2009	121.1	121.1	139.2	139.2	8.9	0.0
	2010–2019	166.4	166.4	166.4	166.4	0.0	0.0
Land cover 2001 (%)	Primary forest	18%	19%	24%	25%	26%	16%
	Secondary forest	2%	3%	3%	3%	3%	8%
	Stunted forest	22%	20%	27%	26%	36%	7%
	Exotic tree plantation	0.1%	0.09%	0.05%	0.05%	0.03%	0.0%
	Shrubland	19%	18%	14%	14%	11%	13%
	Grassland	6%	5%	4%	4%	3%	2%
	Urban	0.12%	0.1%	0.05%	0.05%	0.0%	0.0%
	Water body	2.4%	2.4%	2.6%	2.7%	2.6%	1.0%
	Snow and ice	7%	9%	6%	6%	3%	23%
	Bare land	23%	23%	19%	19%	16%	29%

*The water quality sampling points were located downstream of Lake Inferior (P1), before and after (P2, P3) the confluences with its main tributaries, the Ventisquero (V1) and Manso (M1) rivers, and downstream of Lake Tagua-Tagua (P4), before its mouth in the Reloncaví Fjord (**Figure 1**). Land cover classes are defined in section "Land Cover Change." Reconstruction methods and sources of burned areas are described in section "Wildfires."*

Ammonium was determined by the phenate method (APHA 4500-NH_3 F), total nitrogen was determined by the sodium hydroxide and persulfate digestion method (APHA 4500-N/C) followed by the determination of total N-NO_3. Total phosphorous (Total-P) was measured using the sodium hydroxide and persulfate digestion method (4500-P B/5) followed by the determination of soluble phosphorus using the method of acid ascorbic - blue indophenol (APHA 4500-PE).

Samples for DOC, DIC and DOM quality were filtered (GFF, nominal pore sizes = 0.7 and 0.22 μm) to analyze DOM optical spectroscopy, and DOC replicates were filtered and fixed by adding 100 μL of fuming HCl (Merck) to stop microbial activity, and transported at 4–7°C to the laboratory for subsequent analysis. Note that samples from the deepest point in the fjord (F25) were not available for DOM. DOC concentrations were measured using high-temperature catalytic oxidation (HighTOC, Elementar Systems) as described in Kamjunke et al. (2017). Fluorescence of DOM was measured using a Varian Cary Eclypse fluorescence spectrometer (Santa Clara, CA, United States) as described in Nimptsch et al. (2014). Briefly, excitation matrices from 240 to 450 nm (5 nm steps) and emission from 300 to 600 nm, inner filter corrections and Raman standardization were done using the FDOMcorr toolbox v1.6 for Matlab (Murphy et al., 2010). Parallel Factor Analysis Model (PARAFAC) was performed using DOMFluor toolbox v1.7 for Matlab (Stedmon and Bro, 2008). Four PARAFAC components (i.e. fluorophores C1 to C5) were identified and split-half validated with 1000 iterations with random starts (Stedmon and Bro, 2008).

For the determination of dissolved iron, water samples (volume: 15 ml) were filtered using a 0.2 μm syringe filter and acidified with suprapure nitric acid (MERCK). The samples were analyzed using total-reflection X-ray fluorescence spectrometry (TRXF) following procedures described in Mages et al. (2003). Acidified water samples (10 μl) were prepared onto quartz carriers and internal Ga standard (5 ng, suspended in Suprapur® nitric acid for trace analysis—Sigma-Aldrich) was added. After drying on a hot plate (15 min, 60°C), trace elements were determined using a total reflection X-ray fluorescence spectrometer Picotax (BRUKER).

Land Cover Change

Satellite images were used to analyze the land cover change in the Puelo River Basin. The images were obtained from Landsat 5 and 8 for 2001 (December 16) and 2016 (February 9), respectively. These images have a spatial resolution of 30 m. Using the IDRISI GIS Analysis tool[1], selected images were subjected to standard preprocessing procedure as geometric, radiometric and topographic corrections to reduce the effects of atmosphere and shadows on land surface spectral response (e.g., Echeverria et al., 2006; Fuentes et al., 2017).

The supervised land cover classification of each image was performed in ENVI 4.5 software, which uses maximum likelihood statistics based on training points (Segura and Trincado, 2003). Training point selection for digital supervised classification of the 2001 image were taken from

[1]www.clarklabs.org/terrset/idrisi-gis/

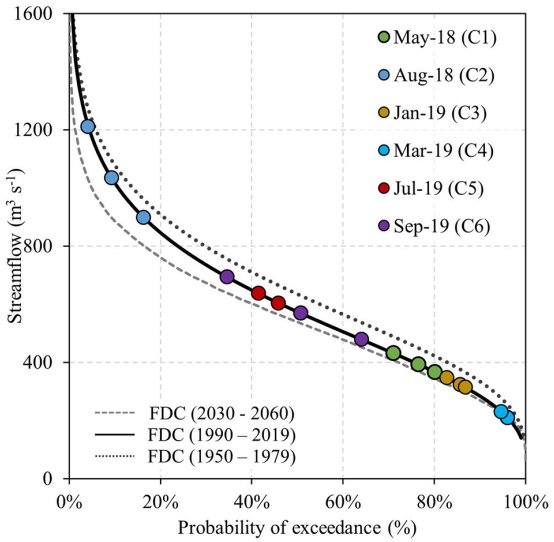

FIGURE 2 | Flow Duration Curve (FDC) of the monthly streamflow of the Puelo River for different periods. The projected streamflows for the period 2030–2060 were obtained from Aguayo et al. (2019). The colors of the circles correspond to the six field campaigns performed in the Puelo River Basin and the Reloncaví Fjord.

CONAF et al. (1999) dataset, a GIS-based data set of thematic maps derived from aerial photographs and satellite imagery from 1998 (Miranda et al., 2018). For the 2016 image classification, 750 training points were obtained from different field campaigns between 2018 and 2019. To increase accuracy of the satellite image classification, the Normalized Difference Vegetation Index (NDVI), Soil Adjusted Vegetation Index (SAVI) and Land Surface Water Index (LSWI) were used as additional spectral bands in both years (Wu et al., 2007).

The spectral information was classified in 10 different land covers categories: primary forests (pristine evergreen forests or those of a natural succession), secondary forest (forests regenerated after a disturbance, whether natural or anthropic), stunted forest (forest under the tree line), exotic tree plantation (commercial plantations mainly of eucalyptus), shrublands, grassland (crop and pastures), urban, water body, snow and ice and bare land. The accuracy assessment consisted of confusion matrices between classified images and independent sampling points collected from aerial photographs and field campaigns. Land cover change analyses were performed using the IDRISI Selva Land Change Modeler module[2]. This analysis consisted of descriptive spatial-temporal statistics of the land covers gains and losses in the time period. The change rates (q) of the different classes were calculated using the equation proposed by Food and Agriculture Organization (1996):

$$q = \left(\frac{A_1}{A_2}\right)^{\frac{1}{t_2 - t_1}} - 1, \quad (1)$$

where A_1 and A_2 are the land cover at time t_1 and t_2, respectively.

[2]www.clarklabs.org/terrset/land-change-modeler/

Wildfires

Past burned areas (>1 ha; 1985–2018) were analyzed as the main potential driver of land cover change in the Puelo River Basin. Burned area reconstruction in the Chilean portion of the basin was performed by applying an algorithm in Google Earth Engine (GEE) (Long et al., 2019). GEE is an open cloud computing platform for geospatial analysis that contains a public catalog of historical satellite images, topography, land cover and other environmental datasets (Gorelick et al., 2017). Taking advantage of the GEE big-data analysis platform, we develop a flexible workflow to reconstruct individual burned area for all fires reported since 1985. This approach processes Landsat images and generates historical burned areas by detecting the multi-temporal reflectance change (before and after the fire) of the Normalized Burn Ratio [NBR = (ρNIR - ρSWIR2)/(ρNIR + ρSWIR2)], which uses the difference between pre- and post-fire reflectance of the near-infrared band (ρNIR) and short-wavelength infrared band (ρSWIR2) extracted from satellite images (Key and Benson, 2003). High values of NBR indicate a burned area that allows the reconstruction of the fire scar in the landscape. All the necessary data are freely available at GEE. This process needs as initial data the ignition point and date, which were compiled by the Chilean National Forestry Corporation (CONAF, 2018). In the Argentinean portion of the basin, the burned areas were obtained directly from MODIS MCD64A1 monthly data (500 m; 2001–2019) and the program of Provincial Agricultural Services (1985–2000).

Statistical Analysis

Water Quality

Nutrient and DOM data were analyzed with a multivariate approach focused on identifying spatial-temporal patterns of coherence between streamflow and water quality variables. Nutrient, DOC, DIC, and DOM data derived from spectroscopic characterization (CDOM (m^{-1}), color (Pt) and PARAFAC components) were first tested and transformed to meet the normality requirement as appropriate. The relationship between nutrients and DOM variables and between samples from all the sites and campaigns was evaluated using a heatmap and a hierarchical clustering approach on the Euclidean distances of the data matrix (*ComplexHeatmap* package v1.10 for R; Gu et al., 2016), which identifies clusters among and within samples and variables.

A non-metric dimensional scaling (NMDS) was used on the Manhattan distance matrix of nutrient concentration (N-total, P-total, NH_4, NO_3, NO_2, and PO_4) and DOM quality descriptors (PARAFAC components, CDOM, ColorPt, and DOC concentration). NH_4 and NO_2 were excluded from the analysis as more than 70% of the cases were below the detection limit. The effect of having total P and PO_4 samples below the detection limit in 50 and 30% of the cases was evaluated and the detection limit value was used (Palarea-Albaladejo and Martín-Fernández, 2015). The relationship between the NMDS of nutrients and DOM quality descriptors and streamflow was assessed by fitting streamflow onto the ordination (*envfit* function) and the result was plotted on the ordination diagram. The significance

of the correlation was assessed through a Monte Carlo test (1,000 permutations). Additionally, the grouping of the factors "Campaign" and "Site" was visualized through hulls plotted for each group using the function *ordihull* and the average of the group scores for each hull (function *ordibar*). The area of those polygons was then tested against areas produced by randomized groups through a permutation test (1,000 permutations) using the function *ordiareatest*. The NMDS was generated by *MetaMDS* function. To assess the effect of the factors campaign and site on DOM quality descriptors, permutation analysis of variance (PERMANOVA; Anderson, 2001) was performed on the corresponding Manhattan dissimilarity matrix (*adonis2* function). All the analyses described above were performed using *stats* v4.1 and *vegan* v2.5 packages for R.

Hydrological Regime

Trends in the hydrological regime of the Puelo River were examined using the Indicators of Hydrologic Alteration software (IHA; Richter et al., 1996). Based on daily data, this tool calculates 33 hydrological metrics that characterize the intra- and inter-annual variability in streamflow conditions, including the magnitude, frequency, duration, timing, and rate of change of streamflow. The metrics were estimated at the Puelo River fluviometric station located near the mouth (PD in **Figure 1**). This station has the most extensive records in the basin and possibly the longest in western Patagonia (water years: 1950–2019). This station adequately represents the hydrological behavior of the streamflows recorded by stations located upstream in Chile (Pearson correlation > 0.95 for the Manso and Puelo Rivers before their confluence; **Figure 1**). Missing daily data were filled with linear regressions with upstream stations (<1% of total data). The magnitude and the significance of the trends were analyzed with the Sen's slope (Sen, 1968) and Mann-Kendall tests (Mann, 1945) (*trend* package v1.1 for R).

Cross-wavelet transform (XWT) and coherence (XWC) analyses were applied to identify significant changes in the association between time series of precipitation and streamflow (Grinsted et al., 2004; Cazelles et al., 2008). XWT evaluates when two time series oscillate in common periods and if there is temporal lag between the peaks of the oscillations, and XWC analyzes the strength of this association (in the form of a correlation and a significance level). A high coherence (∼correlation) between two series for a given oscillation frequency and time period implies that the two series oscillate in a common frequency, and also that the lag between the peaks of the oscillations is constant, which suggests an underlying causal mechanism (Grinsted et al., 2004). XWT was calculated from log (streamflow; PD station in **Figure 1**) or square-root (precipitation; station located near Puerto Montt city 41.5°S), transformed series to attain normality. XWC was calculated in the Undarius High Performance Computer cluster at the Catalan Institute for Water Research, using a Monte Carlo randomization technique as in Grinsted et al. (2004). After XWT and XWC calculations, time series were extracted from correlation and the phase relationship of the most prominent common periods of oscillation shared by the two-time series, and calculated annual means. All data points that did not correspond to statistically significant ($p < 0.05$) associations as identified during XWT were discarded. The correlation and phase relationship of the same common periods of oscillation were extracted for each season and year. All calculations were performed using the *biwavelet* package v0.20.19 for R.

Hydrologic Modeling of LCC

Land Cover Scenarios

The hydrological model aims to evaluate the hydrological impact of three different land cover scenarios (SC), projected to the year 2030 based on observed LCC (2001–2016) and historical burned area (1985–2019). The first scenario (SC-1) considered a matrix of transition probability generated from LCC from 2001 to 2016 in the CA-MARKOV Module of IDRISI Selva v17.0 software[3]. This stochastic model assumes that in a given period pixel persistence or change in either class is dependent only on the immediately previous state, not on historical changes (Zhang and Dai, 2007; Zhang et al., 2011). A cellular automaton model was used to spatialize the Markov model results. This model allowed assessing the spatial changes among pixels, assuming that the changes are dependent on the initial condition and neighboring pixels (Guan et al., 2011; Yang et al., 2012). A standard 5×5 contiguity filter type cellular automaton and a 14-year iteration were used to generate the projected land cover for 2030. The second scenario (SC-2) assumed that the zones most likely to be burned are those where wildfires have been previously occurred. Under this assumption, SC-2 replaced SC-1 land cover with burned areas in those places where wildfires have occurred historically (1985–2019). Finally, the third scenario (SC-3) added to SC-2 new burned areas according to a 2 km buffer around the main lakes and urban or touristic spots, since most of the fires have been recorded in the vicinity of these places [see section "Land Cover Change (LCC)"]. The areas affected by wildfires were considered as bare land in the modeling process in order to evaluate the most extreme hydrological condition. This was the most recurrent condition detected during the post-fire analysis of LCC [see section "Land Cover Change (LCC)"]. Finally, the land cover classes were grouped into six categories: forest (primary, secondary, stunted, and exotic tree plantations), shrubland, grassland, bare land (including urban areas), water body, and snow and ice.

Hydrological Model WEAP

The three land cover scenarios for 2030 were simulated in the WEAP hydrological model (Water Evaluation and Planning; Yates et al., 2005), considering the same climatic conditions for each. The WEAP model, previously used in Chile (e.g., Vicuña et al., 2012; Chadwick et al., 2020; Barría et al., 2021), is a semi-distributed model that represents the relevant hydrological processes using empirical functions that describe the distribution of water in two soil water storages (root and deep storage). In this regard, the snow accumulation and snowmelt are based on the degree-day method, and the potential evapotranspiration (PET) was calculated with the Penman-Monteith equation. As a final output, the streamflow composition of each simulated river

[3]www.clarklabs.org

corresponds to the sum of surface runoff, interflow and baseflow. See Yates et al. (2005) for more details on the equations of the conceptual model.

The WEAP model was previously calibrated and validated for a monthly time step by Aguayo et al. (2021) using the corrected atmospheric products of section "Hydrology and Climate" (period 2000–2019). In this approach, the Puelo River Basin was divided into nine sub-basins (green squares in **Figure 1**), which were subdivided into different hydrological units according to their elevation and land cover type (baseline year 2001). The model reached a Modified Kling-Gupta Efficiency (Kling et al., 2012) of 0.83 and 0.74 for the calibration (2000–2010) and validation (2011–2019) stages, respectively (sub-basin PD in **Figure 1**). The model maintained high correlations (r = 0.78 ± 0.07) and dry biases (β = 0.93 ± 0.11) during the validation stage. These biases were mainly associated with high streamflow events when the probability of exceedance was less than 20%. In contrast, minimum annual streamflows were adequately simulated (r = 0.84). The simulated PET near the Reloncaví Fjord was similar to the time series recorded by an evaporation pan located in the same place (2002–2012; R^2 = 0.87, RMSE = 14 mm). Further details of the calibration/validation process and the parameter estimation can be found in Text S1 and Aguayo et al. (2021).

RESULTS

Water Quality in the Land-Ocean Interface

Nitrogen, phosphorus, dissolved carbon, and iron measured during the six field campaigns in the Puelo River Basin had very low concentrations (**Figure 3** and **Supplementary Table 2**) which are characteristic of well-conserved basins previously reported in southern Chile (**Supplementary Table 3**). In river samples (P1 to P4, Manso and Ventisquero), total nitrogen, phosphorus, dissolved carbon and iron concentration were mostly < 60 μg N L^{-1}, < 10 μg P L^{-1}, < 3.8 mg C L^{-1} and < 10 μg Fe L^{-1}. In contrast, the Reloncaví Fjord had mostly 3–15 times higher mean N, P, C and Fe concentrations (160–400 μg N L^{-1}, 27–74 μg P L^{-1}, 6–13 mg C L^{-1}, 22–26 μg Fe L^{-1}) which also increased remarkably by a factor of three from surface to 25 m depth (**Figure 3** and **Supplementary Table 2**). High values of total dissolved carbon in the fjord corresponded to the inorganic fraction; DOC concentrations were comparable across samples (**Supplementary Table 2**). The Ventisquero (V1) and Manso Rivers (M1) presented different mean values from those found by site in Puelo River's mainstem (**Supplementary Table 2**). The Ventisquero River showed the lowest mean total N and dissolved C concentration (<30 μg N L^{-1} and < 2,14 mg C L^{-1}), thus diluting nutrient concentrations of the mainstem after their confluence. Manso River transported higher nutrient loads, especially TP, leading to increases in P3 (**Figure 3**, **Supplementary Figure 1**, and **Supplementary Table 2**).

The NMDS separated the samples according to their origin of fjord versus basin and into the different sampling campaigns (**Figure 4** and **Supplementary Figure 1**; stress = 0.159). The first dimension was related, on the positive side, to protein-like DOM components, and with nutrients and DIC on the negative side. Fjord samples (F1 and F8) appeared grouped independently of the sampling campaign, and related to nutrients. The fjord's surface layer samples (1 m, F1) appear between the deeper fjord samples (8 m, F8) and the basin samples. The second dimension of the NMDS separated the basin samples by

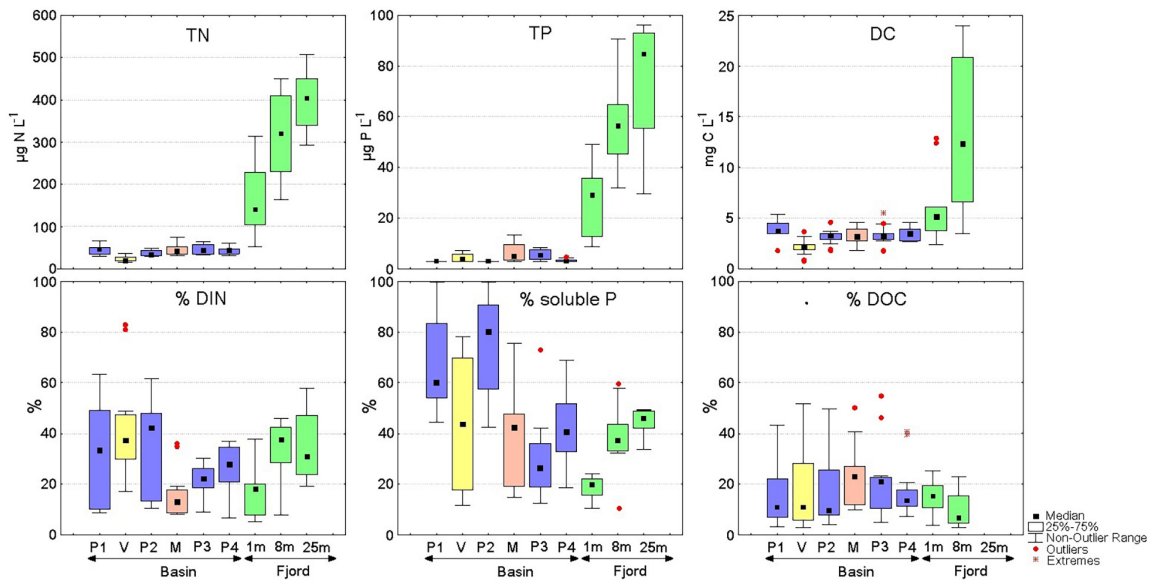

FIGURE 3 | Upper panel: Total nitrogen (TN), total phosphorus (TP) and total dissolved carbon (DC) concentrations measured in the Puelo River (P1-P4), Ventisquero River (V), Manso River (M) and Reloncaví Fjord at three depths (n = 12). Lower panel: Percentage of dissolved inorganic nitrogen (DIN), soluble phosphorous and dissolved organic carbon (DOC) with respect to the concentrations of the upper panel.

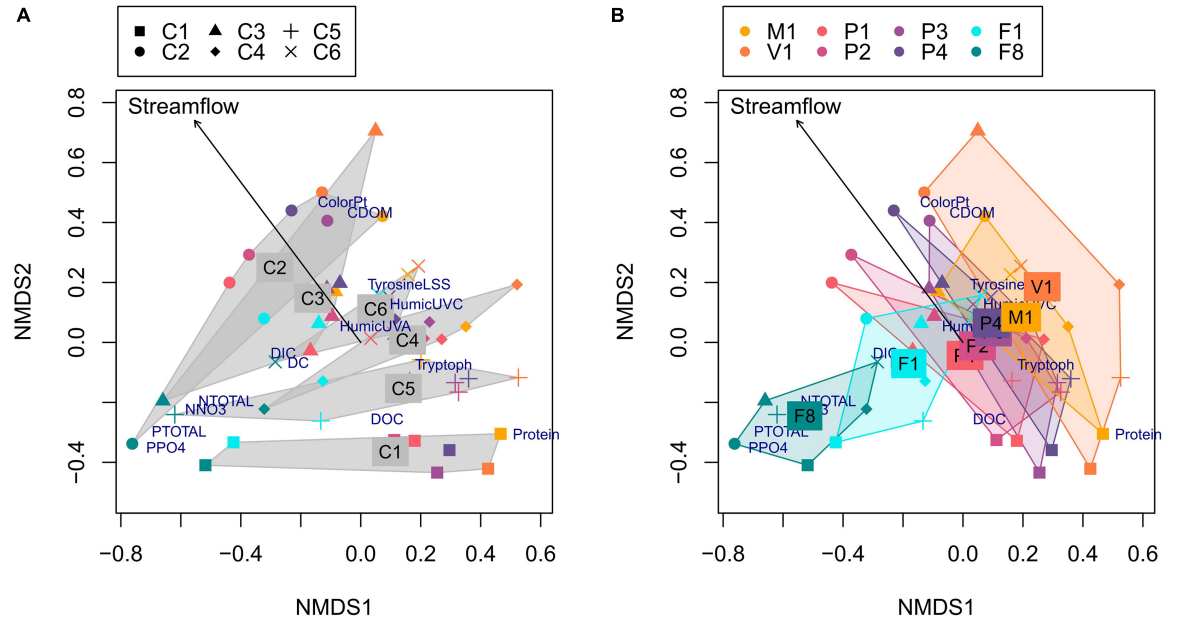

FIGURE 4 | Non-metric dimensional scaling (NMDS) ordination of all samples based on nutrients and DOM descriptors (symbol colors indicate the different sampling sites and shapes show the different campaigns). Labels indicate the nutrients and DOM descriptors. The left panel **(A)** shows hulls for the Campaign groups, labeled at the position of the average group scores. All the hulls except or C3 were significantly smaller than those produced by random groups. The right panel **(B)** shows hulls for the Site groups, labeled at the position of the average group scores. Only the hull for F8 is significantly smaller than those produced by random groups (see **Supplementary Table 4**). The arrow corresponds to streamflow values fitted to the ordination (r^2 = 0.1902, p = 0.01).

their different campaigns based mainly on DOM descriptors. Thus this dimension represents a gradient from colored and humic to protein-like DOM. C2 (Aug. 19) samples presented colored DOM, while those from C1 (May 19) had protein-like DOM. The remaining campaigns appeared ordered in the intermediate values of that second dimension. Streamflow appeared significantly fit to the NMDS ordination (r^2 = 0.19, p = 0.009), with higher streamflow conditions related to positive values of the second axis. Thus, these conditions (**Figure 2**) contribute with humic and colored materials (as in August, 2019), while low streamflows corresponded to higher arrival of protein-like materials from the basin (as in May, 2018). Fjord samples from 1 m are grouped together with Puelo River samples for each campaign. The permutation test for the size of the ordination hulls for campaign show that all the campaigns except C3 had smaller areas than random groups, while the test for sites shows that only F8 had a smaller area than random groups (**Supplementary Table 4**). In agreement with this, the PERMANOVA analysis of nutrients and DOM showed that both campaign and site had a significant effect (**Table 2**; FCampaign = 5.98, FSite = 10.32, p = 0.001 in both cases), although the effect of site was weaker when nutrients were excluded (**Table 2**; FSite = 3.26, p = 0.005, FCampaign = 10.12, p = 0.001).

Natural Flow Regime

Puelo River observational records analysis showed trends in magnitude, timing, duration, and change rate of streamflow (**Supplementary Table 1** and **Figure 5**). The streamflow recorded during summer and autumn showed statistically significant decreasing trends (summer in color palette of **Figure 5A**). The most affected months were January (−6% decade^{-1}; p < 0.001), February (−6% decade^{-1} p < 0.001), March (−4% decade^{-1}; p < 0.05) and May (−9% decade^{-1}; p < 0.05). The magnitude of such trends was also reflected in the Flow Duration Curve for the 1950–1979 and 1990–2019 periods (**Figure 2**). Inter-annual hydrological variability also showed significant changes associated with extreme conditions. Minimum annual streamflows for time windows of 7, 30, and 90 days showed statistically significant trends (**Supplementary Table 1** and **Figure 5A**). The timing of the maximum annual peak streamflow also changed. Only 10% of the years between 1950 and 1990 recorded the peak outside of the autumn or winter. In contrast, since 1990 this percentage has increased to 40% (p < 0.05; **Figure 5B**), and it has become more frequent to observe them in spring. Furthermore, the duration of the high streamflows registered a significant decrease (0.3 days decade^{-1}; color palette of **Figure 5B**). Finally, there were also significant trends in the streamflow fall rate (negative differences between consecutive values; **Supplementary Table 1**). The anomalies in the natural flow regime have coincided with the SAM trend (**Figure 5C**). In recent decades, the SAM positive phase has coincided with very warm ENSOs, which has favored extreme drought conditions in Northwestern Patagonia (e.g., 1998 and 2016 in **Figure 5**). This is not expected, considering that El Niño conditions tend to promote the negative phase of SAM, thus producing a negative correlation between their indices at interannual time-scales (L'Heureux and Thompson, 2006; Ding et al., 2012).

TABLE 2 | PERMANOVA analysis of (a) nutrients (N-total, P-total, NO_3, NO_2, and PO_4) and (b) DOM quality descriptors (PARAFAC components, CDOM, ColorPt, and DOC concentration), with sites and campaigns as factors.

(a) Nutrients	Df	SS	MS	Pseudo-F	P (perm)
Campaign	5	155.2	0.445	7.99	0.001***
Site	5	95.8	0.275	4.93	0.002**
Residual	25	97.1	0.278		
Total	35	348.1	1.000		
(b) DOM	**Df**	**SS**	**MS**	Pseudo-F	P(perm)
Campaign	5	168.7	0.466	10.1	0.001***
Site	7	76.1	0.210	3.23	0.008**
Residual	35	116.7	0.322		
Total	47	361.6	1.000		

*Df, degrees of freedom; SS, sum of squares; MS, mean sum of squares; Pseudo-F, F value by permutation, P(perm), p-values. ** < 0.01, *** < 0.001.*

The cross-wavelet transform and coherence analyses suggested shifts in the response of streamflow to precipitation events during the last decades (**Figure 6**). Beyond the expected year-to-year variability of the correlation (color) and lag (arrows) between streamflow and precipitation at short periods of oscillation (period from weeks to ∼3 months; **Figure 6A**), the analysis showed a significant common oscillation at 180 days (**Figure 6B**), corresponding to the relationship of precipitation peak during early winter and the streamflow peaks during early winter and late spring. For the oscillation at a period of 180 days, a significant increase (tau = 0.224, $p < 0.05$) of the lag between precipitation and streamflow was apparent (**Figure 6C**), from oscillations mostly around phase (lag ∼ 0, i.e. oscillations are synchronous) during the 1970s, to average lags around 20 days (and up to ∼50 days) during the last decade (i.e. streamflow peak had a lag of ∼20 days with respect to the precipitation peak), which is consistent with **Figure 5B**. This indicated that years with the prominent streamflow peak during spring are becoming more frequent. The correlation between the time-series at the period of oscillation of 180 days substantially decreased over years, showing longer lags between precipitation and streamflow (**Figure 6C**). This interpretation is also supported by the correlation between precipitation and streamflow oscillations analyzed at a period of 1 year, which shows consistently high correlation during the last decades (**Figure 6B**). This is expected if the double streamflow peak during winter-spring simplifies to a single peak, which would correlate better with the prominent precipitation peak during winter.

Land Cover Change (LCC)

The overall accuracy for satellite image classification was 85.3% for 2001 and 88.7% for 2016. The highest accuracy (except for water and bare soil) was achieved in primary forests (2001: 84.6%; 2016: 87.1%). The lowest values of accuracy corresponded to shrubland in 2001 and 2016 (76.6 and 81.8%, respectively). Land cover classification showed that 55% of the Puelo River Basin was covered by native forest in 2001 (**Figure 7c** and **Table 3**). Native forest cover rises to 77% without considering the water bodies and high elevated areas of bare land and snow. Other important classes were shrubland (13.5%) and bare land (18.7%) (**Tables 1**, **3**).

Land cover change analysis showed that 91.2% of the total area remained unchanged in the 2001–2016 period (**Figure 7a** and **Table 3**). The main changes corresponded to the increase of secondary forest (+3.7% yr^{-1}), shrubland (+0.2% yr^{-1}) and bare land (+0.5% yr^{-1}) (annual rate of change; **Table 3**). Secondary forest recovery was concentrated in areas with reduced human activity (e.g., Ventisquero River basin; **Figure 7a**). In contrast, the degradation processes associated with the loss of primary forest were located in the Turbio and Epuyén river valleys, where historical wildfires were concentrated (**Figures 7A,B**). Although exotic tree plantations and urban areas represented a minimum area in 2016, these land cover classes reported the highest annual rates of change (7.0 and 5.4%, respectively; **Table 3**).

The reconstruction of the burned area in the Puelo River Basin showed that 649.6 km^2 (7.1% of the basin) were affected by 74 wildfires between 1985 and 2019 (**Figure 7b** and **Table 1**). Of this total, 43 records occurred in Chile (109 km^2) and 31 in Argentina (539 km^2). Only 15 wildfires accumulated 88% of the total burned area (>10 km^2). Of these, only one occurred before 1995 (**Table 1**). The largest wildfires in Chile and Argentina occurred in the surroundings of Tagua-Tagua Lake (1998; 39 km^2) and Puelo Lake (2015; 129 km^2), respectively.

Hydrological Response to LCC

The three land cover scenarios projected toward the year 2030 showed LCC of different magnitude. SC-1 will decrease in primary (−1.1%) and stunted forest (−0.4%) (**Table 3**). SC-2 will add 524 km^2 of bare land in areas historically affected by wildfires (1985–2019) to SC-1, which affected mainly native forest areas (148 km^2), shrubland (197 km^2) and grasslands (24 km^2) (**Figure 7b** and **Table 3**). Finally, SC-3 will add 1,192 km^2 of possible burned areas to SC-2 according to a 2 km buffer around the principal lakes (**Figure 7d** and **Table 3**). Despite the extreme conditions assumed by this scenario, the native forest will decrease from 55.2 to 45.7%, while the bare land will increase from 18.7 to 31.6% (**Table 3**).

The decrease in vegetation cover shown by the three scenarios (e.g., native forest, shrubland) consistently reduced ET, and

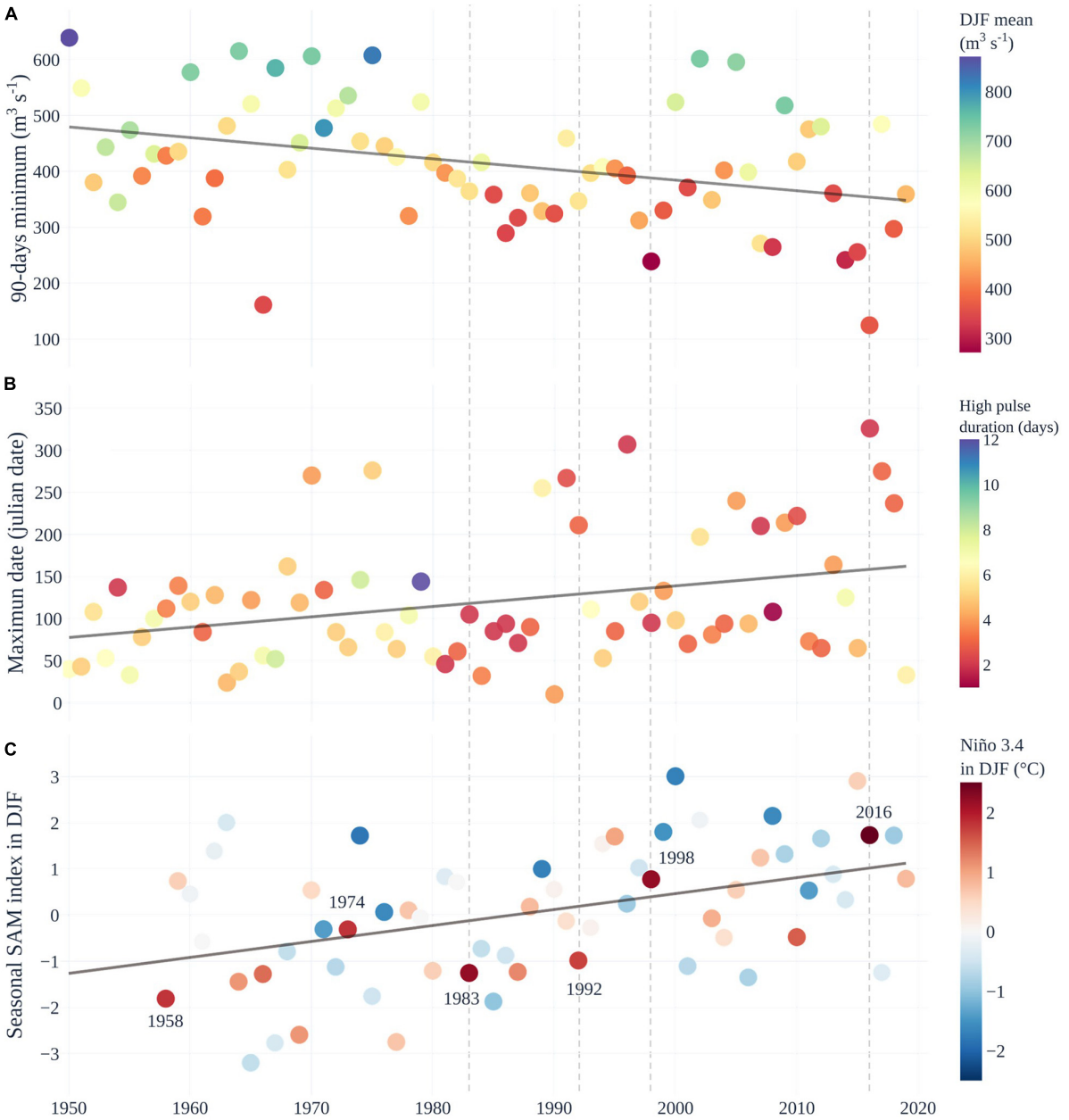

FIGURE 5 | Natural streamflow regime trends of the Puelo River and the climatic context. **(A)** Minimum annual streamflow in a 90-day window. The color palette in **(A)** represents the average streamflow during the summer season (DJF period). **(B)** Julian date of the maximum annual streamflow and high pulse duration (defined by 75th percentile; color palette). The first Julian day corresponds to the first day of the water year (April 1). **(C)** Southern Annular Mode (SAM) index during DJF as in Marshall (2003). The color palette represents the Niño 3.4 index during DJF of the HadISST1 data set. The segmented vertical lines indicate the main ENSO events.

altered internal hydrological processes (**Figure 8**). Reduced vegetation promotes changes in surface hydrological response, reducing infiltration rates and increasing surface runoff. Lower infiltration reduces subsurface flow and percolation into deep storage, which in turn controls base flow. Note that the base flow dominated the streamflow composition during the baseline period (2000–2019) with values of 40 ± 9% (**Figure 8**).

The magnitude of the hydrological response varied according to the scenarios, from non-significant changes (SC-1) to slight changes (SC-3) (**Figure 8**). Note that snow accumulation remained constant in **Figure 8**, since the climatic forcing does not change in the land cover scenarios. Regardless of the scenario evaluated, surface runoff and ET showed the greatest changes (**Figure 8**). Under the worst-case scenario (SC-3), the winter season recorded the largest projected changes in streamflow composition. In this season, the base flow, interflow and runoff showed changes relative to the baseline period of −2.0, −2.4, and 8.6%, respectively (**Figure 8**). Despite the seasonal

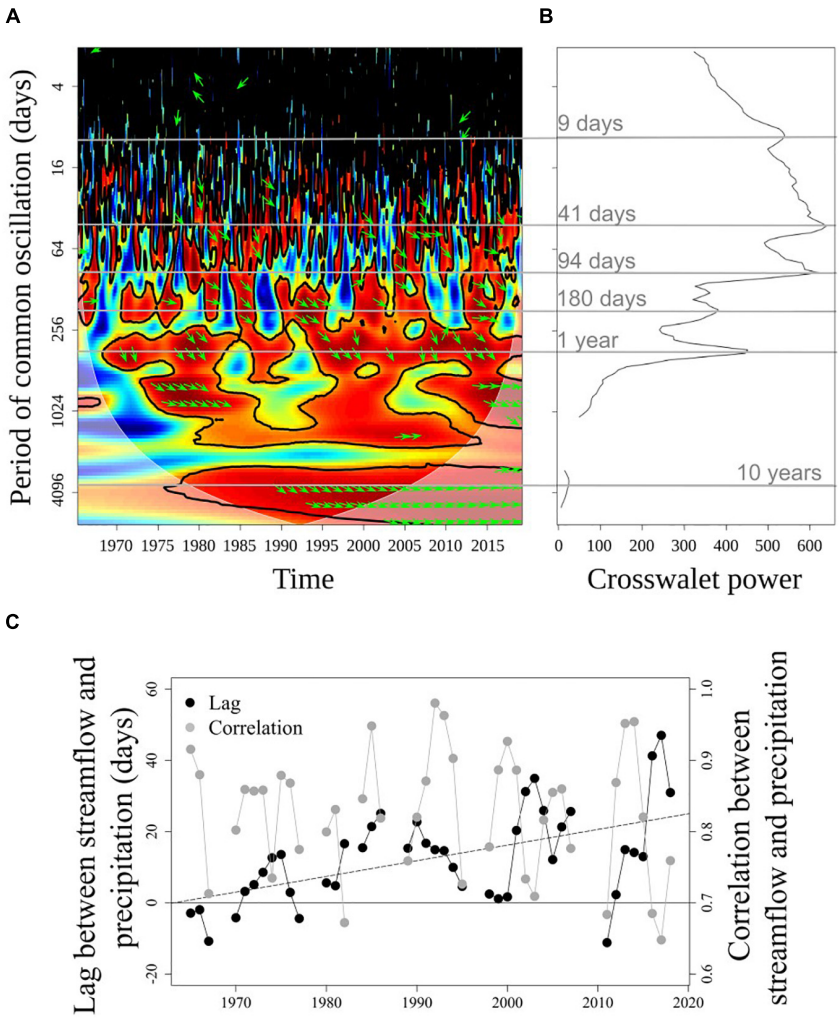

FIGURE 6 | Cross-wavelet transform and coherence analyses for the precipitation (in Puerto Montt) and streamflow time series (PD in **Figure 1**). **(A)** Cross-wavelet coherence plot, with significant regions delimited with a thick continuous line. Red colors denote high correlation. Shaded area is the cone of influence, where interpretations should be cautious. **(B)** Global cross-wavelet power showing the main periods of common oscillation. **(C)** Temporal lag (in days respect the precipitation series) and correlation between precipitation and streamflow analyzed at a period of 180 days. The dashed line is a linear trend for the lag, while the correlation did not show a significant trend. In panels b and c non-significant periods, lags, and correlations are not shown.

changes in hydrological processes, the same scenario indicated an average annual increase of only 1.1% of freshwater input to the Reloncaví Fjord.

DISCUSSION

This study illustrates the importance of water availability and quality of Puelo River Basin as the main freshwater input to the Reloncaví Fjord system. We show that the hydrology of the Puelo River has changed over time, with major shifts in magnitude (lower flows in summer and autumn), duration (minimum annual streamflows), timing (more floods in spring), and frequency (fewer prolonged floods). Concentrations of nitrogen and phosphorus must be highlighted as some of the lowest recorded for temperate rivers, highlighting the relatively pristine nature of the basin. The analysis of spectroscopic DOM descriptors and DOC concentration showed that streamflow and hydrological moment drive DOM composition in the hydrological network. The freshwater inputs from the Puelo River are fundamental to the haline stratification of the Reloncaví Fjord and the dilution of nutrients in the upper brackish layer. Wildfires have been the main driver of land cover change (LCC) in the past. Future LCC projections will reduce the evapotranspiration and subsurface flow, increasing the surface runoff, which will result in slight seasonal changes in freshwater inputs to the fjord. This study highlights the need for large coastal basins with near-reference conditions as indicators, sentinels or model systems for evaluating how could affect future scenarios of global environmental change affecting freshwater inputs (including volume, seasonal, and water quality) in fjord systems of Patagonia.

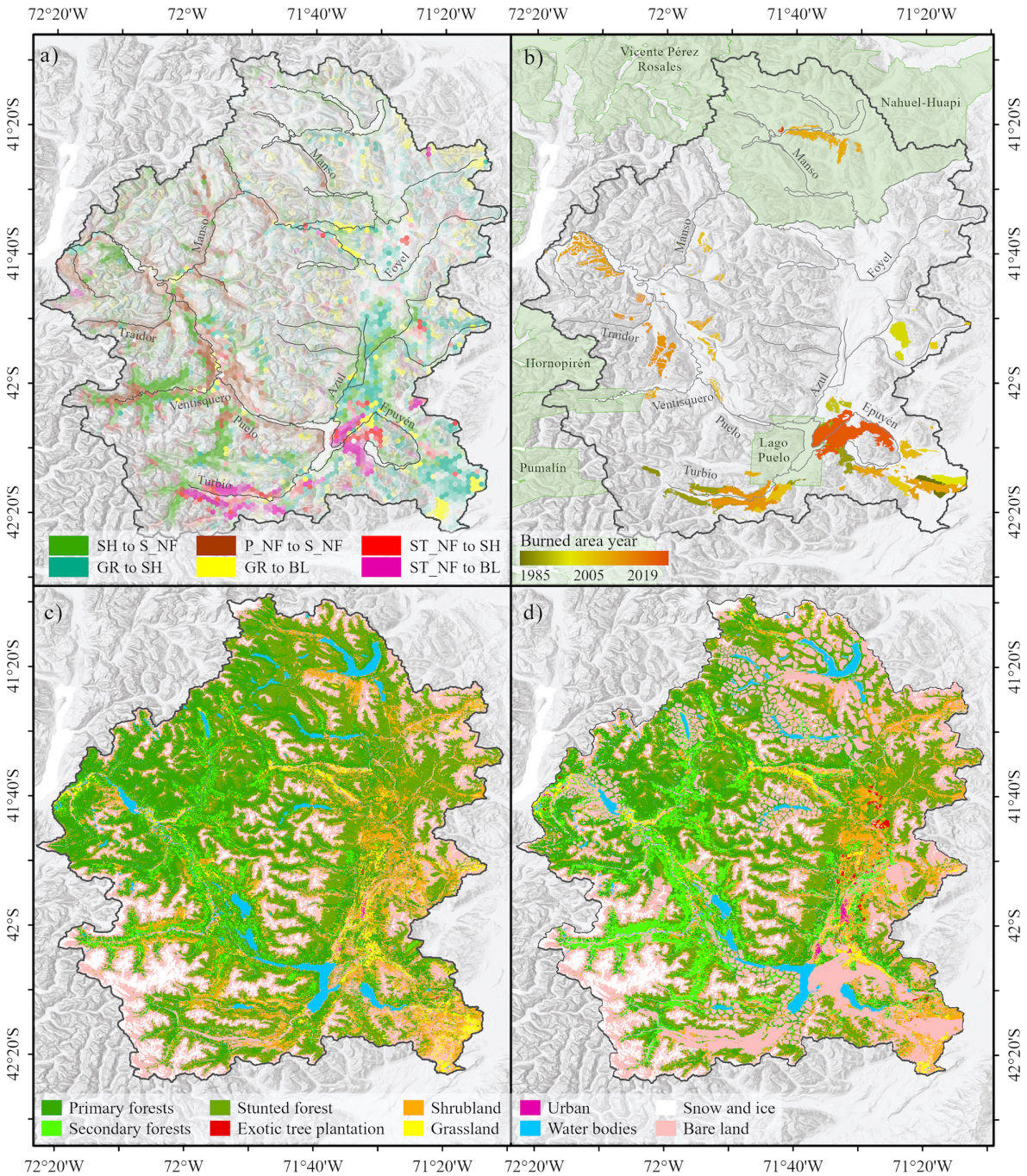

FIGURE 7 | (a) Land cover change in the Puelo River Basin during the 2001–2016 period. The colors in panel **(a)** indicate the six major land cover transitions (74% of the total changes). P_NF, Primary native forests; S_NF, Secondary native forest; ST_NF, Stunted native forest; SH, Shrubland; GR, Grassland; BL, Bare land. **(b)** Historical burned area (1985–2019). **(c)** Land cover in 2001. **(d)** Land cover in 2030 (SC-3), This scenario considered SC-1, the historically burned area in **(b)** and buffer areas around the main lakes and urban or touristic spots.

Natural Flow Regime and Freshwater Quality

Nutrient concentrations in the Puelo River drainage network across seasons are in the lower range of previously reported values for rivers in southern Chile (**Supplementary Table 3**; Oyarzun et al., 1997, 2004; Godoy et al., 1999, 2001; Perakis and Hedin, 2002; Oyarzún and Huber, 2003; Little et al., 2008), and elsewhere (de la Crétaz and Barten, 2007). Nutrient concentrations in the Reloncaví Fjord are much higher than those from the Puelo River. Therefore, the low concentration of N and P in these freshwater

TABLE 3 | Land cover in the Puelo River Basin in 2001, 2016 and 2030 (under the three scenarios).

Land-use cover	Area (%)					Rate of change (% yr^{-1})	
	2001	2016	2030 (SC-1)	2030 (SC-2)	2030 (SC-3)	2001–2016 (Historical)	2016–2030 (SC-1)
Native forest	55.2%	55.0%	53.6%	51.7%	45.7%	−0.03%	−0.17%
Primary forest	25.7%	23.9%	20.1%	19.3%	16.1%	−0.5%	−1.1%
Secondary forest	3.5%	6.1%	9.9%	9.2%	8.6%	3.7%	3.2%
Stunted forest	26.0%	25.0%	23.6%	23.3%	20.9%	−0.3%	−0.4%
Exotic tree plant.	0.1%	0.1%	0.3%	0.3%	0.3%	7.0%	5.5%
Shrubland	13.5%	14.0%	14.5%	12.2%	11.8%	0.2%	0.2%
Grassland	4.0%	2.2%	2.5%	2.2%	2.1%	−4.0%	0.8%
Urban	0.0%	0.1%	0.1%	0.1%	0.1%	5.4%	1.7%
Water bodies	2.7%	2.7%	2.7%	2.7%	2.7%	–	–
Snow and ice	5.8%	5.8%	5.8%	5.8%	5.8%	–	–
Bare land	18.7%	20.1%	20.5%	25.0%	31.6%	0.5%	0.1%

The annual rate of change was determined according to the formula proposed by FAO (1996). Total native forest cover is the sum of primary, secondary and stunted forests.

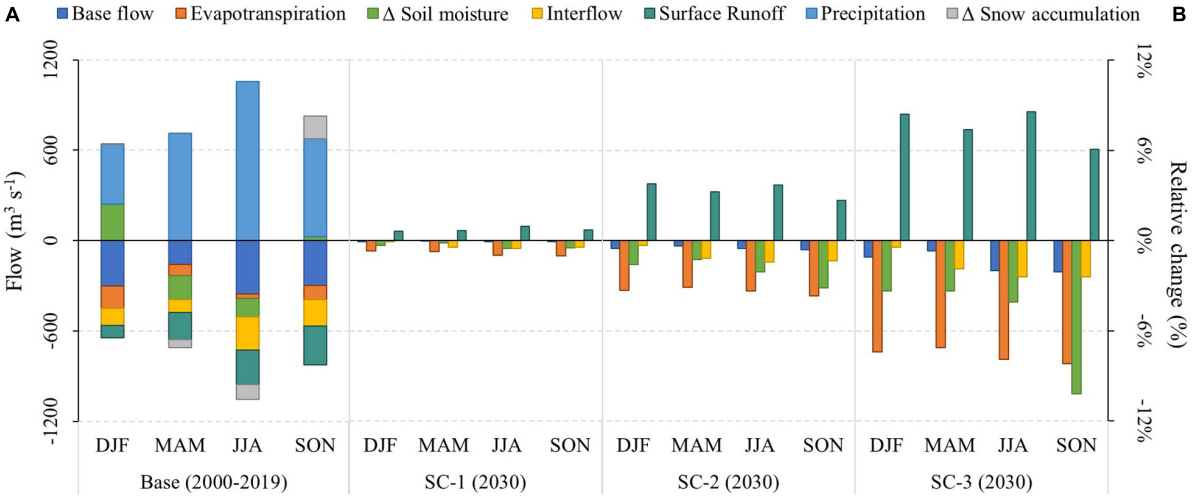

FIGURE 8 | (A) Hydrological balance of the Puelo River Basin using the WEAP model previously calibrated by Aguayo et al. (2021) (2000–2019; sub-basin PD in **Figure 1**). Positive flows (precipitation, soil moisture depletion and snowmelt) represent inflows of water to the basin. Negative flows represent accumulations (as soil moisture or snowpack) or outflows (evapotranspiration, surface runoff, interflow and base flow) from the basin. Note that storages can have a positive or negative sign depending on if they accumulate ($\Delta < 0$) or release water ($\Delta > 0$). **(B)** Relative changes of the hydrological processes for each scenario in relation to the same process during the baseline period. Each scenario represents different land covers in the year 2030. SC-1 projected land cover considering the changes that occurred in the period 2001–2016. SC-2 replaced SC-1 land cover with burned areas in those places where wildfires have occurred historically (1985–2019). SC-3 added to SC-2 new burned areas according to a 2 km buffer around the main lakes and urban areas.

inputs of the Puelo River may play a significant role in the coastal dynamics, influencing the upper layer of the Reloncaví Fjord. Clearly it can be stated out that the enhanced concentrations of dissolved and total fractions of N, P and Fe reported in the fjord are unlikely to be caused by the Puelo River input, as its nutrient and Fe content were always below the fjord samples. Therefore, it can only be speculated what other sources are responsible for the higher N, P and Fe concentration in the fjord; diffuse input from coastal sides, in-sea contamination from salmon farming and others. The NMDS and PERMANOVA analysis showed that nutrients present stronger differences between the fjord and the basin samples than DOM composition and the fjord's surface layer (1 m, mainly fresh and brackish water) nutrient concentrations are between the deeper fjord samples (measured at 8 and 25 m depth in the fjord) and the basin samples (**Supplementary Table 2**). This upper layer can limit the exchanges with deeper layers mostly of oceanic origin (González et al., 2013; Torres et al., 2014). This fjord has likely been more resilient to additional nutrient inputs (salmon farming; Soto et al., 2019) due to both the dilution role of freshwater input and rates of water turnover (Pinilla et al., 2020). Future scenarios of streamflow reduction might reduce water turnover in the fjord and enhance local eutrophication conditions. Hence the pristine conditions of freshwater input could provide important ecosystem services to maintain the resilience of the Reloncaví Fjord ecosystem to global environmental change.

NMDS based on nutrients, spectroscopic DOM descriptors and DOC concentrations (**Figure 4**) shows that streamflow and hydrological conditions drive DOM composition in freshwater. A closer examination of the origin of DOM from the Puelo River to the Reloncaví Fjord during the low streamflow period illustrates the fragile balance between hydrology and biogeochemical function of the river-fjord system. The PERMANOVA result, with both campaign and site being significant, does not allow us to present hydrology as the only control of DOM quality, but this result together with the NMDS sample clustering leads us to conclude that (i) seasonality and streamflow play a major role in it, (ii) the two major tributaries M1 and V1 contribute with low nutrient concentrations and very variable DOM quality (**Figure 4** and **Supplementary Table 4**).

High streamflow conditions during winter are related to humic and colored DOM, in agreement with behavior as a passive pipe; terrestrial DOM is transferred from soils to streams, and then rapidly transported toward the ocean without significant alteration (Raymond et al., 2016; Casas-Ruíz et al., 2020). In contrast, during low streamflow conditions we found an increase in protein-like DOM sources from degraded peptide material (Fellman et al., 2010) coming from the Puelo River Basin. This is likely due to the disconnection of lateral channel processes in the drainage network resulting in longer water residence time, and a large proportion of DOM from autochthonous sources (Casas-Ruiz et al., 2016; Catalán et al., 2016). However, we found a significant effect of site on DOM quality, and we expect some sections of the Puelo River drainage network to have a disproportionate influence on DOM quality and ultimately on the different layers of the Reloncaví Fjord. In order to constrain the link between hydrology and DOC concentration and DOM quality better, we encourage future studies to trace both the hydrograph and concentration response on a finer temporal scale and especially during extreme hydrologic conditions, as those may lead to especially harmful conditions in the fjord.

While our results help to understand the effect that the interplay between hydrological change and LCCs has on DOM composition, it is still unclear whether the relatively small LCC occurring in the Puelo River Basin have sufficient potential to affect fjord-level processes significantly. Targeting compounds at the molecular level (Coppola et al., 2018) might be key to identify the legacy of wildfires in these aquatic systems further. For example, increases in riverine export of dissolved black carbon have been found decades after wildfires in Brazil's Atlantic forest (Dittmar et al., 2012). Changes in the composition of riverine organic matter can alter carbon cycling in fjords due to shifts in both sedimentation rates and light penetration (Ward et al., 2017). However, even considering the constraints of our study, based on the high proportion of native forest in the Manso sub-basin, the projected LCC may reduce the DOM inputs from terrestrial vegetation (colored and typically aromatic) in the Reloncaví Fjord. This could lead to reduced flocculation and sedimentation in the coastal waters (Raymond and Spencer, 2015).

Recent hydrological shifts imply that the routing of water in the basin is undergoing profound changes. Considering the pristine nature of the basin, this also may have measurable yet unknown consequences for the export of DOC and nutrients from soils to rivers, and ultimately for the fjord. Although most studies focus on temperate, boreal and artic regions, it is well known that changes in hydrological regimes influence the export of DOC in relatively undisturbed basins (Winterdahl et al., 2016; Baek et al., 2019; Connolly et al., 2020). Unfortunately, our short-term study in terms of water chemistry cannot illuminate this issue, and there are no long-term records of organic matter and nutrient export from Patagonian basins to support claims related to changes in hydrological regimes. However, there is evidence from other regions that DOM export from snow-melt has a different chemical signature than exports from other flow paths (Burns et al., 2016). Furthermore, changes in timing and magnitude of streamflow in the region represent shifts in natural hydrological regimes (Poff et al., 1997; Poff, 2018), and could have additional biological implications in river networks and fjord ecosystems of this region. For example, the predicted shift in the hydrology of the Puelo River might increase the importance of autochthonous sources and decrease the transport of DOM from humic-like terrestrial sources reaching the fjord, except during storm episodes. Considering the relevance of organic carbon and nutrient exports for the ecological dynamics of the fjord and the expected hydrological changes in the future, understanding how this hydrological shift impacts constituent export from the basin should be a research priority.

Wildfires Are the Main Drivers of Land Cover Changes

The native forest cover in the Puelo River Basin (primary, secondary and stunted forests) showed an annual deforestation rate of 0.03%, with more than 90% of the basin area remaining unchanged during the period 2001–2016 (**Table 3**). As in Gowda et al. (2012), urban areas and exotic tree plantation had a marginal negative net contribution to forest cover throughout the period. However, these land cover classes reported the highest annual rates of change (7 and 5.4%, respectively, **Table 3**). The low LCC rate demonstrates the good conservation status of the Puelo River basin, differing from the values described for south-central Chile (33–42°S), an area that has been subjected to major LCC and is experiencing an annual rate of forest loss ranging between 0 and 5.8% (Miranda et al., 2017). Also the LCC ranges of the Puelo River basin are in the lower range of northwestern Patagonia, where Echeverría et al. (2012) reported an annual deforestation rate close to 1.0% (1985–1999 vs. 1999–2007).

According to our results, wildfires are main drivers of LCC in the Puelo River Basin. The frequency of fires in northwestern Patagonia peaked in the late nineteenth century, due to widespread burning and clearing of forests by European settlers. Fire frequency declined dramatically around 1910 due to the cessation of intentional fires; it has remained low due to current fire suppression (Kitzberger and Veblen, 1999; Veblen et al., 1999). In this study, the historical reconstruction of burned areas in the Puelo River Basin shows that 649.6 km^2 were affected by 74 wildfires between 1985 and 2019 (**Figure 7** and **Table 1**). Mundo et al. (2013) reported a strong negative association

between the density of fire ignitions and their distance to cities in this region (<5 km). This is consistent with the human origin of the fires in the Puelo River Basin, where most of wildfires have occurred around national parks, lakes and urban areas. Although the annual area burned in the Puelo River Basin has not changed over time, more than 90% of wildfires larger than 10 km^2 occurred after 1995. Climate trends might facilitate the spread of large wildfires, which added to the high fuel content in the region could increase the frequency of larger wildfires (Kitzberger and Veblen, 1999; González et al., 2018; Urrutia-Jalabert et al., 2018). In comparable mountain systems from western North America there is a strong link between wildfire activity and climate oscillations (Trouet et al., 2006; Holden et al., 2018).

Synergistic Hydrological Effects Between Climate and LCC

The three LCC scenarios showed changes of different magnitude in the Puelo River landscape. If current LCC trends continue (SC-1), native forest will decrease by 1.6% (relative value for 2001–2030), while if LCC intensifies due to potential wildfires (SC-3), native forest could decrease by up to 9.5% by 2030 (**Table 3**). Under these scenarios, bare land, the most recurrent land cover class after wildfires (**Figure 7**), would increase by 1.8 and 12.9%, respectively (**Table 3**). According to the WEAP model, these land cover transitions promote reductions in infiltration rates, which in turn reduce subsurface flow and percolation into deep storage (**Figure 8**). Reduced percolation can lead to a reduction in base flow, the dominant streamflow component of the Puelo River (40 ± 9%). Consistent with other hydrologic modeling in mountain systems (Havel et al., 2018), other processes observed in the hydrologic response were an increase in surface runoff and a decrease in evapotranspiration. The hydrologic response varied according to the scenario and remained similar between seasons. In the worst scenario for winter (SC-3), the hydrological model predicts changes of −2.0%, −2.4% and 8.6% on the base flow, interflow and runoff, respectively. The magnitude of projected changes is comparable to a deforestation scenario in the Vergara River Basin (Stehr et al., 2010), but lower than what was reported in south-central Chile, where changes in LCC are relatively more drastic and different (intensive forestry; Aguayo et al., 2016; Barrientos et al., 2020; Martínez-Retureta et al., 2020).

The hydrological simulations forced by LCC scenarios were an order of magnitude lower than the previous projections forced by the climate change scenarios. According to dendrochronological reconstructions, recent climate trends are unprecedented in the last centuries (e.g., SAM in **Figure 5C**; Villalba et al., 2012; Morales et al., 2020), which has been evident in the precipitation and temperature of northwestern Patagonia (Pabón-Caicedo et al., 2020). Recently, Aguayo et al. (2021) showed that temperature in northwestern Patagonia has increased during the whole year, but mainly in summer (0.3 ± 0.1°C decade^{-1}). In contrast, precipitation has decreased mainly during the autumn (−8 ± 8% decade^{-1}) and winter (−4 ± 9% decade^{-1}). Based on these climate trends, recent hydrological modeling in northwestern Patagonia projects an increase in the frequency of severe droughts during summer and autumn months (Aguayo et al., 2019, 2021; Pessacg et al., 2020). Lower streamflow conditions during summer are likely due to higher evapotranspiration (Ellenburg et al., 2018), and lower snow accumulation in snow-dominated regions (Barnett et al., 2005). Timing of the streamflow annual peaks have also changed in the Puelo River Basin, migrating from winter to less prolonged spring peaks. The increasing lag between precipitation and streamflow seasonally (from synchronous peaks to a lag of ∼50 days) suggests a shift in the peak streamflow timing (**Figure 6**). We hypothesize that the lower precipitation recorded in winter (maximum daily precipitation), together with a greater height of the 0°C isotherm in spring, allows the maximum annual streamflow to occur in spring.

The importance of various hydrological stressors depends on the local climatic, geographic and hydrological conditions, and the respective future trajectories (e.g., Davis et al., 2015; Yang et al., 2017; Chanapathi and Thatikonda, 2020). Hydrological projections for LCC and climate scenarios show opposite directions in the Puelo River Basin. Considering a moderate emissions scenario to the year 2030 (Shared Socio-economic Pathway Two), Aguayo et al. (2021) projected streamflow changes of −15, −18, 8, and 2% to DJF, MAM, JJA and SON, respectively (multi-model mean for 2020–2040 vs. 2000–2019). These values are an order of magnitude larger than those projected by LCC, since the projected climate trend for NP is one of the largest in the world (Cook et al., 2020). For example, Barría et al. (2021) recently determined that the relative impact of the climate factor is more than 10 times larger than the impact of the observed LLC changes in the Aculeo Lake balance (Central Chile; 33°S). Although these results may discourage conservation, Galleguillos et al. (2021) reported that conservative scenarios focused on native forest protection and restoration could partially mitigate the effect of climate change in Mediterranean basins. Future efforts should focus on understanding the hydrological role of different vegetation cover (e.g., Milkovic et al., 2019), under changing climatic conditions in northwestern Patagonia.

Long-Term Hydrological Trends Are Changing the Fjord System

Changes in climate ultimately result in modified trends of surface hydrology. During the last decades, the Puelo River regime showed a clear trend toward longer and more intense hydrological droughts, with major shifts in magnitude (lower flows in summer and autumn), duration (minimum annual streamflows), timing (more floods in spring), and frequency (fewer prolonged floods) (**Figure 5**). The trends in magnitude were consistent with those previously reported. Recently, Aguayo et al. (2021) showed a decreasing streamflow mainly during autumn (−6% ± 3% decade^{-1}) and summer (−5% ± 2% decade^{-1}) for most of the rivers of northwestern Patagonia. As a result of climate change, these results invite understanding the influence of the Puelo River as a non-stationary driver of the Reloncaví Fjord.

Changes in the natural flow regime during extreme climatic conditions, like during ENSO event in summer and autumn

(e.g., Valle-Levinson et al., 2007; León-Muñoz et al., 2018), could influence the occurrence of anomalous oceanographic events in the Reloncaví Fjord. The reduction in freshwater input drives the weakening of ocean stratification in the upper layer, allowing vertical advection of saline, less oxygenated and nutrient-rich waters (Valle-Levinson et al., 2007). These mechanisms have the potential to affect the production of mussels (*Mytilus chilensis*) and salmon (*Salmo salar* and *Onchorhynchus* spp.) in aquaculture facilities (Soto et al., 2019). For example, an increase in the salinity of the fjord's surface layer can alter environmental conditions that minimize the impacts of caligidosis (sea louse) in salmon (Montory et al., 2018). León-Muñoz et al. (2018) reported that the severe drought during 2016 (the lowest streamflow in 70 years) generated the appropriate conditions for a record harmful algae bloom in northwestern Patagonia. As a consequence, the mortality of salmon in a few days was comparable to the mortality that all salmon farming usually experiences in 2 years (US$ 800 million). This extreme event is also a relevant threat to mussel culture (Chávez et al., 2019; Soto et al., 2020). Coastal sites with high input of freshwater seem to ensure better mussel seed provision, survival and capture, apparently because the wild mussel populations providing the seeds are more successful at lower salinities (Molinet et al., 2015, Molinet et al., 2021). Therefore, the decreasing trend in freshwater input to the Reloncaví Fjord during drought years, and the changes in its timing, could be compromising the future of these two industries (Soto et al., 2020).

CONCLUSION

The Puelo River streamflow showed non-stationary conditions with clear trends toward longer and more intense droughts. Several indicators of the natural flow regime also showed significant trends, such as the timing of the maximum annual peak streamflow, the duration of high streamflows and the streamflow fall rate. Despite the recent increase in wildfires in recent decades, more than 90% of the total area maintained its land cover during the period 2001–2016. Considering these trends, the hydrological simulations based on land cover scenarios toward the year 2030 will slightly influence hydrological processes (e.g., surface runoff, evapotranspiration), and therefore the hydrological regime of the Puelo River will be mostly modulated by climate trends. These climate trends would imply hydrological changes in the opposite direction to those forced by the LCC scenarios. The combined effect of both hydrological stressors and potential decline in water quality (increase in nutrients) is a call for more robust data monitoring and analysis of both drivers. For example, it is essential to advance in the understanding the hydrological role of different vegetation covers under warmer and drier climatic conditions in northwestern Patagonia.

Nutrient concentrations in the drainage network are in the lower range of previously reported values for rivers in southern Chile, and are 3–15 times lower than in the fjord. As result, the fjord′s surface layer limits the exchanges with deeper water layers mostly of oceanic origin. Future decreases in freshwater input might reduce water turnover in the fjord and enhance local eutrophication conditions. Coastal sites with high freshwater input support large-scale salmon aquaculture and ensure better mussel seed survival. Considering the relevance of organic carbon and nutrient exports, understanding how this hydrological shift influences the export of basin constituents warrants further research. For example, to trace both the hydrograph and concentration response on a finer temporal scale during extreme hydrologic conditions, as these may lead to anomalous and extreme events in the fjord (e.g., harmful alga bloom, hypoxia events). This study provides baseline information about present and future threats relevant to the potential of "losing the freshwater-dependent resilience" of the Reloncaví Fjord to future global environmental change. More research is still needed to understand better the influence of water availability and quality on the biogeochemistry, food webs and ecosystem services provided by this river-fjord complex.

DATA AVAILABILITY STATEMENT

The datasets generated for this study can be found in the Zenodo repository (https://doi.org/10.5281/zenodo.4604929). This repository contains hydro-climatic observations, gridded products of precipitation and temperature, land cover for different periods, and the reconstruction of burned areas. The raw data from CHIRPSv2, MODIS MOD11C3, and ERA5 can be found at www.chc.ucsb.edu/data/chirps (last access: June 12, 2021), https://lpdaac.usgs.gov/products/mod11c3v006 (last access: June 12, 2021), and www.ecmwf.int/en/forecasts/datasets/reanalysis-datasets/era5 (last access: June 12, 2021), respectively.

AUTHOR CONTRIBUTIONS

JL-M: conceptualization, methodology, validation, investigation, formal analysis, and writing—original draft. RA and CC: methodology, investigation, software, formal analysis, data curation, visualization, and writing—reviewing and editing. NC: methodology, investigation, software, formal analysis, and writing—reviewing and editing. RM: software, formal analysis, and writing—reviewing and editing. SW and JN: investigation, formal analysis, and writing—reviewing and editing. DS, IA, and AM: writing—reviewing and editing. All authors contributed to the article and approved the submitted version.

FUNDING

This research was supported by projects ANID—FONDECYT: N°11170768 "Potential effects of land use change on fjords of western Patagonia under climate change scenarios" and Interdisciplinary Center for Aquaculture Research (FONDAP INCAR 15110027, ANID). RA was supported by ANID PFCHA/DOCTORADO NACIONAL/2019—21190544. RM and NC participated trough the project C-HydroChange (CGL2017-86788-C3-2-P) of the Spanish Ministry of Economy and Competitiveness.

ACKNOWLEDGMENTS

We thank Directorate of Water (DGA), Meteorological Directorate of Chile (DMC), and the Sub-Secretariat of Water Resources of Argentina (SRHA) for their role in collecting data.

SUPPLEMENTARY MATERIAL

The Supplementary Material for this article can be found online at: https://www.frontiersin.org/articles/10.3389/fmars.2021.628454/full#supplementary-material

REFERENCES

Aguayo, M., Stehr, A., and Link, O. (2016). Respuesta hidrológica de una cuenca de meso escala frente a futuros escenarios de expansión forestal. *Rev. Geogr. Norte Gd.* 65, 197–214. doi: 10.4067/S0718-34022016000300010

Aguayo, R., León-Muñoz, J., Garreaud, R., and Montecinos, A. (2021). Hydrological droughts in the southern Andes (40–45°S) from an ensemble experiment using CMIP5 and CMIP6 models. *Sci. Rep.* 11:5530. doi: 10.1038/s41598-021-84807-4

Aguayo, R., León-Muñoz, J., Vargas-Baecheler, J., Montecinos, A., Garreaud, R., Urbina, M., et al. (2019). The glass half-empty: climate change drives lower freshwater input in the coastal system of the Chilean Northern Patagonia. *Clim. Change* 155, 417–435. doi: 10.1007/s10584-019-02495-6

Alvarez-Garreton, C., Lara, A., Boisier, J. P., and Galleguillos, M. (2019). The impacts of native forests and forest plantation on water supply in Chile. *Forests* 10:473. doi: 10.3390/f10060473

American Public Health Association (2005). *Standard Methods for the Examination of water and wastewater*, 21st Edn. Washington, DC: American Public Health Association.

Anderson, M. J. (2001). A new method for non parametric multivariate analysis of variance. *Austral. Ecol.* 26, 32–46.

Arblaster, J. M., and Meehl, G. A. (2006). Contributions of external forcings to southern annular mode trends. *J. Clim.* 19, 2896–2905. doi: 10.1175/JCLI3774.1

Astorga, A., Moreno, P., and Reid, B. (2018). Watersheds and trees fall together: an analysis of intact forested watersheds in southern Patagonia (41–56° S). *Forests* 9:385. doi: 10.3390/f9070385

Aufdenkampe, A. K., Mayorga, E., Raymond, P. A., Melack, J. M., Doney, S. C., Alin, S. R., et al. (2011). Riverine coupling of biogeochemical cycles between land, oceans, and atmosphere. *Front. Ecol. Environ.* 9:14. doi: 10.1890/100014

Baek, S., Jeon, J., Lee, H., Park, J., and Cho, K. (2019). investigating influence of hydrological regime on organic matters characteristic in a korean watershed. *Water* 11:512. doi: 10.3390/w11030512

Barbier, E. B., Hacker, S. D., Kennedy, C., Koch, E. W., Stier, A. C., and Silliman, B. R. (2011). The value of estuarine and coastal ecosystem services. *Ecol. Monogr.* 81, 169–193. doi: 10.1890/10-1510.1

Barnett, T. P., Adam, J. C., and Lettenmaier, D. P. (2005). Potential impacts of a warming climate on water availability in snow-dominated regions. *Nature* 438, 303–309. doi: 10.1038/nature04141

Barría, P., Chadwick, C., Ocampo-Melgar, A., Galleguillos, M., Garreaud, R., Díaz-Vasconcellos, R., et al. (2021). Water management or megadrought: what caused the Chilean Aculeo Lake drying? *Reg. Environ. Chang.* 21:19.

Barrientos, G., Herrero, A., Iroumé, A., Mardones, O., and Batalla, R. J. (2020). Modelling the effects of changes in forest cover and climate on hydrology of headwater catchments in south-central Chile. *Water* 12:1828. doi: 10.3390/w12061828

Beck, H. E., Zimmermann, N. E., McVicar, T. R., Vergopolan, N., Berg, A., and Wood, E. F. (2018). Present and future Köppen-Geiger climate classification maps at 1-km resolution. *Sci. Data* 5:180214. doi: 10.1038/sdata.2018.214

Boisier, J. P., Alvarez-Garreton, C., Cordero, R. R., Damiani, A., Gallardo, L., Garreaud, R. D., et al. (2018). Anthropogenic drying in central-southern Chile evidenced by long-term observations and climate model simulations. *Elem. Sci. Anthr.* 6:74. doi: 10.1525/elementa.328

Boisramé, G. F. S., Thompson, S. E., Tague, C., and Stephens, S. L. (2019). Restoring a natural fire regime alters the water balance of a sierra nevada catchment. *Water Resour. Res.* 55, 5751–5769. doi: 10.1029/2018WR024098

Burns, M. A., Barnard, H. R., Gabor, R. S., McKnight, D. M., and Brooks, P. D. (2016). Dissolved organic matter transport reflects hillslope to stream connectivity during snowmelt in a montane catchment. *Water Resour. Res.* 52, 4905–4923. doi: 10.1002/2015WR017878

Casas-Ruíz, J. P., Spencer, R. G. M., Guillemette, F., Schiller, D., Obrador, B., Podgorski, D. C., et al. (2020). Delineating the continuum of dissolved organic matter in temperate river networks. *Global Biogeochem. Cycles* 34:e2019GB006495. doi: 10.1029/2019gb006495

Casas-Ruiz, J. P., Tittel, J., von Schiller, D., Catalán, N., Obrador, B., Gómez-Gener, L., et al. (2016). Drought-induced discontinuities in the source and degradation of dissolved organic matter in a Mediterranean river. *Biogeochemistry* 127, 125–139.

Castillo, M. I., Cifuentes, U., Pizarro, O., Djurfeldt, L., and Caceres, M. (2016). Seasonal hydrography and surface outflow in a fjord with a deep sill: the Reloncaví fjord. *Chile. Ocean Sci.* 12, 533–534. doi: 10.5194/os-12-533-2016

Catalán, N., Marcé, R., Kothawala, D. N., and Tranvik, L. J. (2016). Organic carbon decomposition rates controlled by water retention time across inland waters. *Nat. Geosci.* 9, 501–504. doi: 10.1038/ngeo2720

Cazelles, B., Chavez, M., Berteaux, D., Ménard, F., Vik, J. O., Jenouvrier, S., et al. (2008). Wavelet analysis of ecological time series. *Oecologia* 156, 287–304.

Chadwick, C., Gironás, J., Barría, P., Vicuña, S., and Meza, F. (2020). Assessing reservoir performance under climate change. when is it going to be too late if current water management is not changed? *Water* 13:64. doi: 10.3390/w13010064

Chanapathi, T., and Thatikonda, S. (2020). Investigating the impact of climate and land-use land cover changes on hydrological predictions over the Krishna river basin under present and future scenarios. *Sci. Total Environ.* 721:137736. doi: 10.1016/j.scitotenv.2020.137736

Chávez, C., Dresdner, J., Figueroa, Y., and Quiroga, M. (2019). Main issues and challenges for sustainable development of salmon farming in Chile: a socio-economic perspective. *Rev. Aquac.* 11, 403–421. doi: 10.1111/raq.12338

CONAF (2018). *Estadísticas Históricas De Incendios Forestales en Chile*. Available online at: https://www.conaf.cl/incendios-forestales/incendios-forestales-en-chile/estadisticas-historicas/ (accessed January 6, 2020).

CONAF, CONAMA, and Birf. (1999). *Catastro y Evaluación De Los Recursos Vegetacionales Nativos De Chile. Informe nacional con Variables Ambientales*. Santiago: Natural Resources Information Center (CIREN).

CONAF, and UACH. (2014). *Monitoreo De Cambios, Corrección Cartográfica Y Actualización Del Catastro De Recursos Vegetacionales Nativos de la Región de Los Lagos*. Santiago: Natural Resources Information Center (CIREN).

Connolly, C. T., Cardenas, M. B., Burkart, G. A., Spencer, R. G. M., and McClelland, J. W. (2020). Groundwater as a major source of dissolved organic matter to Arctic coastal waters. *Nat. Commun.* 11:1479. doi: 10.1038/s41467-020-15250-8

Cook, B. I., Mankin, J. S., Marvel, K., Williams, A. P., Smerdon, J. E., and Anchukaitis, K. J. (2020). Twenty-First Century Drought Projections in the CMIP6 Forcing Scenarios. *Earth's Futur.* 8, 1–20. doi: 10.1029/2019EF001461

Coppola, A. I., Wiedemeier, D. B., Galy, V., Haghipour, N., Hanke, U. M., Nascimento, G. S., et al. (2018). Global-scale evidence for the refractory nature of riverine black carbon. *Nat. Geosci.* 11, 584–588. doi: 10.1038/s41561-018-0159-8

Cuevas, J. G., Soto, D., Arismendi, I., Pino, M., Lara, A., and Oyarzún, C. (2006). Relating land cover to stream properties in southern Chilean watersheds: trade-off between geographic scale, sample size, and explicative power. *Biogeochemistry* 81, 313–329. doi: 10.1007/s10533-006-9043-5

Dávila, P. M., Figueroa, D., and Müller, E. (2002). Freshwater input into the coastal ocean and its relation with the salinity distribution off austral Chile (35-55°s). *Cont. Shelf Res.* 22, 521–534. doi: 10.1016/S0278-4343(01)00072-3

Davis, J., O'Grady, A. P., Dale, A., Arthington, A. H., Gell, P. A., Driver, P. D., et al. (2015). When trends intersect: The challenge of protecting freshwater ecosystems under multiple land use and hydrological intensification scenarios. *Sci. Total Environ.* 534, 65–78. doi: 10.1016/j.scitotenv.2015.03.127

de la Crétaz, A., and Barten, P. K. (2007). *Land Use Effects on Streamflow and Water Quality in the Northeastern United States*. Boca Raton, FL: CRC Press, doi: 10.1201/9781420008722.ch7

Desmit, X., Thieu, V., Billen, G., Campuzano, F., Dulière, V., Garnier, J., et al. (2018). Reducing marine eutrophication may require a paradigmatic change. *Sci. Total Environ.* 635, 1444–1466.

Díaz, P. A., Peréz-Santos, I., Álvarez, G., Garreaud, R., Pinilla, E., Díaz, M., et al. (2021). Multiscale physical background to an exceptional harmful algal bloom of Dinophysis acuta in a fjord system. *Sci. Total Environ.* 773:145621. doi: 10.1016/j.scitotenv.2021.145621

Ding, Q., Steig, E. J., Battisti, D. S., and Wallace, J. M. (2012). Influence of the tropics on the southern annular mode. *J. Clim.* 25, 6330–6348.

Dittmar, T., de Rezende, C. E., Manecki, M., Niggemann, J., Coelho Ovalle, A. R., Stubbins, A., et al. (2012). Continuous flux of dissolved black carbon from a vanished tropical forest biome. *Nat. Geosci.* 5, 618–622. doi: 10.1038/ngeo1541

Echeverria, C., Coomes, D., Salas, J., Rey-Benayas, J. M., Lara, A., and Newton, A. (2006). Rapid deforestation and fragmentation of Chilean Temperate Forests. *Biol. Conserv.* 130, 481–494. doi: 10.1016/j.biocon.2006.01.017

Echeverría, C., Newton, A., Nahuelhual, L., Coomes, D., and Rey-Benayas, J. M. (2012). How landscapes change: Integration of spatial patterns and human processes in temperate landscapes of southern Chile. *Appl. Geogr.* 32, 822–831. doi: 10.1016/j.apgeog.2011.08.014

Ellenburg, W. L., Cruise, J. F., and Singh, V. P. (2018). The role of evapotranspiration in streamflow modeling – An analysis using entropy. *J. Hydrol.* 567, 290–304. doi: 10.1016/j.jhydrol.2018.09.048

Ellison, D., Morris, C. E., Locatelli, B., Sheil, D., Cohen, J., Murdiyarso, D., et al. (2017). Trees, forests and water: cool insights for a hot world. *Glob. Environ. Chang.* 43, 51–61. doi: 10.1016/j.gloenvcha.2017.01.002

Eyring, V., Arblaster, J. M., Cionni, I., Sedláček, J., Perlwitz, J., Young, P. J., et al. (2013). Long-term ozone changes and associated climate impacts in CMIP5 simulations. *J. Geophys. Res. Atmos.* 118, 5029–5060. doi: 10.1002/jgrd.50316

Farías, L., Sanzana, K., Sanhueza-Guevara, S., and Yevenes, M. A. (2017). dissolved methane distribution in the reloncaví fjord and adjacent marine system during Austral Winter (41°–43° S). *Estuaries and Coasts* 40, 1592–1606. doi: 10.1007/s12237-017-0241-2

Fellman, J. B., Hood, E., and Spencer, R. G. M. (2010). Fluorescence spectroscopy opens new windows into dissolved organic matter dynamics in freshwater ecosystems: a review. *Limnol. Oceanogr.* 55, 2452–2462. doi: 10.4319/lo.2010.55.6.2452

Food and Agriculture Organization (1996). *Forest Resources Assessment 1990. Survey of Tropical Forest Cover and Study of Change Process*. Roma: Food and Agriculture Organization of the United Nations.

Fuentes, R., León-Muñoz, J., and Echeverría, C. (2017). Spatially explicit modelling of the impacts of land-use and land-cover change on nutrient inputs to an oligotrophic lake. *Int. J. Remote Sens.* 38, 7531–7550. doi: 10.1080/01431161.2017.1339928

Funk, C., Peterson, P., Landsfeld, M., Pedreros, D., Verdin, J., Shukla, S., et al. (2015). The climate hazards infrared precipitation with stations—a new environmental record for monitoring extremes. *Sci. Data* 2:150066. doi: 10.1038/sdata.2015.66

Galleguillos, M., Gimeno, F., Puelma, C., Zambrano-Bigiarini, M., Lara, A., and Rojas, M. (2021). Disentangling the effect of future land use strategies and climate change on streamflow in a Mediterranean catchment dominated by tree plantations. *J. Hydrol.* 595:126047. doi: 10.1016/j.jhydrol.2021.126047

Garreaud, R. (2018). Record-breaking climate anomalies lead to severe drought and environmental disruption in western Patagonia in 2016. *Clim. Res.* 74, 217–229. doi: 10.3354/cr01505

Godoy, R., Oyarzún, C., and Bahamondes, J. (1999). Flujos hidroquímicos en un bosque de Nothofagus pumilio en el Parque Nacional Puyehue, sur de Chile. *Rev. Chil. Hist. Nat.* 72, 579–594.

Godoy, R., Oyarzún, C., and Gerding, V. (2001). Precipitation chemistry in deciduous and evergreen Nothofagus forests of southern Chile under a low-deposition climate. *Basic Appl. Ecol.* 2, 65–72. doi: 10.1078/1439-1791-00037

González, H. E., Castro, L. R., Daneri, G., Iriarte, J. L., Silva, N., Tapia, F., et al. (2013). Land-ocean gradient in haline stratification and its effects on plankton dynamics and trophic carbon fluxes in Chilean Patagonian fjords (47-50°S). *Prog. Oceanogr.* 119, 32–47. doi: 10.1016/j.pocean.2013.06.003

González, H. E., Nimptsch, J., Giesecke, R., and Silva, N. (2019). Organic matter distribution, composition and its possible fate in the Chilean North-Patagonian estuarine system. *Sci. Total Environ.* 657, 1419–1431. doi: 10.1016/j.scitotenv.2018.11.445

González, M. E., Gómez-González, S., Lara, A., Garreaud, R., and Díaz-Hormazábal, I. (2018). The 2010-2015 Megadrought and its influence on the fire regime in central and south-central Chile. *Ecosphere* 9:e02300. doi: 10.1002/ecs2.2300

Gorelick, N., Hancher, M., Dixon, M., Ilyushchenko, S., Thau, D., and Moore, R. (2017). Google Earth Engine: planetary-scale geospatial analysis for everyone. *Remote Sens. Environ.* 202, 18–27. doi: 10.1016/j.rse.2017.06.031

Gowda, J. H., Kitzberger, T., and Premoli, A. C. (2012). Landscape responses to a century of land use along the northern Patagonian forest-steppe transition. *Plant Ecol.* 213, 259–272. doi: 10.1007/s11258-011-9972-5

Grinsted, A., Moore, J. C., and Jevrejeva, S. (2004). Application of the cross wavelet transform and wavelet coherence to geophysical time series. *Nonlinear Process. Geophys.* 11, 561–566. doi: 10.5194/npg-11-561-2004

Gu, Z., Eils, R., and Schlesner, M. (2016). Complex heatmaps reveal patterns and correlations in multidimensional genomic data. *Bioinformatics* 32, 2847–2849. doi: 10.1093/bioinformatics/btw313

Guan, D., Li, H., Inohae, T., Su, W., Nagaie, T., and Hokao, K. (2011). Modeling urban land use change by the integration of cellular automaton and Markov model. *Ecol. Modell.* 222, 3761–3772. doi: 10.1016/j.ecolmodel.2011.09.009

Havel, A., Tasdighi, A., and Arabi, M. (2018). Assessing the hydrologic response to wildfires in mountainous regions. *Hydrol. Earth Syst. Sci.* 22, 2527–2550. doi: 10.5194/hess-22-2527-2018

Hernes, P. J., and Benner, R. (2003). Photochemical and microbial degradation of dissolved lignin phenols: Implications for the fate of terrigenous dissolved organic matter in marine environments. *J. Geophys. Res. Ocean.* 108:3291. doi: 10.1029/2002JC001421

Hersbach, H., Bell, B., Berrisford, P., Hirahara, S., Horányi, A., Muñoz-Sabater, J., et al. (2020). The ERA5 global reanalysis. *Q. J. R. Meteorol. Soc.* 146, 1999–2049. doi: 10.1002/qj.3803

Holden, Z. A., Swanson, A., Luce, C. H., Jolly, W. M., Maneta, M., Oyler, J. W., et al. (2018). Decreasing fire season precipitation increased recent western US forest wildfire activity. *Proc. Natl. Acad. Sci. U.S.A.* 115, E8349–E8357. doi: 10.1073/pnas.1802316115

Iriarte, J. L., González, H. E., Liu, K. K., Rivas, C., and Valenzuela, C. (2007). Spatial and temporal variability of chlorophyll and primary productivity in surface waters of southern Chile (41.5–43° S). *Estuar. Coast. Shelf Sci.* 74, 471–480. doi: 10.1016/j.ecss.2007.05.015

Iriarte, J. L., León-Muñoz, J., Marcé, R., Clément, A., and Lara, C. (2017). Influence of seasonal freshwater streamflow regimes on phytoplankton blooms in a Patagonian fjord. *New Zeal. J. Mar. Freshw. Res.* 51, 304–315. doi: 10.1080/00288330.2016.1220955

Iriarte, J. L., Pantoja, S., and Daneri, G. (2014). Oceanographic processes in chilean fjords of patagonia: from small to large-scale studies. *Prog. Oceanogr.* 129, 1–7. doi: 10.1016/j.pocean.2014.10.004

Iroumé, A., and Palacios, H. (2013). Afforestation and changes in forest composition affect runoff in large river basins with pluvial regime and Mediterranean climate. Chile. *J. Hydrol.* 505, 113–125. doi: 10.1016/j.jhydrol.2013.09.031

Jacob, B. G., Tapia, F. J., Daneri, G., Iriarte, J. L., Montero, P., Sobarzo, M., et al. (2014). Springtime size-fractionated primary production across hydrographic and PAR-light gradients in Chilean Patagonia (41-50°S). *Prog. Oceanogr.* 129, 75–84. doi: 10.1016/j.pocean.2014.08.003

Kamjunke, N., Nimptsch, J., Harir, M., Herzsprung, P., Schmitt-Kopplin, P., Neu, T. R., et al. (2017). Land-based salmon aquacultures change the quality and bacterial degradation of riverine dissolved organic matter. *Sci. Rep.* 7:43739. doi: 10.1038/srep43739

Key, C., and Benson, N. (2003). The normalized Burn Ratio (NBR): A Landsat TM Radiometric Measure of Burn Severity. US Geological Survey Northern Rocky Mountain Science Center. U.S. Department of the Interior, U.S. Geological Survey, Northern Rocky Mountain Science Center. Available online at: https://www.frames.gov/catalog/5860 (accessed January 6, 2020).

Khoury, S., and Coomes, D. A. (2020). Resilience of Spanish forests to recent droughts and climate change. *Glob. Chang. Biol.* 26, 7079–7098. doi: 10.1111/gcb.15268

Kitzberger, T., and Veblen, T. T. (1999). Fire-induced changes in northern Patagonian landscapes. *Landsc. Ecol.* 14, 1–15. doi: 10.1023/A:1008069712826

Kling, H., Fuchs, M., and Paulin, M. (2012). Runoff conditions in the upper Danube basin under an ensemble of climate change scenarios. *J. Hydrol.* 42, 264–277. doi: 10.1016/j.jhydrol.2012.01.011

Lara, A., Villalba, R., and Urrutia, R. (2008). A 400-year tree-ring record of the Puelo River summer-fall streamflow in the Valdivian Rainforest eco-region, Chile. *Clim. Change* 86, 331–356. doi: 10.1007/s10584-007-9287-7

León-Muñoz, J., Marcé, R., and Iriarte, J. L. (2013). Influence of hydrological regime of an Andean river on salinity, temperature and oxygen in a Patagonia fjord, Chile. *New Zeal. J. Mar. Freshw. Res.* 47, 515–528. doi: 10.1080/00288330.2013.802700

León-Muñoz, J., Urbina, M. A., Garreaud, R., and Iriarte, J. L. (2018). Hydroclimatic conditions trigger record harmful algal bloom in western Patagonia (summer 2016). *Sci. Rep.* 8:1330. doi: 10.1038/s41598-018-19461-4

L'Heureux, M. L., and Thompson, D. W. J. (2006). Observed Relationships between the El Niño–Southern oscillation and the extratropical zonal-mean circulation. *J. Clim.* 19, 276–287. doi: 10.1175/JCLI3617.1

Little, C., Lara, A., McPhee, J., and Urrutia, R. (2009). Revealing the impact of forest exotic plantations on water yield in large scale watersheds in South-Central Chile. *J. Hydrol.* 374, 162–170. doi: 10.1016/j.jhydrol.2009.06.011

Little, C., Soto, D., Lara, A., and Cuevas, J. G. (2008). Nitrogen exports at multiple-scales in a southern Chilean watershed (Patagonian Lakes district). *Biogeochemistry* 87, 297–309. doi: 10.1007/s10533-008-9185-8

Long, T., Zhang, Z., He, G., Jiao, W., Tang, C., Wu, B., et al. (2019). 30 m Resolution Global Annual Burned Area Mapping Based on Landsat Images and Google Earth Engine. *Remote Sens.* 11, 489. doi: 10.3390/rs11050489

Mages, M., Woelfl, S., Óvári, M., and Tümpling jun, W. v (2003). The use of a portable total reflection X-ray fluorescence spectrometer for field investigation. *Spectrochim. Acta Part B At. Spectrosc* 58, 2129–2138. doi: 10.1016/S0584-8547(03)00197-6

Mann, H. B. (1945). Nonparametric tests against trend. *Econometrica* 13:245. doi: 10.2307/1907187

Marshall, G. J. (2003). Trends in the Southern Annular Mode from Observations and Reanalyses. *J. Clim* 16, 4134–4143.

Martínez-Retureta, R., Aguayo, M., Stehr, A., Sauvage, S., Echeverría, C., and Sánchez-Pérez, J.-M. (2020). Effect of Land Use/Cover Change on the hydrological response of a southern center basin of Chile. *Water* 12:302. doi: 10.3390/w12010302

Milkovic, M., Paruelo, J. M., and Nosetto, M. D. (2019). Hydrological impacts of afforestation in the semiarid Patagonia: a modelling approach. *Ecohydrology* 12:e2113. doi: 10.1002/eco.2113

Milliman, J. D., and Farnsworth, K. L. (2011). *River Discharge to the Coastal Ocean*. Cambridge: Cambridge University Press, doi: 10.1017/CBO9780511781247

Miranda, A., Altamirano, A., Cayuela, L., Lara, A., and González, M. (2017). Native forest loss in the Chilean biodiversity hotspot: revealing the evidence. *Reg. Environ. Chang.* 17, 285–297. doi: 10.1007/s10113-016-1010-7

Miranda, A., Lara, A., Altamirano, A., Zamorano-Elgueta, C., Hernández, H. J., González, M. E., et al. (2018). Monitoreo de la superficie de los bosques nativos de Chile: un desafío pendiente. *Bosque (Valdivia)* 39, 265–275. doi: 10.4067/S0717-92002018000200265

Molinet, C., Astorga, M., Cares, L., Diaz, M., Hueicha, K., Marín, S., et al. (2021). Patrones de distribución vertical del suministro de larvas y spatfall de tres especies de Mytilidae en un fiordo chileno utilizado para el cultivo de mejillones: Insights for mussel spatfall efficiency. *Aquaculture* 535. doi: 10.1016/j.aquaculture.2021.736341

Molinet, C., Díaz, M., Arriagada, C., Cares, L., Marín, S., Astorga, M., et al. (2015). Spatial distribution pattern of Mytilus chilensis beds in the Reloncaví fjord: hypothesis on associated processes. *Rev. Chil. Hist. Nat.* 88:11. doi: 10.1186/s40693-015-0041-7

Montory, J. A., Cumillaf, J. P., Cubillos, V. M., Paschke, K., Urbina, M. A., and Gebauer, P. (2018). Early development of the ectoparasite Caligus rogercresseyi under combined salinity and temperature gradients. *Aquaculture* 486, 68–74. doi: 10.1016/j.aquaculture.2017.12.017

Morales, M. S., Cook, E. R., Barichivich, J., Christie, D. A., Villalba, R., LeQuesne, C., et al. (2020). Six hundred years of South American tree rings reveal an increase in severe hydroclimatic events since mid-20th century. *Proc. Natl. Acad. Sci. U.S.A.* 117, 16816–16823. doi: 10.1073/pnas.2002411117

Mundo, I. A., Wiegand, T., Kanagaraj, R., and Kitzberger, T. (2013). Environmental drivers and spatial dependency in wildfire ignition patterns of northwestern Patagonia. *J. Environ. Manage.* 123, 77–87. doi: 10.1016/j.jenvman.2013.03.011

Murphy, K. R., Butler, K. D., Spencer, R. G. M., Stedmon, C. A., Boehme, J. R., and Aiken, G. R. (2010). Measurement of Dissolved Organic Matter Fluorescence in Aquatic Environments: an interlaboratory comparison. *Environ. Sci. Technol.* 44, 9405–9412. doi: 10.1021/es102362t

Nimptsch, J., Woelfl, S., Kronvang, B., Giesecke, R., González, H. E., Caputo, L., et al. (2014). Does filter type and pore size influence spectroscopic analysis of freshwater chromophoric DOM composition? *Limnologica* 48, 57–64. doi: 10.1016/j.limno.2014.06.003

Nixon, S. W., and Buckley, B. A. (2002). "A strikingly rich zone"—Nutrient enrichment and secondary production in coastal marine ecosystems. *Estuaries* 25, 782–796. doi: 10.1007/BF02804905

Oyarzun, C., Campos, H., and Huber, A. (1997). Exportación de nutrientes en microcuencas con distinto uso del suelo en el sur de Chile (Lago Rupanco, X Región). *Rev. Chil. Hist. Nat.* 70, 507–519.

Oyarzun, C. E., Godoy, R., De Schrijver, A., Staelens, J., and Lust, N. (2004). Water chemistry and nutrient budgets in an undisturbed evergreen rainforest of southern Chile. *Biogeochemistry* 71, 107–123. doi: 10.1007/s10533-004-4107-x

Oyarzún, C. E., and Huber, A. (2003). Nitrogen export from forested and agricultural watersheds of southern Chile. *Gayana. Botánica* 60, 63–68. doi: 10.4067/S0717-66432003000100010

Pabón-Caicedo, J. D., Arias, P. A., Carril, A. F., Espinoza, J. C., Borrel, L. F., Goubanova, K., et al. (2020). Observed and projected hydroclimate changes in the andes. *Front. Earth Sci.* 8:61. doi: 10.3389/feart.2020.00061

Palarea-Albaladejo, J., and Martín-Fernández, J. A. (2015). zCompositions — R package for multivariate imputation of left-censored data under a compositional approach. *Chemom. Intell. Lab. Syst.* 143, 85–96. doi: 10.1016/j.chemolab.2015.02.019

Pantoja, S., Luis Iriarte, J., and Daneri, G. (2011). Oceanography of the Chilean Patagonia. *Cont. Shelf Res.* 31, 149–153. doi: 10.1016/j.csr.2010.10.013

Perakis, S. S., and Hedin, L. O. (2002). Nitrogen loss from unpolluted South American forests mainly via dissolved organic compounds. *Nature* 415, 416–419. doi: 10.1038/415416a

Pessacg, N., Flaherty, S., Solman, S., and Pascual, M. (2020). Climate change in northern Patagonia: critical decrease in water resources. *Theor. Appl. Climatol.* 140, 807–822. doi: 10.1007/s00704-020-03104-8

Pinilla, E., Soto, G., Soto-Riquelme, C., Venegas, O., Salas, P., and Cortes, J. (2020). *Determinación de las Escalas de Intercambio de Agua en Fiordos y Canales de la Región de Los Lagos y Región de Aysén del General Carlos Ibáñez del Campo*. Valparaiso: Instituto de Fomento Pesquero (IFOP), doi: 10.13140/RG.2.2.17813.65762

Poff, N. L. (2018). Beyond the natural flow regime? Broadening the hydro-ecological foundation to meet environmental flows challenges in a non-stationary world. *Freshw. Biol.* 63, 1011–1021. doi: 10.1111/fwb.13038

Poff, N. L., Allan, J. D., Bain, M. B., Karr, J. R., Prestegaard, K. L., Richter, B. D., et al. (1997). The natural flow regime. *Bioscience* 47, 769–784. doi: 10.2307/1313099

Quiñones, R. A., Fuentes, M., Montes, R. M., Soto, D., and León-Muñoz, J. (2019). Environmental issues in Chilean salmon farming: a review. *Rev. Aquac* 11, 375–402. doi: 10.1111/raq.12337

Raymond, P. A., Oh, N.-H., Turner, R. E., and Broussard, W. (2008). *Anthropogenically* enhanced fluxes of water and carbon from the Mississippi River. *Nature* 451, 449–452. doi: 10.1038/nature06505

Raymond, P. A., Saiers, J. E., and Sobczak, W. V. (2016). Hydrological and biogeochemical controls on watershed dissolved organic matter transport: pulse-shunt concept. *Ecology* 97, 5–16. doi: 10.1890/07-1861.1

Raymond, P. A., and Spencer, R. G. M. (2015). "Riverine DOM," in *Biogeochemistry of Marine Dissolved Organic Matter*, eds C. A. Carlson and D. A. Hansell (Amsterdam: Elsevier), 509–533. doi: 10.1016/B978-0-12-405940-5.00011-X

Rebolledo, L., Lange, C. B., Bertrand, S., Muñoz, P., Salamanca, M., Lazo, P., et al. (2015). Late Holocene precipitation variability recorded in the sediments of Reloncaví Fjord (41°S, 72°W), Chile. *Quat. Res.* 84, 21–36. doi: 10.1016/j.yqres.2015.05.006

Richter, B. D., Baumgartner, J. V., Powell, J., and Braun, D. P. (1996). A Method for assessing hydrologic alteration within ecosystems. *Conserv. Biol.* 10, 1163–1174. doi: 10.1046/j.1523-1739.1996.10041163.x

Rulli, M. C., and Rosso, R. (2007). Hydrologic response of upland catchments to wildfires. *Adv. Water Resour.* 30, 2072–2086. doi: 10.1016/j.advwatres.2006.10.012

Saldías, G. S., Sobarzo, M., and Quiñones, R. (2019). Freshwater structure and its seasonal variability off western Patagonia. *Prog. Oceanogr.* 174, 143–153. doi: 10.1016/j.pocean.2018.10.014

Segura, R., and Trincado, G. (2003). Cartografía digital de la Reserva Nacional Valdivia a partir de imágenes satelitales Landsat TM. *Bosque (Valdivia)* 24, 43–52. doi: 10.4067/S0717-92002003000200005

Sen, P. K. (1968). Estimates of the regression coefficient based on Kendall's Tau. *J. Am. Stat. Assoc.* 63:1379. doi: 10.2307/2285891

Sievers, H., and Silva, N. (2008). "Water masses and circulation in austral Chilean channels and fjords," in *Progress in the Oceanographic Knowledge of Chilean Interior Waters, from Puerto Montt to Cape Horn*, eds N. Silva and S. Palma (Valparaíso: Comité Oceanográfico Nacional - Pontificia Universidad Católica de Valparaíso), 53–58.

Silva, N., Vargas, C. A., and Prego, R. (2011). Land–ocean distribution of allochthonous organic matter in surface sediments of the Chiloé and Aysén interior seas (Chilean Northern Patagonia). *Cont. Shelf Res.* 31, 330–339. doi: 10.1016/j.csr.2010.09.009

Soto, D., León-Muñoz, J., Dresdner, J., Luengo, C., Tapia, F. J., and Garreaud, R. (2019). Salmon farming vulnerability to climate change in southern Chile: understanding the biophysical, socioeconomic and governance links. *Rev. Aquac.* 11, 354–374. doi: 10.1111/raq.12336

Soto, D., León-Muñoz, J., Molinet, C., Soria-Galvarro, Y., Videla, J., Opazo, D., et al. (2020). *Informe Mapas de riesgo ante el cambio climático Acuicultura, Proyecto ARClim. Centro de Ciencia del Clima y la Resiliencia y Centro de Cambio Global UC para el Ministerio del Medio Ambiente a traveìs de La Deutsche Gesellschaft für Internationale Zusammenarbeit (GIZ)*. (Chile, Ministerio del Medio Ambiente).

Stedmon, C. A., and Bro, R. (2008). Characterizing dissolved organic matter fluorescence with parallel factor analysis: a tutorial. *Limnol. Oceanogr. Methods* 6, 572–579. doi: 10.4319/lom.2008.6.572

Stehr, A., Aguayo, M., Link, O., Parra, O., Romero, F., and Alcayaga, H. (2010). Modelling the hydrologic response of a mesoscale Andean watershed to changes in land use patterns for environmental planning. *Hydrol. Earth Syst. Sci.* 14, 1963–1977. doi: 10.5194/hess-14-1963-2010

Torres, R., Reid, B., Frangópulos, M., Alarcón, E., Márquez, M., Häusermann, V., et al. (2020). Freshwater runoff effects on the production of biogenic silicate and chlorophyll-a in western Patagonia archipelago (50–51°S). *Estuar. Coast. Shelf Sci.* 241:106597. doi: 10.1016/j.ecss.2020.106597

Torres, R., Silva, N., Reid, B., and Frangopulos, M. (2014). Silicic acid enrichment of subantarctic surface water from continental inputs along the Patagonian archipelago interior sea (41-56°S). *Prog. Oceanogr.* 129, 50–61. doi: 10.1016/j.pocean.2014.09.008

Trouet, V., Taylor, A. H., Carleton, A. M., and Skinner, C. N. (2006). Fire-climate interactions in forests of the American Pacific coast. *Geophys. Res. Lett.* 33:L18704. doi: 10.1029/2006GL027502

Uribe, S. V., Estades, C. F., and Radeloff, V. C. (2020). Pine plantations and five decades of land use change in central Chile. *PLoS One* 15:e0230193. doi: 10.1371/journal.pone.0230193

Urrutia-Jalabert, R., González, M. E., González-Reyes, Á, Lara, A., and Garreaud, R. (2018). Climate variability and forest fires in central and south-central Chile. *Ecosphere* 9:e02171. doi: 10.1002/ecs2.2171

Valle-Levinson, A., Castro, L., Cáceres, M., and Pizarro, O. (2014). Twilight vertical migrations of zooplankton in a Chilean fjord. *Prog. Oceanogr.* 129, 114–124. doi: 10.1016/j.pocean.2014.03.008

Valle-Levinson, A., Sarkar, N., Sanay, R., Soto, D., and León, J. (2007). Spatial structure of hydrography and flow in a Chilean fjord, Estuario Reloncaví. *Estuaries Coasts* 30, 113–126. doi: 10.1007/BF02782972

Vargas, C. A., Martinez, R. A., San Martin, V., Aguayo, M., Silva, N., and Torres, R. (2011). Allochthonous subsidies of organic matter across a lake-river-fjord landscape in the Chilean Patagonia: implications for marine zooplankton in inner fjord areas. *Cont. Shelf Res.* 31, 187–201. doi: 10.1016/j.csr.2010.06.016

Veblen, T. T., Kitzberger, T., Raffaele, E., and Lorenz, D. C. (1999). "Fire History and Vegetation Changes in Northern Patagonia, Argentina," in *Fire and Climatic Change in Temperate Ecosystems of the Western Americas*, eds G. Montenegro, T. T. Veblen, T. W. Swetnam, and W. L. Baker (New York, NY: Springer-Verlag), 265–295. doi: 10.1007/0-387-21710-X_9

Vergara-Jara, M. J., DeGrandpre, M. D., Torres, R., Beatty, C. M., Cuevas, L. A., Alarcón, E., et al. (2019). Seasonal changes in carbonate saturation state and Air-Sea CO 2 fluxes during an annual cycle in a stratified-temperate Fjord (Reloncaví Fjord, Chilean Patagonia). *J. Geophys. Res. Biogeosci.* 124, 2851–2865. doi: 10.1029/2019JG005028

Vicuña, S., McPhee, J., and Garreaud, R. D. (2012). Agriculture vulnerability to climate change in a snowmelt-driven basin in semiarid Chile. *J. Water Resour. Plan. Manag.* 138, 431–441. doi: 10.1061/(ASCE)WR.1943-5452.0000202

Villalba, R., Lara, A., Masiokas, M. H., Urrutia, R., Luckman, B. H., Marshall, G. J., et al. (2012). Unusual Southern Hemisphere tree growth patterns induced by changes in the Southern Annular Mode. *Nat. Geosci.* 5, 793–798. doi: 10.1038/ngeo1613

Wan, Z., Hook, S., and Hulley, G. (2015). *MOD11C3 MODIS/Terra Land Surface Temperature/Emissivity Monthly L3 Global 0.05Deg CMG V006 [Data set]. NASA EOSDIS L. Process*. Oak Ridge, TEN: DAAC, doi: 10.5067/MODIS/MOD11C3.006

Ward, N. D., Bianchi, T. S., Medeiros, P. M., Seidel, M., Richey, J. E., Keil, R. G., et al. (2017). Where carbon goes when water flows: carbon cycling across the aquatic continuum. *Front. Mar. Sci.* 4:7. doi: 10.3389/fmars.2017.00007

Winterdahl, M., Laudon, H., Lyon, S. W., Pers, C., and Bishop, K. (2016). Sensitivity of stream dissolved organic carbon to temperature and discharge: Implications of future climates. *J. Geophys. Res. Biogeosci.* 121, 126–144. doi: 10.1002/2015JG002922

Wu, J., Wang, D., and Bauer, M. E. (2007). Assessing broadband vegetation indices and QuickBird data in estimating leaf area index of corn and potato canopies. *F. Crop. Res.* 102, 33–42. doi: 10.1016/j.fcr.2007.01.003

Yang, L., Feng, Q., Yin, Z., Wen, X., Si, J., Li, C., et al. (2017). Identifying separate impacts of climate and land use/cover change on hydrological processes in upper stream of Heihe River, Northwest China. *Hydrol. Process.* 31, 1100–1112. doi: 10.1002/hyp.11098

Yang, X., Zheng, X.-Q., and Lv, L.-N. (2012). A spatiotemporal model of land use change based on ant colony optimization, Markov chain and cellular automata. *Ecol. Modell.* 233, 11–19. doi: 10.1016/j.ecolmodel.2012.03.011

Yates, D., Sieber, J., Purkey, D., and Huber-Lee, A. (2005). WEAP21—A Demand-, Priority-, and preference-driven water planning model. *Water Int.* 30, 487–500. doi: 10.1080/02508060508691893

Yevenes, M. A., Lagos, N. A., Farías, L., and Vargas, C. A. (2019). Greenhouse gases, nutrients and the carbonate system in the Reloncaví Fjord (Northern Chilean Patagonia): Implications on aquaculture of the mussel, Mytilus chilensis, during an episodic volcanic eruption. *Sci. Total Environ.* 669, 49–61. doi: 10.1016/j.scitotenv.2019.03.037

Zhang, L., and Dai, S. (2007). Application of Markov model to environmental fate of phenanthrene in Lanzhou Reach of Yellow River. *Chemosphere* 67, 1296–1299. doi: 10.1016/j.chemosphere.2006.11.026

Zhang, R., Tang, C., Ma, S., Yuan, H., Gao, L., and Fan, W. (2011). Using Markov chains to analyze changes in wetland trends in arid Yinchuan Plain, China. *Math. Comput. Model.* 54, 924–930. doi: 10.1016/j.mcm.2010.11.017

Conflict of Interest: The authors declare that the research was conducted in the absence of any commercial or financial relationships that could be construed as a potential conflict of interest.

frontiers in Marine Science

ORIGINAL RESEARCH
published: 23 July 2021
doi: 10.3389/fmars.2021.611981

Influence of Estuarine Water on the Microbial Community Structure of Patagonian Fjords

*Javier Tamayo-Leiva[1,2], Jerónimo Cifuentes-Anticevic[1], Pilar Aparicio-Rizzo[2,3], José Ignacio Arroyo[1,4,5,6], Italo Masotti[2,3,7] and Beatriz Díez[1,2,8]**

[1] Department of Molecular Genetics and Microbiology, Faculty of Biological Sciences, Pontifical Catholic University of Chile, Santiago, Chile, [2] Center for Climate and Resilience Research (CR2), University of Chile, Santiago, Chile, [3] Facultad de Ciencias del Mar y de Recursos Naturales, Universidad de Valparaíso, Viña del Mar, Chile, [4] The Santa Fe Institute, Santa Fe, NM, United States, [5] Department of Ecology, Faculty of Biological Sciences, Pontificia Universidad Católica de Chile, Santiago, Chile, [6] Center for Mathematical Modeling, University of Chile, Santiago, Chile, [7] Centro de Observación Marino para Estudios de Riesgos del Ambiente Costero (COSTAR-UV), Universidad de Valparaíso, Viña del Mar, Chile, [8] Center for Genome Regulation (CRG), Santiago, Chile

OPEN ACCESS

Edited by:
Giorgio Bavestrello,
University of Genoa, Italy

Reviewed by:
Sokratis Papaspyrou,
University of Cádiz, Spain
Giovanni Daneri,
Patagonian Ecosystems Investigation Research Center (CIEP), Chile

***Correspondence:**
Beatriz Díez
bdiez@bio.puc.cl

Specialty section:
This article was submitted to Marine Ecosystem Ecology, a section of the journal Frontiers in Marine Science

Received: 29 September 2020
Accepted: 25 June 2021
Published: 23 July 2021

Citation:
Tamayo-Leiva J, Cifuentes-Anticevic J, Aparicio-Rizzo P, Arroyo JI, Masotti I and Díez B (2021) Influence of Estuarine Water on the Microbial Community Structure of Patagonian Fjords. Front. Mar. Sci. 8:611981. doi: 10.3389/fmars.2021.611981

Fjords are sensitive areas affected by climate change and can act as a natural laboratory to study microbial ecological processes. The Chilean Patagonian fjords (41–56°S), belonging to the Subantarctic ecosystem (46–60°S), make up one of the world's largest fjord systems. In this region, Estuarine Water (EW) strongly influences oceanographic conditions, generating sharp gradients of oxygen, salinity and nutrients, the effects of which on the microbial community structure are poorly understood. During the spring of 2017 we studied the ecological patterns (dispersal and oceanographic factors) underlying the microbial community distribution in a linear span of 450 km along the estuarine-influenced Chilean Patagonian fjords. Our results show that widespread microbial dispersion existed along the fjords where bacterioplankton exhibited dependence on the eukaryotic phytoplankton community composition. This dependence was particularly observed under the low chlorophyll-*a* conditions of the Baker Channel area, in which a significant relationship was revealed between SAR11 Clade III and the eukaryotic families Pyrenomonadaceae (Cryptophyte) and Coccomyxaceae (Chlorophyta). Furthermore, dissolved oxygen and salinity were revealed as the main drivers influencing the surface marine microbial communities in these fjords. A strong salinity gradient resulted in the segregation of the Baker Channel prokaryotic communities from the rest of the Patagonian fjords. Likewise, Microbacteriaceae, Burkholderiaceae and SAR11 Clade III, commonly found in freshwater, were strongly associated with EW conditions in these fjords. The direct effect of EW on the microbial community structure and diversity of the fjords exemplifies the significance that climate change and, in particular, deglaciation have on this marine region and its productivity.

Keywords: Patagonian fjords, Subantarctic, Estuarine Water, bacterioplankton, eukaryotic phytoplankton, microbial indicator

INTRODUCTION

One of the world's largest fjord systems is located in the Patagonian region of southern Chile (41–56°S) (Iriarte et al., 2010). This fragmented coastal region, which possesses several islands, rivers and channels (Iriarte et al., 2014; Cuevas et al., 2019), is characterized by high primary production due to the occurrence of phytoplankton blooms throughout the year (Iriarte et al., 2016; Montero et al., 2017). During the austral summer in the Patagonian fjords, high primary production results in carbon sequestration (∼5 mol C m^{-2} $year^{-1}$) that is considered high relative to Patagonia's Atlantic coast (∼1.6 mol C m^{-2} $year^{-1}$) (Torres et al., 2011). Rivers and rainfall runoff, together with glacier melting and vertical mixing, explain this high primary production due to nutrient input (Iriarte et al., 2010; Montero et al., 2017; Cuevas et al., 2019). The Patagonian fjord system is also characterized by sharp vertical and horizontal oxygen and salinity gradients (Iriarte et al., 2014; Cuevas et al., 2019), which are produced by advective transport and mixing of Estuarine Water (EW) with Sub-Antarctic Water (SAAW) (Silva and Vargas, 2014; Vargas et al., 2018). This mixing of EW and SAAW will also likely result in the mixing of entire microbial communities and nutrients in a process termed "community coalescence" (Rillig et al., 2015).

The Patagonian fjord region is considered a vulnerable ecosystem that is highly sensitive to climatic change and anthropogenic activity (Iriarte et al., 2010; Iriarte, 2018; González et al., 2019). Climate forcing by the El Niño-Southern Oscillation and the Southern Annular Mode has been linked to inter-annual variations in environmental conditions, such as higher sea surface temperature, changes in wind direction and intensity, and decreased freshwater discharge to the marine system due to drought (Garreaud, 2018; León-Muñoz et al., 2018). These regional variations can affect the marine microbial community, modifying primary production, and they have even been proposed as possible triggers of harmful algal blooms in the area (Iriarte, 2018; Moreno-Pino et al., 2018). For example, a harmful algal bloom of *Pseudochattonella* cf. *verruculosa* observed in the summer of 2016 was the largest reported to date in this area (León-Muñoz et al., 2018). Additionally, activities and processes, such as aquaculture, freshwater runoff and increased glacier melt (Iriarte, 2018; González et al., 2019), have had an impact on the carbon and nitrogen nutrient input to these coastal areas (Silva and Vargas, 2014; Vargas et al., 2018), subsequently affecting microbial activity (Olsen et al., 2017; González et al., 2019). However, the overall effect of these processes on the local microbial ecology is still unknown.

Most efforts to study microbial communities in the Patagonian fjords have focused on the northern region (41–45°S) (Gutiérrez et al., 2015, 2018; Iriarte et al., 2016; Montero et al., 2017), Baker Channel (48°S) (Gutiérrez et al., 2015) and Cape Horn area (52–56°S) (Moreno-Pino et al., 2018), while microbial communities in the central area (47–52°S) remain underexplored. Analyses of the microbial ecology in this area have shown high heterogeneity of the phytoplankton community, dominated during spring blooms by the diatom genera *Skeletonema*, *Chaetoceros*, *Rhizosolenia,* and *Thalassiosira* (Iriarte et al., 2016; Montero et al., 2017). Additionally, oxygen and salinity were recently suggested as drivers of vertical water stratification that affects the bacterial community distribution of the Puyuhuapi fjord in northern Patagonia (44°S) (Gutiérrez et al., 2018). To date, no broader study has focused on the structure and diversity patterns of bacterioplankton across the Patagonian fjord region.

Here we investigate the influence of EW on the microbial community structure and diversity in the central Patagonian fjord system (47–52°S) over a linear span of 450 km. This survey is necessary to identify the general patterns of microbial communities and specific microorganisms that can be used as possible biological indicators of change in the water conditions of this southern ecosystem, which is susceptible to climatic change and anthropogenic activity. The primary objectives of our analyses were to (i) characterize the environmental conditions, such as temperature, salinity, oxygen and chlorophyll-*a*, in the Estuarine Waters of the central Patagonian fjords; (ii) assess the effect of the environmental conditions and geographic distance on the community structures of both bacterioplankton (bacteria and archaea) and eukaryotic phytoplankton; and finally, (iii) determine the influence of environmental drivers on relevant taxa in the region.

MATERIALS AND METHODS

Study Area and Sampling

The central Patagonian fjord region sampled in this study stretched 450 km, from the Penas Gulf (47°S) to Nelson Strait (52°S), as shown in **Figure 1**. The extent to which areas in this region are influenced by Estuarine and Sub-Antarctic Waters (or modified SAAW) differs. The study transect comprised 23 stations from the Penas Gulf (47.7°S, station 2) to Nelson Strait (51.4°S, station 48) and was divided into ten geographic areas according to the information provided by the Chilean Hydrographic and Oceanographic Service of the Navy. From north to south, the sampling stations were as follows: Penas Gulf (station 2); Baker Channel (stations 10, 8, 7, and 5, oriented in an E–W direction); Bernardo (stations 18C and 18A), Iceberg (station 21B), Falcon (stations 30 and 25) and Penguin (station 33) fjords; Messier Channel (stations 19, 24, 35, 43, and 44); Europa (stations 39 and 36) and Peel (stations 72, 75, and 70) fjords; and Nelson Strait (stations 68 and 48) (**Figure 1**). Sampling was performed onboard the scientific research vessel "*Cabo de Hornos*" (AGS61), operated by the Chilean navy's Hydrographic and Oceanographic Service as part of the program "*Cruceros de Investigación Marina en Areas Remotas*" (CIMAR). Specifically, this CIMAR23f campaign was conducted from October 17 to November 20, 2017.

Surface water at the 23 stations was sampled at two depths (5 and 10 m) using a Niskin bottle-rosette system (46 samples in total). Water samples were analyzed for dissolved oxygen (DO), chlorophyll-*a* (Chl-*a*) and used for microbial biomass concentration. Concurrent with water sample collection, temperature and conductivity profiles for the whole column water were obtained using a Seabird 19 CTD. For Chl-*a*, 1 L water samples were pre-filtered through 200-μm nylon mesh, filtered

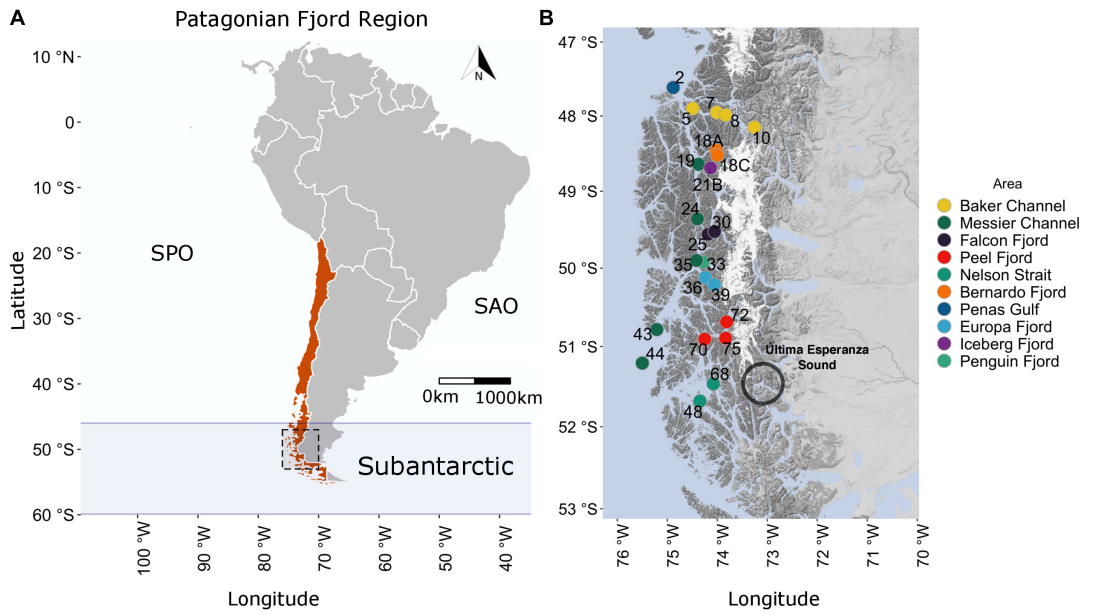

FIGURE 1 | Geographic location and study area of the CIMAR23f campaign. **(A)** Chilean Patagonian fjords as part of the Subantarctic region (46–60°S). Red denotes the Chilean political division within South America. The black dashed square delimits the Patagonian fjord study area. **(B)** Study area (47.5–52°S) and sampling station locations. Colored circles and numbers represent the location and identification number, respectively, of each station. South Pacific Ocean (SPO), South Atlantic Ocean (SAO).

through 0.22-μm cellulose membrane filters and then stored at −20°C until analysis. The Chl-*a* concentration (mg m^{-3}) was subsequently determined fluorometrically using the method described by Parsons et al. (1984). DO (O_2) concentrations (μM) were determined by the modified Winkler method proposed by Strickland and Parsons (1972). For microbial community analysis, seawater (10–15 L) was subjected to serial prefiltration through 200-μm nylon mesh followed by 20-μm polycarbonate filters using a Cole Parmer peristaltic pump system (Model 7553–70, 6 – 600 rpm) at 50 – 100 mL min^{-1} for an average of 1 h. Microbial biomass in the filtrate was then concentrated onto 0.22-μm pore size Sterivex units (Durapore; Millipore) and stored at −20°C until analysis.

DNA Extraction

DNA was extracted according to a modified protocol described in Tillett and Neilan (2000). Briefly, the Sterivex membrane filters were manually removed from the housing before DNA extraction. Next, the biomass on the Sterivex filters was resuspended in xanthogenate buffer [1% potassium ethyl xanthogenate (Sigma-Aldrich, United States), 100 mM Tris-HCl (pH 7.4), 20 mM EDTA (pH 8), 800 mM ammonium acetate] with 1% SDS. The mixture was incubated at 65°C for 2 h (hand-shaken every 30 min). After incubation, the tubes were placed on ice for 30 min. The DNA was then extracted with phenol-chloroform-isoamyl alcohol (25:24:1), and the residual phenol was eliminated with chloroform-isoamyl alcohol (24:1). The extract was cleaned by overnight precipitation with cold isopropanol (−20°C) and subsequently washed with 70% ethanol. DNA was quantified using a Qubit 2.0 Fluorometer (Thermo Fisher Scientific, United States). The quality was assessed by spectrophotometry (A_{260}/A_{280} ratio) and the integrity was verified by standard 1% agarose gel electrophoresis.

Amplicon Sequencing and Processing

The V4–V5 hypervariable region of the 16S rRNA gene was amplified using the primers 515F (5′-GTGYCAGCMG CCGCGGTAA-3′) and 926R (5′-CCGYCAATTYMTTTRAGT TT-3′), according to Parada et al. (2016). Sequencing was conducted on the Illumina MiSeq platform at the Argonne National Laboratory (Lemont, IL, United States). Raw sequences of the 16S rRNA gene were demultiplexed using the q2-demux plugin implemented in the QIIME2 pipeline (Bokulich et al., 2018; Bolyen et al., 2019). The paired-end sequences were trimmed and merged using DADA2 (Callahan et al., 2016) to obtain amplicon sequencing variants (ASVs). The taxonomy of the 16S rRNA ASVs was assigned using the q2-feature-classifier against the SILVA132 database (Quast et al., 2013) via the "classify consensus vsearch" method (Rognes et al., 2016). ASVs that were taxonomically annotated as "Mitochondria" and "Chloroplast" were excluded from the subsequent bacterial and archaeal community analysis. To obtain the taxonomic identity of eukaryotic phytoplankton (phytoplankton community), ASVs that were annotated as "Chloroplast" were separated and re-annotated using the same methodology applied to the aforementioned ASVs but against the PhytoRef database (Decelle et al., 2015), as described in Fuentes et al. (2019). Finally, to remove singletons and rare taxa, ASVs were filtered by total count sum (>4) and prevalence in at least 10% of the samples

(**Supplementary Table 1**). All 16S rRNA sequences used in this study have been deposited in the NCBI Sequence Read Archive (SRA) under BioProject ID PRJNA670217.

Exploratory Data Analysis

Amplicon sequencing variants analyses were conducted using R packages (R Core Team, 2020), including phyloseq (McMurdie and Holmes, 2013) and ampvis2 (Andersen et al., 2018). Graphical support for the microbial community was conducted with ggplot2 (Wickham, 2016), dendextend (Galili, 2015) and ggmap (Kahle and Wickham, 2013). The Ocean Data View (ODV) software was used for oceanographic variables (Schlitzer, 2020). Maps of the oceanographic conditions by depth were made with a spatial resolution of 1 km (GEBCO 2015 grid) and implemented with coastlines and fill coastlines layers. Diversity analyses were performed with the stats (R Core Team, 2020) and vegan (Oksanen et al., 2019) packages in R. Alpha diversity was measured as the number of distinct ASVs or taxonomic ranks in each sample (observed richness). The Shannon and Pielou indexes were applied exclusively to clean ASVs. For clustering and ordinate analysis, the double-zero effect and rare taxa weight were standardized by Hellinger transformation in ASV filter count data. Hellinger-transformed counts were then used to calculate Euclidean distances among samples (Hellinger distance matrix) (Legendre and Gallagher, 2001). Oceanographic variables were standardized using the *z*-score method (mean 0, variance 1). Standardized variables were then used to calculate Euclidean distances among the samples. The Ward2 algorithm (Murtagh and Legendre, 2014), implemented in the vegan package, was used to construct the final dendrogram. Silhouette validation criteria, combined with calculated *p*-values for hierarchical clustering (multiscale bootstrap) implemented in the pvclust package (Suzuki et al., 2019), were used to select the number of clusters (k) in each dataset (Rousseeuw, 1987). Exploratory analysis of the main factors affecting the microbial community structure (i.e., prokaryotic plankton and eukaryotic phytoplankton) was conducted via principal component analysis (PCA) using the 'envfit' test function in the vegan package.

Network Reconstruction

Briefly, microbial network analyses were conducted in R using spieceasi (Kurtz et al., 2015) and plotted with ggnet (Briatte, 2020). The best taxonomic hit grouped the clean prokaryotic and eukaryotic ASVs. For network reconstruction and interaction estimation, the neighborhood selection method (Meinshausen and Bühlmann method) (Meinshausen and Bühlmann, 2006) was applied with an nlambda of 20. The network was processed in igraph (Csardi and Nepusz, 2006) for further attribute analyses (i.e., degree and betweenness). Regression coefficient values calculated by the SPIEC-EASI method were used to estimate the positive or negative correlation of edges.

Statistical Analysis

The relation between environmental variables (i.e., temperature, DO, salinity, and Chl-*a*) and ecological indexes (i.e., Shannon and Pielou) were studied via permutational analysis of variance (PERMANOVA) (Anderson, 2001) using the adonis2 function in the R vegan package (9,999 permutations). Classification of fjord areas was included as the explanatory factor for environmental (df = 9, n = 46) and ecological (df = 9, n = 45) indexes. Additionally, Spearman's rank correlation (*rho*) was performed among environmental variables ($p < 0.01$) (Kendall, 1948). To study the relationship among the environmental and ecological dissimilarity matrices, a Mantel test with a Spearman's rank correlation (*rho*) was performed in R. Mantel tests (9,999 permutations), facilitated by the mantel function in the vegan package, were performed between the Hellinger distance matrix (i.e., prokaryotic plankton and eukaryotic phytoplankton), Euclidean distance matrix (independent and joined variables) or the matrix of the Haversine distance between geographical coordinates (i.e., latitude and longitude) among samples (Mantel, 1967; Legendre and Fortin, 2010). Adjusted *p*-values were obtained using the stats package and Benjamini–Hochberg (BH) *post hoc* tests (Benjamini and Hochberg, 1995). Distance decay analysis was performed as a simple linear regression analysis of the Jaccard similarity index log between samples versus Haversine distance between sites. Statistical analyses were performed using R software with the stats, vegan, hmisc (Harrell, 2020) and corrplot (Wei and Simko, 2017) packages.

To explore spatial autocorrelation in the collected data, a Mantel correlogram analysis was performed with the vegan package function "mantel.correlog," using the stations' latitude and longitude values (XY option), and 9,999 permutations (**Supplementary Figure 1**). The spatial autocorrelation observed for the oceanographic conditions between neighboring samples was then considered using two approaches, as suggested by Dale and Fortin (2002), and applied to all statistical analyses in this study. First, the *p*-values were adjusted to a more restrictive type I error (i.e., $p < 0.01$) for non-permutational analyses [i.e., Spearman's rank correlation (rho), linear regression and PCA envfit]. Second, when possible, analyses that allow randomization or permutation methods were applied (i.e., PERMANOVA, Mantel test and bootstrap).

RESULTS

Oceanographic Conditions of the Subantarctic Patagonian Fjords

Oceanographic conditions in the Patagonian fjord region showed spatial autocorrelation (**Supplementary Figure 1**) and an evident freshwater influence along the study area, as illustrated by salinity, temperature and DO profiles (**Supplementary Figure 2**). The vertical distribution of salinity evidenced a two-layer structure with a remarkable halocline within the first meters (∼0–30 m), especially at sites directly influenced by freshwater (i.e., stations 10, 18A, 21B, 30, 39, and 72). A similar pattern was observed for the DO and temperature profiles (**Supplementary Figure 2**), with a clear oxycline and thermocline in the first meters (∼0–30 m) of the water column. In addition, temperature profiles displayed thermal inversions at some stations (**Supplementary Figure 2**).

At 5 and 10 m depth, where microbial communities were studied, temperature showed an overall similar pattern, with

more considerable differences between depths at the Falcon, Iceberg and Penguin fjords (**Figure 2A**). Along the study area, mean temperature values ranged between 7.05°C (Falcon Fjord) and 10.86°C (Iceberg Fjord) (**Table 1**), with significant differences among defined areas (PERMANOVA R^2 = 0.97; p = 0.0398). Salinity values at 5 and 10 m were similar (**Figure 2B**), except for the Baker Channel area (**Figure 2B**). The study sites did not show significant differences in salinity (PERMANOVA R^2 = −10.24; p = 0.9751), with mean values normally below 28 (**Table 1**). Only stations influenced by oceanic water, specifically those located in the Messier Channel and Penas Gulf areas (**Figure 1**), showed salinity values above 28 (**Figure 2B** and **Table 1**).

The mean DO concentrations in this study ranged between 281.74 and 402.67 μM (**Table 1**), with non-significant differences between areas (PERMANOVA R^2 = 0.80; p = 0.3567). DO concentrations and saturation percentages demonstrated a well-oxygenated surface layer, with higher DO values at 5 m, especially in the Falcon and Penguin fjords (**Figure 2C** and **Table 1**), rather than at 10 m depth where several areas (Baker Channel, Bernardo, Iceberg and Falcon fjords) showed undersaturated mean values (oxygen saturation <100%, **Supplementary Table 2**). Chl-*a* values over 3 mg m^{-3} were detected at both 5 and 10 m in the Messier Channel (stations 35, 43, and 44) and Peel Fjord (stations 70 and 72) areas (**Figure 2D**). Meanwhile, the lowest Chl-*a* concentrations (<1 mg m^{-3}) were observed in the Penas Gulf, Baker Channel and Nelson Strait areas (**Figure 2D**). Although mean values ranged from 0.12 to 9.60 mg m^{-3}, non-significant differences between areas were detected for Chl-*a* (PERMANOVA R^2 = −1.27; p = 0.8678) (**Table 1**).

Among the environmental variables (temperature, salinity and DO), non-significant ($p > 0.01$) correlations were detected. However, Spearman's correlation analysis showed significant associations between depth and these variables (i.e., temperature, salinity and DO). For instance, depth was negatively correlated with DO (R = −0.463; $p < 0.01$) and temperature (R = −0.364; $p < 0.05$), but positively correlated with salinity (R = 0.477; $p < 0.001$) (**Supplementary Figure 3**). Temperature, salinity and DO conditions in the region were used to identify the presence of estuarine freshwater (EFW; $S < 11$), estuarine brackish water (EBW; S = 11–21) and estuarine saltwater (ESW; S = 21–31) in the first ∼24 m, followed by modified Subantarctic water (MSAAW; S = 31–33) between ∼25–69 m and Subantarctic water (SAAW; $S > 33$) below 70 m (**Supplementary Figure 2**).

Effect of Oceanographic and Geographic Factors on the Microbial Community Structure

Alpha diversity analyses were performed to determine the microbial community diversity of species within each fjord. The

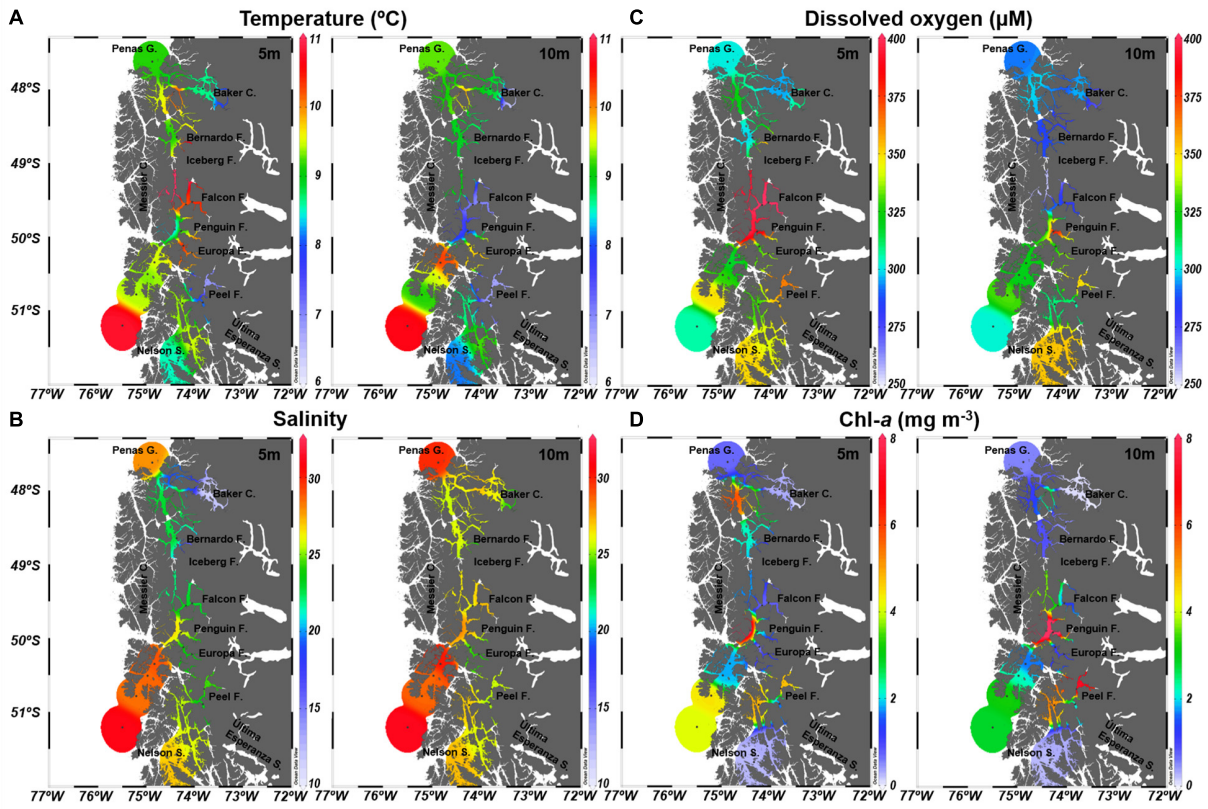

FIGURE 2 | Oceanographic conditions of the Chilean Subantarctic Patagonian fjord region. Study area and station locations during the CIMAR23f campaign from October 17 to November 20, 2017 (austral spring). **(A)** Temperature, **(B)** Salinity, **(C)** Dissolved oxygen, and **(D)** Chlorophyll-*a*.

TABLE 1 | Variability of oceanographic conditions in the Patagonian fjords at 5 and 10 m depth.

Area	Stations	Samples		Temperature (°C)								Salinity							
				5 m				10 m				5 m				10 m			
		5 m	10 m	Mean	Sd	Min	Max	Mean	Sd	Min	Max	Mean	Sd	Min	Max	Mean	Sd	Min	Max
Baker C.	05/07/08/10	4	4	8.5	0.39	7.92	8.74	8.32	1.25	6.44	9.03	15.23	4.42	10.94	19.72	26.07	1.29	24.23	27.23
Messier C.	19/24/35/43/44	5	5	9.75	1.32	8.1	11.37	9.05	1.15	7.43	10.67	26.37	3.71	22.14	31.02	28.16	2.1	25.95	31.24
Falcon f.	25/30	2	2	10.3	0.18	10.17	10.42	7.05	0.08	6.99	7.11	23.14	0.37	22.87	23.4	26.64	1.09	25.87	27.41
Peel f.	70/72/75	3	3	8.12	1.29	6.83	9.4	7.45	1.08	6.81	8.69	24.44	1.12	23.3	25.54	25.93	0.85	25.29	26.9
Nelson S.	48/68	2	2	9	0.68	8.52	9.49	8.69	0.76	8.16	9.23	26.41	0.82	25.83	26.99	26.54	0.97	25.85	27.22
Bernardo f.	18A/C	2	2	9.52	0.14	9.42	9.62	8.75	0.02	8.73	8.76	22.17	2.21	20.61	23.74	25.86	0.52	25.49	26.23
Penas G.	2	1	1	9.16	NA	9.16	9.16	9.28	NA	9.28	9.28	27.98	NA	27.98	27.98	29.76	NA	29.76	29.76
Europa f.	36/39	2	2	10.22	0.33	9.99	10.45	9.76	0.07	9.71	9.81	23.66	0.14	23.56	23.76	24.3	0.09	24.24	24.36
Iceberg f.	21B	1	1	10.86	NA	10.86	10.86	8.79	NA	8.79	8.79	15.4	NA	15.4	15.4	24.07	NA	24.07	24.07
Penguin f.	33	1	1	9.34	NA	9.34	9.34	8.05	NA	8.05	8.05	25.69	NA	25.69	25.69	27.15	NA	27.15	27.15

Area	Stations	Samples		Dissolved oxygen (μM)								Chlorophyll-*a* (mg m^{-3})							
				5 m				10 m				5 m				10 m			
		5 m	10 m	Mean	Sd	Min	Max	Mean	Sd	Min	Max	Mean	Sd	Min	Max	Mean	Sd	Min	Max
Baker C.	05/07/08/10	4	4	302.43	7.10	296.12	309.40	289.85	12.19	273.16	300.24	0.26	0.12	0.09	0.33	0.12	0.12	0.02	0.29
Messier C.	19/24/35/43/44	5	5	349.65	48.28	296.87	400.54	296.30	28.14	255.18	331.42	4.56	3.36	1.78	10.2	3.8	2.74	0.92	8.33
Falcon f.	25/30	2	2	402.67	3.08	400.49	404.85	286.17	9.10	279.73	292.60	0.75	0.02	0.74	0.76	2.25	1.91	0.9	3.6
Peel f.	70/72/75	3	3	349.79	17.53	330.53	364.81	322.56	25.51	305.23	351.85	3.77	1.92	1.55	4.9	4.87	2.81	1.9	7.48
Nelson S.	48/68	2	2	347.28	5.60	343.32	351.24	353.15	0.56	352.76	353.55	0.3	0.06	0.25	0.34	0.3	0.04	0.28	0.33
Bernardo f.	18A/C	2	2	321.53	30.14	300.22	342.85	281.74	1.88	280.41	283.07	2.26	1.63	1.1	3.41	0.46	0.07	0.41	0.51
Penas G.	2	1	1	NA	NA	NA	NA	292.85	NA	292.85	292.85	0.69	NA	0.69	0.69	0.54	NA	0.54	0.54
Europa f.	36/39	2	2	331.43	6.79	326.63	336.23	329.44	10.11	322.29	336.59	0.85	0.57	0.45	1.26	0.95	0.25	0.77	1.12
Iceberg f.	21B	1	1	357.62	NA	357.62	357.62	290.42	NA	290.42	290.42	1.05	NA	1.05	1.05	0.38	NA	0.38	0.38
Penguin f.	33	1	1	390.20	NA	390.20	390.20	395.20	NA	395.20	395.20	0.83	NA	0.83	0.83	9.6	NA	9.6	9.6

bacterioplankton communities and eukaryotic phytoplanktonic (hereafter referred to as phytoplankton) communities showed similar alpha diversity patterns among the study areas, with the highest observed richness values observed in the Messier Channel, Peel Fjord and Baker Channel, and the lowest observed richness values in the Penas Gulf (**Supplementary Table 3**). PERMANOVA, which was applied to investigate the difference between fjord areas, showed a significant difference in the diversity (Shannon index) and evenness (Pielou index) of ASVs from the bacterioplankton communities (PERMANOVA: Shannon index $R^2 = 0.56$, $p = 0.0003$; Pielou index $R^2 = 0.40$, $p = 0.0252$). Conversely, a non-significant difference was found for phytoplankton using the same indexes (PERMANOVA: Shannon index $R^2 = 0.36$, $p = 0.0617$; Pielou index $R^2 = 0.29$, $p = 0.1756$).

To determine the variation in species composition (i.e., beta diversity) among samples in the Patagonian fjords and the effect of oceanographic variables, a PCA plus envfit analysis was performed. The PCA results show that the first three axes (i.e., PC1, PC2, and PC3) explained 73.8 and 46.6% of the variance for bacterioplankton and phytoplankton, respectively (**Figure 3**). DO was identified as the main factor inducing variation in the diversity of both communities in the Patagonian fjords (**Figure 3**). In the Europa Fjord, bacteria and phytoplankton responded differentially to DO concentrations. Additionally, lower salinity values showed an influence on Baker Channel bacterioplankton (**Figure 3A**). Accordingly, salinity seemed to induce separation of the bacterioplankton assemblages from the Baker Channel and Penas Gulf (**Figure 3A**). This effect was more pronounced for the bacterioplankton communities located in the Baker Channel at 5 m depth, where the mean salinity value was 15 (**Table 1**).

Beta diversity-based cluster analyses of samples were performed to determine regional diversity (**Figure 4** and **Supplementary Figure 4**). The results reveal two separate clusters of bacterioplankton (B1 and B2) and four clusters of phytoplankton (P1–P4) (**Figure 4A**). A geographical division of the Patagonian fjords is reflected in the cluster distribution of both communities (**Figure 4A**). The more northern stations, represented by samples from Penas Gulf (47°S) and Baker Channel (48°S), grouped with samples from south of Messier Channel (51°S) (clusters B2 and P4). The central area from Bernardo Fjord to Falcon Fjord (48.8–49.5°S), instead grouped exclusively as part of clusters B1 and P1. Finally, stations in the southern fjord region (50–52°S; **Figure 1**) were heterogeneously represented by a high diversity of groups dispersed within the six different clusters.

The effect of oceanographic variables on beta diversity was then assessed using a Mantel test with Spearman's correlation (*rho*). The results confirm that the environment modulates microbial community clusters differentially. For instance, the bacterioplankton community structure of cluster B2 correlated much stronger with salinity and DO ($R = 0.5875$, $p = 0.0018$) than that of cluster B1 ($R = 0.243$, $p = 0.0283$) (**Table 2**). Meanwhile, phytoplankton of cluster P1 showed a weak but significant correlation with temperature ($R = 0.3205$, $p = 0.0093$), and those of cluster P4 showed a moderate correlation with salinity ($R = 0.4729$, $p = 0.0283$) (**Table 2**). Finally, geographical distance (i.e., Haversine distance) between samples, as well as the correlation of diversity between communities, were studied. Geographic distance showed a weak correlation for both communities (bacterioplankton $R = 0.\ 2398$, $p = 0.0024$; phytoplankton $R = 0.2265$, $p = 0.0018$), thus their dissimilarity weakly correlated with the distance between samples. However, a high correlation was observed between the bacterioplankton and phytoplankton communities ($R = 0.687$, $p = 0.0018$) (**Supplementary Table 4** and **Figure 4B**).

Microbial Core Taxa, Indicators and Interactions in the Patagonian Fjords

To identify the microbial taxonomic composition, and the impact of environmental variables on specific taxa, we focused on identifying the microbial core taxa based on the decreasing prevalence of taxa among samples (**Supplementary Table 5**). The results showed that no bacterioplankton or phytoplankton ASVs were shared by all samples ($n = 45$), signifying a highly variable microbial community in the study area. However, when analyzing bacterioplankton at the species level, as well as phytoplankton at the phylum level, it was possible to detect core taxa (**Supplementary Table 5**). Fifteen bacterioplankton families (9 orders), dominated by Flavobacteriaceae (Flavobacteriales), Rhodobacteraceae (Rhodobacterales) and Pelagibacteraceae SAR11 Clade I (SAR11 clades) (**Supplementary Table 6**), represented the core taxa and the most abundant bacterioplankton taxa in these Patagonia fjords. In contrast, although the phytoplankton composition was dominated by the families Thalassiosiraceae, Skeletonemataceae, and Bathycoccaceae (**Supplementary Table 7**), none represented the core (**Supplementary Table 5**). To confirm if the observed community differences respond to geographic barriers, a distance decay analysis was performed. The results showed a non-significant ($p > 0.01$) association between the shared ASVs (Jaccard similarity index) and geographical distance (km) between sites (ln prokaryotic $R^2 = 0.007$, $p = 0.03$; phytoplankton $R^2 = 0.008$, $p = 0.04$) (**Figure 4C**). The same dispersion analysis performed at different taxonomic levels shows a higher dispersion of taxa in the Patagonian fjord communities.

Additionally, we analyzed the effect of environmental factors on specific taxa to identify potential microbial indicators of environmental change within the Patagonian fjords. Here, we defined microbial indicators as those families with a moderate to strong correlation (i.e., $R \geq 0.5$ or ≤ -0.5) with one or more oceanographic factors. The analysis identified 29 families (dominated by bacteria) that were influenced by at least one oceanographic factor, while eight families were affected by more than one factor. As expected, DO was identified as a critical factor, affecting 14 families (bacteria 12; archaea 2) (**Figure 5**). Additionally, several families including Gimesiaceae, Beijerinckiaceae and the NS9 marine group, showed a conserved pattern of correlations and were significantly associated with low temperature and low DO concentrations. In contrast, the bacterial families SAR11 Clade III, Burkholderiaceae and

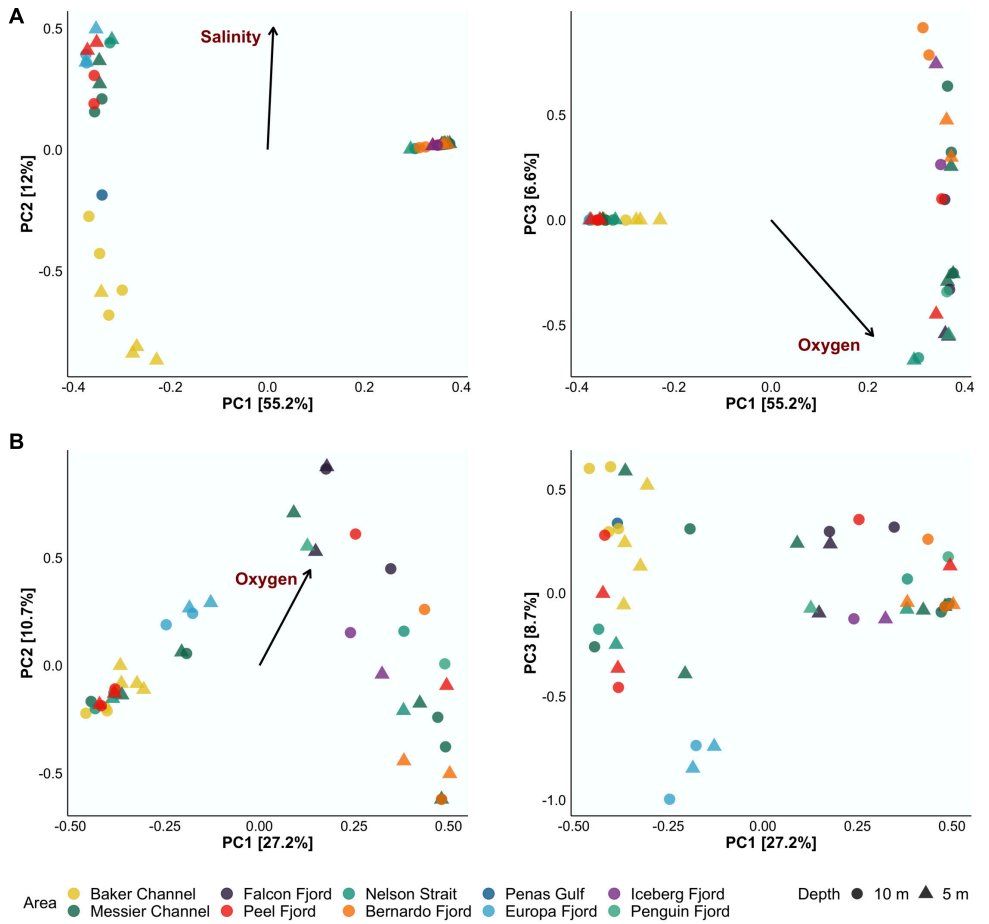

FIGURE 3 | Principal component analysis (PCA) of the 45 samples analyzed for bacterioplankton **(A)** and phytoplankton **(B)** communities. The left side of panels **(A,B)** shows PC1 and PC2, while the right side shows PC1 and PC3. Samples were collected from 5 m (triangles) and 10 m (circles) depth. Only oceanographic variables with values of significance ($p < 0.01$) via envfit were plotted (black arrow and red labels). The relative contribution (eigenvalue) of each axis to the total inertia in the data is indicated as a percentage on the axis titles.

Microbacteriaceae were negatively correlated with salinity and Chl-*a*. These bacterial families also showed a positive correlation with the eukaryotic families Coccomyxaceae and Pyrenomonadaceae. Furthermore, Coccomyxaceae and Pyrenomonadaceae, which were negatively correlated with Chl-*a*, were the only phytoplankton families to show a significant correlation with an abiotic factor (**Figure 5**).

Finally, the relationship previously observed in the Mantel test (**Figure 4C**) between bacterioplankton and phytoplankton taxa (612 and 33 ASVs, respectively) was analyzed in more detail via network reconstruction (**Figure 6**). The analysis yielded high modularity within the community. This network was mainly dominated by generalist bacteria present in more than one cluster (**Figure 6A**), while most connected nodes belonged to ASVs within the major bacterioplankton groups (clusters B1 and B2). All phytoplankton ASVs were located, with high connectivity, at the network center (**Figure 6A**). According to the beta diversity analysis, phytoplankton ASVs that were abundant in cluster P1 correlated more with cluster B1 while ASVs from cluster P4 interacted more with cluster B2. Subsequently, to better understand specific inter-domain interactions, we performed a new correlation analysis by selecting all bacterioplankton families that correlated (i.e., $R \geq 0.5$ or ≤ -0.5) with phytoplanktonic taxa. The results show interactions between 27 bacterioplankton and 10 phytoplankton families (**Figure 6B**). The Pyrenomonadaceae and Coccomyxaceae families accounted for most of the positive correlations with bacteria, especially Schleiferiaceae, Spirosomaceae, Sporichthyaceae, and TRA3-20 (**Figure 6B**). At the same time, Noelaerhabdaceae (order Isochrysidales) exhibited stronger negative correlations with bacteria (i.e., Methylophilaceae) (**Figure 6B**).

DISCUSSION

Oceanographic Heterogeneity in the Patagonia Fjord

Oceanographic conditions along the study area showed a clear stratification in the water column. This stratification is associated with the presence of the Estuarine Water (EW) in the first

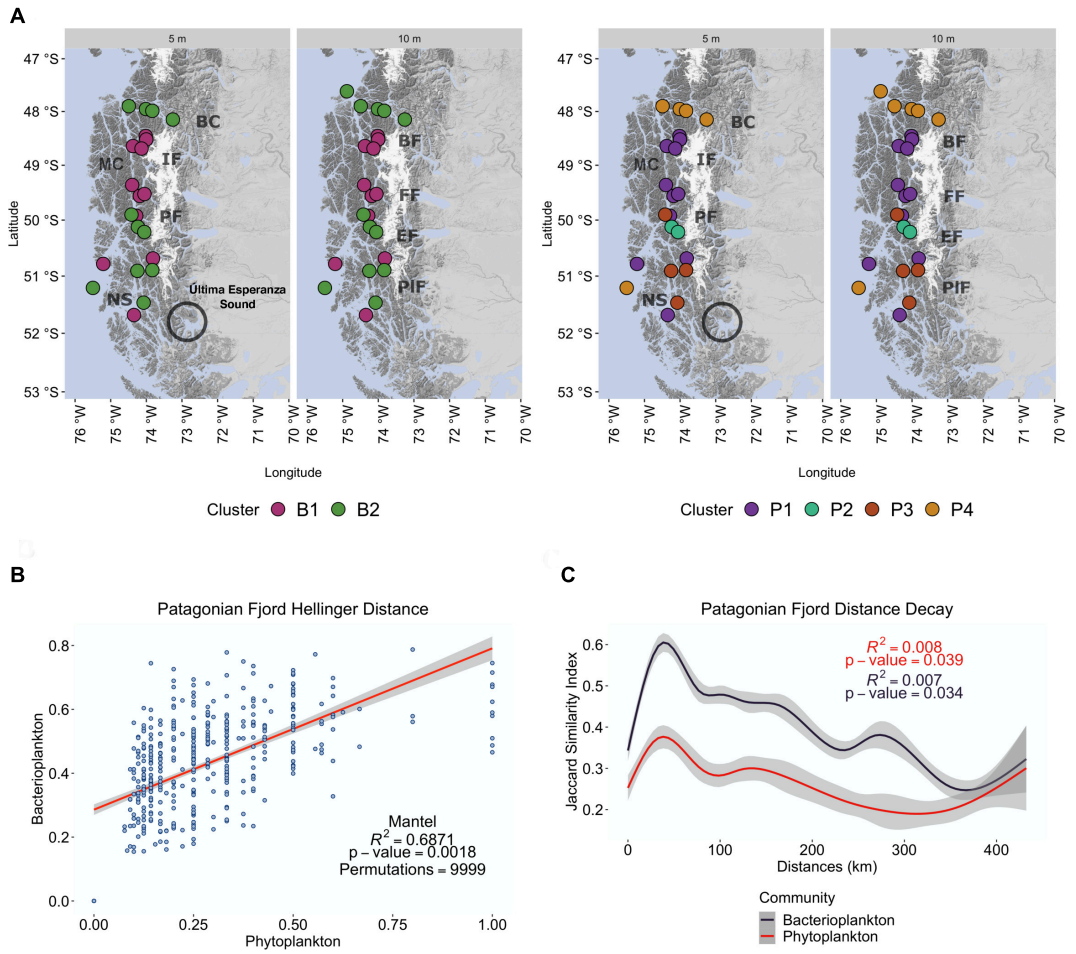

FIGURE 4 | Cluster analysis of the Patagonian fjord microbial community distribution. **(A)** Geographical distribution of bacterioplankton clusters (colored areas labeled as B1 and B2) and phytoplankton clusters (colored areas labeled as P1 to P4) throughout the Chilean Patagonian fjords. Baker Channel (BK), Bernardo Fjord (BF), Messier Channel (MC), Iceberg Fjord (IF), Falcon Fjord (FF), Penguin Fjord (PF), Europa Fjord (EF), Peel Fjord (PIF), Nelson Strait (NS). Última Esperanza Sound is also shown due to its substantial fluvial contribution to the region. **(B)** Beta diversity correlation of communities. Mantel test with Spearman's correlation (*rho*) of the Hellinger distance matrix between the microbial communities. **(C)** Microbial community distance decay was calculated as the linear regression of the log Jaccard similarity index and the linear distance among samples. Bacterioplankton communities (dark blue). Phytoplankton communities (red).

24 m, followed by the Modified Sub-Antarctic Water (MSAAW) and deeper down by the Sub-Antarctic Water (SAAW) as has been previously described in the area (Silva and Vargas, 2014). Additionally, 3 types of EW, previously identified in the area (Silva and Guzmán, 2006), could be distinguished in the first meters of the water column. At 5 and 10 m depth, the Estuarine Salty Water (ESW) clearly dominates in the study area, with only Estuarine Brackish Water (EBW) present at 5 m in the Baker Channel and the Iceberg fjord. In agreement with previous results from central Patagonia (∼47–53°S) (Silva and Vargas, 2014; Torres et al., 2014), a low salinity, high oxygen surface layer was detected throughout the study area, even in stations located far from a direct freshwater input (i.e., stations 2, 43, 48, and 68), denoting a strong influence of freshwater along the region. Substantial fluvial input has been described in the region, mainly related to Baker Channel and Última Esperanza Sound (González et al., 2013; Silva and Vargas, 2014). The freshwater contribution from rivers and glaciers is characterized by low nitrate and phosphate, but high silicate and organic matter, playing a key role in local dynamics through mixing/stratification processes and influencing the phytoplankton community (González et al., 2013; Silva and Vargas, 2014; Vargas et al., 2018). The salinity and DO conditions associated with EW have been shown to influence the establishment of estuarine microbial communities in northern Patagonia (41°S), delimiting their ecological niches (Gutiérrez et al., 2018). This agrees with our observation in the central Patagonian area, where salinity and DO are also significant drivers of the bacterioplankton structure. These results show a different response of the fjord microbial community structure relative to the general pattern observed in other oceanographic regions where temperature is the main driver (Sunagawa et al., 2015). Our results also confirm the presence of Estuarine Waters, mainly Estuarine Salty Water (ESW, S = 21–31) along the study area, highlighting a conserved pattern of estuarine influence

TABLE 2 | Correlation of Patagonian fjord microbial clusters with oceanographic parameters.

Mantel test	Cluster B1		Cluster B2		Cluster P1		Cluster P2		Cluster P3		Cluster P4	
Comparison	***R***	***P*-value**	***R***	***P*-value**	***R***	***P*-value**	***R***	***P*-value**	***R***	***P*-value**	***R***	***P*-value**
Hell dist + depth	0.0556	0.2477	0.0591	0.2300	−0.0112	0.6551	−0.414	1.0000	−0.0089	0.7573	0.0817	0.3144
Hell dist + temp	0.0712	0.3318	0.1602	0.1242	0.3205	0.0093**	−0.3714	0.9375	0.2616	0.2104	0.265	0.1507
Hell dist + oxy	0.1887	0.0653	0.3087	0.0170*	0.1462	0.1022	−0.0286	0.5510	0.4056	0.2050	−0.1617	0.9556
Hell dist + sal	0.0182	0.5639	0.4377	0.0024**	0.1408	0.1807	−0.3714	0.9162	−0.0733	0.6917	0.4729	0.0283*
Hell dist + Chl-*a*	−0.0004	0.6372	0.0736	0.3144	−0.1547	1.0000	−0.6	1.0000	0.4625	0.1102	0.1344	0.3144
Hell dist + oxy and sal	0.2432	0.0283*	0.5875	0.0018**	0.2693	0.0144*	−0.2571	0.7759	0.393	0.2104	0.4664	0.0283*
Hell dist + oxy, sal and depth	0.164	0.0771	0.336	0.0108*	0.1353	0.1102	−0.5429	0.9000	0.1883	0.2642	0.3005	0.1116
Hell dist + env (all)	0.1296	0.1221	0.3006	0.0112*	0.1378	0.1102	−0.3714	0.9162	0.3131	0.1242	0.3197	0.0996
Hell dist + geo dist	0.6169	0.0018**	0.7349	0.0018**	0.0894	0.2564	−0.414	1.0000	0.5085	0.1012	0.2838	0.1242

*Mantel test with Spearman's correlation (rho) of the Hellinger distance matrix for the bacterioplankton (prokaryotic plankton) clusters (B1 and B2) and eukaryotic phytoplankton clusters (P1–P4) versus Euclidean distances of the environmental factors, or Haversine distances between samples. Values of significance after Benjamini–Hochberg (BH) false discovery rate (FDR) correction are shown. Significance codes: 0.01 '**' 0.05 '*'.*

along 450 km of the Chilean Patagonian fjord region. Freshwater input with low nutrients (nitrate and phosphate) and high sediment material, which limits light penetration in the column water, probably negatively affects phytoplankton biomass. In this regard, the lowest Chl-*a* concentrations observed in this study, namely in the Baker Channel and Nelson Strait areas, were correlated with a direct freshwater influence. In contrast, the highest Chl-*a* values were detected along the Messier Channel area (stations 19, 24, 35, 43, and 44), where local dynamics allow for the arrival of SAAW, which is characterized by nutrient-rich waters (Silva and Vargas, 2014; Cuevas et al., 2019). The relationship between low Chl-*a* and high freshwater input has been previously reported in several areas of Patagonia (Vargas et al., 2018; Cuevas et al., 2019) and other glacier regions, such as Maxwell Bay (King George Island, Antarctic Peninsula) (Meredith et al., 2018).

Patagonia Fjord Microbial Community Structure

Freshwater and intertidal waters are characterized by a higher microbial richness than marine waters (Wang et al., 2012). This is reflected in the present study, with areas such as Peel Fjord and Baker Channel showing higher richness and sharp environmental gradients in the surface of the water column, which can be explained by the mixing of sediment and microorganisms from freshwater input (Wang et al., 2012; Rocca et al., 2020). In contrast, due to its connection with an enclosed area containing many fjords, the high richness observed in the Messier Channel area was probably associated with the arrival of sediments and EW, thus accumulating the microbial richness of these fjords. The mixing of these microbial communities (i.e., community coalescence) triggers a structural change that shapes the communities of the Patagonian fjords. However, as in other aquatic environments, the mixing process in this region is not random but facilitated by estuarine circulation, specifically driven by the constant mixing of EW and SAAW that can generate sharp gradients, as observed in this study. This prompts constant community coalescence and the selection of species better adapted to dispersion and mixing (Castledine et al., 2020; Mestre and Höfer, 2020). However, heterogeneous water mixing (i.e., differential mixing between water masses along the fjord system) was also noticed between stations in the study area. These different gradients can also induce variations in the community coalescence mixing ratio and microbial structure (Rillig et al., 2015; Castledine et al., 2020). This was demonstrated by our cluster analysis, in that geographically heterogeneous community structures respond differentially to the measured oceanographic conditions, even when several taxa are shared between clusters, emphasizing the importance of biotic interactions in these communities. Furthermore, evidence suggests that the microbial coalescence process favors system function over the prevalence of input members, selecting the best-adapted taxa, even from the rare biosphere, to ensure productivity of the system (Rillig and Mansour, 2017; Sierocinski et al., 2017; Rocca et al., 2020). Further analysis is now needed to determine if the primary productivity pattern is conserved within different communities of the Patagonian fjords.

The network analysis suggests high modularity in the Patagonian communities (i.e., bacterioplankton and phytoplankton), observing two divergent modules made up of positive biotic connections within modules and negative connections between modules. Modular communities, such as those observed here, have been proposed to emerge after particular coalescence events. These coalescence events produce mixed communities that are adapted to the new resulting environment, while maintaining most of their original species interactions. However, modularity also can be observed when a structured environment limits the mixing between communities,

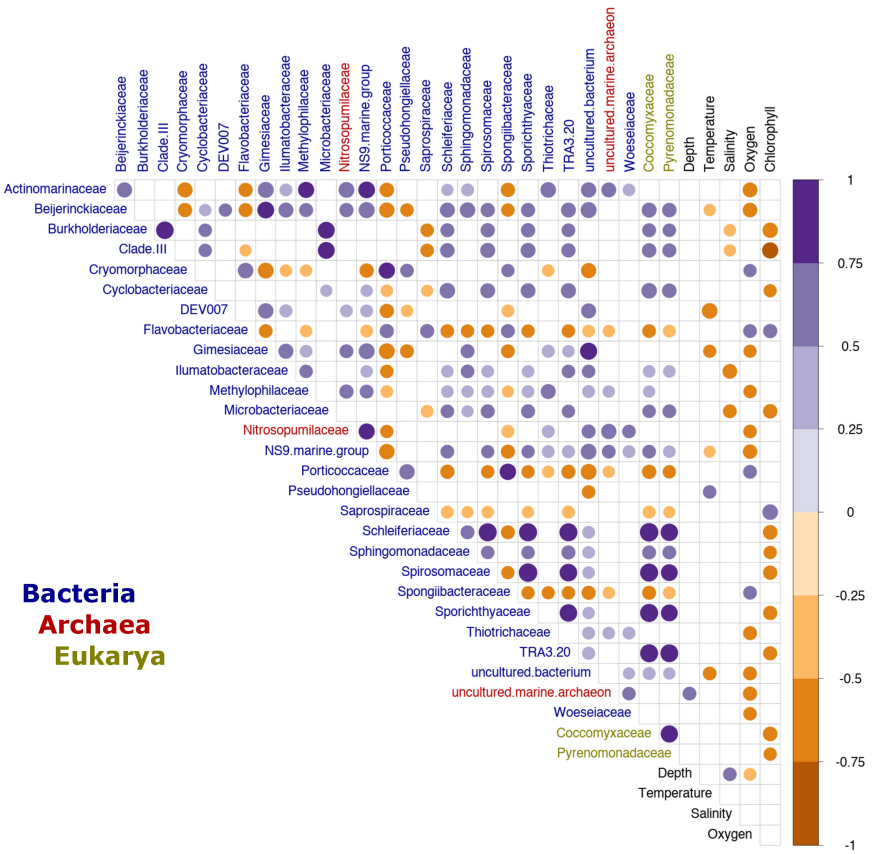

FIGURE 5 | Indicator families from the Patagonian fjord microbial communities. Correlation analysis between environmental variables and fjord families. Only taxa with a significant correlation ($p < 0.01$) and a moderate to strong effect ($R \geq 0.5$ or ≤ -0.5) with at least one oceanographic factor are shown. The color gradient represents the Spearman's correlation coefficient values. Only values with significance ($p < 0.01$), after Benjamini–Hochberg (BH) FDR correction, are shown. The labels are colored by domain according to the legend at the bottom of the plot. Clade III refers to Pelagibacteraceae subgroup III.

thereby supporting localized interactions (Castledine et al., 2020). The lack of overlap between the two observed modules and their different ecological potentials could be associated here with the gradients caused by heterogeneous mixing of the water masses in the Patagonian fjords (i.e., EW and SAAW); that is, local conditions limit mixing of the communities. Nevertheless, some strong biotic connections were observed between bacterioplankton and phytoplankton at the community and family levels. In the Baker Channel, some localized correlations associated with its differential and specific ecological conditions were also observed. The low dispersion barriers in the area allow dispersion of microorganisms in conjunction with local selection, limiting microbial interactions. In that sense a few ubiquitous and more generalist (i.e., better-adapted) families were distributed throughout the microbial communities of the different fjords. New experiments are now needed to better address the differential mixing ratios affecting the community structures, interactions and productivity in the Patagonian fjords.

Along the 450 km of the Patagonian fjords studied here, the bacterioplankton community was characterized by the dominance of Flavobacteriales, Rhodobacterales and SAR11 Clade I (Pelagibacteraceae). These bacterial groups have been previously described as abundant in this region (Gutiérrez et al., 2018) and in other fjords, such as Arctic Svalbard (Cardman et al., 2014). Flavobacteriales and Rhodobacterales are commonly attached to phytoplankton cells during blooms (Buchan et al., 2014) and are specialized for algal polysaccharide remineralization (Teeling et al., 2016; Kappelmann et al., 2019). In that sense, the high abundance of these bacteria, which were collected during the spring of 2017, could be related to the typical seasonal occurrence of spring phytoplankton blooms (Gutiérrez et al., 2018; Cuevas et al., 2019; Saldías et al., 2019). In agreement with Gutierrez et al., who studied the surface waters of Puyuhuapi fjord in northern Patagonia (Gutiérrez et al., 2018), our results show that the abundant and global marine generalist SAR11 is ubiquitous in the Patagonian fjords. However, the present study also reveals the presence of different sub-clades of SAR11 that are associated with different niches. In particular, SAR11 Clade I (i.e., ecotype SAR11 Clade Ia.1), which has been mainly associated with cold marine waters at high latitudes, was the most abundant sub-clade present in the Patagonian fjords. Meanwhile, Clade III (i.e., ecotype SAR11 Clade III.b), related to freshwater (Brown et al., 2012; Giovannoni, 2017), was associated with the low salinity (i.e., EW) and low Chl-*a* waters,

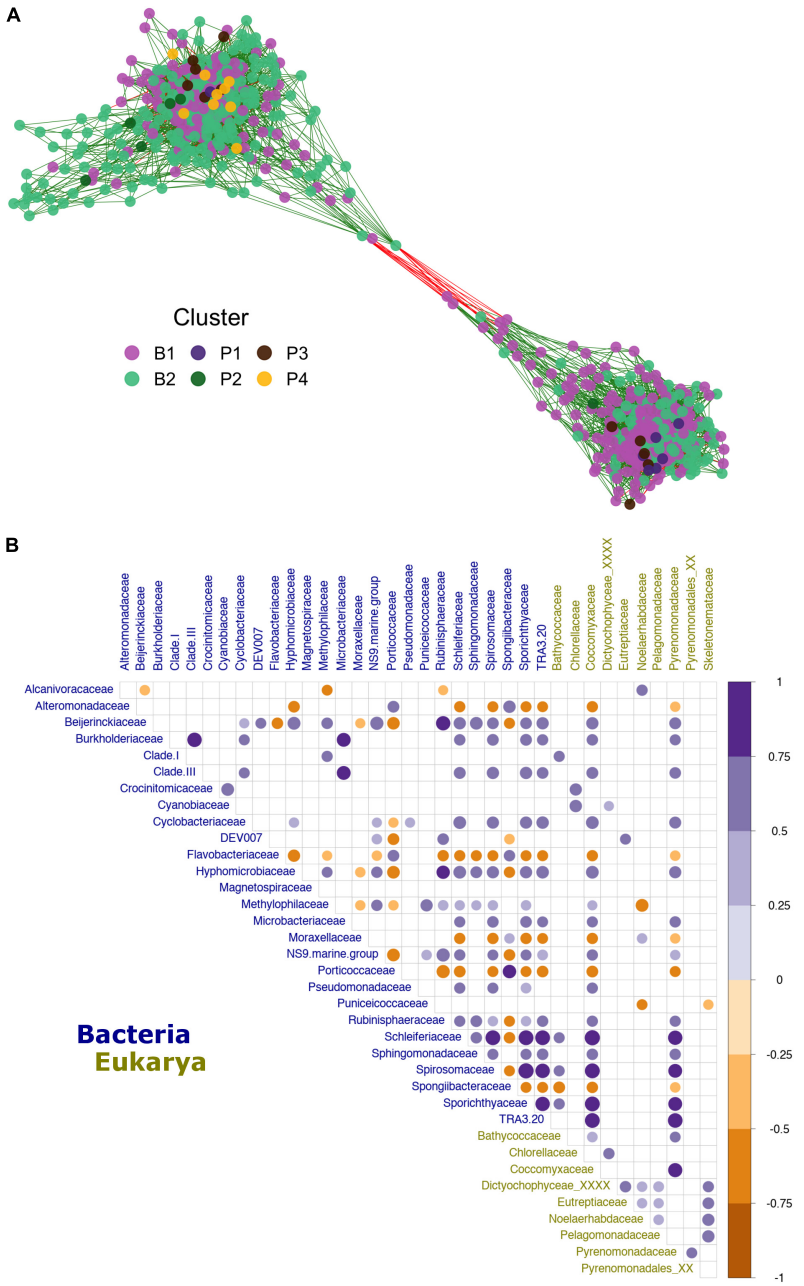

FIGURE 6 | Patagonian fjord microbial network and inter-domain interactions. **(A)** Microbial co-occurrence network. The node color (ASV) was assigned according to the group with the highest relative abundance observed for the node. Vertices are colored according to the positive (green) or negative (red) correlation between nodes. **(B)** Correlation between microbial families influenced by interactions with phytoplankton ($R \geq 0.5$ or ≤ -0.5). The color gradient presents the degree of pair Spearman's correlation, with blue representing positive correlations and dark yellow representing negative correlations. Only values of significance ($p < 0.01$), after Benjamini–Hochberg (BH) FDR correction, are shown. The labels are colored by domain according to the legend at the bottom of the plot. Clades I and III refer to Pelagibacteraceae subgroups I and III, respectively.

such as those observed in the Baker Channel. Nevertheless, the conclusions presented in this study should be taken with a degree of caution given the inherent limitations of current molecular techniques applied to measure the full diversity or taxonomy of microbial communities. Limitations in DNA extraction and library construction that may over- or under-represent estimates of microbial communities members have not yet been solved (Oyola et al., 2012; Vincent et al., 2017). In addition, a major technical limitation in this study was the use of a single molecular marker (i.e., the 16S rRNA gene), which is unable to resolve the finest taxonomic discrepancies and relies heavily on database annotation (Rosselló-Móra and Amann, 2015).

The Patagonian fjord phytoplanktonic community was dominated by the orders Thalassiosirales (Thalassiosiraceae and Skeletonemataceae) and Mamiellales (Bathycoccaceae), which have been previously described in the region (Takeuchi and Kohshima, 2004; González et al., 2013; Iriarte et al., 2013; Fernández et al., 2017; Montero et al., 2017; Fuentes et al., 2019). However, the families Pyrenomonadaceae and Coccomyxaceae exhibited a higher correlation with bacterioplankton families. Pyrenomonadaceae and Coccomyxaceae were especially abundant in areas of low salinity and low Chl-*a,* such as the Baker Channel. These two families are mainly comprised of genera identified in terrestrial and freshwater environments (Guiry and Guiry, 2020), supporting the introduction of microorganisms into these fjords by freshwater inputs. The distinctive oceanographic conditions found in the Baker area explain the segregated microbial communities when compared to the rest of the Patagonian fjord areas and reveal possible specific interactions between the phytoplankton families Coccomyxaceae and Pyrenomonadaceae and some bacterial families (i.e., Schleiferiaceae, Spirosomaceae, Sporichthyaceae, TRA3-20, and SAR11 Clade III). How these interactions impact the system, and if these interactions are direct (i.e., mutualism) or indirect (i.e., trophic cascades), should be addressed in future studies.

Microbial Indicators of Environmental Changes in the Patagonia Fjords

Microorganisms are crucial for the formation of an ecosystem. Thus, the essential role of the microbiome within the environmental structure can be studied and associated in relation to normal or perturbed ecological conditions (Glasl et al., 2017; Astudillo-García et al., 2019). Consequently, microbiomes have been used to assess the impact of climate change in highly sensitives ecosystems, such as agricultural soils (Schloter et al., 2018), coral reefs (Glasl et al., 2017), and fjords (Gutiérrez et al., 2015; Eregno et al., 2018). Microbial communities respond rapidly to environmental changes, making them a potential tool to complement current monitoring systems (Glasl et al., 2017; Rocca et al., 2020). However, both the environment and microbial communities are highly dynamic, so the use of these communities as biological indicators presents different challenges, such as understanding system stability and how temporal variation impacts the community structure (Astudillo-García et al., 2019). The use of microbial communities or specific taxa to analyze the health of a natural system will largely depend on our knowledge of the microbial diversity, ecology and stability of the system (Astudillo-García et al., 2019). Exploring the diversity of the microbial diversity is important for understanding their complexity, variation and conservation within an specific environment, which will ultimately improve our understanding of how microorganisms interact with the system (Colwell, 1997; Astudillo-García et al., 2019). Efforts to obtain information on the microbial communities of a given system also help to establish a reference for the analysis of other similar regions.

In the Patagonia region, inter-annual variations (e.g., El Niño-Southern Oscillation and Southern Annular Mode) (Garreaud, 2018) can impact the planktonic community, causing increased harmful algal blooms (León-Muñoz et al., 2018). In this study, the negative associations of SAR11 Clade III with salinity and Chl-*a* conditions highlight this taxon as a potential indicator of freshwater input into the fjords, especially in the Baker Channel area, which features high freshwater runoff, sediment load penetration and decreased light penetration (González et al., 2013). SAR11 Clade III has not only been previously associated with freshwater (Giovannoni, 2017), but it has also been suggested as a tool to monitor climate change mediated by ocean warming (i.e., by following the migration of tropical ecotypes to polar regions) (Brown et al., 2012). Considering that global climate change is influencing precipitation in the Patagonia region (Garreaud, 2018), with precipitation trends decreasing over north-central Patagonia and increasing south of 50°S (Garreaud et al., 2013), changes in the abundance of SAR11 Clade III could also be a potential indicator of possible climate change effects in the region.

In contrast to the conditions observed in freshwater-influenced stations, Beijerinckiaceae, Gimesiaceae (PVC group; Planctomycetes) and the NS9 marine group (Flavobacteriia; Flavobacteriales) were identified as potential indicators of the low temperature and low DO waters upwelled from the MSAAW. These bacteria have been associated with different depths in the water column (Muck et al., 2019). The NS9 marine group has been commonly found below the deep chlorophyll maximum (DCM) (Cram et al., 2015). Planctomycetes are highly diverse (i.e., genetically) and widespread in aquatic environments (Dedysh and Ivanova, 2019), in which the Gimesiaceae family, in particular, has been associated with deep waters, mainly in lakes (Rojas-Jimenez et al., 2019). In this region, due to the potential changes in freshwater input under the current climate change scenario, alterations to the typical salinity and oxygen concentration could disrupt the dominance of certain taxa in the surface of the column water. This could modify the interactions between surface and subsurface microorganisms in the Patagonian fjords. Further analyses are needed to fully understand how these changes in community structure and interactions could impact the high productivity of the Patagonian fjord system.

CONCLUSION

The microbial dispersion observed in the central Patagonian fjord area could be due to both estuarine circulation and the normal coalescence process that homogenize microbial communities over hundreds of kilometers within this ecosystem. However, particular local conditions seem to influence the interactions of microorganisms that are possibly co-evolving in these communities. Thus, our results suggest that Patagonia fjords are an ideal location to study selective ecological pressure on microbial coalescent communities. In addition, the microbial communities in Patagonia showed that while high dispersion homogenizes the community, established biotic interactions allow bacterioplankton and phytoplankton to respond differentially to environmental factors.

Thus, the significant association identified in this study between bacterioplankton and phytoplankton (i.e., beta diversity and family-level microbial composition) suggests that although abiotic factors directly or indirectly affect particular taxa within the microbial assemblages (e.g., indicators), biological interactions can permeate the entire community structure of the Patagonian fjords. However, particular taxa, such as the SAR11 Clade III, Burkholderiaceae and Microbacteriaceae families, should be further analyzed and potentially used as indicators of freshwater input into the Patagonian fjord region, an ecosystem highly susceptible to climate change. Meanwhile, Gimesiaceae, Beijerinckiaceae and the NS9 marine group could be used to monitor the impact of marine waters upwelled from the SAAW or MSAAW in these fjords. Due to changes in freshwater input under the current climate change scenario, alterations to the typical salinity and DO concentration may disrupt common interactions between surface and subsurface microorganisms in the region. Altogether, this study of the marine microbial communities in the Patagonia fjords, as indicators of environmental variations in Subantarctic fjords, may help us to understand the potential impact of climate change on Patagonian biodiversity and productivity, and ultimately in other fjords worldwide.

DATA AVAILABILITY STATEMENT

The datasets generated for this study can be found in online repositories. The names of the repository/repositories and accession number(s) can be found below: National Center for Biotechnology Information (NCBI), Sequence Read Archive (SRA), BioProject accession ID PRJNA670217.

AUTHOR CONTRIBUTIONS

JT-L collected and processed the samples in the field. JT-L, JC-A, PA-R, JA, and IM processed and analyzed sequence data, analyzed oceanographic data, helped with the discussion, and critically reviewed and edited the manuscript for journal submission. JT-L and BD wrote the manuscript. All authors contributed to the article and approved the submitted version.

FUNDING

This research was funded by "*Cruceros de Investigación Marina en Areas Remotas* (CIMAR)" – CIMAR Fiordos 23 (CONA C23F 17-02) of the "*Servicio Hidrográfico y Oceanográfico de la Armada*" (SHOA), the Center for Climate and Resilience Research (CR)2 (ANID/FONDAP/1511000), and the Center for Genome Regulation (CRG) (ANID/FONDAP/15200002). Additionally, JT-L was supported by the National Agency for Research and Development (ANID) National Doctoral Scholarship (no. 21171048) during the analysis and writing of this manuscript. JA thanks ANID National Doctoral Scholarship (no. 21130515) for additional funding support.

ACKNOWLEDGMENTS

We would like to thank the scientific research ship "*Cabo de Hornos*" (AGS61) of the Chilean navy, their crew and the "*Servicio Hidrográfico y Oceanográfico de la Armada*" (SHOA) for their help and logistical support during the CIMAR23f campaign. We also thank Christina Ridley for her help in correcting the English version of the manuscript, and the BLOOM laboratory team, especially Antonieta Jojot, Juan Ayala, and Viviana Catalan, for sampling and sample processing. The comments of the editor and reviewers helped us to improve the manuscript.

SUPPLEMENTARY MATERIAL

The Supplementary Material for this article can be found online at: https://www.frontiersin.org/articles/10.3389/fmars.2021.611981/full#supplementary-material

REFERENCES

Andersen, K. S., Kirkegaard, R. H., Karst, S. M., and Albertsen, M. (2018). ampvis2: an R package to analyse and visualise 16S rRNA amplicon data. *Biorxiv* [Preprint] doi: 10.1101/299537

Anderson, M. J. (2001). A new method for non-parametric multivariate analysis of variance. *Austral. Ecol.* 26, 32–46. doi: 10.1111/j.1442-9993.2001.01070.pp.x

Astudillo-García, C., Hermans, S. M., Stevenson, B., Buckley, H. L., and Lear, G. (2019). Microbial assemblages and bioindicators as proxies for ecosystem health status: potential and limitations. *Appl. Microbiol. Biotechnol.* 103, 6407–6421. doi: 10.1007/s00253-019-09963-0

Benjamini, Y., and Hochberg, Y. (1995). Controlling the false discovery rate: a practical and powerful approach to multiple testing. *J. R. Stat. Soc. Ser. B* 57, 289–300. doi: 10.1111/j.2517-6161.1995.tb02031.x

Bokulich, N. A., Kaehler, B. D., Rideout, J. R., Dillon, M., Bolyen, E., Knight, R., et al. (2018). Optimizing taxonomic classification of marker-gene amplicon sequences with QIIME 2's q2-feature-classifier plugin. *Microbiome* 6:90. doi: 10.1186/s40168-018-0470-z

Bolyen, E., Rideout, J. R., Dillon, M. R., Bokulich, N. A., Abnet, C. C., Al-Ghalith, G. A., et al. (2019). Reproducible, interactive, scalable and extensible microbiome data science using QIIME 2. *Nat. Biotechnol.* 37, 852–857. doi: 10.1038/s41587-019-0209-9

Briatte, F. (2020). *Ggnet: Functions to Plot Networks With ggplot2. R package version 0.1.0.* Available online at: https://github.com/briatte/ggnet (accessed November 28, 2020).

Brown, M. V., Lauro, F. M., DeMaere, M. Z., Muir, L., Wilkins, D., Thomas, T., et al. (2012). Global biogeography of SAR11 marine bacteria. *Mol. Syst. Biol.* 8:595. doi: 10.1038/msb.2012.28

Buchan, A., LeCleir, G. R., Gulvik, C. A., and Gonzalez, J. M. (2014). Master recyclers: features and functions of bacteria associated with phytoplankton blooms. *Nat. Rev. Microbiol.* 12, 686–698. doi: 10.1038/nrmicro3326

Callahan, B. J., McMurdie, P. J., Rosen, M. J., Han, A. W., Johnson, A. J. A., and Holmes, S. P. (2016). DADA2: high-resolution sample inference from illumina amplicon data. *Nat. Methods* 13, 581–583. doi: 10.1038/nmeth.3869

Cardman, Z., Arnosti, C., Durbin, A., Ziervogel, K., Cox, C., Steen, A. D., et al. (2014). Verrucomicrobia are candidates for polysaccharide-degrading bacterioplankton in an arctic fjord of svalbard. *Appl. Environ. Microbiol.* 80, 3749–3756. doi: 10.1128/AEM.00899-14

Castledine, M., Sierocinski, P., Padfield, D., and Buckling, A. (2020). Community coalescence: an eco-evolutionary perspective. *Philos. Trans. R. Soc. B Biol. Sci.* 375:20190252. doi: 10.1098/rstb.2019.0252

Colwell, R. R. (1997). Microbial diversity: the importance of exploration and conservation. *J. Ind. Microbiol. Biotechnol.* 18, 302–307. doi: 10.1038/sj.jim.2900390

Cram, J. A., Chow, C. E. T., Sachdeva, R., Needham, D. M., Parada, A. E., Steele, J. A., et al. (2015). Seasonal and interannual variability of the marine bacterioplankton community throughout the water column over ten years. *ISME J.* 9, 563–580. doi: 10.1038/ismej.2014.153

Csardi, G., and Nepusz, T. (2006). The igraph software package for complex network research. *InterJournal* 1695, 1–9.

Cuevas, L. A., Tapia, F. J., Iriarte, J. L., González, H. E., Silva, N., and Vargas, C. A. (2019). Interplay between freshwater discharge and oceanic waters modulates phytoplankton size-structure in fjords and channel systems of the chilean patagonia. *Prog. Oceanogr.* 173, 103–113. doi: 10.1016/j.pocean.2019.02.012

Dale, M. R. T., and Fortin, M. J. (2002). Spatial autocorrelation and statistical tests in ecology. *Ecoscience* 9, 162–167. doi: 10.1080/11956860.2002.11682702

Decelle, J., Romac, S., Stern, R. F., Bendif, E. M., Zingone, A., Audic, S., et al. (2015). PhytoREF: a reference database of the plastidial 16S rRNA gene of photosynthetic eukaryotes with curated taxonomy. *Mol. Ecol. Resour.* 15, 1435–1445. doi: 10.1111/1755-0998.12401

Dedysh, S. N., and Ivanova, A. A. (2019). Planctomycetes in boreal and subarctic wetlands: diversity patterns and potential ecological functions. *FEMS Microbiol. Ecol.* 95:fiy227. doi: 10.1093/femsec/fiy227

Eregno, F. E., Tryland, I., Tjomsland, T., Kempa, M., and Heistad, A. (2018). Hydrodynamic modelling of recreational water quality using *Escherichia coli* as an indicator of microbial contamination. *J. Hydrol.* 561, 179–186. doi: 10.1016/j.jhydrol.2018.04.006

Fernández, L. D., Hernández, C. E., Schiaffino, M. R., Izaguirre, I., and Lara, E. (2017). Geographical distance and local environmental conditions drive the genetic population structure of a freshwater microalga (Bathycoccaceae; Chlorophyta) in Patagonian lakes. *FEMS Microbiol. Ecol.* 93:fix125. doi: 10.1093/femsec/fix125

Fuentes, S., Arroyo, J. I., Rodríguez-Marconi, S., Masotti, I., Alarcón-Schumacher, T., Polz, M. F., et al. (2019). Summer phyto- and bacterioplankton communities during low and high productivity scenarios in the Western Antarctic Peninsula. *Polar Biol.* 42, 159–169. doi: 10.1007/s00300-018-2411-5

Galili, T. (2015). Dendextend: an R package for visualizing, adjusting, and comparing trees of hierarchical clustering. *Bioinformatics* 31, 3718–3720. doi: 10.1093/bioinformatics/btv428

Garreaud, R., Lopez, P., Minvielle, M., and Rojas, M. (2013). Large-scale control on the patagonian climate. *J. Clim.* 26, 215–230. doi: 10.1175/JCLI-D-12-00001.1

Garreaud, R. D. (2018). Record-breaking climate anomalies lead to severe drought and environmental disruption in western Patagonia in 2016. *Clim. Res.* 74, 217–229. doi: 10.3354/cr01505

Giovannoni, S. J. (2017). SAR11 bacteria: the most abundant plankton in the oceans. *Ann. Rev. Mar. Sci.* 9, 231–255. doi: 10.1146/annurev-marine-010814-015934

Glasl, B., Webster, N. S., and Bourne, D. G. (2017). Microbial indicators as a diagnostic tool for assessing water quality and climate stress in coral reef ecosystems. *Mar. Biol.* 164:91. doi: 10.1007/s00227-017-3097-x

González, H. E., Castro, L. R., Daneri, G., Iriarte, J. L., Silva, N., Tapia, F., et al. (2013). Land–ocean gradient in haline stratification and its effects on plankton dynamics and trophic carbon fluxes in Chilean Patagonian fjords (47–50°S). *Prog. Oceanogr.* 119, 32–47. doi: 10.1016/j.pocean.2013.06.003

González, H. E., Nimptsch, J., Giesecke, R., and Silva, N. (2019). Organic matter distribution, composition and its possible fate in the Chilean North-Patagonian estuarine system. *Sci. Total Environ.* 657, 1419–1431. doi: 10.1016/j.scitotenv.2018.11.445

Guiry, M. D., and Guiry, G. M. (2020). *AlgaeBase.* Available online at: https://www.algaebase.org (accessed August 2, 2020).

Gutiérrez, M. H., Galand, P. E., Moffat, C., and Pantoja, S. (2015). Melting glacier impacts community structure of bacteria, archaea and fungi in a Chilean Patagonia fjord. *Environ. Microbiol.* 17, 3882–3897. doi: 10.1111/1462-2920.12872

Gutiérrez, M. H., Narváez, D., Daneri, G., Montero, P., Pérez-Santos, I., and Pantoja, S. (2018). Linking seasonal reduction of microbial diversity to increase in winter temperature of waters of a Chilean Patagonia Fjord. *Front. Mar. Sci.* 5:277. doi: 10.3389/fmars.2018.00277

Harrell, F. E. Jr. (2020). *Hmisc: Harrell Miscellaneous. R package version 4.5.0.* Available online at: https://cran.r-project.org/package=Hmisc (accessed February 28, 2021).

Iriarte, J., León-Muñoz, J., Marcé, R., Clément, A., and Lara, C. (2016). Influence of seasonal freshwater streamflow regimes on phytoplankton blooms in a Patagonian fjord. *New Zeal. J. Mar. Freshw. Res.* 51, 304–315. doi: 10.1080/00288330.2016.1220955

Iriarte, J. L. (2018). Natural and human influences on marine processes in Patagonian subantarctic coastal waters. *Front. Mar. Sci.* 5:360. doi: 10.3389/fmars.2018.00360

Iriarte, J. L., González, H. E., and Nahuelhual, L. (2010). Patagonian Fjord ecosystems in southern Chile as a highly vulnerable region: problems and needs. *Ambio* 39, 463–466. doi: 10.1007/s13280-010-0049-9

Iriarte, J. L., Pantoja, S., and Daneri, G. (2014). Oceanographic processes in Chilean fjords of Patagonia: from small to large-scale studies. *Prog. Oceanogr.* 129, 1–7. doi: 10.1016/j.pocean.2014.10.004

Iriarte, J. L., Pantoja, S., González, H. E., Silva, G., Paves, H., Labbé, P., et al. (2013). Assessing the micro-phytoplankton response to nitrate in Comau Fjord (42 S) in Patagonia (Chile), using a microcosms approach. *Environ. Monit. Assess.* 185, 5055–5070. doi: 10.1007/s10661-012-2925-1

Kahle, D., and Wickham, H. (2013). ggmap: spatial visualization with ggplot2. *R J.* 5, 144–161. doi: 10.32614/rj-2013-014

Kappelmann, L., Krüger, K., Hehemann, J.-H., Harder, J., Markert, S., Unfried, F., et al. (2019). Polysaccharide utilization loci of North Sea Flavobacteriia as basis for using SusC/D-protein expression for predicting major phytoplankton glycans. *ISME J.* 13, 76–91. doi: 10.1038/s41396-018-0242-6

Kendall, M. G. (1948). *Rank Correlation Methods*. Oxford: Griffin.

Kurtz, Z. D., Müller, C. L., Miraldi, E. R., Littman, D. R., Blaser, M. J., and Bonneau, R. A. (2015). Sparse and compositionally robust inference of microbial ecological networks. *PLoS Comput. Biol.* 11:e1004226. doi: 10.1371/journal.pcbi.1004226

Legendre, P., and Fortin, M. J. (2010). Comparison of the Mantel test and alternative approaches for detecting complex multivariate relationships in the spatial analysis of genetic data. *Mol. Ecol. Resour.* 10, 831–844. doi: 10.1111/j.1755-0998.2010.02866.x

Legendre, P., and Gallagher, E. D. (2001). Ecologically meaningful transformations for ordination of species data. *Oecologia* 129, 271–280. doi: 10.1007/s004420100716

León-Muñoz, J., Urbina, M. A., Garreaud, R., and Iriarte, J. L. (2018). Hydroclimatic conditions trigger record harmful algal bloom in western Patagonia (summer 2016). *Sci. Rep.* 8:1330. doi: 10.1038/s41598-018-19461-4

Mantel, N. (1967). The detection of disease clustering and a generalized regression approach. *Cancer Res.* 27, 209–220.

McMurdie, P. J., and Holmes, S. (2013). phyloseq: an R package for reproducible interactive analysis and graphics of microbiome census data. *PLoS One* 8:e61217. doi: 10.1371/journal.pone.0061217

Meinshausen, N., and Bühlmann, P. (2006). High-dimensional graphs and variable selection with the Lasso. *Ann. Stat.* 34, 1436–1462. doi: 10.1214/009053606000000281

Meredith, M. P., Falk, U., Bers, A. V., Mackensen, A., Schloss, I. R., Ruiz Barlett, E., et al. (2018). Anatomy of a glacial meltwater discharge event in an Antarctic cove. *Philos. Trans. R. Soc. A Math. Phys. Eng. Sci.* 376:20170163. doi: 10.1098/rsta.2017.0163

Mestre, M., and Höfer, J. (2020). The microbial conveyor belt: connecting the globe through dispersion and dormancy. *Trends Microbiol* 29, 482–492. doi: 10.1016/j.tim.2020.10.007

Montero, P., Pérez-Santos, I., Daneri, G., Gutiérrez, M. H., Igor, G., Seguel, R., et al. (2017). A winter dinoflagellate bloom drives high rates of primary production in a Patagonian fjord ecosystem. *Estuar. Coast. Shelf Sci.* 199, 105–116. doi: 10.1016/j.ecss.2017.09.027

Moreno-Pino, M., Krock, B., De la Iglesia, R., Echenique-Subiabre, I., Pizarro, G., Vásquez, M., et al. (2018). Next generation sequencing and mass spectrometry reveal high taxonomic diversity and complex phytoplankton-phycotoxins

patterns in Southeastern Pacific fjords. *Toxicon* 151, 5–14. doi: 10.1016/j.toxicon.2018.06.078

Muck, S., De Corte, D., Clifford, E. L., Bayer, B., Herndl, G. J., and Sintes, E. (2019). Niche differentiation of aerobic and anaerobic ammonia oxidizers in a high latitude deep oxygen minimum zone. *Front. Microbiol* 10:2141. doi: 10.3389/fmicb.2019.02141

Murtagh, F., and Legendre, P. (2014). Ward's hierarchical agglomerative clustering method: which algorithms implement ward's criterion? *J. Classif.* 31, 274–295. doi: 10.1007/s00357-014-9161-z

Oksanen, J., Blanchet, F. G., Friendly, M., Kindt, R., Legendre, P., McGlinn, D., et al. (2019). *Vegan: Community Ecology Package. R package version 2.5.7.* Available online at: https://cran.r-project.org/package=vegan (accessed November 28, 2020).

Olsen, L. M., Hernández, K. L., Ardelan, M., Van Iriarte, J. L., Bizsel, K. C., and Olsen, Y. (2017). Responses in bacterial community structure to waste nutrients from aquaculture: an in situ microcosm experiment in a Chilean fjord. *Aquac. Environ. Interact.* 9, 21–32. doi: 10.3354/aei00212

Oyola, S. O., Otto, T. D., Gu, Y., Maslen, G., Manske, M., Campino, S., et al. (2012). Optimizing illumina next-generation sequencing library preparation for extremely at-biased genomes. *BMC Genomics* 13:1. doi: 10.1186/1471-2164-13-1

Parada, A. E., Needham, D. M., and Fuhrman, J. A. (2016). Every base matters: assessing small subunit rRNA primers for marine microbiomes with mock communities, time series and global field samples. *Environ. Microbiol.* 18, 1403–1414. doi: 10.1111/1462-2920.13023

Parsons, T. R., Maita, Y., and Lalli, C. M. (1984). *A Manual of Chemical and Biological Methods for Seawater Analysis*. Oxford: Pergamon Press.

Quast, C., Pruesse, E., Yilmaz, P., Gerken, J., Schweer, T., Yarza, P., et al. (2013). The SILVA ribosomal RNA gene database project: improved data processing and web-based tools. *Nucleic Acids Res.* 41, 590–596. doi: 10.1093/nar/gks1219

R Core Team. (2020). *R: A Language and Environment for Statistical Computing. R version 3.6.3.* Available online at: https://www.r-project.org/ (accessed February 28, 2021).

Rillig, M. C., Antonovics, J., Caruso, T., Lehmann, A., Powell, J. R., Veresoglou, S. D., et al. (2015). Interchange of entire communities: microbial community coalescence. *Trends Ecol. Evol.* 30, 470–476. doi: 10.1016/j.tree.2015.06.004

Rillig, M. C., and Mansour, I. (2017). Microbial ecology: community coalescence stirs things up. *Curr. Biol.* 27, R1280–R1282. doi: 10.1016/j.cub.2017.10.027

Rocca, J. D., Simonin, M., Bernhardt, E. S., Washburne, A. D., and Wright, J. P. (2020). Rare microbial taxa emerge when communities collide: freshwater and marine microbiome responses to experimental mixing. *Ecology* 101:e02956. doi: 10.1002/ecy.2956

Rognes, T., Flouri, T., Nichols, B., Quince, C., and Mahé, F. (2016). VSEARCH: a versatile open source tool for metagenomics. *PeerJ* 4:e2584. doi: 10.7717/peerj.2584

Rojas-Jimenez, K., Araya-Lobo, A., Quesada-Perez, F., Akerman-Sanchez, J., Delgado-Duran, B., Ganzert, L., et al. (2019). Variation of bacterial communities along the vertical gradient in Lake Issyk Kul, Kyrgyzstan. *Biorxiv*. [Preprint] doi: 10.1101/864355 Biorxiv: 864355,

Rosselló-Móra, R., and Amann, R. (2015). Past and future species definitions for Bacteria and Archaea. *Syst. Appl. Microbiol.* 38, 209–216. doi: 10.1016/j.syapm.2015.02.001

Rousseeuw, P. J. (1987). Silhouettes: a graphical aid to the interpretation and validation of cluster analysis. *J. Comput. Appl. Math.* 20, 53–65. doi: 10.1016/0377-0427(87)90125-7

Saldías, G. S., Sobarzo, M., and Quiñones, R. (2019). Freshwater structure and its seasonal variability off western Patagonia. *Prog. Oceanogr.* 174, 143–153. doi: 10.1016/j.pocean.2018.10.014

Schlitzer, R. (2020). *Ocean Data View. Version 5.2.0.* Available online at: https://www.odv.awi.de (accessed February 18, 2020).

Schloter, M., Nannipieri, P., Sørensen, S. J., and van Elsas, J. D. (2018). Microbial indicators for soil quality. *Biol. Fertil. Soils* 54, 1–10. doi: 10.1007/s00374-017-1248-3

Sierocinski, P., Milferstedt, K., Bayer, F., Großkopf, T., Alston, M., Bastkowski, S., et al. (2017). A single community dominates structure and function of a mixture of multiple methanogenic communities. *Curr. Biol.* 27, 3390–3395. doi: 10.1016/j.cub.2017.09.056

Silva, N., and Guzmán, D. (2006). Condiciones oceanográficas físicas y químicas, entre boca del guafo y fiordo aysén (crucero cimar 7 fiordos). *Cienc. Y Tecnol. del Mar* 29, 25–44.

Silva, N., and Vargas, C. A. (2014). Hypoxia in chilean patagonian fjords. *Prog. Oceanogr.* 129, 62–74. doi: 10.1016/j.pocean.2014.05.016

Strickland, J. D. H., and Parsons, T. R. (1972). *A Practical Handbook of Seawater Analysis*, 167th Edn. Ottawa, CA: Fisheries research board of Canada.

Sunagawa, S., Coelho, L. P., Chaffron, S., Kultima, J. R., Labadie, K., Salazar, G., et al. (2015). Structure and function of the global ocean microbiome. *Science* 348:1261359. doi: 10.1126/science.1261359

Suzuki, R., Terada, Y., and Shimodaira, H. (2019). *Pvclust: Hierarchical Clustering with P-Values via Multiscale Bootstrap Resampling. R package version 2.2.0.* Available online at: https://cran.r-project.org/package=pvclust (accessed November 19, 2019).

Takeuchi, N., and Kohshima, S. (2004). A snow algal community on Tyndall Glacier in the Southern Patagonia Icefield, Chile. *Arctic Antarct. Alp. Res.* 36, 92–99. doi: 10.1657/1523-04302004036

Teeling, H., Fuchs, B. M., Bennke, C. M., Krüger, K., Chafee, M., Kappelmann, L., et al. (2016). Recurring patterns in bacterioplankton dynamics during coastal spring algae blooms. *Elife* 5:e11888. doi: 10.7554/eLife.11888

Tillett, D., and Neilan, B. A. (2000). Xanthogenate nucleic acid isolation from cultured and environmental cyanobacteria. *J. Phycol.* 36, 251–258. doi: 10.1046/j.1529-8817.2000.99079.x

Torres, R., Pantoja, S., Harada, N., González, H. E., Daneri, G., Frangopulos, M., et al. (2011). Air-sea CO2 fluxes along the coast of Chile: from CO2 outgassing in central northern upwelling waters to CO2 uptake in southern Patagonian fjords. *J. Geophys. Res. Ocean* 116, 1–17. doi: 10.1029/2010JC006344

Torres, R., Silva, N., Reid, B., and Frangopulos, M. (2014). Silicic acid enrichment of subantarctic surface water from continental inputs along the Patagonian archipelago interior sea (41-56°S). *Prog. Oceanogr.* 129, 50–61. doi: 10.1016/j.pocean.2014.09.008

Vargas, C. A., Cuevas, L. A., Silva, N., González, H. E., De Pol-Holz, R., and Narváez, D. A. (2018). Influence of glacier melting and river discharges on the nutrient distribution and DIC Recycling in the Southern Chilean Patagonia. *J. Geophys. Res. Biogeosciences* 123, 256–270. doi: 10.1002/2017JG003907

Vincent, A. T., Derome, N., Boyle, B., Culley, A. I., and Charette, S. J. (2017). Next-generation sequencing (NGS) in the microbiological world: how to make the most of your money. *J. Microbiol. Methods* 138, 60–71. doi: 10.1016/j.mimet.2016.02.016

Wang, Y., Sheng, H. F., He, Y., Wu, J. Y., Jiang, Y. X., Tam, N. F. Y., et al. (2012). Comparison of the levels of bacterial diversity in freshwater, intertidal wetland, and marine sediments by using millions of illumina tags. *Appl. Environ. Microbiol.* 78, 8264–8271. doi: 10.1128/AEM.01821-12

Wei, T., and Simko, V. (2017). *R Package "Corrplot": Visualization of a Correlation Matrix. R version 0.89.* Available online at: https://github.com/taiyun/corrplot (accessed June 6, 2021).

Wickham, H. (2016). *Ggplot2: Elegant Graphics for Data Analysis. R package version 3.3.4.* New York, NY: Springer-Verlag. (accessed June 16, 2021).

Conflict of Interest: The authors declare that the research was conducted in the absence of any commercial or financial relationships that could be construed as a potential conflict of interest.

Publisher's Note: All claims expressed in this article are solely those of the authors and do not necessarily represent those of their affiliated organizations, or those of the publisher, the editors and the reviewers. Any product that may be evaluated in this article, or claim that may be made by its manufacturer, is not guaranteed or endorsed by the publisher.

frontiers in Marine Science

ORIGINAL RESEARCH
published: 26 July 2021
doi: 10.3389/fmars.2021.635430

Hard-Bottom Megabenthic Communities of a Chilean Fjord System: Sentinels for Climate Change?

Federico Betti[1], Francesco Enrichetti[1], Giorgio Bavestrello[1], Andrea Costa[1], Alessandra Moreni[1], Marzia Bo[1], Paula Ortiz Saini[2] and Giovanni Daneri[2,3]*

[1] DISTAV, Università degli Studi di Genova, Genova, Italy, [2] Centro de Investigación en Ecosistemas de la Patagonia (CIEP), Coyhaique, Chile, [3] Centro de Investigación Oceanográfica COPAS Sur-Austral, Universidad de Concepción, Concepción, Chile

OPEN ACCESS

Edited by:
Susana Carvalho, King Abdullah University of Science and Technology, Saudi Arabia

Reviewed by:
Alejandro Perez Matus, Pontificia Universidad Católica de Chile, Chile
Simone Baldanzi, Universidad de Valparaiso, Chile

***Correspondence:**
Giorgio Bavestrello
giorgio.bavestrello@unige.it

Specialty section:
This article was submitted to Marine Ecosystem Ecology, a section of the journal Frontiers in Marine Science

Received: *30 November 2020*
Accepted: *02 July 2021*
Published: *26 July 2021*

Citation:
Betti F, Enrichetti F, Bavestrello G, Costa A, Moreni A, Bo M, Ortiz Saini P and Daneri G (2021) Hard-Bottom Megabenthic Communities of a Chilean Fjord System: Sentinels for Climate Change? Front. Mar. Sci. 8:635430. doi: 10.3389/fmars.2021.635430

Chilean Patagonia hosts one of the extensive fjord systems in the world, spanning more than 1,600 km between 41 and 55°S, and with a complex geomorphology and hydrography that supports rich and unique assemblages of marine fauna. The biodiversity of benthic organisms is possibly further enhanced by the geographic position of the region that extends far south into subantarctic waters. However, we currently lack an exhaustive picture of the zonation and ecological functioning of the benthic communities within Chilean fjords. The present study provides a detailed examination of the hard substrata megabenthic communities inhabiting the Puyuhuapi and Jacaf fjord system, in the Aysén Region of Chile. Fifty-nine stations scattered along these fjords were explored through SCUBA diving surveys, at depths between 5 and 30 m, and 16 stations were characterized in terms of benthic cover and diversity using replicated underwater photography. Ten hard bottom megabenthic communities were identified within the fjords, with some communities newly described for this region. Community composition varied both along-fjord, and with depth, and was apparently driven by variation in environmental properties. Our characterization of these fjord communities improves overall knowledge of the functioning of the fjords, and provides a useful baseline against which future anthropogenic pressures can be assessed. Future shifts in bathymetric and geographical distributions might indicate detrimental effects of climate changes, and we therefore propose that characteristic communities could be adopted as "sentinels" for overall environmental status of these unique fjord ecosystems. In this regard, detailed mapping of the distribution of megabenthic communities can provide a fundamental tool that assists in best management practices for these ecosystems.

Keywords: Chilean Patagonia, megabenthic diversity, global warming, sentinel species, cold water benthic communities

INTRODUCTION

Fjords are deep, narrow incisions of high latitude coastlines derived from ice cap retreat and subsequent erosion by glaciers (e.g., Howe et al., 2010). Fjords represent some of the most biogeochemically dynamic environments on earth, and link terrestrial environments along coastlines to the open ocean (Walsh, 1991; Gattuso et al., 1998). The coastline of Chilean Patagonia represents one of the most extensive fjord regions in the world, extending for 1,600 linear km between 41 and 55°S, and characterized by highly heterogeneous geomorphological and hydrographical conditions (Silva and Palma, 2008; Pantoja et al., 2011; Sánchez et al., 2011). The water column in Patagonian fjords is estuarine in nature, driven by the interaction between intrusion of oceanic subantarctic waters and freshwater input derived from extremely high rainfall (annual mean varies between 1,500 and 4,500 mm) and melting of coastal glaciers (Lopez et al., 2010; Pantoja et al., 2011). Freshwater generates a buoyant brackish surface layer in the fjords, up to depths of 10 m. Salinity, temperature, and depth of this surface layer varies considerably during the year as a result of seasonal variation in freshwater input, whilst properties of deeper oceanic waters remain relatively stable. The interactions of oceanic water (rich in nitrogen and phosphorous) and freshwater (rich in silica) sustain high levels of primary production within the fjords that fuel high biomass and productivity of associated zooplankton and benthic organisms (Häussermann and Försterra, 2009; González et al., 2010). Moreover, the biogeographical importance of the Chilean fjord region is enhanced by its unique geographical position that provides an extensive transition area between the southern Antarctic coasts and the temperate northern Chilean waters (Brattström and Johanssen, 1983; Escribano et al., 2003).

This combination of geographical, geomorphological, and hydrological features in Patagonian fjords shape a rich and unique megabenthic community comprising about 1,650 species of identified megafaunal organisms (Häussermann and Försterra, 2009). These communities are characterized by a high diversity of endemic species (due to the relative isolation of the fjords and their peculiar environmental traits), deep-water species emergences (facilitated by the low penetration level of light through the turbid superficial layer), and the occurrence of species typically found in the Antarctic region (Brattström and Johanssen, 1983; Escribano et al., 2003; Häussermann and Försterra, 2009; Betti et al., 2017). Various zoological studies have been conducted on many fjord benthic taxa, both of soft and hard bottoms, including foraminiferans (Hromic et al., 2006), sponges (Bertolino et al., 2019, 2020), cnidarians (Försterra and Häussermann, 2003; Häussermann and Försterra, 2007; Sinniger and Häussermann, 2009), molluscs (Schwabe et al., 2006; Cárdenas et al., 2008), polychaetes (Cañete et al., 1999), pycnogonids (Melzer et al., 2006), and crustaceans (Mutschke and Gorny, 1999; Schmidt and Brandt, 2001; Betti et al., 2020).

Despite this extensive literature, a detailed overall picture of the zonation and environmental factors influencing the megabenthic communities of the Chilean fjords is yet to emerge. The megabenthic diversity of a temperate fjord has been investigated in a recent study (Villalobos et al., 2021); in addition, Betti et al. (2017) described the hard substrata infralittoral benthic communities and their variations inside the Seno Magdalena, a 14 km long and narrow indentation of the Isla Magdalena (44.656944°S, 7.80222°W). Five main communities were identified on the basis of 60 recorded Operative Taxonomic Units (OTUs), with distributions related to differences in salinity, turbidity and terrigenous input. More recently, the main soft-bottom communities of the Puyuhuapi Fjord have been identified in a study describing wide, previously unrecorded, aggregations of the squat lobster *Munida gregaria* (Fabricius, 1793) (Betti et al., 2020).

The present study aims to describe the hard-bottom megabenthic communities throughout the Puyuhuapi–Jacaf fjord system, attempting to identify the recurrent assemblages, their ecological role, their geographical variations, and the main environmental factors driving their distribution. This more localized information should help in understanding the dynamics of fjord ecosystems on the larger regional scale, and provide baseline data for their management and conservation.

MATERIALS AND METHODS

Site Description

The Puyuhuapi–Jacaf fjord system is located in the Aysén Region of northern Chilean Patagonia (**Figure 1A**). The system is composed of two fjords, which delimit the Isla Magdalena, a large island located in the central portion of the Moraleda Channel and subjected to protection (*Parque Nacional Isla Magdalena*) (**Figure 1B**). The Puyuhuapi Fjord borders the southeastern coast of the Magdalena Island. It is about 90 km long and 7 km width, with a large mouth connected to the Moraleda Channel located in its southern portion. The Puyuhuapi Fjord runs approximately SW–NE, ending in a large bay nearby the Ventisquero Sound (**Figure 1B**). At around 15 km from the head of the Puyuhuapi Fjord, the Jacaf Fjord runs approximately NW for 55 km, delimiting the northern border of the Isla Magdalena before joining the Moraleda Channel.

The main circulation of subsurface water is counter clockwise (**Figure 1B**): oceanic waters enter the Puyuhuapi Fjord from the South, flow NE, before entering the Jacaf Fjord and finally exiting into the Moraleda Channel (Schneider et al., 2014). Ten main rivers discharge into the Puyuhuapi Fjord, with the largest being the Cisnes River, with an average flow rate of 233 $m^3\ s^{-1}$ (Prado-Fiedler and Castro, 2008), and with its mouth located in the central portion of the fjord (**Figure 1B**). River runoff, together with rainfall of up to 3,000 mm y^{-1} (DGA, 2003), contributes to create a brackish surface layer that is up to 7–10 m deep, highly stratified, and only partially mixed during winter months (González et al., 2011; Betti et al., 2017, 2020). Spatial variation in riverine input results in a fresher northern section and a more haline southern section to the Puyuhuapi Fjord, with the partial exception of winter months, when the intrusion of oceanic water via the Jacaf Fjord can locally reverse this pattern (Schneider et al., 2014). The sharp haline stratification in the fjord system reduces vertical mixing and results in a marked decrease in dissolved

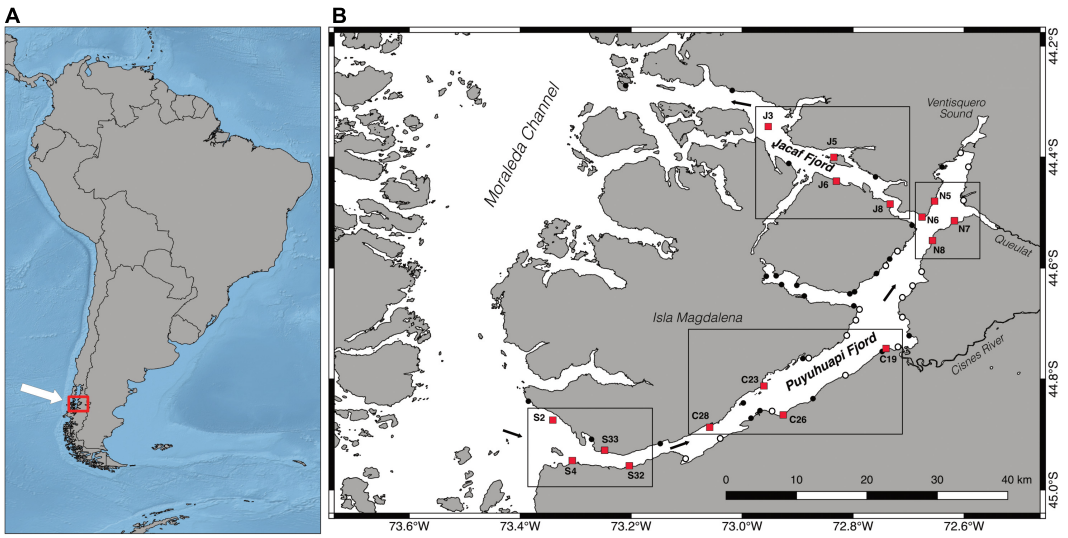

FIGURE 1 | Location of the study area **(A)** and explored stations **(B)**. White circles indicate non-cohesive seafloors, black circles indicate rocky bottoms, red squares indicate the stations selected for investigations, and black arrows indicate the main direction of water circulation. Frames and code letters identify the four macro-areas considered in this study: S, southern Puyuhuapi; C, central Puyuhuapi; N, northern Puyuhuapi; and J, Jacaf Fjord.

oxygen, from concentrations close to saturation near to surface, to 50% saturation at 50–100 m depth (Schneider et al., 2014).

Data Collection and Sampling Design

Between 2014 and 2019, a total of 59 stations were randomly chosen along the Puyuhuapi and Jacaf fjords (**Figure 1B**) and were subsequently explored by SCUBA diving. To avoid seasonality variations, all campaigns were conducted during the month of March. After a visual characterization, these stations were classified according to main seafloor type in rocky vs. soft bottoms (following Betti et al., 2020). Of the total stations, 18 were dominated by soft bottoms and were not considered in the present study, but instead analyzed using a different methodology [the results were published in Betti et al. (2020)]. Six stations characterized by hard substrata were localized in the small lateral inlet of Seno Magdalena and were reported in a different study (Betti et al., 2017). Among the remaining rocky sites, 16 were characterized by similar vertical or sub-vertical rocky cliffs and were used as representative sites for hard-bottoms megabenthic communities of the Puyuhuapi–Jacaf fjord system. The selected stations were located in four different "macro-areas" (four sites for each macro-area), corresponding to different sections of the Puyuhuapi and Jacaf fjords: S, including the stations scattered in the southern portion of the Puyuhuapi Fjord; C, including the stations in the central portion of the Puyuhuapi Fjord; N, representing the northern part of the fjord, and J, including the sites located in the Jacaf Fjord. Within each station, six different depths were investigated, namely 5, 10, 15, 20, 25, and 30 m. For each depth, five replicates photographs of 50 × 35 cm^2 areas were taken, each representing the sampling unit (SU) adopted in this study. Images were shot using a Nikon D7000 camera and Tokina 10–17 mm lens in underwater housing and were later analyzed to identify the taxa present at up to the lowest possible taxonomic level. Voucher samples for those species for which identification through the video footage was difficult were manually collected and subsequently dried or fixed in absolute ethanol for further taxonomic identification. When specific identification was not possible, other OTUs were adopted.

Diversity Patterns

To characterize the rocky benthic communities of the Puyuhuapi–Jacaf fjord system, differences among macro-areas were investigated in terms of cover, species richness (SR), abundance of organisms, and diversity. The percentage cover of cyanobacteria, algae, and metazoans was calculated for each photographic area using the ImageJ64 software package: the standard frame of the pictures was used to calibrate the tools allowing the precise measures of each organism's perimeter in each picture. SR was calculated as number of species per SU, equally considering metazoan organisms identified as morphospecies under different taxonomic levels (species, genus, or higher taxa). Local abundance of organisms was calculated considering the number of organisms per SU. Megabenthic diversity was estimated for each SU using two indices that give complementary information on the community and possess different statistical properties: (i) the Shannon's diversity index (H′) applied to the densities of individuals and based on the natural logarithm, which provides an indication of community composition and frequency of species in a community (Shannon, 1948; Magurran, 2013), (ii) Simpson's diversity index (1-D; Magurran, 2013) which ranges from 0 to 1 and represents the probability that two individuals drawn at random from the community belong to different species.

In order to detect differences in terms of cover of cyanobacteria, algae, and metazoans among the four investigated macro-areas, a one-way analysis of variance (ANOVA) was

conducted considering the entire dataset [data normally distributed, sqrt(x) transformed, with n = 431]. In order to describe the community and to identify the effect of environmental predictors, a series of Generalized Linear Mixed Models (GLMMs) was built, on four different metrics: abundance, SR, and diversity indices. To model community metrics, depth, and distance from Puyuhuapi mouth were considered as predictors, SU as a random effect. Different error distributions and link functions were employed, on the basis of the response metrics: (i) Poisson error distribution and log link for count derived metrics (i.e., local abundance and SR; O'Hara and Kotze, 2010), (ii) gaussian distribution and identity link for Shannon diversity index (Leps et al., 2015), and (iii) binomial distribution and logit link for Simpson's diversity index, using sample count as prior weight for the number of trials (Warton and Hui, 2011). Analyses were performed using Past 3.20 (Hammer et al., 2011) and package "Lme4" (Bates et al., 2007) within the R environment.

Community Analysis

To identify the major megabenthic communities of the Puyuhuapi and Jacaf fjords, a matrix of 431 observations (SU) per 95 variables (OUT abundance values) was created. Those species that accounted for fewer than three individuals throughout the whole dataset were considered rare and removed from the multivariate analyses. In addition, to reduce the background noise produced by the large number of samples with low abundance, only SUs with more than 10 individuals were included in the statistical analyses. Species associations were determined using the clustering algorithm Ward's minimum variance method, constructed over square-root Bray–Curtis dissimilarity measures that were previously calculated from the square-root transformed abundance data. Clustering was performed using the function *hclust* of the package *stats* in the R environment. The optimal number of groups in which to split the dataset was determined using the *silhouette* function included in the *cluster* package. A distance-based permutational multivariate analysis of variance (PERMANOVA, number of permutations = 999) was run to determine statistically significant differences between groups, using the *adonis* function included in the *vegan* package (Oksanen et al., 2016). The indicator value (IndVal) was used to determine the relative importance of all taxa in each community, identifying those species that can be considered characteristic of each association (Dufrêne and Legendre, 1997; Dominguez-Carrió, 2018). IndVal measures were computed using the function *indval* included in the *labdsv* package (Roberts, 2016). Finally, the spatial distribution of all the identified megabenthic communities was mapped using the open-source software Quantum GIS.

Environmental Parameters

To better understand which factors contribute most significantly to variations in species composition among megabenthic communities, two environmental parameters were used to characterize each SU, namely water depth and distance from the fjord mouth. A distance-based redundancy analysis (dbRDA) was computed over the square-root of Bray–Curtis dissimilarity measures and the environmental matrix, with standardized values using the function *capscale* included in the *vegan* package (Oksanen et al., 2016).

RESULTS

Diversity Patterns

The exploration of the 16 selected stations within the Puyuhuapi–Jacaf fjord system provided a total of 456 photographic quadrants, corresponding to a total explored area of 79.8 m^2. **Table 1** summarizes the main features of the macro-areas, while a detailed description of the stations is given in **Supplementary Material 1**.

On average, 95% of substrata were covered by organisms, with macroalgae – always dominated by a coralline encrusting red alga (Order Corallinales) – the most important group, on average occupying 67% of the total biotic cover (**Figure 2A**). Cyanobacteria contributed on average 17% to total cover, with all the other components combined accounting for about 16% of total cover. Significant differences were shown among the four investigated macro-areas (J, N, C, and S) in terms of cyanobacteria (one-way ANOVA, df = 3, MS = 3386.59, $F = 41.52$, $p < 0.001$, and Tukey's pairwise test J≠N≠C≠S) and algal cover (one-way ANOVA, df = 3, MS = 1003.69, $F = 13.09$, $p < 0.001$, and Tukey's pairwise test J = N≠C≠S).

A total of 51,517 individual metazoans – belonging to 137 OTUs – were identified in the photographic quadrants (**Supplementary Material 2**). Up to 67% of the taxa could be identified to species (51%) or genus level (16%). Porifera, with 35 OTUs (23% of the total identified taxa) represented the most diverse group, followed by Mollusca (22%), Echinodermata (16%), and Cnidaria (15%) (**Figure 2B**). Annelids were the most abundant group (50% of total abundance), followed by echinoderms (21%), poriferans (8%), and cnidarians (8%) (**Figure 2C**). The remaining phyla contributed 14% of the total number of organisms. The polychaete *Spiochaetopterus* sp., occurred in about 63% of the samples, and represented the most abundant organism with more than 12,500 individuals observed (**Supplementary Material 2**). Other abundant polychaetes were Spirorbinae (8,632 individuals, in 53% of SUs) and *Chaetopterus variopedatus* (Renier, 1804) (4,126 individuals, in 39% of SUs). The holothurian *Psolus* sp. (3,190 individuals, in 47% of SUs), the sea urchin *Loxechinus albus* (Molina, 1782) (2,901 individuals, in 25% of SUs) and the sea anemone *Metridium* cfr. *Senile* (Linnaeus, 1761) (2,710 individuals, in 10% of SUs) were also particularly abundant.

Generalized Linear Mixed Models conducted on local abundance showed a significant effect of distance from fjord mouth (Wald test: $\chi^2 = 4.41$, Df = 1, $p < 0.05$; **Table 2**), with the abundance decreasing with distance, while no significant effect of depth was observed (Wald test: $\chi^2 = 2.29$, Df = 1, $p = 0.13$; **Table 2**). SR was also negatively affected by distance from fjord mouth (**Table 2**; Wald test: $\chi^2 = 23.55$, Df = 1, and $p < 0.001$) and positively affected by sampling depth (**Table 2** and **Figure 3**; Wald test: $\chi^2 = 156.95$, Df = 1, and $p < 0.001$). Finally, the same pattern has been observed for

TABLE 1 | Overall differences in species composition and diversity of the invertebrate megafauna between the four study macro-areas.

Area	n° of SU	Av. n° spp. per SU (± SD)	Av. n° org. per SU (± SD)	Av. H per SU (± SD)	Number of species									
					POR	CNI	MOL	ANN	ART	BRY	BRA	ECH	CHO	Tot.
Jacaf	105	7.7 (± 3.2)	102.2 (± 82.4)	1.2 (± 0.5)	15	5	15	7	0	5	2	12	2	63
Puyuhuapi N	97	8.9 (± 4.2)	158.8 (± 135.6)	1.3 (± 0.5)	16	5	18	6	2	3	1	14	2	67
Puyuhuapi C	112	9.8 (± 4.1)	128.3 (± 94)	1.5 (± 0.4)	22	7	17	7	2	5	2	12	5	79
Puyuhuapi S	117	9.4 (± 3.8)	94.1 (± 58.8)	1.6 (± 0.6)	22	10	15	7	0	5	2	14	2	77

SU, Sampling Unit; SD, Standard Deviation; POR, Porifera; CNI, Cnidaria; MOL, Mollusca; ANN, Annelida; ART, Arthropoda; BRY, Bryozoa; BRA, Brachiopoda; ECH, Echinodermata; CHO, Chordata.

diversity indices, both Shannon's (**Figure 4**) and Simpson's diversity indices being affected significantly and positively by depth (Wald test Shannon's H′: $\chi^2 = 249.95$, Df = 1, $p < 0.001$; Wald test Simpson's 1-D: $\chi^2 = 162.79$, Df = 1, $p < 0.001$; **Table 2** and **Figure 3**) while negatively by distance from Puyuhuapi mouth (Wald test Shannon's H′: $\chi^2 = 53.99$, Df = 1, $p < 0.001$; Wald test Simpson's 1-D: $\chi^2 = 38.20$, Df = 1, $p < 0.001$; **Table 2**).

Megabenthic Communities

The clustering of 431 SUs was judged to be suitable for statistical analysis, and provided a total of 10 communities (**Table 3** and **Figure 5**) that were significantly different from each other based upon species composition (PERMANOVA, df = 9, MS = 5.90, $F = 33.62$, and $p < 0.001$). The geographical distribution of the 10 megabenthic communities is shown in **Figure 6**, and a comprehensive list of the most important species characterizing each community (based on the IndVal index) is provided in **Table 4**. A description of each identified community follows:

Community 1: *Psolus* sp. Aggregations

Small passive filter feeder holothurians belonging to the genus *Psolus* tend to aggregate in large numbers on vertical and sub-vertical walls, with a maximum recorded density of 1,023 individuals per m^2 (ind. m^{-2}). The aggregations are typically found between 5 and 25 m depth and are widespread along the Puyuhuapi and Jacaf fjords, being more common in the latter (**Figure 5a**).

Community 2: *Spiochaetopterus* sp. and *Heterocucumis godeffroyi* Gardens

This community occurred between 10 and 30 m depth and was more common in the Jacaf Fjord and the southern Puyuhuapi area. Polychaetes belonging to the genus *Spiochaetopterus* produce long and thin membranaceus tubes and can create wide and extremely dense aggregations (up to 1,886 ind. m^{-2}) that protrude from rocky walls and overhangs. Using two long palps, these worms capture organic matter from the water column. The passive filter feeding holothurian *H. godeffroyi* (Semper, 1867) is associated with these polychaete gardens, living amongst the tubes and reaching a maximum density of 194 ind. m^{-2} (**Figure 5b**).

Community 3: Serpulidae Aggregations

This community is characterized by patches of bare rocks covered only with unidentified serpulid polychaetes, which reach a maximum density of 109 ind. m^{-2}; the polyplacophoran *Chiton boweni* King 1832 is also often associated with these serpulids. This community is particularly frequent in the Jacaf Fjord, typically at depths of 25–30 m, but can also be occasionally found at depths of 5–10 m in the southern and central Puyuhuapi, mainly dominated by *C. boweni* (**Figure 5c**).

Community 4: *Loxechinus albus* Aggregations

The sea urchin *L. albus*, reaching maximum densities of 1,211 ind. m^{-2}, is often associated with the gastropod *Crepipatella dilatata* (Lamarck, 1882) and another common sea urchin, *Arbacia dufresnii* (Blainville, 1825). The predatory sea star *Cosmasterias lurida* (Philippi, 1858) is also usually present. The community typically occurred at depths of 5–15 m in all studied areas (**Figure 5d**).

Community 5: *Pentactella leonina* Aggregations

This community was found almost exclusively along the Jacaf Fjord at depths of 5–15 m (**Table 3**). In the Puyuhuapi Fjord, the community was recorded only once at 15 m depth in the central portion of the fjord. The characteristic species was *P. leonina* (Semper, 1867), a holothurian that passively filters large particles and reached a maximum density of 1,023 ind. m^{-2}. The small sea star *Asterina fimbriata* Perrier, 1875 was often found in the same environment (**Figure 5e**).

Community 6: Community of Deep Walls and Crevices

This was the most commonly observed community in the study area, and is widespread below 5 m depth in water more influenced by oceanic water (**Table 3**). The community was particularly notable in the central portion of the Puyuhuapi Fjord but was poorly represented in the Jacaf Fjord. The community is constituted mainly by spirorbin polychaetes, together with encrusting bryozoans. Other important taxa are the sponges *Axinella crinita* Thiele, 1905, and *Neopodospongia tupecomareni* Hajdu, Desqueyroux-Faúndez, Carvalho, Lôbo-Hajdu & Willenz, 2013, and an unidentified erect yellow sponge, the hard corals *Desmophyllum dianthus* (Esper, 1794), and *Caryophyllia huinayensis* Cairns, Häussermann & Försterra, 2005, the erect bryozoans *Aspidostoma giganteum* (Busk,

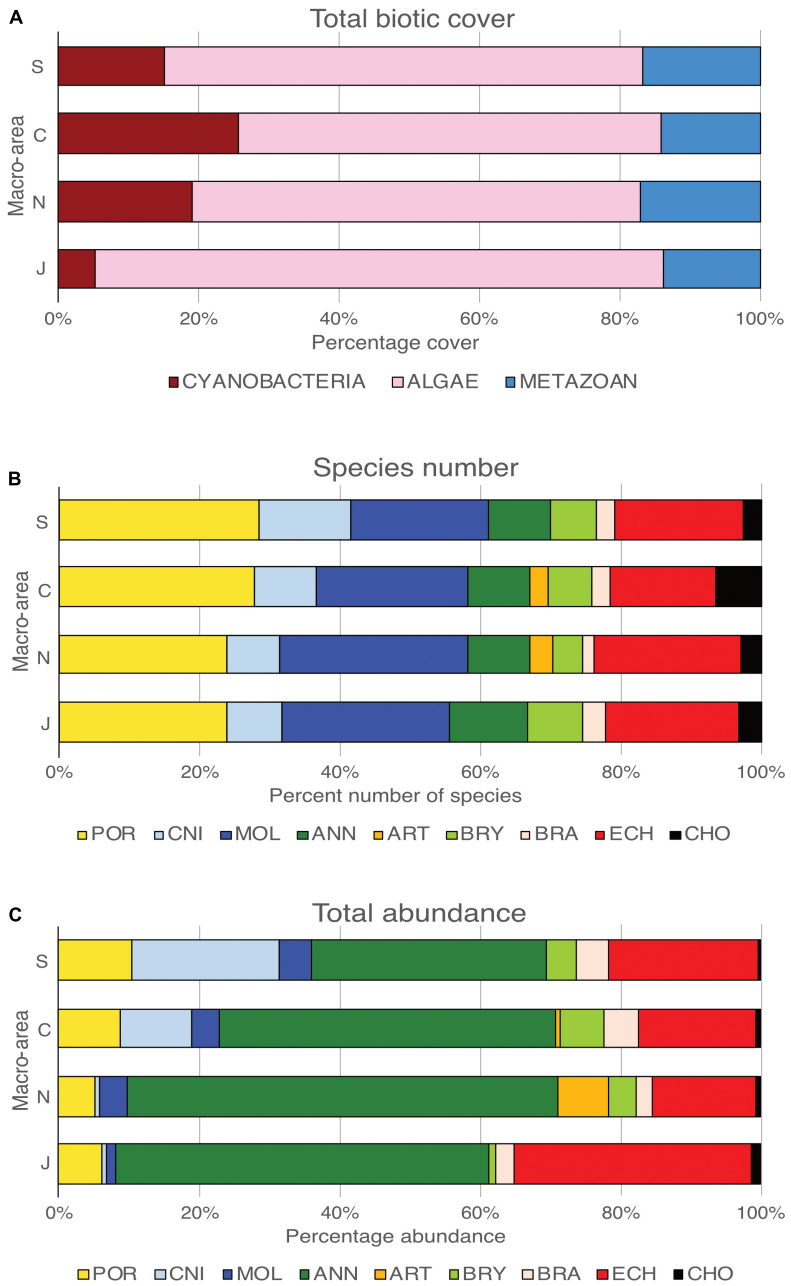

FIGURE 2 | Diversity of megafauna species along the Puyuhuapi–Jacaf fjords. Total biotic cover of Cyanobacteria, algae, and metazoans **(A)**, percentage of the number of species **(B)**, and total abundance **(C)** of megafauna for each phylum in each of the four macro-areas.

1854), and *Reteporella magellensis* (Busk, 1884), and the brachiopod *Magellania venosa* (Dixon, 1789). This brachiopod may occasionally form dense facies (**Figure 5f**).

Community 7: *Chaetopterus variopedatus* Aggregations

The principal representatives of this community are the polychaete *C. variopedatus* which produces membranous tubes attached to the rocks, and various species of encrusting sponges. The maximum recorded density of the polychaete was 1,309 tubes m^{-2}. Other species typical of the community are the sponges *Clathrina fiordica*, *Scopalina* sp. and an unidentified massive yellow sponge, together with the encrusting ascidian *Didemnum studeri*. This community showed the highest average number of species per SU and the highest diversity H′ (**Table 3**) (**Figure 5g**).

Community 8: *Aulacomya atra* Belts

Reaching a maximum density of 594 ind. m^{-2}, the ribbed mussel *A. atra* (Molina, 1782) created extensive large belts between the intertidal zone and the deepest extent of the brackish layer. This

community occurred throughout the Puyuhuapi Fjord but was not observed in the Jacaf Fjord. Different species of barnacles were often observed associated with the mussels, together with the small sea star *Anasterias antarctica* (Lutken, 1857). This community showed the lowest average number of species per SU and the lowest H′ (**Table 3**) (**Figure 5h**).

Community 9: Deep Gorgonian Forests

This community is mainly constituted by large aggregations of the gorgonian *Thouarella* cfr. *variabilis* Wright & Studer, 1889, reaching a maximum density of 194 ind. m^{-2}. Accessory species within the community are the whip gorgonian *Primnoella chilensis* (Phillipi, 1894), the epibiont ophiuroid *Astrotoma agassizii* Lyman, 1875 – sometimes living on branches of *T.* cfr. *Variabilis* – and an unidentified brachiopod. This community was present only at depths of 25–30 m in the central Puyuhuapi Fjord, and occurred only once in the northern portion. The community was absent from the Jacaf Fjord (**Figure 5i**).

Community 10: *Metridium* cfr. *senile* Gardens

The sea anemone *M.* cfr. *senile* creates large aggregations of up to more than 1,500 ind. m^{-2}, representing the highest average number of individuals per SU observed in any of the communities (**Table 3**). The polyplacophoran *Chiton* sp. is often associated with this community. This community occurred only at depths of 5–15 m in the southern and central Puyuhuapi Fjord (**Figure 5j**).

Relationship With Environmental Parameters

Based on the dbRDA, the selected factors only partially explained total variability in species composition, with the first two axes explaining about 16% of the constrained variance (CAP1: 12.3%, CAP2: 3.6%; **Figure 7A**). Depth and distance from the fjord's mouth represent good predictors in modeling the spatial distribution of benthic fauna (**Figure 7B**). The biplot shows that the shallow area at the mouth of the fjord, characterized by well-oxygenated waters with intermediate levels of salinity, is dominated by the sea anemone *M.* cfr. *senile*. The communities dominated by *P. leonina* and *A. atra* tend to prosper in shallow, low-salinity, and well-oxygenated waters of the central portion of the Puyuhuapi Fjord. With increasing salinity and depth, communities are dominated by *Spiochaetopterus* sp., *H. godeffroyi*, *C. variopedatus*, *Psolus* sp., *C. dilatata,* and echinoderms. In addition, *Spiochaetopterus* sp. results particularly abundant also at shallow depth in the Jacaf Fjord. Finally, spirorbin polychaetes, brachiopods and encrusting bryozoans are the most representative organisms in deeper water, where salinity levels are more stable and oxygen saturation is lower than in shallower water.

TABLE 2 | Generalized Linear Mixed Models (GLMMs) parameter estimates for four community metrics: local abundance of organisms, species richness (SR), Shannon's diversity index (H′), and Simpson's diversity index (1-D).

Community metric	Parameter	Estimate	Z(*t*)-value	*p*-value
Local abundance	Intercept	4.19	39.14	$p < 0.001$
	Depth	0.07	1.52	$p = 0.13$
	Distance	−0.09	−2.10	$p < 0.05$
Species richness (SR)	Intercept	2.10	101.82	$p < 0.001$
	Depth	0.25	12.53	$p < 0.001$
	Distance	−0.09	−4.85	$p < 0.001$
Shannon's H′	Intercept	1.36	65.72	$p < 0.001$
	Depth	0.32	15.81	$p < 0.001$
	Distance	−0.15	−7.34	$p < 0.001$
Simpson's 1-D	Intercept	0.50	11.61	$p < 0.001$
	Depth	0.56	12.76	$p < 0.001$
	Distance	−0.27	−6.18	$p < 0.001$

Depth = depth of the sampling unit; Distance = distance from Puyuhuapi mouth.

DISCUSSION

A Diversity Hotspot

In recent years, the Puyuhuapi and Jacaf fjords have attracted an increasing number of studies, from oceanographic (e.g., Schneider et al., 2014; Pérez-Santos et al., 2018; Montero et al., 2021), to biochemical (e.g., Daneri et al., 2012), and zoological (e.g., Försterra et al., 2016; Betti et al., 2017, 2020; Bertolino et al., 2019, 2020) perspective. Therefore, our study of the benthic communities along the coastline of the two fjords complements this previous information to improve our understanding of how ecosystems function in this region. The Puyuhuapi and Jacaf fjord system can be considered very rich and complex because of the sheer number of megafauna species sustained, accounting for 137 identified metazoan taxa of hard bottoms. The high number of species observed is related to the large total sampled area (about 80 m^{-2} along a 150 km stretch; **Supplementary Material 3**), but also to the high diversification of the environmental conditions occurring along the rocky walls of the fjords. We identified ten distinct megabenthic communities, all typically dominated by heterotrophic suspension feeders, a functional group that plays a fundamental role in the transfer of matter and energy from the pelagic to the benthic realm. These communities are also structured to varying extents by conspicuous habitat-forming species, such as sponges, anthozoans, polychaetes, mussels, and bryozoans, all capable of modifying surrounding biotic and abiotic environmental properties. As a consequence, individuals within these communities build the so-called marine animal forests that are characterized by high complexity and biodiversity of benthic macrofauna (Försterra et al., 2016; Rossi et al., 2017).

Försterra et al. (2016) reported ten megabenthic aggregations structured by habitat-forming species throughout the whole region of Chilean Patagonian. Two of these aggregations, namely "mussel beds" and "gorgonian gardens," closely overlap with communities 8 and 9 identified in the present study, and these were also recently reported in the small Seno Magdalena inlet that extends in an approximately NW direction about halfway along the Puyuhuapi Fjord (Betti et al., 2017). Most of the remaining aggregations discussed by Försterra et al. (2016) are also reported in the present study, but are present as separate mono or paucispecific facies within several other communities. For example, "sponge fields" were distributed within communities

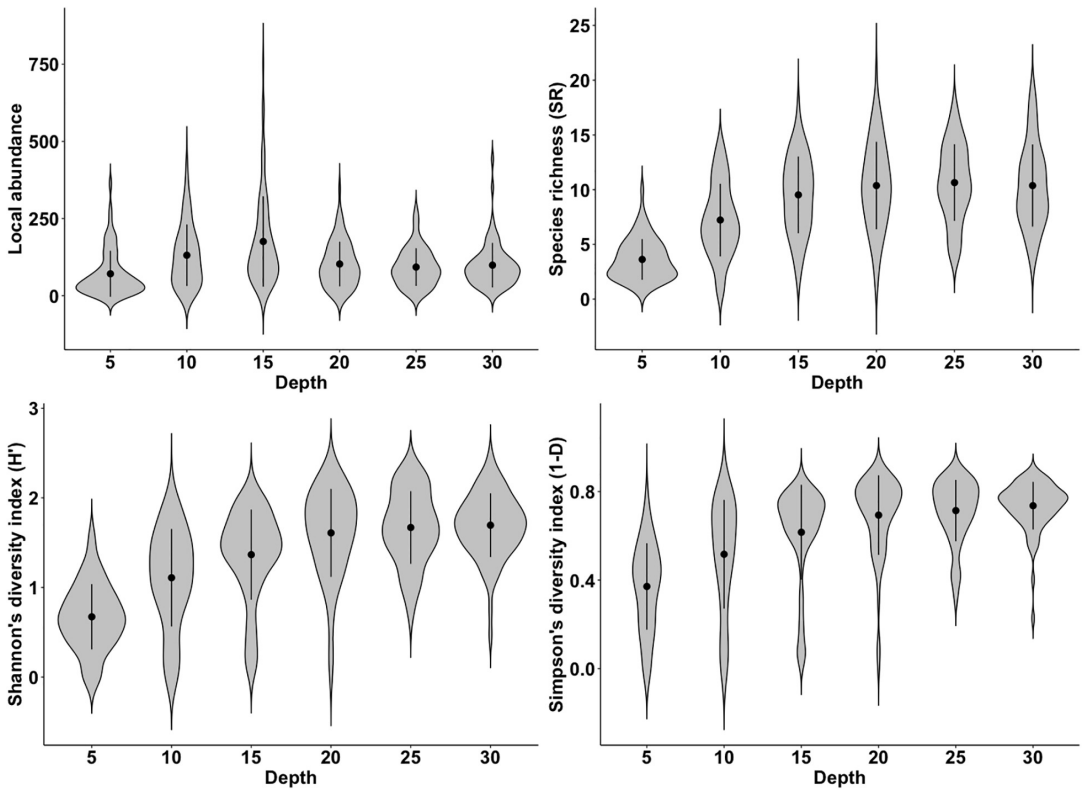

FIGURE 3 | Variation of four community metrics [local abundance of organisms, species richness (SR), Shannon's diversity index (H′), and Simpson's diversity index (1-D)] in relation to depth of sampling, expressed in meters. Blacks dots and vertical lines represent, respectively the mean and the Standard Deviation for each violin-plot.

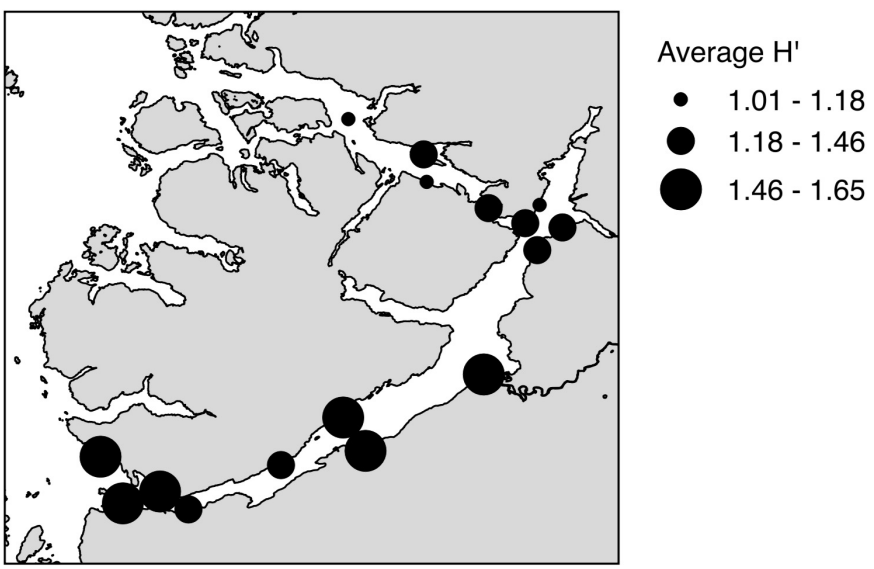

FIGURE 4 | Map representing average Shannon index H′ for the investigated sites.

6 and 7. The aggregation "polychaete fields" partially overlaps with community 7 (being both dominated by *C. variopedatus*) and, to a minor extent, with communities 2, 3, and 6. Similarly, aggregations of barnacles and ascidians may occur within communities 8 and 7, respectively. Community 6 consisted of deep walls and crevices and was more diversified. This included

TABLE 3 | Main features of the 10 communities identified in this study.

ID	Characteristic species	Depth range (m)	Occupancy (%SU)	JAC	PUY_N	PUY_C	PUY_S	Av. n° spp. per SU (±SD)	Av. n° org. per SU (±SD)	Av. H′ per SU (±SD)
1	*Psolus* sp.	5–25	10.2	21	5	7	11	6.9 (± 2.5)	48.5 (± 47)	1.4 (± 0.5)
2	*Spiochaetopterus* sp.	10–30	17.4	26	12	8	29	9.0 (± 2.7)	164.3 (± 146.6)	1.2 (± 0.5)
3	Serpulidae	5–30	7.4	20	2	5	5	7.0 (± 2.8)	54.3 (± 41.1)	1.3 (± 0.4)
4	*Loxechinus albus*	5–30	5.3	3	6	8	6	4.9 (± 2.6)	128.3 (± 119)	0.8 (± 0.4)
5	*Pentactella leonina*	5–15	4.4	16	-	3	-	5.7 (± 2.4)	106.5 (± 63.5)	0.9 (± 0.5)
6	Spirorbinae	5–30	26.7	12	30	48	25	11.7 (± 3.2)	123.9 (± 65.3)	1.7 (± 0.3)
7	*Chaetopterus variopedatus*	10–25	13.9	7	25	13	15	12.5 (± 2.8)	154.4 (± 88.7)	1.9 (± 0.3)
8	*Aulacomya atra*	5	4.9	-	13	3	5	3.1 (± 1.3)	96.6 (± 70.3)	0.5 (± 0.5)
9	*Thouarella* cfr. *Variabilis*	25–30	4.6	-	4	10	6	7.2 (± 2.1)	57.6 (± 30.7)	1.4 (± 0.4)
10	*Metridium* cfr. *senile*	5–15	5.1	-	-	7	15	6.6 (± 2.8)	166.3 (± 99.4)	1.0 (± 0.4)

ID, indicates the identified community; SU, Sampling Unit; SD, Standard Deviation; JAC, Jacaf; PUY_N, northern Puyuhuapi; PUY_C, central Puyuhuapi; PUY_S, Southern Puyuhuapi.

five of the aggregations proposed by Försterra et al. (2016), dominated by sponges, *D. dianthus*, polychaetes, bryozoans, and brachiopods, and the remaining four aggregations identified in Seno Magdalena by Betti et al. (2017). Community 4, represented by aggregations of the sea urchin *L. albus*, is widespread at the same depth range throughout northern Patagonia, with maximum densities comparable to those observed in the Puyuhuapi Fjord (Molinet et al., 2016; Contreras et al., 2019). Finally, three of the communities reported here are the first descriptions in the scientific literature for fjord ecosystems, and these were dominated by holothurians (1 and 5), and sea anemones (10).

From a wider perspective, the uniqueness of the fjords' ecosystems with respect to megafaunal assemblages is confirmed by the striking structural differences of the assemblages observed along the northern Chilean coasts (outside the fjord region) where kelp forests dominate the coastal hard seafloors, and barrens grounds are common (Pérez-Matus et al., 2007; Stotz et al., 2016). In these areas macroalgae result more frequent and only very few species (i.e., *L. albus*) are in common with the Patagonian fjords.

Fjord Functioning

Benthic diversity is clearly unevenly distributed with regard to bathymetry: shallow environments within the surface brackish layer are subject to high variability in environmental properties (in particular, seasonal temperature oscillations are much more variable than in the oceanic layer), and a generally lower salinity, and are therefore less populated by benthos than the underlying layers influenced more by oceanic water. Similar patterns have already been described in the Seno Magdalena Inlet (Betti et al., 2017). Halocline and thermocline are known to greatly influence the distribution in the fjords of sessile and vagile species, as well as their larval stages (e.g., Landaeta and Castro, 2006; Bustos et al., 2007; Landaeta et al., 2007; Meerhoff et al., 2013; Villalobos et al., 2021). Salinity horizontal gradients (due to increasing distance from freshwater inputs, such as rivers) are also known to influence the distribution of the species in the fjords, both on hardgrounds (Kuklinski, 2013; Villalobos et al., 2021) and soft seafloors (Betti et al., 2020). The low light penetration through the turbid brackish layer may also partially explain our observations of poor algal biodiversity, as well as the dominance by red crustose coralline algae below the surface layer: these are adapted to low light conditions and find little competition within the layer influenced by oceanic water, thus potentially explaining their wide and consistent coverage below the halocline.

From the mouth of the Puyuhuapi Fjord to the seaward end of the Jacaf Fjord, the composition of hard bottom macrobenthic communities show a significant constant decrease in terms of organisms' abundance, SR, Shannon, and Simpson indices. In particular, a slight decrease in abundance of passive predators (such as sea anemones) and active filter feeders (e.g., sponges, bryozoans, brachiopods, barnacles, the gastropod *C. dilatata,* and ascidians) is coupled with an increase in the diversity of passive filter feeders (e.g., other anthozoans, tubeworms, and holothurians). This is likely related to the variations in the characteristics of the water column throughout the fjord system. At the mouth of the Puyuhuapi Fjord, the oceanic waters from the Moraleda Channel are turbulent and rich in plankton, and thus favor passive predators such as sea anemones. Further along the fjord the amount of detritus increases, possibly favoring passive filter feeders such as holothurians that feed on larger particles. More extensive information is clearly required on dissolved and particulate organic matter cycling, local current regimes, turbidity, and other properties of the water column; these data might facilitate a better understanding of how the megabenthic communities are shaped along the fjords.

A Baseline for Further Studies

The analysis of the megabenthic communities in the present study represents a "snapshot" of the current status of the fjords. This provides an important baseline in an era of potentially significant shifts to these ecosystems caused both by direct anthropogenic stresses and the effects of climate change. Among the more direct impacts, both fishery and aquaculture activities are a constant threat to Patagonian fjord ecosystems;

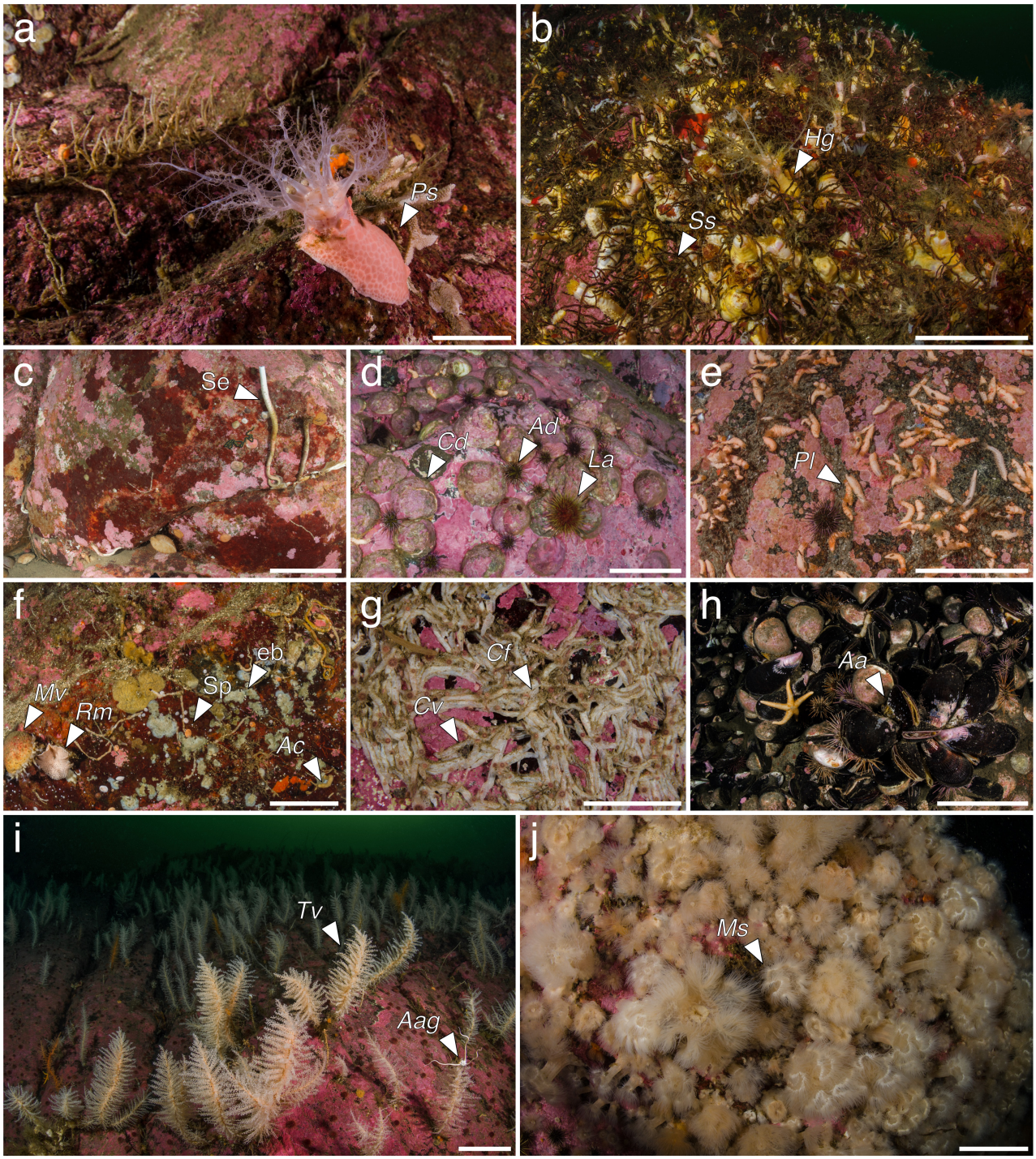

FIGURE 5 | Megabenthic communities identified along the Puyuhuapi–Jacaf fiord system. *Psolus* sp. (*Ps*) aggregations **(a)**; *Spiochaetopterus* sp. (*Ss*) and *Heterocucumis godeffroyi* (*Hg*) gardens **(b)**; Serpulidae (Se) aggregations **(c)**; *Loxechinus albus* (*La*) aggregations **(d)** including *Arbacia dufresnii* (*Ad*) and *Crepipatella dilatata* (*Cd*); *Pentactella leonina* (*Pl*) aggregations **(e)**; community of deep walls and crevices **(f)** including Spirorbinae (Sp), encrusting bryozoans (eb), *Axinella crinita* (*Ac*), *Reteporella magellensis* (*Rm*), and *Magellania venosa* (*Mv*); *Chaetopterus variopedatus* (*Cv*) aggregations **(g)** including *Clathrina fjordica* (*Cf*); *Aulacomya atra* (*Aa*) belt **(h)**, deep gorgonian forests **(i)** including *Thouarella* cfr. *variabilis* (*Tv*) and *Astrotoma agassizii* (*Aag*); *Metridium* cfr. *senile* (*Ms*) gardens **(j)**. Scale bars: **(a)** 2 cm; **(b–i)** 10 cm; **(j)** 5 cm.

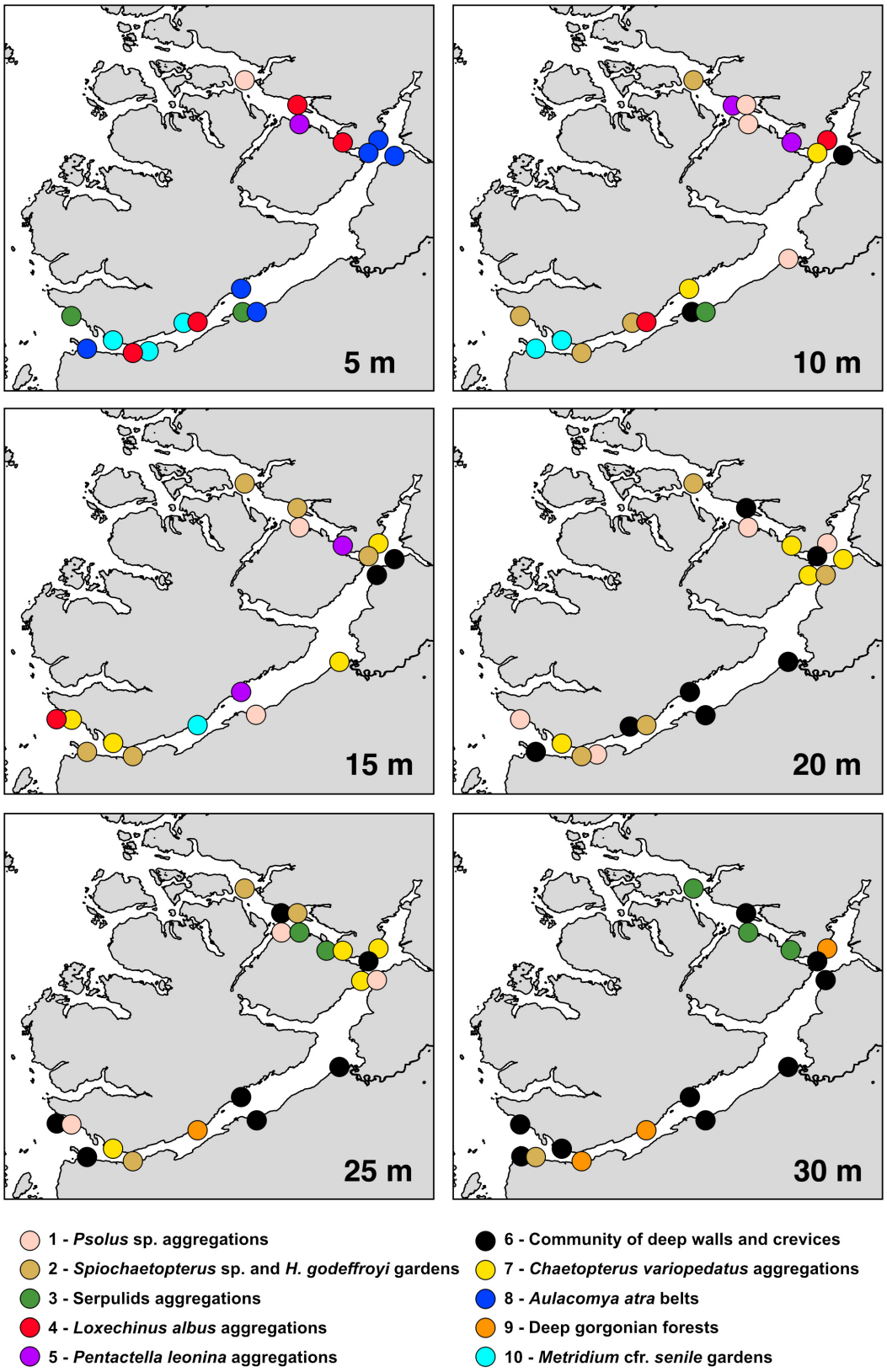

FIGURE 6 | Distribution maps. Spatial distribution of the 10 megabenthic communities identified in the cluster analysis at the six analyzed depths along the Puyuhuapi–Jacaf fiord system.

already some communities, such as *L. albus* aggregations, are declining as a result of intense fishing activities (Contreras et al., 2019). Moreover, a decreasing trend in hardgrounds megafaunal abundance due to aquaculture has been recorded (Häussermann et al., 2013). Regarding climate changes, increasing temperature, and sea levels will have relatively slow impacts on ecosystems, but other indirect effects are already evident. Recent studies have highlighted a historical decline in precipitation and streamflow in the fjords of northern Patagonia (down to 48° S) resulting from climate changes (i.e., Lara et al., 2008; Iriarte et al., 2016; Garreaud, 2018). This variation in freshwater inputs into fjords is likely to influence the volume and chemistry of the brackish surface layer, with consequences for phytoplankton communities that represent the base of the food chain for benthos. Clearly, fjords such as Puyuhuapi and Jacaf may act as a "sentinel" area that could highlight impacts of climate

TABLE 4 | Summary of the main species characterizing the 10 megabenthic communities identified in this study, with ecological information.

ID	Species	IndVal	Occupancy (%)	Tot. abundance	Av. density (org. m^{-2})	Max density (org. m^{-2})
1	*Psolus* sp.	0.23	46.6	3,190	42.29	1,022.86
2	*Spiochatopterus* sp.	0.35	63.1	12,572	166.68	1,885.71
	Heterocucumis godeffroyi	0.22	32.0	584	7.74	194.29
3	Serpulidae	0.15	16.7	249	3.30	108.57
	Chiton boweni	0.07	2.6	19	0.25	11.43
4	*Loxechinus albus*	0.42	25.3	2,901	38.46	1,211.43
	Crepipatella dilatata	0.19	6.0	414	5.49	422.86
	Arbacia dufresnii	0.18	58.7	1,361	18.04	257.14
	Cosmasterias lurida	0.09	7.2	40	0.53	22.86
5	*Pentactella leonina*	0.65	29.2	2,332	30.92	1,022.86
	Asterina fimbriata	0.38	5.1	79	1.05	68.57
	Asteroidea 1	0.08	7.2	44.85	0.59	56.29
6	Spirorbinae	0.36	52.7	8,632	114.44	1,605.71
	Encrusting Bryozoa	0.26	39.4	1,742	23.10	857.14
	Axinella crinita	0.16	40.4	446	5.91	68.57
	Desmophyllum dianthus	0.15	5.6	142	1.88	137.14
	Demospongiae 3	0.14	13.5	136	1.80	40.00
	Aspidostoma giganteum	0.13	4.4	137	1.82	148.57
	Reteporella magellensis	0.13	5.3	46	0.61	40.00
	Caryophyllia huinayensis	0.09	11.1	392	5.20	245.71
	Neopodospongia tupecomareni	0.09	8.4	113	1.50	80.00
	Magellania venosa	0.08	7.0	74	0.98	40.00
	Fusitriton magellanicus	0.07	7.0	49	0.65	28.57
7	*Chaetopterus variopedatus*	0.24	39.4	4,126	54.70	1,308.57
	Encrusting porifera	0.21	73.1	2,255	29.90	462.86
	Clathrina fiordica	0.13	24.1	382	5.06	262.86
	Demospongiae 5	0.12	8.6	117	1.55	62.86
	Scopalina sp.	0.10	13.9	208	2.76	51.43
	Actiniaria 3	0.10	1.4	89	1.18	177.14
	Nassarius gayi	0.09	10.0	206	2.73	177.14
	Didemnum studeri	0.09	17.9	248	3.29	245.71
	Tritonia challengeriana	0.08	10.4	56	0.74	17.14
	Demospongiae 1	0.05	0.7	6	0.08	17.14
8	*Aulacomya atra*	0.67	5.3	760	10.08	594.29
	Sessilia 1	0.34	3.9	852	11.30	1,600.00
	Anasterias antarctica	0.27	1.6	13	0.17	17.14
	Elminius kingii	0.27	1.6	319	4.23	685.71
9	*Thouarella* cfr. *variabilis*	0.77	7.7	292	3.87	194.29
	Brachiopoda 1	0.35	32.7	1,763	23.37	337.14
	Astrotoma agassizii	0.15	0.7	4	0.05	11.43
	Primnoella chilensis	0.09	13.5	77	1.02	28.57
	Demospongiae 4	0.07	1.4	7	0.09	11.43
10	*Metridium* cfr. *senile*	0.76	10.4	2,710	35.93	1,542.86
	Chiton sp.	0.11	5.1	42	0.56	45.71

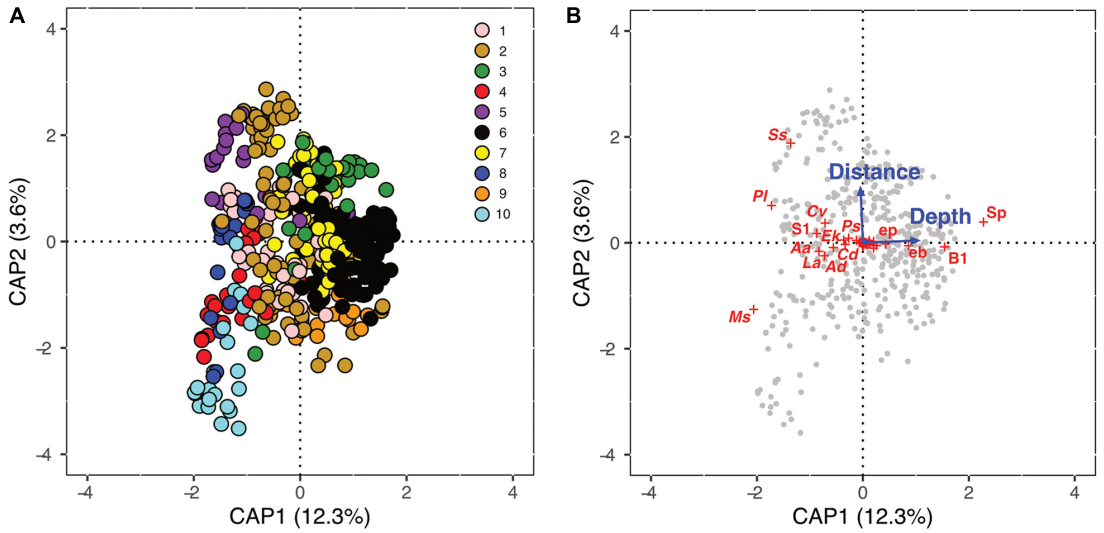

FIGURE 7 | Distance-based redundancy analysis (dbRDA). Results of the dbRDA performed over Bray–Curtis dissimilarity matrix of square-root transformed density data. Samples are represented as colored [**(A)**; color code is referred to **Figure 6**] or gray **(B)** dots, environmental variables represented as blue solid lines with arrows and species as red crosses. Names of the species with the highest scores are also shown in the biplot. *Aa*: *Aulacomya atra*, *Ad*: *Arbacia dufresnii*, B1: Brachiopoda 1, *Cd*: *Crepipatella dilatata*, *Cv*: *Chaetopterus variopedatus*, eb: encrusting bryozoans, *Ek*: *Elminius kingii*, ep: encrusting poriferans, *La*: *Loxechinus albus*, *Ms*: *Metridium* cfr. *senile*, *Pl*: *Pentactella leonina*, *Ps*: *Psolus* sp., S1: Sessilia 1, Sp: Spirorbinae, and *Ss*: *Spiochaetopterus* sp.

change if effectively monitored. A decrease in the influence of the brackish freshwater input could result in emergence of communities and species that characterize the oceanic layer, coupled with a reduction in communities typical of low salinity shallow waters, such as *A. atra* belts (found here only in the brackish layer), *L. albus* aggregations and *M.* cfr. *senile* gardens. The reduction of the typically turbid surface layer may cause an increase in light penetration through the water column, potentially increasing the presence and cover of non-Corallinales macroalgae. Reduced riverine input of organic material might induce a community shift in the Jacaf Fjord, particularly in communities characterized by large particle passive filter feeders such as *P. leonina* and *Psolus* sp. aggregations, and the communities dominated by gardens of *Spiochaetopterus* sp. and *H. godeffroyi*. Therefore, filter feeding Holothuroidea might represent a realistic and sensitive target species for monitoring activities, because a decrease in their abundance might provide an early warning of changes within fjord ecosystems.

A unique characteristic of Patagonian fjords is their latitudinal range; these fjords host many Antarctic species at the northern reach of their geographical distribution, and these species are clearly sensitive to global warming and associated effects of climate change. For instance, cold-water corals (CWCs) are known to be threatened both by warming and subsequent oxygen reduction within the water column (i.e., Jantzen et al., 2013). Therefore, the CWCs *C. huinayensis* and *D. dianthus*, both present in the Puyuhuapi Fjord, provide promising examples of potentially important sentinel species. On the contrary, brachiopods living in British Columbia fjords demonstrated a good tolerance to low oxygen concentrations (Tunnicliffe and Wilson, 1988); therefore, Chilean species such as *M. venosa* might be favored by an eventual oxygen reduction. Benthic macrofauna of European fjords showed an abrupted change in diversity, abundance and biomass at oxygen concentrations of approximately 2 mg O_2 liter^{-1}, with molluscs being the most tolerant species (Rosenberg, 1980).

Finally, ocean acidification, derived from CO_2 emissions generated by anthropic activities, is considered one of the major threats to marine organisms all over the World (Fabry et al., 2008); nevertheless, the effects of acidification on benthic communities is still unclear, due to a high variability of processes influencing the small-scale phenomenon (e.g., river discharges, upwelling, ice melting, eutrophication, and pollution) (e.g., Salisbury et al., 2008; Vargas et al., 2017). Establishing a baseline can help in detecting early effects of acidification on fjords ecosystems; calcifiers organisms, such as gastropods and bivalves (e.g., Thomsen et al., 2012), and also CWCs (Turley et al., 2007) may represent valid sentinel species. Globally, brachiopods appear to be less impacted by ocean acidification (Cross et al., 2015, 2016), probably thanks to compensating mechanisms (Cross et al., 2019), but microstructural changes have been observed in the shell of the Chilean fjords' species *M. venosa* (Ye et al., 2019). With warming and climate change seriously threatening these Chilean fjords benthic communities, it is imperative to reduce general stress levels on all organisms, and on the ecosystem itself. This can be achieved through effective management of other potential anthropogenic impacts, such as fishery and aquaculture activities. In order to protect benthic communities and fjord ecosystems from challenges brought about by climate change, comprehensive and continuous monitoring, and

mapping activities are an important tool to verify the effectiveness of these management plans.

DATA AVAILABILITY STATEMENT

The raw data supporting the conclusions of this article will be made available by the authors, without undue reservation.

AUTHOR CONTRIBUTIONS

All authors greatly contributed to the manuscript. FB: project coordination, sampling activity, and manuscript writing. FE: sampling activity, data analysis, conceptualization, and manuscript writing. GB: conceptualization, project coordination, and manuscript reviewing. AC and MB: data analysis and manuscript reviewing. AM: data analysis. PO: manuscript reviewing. GD: project coordination and manuscript reviewing. All authors contributed to the article and approved the submitted version.

SUPPLEMENTARY MATERIAL

The Supplementary Material for this article can be found online at: https://www.frontiersin.org/articles/10.3389/fmars.2021.635430/full#supplementary-material

Supplementary Material 1 | Biological characteristics of the 16 stations explored in this study.

Supplementary Material 2 | Comprehensive list of the species identified in this study.

Supplementary Material 3 | Species accumulation curves, built using the Mao Tau sample-based rarefaction method, and divided by macro-areas. S = southern portion of the Puyuhuapi Fjord, C = central portion of the Puyuhuapi Fjord; N = northern part of the Puyuhuapi Fjord, J = Jacaf Fjord. Shaded areas represent 95% confidence intervals.

REFERENCES

Bates, D., Sarkar, D., Bates, M. D., and Matrix, L. (2007). *The Lme4 Package. R Package Version 2.1.74*.

Bertolino, M., Costa, G., Bavestrello, G., Pansini, M., and Daneri, G. (2020). New sponge species from seno magdalena, puyuhuapi fjord and jacaf canal (Chile). *Eur. J. Taxon* 715, 1–49.

Bertolino, M., Costa, G., Reboa, A., Bavestrello, G., Pansini, M., Betti, F., et al. (2019). The sponge fauna of the seno magdalena and puyuhuapi fjord (Chile), with a description of two new species. *Zootaxa* 4623, 306–320. doi: 10.11646/zootaxa.4623.2.5

Betti, F., Bavestrello, G., Bo, M., Enrichetti, F., Loi, A., Wanderlingh, A., et al. (2017). Benthic biodiversity and ecological gradients in the Seno Magdalena (Puyuhuapi Fjord, Chile). *Estuar. Coast. Shelf Sci.* 198, 269–278. doi: 10.1016/j.ecss.2017.09.018

Betti, F., Castro, L. R., Bavestrello, G., Enrichetti, F., and Daneri, G. (2020). Distribution, abundance and ecological requirements of the benthic phase of *Munida gregaria* (Anomura; Munididae) in the Puyuhuapi Fjord (Chilean Patagonia). *Reg. Stud. Mar. Sci.* 40:101534. doi: 10.1016/j.rsma.2020.101534

Brattström, H., and Johanssen, A. (1983). Ecological and regional zoogeography of the marine benthic fauna of Chile. Report No. 49 of the Lund University Chile Expedition 1948-49. *Sarsia* 68, 233–339.

Bustos, C. A., BalbontÍn, F., and Landaeta, M. F. (2007). Spawning of the southern hake *Merluccius australis* (Pisces: Merlucciidae) in Chilean fjords. *Fish. Res.* 83, 23–32. doi: 10.1016/j.fishres.2006.08.010

Cañete, J. I., Leighton, G. L., and Aguilera, F. F. (1999). Polychaetes from Aysén Fjord, Chile: distribution, abundance and biogeographical comparison with the shallow soft-bottom polychaete fauna from Antarctica and the Magellan Province. *Sci. Mar.* 63, 243–252. doi: 10.3989/scimar.1999.63s1243

Cárdenas, J., Aldea, C., and Valdovinos, C. (2008). Chilean marine Mollusca of northern Patagonia collected during the Cimar-10 fjords cruise. *Gayana* 72, 202–240.

Contreras, C., Niklitschek, E., Molinet, C., Díaz, P., and Díaz, M. (2019). Fishery-induced reductions in density and size truncation of sea urchin Loxechinus albus affects diversity and species composition in benthic communities. *Estuar. Coast. Shelf Sci.* 219, 409–419. doi: 10.1016/j.ecss.2019.02.030

Cross, E. L., Harper, E. M., and Peck, L. S. (2019). Thicker shells compensate extensive dissolution in brachiopods under future ocean acidification. *Environ. Sci. Technol.* 53, 5016–5026. doi: 10.1021/acs.est.9b00714

Cross, E. L., Peck, L. S., and Harper, E. M. (2015). Ocean acidification does not impact shell growth or repair of the Antarctic brachiopod *Liothyrella uva* (Broderip, 1833). *J. Exp. Mar. Biol. Ecol.* 426, 29–35. doi: 10.1016/j.jembe.2014.10.013

Cross, E. L., Peck, L. S., Lamare, M. D., and Harper, E. M. (2016). No ocean acidification effects on shell growth and repair in the New Zealand brachiopod *Calloria inconspicua* (Sowerby, 1846). *ICES J. Mar. Sci.* 73, 920–926. doi: 10.1093/icesjms/fsv031

Daneri, G., Montero, P., Lizárraga, L., Torres, R., Iriarte, J. L., Jacob, B., et al. (2012). Primary Productivity and heterotrophic activity in an enclosed marine area of central Patagonia (Puyuhuapi channel; 44° S, 73° W). *Biogeosci. Discuss.* 9, 5929–5968.

DGA. (2003). *Dirección General de Aguas*. Chile. Available online at: http://www.dga.cl.

Dominguez-Carrió, C. (2018). *ROV-Based Ecological Study and Management Proposal for the Offshore Marine Protected Area of Cap de Creus (NW Mediterranean)*. Ph.D. thesis. Barcelona: Universitat de Barcelona.

Dufrêne, M., and Legendre, P. (1997). Species assemblages and indicator species: the need for a flexible asymmetrical approach. *Ecol. Monogr.* 67, 345–366. doi: 10.2307/2963459

Escribano, R., Fernández, M., and Aranís, A. (2003). Physical-chemical processes and patterns of diversity of the Chilean eastern boundary pelagic and benthic marine ecosystems: an overview. *Gayana* 67, 190–205.

Fabry, V. J., Seibel, B. A., Feely, R. A., and Orr, J. C. (2008). Impacts of ocean acidification on marine fauna and ecosystem processes. *ICES J. Mar. Sci.* 65, 414–432. doi: 10.1093/icesjms/fsn048

Försterra, G., Häussermann, V., and Laudien, J. (2016). "Animal forests in the Chilean fjords: discoveries, perspectives and threats in shallow and deep waters," in *Marine Animal Forests*, eds S. Rossi, L. Bramanti, A. Gori, and C. Orejas (Cham: Springer).

Försterra, G., and Häussermann, V. (2003). First report on large scleractinian (Cnidaria: Anthozoa) accumulations in cold-temperate shallow water of south Chilean. *Zool. Verh.* 345, 117–128.

Garreaud, R. D. (2018). Record-breaking climate anomalies lead to severe drought and environmental disruption in western Patagonia in 2016. *Clim. Res.* 74, 217–229. doi: 10.3354/cr01505

Gattuso, J. P., Frankignoulle, M., and Wollast, R. (1998). Carbon and carbonate metabolism in coastal aquatic ecosystems. *Ann. Rev. Ecol. Syst.* 29, 405–434. doi: 10.1146/annurev.ecolsys.29.1.405

González, H. E., Calderón, M. J., Castro, L., Clement, A., Cuevas, L. A., Daneri, G., et al. (2010). Primary production and plankton dynamics in the Reloncaví fjord and the interior sea of Chiloé, Northern Patagonia, Chile. *Mar. Ecol. Prog. Ser.* 402, 13–30. doi: 10.3354/meps08360

González, H. E., Castro, L., Daneri, G., Iriarte, J. L., Silva, N., Vargas, C. A., et al. (2011). Seasonal plankton variability in Chilean Patagonia fjords: carbon flow through the pelagic food web of Aysen Fjord and plankton dynamics in the

Moraleda Channel basin. *Cont. Shelf Res.* 31, 225–243. doi: 10.1016/j.csr.2010.08.010

Hammer, Ø, Harper, D. A. T., and Ryan, P. D. (2011). *Reference Manual of PAST, Paleontological Statistics, Version 2.09. Natural History Museum*. Oslo: University of Oslo.

Häussermann, V., and Försterra, G. (2007). Large assemblages of cold-water corals in Chile: a summary of recent findings and potential impacts. *Bull. Mar. Sci.* 81, 195–207.

Häussermann, V., and Försterra, G. (2009). *Marine Benthic Fauna of Chilean Patagonia*. Santiago: Nature in Focus.

Häussermann, V., Försterra, G., Melzer, R. R., and Meyer, R. (2013). Gradual changes of benthic biodiversity in Comau Fjord, Chilean Patagonia – lateral observations over a decade of taxonomic research. *Spixiana* 36, 161–171.

Howe, J. A., Austin, W. E. N., Forwick, M., Paetzel, M., Harland, R., and Cage, A. G. (2010). Fjord systems and archives: a review. *Geol. Soc. Lond. Special Publ.* 344, 5–15.

Hromic, T., Ishman, S., and Silva, N. (2006). Benthic foraminiferal distributions in Chilean fjords: 47 S to 54 S. *Mar. Micropaleontol.* 59, 115–134. doi: 10.1016/j.marmicro.2006.02.001

Iriarte, J., León-Muñoz, J., Marcé, R., Clément, A., and Lara, C. (2016). Influence of seasonal freshwater streamflow regimes on phytoplankton blooms in a Patagonian fjord. *New Zeal. J. Mar. Freshw. Res.* 51, 304–315. doi: 10.1080/00288330.2016.1220955

Jantzen, C., Häussermann, V., Försterra, G., Laudien, J., Ardelan, M., Maier, S., et al. (2013). Occurrence of a cold-water coral along natural pH gradients (Patagonia, Chile). *Mar. Biol.* 160, 2597–2607. doi: 10.1007/s00227-013-2254-0

Kuklinski, P. (2013). Biodiversity and abundance patterns of rock encrusting fauna in a temperate fjord. *Mar. Environ. Res.* 87-88, 61–72. doi: 10.1016/j.marenvres.2013.03.005

Landaeta, M. F., and Castro, L. R. (2006). Larval distribution and growth of the rockfish, *Sebastes capensis* (Sebastidae, Pisces), in the fjords of southern Chile. *ICES J. Mar. Sci.* 63, 714–724. doi: 10.1016/j.icesjms.2006.01.002

Landaeta, M. F., Martinez, R. A., Bustos, C. A., and Castro, L. R. (2007). Distribution of microplankton and fish larvae related to sharp clines in a Patagonian fjord. *Rev. Biol. Mar. Oceanogr.* 48, 401–407. doi: 10.4067/s0718-19572013000200020

Lara, A., Villalba, R., and Urrutia, R. A. (2008). 400-year tree-ring record of the Puelo River summer–fall streamflow in the Valdivian Rainforest eco-region, Chile. *Clim. Change* 86, 331–356. doi: 10.1007/s10584-007-9287-7

Leps, M., Tonkin, J. D., Dahm, V., Haase, P., and Sundermann, A. (2015). Disentangling environmental drivers of benthic invertebrate assemblages: the role of spatial scale and riverscape heterogeneity in a multiple stressor environment. *Sci. Total Environ.* 536, 546–556. doi: 10.1016/j.scitotenv.2015.07.083

Lopez, P., Chevallier, P., Favier, V., Pouyaud, B., Ordenes, F., and Oerlemans, J. (2010). A regional view of fluctuations in glacier length in southern South America. *Glob. Planet. Change* 71, 85–108. doi: 10.1016/j.gloplacha.2009.12.009

Magurran, A. E. (2013). *Measuring Biological Diversity*. Hoboken, NJ: Wiley.

Meerhoff, E., Castro, L., and Tapia, F. (2013). Influence of freshwater discharges and tides on the 354 abundance and distribution of larval and juvenile *Munida gregaria* in the Baker river estuary, Chilean Patagonia. *Cont. Shelf Res.* 61, 1–11. doi: 10.1016/j.csr.2013.04.025

Melzer, R. R., Schrodl, M., Haussermann, V., Forsterra, G., and Bravo, M. F. M. (2006). Pycnogonids on cnidarians at fjord Comau, Southern Chile: a report on 2005 SCUBA collections. *Spixiana* 29, 237–242.

Molinet, C., Barahona, N., Díaz, M., Díaz, P. A., Millanao, M. O., Araya, P., et al. (2016). Using drift video transects and maximum likelihood geostatistics for quantifying and monitoring exploited subpopulations of Loxechinus albus at a mesoscale. *Mar. Coast. Fish.* 8, 70–80. doi: 10.1080/19425120.2015.1121939

Montero, P., Coppari, M., Betti, F., Bavestrello, G., and Daneri, G. (2021). Feeding of *Aulacomya atra* under different organic matter sources (autochthonous and allochthonous) in a Chilean Patagonia fjord ecosystem. *Front. Mar. Sci.* doi: 10.3389/fmars.2021.612406

Mutschke, E., and Gorny, M. (1999). The benthic decapod fauna in the channels and fjords along the South Patagonian Icefield, Southern Chile. *Sci. Mar.* 63, 315–319. doi: 10.3989/scimar.1999.63s1315

O'Hara, R., and Kotze, J. (2010). Do not log-transform count data. *Met. Ecol. Evol.* 1, 118–122. doi: 10.1111/j.2041-210x.2010.00021.x

Oksanen, J., Blanchet, F. G., Kindt, R., Legendre, P., Minchin, P. R., O'Hara, R. B., et al. (2016). *Package "Vegan", Version 2.3–5. CRAN Repository, 1-295*.

Pantoja, S., Iriarte, J. L., and Daneri, G. (2011). Oceanography of the Chilean Patagonia. *Cont. Shelf Res.* 31, 149–153. doi: 10.1016/j.csr.2010.10.013

Pérez-Matus, A., Ferry-Graham, L. A., Cea, A., and Vásquez, A. (2007). Community structure of temperate reef fishes in kelp-dominated subtidal habitats of northern Chile. *Mar. Freshw. Res.* 58, 1069–1085. doi: 10.1071/mf06200

Pérez-Santos, I., Castro, L., Ross, L., Niklitschek, E., Mayorga, N., Cubillos, L., et al. (2018). Turbulence and hypoxia contribute to dense biological scattering layers in a Patagonian fjord system. *Ocean Sci.* 14, 1185–1206. doi: 10.5194/os-14-1185-2018

Prado-Fiedler, R., and Castro, J. S. (2008). Aporte fluvial y pluvial de nitrogeno y fosforo al fiordo Aysén y canales Jacaf-Ventisquero-Puyuhuapi, *Ciencia y Tecnologia del Mar*. 31, 75–95.

Roberts, D. W. (2016). *Labdsv: Ordination and Multivariate Analysis for Ecology. R Package Version 1.8–0*.

Rosenberg, R. (1980). "Effect of oxygen deficiency on benthic macrofauna in fjords," in *Fjord Oceanography*, eds Freeland, et al. (New York, NY: Plenum Press), 499–514. doi: 10.1007/978-1-4613-3105-6_45

Rossi, S., Bramanti, L., Gori, A., and Orejas, C. (Eds.) (2017). *Marine Animal Forests: the Ecology of Benthic Biodiversity Hotspots (pp. 1-1366)*. Cham: Springer International Publishing.

Salisbury, J., Green, M., Hunt, C. W., and Campbell, J. (2008). Coastal acidification by rivers: a threat to shellfish? *Eos* 89, 513–528. doi: 10.1029/2008eo500001

Sánchez, N., Gonzales, H. E., and Iriarte, J. L. (2011). Trophic interactions of pelagic crustaceans in Comau fjord (Chile): their role in the food web structure. *J. Plankton Res.* 33, 1212–1229. doi: 10.1093/plankt/fbr022

Schmidt, A., and Brandt, A. (2001). The tanaidacean fauna of the Beagle Channel (southern Chile) and its relationship to the fauna of the Antarctic continental shelf. *Antarct. Sci.* 13, 420–429. doi: 10.1017/s095410200100058x

Schneider, W., Pérez-Santos, I., Ross, L., Bravo, L., Seguel, R., and Hernández, F. (2014). On the hydrography of Puyuhuapi Channel, Chilean Patagonia. *Prog. Oceanogr.* 129, 8–18. doi: 10.1016/j.pocean.2014.03.007

Schwabe, E., Försterra, G., Häussermann, V., Melzer, R. R., and Schroedl, M. (2006). Chitons (Mollusca: Polyplacophora) from the southern Chilean Comau Fjord, with reinstatement of *Tonicia calbucensis* Plate, 1897. *Zootaxa* 1341, 1–27. doi: 10.11646/zootaxa.1341.1.1

Shannon, C. E. (1948). A mathematical theory of communication. *Bell Syst. Tech. J.* 27, 379–423.

Silva, N., and Palma, S. (2008). "The CIMAR program in the austral Chilean channels and fjords," in *Progress in the Oceanographic Knowledge of Chilean Interior Waters, From Puerto Montt to Cape Horn*, eds N. Silva and S. Palma (Valparaíso: Comité Oceanográfico Nacional - Pontificia Universidad Católica de Valparaíso), 11–15.

Sinniger, F., and Häussermann, V. (2009). Zoanthids (Cnidaria: Hexacorallia: Zoantharia) from shallow waters of the southern Chilean fjord region, with descriptions of a new genus and two new species. *Org. Divers. Evol.* 9, 23–36. doi: 10.1016/j.ode.2008.10.003

Stotz, W. B., Aburto, J., Caillaux, L. M., and González, S. A. (2016). Vertical distribution of rocky subtidal assemblages along the exposed coast of north-central Chile. *J. Sea Res.* 107, 34–47. doi: 10.1016/j.seares.2015.11.006

Thomsen, J., Casties, I., Pansch, C., Körtzinger, A., and Melzner, F. (2012). Food availability outweighs ocean acidification effects in juvenile *Mytilus edulis*: laboratory and field experiments. *Global Change Biol.* 19, 1017–1027. doi: 10.1111/gcb.12109

Tunnicliffe, V., and Wilson, K. (1988). Brachiopod populations: distribution in fjords of British Columbia (Canada) and tolerance of low oxygen concentrations. *Mar. Ecol.* 47, 117–128. doi: 10.3354/meps047117

Turley, C. M., Roberts, J. M., and Guinotte, J. M. (2007). Corals in deep-water: will the unseen hand of ocean acidification destroy cold-water ecosystems? *Coral Reefs* 26, 445–448. doi: 10.1007/s00338-007-0247-5

Vargas, C. A., Lagos, N. A., Lardies, M. A., Duarte, C., Manriquez, P. H., Aguilera, V. M., et al. (2017). Species-specific responses to ocean acidification should account for local adaptation and adaptive plasticity. *Nat. Ecol. Evol.* 1:84.

Villalobos, V., Valdiviav, N., Försterra, G., Ballyram, S., Espinoza, J. P., Burgos-Andrade, K., et al. (2021). Depth-dependent diversity patterns of rocky subtidal macrobenthic communities along a temperate fjord in Northern Chilean Patagonia. *Front. Mar. Sci.* 8:635855.

Walsh, J. J. (1991). Importance of continental margins in the marine biogeochemical cycling of carbon and nitrogen. *Nature* 350, 53–55. doi: 10.1038/350053a0

Warton, D. I., and Hui, F. K. (2011). The arcsine is asinine: the analysis of proportions in ecology. *Ecology* 92, 3–10. doi: 10.1890/10-0340.1

Ye, F., Jurikova, H., Angiolini, L., Brand, U., Crippa, G., Henkel, D., et al. (2019). Variation in brachiopod microstructure and isotope geochemistry under low-pH–ocean acidification conditions. *Biogeosciences* 16, 617–642. doi: 10.5194/bg-16-617-2019

Conflict of Interest: The authors declare that the research was conducted in the absence of any commercial or financial relationships that could be construed as a potential conflict of interest.

Publisher's Note: All claims expressed in this article are solely those of the authors and do not necessarily represent those of their affiliated organizations, or those of the publisher, the editors and the reviewers. Any product that may be evaluated in this article, or claim that may be made by its manufacturer, is not guaranteed or endorsed by the publisher.

frontiers in Marine Science

BRIEF RESEARCH REPORT
published: 29 July 2021
doi: 10.3389/fmars.2021.612406

Feeding of *Aulacomya atra* Under Different Organic Matter Sources (Autochthonous and Allochthonous) in a Chilean Patagonia Fjord Ecosystem

*Paulina Montero[1,2], Martina Coppari[3], Federico Betti[4], Giorgio Bavestrello[4] and Giovanni Daneri[1,2]**

[1] Centro de Investigación en Ecosistemas de la Patagonia (CIEP), Coyhaique, Chile, [2] Centro de Investigación Oceanográfica COPAS Sur-Austral, Universidad de Concepción, Concepción, Chile, [3] Dipartimento di Scienze della Vita e dell'Ambiente, Università Politecnica delle Marche, Ancona, Italy, [4] Dipartimento di Scienze della Terra, dell'Ambiente e della Vita, Università degli Studi di Genova, Genoa, Italy

OPEN ACCESS

Edited by:
Angel Borja, Technological Center Expert in Marine and Food Innovation (AZTI), Spain

Reviewed by:
José Lino Vieira De Oliveira Costa, University of Lisbon, Portugal
Ursula Felicitas Marianne Witte, University of Aberdeen, United Kingdom

***Correspondence:**
Giovanni Daneri
gdaneri@ciep.cl

Specialty section:
This article was submitted to Marine Ecosystem Ecology, a section of the journal Frontiers in Marine Science

Received: *30 September 2020*
Accepted: *30 June 2021*
Published: *29 July 2021*

Citation:
Montero P, Coppari M, Betti F, Bavestrello G and Daneri G (2021) Feeding of Aulacomya atra Under Different Organic Matter Sources (Autochthonous and Allochthonous) in a Chilean Patagonia Fjord Ecosystem. Front. Mar. Sci. 8:612406. doi: 10.3389/fmars.2021.612406

Aulacomya atra is an active suspension feeder, spatially dominant in the shallow-water hard-bottom benthic communities of the Chilean Patagonia fjords. In this region, the vertical flux of autochthonous organic matter (OM) reaching the benthos is augmented by allochthonous OM both from a terrestrial origin and from intensive salmon farming. This mixed pool of OM represents a potential source of food for a variety of benthic consumers, but to date little is known about the degree of utilization of these materials by filter feeders organisms. In this context, feeding experiments on *A. atra* in Puyuhuapi Fjord, Chilean Patagonia, were conducted during summer and winter 2018–2019. These experiments were designed to determine ingestion rates (IR) of *A. atra* fed with autochthonous (bacterial and microplanktonic community) and allochthonous (salmon food pellet) OM. Additionally, samples of *A. atra* tissues and suspended particulate organic matter (SPOM) were taken from the study area for stable isotope analysis. Data from laboratory experiments indicated that *A. atra* can feed on both autochthonous and allochthonous OM, but higher IR were detected in individuals fed with salmon food pellets. Because the IR is sensitive to food particle density rather than specific type of food, diet preferences of *A. atra* in feeding experiments could not be determined. Stable isotope analyses indicate that *A. atra* in natural environment preferentially exploits food with an isotopic signal corresponding to autochthonous OM, highlighting the primary role of phytoplankton carbon in their diet. Extensive utilization of terrestrially derived OM is therefore unlikely, although utilization of OM derived from salmon farming is not precluded because of the overlap in isotopic signal between food pellets and marine plankton.

Keywords: *Aulacomya atra*, ingestion rate, stable isotopes, autochthonous and allochthonous food, Puyuhuapi Fjord

INTRODUCTION

In aquatic ecosystems, animals that feed on particles suspended in the water are collectively known as filter feeders (Jørgensen, 1990). Bivalves tend to be the dominant suspension feeders in benthic communities (Sebens et al., 2016; Filgueira et al., 2019), filtering large volumes of water whilst retaining a wide range of particle sizes (ca. 4–35 μm diameter) (Voudanta et al., 2016). By filtering water to satisfy their nutritional demands, these organisms remove substantial quantities of microscopic particles from seston, such as bacteria, phytoplankton, detritus, and suspended sediments (Wright et al., 1982; Langdon and Newell, 1996; Prins et al., 1998; Kreeger and Newell, 2000; Cranford et al., 2011). Therefore, these bottom dwelling organisms process large amounts of suspended organic matter (OM) and are often major agents of pelagic-benthic coupling and nutrient cycling (Norkko et al., 2001). The total amount of OM consumed by bivalves is largely determined by their ingestion rate (IR) (Riisgård, 1988) which is a parameter of great ecological importance, and critical to the understanding of their impact on particles fluxes in coastal environments (Winter, 1978). Filter feeding behavior in bivalves is known to be responsible for fluctuations in both the abundance and the composition of seston (Bayne, 1998; Prins et al., 1998). Several studies have suggested that bivalve grazing can control phytoplankton abundance (Cloern, 1982; Prins et al., 1998; Lonsdale et al., 2009; Lucas et al., 2016), favor small phytoplankton organisms (Greene et al., 2011; Jacobs et al., 2016; Cranford, 2019) and decrease phytoplankton production (Dolmer, 2000). Phytoplankton is clearly a major source of nutrition for these organisms (Vaughn and Hoellein, 2018), but bacteria and detritus from terrestrial origins have also been described as important food source for bivalves during periods of low phytoplankton abundance (Langdon and Newell, 1990; Kreeger and Newell, 1996). Mussels are also known to filter small particles of salmon feed (Reid et al., 2010; MacDonald et al., 2011) and fecal pellets from salmon farming areas (Reid et al., 2010), incorporating this waste material as a food source (Gao et al., 2006; Redmond et al., 2010; Handå et al., 2012a,b). Several studies have indicated that bivalves growing adjacent to salmon farming areas remove OM advected from cages by increasing their growth rates (Lander et al., 2004; Peharda et al., 2007; Sarà et al., 2009) and helping to reduce the negative ecological impacts of the salmon industry (Lefebvre et al., 2000; MacDonald et al., 2011) such as the increase in load of OM in the water column and seafloor (Quiñones et al., 2019).

In Chilean Patagonian fjords, salmon farming represents the principal aquaculture activity (Buschman et al., 2006). This industry releases large quantities of organic and inorganic wastes (uneaten feed, feces and excretory products) that modify the particulate and dissolved materials in the water column (Quiñones et al., 2019) and represent a permanent input of allochthonous OM into the local fjord ecosystem (Iriarte et al., 2014). This allochthonous OM, together with high levels of autochthonous OM produced by phytoplankton in Chilean fjords (Montero et al., 2011, 2017a,b), provides a heterogeneous pool of organic substrates available as food for benthic consumers.

Several studies have addressed trophic structure of benthic communities (Mayr et al., 2011; Zapata-Hernández et al., 2014; Andrade et al., 2016; Quiroga et al., 2016), but little information is available on the ecological role of bivalves species in the structure and functioning of Patagonian fjord ecosystems. One of the key suspension feeder in the Patagonian fjords is the ribbed mussel *Aulacomya atra* (Molina, 1782), which normally inhabits protected and semi-protected shallow rocky shores (Betti et al., 2017), and is often found in close vicinity to salmon farms. Despite its importance in bentho-pelagic carbon fluxes of the Patagonian fjords, little is known about the feeding behavior of *A. atra*, including its potential role in processing the uneaten salmon feed. The aim of the present study was to determine the capacity of *A. atra* to assimilate and ingest OM derived both from salmon feed (allochthonous), and from a phytoplankton and bacterial origin (autochthonous) by means of stable isotope analysis and experimental feeding studies conducted in Puyuhuapi Fjord, Chilean Patagonia, during summer and winter periods between 2018 and 2019.

MATERIALS AND METHODS

Study Area and Sampling of *Aulacomya atra*

The study was conducted in Puyuhuapi Fjord which extends for about 90 km between 44°19′ S and 44°57′ S in northern Chilean Patagonia (**Figure 1**), and runs in a N–NE direction, connecting directly to the open sea via the Moraleda Channel at its mouth, and through the Jacaf Channel near the head (Schneider et al., 2014). The hydrography of this area is characterized by an estuarine type of circulation with a vertical two layer structure, comprised of a highly variable 5–10 m deep freshwater layer overlying a more uniform, saltier sub-pycnocline layer (Schneider et al., 2014 and references therein). The deeper saline water originates from Sub-Antarctic Surface Water (SAAW) characteristic of open ocean environments in these latitudes (Chaigneau and Pizarro, 2005). The freshwater upper layer is mainly supplied by the Cisnes River and by rain runoff (Schneider et al., 2014). The surface outflow of buoyant freshwater in the fjord carries high concentrations of silicic acid derived from rivers, while SAAW waters are typically enriched with nitrate and orthophosphate (Silva, 2008). Surface salinity is higher in the north than in the south, suggesting an intrusion of oceanic surface waters into the north of Puyuhuapi Fjord through the Jacaf Channel, forced by westerly winds (Schneider et al., 2014).

Aulacomya atra was collected in the Puyuhuapi Fjord during summer (February) and winter (July) in 2 years, 2018 and 2019 (**Supplementary Table 1**). Samples of *A. atra* for both feeding experiments and stable isotopes analysis were collected by scuba diving at depths ranging from 5 to 10 m at several sampling stations (**Figure 1**). After collection, mussels for the feeding experiment were transferred to the field laboratory, cleaned of epibionts and debris, and maintained in a 200-liters seawater tank with constant aeration and at ambient temperature prior to the experimental protocols (approximately 24 h after collection).

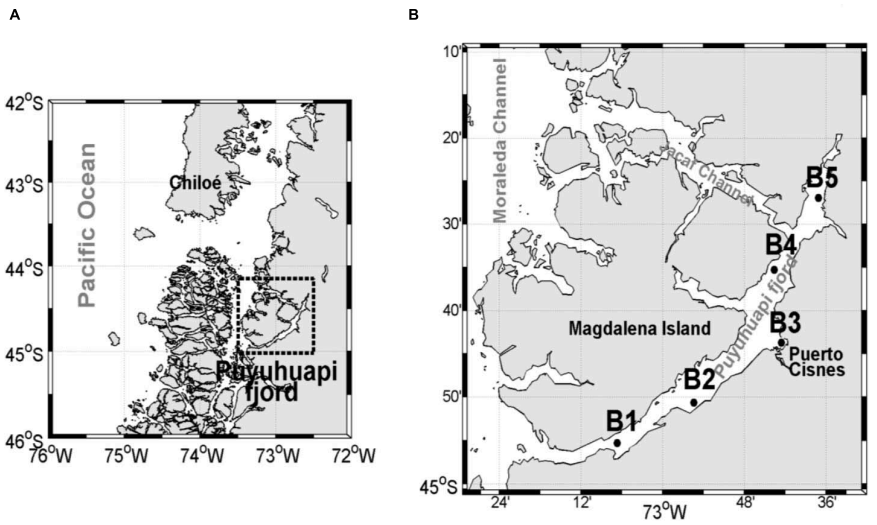

FIGURE 1 | (A) Location of the study area in Chilean Patagonia, **(B)** close-up of the study area with the position of the sampling stations along the Puyuhuapi Fjord.

Mussels for the stable isotopes analysis were treated as described in detail in section "Stable Isotopes."

Feeding Experiments

The feeding experiments were performed using plastic aquaria, each of 6-liters capacity and provided with a pumped air supply (3 L/min). Three different type of food (treatments) were tested: bacterial community, planktonic community, and allochthonous OM derived from salmon food pellets.

The first treatment – referred here as the bacterial community treatment (BC_T) – was prepared by gravity filtering seawater onto 22-μm mesh to remove large zooplankton and microphytoplankton. A peristaltic pump was then used to gently filter this water through 0.8-μm pore size sterile membrane filters (Millipore) in order to separate bacteria from the rest of the planktonic community (including potential predators). The second treatment – referred here as planktonic community treatment (PC_T) – was prepared by gravity filtering seawater onto 150-μm mesh to remove larger plankton. The third treatment consisted of 0.2-μm filtered seawater amended with salmon food pellets (SFP_T). This treatment was prepared by gravity filtering seawater onto 22-μm mesh. Then, a peristaltic pump was used to gently filter this water through 0.2-μm sterile membrane filters (Millipore), in order to remove bacteria and other microorganisms. Finally, 1 g of salmon food pellet was finely ground into particles <1 mm using a mortar; this powder was then added to the filtered water. For each treatment, an experimental and a control aquaria were used. At the beginning of each experiment, both aquaria were filled with the filtered water (BC_T, PC_T, SFP_T water, depending on the treatment) and one specimen of *A. atra* was placed in each experimental aquarium, whilst the control ones remained without individuals. The experiments began as soon as *A. atra* valves opened. Triplicate water samples of 500 mL were taken from experimental and control aquaria at the initial time ($t1$), and again 1 h later ($t2$). Samples from $t1$ and $t2$ were processed for particulate organic carbon (POC) analyses. Total POC was measured by filtering 500 mL water samples on pre-combusted GF/F glass microfiber filters (4 h at 450°C) which were then frozen at –20°C until analysis. Prior to the analysis, filters were defrosted and acidified with HCL. After acidification, the HCL was removed and the filters were dried at 50°C for 24 h. Filters were analyzed at the Laboratory of Biogeochemistry and Applied Stable Isotopes (LABASI, PUC), Chile.

The rate of change in POC concentration from control (kc) and experimental (kg) aquaria was calculated according to Frost (1972) equation:

$$C_2 = C_1 e^{k(t2-t1)}$$

where C_1 and C_2 are POC concentrations (mg C L^{-1}) at initial ($t1$) and final time ($t2$), respectively, and k (h^{-1}) corresponds to the rate of change in POC concentration during the experiments. The grazing coefficient is g (h^{-1}) and was calculated according to Ribes et al. (1998) equation:

$$g = kc - kg$$

where kc and kg are the rates of change in POC concentration from control and experimental aquaria, respectively.

The clearance rate, CR (volume swept clear per individual per time) was calculated according to Ribes et al. (1998) equation:

$$CR = V\left(\frac{g}{n}\right)$$

where V is the volume of the aquaria (L), n is the number of *A. atra* in the experimental aquaria and g is the grazing coefficient (h^{-1}). For comparative purposes, clearance rates were also standardized (CR_s) to constant biomass of 1 g *A. atra* dry flesh weight (Cranford et al., 2011). Finally, the ingestion rate, I (particles ingested per individual per time) was calculated as

the product of CR (L individual^{-1} h^{-1}) and the concentration of POC (mg L^{-1}) using Ribes et al. (1998) formula:

$$I = CR \times C$$

where C is the initial POC concentration (C_1) in the experimental aquaria, calculated according to the following equation (Frost, 1972; Saiz, 1993):

$$C = \frac{C_1[e\{(kc - kg)\ (t2 - t1)\} - 1]}{(t2 - t1)\ (kc - kg)}$$

When the rate of change in POC concentrations was higher in experimental (*kg*) than in control (*kc*) aquaria, negative grazing coefficients (*g*) were obtained. Negative *g* are reported in **Table 1**; according to previous studies, negative values were set up to zero (Strom and Fredrickson, 2008; Stoecker et al., 2014, 2015; Anderson et al., 2018; Menden-Deuer et al., 2018; Anderson and Harvey, 2019), in order to calculate the mean and standard error of grazing in each treatment, and subsequently to estimate means and standard deviations in CR and IR. The significance of grazing (*g* values > 0) for each food type (treatments) was tested by comparing the rate of change in POC concentration from control (*kc*) and experimental (*kg*) aquaria using a two-tailed Wilcoxon test. Individual values of *kc* and *kg* for each experiment (**Table 1**) correspond to the average of three replicates obtained from control (**Supplementary Table 1**) and experimental (**Supplementary Table 2**) aquaria, respectively. Wilcoxon test was applied to seven experiments conducted under PC_T (autochthonous source), nine under BC_T (autochthonous source), and five under SFP_T (allochthonous source). In this last case, Wilcoxon test considered an alpha = 0.1 due the low number of sampling points.

To examine the relationship between CR and size/weight of the individuals under study, after each experiment, shell lengths and dry (24 h at 60°C) flesh weights were determined for each individual.

The non-parametric Kruskal–Wallis test (H) was used to examine differences in *g*, CR and IR between the different food sources (treatments). Kolmogorov-Smirnov test (K-S) was used to examine seasonal differences in CR and CRs.

Stable Isotopes

Three specimens of *A. atra* were collected from each sampling station for stable isotopes analysis in the study area (**Figure 1**). After collection, mussels were maintained in filtered seawater (0.2 μm) in a plastic container for 24 h and were then rinsed with distilled water and frozen at –20°C. Frozen samples were thawed and dissected. *A. atra* tissues were lyophilized and grounded prior to analysis.

In order to measure the stable isotope composition in suspended particulate organic matter (SPOM), samples were monthly collected from three depths (2, 10, and 20 m) from March to May 2018 and from July 2018 to February 2019 at sampling station B4. In addition, samples from 2 and 20 m depth were obtained from station B3 between March and May 2018 and in July 2018. Water samples (5 L) were filtered under gentle vacuum through GF/F filters (pre combusted for 4 h at 450°C) and refrigerated prior to analysis. The isotopic signal from salmon food pellets used in the feeding experiments of February/July 2018 and February 2019 was also measured. Tissues, filters and salmon food pellets samples were analyzed at the Laboratory of Biogeochemistry and Applied Stable Isotopes (LABASI, PUC, Chile) with an Isotope Ratio Mass Spectrometer (Thermo Fisher Scientific, Delta V Advantage IRMS) coupled with and Elemental Analyzer (Flash, EA 2000). Data are expressed in the standard ∂ unit notation:

$$\partial^{13}C \text{ or } \partial^{15}N = \left(\left(\frac{Rsample}{Rstandard}\right) - 1\right) \times 1000‰$$

where R represents the $^{13}C/^{12}C$ or $^{15}N/^{14}N$ ratio for carbon and nitrogen, respectively, reported relative to VPDB for carbon and to atmospheric N_2 for nitrogen.

The non-parametric Kruskal–Wallis test (H) was used to examine seasonal differences in carbon ($\partial^{13}C$) and nitrogen ($\partial^{15}N$) signals from *A. atra* tissue and SPOM samples. In addition, isotopic signals ($\partial^{13}C$ and $\partial^{15}N$) from different sampling stations were also examined using test H.

To assess the potential contribution of the different carbon sources (allochthonous and autochthonous) in the diet of *A. atra,* and in the SPOM samples, an isotopic mixing model was used (Dauby, 1989; Fry, 2006). Allochthonous terrestrial OM (TOM) is isotopically lighter than its marine counterpart (Bianchi, 2007). In Chilean fjords TOM has an average $\delta^{13}C$ isotopic signals of −29‰ while autochthonous marine OM (MOM) has an average $\delta^{13}C$ isotopic signal of −1‰ (Vargas et al., 2011; Lafon et al., 2014; González et al., 2019). The isotopic mixing model considered three end members recorded in this study: (i) autochthonous OM from a marine source with a $\partial^{13}C$ of −18.3 (measured at station B4, 2 m depth), (ii) allochthonous OM from a terrestrial source with a $\partial^{13}C$ of −29.9 (measured at station B4, 20 m depth), and (iii) allochthonous OM from salmon food pellets used in feeding experiments with a $\partial^{13}C$ of −21.94.

RESULTS AND DISCUSSION

Differences in rates of change of POC concentrations in control (**Supplementary Table 2**) and experimental (**Supplementary Table 3**) aquaria were used to calculate grazing by *A. atra* (**Table 1**). The highest average grazing values were recorded on bacterial community (0.20 h^{-1} ± SE 0.08) and salmon food pellet treatment (0.26 h^{-1} ± SE 0.12), while planktonic community treatment showed the lowest (0.05 h^{-1} ± SE 0.02). Grazing values greater than zero; obtained when the rate of change of POC concentration was significantly higher under control conditions than in experimental aquaria (**Figure 2A**), indicated that *A. atra* was able to feed on both of the autochthonous sources of OM (bacterial and total microplanktonic community; Wilcoxon test, $p < 0.05$) and on the allochthonous source (ground salmon food pellet; Wilcoxon test, $p < 0.1$). The present study therefore confirms observations that ribbed mussels are omnivores, feeding on a wide array of organic particles (Kreeger et al., 2018), and highlights the ability of

TABLE 1 | Variables calculated during the feeding experiments.

Date	(h^{-1}) *Kc*	(h^{-1}) *Kg*	(h^{-1}) *g*	Treatment	L ind^{-1} h^{-1} C rate	mg C ind^{-1} h^{-1} I rate	g D Weight	mm Length	L g^{-1} h^{-1} C rate (s)
22-February-18	−0.44	−0.06	**−0.38**	PC_T	0	0	6	132	0
25-February-18	0.06	0.16	**−0.11**	PC_T	0	0	7	120	0
22-February-19	0.49	1.17	**−0.68**	PC_T	0	0	7	115	0
22-February-19	0.33	0.82	**−0.49**	PC_T	0	0	5	100	0
16-July-18	−0.12	0.05	**−0.17**	PC_T	0	0	6	112	0
22-February-18	0.34	0.33	0.01	PC_T	0.08	0.04	8	126	0.01
25-February-18	0.06	−0.06	0.11	PC_T	0.68	0.17	2	106	0.34
16-July-18	−0.34	−0.39	0.06	PC_T	0.34	0.12	6	111	0.06
25-February-19	0.10	−0.12	0.22	PC_T	1.30	0.31	8	106	0.16
09-July-19	−0.03	−0.21	0.18	PC_T	1.06	0.19	6	98	0.18
09-July-19	−0.03	−0.04	0.01	PC_T	0.08	0.01	4	97	0.02
10-July-19	−0.05	−0.10	0.05	PC_T	0.30	0.04	6	101	0.05
21-February-18	0.18	0.25	**−0.07**	BC_T	0	0	13	128	0
25-February-18	0.10	0.19	**−0.10**	BC_T	0	0	6	119	0
26-February-18	0.07	0.16	**−0.08**	BC_T	0	0	11	115	0
21-February-18	0.23	0.20	0.03	BC_T	0.16	0.03	7	137	0.02
17-July-18	0.17	−0.002	0.17	BC_T	1.03	0.28	7	109	0.15
23-February-19	1.06	0.07	1.00	BC_T	5.98	1.31	12	118	0.50
23-February-19	1.33	1.15	0.19	BC_T	1.11	0.10	3	112	0.37
25-February-19	0.67	0.27	0.40	BC_T	2.39	0.41	4	95	0.60
25-February-19	0.60	0.29	0.31	BC_T	1.88	0.33	4	110	0.47
08-July-19	0.02	−0.10	0.13	BC_T	0.76	0.10	5	92	0.15
08-July-19	−0.14	−0.17	0.04	BC_T	0.24	0.03	6	110	0.04
09-July-19	0.02	−0.11	0.12	BC_T	0.73	0.10	4	111	0.18
21-February-18	−0.54	0.40	**−0.94**	SFP_T	0	0	6	125	0
26-February-18	−0.68	0.29	**−0.97**	SFP_T	0	0	5	103	0
23-February-19	−0.83	−0.47	**−0.37**	SFP_T	0	0	7	101	0
21-February-18	0.29	0.27	0.02	SFP_T	0.13	0.25	6	111	0.02
26-February-18	0.18	−0.07	0.24	SFP_T	1.40	2.19	4	109	0.36
17-July-18	1.69	0.85	0.85	SFP_T	5.07	11.38	7	124	0.72
23-February-19	1.23	0.59	0.64	SFP_T	3.82	20.89	7	106	0.55
26-February-19	0.32	−0.01	0.33	SFP_T	1.98	10.41	5	105	0.40

Kc, rate of change in POC concentration in control aquaria; Kg, rate of change in POC concentration in experimental aquaria; g, grazing coefficient; C rate, clearance rate by individual; C rate (s), clearance rate standardized by weight; I rate, ingestion rate by individual; D weight and length, dry weight and length of Aulacomya atra in feeding experiments. Negative values in bold were substituted by zero to calculate C rate and I rate.

A. atra to filter both small (bacterial community <0.8 μm) and large (ground salmon food pellet <1 mm) food particles. Bacteria are generally too small to be efficiently retained by the gills of most bivalves, however, the particular morphology of gills of ribbed mussels – such as *A. atra* and *Geukensia demissa* (Dillwyn, 1817) – makes these species very effective grazers of bacteria (Wright et al., 1982; Stuart and Klumpp, 1984; Langdon and Newell, 1990). The bacterial community therefore makes an appreciable contribution to the diet of these species (Stuart et al., 1982; Kreeger and Newell, 1996). Bacterial ingestion by *A. atra* may also represent an important step in the vertical transfer of food and energy in Patagonian fjord ecosystems, and could be a particularly important route for allochthonous OM (from terrestrial origin or from salmon farming waste) entering indirectly into the benthic food web as material assimilated by bacterial community (Zapata-Hernández et al., 2014).

Consumption of salmon waste particles (uneaten food and feces) by blue mussels (*Mytilus edulis*; Linnaeus, 1758) under laboratory conditions has been described in the literature (Reid et al., 2010; MacDonald et al., 2011; Handå et al., 2012b). These studies have shown that mussels not only have the ability to efficiently capture and ingest particulate organic material (POM) from salmon feed and feces, but in some cases, mussels can in fact select fish feed particles and utilize them more efficiently than feces particles (Handå et al., 2012b). POM derived from salmon cages has previously been shown to be a food source as important as microalgae for mussels (Reid et al., 2010). In feeding experiments, clearance rates (CR) measured in bacterial (0–5.98 L ind^{-1} h^{-1}) and salmon food pellet (0–5.07 L ind^{-1} h^{-1}) treatments were quite similar and showed a range of values greater than those measured in planktonic community treatment (0–1.30 L ind^{-1} h^{-1}) (**Figure 2B**). However, no significant differences were observed between the different food sources

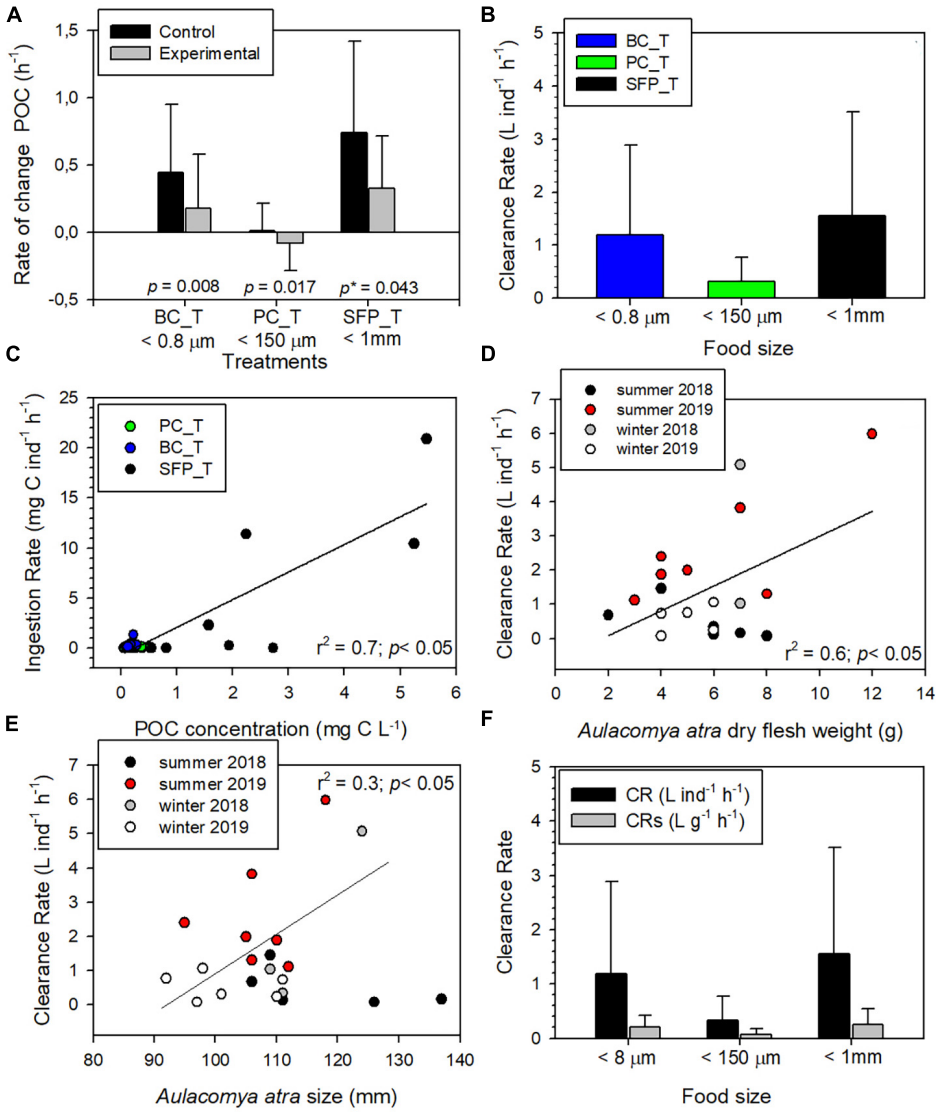

FIGURE 2 | (A) Rate of change in POC concentrations (average ± SD) from feeding experiments in control and experimental aquaria under bacterial community (BC_T), planktonic community (PC_T) and salmon food pellet (SFP_T) treatments. The mean value in both control and experimental aquaria correspond to all experiments carried out under the same treatment with a grazing coefficient > 0 (**Table 1**), *p*: *p*-value with alpha = 0.05, *p**: *p*-value with alpha = 0.1. **(B)** *Aulacomya atra* clearance rate (average ± SD) in each type of treatment. The mean value correspond to all experiments carried out under the same treatment. **(C)** Relation between POC concentration and ingestion rate (IR) of *A. atra* during feeding experiments. **(D)** Clearance rate as a function of dry flesh weight in *A. atra* during sampling campaigns. **(E)** Clearance rate as a function of *A. atra* size during sampling campaigns. **(F)** Comparison between clearance rates by individual (CR) and those standardized by weight (CRs) in each treatment.

(Kruskal–Wallis test, $p > 0.05$). The highest ingestion rates (IR) (2.19 to 20.9 mg C ind^{-1} h^{-1}) were obtained for salmon food pellet treatment (allochthonous OM) (**Figure 2C**) indicating that *A. atra* was able to capture and ingest salmon feed more efficiently than bacteria and microplanktonic organisms (Kruskal–Wallis test, $p < 0.05$). In contrast, highest IR values of between 0.17 and 0.31 mg C ind^{-1} h^{-1} recorded under autochthonous feeding conditions were significantly lower (Kruskal–Wallis test, $p < 0.05$) for the planktonic community treatment than the range of 0.28–1.31 mg C ind^{-1} h^{-1} recorded in bacterial treatment (**Figure 2C** and **Table 1**). These results do not necessarily represent a selection or preference of *A. atra* for a given food type since the diets provided in this study were not mixed. Highest IR values were associated with higher POC concentration (IR and POC concentration were positively correlated, **Figure 2C**, $r^2 = 0.73$, $p < 0.05$). Overall, salmon food pellet treatment with POC concentration >2 mg C L^{-1} had a greater IR (>10 mg C ind^{-1} h^{-1}) than those treatments with a lower POC concentration (**Figure 2C**).

Clearance rates (values > 0) was positively correlated to dry flesh weight of *A. atra* (more clearly observed during the 2019 summer campaign; $r^2 = 0.64$, $p < 0.05$) and with *A. atra* size

(more clearly observed during winter campaigns and summer 2019; $r^2 = 0.3$, $p < 0.05$), suggesting that in most cases, an increase in weight and/or size of *A. atra* results in a higher CR (**Figures 2D,E**). The weight-standardized clearance rate (CRs) showed the same pattern as CR, although the values observed were lower (**Figure 2F**). Seasonally, CR and CRs were both significantly higher in summer than in winter (Kolmogorov-Smirnov test, $p < 0.05$), probably associated with the influence of water temperature on bivalve metabolic rates. Indeed, greater CR values are generally associated with high temperature (Haure et al., 1998; Sylvester et al., 2005; Kang et al., 2016). During summer, experiments were conducted within the 15–18°C temperature range whereas in the winter period the temperature range was lower (8–10°C). CR and IR values measured in this study for *A. atra* well agree with those reported in previous laboratory studies, both with *A. atra* (Griffiths and King, 1979) and with other species of mussels such as *M. edulis* (MacDonald et al., 2011; Handå et al., 2012b).

Stable isotopes show long-term nutrition, yielding accurate information about the characteristics of the assimilated food (Valiela, 1995), being among the most suitable tools to describe trophic relationships in coastal ecosystems (Wada et al., 1991). In this study carbon (∂^{13}C) and nitrogen (∂^{15}N) signatures from samples of *A. atra* tissue and SPOM from the Puyuhuapi Fjord were plotted together (**Figure 3A**). ∂^{13}C and ∂^{15}N values of *A. atra* tissues did not differ significantly (Kruskal–Wallis test, $p > 0.05$) among sampling station throughout the study period (B1: ∂^{13}C −18.5 ± 0.9‰, ∂^{15}N 9.5 ± 0.7‰; B2: ∂^{13}C −19.5 ± 1.7‰, ∂^{15}N 9.3 ± 0.7‰; ‰; B3: ∂^{13}C −20.1 ± 2.2‰, ∂^{15}N 9.1 ± 0.2‰; B4: ∂^{13}C −19.9 ± 1.2‰, ∂^{15}N 8.4 ± 0.4‰;

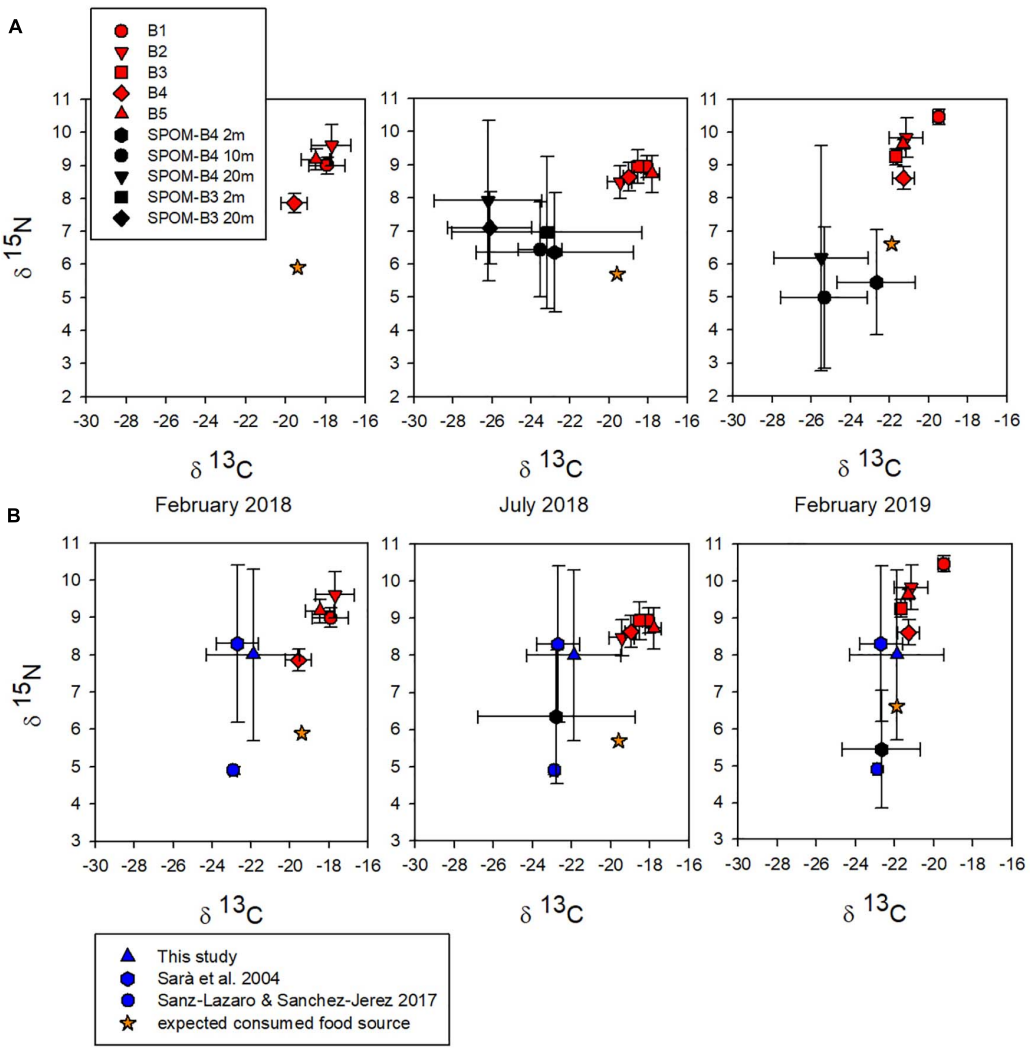

FIGURE 3 | (A) ∂^{13}C and ∂^{15}N biplot showing stable isotopic composition of *Aulacomya atra* tissues (red shapes) and of suspended particulate organic matter (SPOM) (black shapes). Samples of *A. atra* were obtained from different sampling stations across the Puyuhuapi Fjord (from B1 to B5). Samples of SPOM were obtained from different sampling depths (2, 10, and 20 m) in B4 and B3 stations. The orange star indicates the expected isotopic signature of the preferred food source. **(B)** ∂^{13}C and ∂^{15}N biplot showing stable isotopic composition in *A. atra* tissues and in pellet salmon food from this study and others.

B5: ∂^{13}C −19.2 ± 1.9‰, ∂^{15}N 9.2 ± 0.5‰) (**Figure 3A** and **Supplementary Table 4**). Likewise, the ∂^{15}N of *A. atra* tissues was quite similar seasonally (February 2018: 8.9 ± 0.8‰, July 2018: 8.7 ± 0.2‰ and February 2019: 9.6 ± 0.7‰) and showed no significant differences (Kruskal–Wallis test, $p > 0.05$) (**Figure 3A** and **Supplementary Table 4**). On the contrary, ∂^{13}C values of *A. atra* tissues were significantly different (Kruskal–Wallis test, $p < 0.05$) between February 2018 (−18.4 ± 0.8‰), July 2018 (−18.6 ± 0.7‰) and February 2019 (−20.9 ± 0.9‰) (**Figure 3A** and **Supplementary Table 4**). These seasonal differences observed in ∂^{13}C values might be related to the different food source (i.e., autochthonous vs. allochthonous) that was available in the water column for consumption of *A. atra*. In fact, ∂^{13}C values in SPOM samples – that include a wide range of potential food source for filter feeder organisms – between March and July 2018 at surface layer (2–10 m) ranged from −18.3 to −27.1‰, while between August 2018 and February 2019 ranged from −21.5 to −29.7‰ (**Figure 3A**). Different seasonal ranges observed in the isotopic signal of SPOM were possibly determined by the contribution of oceanic surface water and the increase in freshwater discharge, that usually occur in the Puyuhuapi Fjord during winter and spring months, respectively (Schneider et al., 2014). Oceanic waters are indicative of a strong marine component (∂^{13}C average = −19‰), while freshwater discharge has a high terrestrial signature (∂^{13}C average = −29‰) (Vargas et al., 2011; Lafon et al., 2014; González et al., 2019). In addition, depleted values of ∂^{15}N with values low 4‰ (as those observed between August 2018 and February 2019 in the study area) are indicative of a high terrestrial signal (Sepúlveda et al., 2011). ∂^{13}C and ∂^{15}N values of SPOM from 2 and 20 m did not show significant differences between sampling station B3 and B4 (Kruskal–Wallis test, $p < 0.05$; **Figure 3**).

Average ∂^{13}C values of SPOM (2–20 m) among March 2018 and July 2018 (−24.4 ± 1.7‰) and between August 2018 and February 2019 (−25.2 ± 0.4‰) were significantly more depleted (Kruskal–Wallis test, $p > 0.05$) than those measured in *A. atra* tissues in July 2018 (−18.6 ± 0.7‰) and February 2019 (−20.9 ± 0.9‰) (**Figure 3A** and **Supplementary Table 4**). Likewise, average ∂^{15}N values of SPOM between March 2018 and July 2018 (6.9 ± 0.6‰) and between August 2018 and February 2019 (5.5 ± 0.6‰) were significantly lower (Kruskal–Wallis test, $p > 0.05$) than those measured in *A. atra* tissues in July 2018 (8.7 ± 0.2‰) and February 2019 (9.6 ± 0.7‰) (**Figure 3A** and **Supplementary Table 4**). These ∂^{13}C and ∂^{15}N signatures of *A. atra* tissues and SPOM samples well agree with previous reports in Chilean fjords (Mayr et al., 2011; Andrade et al., 2016) and with studies on bivalves in fish farming areas (Mazzola and Sarà, 2001; Gao et al., 2006; Redmond et al., 2010).

Since the potential food sources ingested by *A. atra* are those which are depleted by 1‰ in ∂^{13}C and by ∼ 3‰ in ∂^{15}N compared to the tissues of this consumer (Minagawa and Wada, 1984; Rau et al., 1990; Post, 2002), we might expect that the preferentially exploited food source shows values of −19.4‰ ∂^{13}C and 5.9‰ ∂^{15}N in February 2018, −19.6‰ ∂^{13}C and 5.7‰ ∂^{15}N in July 2018 and −21.9‰ ∂^{13}C and 6.6‰ ∂^{15}N in February 2019 (**Figure 3**). These isotopic ratios were close to the more enriched range of SPOM isotopic signal from 2m deep in the water column (**Figure 3**) that mainly correspond to autochthonous organic production by marine phytoplankton, with ranges of ∂^{13}C between −18 and −22‰ (Goericke and Fry, 1994) and ∂^{15}N between 6 and 7‰ (Wada et al., 1987). In this context, the results indicate that *A. atra* preferentially exploits food resources with signals consistent with autochthonous marine OM in Puyuhuapi Fjord. However, the average isotopic composition of the salmon food pellets used in feeding experiments from this study (∂^{13}C −21.9 ± 2.4‰, ∂^{15}N 8.0 ± 2.3‰) and in other studies (∂^{13}C −22.7 ± 1.1‰, ∂^{15}N 8.3 ± 2.1‰ from Sarà et al., 2004 and ∂^{13}C −22.9 ± 0.2‰, ∂^{15}N 4.9 ± 0.1‰ from Sanz-Lazaro and Sanchez-Jerez, 2017; **Figure 3B**) overlaps with marine phytoplankton signal in SPOM samples, mainly in February 2019 (**Figure 3B**). Estimating the contribution of this allochthonous salmon feed material to the diet of *A. atra* is therefore not so clear cut. The mixing equations clarify this point and indicate that both allochthonous material derived from uneaten salmon feed and autochthonous materials highly contribute to its diet (**Supplementary Table 5**). In February and July 2018, the greatest relative contributions (92–99%) came from autochthonous OM, while the terrestrial contribution to the diet of *A. atra* was minimal (1–23%) throughout the study (**Supplementary Table 5**). Regarding SPOM samples, the highest relative contributions were from autochthonous OM (40–60%) and allochthonous material from salmon pellet food (58–87%) in surface waters (2–10 m). In subsurface waters (20 m) the highest contributions (40–70%) were mainly from allochthonous terrestrial material (**Supplementary Table 5**).

The influence of allochthonous carbon sources on hard-bottom benthic communities in Chilean fjords has been poorly studied to date. Some authors have suggested that allochthonous material from a terrestrial origin plays a minor role as a food for suspension feeders (Mayr et al., 2011; Zapata-Hernández et al., 2014) and that autochthonous OM from phytoplankton production provides one of the principal food sources to these populations (Andrade et al., 2016). Our data confirm that phytoplankton carbon plays a primary role in the diet of *A. atra* and apparently excluding extensive utilization of terrestrially derived OM. However, the present study cannot preclude significant utilization of OM derived from salmon farming.

DATA AVAILABILITY STATEMENT

The original contributions presented in the study are included in the article/**Supplementary Material**, further inquiries can be directed to the corresponding author.

AUTHOR CONTRIBUTIONS

PM: study design, data collection, analysis of data, interpretation of results, and manuscript leader. MC: study design, data collection, analysis of data, and manuscript revision. FB: data collection and manuscript revision. GB: manuscript revision. GD: study design, critical revision, and edition of final version

of the manuscript. All authors contributed to the writing of the manuscript.

FUNDING

This research was funded by FIC No 40000236-0 and (partially) by COPAS Sur-Austral ANID PIA APOYO CCTE AFB 170006 and Programa Regional CONICYT R17A10002, Laboratorio EcoClimático Región de Aysén.

ACKNOWLEDGMENTS

The authors thank the technical staff of Centro de Investigación en Ecosistemas de la Patagonia (CIEP) for support during field work.

SUPPLEMENTARY MATERIAL

The Supplementary Material for this article can be found online at: https://www.frontiersin.org/articles/10.3389/fmars.2021.612406/full#supplementary-material

Supplementary Table 1 | Date, season, and geographical coordinates of *Aulacomya atra* sampling sites in the Puyuhuapi Fjord.

Supplementary Table 2 | Initial (C1) and final (C2) POC concentration [mean ± standard deviation (SD)] in control aquaria from different treatments during feeding experiments. Kc corresponds to rate of change in POC concentration estimated in control aquaria during feeding experiments. PC_T, planktonic community treatment; BC_T, bacterial community treatment; and SFP_T, salmon food pellet treatment.

Supplementary Table 3 | Initial (C1) and final (C2) POC concentration [mean ± standard deviation (SD)] in experimental aquaria from different treatments during feeding experiments. Kg corresponds to rate of change in POC concentration estimated in experimental aquaria during feeding experiments. PC_T, planktonic community treatment; BC_T, bacterial community treatment; and SFP_T, salmon food pellet treatment.

Supplementary Table 4 | $\partial^{13}C$ and $\partial^{15}N$ values [mean ± standard deviation (SD)] measured in *Aulacomya atra* tissues and in suspended particulate organic matter (SPOM) in the Puyuhuapi Fjord during the study period. For the location of the sampling station in the Puyuhuapi Fjord, refer to **Figure 1**.

Supplementary Table 5 | Possible contributions (%) of the three main carbon sources to the carbon isotopic signal of *Aulacomya atra* and suspended particulate organic matter (SPOM) estimated using the mixing model (Dauby, 1989; Fry, 2006). Three $\delta^{13}C$ end-member obtained in this study were used in the mixing model: autochthonous marine end-member $\delta^{13}C$ (−18.3), allochthonous terrestrial end-member $\delta^{13}C$ (−29.9) and allochthonous pellet end-member $\delta^{13}C$ (−21.9).

REFERENCES

Anderson, S. R., Diou-Cass, Q. P., and Harvey, E. L. (2018). Short-term estimates of phytoplankton growth and mortality in a tidal estuary. *Limnol. Oceanogr.* 63, 2411–2422. doi: 10.1002/lno.10948

Anderson, S. R., and Harvey, E. L. (2019). Seasonal variability and drivers of microzooplankton grazing and phytoplankton growth in a subtropical estuary. *Front. Mar. Sci.* 6:174. doi: 10.3389/fmars.2019.00174

Andrade, C., Ríos, C., Gerdes, D., and Brey, T. (2016). Trophis structure of shallow-water benthic communities in the sub-Antartic Strait of Magellan. *Polar Biol.* 39, 2281–2297. doi: 10.1007/s00300-016-1895-0

Bayne, B. L. (1998). The physiology of suspension feeding by bivalve molluscs: an introduction to the Plymouth "TROPHEE" workshop. *J. Exp. Mar. Biol. Ecol.* 219, 1–19. doi: 10.1016/s0022-0981(97)00172-x

Betti, F., Bavestrello, G., Bo, M., Enrichetti, F., Loi, A., Wabderlingh, A., et al. (2017). Benthic biodiversity and ecological gradients in the Seno Magdalena (Puyuhuapi Fjord. Chile). *Estuar. Coast. Shelf Sci.* 198, 269–278. doi: 10.1016/j.ecss.2017.09.018

Bianchi, T. S. (2007). *Biogeochemistry of Estuaries*. Oxford: Oxford University Press, 706.

Buschman, A. H., Riquelme, V., Hernández-González, M. C., Varela, D., Jiménez, J. E., Henríquez, L. A., et al. (2006). A review of the impacts of salmonid farming on marine coastal ecosystems in the southeast Pacific. *ICES J. Mar. Sci.* 63, 1338–1345. doi: 10.1016/j.icesjms.2006.04.021

Chaigneau, A., and Pizarro, O. (2005). Mean surface circulation and mesoscale turbulent flow characteristics in the eastern South Pacific from satellite tracked drifters. *J. Geophys. Res.* 110:C05014. doi: 10.1029/2004JC002628

Cloern, J. E. (1982). Does the benthos control phytoplankton biomass in south san francisco bay? *Mar. Ecol. Prog. Ser.* 9, 191–202. doi: 10.3354/meps009191

Cranford, P. J. (2019). "Magnitude and Extent of waterclarification services provided by bivalvesuspension feeding," in *Goods and Services of Marine Bivalves*, eds A. C. Smaal, J. G. Ferreira, J. Grant, J. K. Petersen, and Ø Strand (Cham: Springer), doi: 10.1007/978-3-319-96776-9_8

Cranford, P. J., Ward, J. E., and Shumway, S. E. (2011). "Bivalve filter feeding: variability and limits of the aquaculture biofilter," in *Shellfish Aquaculture and the Environment*, 1st Edn, ed. S. E. Shumway (Hoboken, NJ: Wiley-Blackwell), 81–124. doi: 10.1002/9780470960967.ch4

Dauby, P. (1989). The stable isotope ratios in benthic food webs of the Gulf of Calvi, Corsica. *Cont. Shelf Res.* 9, 181–195. doi: 10.1016/0278-4343(89)90091-5

Dillwyn, L. W. (1817). *A Descriptive Catalogue of Recent Shells, Arranged According to the Linnean Method, Whit Particular Attention to the Synonymy*, 1: 1–580, Vol. 2. London: John and Arthur Arch, 581–1092.

Dolmer, P. (2000). Feeding activity of mussels *Mytilus edulis* related to near-bed currents and phytoplankton biomass. *J. Sea Res.* 44, 221–231. doi: 10.1016/S1385-1101(00)00052-6

Filgueira, R., Strohmeier, T., and Strand, Ø (2019). "Regulating services of bivalve molluscs in the context of the carbon cycle and implications for ecosystem valuation," in *Goods and Services of Marine Bivalves*, eds A. C. Smaal, J. G. Ferreira, J. Grant, J. K. Petersen, and Ø Strand (Cham: Springer), doi: 10.1007/978-3-319-96776-9_12

Frost, B. W. (1972). Effects of size and concentration of food particles on the feeding behaviour of the marine planktonic copepod *Calanus pacificus*. *Limnol. Oceanogr.* 17, 805–815. doi: 10.4319/lo.1972.17.6.0805

Fry, B. (2006). *Stable Isotope Ecology*. New York, NY: Springer, doi: 10.1007/0-387-33745-8

Gao, Q. F., Shin, P. K. S., Lin, G. H., Chen, S. P., and Cheung, S. G. (2006). Stable isotope and fattyacid evidence for uptake of organic waste by green-lipped mussels *Pernaviridis* in a polyculture fish farm system. *Mar. Ecol. Prog. Ser.* 317, 273–283. doi: 10.3354/meps317273

Goericke, R., and Fry, B. (1994). Variations of marine plankton $\delta^{13}C$ with latitude, temperature, and dissolved CO_2 in the world ocean. *Glob. Biogeochem. Cycles* 8, 85–90. doi: 10.1029/93gb03272

González, H. E., Nimptsch, J., Giesecke, R., and Silva, N. (2019). Organic matter distribution, composition and its possible fate in the Chilean North-Patagonian estuarine system. *Sci. Total Environ.* 657, 1419–1431. doi: 10.1016/j.scitotenv.2018.11.445

Greene, V. E., Sullivan, L. J., Thompson, J. K., and Kimmerer, W. J. (2011). Grazing impact of the invasive clam *Corbula amurensis* on the microplankton assemblage of the northern San Francisco Estuary. *Mar. Ecol. Prog. Ser.* 431, 183–193. doi: 10.3354/meps09099

Griffiths, C. L., and King, J. A. (1979). Some relationships between size, food availability andenergy balance in the ribbed mussel *Aulacomyaater*. *Mar. Biol.* 51, 141–149. doi: 10.1007/bf00555193

Handå, A., Min, H., Wang, X., Broch, O. J., Reitan, K. I., Reinertsen, H., et al. (2012a). Incorporation of fish feed and growth of blue mussels (*Mytilus edulis*)

in close proximity to salmon (*Salmo salar*) aquaculture: Implications for integrated multi-trophic aquaculture in Norwegian coastal waters. *Aquaculture* 356–357, 328–341. doi: 10.1016/j.aquaculture.2012.04.048

Handå, A., Ranheim, A., Olsen, A. J., Altin, D., Reitan, K. I., Olsen, Y., et al. (2012b). Incorporation of salmon fish feed and feces components in mussel (*Mytilus edulis*): implications for integrated multi-trophic aquaculture in cool-temperate North Atlantic waters. *Aquaculture* 370–371, 40–53. doi: 10.1016/j.aquaculture.2012.09.030

Haure, J., Penisson, C., Bougrier, S., and Baud, J. P. (1998). Influence of temperature on clearance and oxygen consumption rates of the flat oyster *Ostrea edulis*: determination of allometric coefficients. *Aquaculture* 169, 211–224. doi: 10.1016/s0044-8486(98)00383-4

Iriarte, J. L., Pantoja, S., and Daneri, G. (2014). Oceanographic processes in Chilean fjords of Patagonia: from small to large-scale studies. *Prog. Oceanogr.* 129, 1–7. doi: 10.1016/j.pocean.2014.10.004

Jacobs, P., Riegman, R., and van der Meers, J. (2016). Impact of introduced juvenile mussel cultures onthe pelagic ecosystem of the western Wadden Sea, The Netherlands. *Aquac. Environ. Interact.* 8, 553–566. doi: 10.3354/aei00196

Jørgensen, C. B. (1990). *Bivalve Filter Feeding: Hydrodynamics, Bioenergetics, Physiology and Ecology*. Fredensborg: Olsen & Olsen, 140.

Kang, C. K., Choy, E. J., Hur, Y. B., and Myeong, J. I. (2016). Isotopic evidence of particle size-dependent food partitioning in cocultured sea squirt *Halocynthia roretzi* and Pacific oyster *Crassostrea gigas*. *Aquat. Biol.* 6, 289–302. doi: 10.3354/ab00126

Kreeger, D. A., Gatenby, C. M., and Bergstrom, P. W. (2018). Restoration potential of several native species of bivalve molluscs for water quality improvement in mid-Atlantic watersheds. *J. Shellfish Res.* 37, 1121–1157. doi: 10.2983/035.037.0524

Kreeger, D. A., and Newell, R. I. E. (1996). Ingestion and assimilation of carbon from cellulotyc bacteria and heterotrophic flagellates by the mussels *Geukensia demisa* and *Mytilus edulis* (Bivalvia, Mollusca). *Aquat. Microb. Ecol.* 11, 205–214. doi: 10.3354/ame011205

Kreeger, D. A., and Newell, R. I. E. (2000). "Trophic complexity between primary producers and invertebrate consumers in salt marshes," in *Concepts and Controversies in Tidal Marsh Ecology*, eds M. P. Weinstein and D. A. Kreeger (New York, NY: Kluwer Press), 187–220. doi: 10.1007/0-306-47534-0_10

Lafon, A., Silva, N., and Vargas, C. A. (2014). Contribution of allochthonous organic carbon across the Serrano River Basin and the adjacent fjord system in southern Chilean Patagonia: insights from the combined use of stable isotopes and fatty acid biomarkers. *Prog. Oceanogr.* 129, 98–113. doi: 10.1016/j.pocean.2014.03.004

Lander, T., Barrington, K., Robinson, S., MacDonald, B., and Martin, J. (2004). Dynamics of the blue mussel as an extractive organism in an integrated multi-trophic aquaculture system. *Bull. Aquac. Assoc. Can.* 104, 19–28. doi: 10.1016/j.aquaculture.2012.09.029

Langdon, C. J., and Newell, R. I. E. (1990). Utilization of detritus and bacteria as food sources by two bivalve suspension-feeders, the oyster *Crassotrea virginica* and the mussel *Geukensia demisa*. *Mar. Ecol. Prog. Ser.* 58, 299–310. doi: 10.3354/meps058299

Langdon, C. J., and Newell, R. I. E. (1996). "Digestion and nutrition of larvae and adults," in *The Eastern Oyster Crassostrea virginica*, eds V. S. Kennedy, R. I. E. Newell, and A. F. Eble (College Park, MD: Maryland Sea Grant College), 231–270.

Lefebvre, S., Barillé, L., and Clerc, M. (2000). Pacific oyster (*Crassostrea gigas*) feeding responses to a fish-farm effluent. *Aquaculture* 187, 185–198. doi: 10.1016/s0044-8486(99)00390-7

Linnaeus, C. (1758). *Systema Naturae per Regna Tria Naturae, Secundum Classes, Ordines, Genera, Species, Cum Characteribus, Differentiis, Synonymis, Locis. Editio Decimal, Reformarta*, 10th revised Edn, Vol. 1. 824.

Lonsdale, D. J., Cerrato, R. M., Holland, R., Mass, A., Holt, L., Schaffner, R. A., et al. (2009). Influence of suspension-feeding bivalves on the pelagic food webs of shallow, coastal embayments. *Aquat. Biol.* 6, 263–279. doi: 10.3354/ab00130

Lucas, J., Koester, I., Wichels, A., Niggemann, J., Dittmar, T., Callies, U., et al. (2016). Short-term dynamics of North Sea bacterioplankton-dissolved organic matter coherence on molecular level. *Front. Microbiol.* 7:321. doi: 10.3389/fmicb.2016.00321

MacDonald, B. A., Robinson, S. M. C., and Barrington, K. A. (2011). Feeding activity of mussels (*Mytilus edulis*) held in the field at an integrated multi-trophic aquaculture (IMTA) site (*Salmo salar*) and exposed to fish food in the laboratory. *Aquaculture* 314, 244–251. doi: 10.1016/j.aquaculture.2011.01.045

Mayr, C., Försterra, G., Häussermann, V., Wunderlich, A., Grau, J., Zieringer, M., et al. (2011). Stable isotope variability in a Chilean fjord food web: implications for N- and C-cycles. *Mar. Ecol. Prog. Ser.* 428, 89–104. doi: 10.3354/meps09015

Mazzola, A., and Sarà, G. (2001). The effect of fish farming organic waste on food availability for bivalve molluscs (Gaeta Gulf, Central Tyrrhenian, MED): stable carbon isotopic analysis. *Aquaculture* 192, 361–379. doi: 10.1016/s0044-8486(00)00463-4

Menden-Deuer, S., Lawrence, C., and Franzè, G. (2018). Herbivorous protist growth and grazing rates at in situ and artificially elevated temperatures during an Artic phytoplankton spring bloom. *PeerJ* 6:e5264. doi: 10.7717/peerj.5264

Minagawa, M., and Wada, E. (1984). Stepwise enrichment of 15N along food chains: further evidence and the relation between δ^{15}N and animal age. *Geochem. Cosmochim. Acta* 48, 1135–1140. doi: 10.1016/0016-7037(84)90204-7

Molina, J. I. (1782). *Saggio Sulla Storia Natural del Chile, del Signor Abate Giovanni Ignazio Molina*. Bologna: Nella Stamperia di S. Tommaso d'Aquino, 202.

Montero, P., Daneri, G., González, H. E., Iriarte, J. L., Tapia, F., Lizárraga, L., et al. (2011). Seasonal variability of primary production in a fjord ecosystem of the Chilean Patagonia: implications for the transfer of carbon within pelagic food webs. *Cont. Shelf Res.* 31, 202–215. doi: 10.1016/j.csr.2010.09.003

Montero, P., Daneri, G., Tapia, F., Iriarte, J. L., and Crawford, D. (2017a). Diatom blooms and primary production in a channel ecosystem of central Patagonia. *Lat. Am. J. Aquat. Res.* 45, 999–1016. doi: 10.3856/vol45-issue5-fulltext-16

Montero, P., Pérez-Santos, I., Daneri, G., Gutiérrez, M. H., Igor, G., Seguel, R., et al. (2017b). A winter dinoflagellate bloom drives high rates of primary production in a Patagonian fjord ecosystem. *Estuar. Coast. Shelf Sci.* 199, 105–116. doi: 10.1016/j.ecss.2017.09.027

Norkko, A., Hewitt, J. E., and Thrush, S. F. (2001). Benthic-pelagic coupling and suspension-feeding bivalves: linking site-specific sediment flux and biodeposition to benthic community structure. *Limnol. Oceanogr.* 56, 2067–2072. doi: 10.4319/lo.2001.46.8.2067

Peharda, M., Richardson, C. A., Mladineo, I., Sestanovic, S., Popovic, Z., Bolotin, J., et al. (2007). Age, growth and population structure of *Modiolus barbatus* from the Adriatic. *Mar. Biol.* 151, 629–638. doi: 10.1007/s00227-006-0501-3

Post, D. M. (2002). Using stable isotopes to estimate trophic position: models, method, and assumptions. *Ecology* 83, 703–718. doi: 10.1890/0012-9658(2002)083[0703:usitet]2.0.co;2

Prins, T. C., Smaal, A. D., and Dame, R. F. (1998). A review of the feedbacks between bivalve grazing and ecosystem processes. *Aquat. Ecol.* 31, 349–358.

Quiñones, R. A., Fuentes, M., Montes, R. M., Soto, D., and León-Muñoz, J. (2019). Environmental issues in Chilean salmon farming: a review. *Rev. Aquac.* 11, 375–402. doi: 10.1111/raq.12337

Quiroga, E., Ortíz, P., González-Saldías, R., Reid, B., Tapia, F. J., Pérez-Santos, I., et al. (2016). Seasonal benthic patterns in a glacial Patagonian fjord: the role of suspended sediment and terrestrial organic matter. *Mar. Ecol. Prog. Ser.* 561, 31–50. doi: 10.3354/meps11903

Rau, G. H., Teyssie, J. L., Rassoulzadegan, F., and Fowler, S. W. (1990). ^{13}C/^{12}C and ^{15}N/^{14}N variations among size-fractionated marine particles: implications for their origin and trophic relationships. *Mar. Ecol. Prog. Ser.* 59, 33–38. doi: 10.3354/meps059033

Redmond, K. J., Magnesen, T., Hansen, P. K., Strand, Ø, and Meier, S. (2010). Stable isotopes and fatty acids as tracers of the assimilation of salmon fish feed inblue mussels (*Mytilus edulis*). *Aquaculture* 298, 202–210. doi: 10.1016/j.aquaculture.2009.10.002

Reid, G. K., Liutkus, M., Bennett, A., Robinson, S. M. C., MacDonald, B., and Page, F. (2010). Absorption efficiency of blue mussels (*Mytilus edulis* and *M. trossulus*) feeding on Atlantic salmon (*Salmo salar*) feed and fecal particulates: implications for integrated multi-trophic aquaculture. *Aquaculture* 299, 165–169. doi: 10.1016/j.aquaculture.2009.12.002

Ribes, M., Coma, R., and Gili, J. M. (1998). Seasonal variations of in situ feeding rates by the temperate ascidian *Halocynthia papillosa*. *Mar. Ecol. Progr. Ser.* 175, 201–213.

Riisgård, H. U. (1988). Efficiency of particle retention and filtration rate in 6 species of northeast American bivalves. *Mar. Ecol. Prog. Ser.* 45, 217–223. doi: 10.3354/meps045217

Saiz, E. (1993). Sources of variability in zooplankton feeding experiments: the importance of accurate determination of algal growth rates. *Sci. Mar.* 57, 23–29.

Sanz-Lazaro, C., and Sanchez-Jerez, P. (2017). Mussels do not directly assimilate fish farm wastes: shifting the rationales of integrated multitrophic aquaculture

to a broader scale. *J. Environ. Manag.* 201, 82–88. doi: 10.1016/j.jenvman.2017.06.029

Sarà, G., Scilipoti, D., Mazzola, A., and Modica, A. (2004). Effects of fish farming waste to sedimentary and particulate organic matter in a southern Mediterranean area (Gulf of Castellammare, Sicily): a multiple stable isotope study ($d^{13}C$ and $d^{15}N$). *Aquaculture* 234, 199–213. doi: 10.1016/j.aquaculture.2003.11.020

Sarà, G., Zenone, A., and Tomasello, A. (2009). Growth of *Mytilus galloprovincialis* (mollusca, bivalvia) close to fish farms: a case of integrated multi-trophic aquaculture within the Tyrrhenian Sea. *Hydrobiologia* 636, 129–136. doi: 10.1007/s10750-009-9942-2

Schneider, W., Pérez-Santos, I., Ross, L., Bravo, L., Seguel, R., and Hernández, F. (2014). On the hydrography of Puyuhuapi Channel (Chilean Patagonia). *Prog. Oceanogr.* 129, 8–18. doi: 10.1016/j.pocean.2014.03.007

Sebens, K., Sarà, G., and Nishizaki, M. (2016). "Energetics, particle capture, and growth dynamics of benthic suspension feeders," in *Marine Animal Forest*, ed. S. Rossi (Cham: Springer), doi: 10.1007/978-3-319-17001-5_17-1

Sepúlveda, J., Pantoja, S., and Hughen, K. A. (2011). Sources and distribution of organic matter in northern Patagonia fjords, Chile (∼44–47°S): a multi-tracer approach for carbon cycling assessment. *Continent. Shelf Res.* 31, 315–329. doi: 10.1016/j.csr.2010.05.013

Silva, N. (2008). "Dissolved oxygen, pH, and nutrients in the austral Chilean channels and fjords," in *Progress in the Oceanographic Knowledge of Chilean Interior Waters, from Puerto Montt to Cape Horn*, eds N. Silva and S. Palma (Valparaíso: Pontificia Universidad Católica de Valparaíso), 37–43.

Stoecker, D. K., Nejstgaard, J. C., Madhusoodhanan, R., Pohnert, G., Wolfram, S., Jakobsen, H. H., et al. (2015). Understimation of microzooplankton grazing in dilution experiments due to inhibition of phytoplankton growth. *Limnol. Oceanogr.* 60, 1426–1438. doi: 10.1002/lno.10106

Stoecker, D. K., Weigel, A., and Goes, J. I. (2014). Microzooplankton grazing in the Eastern Bering in summer. *Deep Sea Res. II* 109, 145–156. doi: 10.1016/j.dsr2.2013.09.017

Strom, S. L., and Fredrickson, K. A. (2008). Intense stratification leads to phytoplankton nutrient limitation and reduced microzooplankton grazing in the southeastern Bering Sea. *Deep Sea Res. II* 55, 1761–1774. doi: 10.1016/j.dsr2.2008.04.008

Stuart, V., Field, J. G., and Newell, R. C. (1982). Evidence for absorption of kelp detritus by the ribbed mussel *Aulacomya ater* using a new ^{51}Cr-labelled microsphere technique. *Mar. Ecol. Prog. Ser.* 9, 263–271. doi: 10.3354/meps009263

Stuart, V., and Klumpp, D. W. (1984). Evidence for food-resource partitioning by kelp-bed filter feeders. *Mar. Ecol. Prog. Ser.* 16, 27–37. doi: 10.3354/meps016027

Sylvester, F., Dorado, J., Boltovskoy, D., Juarez, A., and Cataldo, D. (2005). Filtration rates of the invasive pest bivalve *Limnoperna fortunei* as a function of size and temperature. *Hydrobiologia* 534, 71–80. doi: 10.1007/s10750-004-1322-3

Valiela, I. (1995). *Marine Ecological Processes*, 2nd Edn. New York, NY: Springer-Verlag, 696. doi: 10.1007/978-1-4757-4125-4

Vargas, C. A., Martínez, R. A., San Martin, V., Aguayo, M., Silva, N., and Torres, T. (2011). Allochthonous subsidies of organic matter across a lake–river–fjord landscape in the Chilean Patagonia: Implications for marine zooplankton in inner fjord areas. *Cont. Shelf Res.* 31, 187–201. doi: 10.1016/j.csr.2010.06.016

Vaughn, C. C., and Hoellein, T. J. (2018). Bivalve impacts in freshwater and marine ecosystems. *Ann. Rev. Ecol. Evol. Syst.* 49, 183–208. doi: 10.1146/annurev-ecolsys-110617-062703

Voudanta, E., Kormas, K. A., Monchy, S., Delegrange, A., Vincent, D., Genitsaris, S., et al. (2016). Mussel biofiltration effects on attached bacteria and unicellular eukaryotes in fish-rearing seawater. *PeerJ* 4:e1829. doi: 10.7717/peerj.1829

Wada, E., Mizutani, H., and Minagawa, M. (1991). The use of stable isotopes for food web analysis. *Crit. Rev. Food Sci. Nutr.* 30, 361–371. doi: 10.1080/10408399109527547

Wada, E., Minagawa, M., Mizutani, H., Tsuji, T., Imaizum, R., and Karasawa, K. (1987). Biogeochemical studies on the transport of organic matter along the Otsuchi River watershed, Japan. doi: 10.1016/0272-7714(87)90075-8

Winter, J. E. (1978). A review on the knowledge of suspension-feeding in lamellibranchiate bivalves, with special reference to artificial aquaculture systems. *Aquaculture* 13, 1–33. doi: 10.1016/0044-8486(78)90124-2

Wright, R. T., Coffin, R. B., Ersing, C. P., and Pearson, D. (1982). Field and laboratory measurements of bivalve filtration of natural marine bacterioplankton. *Limnol. Oceanogr.* 27, 91–98. doi: 10.4319/lo.1982.27.1.0091

Zapata-Hernández, G., Sellanes, J., Mayr, C., and Muñoz, P. (2014). Benthic food web in the Comau fjord, Chile (42°S): preliminary assessment including a site with chemosynthetic activity. *Prog. Oceanogr.* 129, 149–158. doi: 10.1016/j.pocean.2014.03.005

Conflict of Interest: The authors declare that the research was conducted in the absence of any commercial or financial relationships that could be construed as a potential conflict of interest.

Publisher's Note: All claims expressed in this article are solely those of the authors and do not necessarily represent those of their affiliated organizations, or those of the publisher, the editors and the reviewers. Any product that may be evaluated in this article, or claim that may be made by its manufacturer, is not guaranteed or endorsed by the publisher.

frontiers in Marine Science

ORIGINAL RESEARCH
published: 01 October 2021
doi: 10.3389/fmars.2021.621822

General Hydrography of the Beagle Channel, a Subantarctic Interoceanic Passage at the Southern Tip of South America

Ricardo Giesecke[1,2], Jacobo Martín[3,4], Andrea Piñones[1,2,5], Juan Höfer[2,6,7], Jose Garcés-Vargas[1,2], Ximena Flores-Melo[3], Emilio Alarcón[2,8], Xavier Durrieu de Madron[9], François Bourrin[9] and Humberto E. González[1,2]*

[1] Instituto de Ciencias Marinas y Limnológicas, Universidad Austral de Chile, Valdivia, Chile, [2] Centro FONDAP de Investigación en Dinámica de Ecosistemas Marinos de Altas Latitudes (IDEAL), Valdivia, Chile, [3] Centro Austral de Investigaciones Científicas (CADIC-CONICET), Ushuaia, Argentina, [4] Instituto de Ciencias Polares, Ambiente y Recursos Naturales, Universidad Nacional de Tierra del Fuego (ICPA-UNTDF), Ushuaia, Argentina, [5] Centro COPAS-Sur Austral, Universidad de Concepción, Concepción, Chile, [6] Escuela de Ciencias del Mar, Pontificia Universidad Católica de Valparaíso, Valparaíso, Chile, [7] Fundación San Ignacio de Huinay, Huinay, Chile, [8] Centro de Investigación en Ecosistemas de la Patagonia, Coyhaique, Chile, [9] CEFREM, CNRS - Université de Perpignan Via Domitia, Perpignan, France

OPEN ACCESS

Edited by:
Giorgio Bavestrello, University of Genoa, Italy

Reviewed by:
John Klinck, Old Dominion University, United States
Gregory Lane-Serff, The University of Manchester, United Kingdom

***Correspondence:**
Ricardo Giesecke
ricardo.giesecke@uach.cl

Specialty section:
This article was submitted to Coastal Ocean Processes, a section of the journal Frontiers in Marine Science

Received: *27 October 2020*
Accepted: *19 August 2021*
Published: *01 October 2021*

Citation:
Giesecke R, Martín J, Piñones A, Höfer J, Garcés-Vargas J, Flores-Melo X, Alarcón E, Durrieu de Madron X, Bourrin F and González HE (2021) General Hydrography of the Beagle Channel, a Subantarctic Interoceanic Passage at the Southern Tip of South America. Front. Mar. Sci. 8:621822. doi: 10.3389/fmars.2021.621822

The Beagle Channel (BC) is a long and narrow interoceanic passage (∼270 km long and 1–12 km wide) with west-east orientation and complex bathymetry connecting the Pacific and Atlantic oceans at latitude 55°S. This study is the first integrated assessment of the main oceanographic features of the BC, using recent oceanographic observations from cruises, moored instruments and historical observations. The waters transported into the BC are supplied mainly by the Cape Horn Current, which carries Subantarctic Water (SAAW) at depth (100 m below surface) along the Pacific Patagonian continental shelf break. SAAW enters the continental shelf via a submarine canyon at the western entrance of the BC. The SAAW is diluted by fresh, nutrient depleted (nitrate, phosphate and silicic acid) Estuarine Water (EW) from Cordillera Darwin Ice Field (CDIF) forming modified SAAW (mSAAW). Freshwater inputs from the CDIF generate a two-layer system with a sharp pycnocline which delimits the vertical distribution of phytoplankton fluorescence (PF). Two shallow sills (<70 m) along the BC contribute to EW and mSAAW mixing and the homogenization of the entire water column east of the sills, coherent with Bernoulli aspiration. The central section of the BC, extending ∼100 km toward the east, is filled by a salty (31–32) variety of EW. In winter, this central section is nearly vertically homogeneous with low nutrient concentrations (0.9–1.1 μM PO4 and 7.5–10 μM NO3) and PF. The temporal variability of seawater temperature from 50 to 195 m in the central section of the BC was found to be mostly dominated by the annual and semiannual cycles and influenced by tidal forcing. The middle section of the BC was less influenced by oceanic inputs and its basin-like structure most likely favors retention, which was observed from the weakly stratified water column at the mooring site. Toward the east, the central section bathymetry is disrupted at Mackinlay Strait where another shallow

sill separates the middle channel from the shallow eastern entrance that connects to the Atlantic Ocean. In this section, a weakly stratified two-layer system is formed when the eastward surface outflow (salty-EW) flows over a deeper, denser tongue of oceanic mSAAW.

Keywords: Beagle Channel, hydrography and bathymetry, micro-basins, interoceanic channel, southern Patagonia

INTRODUCTION

Southern Patagonia Under a Climate Change Scenario

The effects of climate change are expected to be more rapid and dramatic in high-latitude polar and subpolar environments (IPCC, 2014). Some of the most noticeable impacts are (a) the retreat of glaciers (due to melting and an increase in rainfall as compared to snowfall), and (b) the variation of atmospheric frontal systems and the resulting increase in extreme events, which ultimately modify both oceanic circulation and water properties, affecting the structure and function of marine ecosystems (Mackas et al., 2006).

The southern Patagonia icefields are among the last relics of the last glaciation. They comprise one of the largest fjord regions worldwide (Vargas et al., 2018), together with the fjord systems of Iceland, Scandinavia, Greenland, Alaska, and British Columbia. At the same time, they make up one of only two Subantarctic fjord regions, the other being the southern island of New Zealand. Situated at the southernmost extension of land before Antarctica, Tierra del Fuego and southern Patagonia constitute unique ecosystems and provide a natural laboratory for monitoring the effects of ongoing climate change.

The southern tip of the South America has a high geomorphological complexity, with fjords and protected embayments that are well-suited to the industrial production of aquatic marine organisms (e.g., salmon, blue mussels, and macroalgae), thanks to the calm and pristine waters, the high availability of phytoplankton (for blue mussels) and the temperature suitable for salmon farms. In the last decades, the salmon farm industry in particular has expanded toward the south in search of new areas to establish sites of aquaculture production. This move has been driven by the necessity to vacate the eutrophic waters generated by intensive aquaculture, with their inherent enhanced oxygen depletion and the various diseases engendered by the bad practices of the aquaculture industry during the last five decades (Buschmann et al., 2009; Pantoja et al., 2011). Aquaculture is now spreading toward the southern tip of South America, where still pristine environments are already facing the challenges of climate change; this increasing industrial pressure threatens these unique ecosystems, about which much has yet to be understood.

Studying this region is a challenge in its own right, due to the complex geomorphology and the difficulty to access most of the channels, which cover a vast surface area (∼132,291 km^2). Furthermore, the region is subject to complex interactions between atmosphere, land, cryosphere, and ocean, and is under the strong influence of oceanographic features such as the Cape Horn Current (CHC) (Strub, 1998; Strub et al., 2019). The CHC originates where the South Pacific Current from the west divides at around 40–45°S, with the CHC going southward (Strub et al., 2019). The CHC is described as a surface current moving southward along the western shelf of Patagonia (Talley et al., 2011; Strub et al., 2013), transporting Subantarctic Water (SAAW) with a salinity in the range 33–34.2 and temperature between 7 and 9°C (Palma and Silva, 2004) along the coast. Close to the continent, the SAAW is diluted by fresh water from continental runoff, referred to as Estuarine Water (EW; salinity 1–32) which is subdivided in fresh-EW (salinity 1–11), brackish-EW (11–21) and salty-EW (21–31) (Silva et al., 1998; Valdenegro and Silva, 2003). As a result of the mixing of SAAW and EW, modified Subantarctic water (mSAAW) with a salinity in the range 32–33 (Sievers et al., 2002) is formed. Due to complex bathymetry, there is a permanent input of SAAW into several fjords and channels, while others have limited or no exchange with SAAW, due to the presence of shallow sills which hinder its circulation (Palma and Silva, 2004). SAAW usually enters the fjords and channels of southern Patagonia between 50 and 75 m depth (Valdenegro and Silva, 2003; Sievers and Silva, 2006), filling a series of microbasins and modifying the physical and chemical properties (Valdenegro and Silva, 2003; Sievers and Silva, 2006; Brun et al., 2020). On the other hand, the freshwater inputs from rivers, coastal runoff, and the thawing of glaciers flow out at the surface, mixing with SAAW and transporting dissolved as well as particulate organic and inorganic matter into the channels and fjords (Valdenegro and Silva, 2003; Giesecke et al., 2019). This creates unique environments that shape ecosystem structure and functioning (Hamamé and Antezana, 1999; Palma and Silva, 2004).

Southern Patagonia faces strong westerlies throughout the year, with an intensification during the austral spring and summer (Garreaud et al., 2009), but these wind regimes are gradually being modified due to climate change. Records from the last four decades indicate that the prevailing zonal (east-west) wind in the region has increased in intensity at a rate of 0.2–0.3 m s^{-1} per decade (Garreaud et al., 2013). Since 1990, there has been a significant increase in rainfall during the austral winter (June, 200 mm per decade) and a gradual decrease in spring and summer (González-Reyes et al., 2017). Atmospheric temperature is linked with the temporal variability of the Southern Annular Mode (SAM), generally defined as the mean sea level pressure difference between 40 and 65^{o}S. The SAM can shift between positive and negative phases associated with the North-South movement of the west wind belt and the path of frontal systems. Since 1940, a trend toward positive SAM phases has been predominant, favoring higher atmospheric

temperatures associated with rising greenhouse gas emissions and increased ozone depletion (Abram et al., 2014).

The Beagle Channel

The Beagle Channel is the southernmost channel of the South American continent and one of the most prominent, due to the fact that it forms an uninterrupted conduit between the Pacific and the Atlantic oceans. This channel is a former tectonic valley that was completely covered by ice during the last glaciation (Bujalesky, 2011). The erosive action of glaciers and the subsequent deposits have shaped its present-day abrupt bathymetry, which includes semi-isolated basins (up to 400 m deep) and embayments separated by a series of shallow topographic sills (Bujalesky, 2011). The Channel has a Y-shape, with two arms at its Pacific end, hereafter named north-western and southern branches; these arms converge at 69 °W to form a single channel (**Figure 1b**). North of the north-western branch, the CDIF supplies large inputs of freshwater (glacial meltwater) into the Beagle Channel via several fjords and rivers, while the southern branch receives melt and rainwater from surrounding continental runoff. At the eastern end of the north-western section, the main topographic sill is located at Diablo Island (close to Punta Divide, **Figure 1e**), where the Channel narrows from 2 km to 1 km and the sill rises to a depth <50 m. In the southern arm another shallow sill (∼100 m depth) is located at Fleuriais Bay (**Figure 1d**). The eastern section of the Beagle Channel basin (between Punta Divide and Gable Island) is separated from the Atlantic Ocean by shallow (30 m deep) and narrow topographic sills at Mackinlay Strait and Murray Channel, respectively (**Figure 1f**; Bujalesky, 2011). These topographic sills limit the circulation of water masses along the Channel (Valdenegro and Silva, 2003), leading to the formation of microbasins with distinct biotic and abiotic properties (Hamamé and Antezana, 1999; Diez et al., 2018).

The entire western section of the Beagle Channel is surrounded by the CDIF. Some of the glaciers of the CDIF are connected to the Channel through fjords located on either side of its north-western branch, while others flow directly into the main channel. In the southern branch of the Channel, glaciers are less numerous and are restricted to mountain tops. The eastern limit of the CDIF is located at Yendegaia Bay. Eastward from Yendegaia Bay, the number and extension of mountain glaciers tend to diminish, while dense river networks play a major role in supplying freshwater to the Channel. These freshwater discharges into the Channel are at present poorly constrained, while observations in the middle sector of the Channel show a clear seasonal pattern, with higher freshwater inputs during the spring/summer (October to January) (Iturraspe et al., 1989). The tidal regime is mixed semidiurnal with a tidal range of 2.3 m (D'Onofrio et al., 1989). It is generally agreed that the main circulation in the region is eastward, transporting waters of Pacific origin into the southwest Atlantic around Cape Horn and through the Strait of Magellan (Brun et al., 2020; Guihou et al., 2020 and references therein). Although the circulation is not well constrained in the particular case of the Beagle Channel, available observations and modeling efforts (e.g., Balestrini et al., 1990, 1998) also indicate an eastward net transport of surface waters flowing above the sills. Balestrini et al. (1990), for example, deployed near-surface current meters for periods of 48 h at 20 locations in the middle section of the Beagle Channel, and were able to describe current reversals associated with tides and residual currents. In all recording stations that were not influenced by very local bathymetric effects, the residual currents presented consistent eastward directions and current speeds between 2.6 and 13.7 cm s^{-1} (Balestrini et al., 1990). Comparable observations were obtained by Speroni et al. (2003) by means of a near-bottom current meter deployed in Mackinlay Strait.

More complex circulation patterns, including recirculating cells, have been observed in embayments such as Ushuaia Bay (Flores-Melo et al., 2020). Less is known about the deep circulation in sectors that are deep enough to host a two-layer system in which the mechanical action of winds, tides and waves is insufficient to mix the entire water column. In fact, both wind intensity and, in particular, wave height are significantly limited with respect to other locations of Southern Patagonia or the Drake Passage, owing to the sheltering effect provided by mountain ranges along the Beagle Channel.

The rapid growth of human settlements, maritime traffic, and industrial endeavors in the Channel call for the establishment of a baseline of the physical, chemical, and biological features of this ecosystem. Despite the relevance of the area, the Beagle Channel is at present understudied, and a complete description of the physical environment is lacking. Research in the Channel has been hindered by its remote location and also by the fact that the Channel is shared between Chile and Argentina, meaning that most research surveys have been conducted within the respective borders of each country. Indeed, coordinated efforts to study the entire Channel have been set up only recently.

This study aims to compile, for the first time, high resolution hydrographical data collected along the Chilean and Argentinian sections of the Beagle Channel in order to provide a detailed description of water mass properties at all depths throughout the Channel.

MATERIALS AND METHODS

Along-Channel Hydrographic Transects

Since October 2016, the IDEAL center (Research Center: Dynamics of High Latitude Marine Ecosystems) has conducted hydrographic transects yearly from the western end of the north-western branch of the BC to Yendegaia Bay (**Figures 1a–c**). While during winter 2017 (July–August), simultaneous to the IDEAL transect, a full oceanographic survey onboard M/O Bernardo Houssay (PNA, Argentina) was conducted from nearby Yendegaia Bay to the eastern limit of the BC, thus generating for the first time a full, high resolution, hydrographic section along the entire Channel. The last survey was held during July 2018 along the northern and southern branch of the BC. In all the surveys, factory-calibrated CTDs (equipped with chlorophyll fluorescence and dissolved oxygen sensors), were used. The

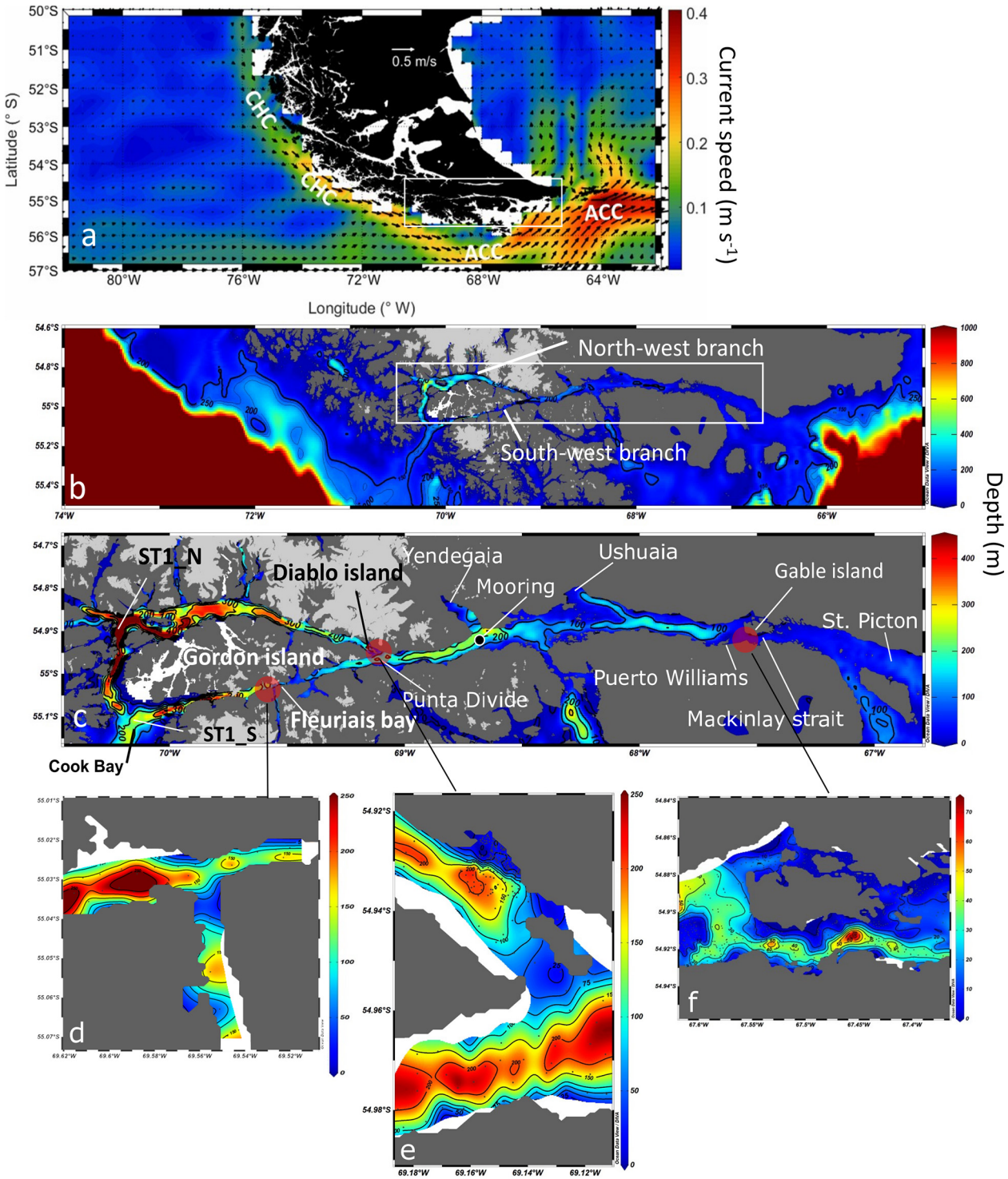

FIGURE 1 | (a) Map of the annual mean surface currents (m s^{-1}, 1992– 2019) at the southern tip of South America. Currents derived from the Ocean Surface Current Analysis Project (Bonjean and Lagerloef, 2002). The names of the main currents are indicated in white letters: ACC = Antarctic Circumpolar Current and CHC = Cape Horn Current. **(b)** Map of the study area bathymetry, including the 200 m isobath, highlighting canyon entrances and the NW and SW branches of the Beagle Channel. **(c)** Detailed bathymetry along the Beagle Channel including the principal toponymy. Light gray areas indicate the location of the Cordillera Darwin Ice Field, while white areas at the western section of Gordon Island denote a lack of bathymetric data. Detailed bathymetry of the main topographic sills along the Beagle Channel at **(d)** Fleuriais Bay, **(e)** Diablo Island, **(f)** Mackinlay Strait. Bathymetric charts of the Chilean Beagle Channel were provided by the Chilean Navy (SHOA), while bathymetry from the Argentinian sector was digitized from chart H-477 (Argentinian Naval Hydrographic Service, SHN). The bathymetry of the continental shelf and slope was obtained from the General Bathymetric Chart of the Oceans (IOC et al., 2003).

details are given in **Table 1**. The raw data from the CTDs were processed individually cast by cast, according to the protocol recommended by SBE and averaged to a vertical resolution of 0.5 m. Data visualization and further analysis were performed using the Ocean Data View software (Schlitzer, 2020).

Water Chemistry Along the Beagle Channel From Historical CIMAR-FJORD Campaigns

Similar spatial coverage of the Beagle Channel but at lower spatial resolution was obtained through two research cruises sponsored by the Chilean Navy CIMAR 3 (1998) and CIMAR 16 (2010) (see **Table 1**). During both cruises, a rosette equipped with 24 Niskin bottles collected water samples at discrete depths for the analysis of macronutrients (nitrate (NO_3^-), phosphate (PO_4^{-3}) and silicic acid ($Si(OH)_4$). Water samples (50 mL) were fixed with mercury chloride, stored at −20°C in acid-cleaned high-density polyethylene bottles and analyzed as described by Atlas et al. (1971) (for more details see Valdenegro and Silva, 2003). These data were provided by the Chilean National Oceanographic and Hydrographic Data Center (CENDHOC).

Time Series From an Oceanographic Mooring and Atmospheric Conditions

An instrumented mooring was deployed from 21 July 2017 through 28 September 2019 in the middle section of the Beagle Channel (54°55′ 3.83′′S; 68°38′ 48.72′′W, see **Figure 1c**) and over a water depth of 280 m. Temperature and conductivity loggers (Star Oddi) with a recording interval of 1 h were deployed at 50, 100, and 195 m depth. The latter was also equipped with a pressure sensor to confirm the final depth of each sensor after deployment. Due to the remoteness of the mooring site, the turnaround took place once a year. Prior to deployment and after recovery, a CTD (SeaBird 25plus) profile was conducted at the mooring site to calibrate the sensors and adjust for any potential drift during their deployment. Conductivity sensors underwent a considerable drift due to fouling and were ultimately discarded from further analysis.

Hourly temperature records at 50 m and 195 m were registered and analyzed for the period July 22, 2017 to September 27, 2019, while temperature at 100 m was recorded from July 22, 2017 to July 19, 2018 only.

Wind and atmospheric temperature data were obtained from the fifth major global European Centre for Medium-Range Weather Forecasts (ECMWF) global reanalysis (ERA5) (Hersbach et al., 2020). The data have a horizontal resolution of 0.25 × 0.25 degrees. A grid of data points around the Beagle Channel was selected and analyzed. The grid point closest to the location of the mooring was selected to be analyzed in the temporal domain using time series analyses (Emery and Thomson, 1998). The ERA5 reanalysis, satellite wind products and *in situ* weather stations had previously been used to determine the spatiotemporal variability of the surface winds along Southern Patagonia (Pérez-Santos et al., 2019): the study validated surface wind reanalysis to surface *in situ* and satellite observations, and obtained satisfactory correlation coefficients (0.5 – 0.9) and RMSE between 2 and 4 m s^{-1}. With this in mind, and considering that the study region is characterized by rugged topography that can shape and shift surface winds, caution must be employed when using the global scaled wind products provided by ERA5 to interpret the role of surface winds at smaller spatial scales: for this reason, we limit and focus the use of surface winds to determine main modes of temporal variability only.

To determine the principal modes of temporal variability in ocean and atmospheric conditions, hourly time series of ocean and atmospheric temperatures and winds were fit with annual and semi-annual harmonics. A residual was obtained by removing the annual and semi-annual cycles, the mean, and the trend. Afterward, spectra were calculated on the residual hourly time series by using fast Fourier transform.

TABLE 1 | Summary of each sampling campaign along the Beagle Channel (BC) included in this study, as well as and the instrumental mooring deployed at the central section of the BC.

Survey	Date	Spatial range	CTD model	Biogeochemistry analyses	CTD casts/sampling stations
CIMAR-3	October 1998	full BC	–	yes	7
CIMAR-16	Oct-Nov 2010	full BC	–	yes	7
IDEAL-2016	October 2016	NW branch to Yendegaia	SBE 19plus	no	16
IDEAL-2017	July 2017	NW branch to Yendegaia	Seabird 25plus	no	11
Houssay-17	August 2017	Yendegaia to eastern limit of BC	Seabird 911plus	no	39
IDEAL-2018	July 2018	NW branch to Yendegaia	Seabird 25plus	no	13
IDEAL-2018	July 2018	Southern branch	Seabird 25plus	no	6
Survey	**Date**	**Spatial range**	**Sensors**	**Biogeochemistry analyses**	**Depths (m)**
Mooring Beagle	21 Jul. 2017 to 28 Sept. 2019	Mid-section Beagle Channel	Star-Oddi (Temperature)	no	50, 195
Mooring Beagle	21 Jul. 2017 to 19 Jul. 2018	Mid-section Beagle Channel	Star-Oddi (Temperature)	no	100

Subtidal variability in temperature and atmospheric conditions was also analyzed by calculating daily averages of time series and estimating the spectra for all variables. Cross-correlations (Emery and Thomson, 1998) were used to determine relationships between wind and ocean temperature at subtidal temporal scales. Cross-correlations were estimated between the daily averaged along-channel wind components, wind magnitude and ocean temperature at 50 m and 195 m. A significance level of 95% was used.

RESULTS

Bathymetric and Hydrographic Features Along the Beagle Channel

The continental slope outside of the western section of the Beagle Channel is a relatively narrow (53 km) and steep margin. It is intersected by a submarine canyon which is 4 km wide and 250 m deep, on a continental shelf less than 100 m deep (**Figure 1b**). This canyon connects the two western branches of the Beagle Channel. The entrance of the NW branch presents a bathymetric depression which reaches a depth of 674 m and is the deepest part of the study area. The entrance of the SW branch, on the other hand, is on average shallower, reaching a maximum depth of 400 m. The seafloor in both branches gradually ascends eastward over an uneven bathymetry. This deep section extends across 70 km along the NW branch and 40 km along the SW branch, ending with narrow (1 km) and shallow topographic sills at Diablo Island (∼50 m) and Fleuriais Bay (∼100 m) in the NW and SW branch, respectively (**Figures 1d,e**). The seafloor deepens abruptly eastward from each sill, reaching a maximum depth of ∼250 m. Both channels converge in the Punta Divide, forming a microbasin which ends in the east at Ushuaia Bay. The depth profile of the eastern section off Ushuaia Bay decreases significantly, forming a narrow valley with depths of ∼150 m along the center of the Beagle Channel. In comparison, the borders of the Channel have a relatively shallow bottom depth (<100 m). Toward the east, there is another shallow (<30 m depth) and narrow (1.5 km wide) sill at Mackinlay Strait. East of this sill, the depth of the Channel is relatively shallow (<40 m), until reaching a transitory depression around 120 m deep in Picton Strait. Eastward from Picton Island, the Channel opens onto a broad and shallow continental shelf (depth < 75 m) that ends rather abruptly at approximately 66.2 °W, where it reaches the continental slope.

At depth in the western section of the Beagle Channel, we observed relatively warm (8–9°C; **Figures 2**, **3B**), saline (>33; **Figures 3A**, **4A–C**), and less oxygenated (6.6–6.8 mL L^{-1}; **Figures 3C**, **5A–C**) SAAW across several kilometers inside both channels. This water mass enters the north-western and southern branches of the Beagle Channel through deep canyons following the 25.5 kg m^{-3} isopycnal. This water mass flows along the NW and SW branches below 100 m depth until it reaches the sills in both branches, where its eastward movement is prevented (**Figures 6A–D**). At the surface in the western section of both branches, the input of diluted (salinity < 30), cold (5–6°C) and more oxygenated (7–7.4 mL L^{-1}) water from the Cordillera Darwin Ice Field (CDIF) combined with continental runoff, forms surficial Estuarine Water (fresh-EW), which then mixes with the SAAW at depth, forming the mSAAW between 50 and 100 m (**Figure 7**). Over both sills (at Diablo Island and Fleuriais Bay) and to the east of them an isopycnal rise (σ_θ = 24.75 kg m^{-3}) was seen to occur during every cruise (**Figures 4A**, **6A**).

The vertical structure was slightly different according to the years and months sampled along the NW branch. During October 2016 (onset of austral spring), the SAAW in the NW branch was slightly colder, and estuarine water (fresh-EW *sensu* Valdenegro and Silva (2003) was slightly warmer and less oxygenated at the surface. During July 2017 and July 2018, the temperature of the SAAW increased by 0.5°C, while surface fresh-EW remained almost the same (**Figures 2A–C**), albeit slightly more oxygenated than during 2016 (**Figures 5A–C**). Oxygen concentration in the upper 50 m of the water column is closely coupled with both Chl-a fluorescence along the entire transect (**Figures 3A–C**), and with the vertical structure of the water column. Chl-a fluorescence values were highest in the western part of the Channel during 2017 and 2018 (west of the Diablo Island sill), where the vertical structure of the water column was clearly defined by the upper fresh-EW and the lower SAAW, both separated by a pycnocline (σ_θ = 24.75 kg m^{-3}) which further limited the vertical distribution of phytoplankton fluorescence (**Figures 3A–C**).

East of the ∼50 and ∼100-m deep sills in both western branches, mixing disrupts the pycnocline and the water column showed vertical mixing from surface to bottom (down to 250 m). This homogenization results in higher dissolved oxygen concentrations and lower Chl-a fluorescence when considering the entire water column. During 2017, the section east of Yendegaia Bay was sampled, allowing us to follow the hydrography along the entire Beagle Channel. Toward the east of the Channel as the seafloor gradually rises, water temperature decreased slightly (0.5°C), while salinity remained relatively constant through the entire water column. Along the middle section of the Channel between these two sills (at Diablo Island and Fleuriais Bay) and the Mackinlay sill, the main water mass filling the entire basin is consistent with salty-EW (sensu Sievers et al., 2002; Palma and Silva, 2004), as defined by a salinity 31–32 (**Figure 7**) with a potential density of 24.5–25.25 kg m^{-3}, and temperature ranging between 5.25 and 7.2°C. The most noticeable feature of this section was the increase in Chl-a fluorescence along the eastern section (**Figure 3B**), where bottom depth becomes shallower, coinciding with an increase in dissolved oxygen at the surface (**Figure 5B**). East of the sill at Mackinlay Strait (eastern section of the Beagle Channel), we observed more saline, oxygenated and slightly warmer waters, consistent with mSAAW, which enter beneath the less saline and colder waters that flow out of the Beagle Channel, thus creating a shallow pycnocline that follows the 25.5 kg m^{-3} isopycnal at 20 m depth (**Figure 4B**).

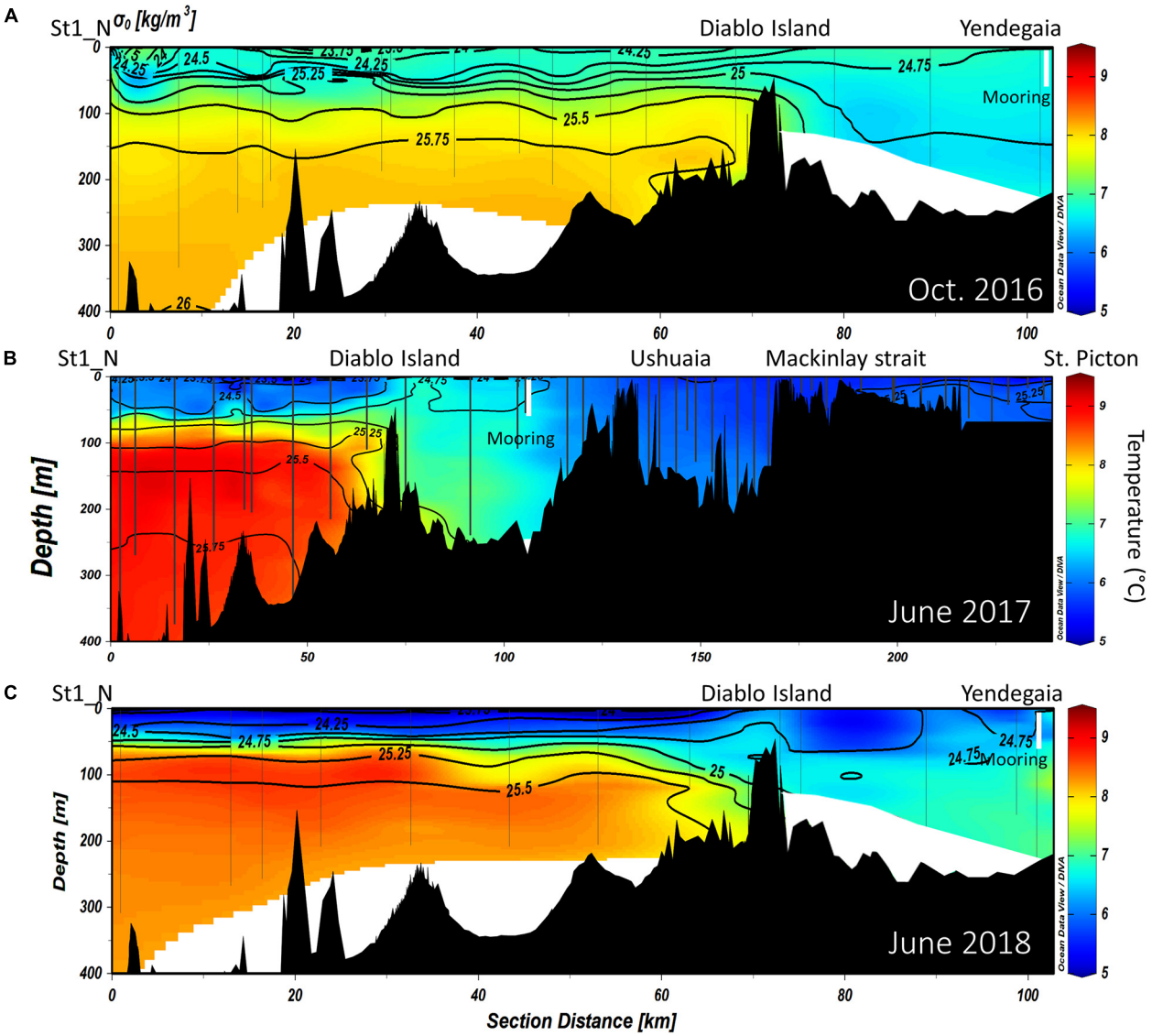

FIGURE 2 | Vertical distribution of potential temperature (°C) overlaid by isopycnals of potential density along the NW branch of the Beagle Channel, during the **(A)** October 2016, **(B)** June 2017 and **(C)** June 2018 campaigns. Interpolated contours are created from individual CTD profiles (positions shown as vertical lines), where St1_N (left side of the figure) represents the westernmost station, and Yendegaia station the eastern part, sampled during 2016 and 2018. During 2017 **(B)** the westernmost station extends from St1_N to St. Picton at the eastern end of the Beagle Channel. The position of the instrumented mooring is indicated by a vertical white line.

Nutrient Distribution (CIMAR 3 and CIMAR 16 Cruises)

During the CIMAR 3 (Oct-1998) cruise (**Figures 8A–C**), the highest concentrations of macronutrients (silicic acid, nitrate and phosphate) were found at depth, related to the inflow of SAAW at the northwestern entrance of the Beagle Channel, while the lowest values were observed at the surface where the high input of meltwater from the CDIF is transported from the fjords into the Channel, forming the fresh-EW and brackish-EW. Nitrate and phosphate (**Figures 8A,B**) followed the same pattern as that observed for the physical properties along the Channel, with higher concentrations associated with the inflow of SAAW at the NW section of the Beagle Channel, west of the Diablo Island sill (**Figures 8A–C**). Phosphate (**Figure 8A**) and nitrate (**Figure 8B**) concentrations were highest at depth (>100 m depth) (1.3–1.6 μM PO_4 and 12.5–17.5 μM NO_3) where SAAW was observed, while silicic acid (**Figure 8C**) showed a more heterogeneous distribution with few maxima at 200m depth (6–8 μM). The upper water column (<100 m depth) had the lowest nutrient concentrations observed (<0.9 μM PO_4, < 9 μM NO_3 and <2 μM $Si(OH)_4$) along the entire BC, which coincides with the section where maximum flow of meltwater from the CDIF reaches the BC, forming the fresh and brackish-EW. East of the Diablo Island sill, a disruption

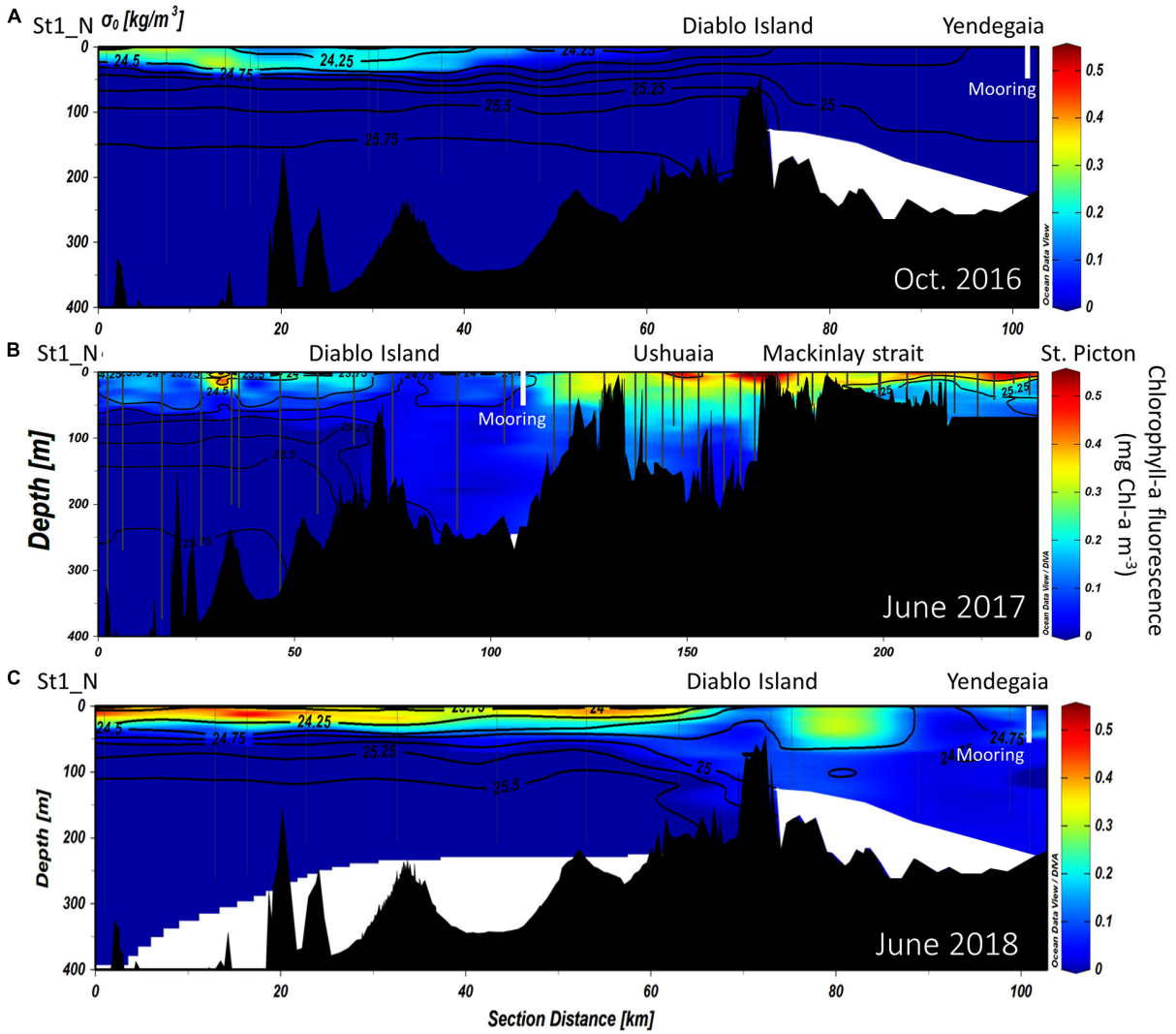

FIGURE 3 | Vertical distribution of chlorophyll-a fluorescence (mg Chl-a m^{-3}), overlaid by isopycnals of potential density along the NW branch of the Beagle Channel, during the **(A)** October 2016, **(B)** June 2017 and **(C)** June 2018 campaigns. Interpolated contours are created from individual CTD profiles (positions shown as vertical lines) where St1_N (left side of the figure) represents the westernmost station, and Yendegaia station the eastern part, sampled during 2016 and 2018. During 2017 **(B)**, the westernmost station extends from St1_N to St. Picton at the eastern end of the Beagle Channel. The position of the instrumented mooring is indicated by a vertical white line.

of the vertical distribution of nutrients was observed, causing an almost complete vertical homogenization of nitrate and phosphate through the entire water column of salty-EW which fills the central section of the BC (**Figure 7**). This relatively homogeneous nutrient distribution (0.9–1.1 μM PO_4 and 7.5–10 μM NO_3) extends throughout the water column, along the entire Channel until it reaches the Atlantic Ocean. A significant increase of phosphate was observed at 100 m depth (1.47 μM PO_4) and a lesser increase of nitrate was recorded in a station 20 km west of Mackinlay Strait (**Figures 8A,B**). Silicic acid concentrations were lowest east of Diablo Island, with some maxima [5–6 μM $Si(OH)_4$] at intermediate depths reaching Mackinlay Strait. Slightly higher silicic acid concentrations were recorded in shallow stations from Ushuaia toward the eastern opening to the Atlantic. Twelve years later, during the CIMAR 16 cruise (Oct–Nov. 2010, **Figures 9A–C**), the same stations were sampled. Slight increases in phosphate (∼0.1 μM PO_4, **Figure 9A**) and nitrate (∼0.5 μM NO_3, **Figure 9B**) were observed at depth in the western part of the Beagle Channel, following a similar pattern as that observed in 1998. Higher concentrations of phosphate, nitrate and silicic acid were observed at stations where SAAW was present. At the surface, and close to the CDIF, a depletion of nutrients (fresh- and brackish-EW) was recorded, and east of the Diablo Island sill could be seen a homogenization of nutrients through the water column, with few maxima at depth west of Mackinlay Strait, similar to the pattern observed during the CIMAR 3 cruise. The major difference was the decrease of silicic acid

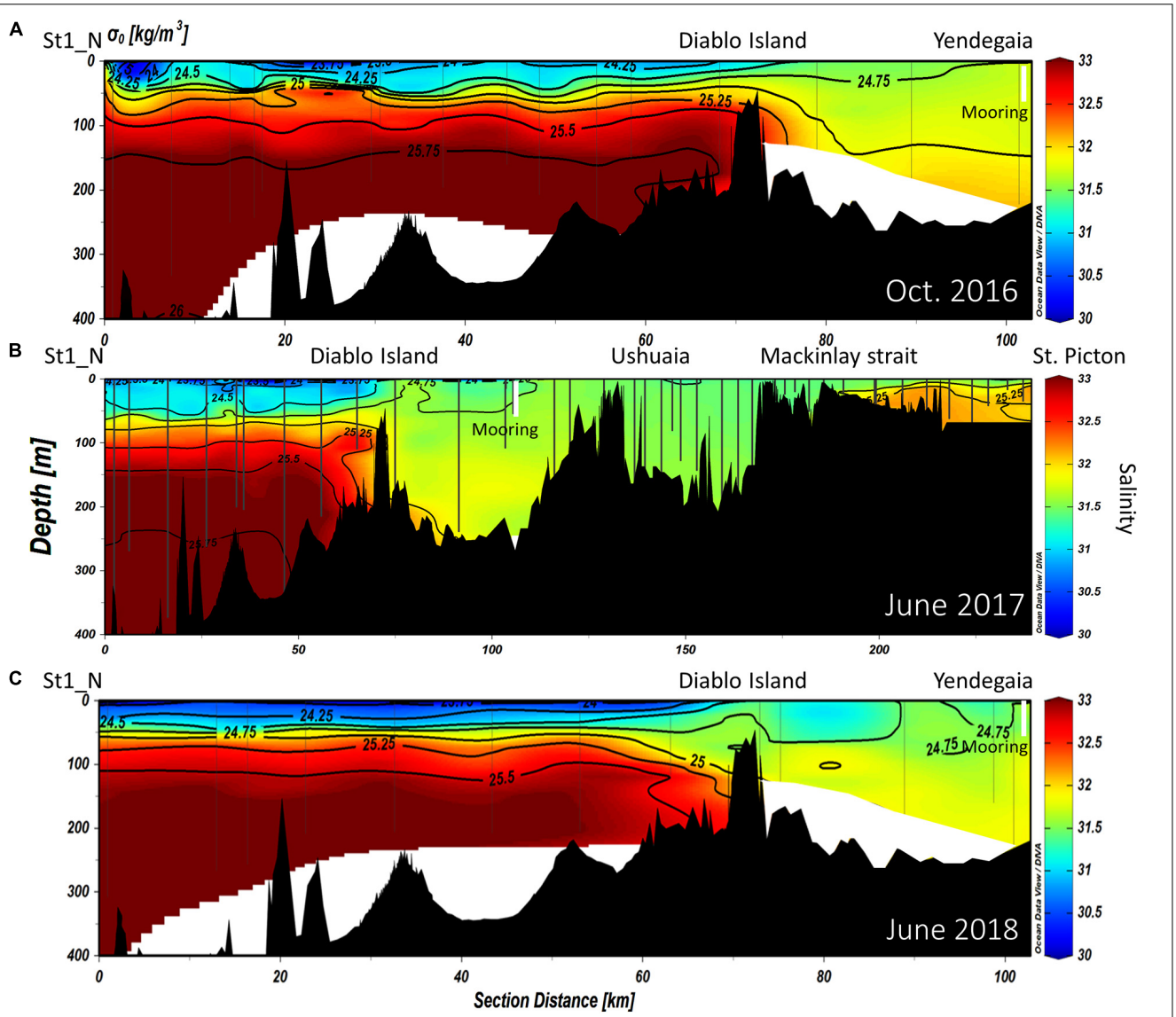

FIGURE 4 | Vertical distribution of salinity (EOS-80), overlaid by isopycnals of potential density along the NW branch of the Beagle Channel during the **(A)** October 2016, **(B)** June 2017, and **(C)** June 2018 campaigns. Interpolated contours are created from individual CTD profiles (positions shown as vertical lines), where St1_N (left side of the figure) represents the westernmost station, and Yendegaia station the eastern part, sampled during 2016 and 2018. During 2017 **(B)** the westernmost station extends from St1_N to St. Picton at the eastern end of the Beagle Channel. The position of the instrumented mooring is indicated by a vertical white line.

at the surface along the entire transect, with concentrations <1.5 μM in the upper 150 m. The entire Beagle Channel showed a noticeable nitrate limitation which was consistent among all water masses (**Figures 10A,B**) with a N : P ratio of 8.42 and 8.25 during CIMAR 3 (**Figure 10A**) and CIMAR 16 (**Figure 10B**), respectively. In contrast to the N : P ratio, the N : Si ratio showed a differential limitation related to the different water masses (**Figures 10C,D**). There was a relative silicic acid limitation in SAAW despite its higher nutrient concentration, compared to the mSAAW and whole EW. The fresh and brackish-EW was the water mass with the lowest nutrient concentration, with an $Si(OH)_4$:NO_3 ratio close to 1 during both CIMAR cruises (**Figures 10C,D**).

Time Series of Temperature and Atmospheric Variables in the Middle Section of the Beagle Channel

The temporal variability in water and atmospheric temperature at low frequencies was dominated by the annual cycle (**Figures 11**, **12A–C**), which explained 75–89% and 53% of the variability, respectively (**Table 2**). A lower percentage of the temporal variability of the water temperature was explained by the semi-annual cycle (2–5%). This explains the significant control exerted by summer and winter seasons in the vertical structure of the water column from the surface (50 m) to 195 m depth in the middle section of the BC. The influence

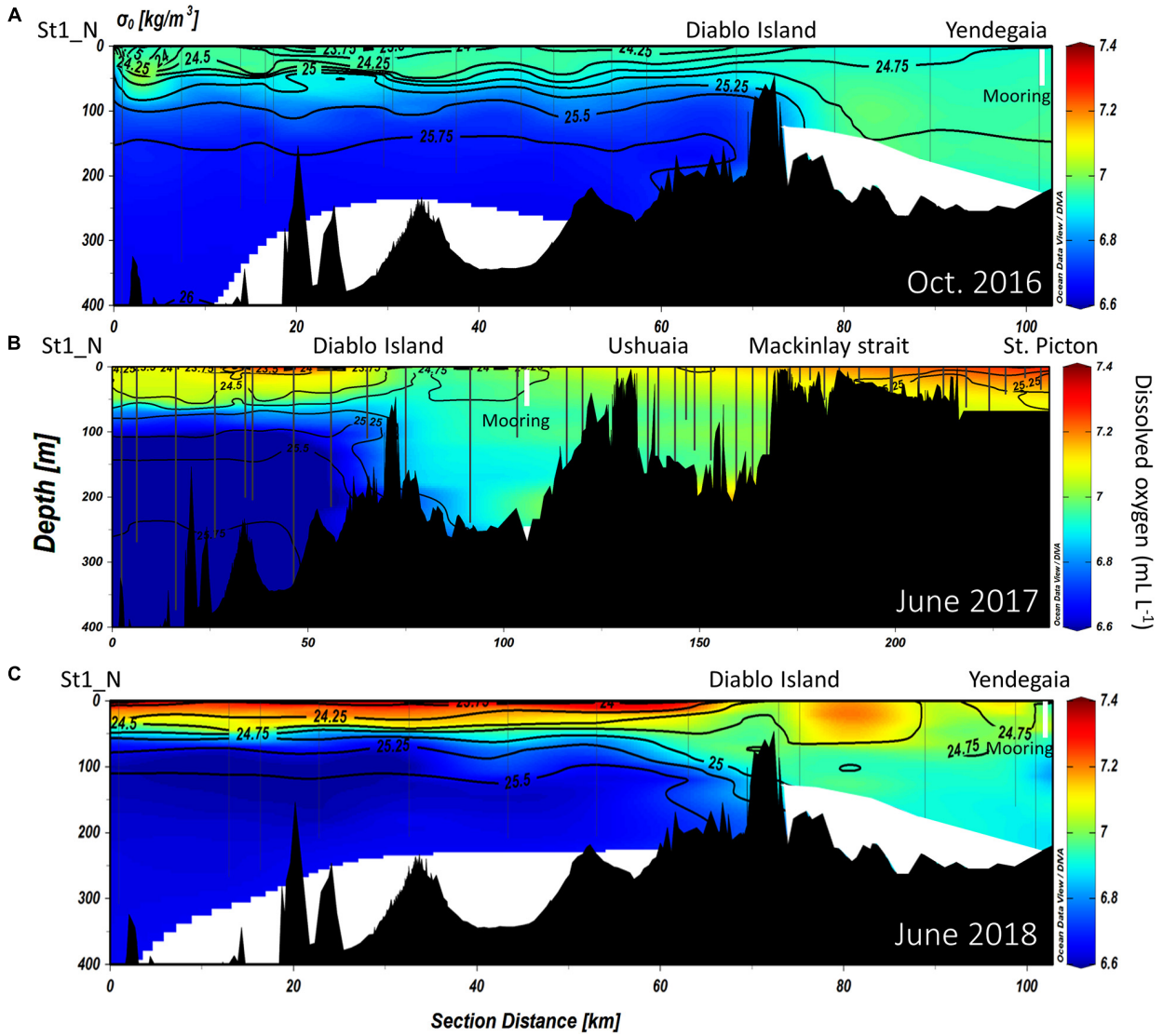

FIGURE 5 | Distribution of dissolved oxygen concentration (mL L^{-1}), overlaid by isopycnals of potential density along the NW branch of the Beagle Channel, during the **(A)** October 2016, **(B)** June 2017 and **(C)** June 2018 campaigns. Interpolated contours are created from individual CTD profiles (positions shown as vertical lines) where St1_N (left side of the figure) represents the westernmost station, and Yendegaia station the eastern part, sampled during 2016 and 2018. During 2017 **(B)** the westernmost station extends from St1_N to St. Picton at the eastern end of the Beagle Channel. The position of the instrumented mooring is indicated by a vertical white line.

of the annual cycle from the surface (50 m) to the depths of the Beagle Channel (195 m) showed a temporal lag of 27 days, and 0 days lag between the surface (50 m) and the subsurface (100 m) (**Table 3**). Correlations among different annual signals, including the atmosphere, showed similar lagged correlations between the annual cycle of the atmosphere and temperatures at 50 and 100 m (r^2 = 0.85 and 0.83, respectively), while atmospheric temperature and measurements taken at 195 m showed a delay of 63 days at the maximum correlation (r^2 = 0.69) (**Table 3**). Once the annual and semi-annual cycles were removed, a peak of energy in ocean temperature variability was explained by high-frequency fluctuations dominated by the semidiurnal tidal periods. Spectral density for the three ocean time series peaked at 12.4 h, although this was more noticeable at 50 m and 100 m than at 195 m (**Figure 11**). The highest energies in the temperature spectrum were observed at 26 days for 50 m and 195 m, while a band of energy between 9 and 17 days was noted for the 100 m temperature time series. A weak cross-correlation was observed between wind magnitude and the residual of ocean temperature (results not shown). The largest temperature gradient from surface (50 m) to depth (195 m) was observed during summer and early fall (January to mid-April), reaching 1.5°C (**Figure 12C**). The mooring was positioned off Yendegaia Bay, east of Diablo Island in the middle section of the Beagle Channel, which is less influenced by oceanic inputs. The basin-like structure of

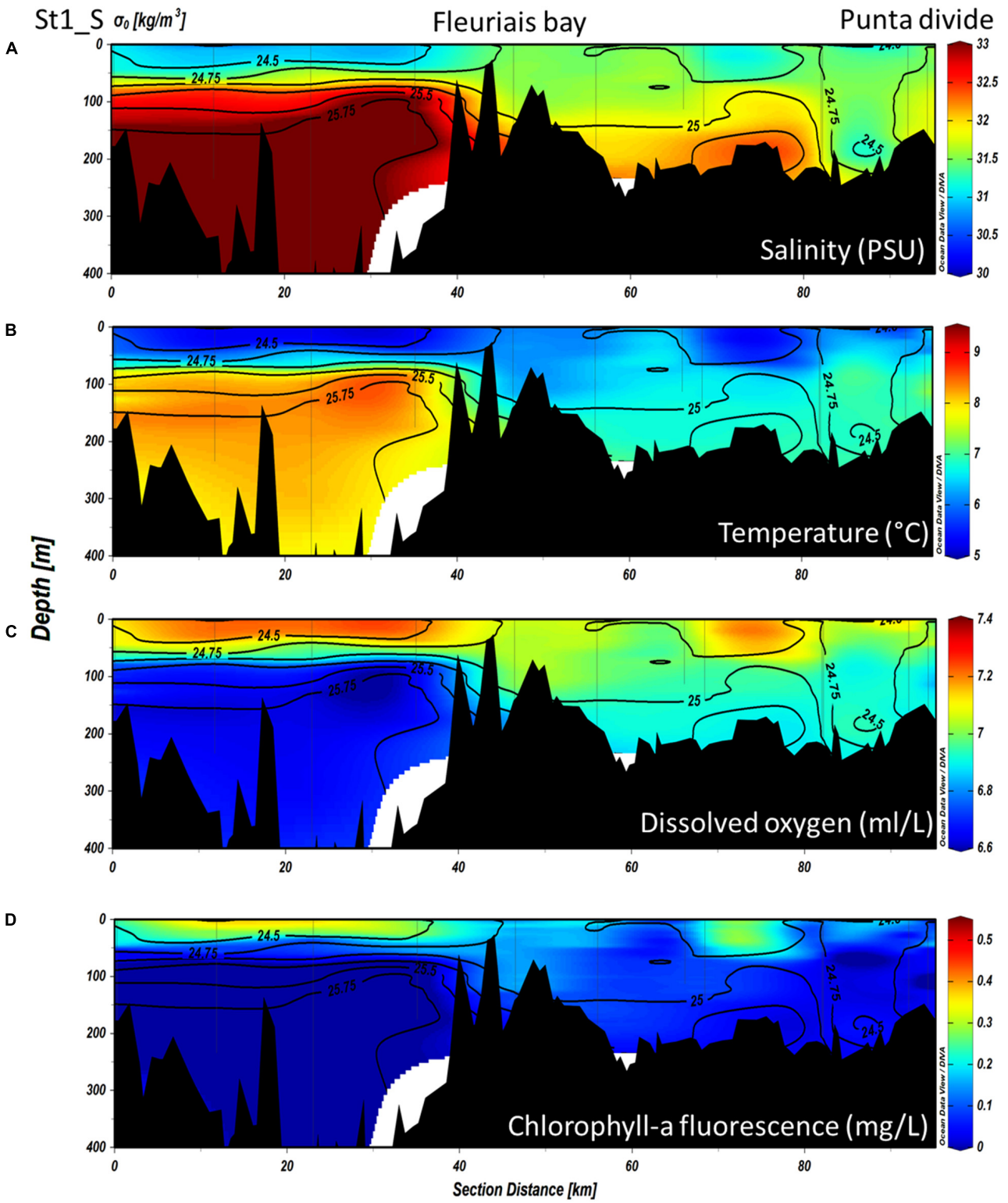

FIGURE 6 | Vertical distribution of **(A)** salinity (PSS-78), **(B)** potential temperature (°C), **(C)** dissolved oxygen (mL L^{-1}) and **(D)** chlorophyll fluorescence (mg m^{-3}), overlaid by isopycnals of potential density along the south-western branch of the Beagle Channel, during the June 2018 campaign. Interpolated contours are created from individual CTD profiles (positions shown as vertical lines) where St1_S (left side of the figure) represents the westernmost station, and Punta Divide station the eastern part, sampled in the south-western branch.

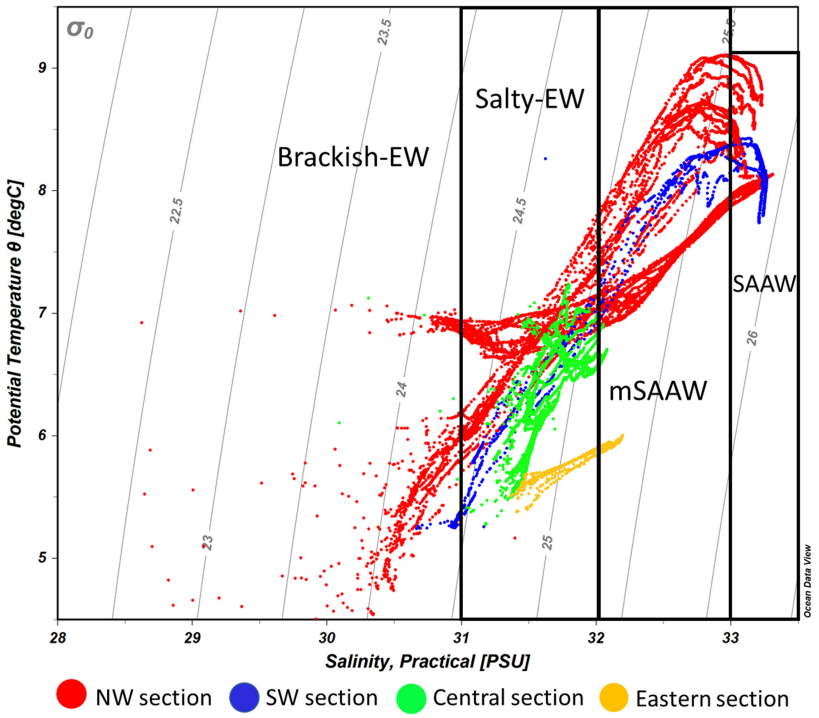

FIGURE 7 | Potential temperature-salinity diagram of all CTD profiles during the different surveys carried out along the Beagle Channel. Light gray lines represent density anomalies (kg m^{-3}). Color codes represent the profiles carried out in each of the described microbasins reported along the Beagle Channel. The NW section (red) includes all the profiles from ST1_N to the Diablo Island sill. The SW section (blue) ranges between ST1_S station and the Fleuriais Bay sill, the central section (green) extends west of the sills in both western branches to the Mackinlay Strait sill, while the eastern section (yellow) indicates all the profiles carried out east of the Mackinlay Strait sill. SAAW, Subantarctic Water; mSAAW, modified Subantarctic water and EW, Estuarine Water which is subdivided into (salty-EW and brackish-EW according to the definition provided by Silva et al. (1998) and Valdenegro and Silva (2003).

this section of the Channel favors retention, and is most likely responsible for the weak temperature gradient found between 50 and 195 m depth.

DISCUSSION

Physical and Chemical Water Column Structure of the Beagle Channel

The hydrography along the Beagle Channel shows a coherence between different sampling events, from the cruises in October 1998 and November 2010, as well as the most recent campaigns in October 2016, July 2017, and July 2018. The system is dominated by (a) the inflow of warm, saline, less oxygenated and nutrient-rich waters characteristic of SAAW, to the western section of the Channel, and (b) by the presence of surface fresh-EW with oxygen-rich and nutrient-poor characteristics. The fresh-EW results from the inflow of cold freshwater from the CDIF glaciers and continental runoff on both shores of the two western branches of the Beagle Channel. Accordingly, a sharp pycnocline develops, separating the lighter fresh-EW from the subsurface tongue of SAAW. The latter fills the entire western section below 75 m depth from the Pacific entrance as far as the sills at Diablo Island (north-western branch) and Fleuriais Bay (southern branch). However, these shallow sills prevent the spreading of SAAW toward the east into the middle section of the BC. Lower dissolved oxygen concentrations west of the sills in the NW and SW branches suggest a long residence time and a slow exchange of SAAW and mSAAW. Eastward from these sills, the vertical structure of the water column changes abruptly from stratified to completely mixed from surface to bottom (down to 250 m depth). The mixed water column has properties that indicate the mixing of fresh-EW with the upper limit of the mSAAW, resulting in salty-EW (31-32) (Sievers et al., 2002; Valdenegro and Silva, 2003). Downstream from these sills, upward pumping of the mSAAW may take place due to Bernoulli aspiration (Kinder and Bryden, 1990), as has been observed for similar environments involving sills along channels (Seim and Gregg, 1997). In fact, Bernoulli aspiration has been registered in the neighboring Magellan Strait (Valle-Levinson et al., 2006), which also connects the Pacific and Atlantic oceans, and provides bathymetric and hydrological along-channel gradients comparable to those of the BC. Briefly, as surface flow accelerates upon encountering the sill, pressure diminishes (Venturi effect), which allows the upward pumping of deep and denser waters; this, in turn, raises the pycnocline. Eventually, the outcrop and overflow of the denser waters toward the downstream side of the sill will be caused by this up-sill suction effect. We presume that only a fraction of the mSAAW is pumped, but it may be enough to increase the density of the brackish-EW near the surface, east of the

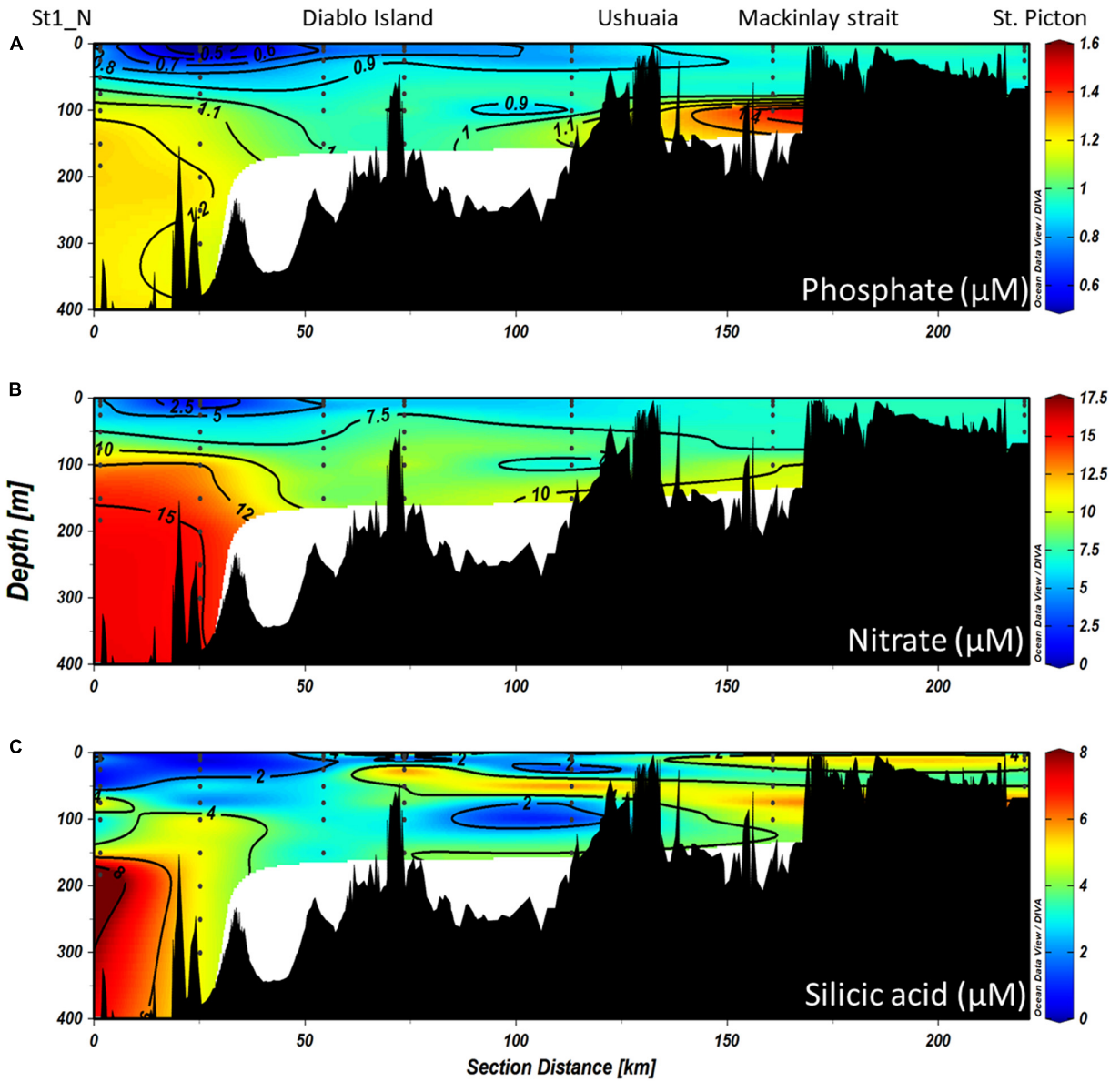

FIGURE 8 | Vertical distributions of **(A)** phosphate, **(B)** nitrate, and **(C)** silicic acid along the entire northern branch of the Beagle Channel during the CIMAR 3 campaign in October 1998. The left of the figures represents the western part of the Beagle Channel, while the right side corresponds to the most eastern part sampled (St. Picton). Black dots represent the stations and depths sampled.

sills, and may thus trigger convective mixing of the entire water column. Such up-sill suction of the SAAW is not evident in our data due to a lack of spatial resolution close to the sill, but previous and more detailed hydrographical profiles conducted along the Diablo Island sill do document this (**Figure 2** in Hamamé and Antezana, 1999). Both the up-sill pumping of deep waters and the complete vertical mixing downstream of the sill, observed in Hamamé and Antezana (1999), are consistent with observations from other locations with similar hydrographic settings (Seim and Gregg, 1997; Valle-Levinson et al., 2006). On the other hand, such a suction effect has not been observed in the other major sill to the east, at Gable Island, which may be due to a smoother bathymetric transition and a wider channel in comparison with the sector around Diablo Island. East of Gable Island, the two-layer structure observed corresponds to the outflow of fresher waters from the middle section of the Channel; these overly a tongue of water with distinctive higher temperature and salinity, corresponding to mSAAW. The transport of this less saline surface water from the Beagle Channel has been characterized by the transport of nutrient-depleted and high humic-like components associated with highly degraded terrigenous humic material along the eastern margin of the continent toward the Atlantic Ocean (Garzón et al., 2016). In this way, the entire Beagle Channel can be understood as a dilution

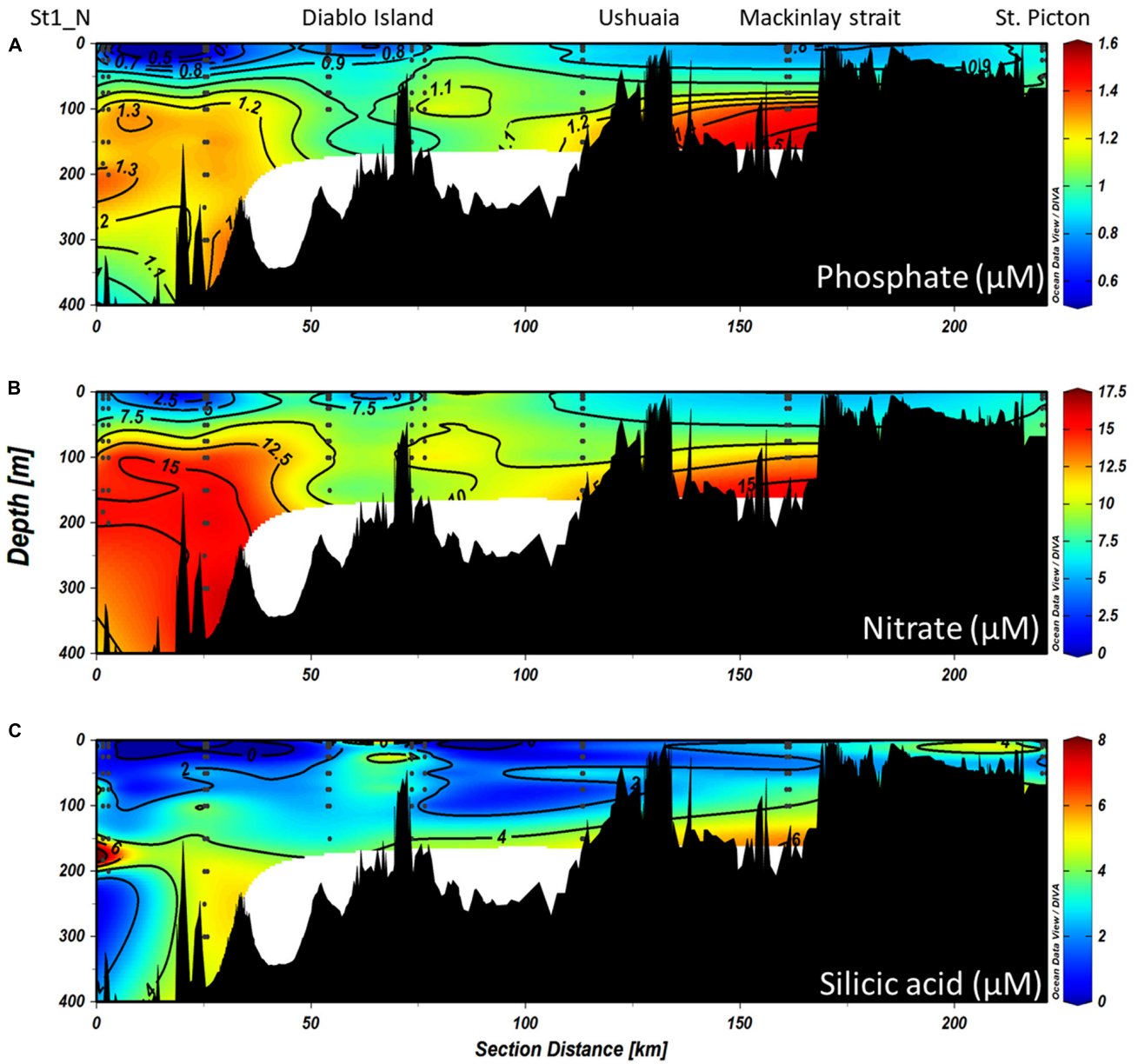

FIGURE 9 | Vertical distributions of **(A)** phosphate, **(B)** nitrate, and **(C)** silicic acid along the entire NW branch of the Beagle Channel during the CIMAR 16 campaign in November 2010. The left of the figures represents the western part of the channel, while the right side corresponds to the most eastern part sampled (St. Picton). Black dots represent the stations and depths sampled.

basin, limited by SAAW in the western section and with a less saline mSAAW at the eastern end. The eastward outflow of the middle Beagle Channel may play a role in the total transport of water properties from the Pacific to the Atlantic Patagonian Shelf, which has a major impact on the hydrography, circulation and ecology of that area (Guihou et al., 2020 and references therein).

The temporal variability of temperature at different depths was described for a region off Yendegaia Bay (**Figure 12**), in the middle section of the Beagle Channel (between the Diablo Island – Fleuriais Bay sills and Mackinlay sill). As mentioned previously, this region is characterized by a relatively homogenous water column (during winter and spring; Aug-Dec), a feature that is permanent in time and changes only slightly during summer months (Dec-Mar). During summer, the atmospheric conditions contribute to both the stratification and the mixing of near-surface waters at the same time. Westerlies increase mainly in November through March (Garreaud et al., 2013), likely contributing to the mixing of the upper water column, whereas higher solar radiation enhances stratification, and hence the relatively homogenous water column, even during summer months (**Figure 12C**). The most significant temporal driver is dominated by the annual

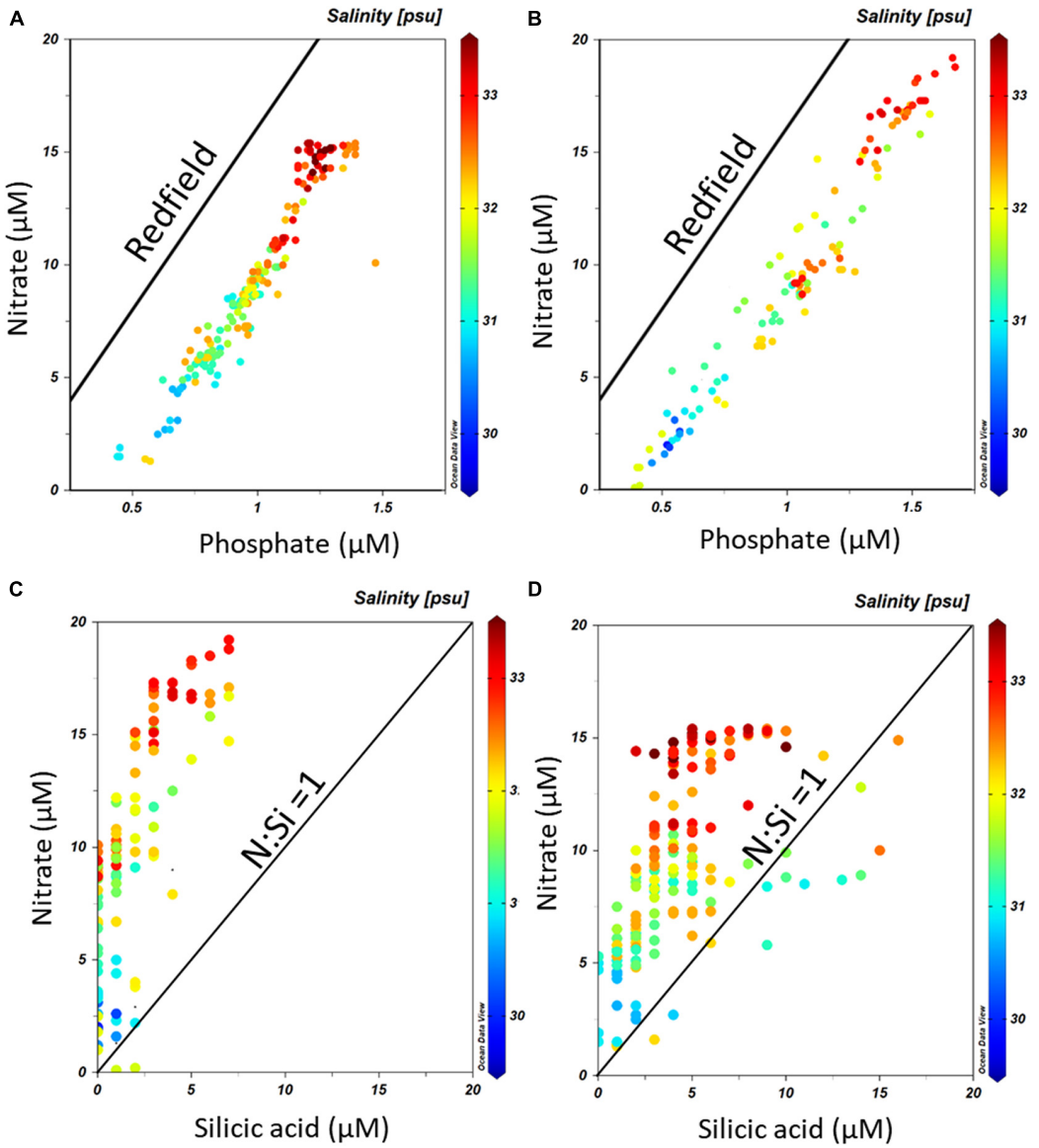

FIGURE 10 | PO_4–NO_3 relationships along the Beagle Channel during **(A)** the CIMAR 3 and **(B)** the CIMAR 16 cruises, during October 1998 and November 2010, respectively. The solid line indicates the Redfield ratio (1:16). $Si(OH)_4$ – NO_3 relationships along the Beagle Channel during **(C)** the CIMAR 3 and **(D)** the CIMAR 16 cruises. The solid line indicates the optimum $Si(OH)_4$: NO_3 for diatoms, according to Ragueneau et al. (2000). The color bar represents the salinity (PSS-78) recorded at each sampling point.

signal, followed by higher frequencies dominated by semidiurnal tides (D'Onofrio et al., 1989).

Chemical Features Along the Beagle Channel

In the Beagle Channel, the highest nutrient concentrations are associated with the inflow of SAAW along the western section of the Channel, while at the surface, nutrient-poor waters are formed by river and glacier runoff. This structure is common to the Patagonian fjords (Silva and Vargas, 2014; Vargas et al., 2018; Cuevas et al., 2019). Generally speaking, this two-layer structure promotes the development of moderate phytoplankton biomass (<0.6 mg Chl-a m^{-3}) which is restricted to the upper part of the pycnocline, where diffusion and turbulence favor vertical transport of nutrients from the SAAW toward the upper water column, thus promoting phytoplankton growth (Hamamé and Antezana, 1999; Cuevas et al., 2019). It must be noted that most of the cruises were carried out during the austral winter (July), therefore low phytoplankton biomass is to be expected due to light limitation (Almandoz et al., 2011). Similarly, the sills in the Channel may play an important role in the mixing of the entire water column (mSAAW and brackish-EW), which in turn disrupts the vertical structure of the water column from surface to bottom. This water mixing moves phytoplankton cells

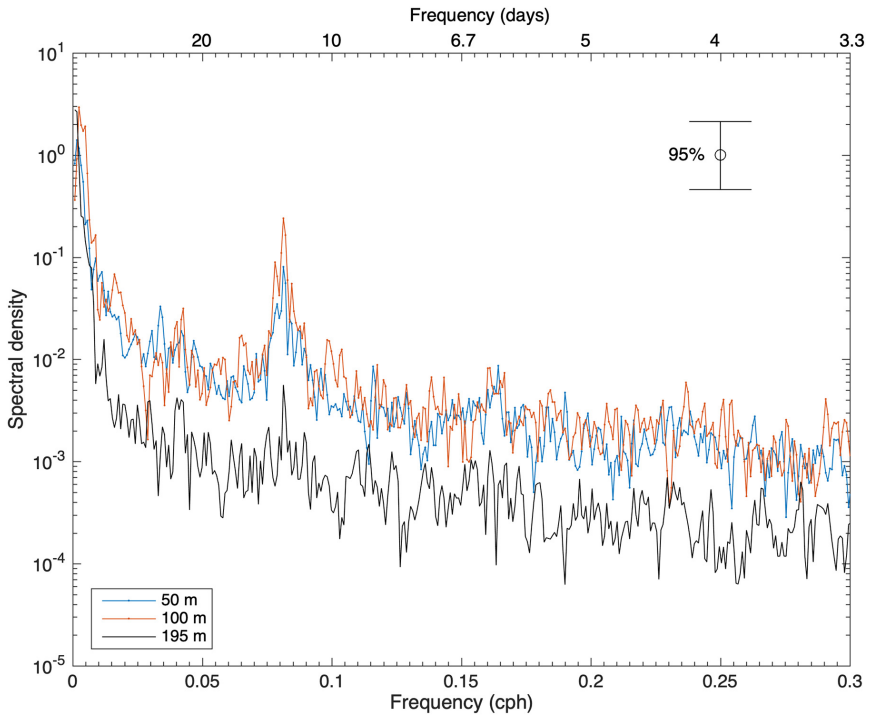

FIGURE 11 | Spectral densities of ocean temperature at 50, 100, and 195 m. Frequency is in cycles per hour (cph) (bottom horizontal axis) and period in days (top horizontal axis). A significance level of 95% was used.

throughout the entire water column, displacing them at times below the photic layer, which in turn reduces light availability and further limits primary production and phytoplankton growth. However, even during the austral spring (October 2016), phytoplankton biomass did not increase and high Chl-a fluorescence was confined to a small area at the NW branch, where larger inputs of freshwater were observed (**Figures 3A–C**). Similarly, east of Ushuaia where bathymetry becomes shallower, higher fluorescence was recorded (**Figure 7B**). The latter may be the consequence of a resuspension of nutrients from the shallow sediments at Mackinlay Strait, as well as a potential inflow of mSAAW along the east entrance of the BC. This water mass flows over a relatively wide (150 km) and shallow (<100 m) continental platform where it can carry nutrients toward the Beagle Channel, promoting primary production. Unfortunately, current measurements along the Beagle Channel are scarce, and are mainly limited to surface currents in the middle section of the Channel (Balestrini et al., 1990). In order to reveal the role of mSAAW on the biogeochemistry and productivity of the eastern section of the BC, the extent and recurrence of mSAAW intrusions across the eastern section should be assessed in the near future.

The productivity of southern Patagonia follows a pronounced seasonal pattern, with an increase in biomass starting in October (reaching between 3 and 8 mg Chl-a m^{-3}) and lasting until March (Iriarte et al., 2001; Almandoz et al., 2011). Photosynthetically active solar radiation then decreases (Cuevas et al., 2019) and chlorophyll biomass diminishes to < 0.5 mg m^{-3} (Almandoz et al., 2011). Phytoplankton in the Beagle Channel may be limited primarily by low irradiance, or by the low nutrient concentrations in fresh and brackish-EW. The low N : P ratio through the entire Beagle Channel likely causes nitrate limitation (**Figures 10A,B**), which restricts phytoplankton growth. Indeed, nutrient limitation, and especially nitrate limitation, is a common feature hampering phytoplankton growth in the upper waters of southern Patagonia (Iriarte et al., 2001; Valdenegro and Silva, 2003; Iriarte et al., 2013; Vargas et al., 2018; Cuevas et al., 2019). In some areas of the Beagle Channel there may also be a silicic acid colimitation (**Figures 10C,D**). The low concentrations of silicic acid in surface waters is likely associated with glacier meltwater inputs. The concentration of silicic acid in coastal runoff depends on variables controlling weathering processes, such as temperature, precipitation, lithogenic structure of the soil, types of vegetation, transport time, etc. The Patagonian freshwater input south of 51 °S is characterized by low levels of silicic acid, due to the small mineral area exposed, low temperatures, reduced runoff, and low volcanic activity, which combine to reduce the weathering flux of silicates to coastal waters (Torres et al., 2011, 2014). Diatoms tend to dominate phytoplankton communities under high phosphate (PO_4), nitrate (NO_3) and silicic acid ($Si(OH)_4$) concentrations (Sarthou et al., 2005) with a $Si(OH)_4$:NO_3 uptake ratio of 1:1 under no iron limitation (Ragueneau et al., 2000). The stoichiometry of macronutrients recorded within the Beagle Channel favors other phytoplankton groups rather than diatoms, which explains why small phytoflagellates and other

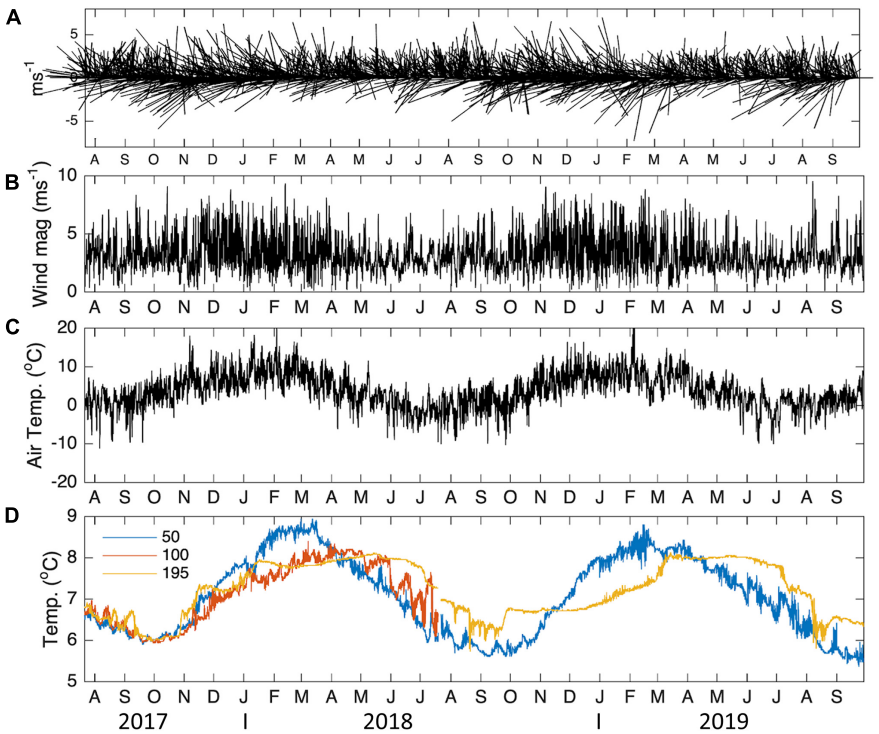

FIGURE 12 | Temporal variability of daily **(A)** wind vectors, **(B)** wind magnitude, **(C)** air temperature and **(D)** ocean temperature, at 50, 150, and 195 m depth. The wind stick plot reports the wind in m s^{-1} and the direction from which it originates. Temperatures are expressed in °C. Wind and atmospheric temperature were obtained from the ERA5 reanalysis corresponding to the location closest to the mooring.

pico- and nanophytoplankton tend to dominate the phytoplankton community in the Beagle Channel (Almandoz et al., 2011). Likewise, the low concentration of nutrients in the surface waters may partially drive the overall low phytoplankton biomass recorded in the Channel.

During the 2017 cruise, the eastern section of the Channel showed an increase in surface Chl-a fluorescence east of Ushuaia where the seafloor rises, reducing the depth of the water column. This bathymetry may favor the resuspension of nutrient-rich sediments, while an increased human footprint may produce a nutrient-rich runoff compared to the western part of the Beagle Channel (Torres et al., 2009; Amin et al., 2011). As observed during the CIMAR 3 and 16 cruises, higher nutrient concentrations occur at depth in the eastern section of the Channel, coinciding with the region where higher Chl-a fluorescence was recorded in 2017. The only time series report on the eastern section of the Channel (Almandoz et al., 2011) shows a clear seasonality in nutrient concentration, with higher nutrient concentrations at surface during winter (NO_3 10–16 μM, PO_4 2 μM and SiOH 4–8 μM), which is consistent with our observations. During spring and summer (October—March), nutrients tend to drop below 2 μM (NO_3), 1 μM (PO_4), and 3 μM (SiOH), which can be associated with phytoplankton uptake when phytoplankton biomass may reach 9 μg Chl-a L^{-1} (Almandoz et al., 2011). Almandoz et al. (2011) also found species of benthic diatoms in the eastern section of the Channel (west of Mackinlay Strait), which further confirms the presence of resuspension in this area, enabling the advection of nutrients to upper waters in this shallow section of the Channel. However, we cannot rule out the possibility of episodic intrusions of mSAAW at depth from the east, which may also transport nutrients into the middle section of the Beagle Channel. The advection of mSAAW may, in fact, be important in both branches of the western section of the Channel due to the presence of deep submarine canyons which may enable the direct inflow of mSAAW. Unlike in the eastern section of the Channel, the deep bathymetry (>200 m) of the western section may hamper the transfer of mSAAW nutrients into surface waters, which in turn may limit phytoplankton growth and the overall effectiveness of deep nutrient inflow through the western end of the Beagle Channel.

The presence of four microbasins along the Beagle Channel creates distinct semi-isolated systems with particular physicochemical properties that are subject to the interplay of SAAW and mSAAW at depth and fresh-EW at the surface. This favors the formation of particular biological niches with both chlorophyll and nutrient discontinuities (Hamamé and Antezana, 1999) and distinctive planktonic communities (Palma and Silva, 2004), reinforcing the idea that these discontinuities can produce ecosystems which are structurally and functionally unique. Further efforts should be focused on increasing process-oriented studies within each of the semi-enclosed basins, as well as on improving spatial and temporal monitoring procedures to shed light on the dynamics of this interoceanic passage.

TABLE 2 | Percentage explained by annual and semi-annual signals in atmospheric temperature (AT), ocean temperature (T50, T195), and wind magnitude (Wind Mag), for the two-year time series.

Temporal signal	T50	T100(*)	T195	AT	Wind Mag
182 days	1.60%	8.00%	5.40%	0.20%	0.60%
365 days	88.70%	49.60%	74.90%	52.60%	4.80%

**The percentage explained by annual and semi-annual signals for 100 m ocean temperature was done for only one year of data.*

TABLE 3 | Cross-correlation analysis between the annual and semi-annual signal of atmospheric temperature (AT) and ocean temperatures at 50, 100, 195 m and lags (in days) associated with the maximum correlations observed using a 95% confidence level.

Variable pairs	Correlation coefficient	Lag (days)
AT—T50	0.8474	25.46
AT—T100	0.8306	28.38
AT—T195	0.6893	63.12
T50-T100	0.9208	0
T50-T195	0.8824	26.62
T100-T195	0.777	35.83

Expected Future Changes in the Beagle Channel and Possible Consequences

Currently, most of the Beagle Channel is still subject to relatively low human pressure, with the exception of the two cities in the eastern section: Ushuaia (67,600 inhabitants, Census 2015) and Puerto Williams (1,868 inhabitants, Census 2018). Currently, the region is facing a major threat due to the expansion of aquaculture toward higher latitudes. This concerns the salmon industry in particular, and can alter nutrient stoichiometry, as has already been observed in central and northern Chilean Patagonia (Iriarte, 2018). In the near future, local anthropogenic activities (city wastewater, industrial activities, navigation and aquaculture) may exert an important impact on the chemical composition of the Beagle Channel waters, and even alter biological productivity, if proper management plans are not implemented now. The major impacts on this region are associated with increased nutrient inputs (especially nitrogen) due to changes in land-use and aquaculture. Microcosm experiments in northern Patagonia have shown that the addition of ammonium due to aquaculture promotes the development of large amounts of autotrophic biomass and bacterial production (Olsen et al., 2017), which could lead to oxygen depletion events in the photic layer. These events, even when sporadic, will affect the entire pelagic community, causing major changes both within the trophic webs of the ecosystem and to the biogeochemistry of the water column and benthos. Due to the pronounced seasonality of marine high latitude ecosystems, the productive period is limited to spring and summer (from October to mid-March, Almandoz et al., 2011) when the net uptake of CO_2 exceeds the community respiration, creating a net sink of CO_2 (Torres et al., 2011). During the remaining months, Chl-a concentration falls to < 1 μg Chl-a L^{-1} (Almandoz et al., 2011) and heterotrophic processes tend to dominate (e.g., Torres et al., 2011; Vergara-Jara et al., 2019). In a scenario of intensive aquaculture, we might expect higher loads of dissolved and particulate organic matter as well as an increase in nutrients (N and P mainly), which will primarily be remineralized by heterotrophic organisms, thus increasing pCO_2 levels and altering the carbonate chemistry of the seawater. On the other hand, increasing loads of inorganic (NH_4, NO_3) and organic nitrogen might also enhance the recurrence of Harmful Algal Blooms (HABs) (Anderson et al., 2002) of the type that already occur in the area (Almandoz et al., 2014, 2019). The current state of the Beagle Channel, and in particular east of the Punta Divide, is particularly vulnerable due to the reduced water exchange between basins. This reduced exchange is thought to promote eutrophication, while vertical mixing of the water column may favor the resuspension of cysts of toxic phytoplankton from the sediments. HABs (especially *Alexandrium catenella*) have been monitored by the Chilean Institute for Fisheries Development (IFOP) since 2006 along the Beagle Channel. HABs have occurred at several locations along the Channel, particularly during the onset of summer (Benavides et al., 1995). One of the largest HABs was recorded between November 1991 and April 1992; it started close to Ushuaia and then spread westward during its development. This HAB caused a high toxicity in blue mussels (80 μg STXeq. 100 g^{-1}) that lasted until the end of 1992 (Benavides et al., 1995). If nutrient inputs increase in the future (e.g., city sewage, aquaculture inputs), it is likely that the middle and eastern sections of the Channel will be affected. In addition, the current decrease in rainfall observed over the last decades during spring and summer in the Magellan region (González-Reyes et al., 2017) may trigger the development of HABs in the Beagle Channel, as has already been the case in northern Patagonia (León-Muñoz et al., 2018).

Similarly, changes in glacial meltwater runoff, as well as sea water temperature and stratification, may alter the occurrence of HABs in the western part of the Beagle Channel in the near future (e.g., Richlen et al., 2016; León-Muñoz et al., 2018; Joli et al., 2018). Previous studies have shown that the warming of the Beagle Channel waters will reduce the abundance of diatoms, which will shift the composition of the plankton community and may, in turn, favor other phytoplankton groups (Moreau et al., 2014). These changes may reduce the efficiency of the biological carbon pump in the Beagle Channel due to the loss of fast sinking diatom frustules, while other groups more prone to developing into HABs (e.g., dinoflagellates) might be favored by the reduction of diatom biomass.

Observations from the last four decades indicate that the prevailing zonal (west-east) wind in the region has increased its intensity to a rate of 0.2–0.3 m s^{-1} per decade (Garreaud et al., 2013). This increase has been related to an increase in rainfall at a rate of 200 mm per decade in areas south of 50 °S. In this region, low frequency forcing is strongly influenced and dominated by the SAM, which in recent decades has shifted to positive polarities, favoring higher atmospheric temperatures. Since 1990, records of rainfall in Punta Arenas have shown a significant increase over the austral winter months (June) and a decrease during spring and summer (González-Reyes et al., 2017). These fluctuations reflect an increase in the minimum air

temperature and an intensification of the effect of the circumpolar atmospheric circulation, respectively (Garreaud et al., 2013). The IPCC projections for atmospheric conditions in the Magellan region in 2050 indicate that, under a business-as-usual scenario (RCP 8.5 scenario), rainfall will increase by about 10 % and the average air temperature will rise by 0.5°C, strengthening and confirming the present-day trends.

The hydrography of the Beagle Channel is primarily constrained by the presence of sills at both ends. This bathymetric configuration is characterized by limited exchange which restricts the permanent flow, in turn generating specific physical, chemical and biological conditions. This situation makes the Beagle Channel a remarkable study area, where each basin has its own dynamics which likely respond differently to external forcing and stressors, such as nutrient discharge, freshwater inputs from glacier melting and rainfall, and large-scale processes such as atmospheric oscillations (SAM, ENSO). Further research should focus on studying the circulation along different sections of the Beagle Channel, as well as on implementing and validating coupled atmosphere-ocean-glacial models in order to determine residence times and identify regions of higher retention. Such studies will help to better understand the main circulation features, forcings, and the spatio-temporal changes that currently drive Beagle Channel dynamics, while establishing a baseline to monitor and manage potential threats to this still near-pristine environment.

DATA AVAILABILITY STATEMENT

The datasets presented in this study can be found in online repositories. The names of the repository/repositories and accession number(s) can be found below: https://doi.pangaea.de/10.1594/PANGAEA.934063 and https://doi.pangaea.de/10.1594/PANGAEA.934046.

AUTHOR CONTRIBUTIONS

RG planned and led the Chilean campaigns between 2016 and 2017 in which JH, JG-V, EA, and HG participated. JG-V led the 2018 campaign. JH and JG-V preformed and processed all the CTDs casts of the campaign performed by the IDEAL center. AP preformed the time series analysis from the fixed station, as well as the atmospheric data. JM compiled and processed the hydrographic data from the Argentinian section of the BC and led the Houssay-17 campaign where XF-M, XD, and FB participated. All authors contributed to discussion and writing of the manuscript.

FUNDING

This research was supported by the *Agencia Nacional de Investigación y Desarrollo* (ANID) through project FONDAP IDEAL, grant number 15150003, projects HYDRO-USHUAIA (ECOS-SUD/MINCyT) and P-UE 2016: 22920160100077CO (CONICET), and by the German Federal Ministry of Education and Research (BMBF), grant number LAT16STRUC-039. The project leading to this publication has received funding from the Excellence Initiative of Aix-Marseille University – A*Midex, a French "Investissements d'Avenir programme" AMX-19-IET-012.

ACKNOWLEDGMENTS

We would like to thank the Chilean and Argentinean Navy for providing bathymetry charts, as well as the captain and crew of the Forrest vessel for their professional assistance and help during sampling procedures. We acknowledge the support of *Prefectura Naval Argentina*, MINCYT and thank Gustavo Ferreyra for making possible the cruise onboard M/O Bernardo Houssay and two reviewers for valuable comments on the manuscript. We would like to express our gratitude and our respects to Nelson Silva who passed away in August 2020. His pioneer work and passion for chemical oceanography research in Patagonia ecosystems opened new avenues for those of us who came after him.

REFERENCES

Abram, N. J., Mulvaney, R., Vimeux, F., Phipps, S. J., Turner, J., and England, M. H. (2014). Evolution of the southern annular mode during the past millennium. *Nat. Clim. Change* 4, 564–569. doi: 10.1038/nclimate2235

Almandoz, G. O., Cefarelli, A. O., Diodato, S., Montoya, N. G., Benavides, H. R., Carignan, M., et al. (2019). Harmful phytoplankton in the Beagle Channel (South America) as a potential threat to aquaculture activities. *Mar. Pollut. Bull.* 145, 105–117. doi: 10.1016/j.marpolbul.2019.05.026

Almandoz, G. O., Hernando, M. P., Ferreyra, G. A., Schloss, I. R., and Ferrario, M. E. (2011). Seasonal phytoplankton dynamics in extreme southern South America (Beagle Channel, Argentina). *J. Sea Res.* 66, 47–57. doi: 10.1016/j.seares.2011.03.005

Almandoz, G. O., Montoya, N. G., Hernando, M. P., Benavides, H. R., Carignan, M. O., and Ferrario, M. E. (2014). Toxic strains of the *Alexandrium ostenfeldii* complex in southern South America (Beagle Channel, Argentina). *Harmful Algae* 37, 100–109. doi: 10.1016/j.hal.2014.05.011

Amin, O., Comoglio, L., Spetter, C., Duarte, C., Asteasuain, R., Freije, R. H., et al. (2011). Assessment of land influence on a high-latitude marine coastal system: Tierra del Fuego, southernmost Argentina. *Environ. Monit. Assess.* 174, 63–73. doi: 10.1007/s10661-010-1493-5

Anderson, D. M., Glibert, P. M., and Burkholder, J. M. (2002). Harmful algal blooms and eutrophication: nutrient sources, composition, and consequences. *Estuaries* 25, 704–726. doi: 10.1007/bf02804901

Atlas, E., Hager, S., Gordon, L., and Park, P. (1971). *A Practical Manual for Use of the Technicon Autoanalyzer in Sea Water Nutrient Analyses. Technical Report*. Corvallis, OR: Oregon State University, 215.

Balestrini, C. F., Vinuesa, J., Speroni, J., Lovrich, G., Mattenet, C., Cantú, C., et al. (1990). *Estudio de las Corrientes Marinas en los alrededores de la Península Ushuaia*. Buenos Aires: CADIC–Centro Austral de Investigaciones Científicas, Comunicación Científica.

Balestrini, C., Manzella, G., and Lovrich, G. A. (1998). *Simulación de Corrientes en el Canal Beagle y Bahía Ushuaia, Mediante un Modelo Bidimensional. Inf Téc N° 98*. Buenos Aires: Servicio de Hidrografía Naval, 1–58.

Benavides, H., Prado, L., Díaz, S., and Carreto, J. I. (1995). "An exceptional bloom of *Alexandrium catenella* in the Beagle Channel, Argentina," in *Harmful Algal Blooms*, eds P. Lassus, G. Arzul, E. Erard, P. Gentien, and C. Marcaillou (Paris: Lavoisier), 113–119.

Bonjean, F., and Lagerloef, G. S. E. (2002). Diagnostic model and analysis of the surface currents in the tropical Pacific Ocean. *J. Phys. Oceanogr.* 32, 2938–2954. doi: 10.1175/1520-0485(2002)032<2938:dmaaot>2.0.co;2

Brun, A. A., Ramirez, N., Pizarro, O., and Piola, A. R. (2020). The role of the Magellan Strait on the southwest South Atlantic shelf. *Estuar. Coast. Shelf Sci.* 237:106661. doi: 10.1016/j.ecss.2020.106661

Bujalesky, G. G. (2011). The flood of the Beagle Valley (11000 YR B.P.), Tierra del Fuego. *Anal. Inst. Patagonia* 39, 5–21. doi: 10.4067/s0718-686x2011000100001

Buschmann, A. H., Cabello, F., Young, K., Carvajal, J., Varela, D. A., and Henríquez, L. (2009). Salmon aquaculture and coastal ecosystem health in Chile: analysis of regulations, environmental impacts and bioremediation systems. *Ocean Coast. Manag.* 52, 243–249. doi: 10.1016/j.ocecoaman.2009.03.002

Cuevas, L. A., Tapia, F. J., Iriarte, J. L., González, H. E., Silva, N., and Vargas, C. A. (2019). Interplay between freshwater discharge and oceanic waters modulates phytoplankton size-structure in fjords and channel systems of the Chilean Patagonia. *Prog. Oceanogr.* 173, 103–113. doi: 10.1016/j.pocean.2019.02.012

D'Onofrio, E., Orsi, A., and Locarnini, R. (1989). *Estudio de Marea en la Costa de Tierra del Fuego. Servicio de Hidrografía Naval*, Vol. 49. Buenos Aires: Servicio de Hidrografía Naval, 1–81.

Diez, M. J., Cabreira, A. G., Madirolas, A., Martín, J., Scioscia, G., Schiavini, A., et al. (2018). Winter is cool: spatio-temporal patterns of the squat lobster *Munida gregaria* and the Fuegian sprat *Sprattus fuegensis* in a sub-Antarctic estuarine environment. *Polar Biol.* 41, 2591–2605. doi: 10.1007/s00300-018-2394-2

Emery, W. J., and Thomson, R. E. (1998). Data analysis methods in physical oceanography. *Oceanogr. Lit. Rev.* 1:2.

Flores-Melo, X., Martín, J., Kerdel, L., Bourrin, F., Colloca, C. B., Menniti, C., et al. (2020). Particle dynamics in Ushuaia Bay (Tierra del Fuego)-potential effect on dissolved oxygen depletion. *Water* 12:324. doi: 10.3390/w12020324

Garreaud, R. D., Vuille, M., Compagnucci, R., and Marengo, J. (2009). Present-day south American climate. *Palaeogeogr. Palaeoclimatol. Palaeoecol.* 281, 180–195. doi: 10.1016/j.palaeo.2007.10.032

Garreaud, R., Lopez, P., Minvielle, M., and Rojas, M. (2013). Large-scale control on the Patagonian climate. *J. Clim.* 26, 215–230. doi: 10.1175/jcli-d-12-00001.1

Garzón, J. C., Martinez, A. M., Barrera, F., Pfaff, F., Koch, B. P., Freije, R. H., et al. (2016). The Pacific-Atlantic connection: biogeochemical signals in the southern end of the Argentine shelf. *J. Mar. Syst.* 163, 95–101. doi: 10.1016/j.jmarsys.2016.07.008

Giesecke, R., Höfer, J., Vallejos, T., and González, H. E. (2019). Death in southern Patagonian fjords: copepod community structure and mortality in land-and marine-terminating glacier-fjord systems. *Prog. Oceanogr.* 174, 162–172. doi: 10.1016/j.pocean.2018.10.011

González-Reyes, A., Aravena, J. C., Muñoz, A. A., Soto-Rogel, P., Aguilera-Betti, I., and Toledo-Guerrero, I. (2017). Variabilidad de la precipitación en la ciudad de Punta Arenas, Chile, desde principios del siglo XX. *Anal. Inst. Patagonia* 45, 31–44. doi: 10.4067/s0718-686x2017000100031

Guihou, K., Piola, A. R., Palma, E. D., and Chidichimo, M. P. (2020). Dynamical connections between large marine ecosystems of Austral South America based on numerical simulations. *Ocean Sci.* 16, 271–290. doi: 10.5194/os-16-271-2020

Hamamé, M., and Antezana, T. (1999). Chlorophyll and zooplankton in microbasins along the Strait of Magellan—Beagle Channel passage. *Sci. Mar.* 63, 35–42. doi: 10.3989/scimar.1999.63s135

Hersbach, H., Bell, B., Berrisford, P., Hirahara, S., Horányi, A., Muñoz-Sabater, J., et al. (2020). The ERA5 global reanalysis. *Q. J. R. Meteorol. Soc.* 146, 1999–2049.

IOC, IHO, and BODC (2003). *Centenary Edition of the GEBCO Digital Atlas", Published on CD-ROM on Behalf of the Intergovernmental Oceanographic Commission and the International Hydrographic Organization as part of the General Bathymetric Chart of the Oceans*. Liverpool: British Oceanographic Data Centre.

IPCC (2014). "Climate change. synthesis report," in *Contributions of Working Groups I, II and III to the Fifth Assessment Report of the Intergovernmental Panel on Climate Change*, eds R. K. Pachauri and L. A. Meyer (Geneva: IPCC), 151.

Iriarte, J. L. (2018). Natural and human influences on marine processes in Patagonian Subantarctic coastal waters. *Front. Mar. Sci.* 5:360. doi: 10.3389/fmars.2018.00360

Iriarte, J. L., Kusch, A., Osses, J., and Ruiz, M. (2001). Phytoplankton biomass in the sub-Antarctic area of the Straits of Magellan (53 S), Chile during spring-summer 1997/1998. *Polar Biol.* 24, 154–162. doi: 10.1007/s003000000189

Iriarte, J. L., Pantoja, S., González, H. E., Silva, G., Paves, H., Labbé, P., et al. (2013). Assessing the micro-phytoplankton response to nitrate in Comau Fjord (42 S) in Patagonia (Chile), using a microcosms approach. *Environ. Monit. Assess.* 185, 5055–5070. doi: 10.1007/s10661-012-2925-1

Iturraspe, R., Sottini, R., Schroeder, C., and Escobar, J. (1989). *Hidrología y Variables Climáticas del Territorio de Tierra del Fuego*, Vol. 7. Ushuaia: Información Básica. Contribución Científica CADIC, 201.

Joli, N., Gosselin, M., Ardyna, M., Babin, M., Onda, D. F., Tremblay, J. -É, et al. (2018). Need for focus on microbial species following ice melt and changing freshwater regimes in a Janus Arctic Gateway. *Sci. Rep.* 8:9405.

Kinder, T. H., and Bryden, H. L. (1990). "Aspiration of deep waters through straits," in *The Physical Oceanography of Sea Straits. NATO ASI Series (Mathematical and Physical Sciences)*, Vol. 318, ed. L. J. Pratt (Dordrecht: Springer), doi: 10.1007/978-94-009-0677-8_14

León-Muñoz, J., Urbina, M. A., Garreaud, R., and Iriarte, J. L. (2018). Hydroclimatic conditions trigger record harmful algal bloom in western Patagonia (summer 2016). *Sci. Rep.* 8:1330.

Mackas, D. L., Strub, P. T., Thomas, A. C., and Montecino, V. (2006). "Eastern Ocean Boundaries Pan-regional overview," in *The sea, the Global Coastal Ocean*, Vol. 14A, eds A. R. Robinson and K. H. Brink (Cambridge, MA: Harvard Press Ltd.), 21–59.

Moreau, S., Mostajir, B., Almandoz, G. O., Demers, S., Hernando, M., Lemarchand, K., et al. (2014). Effects of enhanced temperature and ultraviolet B radiation on a natural plankton community of the Beagle Channel (southern Argentina): a mesocosm study. *Aquat. Microb. Ecol.* 72, 155–173. doi: 10.3354/ame01694

Olsen, L. M., Hernandez, K. L., Ardelan, M., Iriarte, J. L., Bizsel, K. C., and Olsen, Y. (2017). Responses in bacterial community structure to waste nutrients from aquaculture: an *in situ* microcosm experiment in a Chilean fjord. *Aquat. Environ. Int.* 9, 21–32. doi: 10.3354/aei00212

Palma, S., and Silva, N. (2004). Distribution of siphonophores, chaetognaths, euphausiids and oceanographic conditions in the fjords and channels of southern Chile. *Deep Sea Res. II* 51, 513–535. doi: 10.1016/j.dsr2.2004.05.001

Pantoja, S., Luis Iriarte, J., and Daneri, G. (2011). Oceanography of the Chilean Patagonia. *Cont. Shelf Res.* 31, 149–153. doi: 10.1016/j.csr.2010.10.013

Pérez-Santos, I., Seguel, R., Schneider, W., Linford, P., Donoso, D., Navarro, E., et al. (2019). Synoptic-scale variability of surface winds and ocean response to atmospheric forcing in the eastern austral Pacific Ocean. *Ocean Sci.* 15, 1247–1266. doi: 10.5194/os-15-1247-2019

Ragueneau, O., Tréguer, P., Leynaert, A., Anderson, R. F., Brzezinski, M. A., DeMaster, D. J., et al. (2000). A review of the Si cycle in the modern ocean: recent progress and missing gaps in the application of biogenic opal as a paleoproductivity proxy. *Glob. Planet. Change* 26, 317–365. doi: 10.1016/s0921-8181(00)00052-7

Richlen, M. L., Zielinski, O., Holinde, L., Tillmann, U., Cembella, A., Lyu, Y., et al. (2016). Distribution of *Alexandrium fundyense* (Dinophyceae) cysts in Greenland and Iceland, with an emphasis on viability and growth in the Arctic. *Mar. Ecol. Prog. Ser.* 547, 33–46. doi: 10.3354/meps11660

Sarthou, G., Timmermans, K. R., Blain, S., and Tréguer, P. (2005). Growth physiology and fate of diatoms in the ocean: a review. *J. Sea Res.* 53, 25–42. doi: 10.1016/j.seares.2004.01.007

Schlitzer, R. (2020). *Ocean Data View*. Bremerhaven: Alfred Wegener Institute.

Seim, H. E., and Gregg, M. C. (1997). The importance of aspiration and channel curvature in producing strong vertical mixing over a sill. *J. Geophys. Res.* 102, 3451–3472. doi: 10.1029/96jc03415

Sievers, H. A., and Silva, N. (2006). "4.1 Masas de agua y circulación en los canales y fiordos australes," in *Avances en el Conocimiento Oceanográfico de las Aguas Interiores Chilenas, Puerto Montt a Cabo de Hornos*, eds N. Silva and S. Palma (Valparaíso: Comité Oceanográfico Nacional—Pontificia Universidad Católica de Valparaíso), 53–58.

Sievers, H., Calvete, C., and Silva, N. (2002). Distribución de características físicas, masas de agua y circulación general para algunos canales australes entre el Golfo

de Penas y el Estrecho de Magallanes (Crucero CIMAR-2 fiordos). *Chile. Rev. Cien. Tec. Mar* 25, 1–43.

Silva, N., and Vargas, C. A. (2014). Hypoxia in Chilean Patagonian fjords. *Prog. Oceanogr.* 129, 62–74. doi: 10.1016/j.pocean.2014.05.016

Silva, N., Calvete, C., and Sievers, H. (1998). Masas de agua y circulación general para algunos canales australes entre Puerto Montt y Laguna San Rafael, Chile (Crucero CIMAR-Fiordo 1). *Cienc. Tecnol. Mar.* 22, 17–47. doi: 10.4067/s0718-686x2011000200002

Speroni, J., Dragani, W., and Mazio, C. (2003). *Programa de Mediciones de Corrientes en el Canal Beagle. Informe Técnico N° 01 /03*. Buenos Aires: Servicio de Hidrografia Naval.

Strub, P. T. (1998). Coastal ocean circulation off western South America. *Glob. Coast. Ocean Reg. Stud. Synth.* 11, 273–315.

Strub, P. T., Combes, V., Shillington, F. A., and Pizarro, O. (2013). "Chapter 14–currents and processes along the Eastern Boundaries," in *International Geophysics*, eds G. Siedler, S. M. Griffies, J. Gould, and J. A. Church (Cambridge, MA: Academic Press), 339–384. doi: 10.1016/B978-0-12-391851-2.00014-3

Strub, P. T., James, C., Montecino, V., Rutllant, J. A., and Blanco, J. L. (2019). Ocean circulation along the southern Chile transition region (38°–46° S): mean, seasonal and interannual variability, with a focus on 2014–2016. *Prog. Oceanogr.* 172, 159–198. doi: 10.1016/j.pocean.2019.01.004

Talley, L. D., Pickard, G. L., Emery, W. J., and Swift, J. H. (2011). *Descriptive Physical Oceanography: an Introduction*, 6th Edn. Amsterdam: Academic Press, 555.

Torres, A. I., Gil, M. N., Amín, O. A., and Esteves, J. L. (2009). Environmental characterization of a eutrophicated semi-enclosed system: nutrient budget (Encerrada Bay, Tierra del Fuego Island, Patagonia, Argentina). *Water Air Soil Pollut.* 204, 259–270. doi: 10.1007/s11270-009-0042-8

Torres, R., Frangopulos, M., Hamame, M., Montecino, V., Maureira, C., Pizarro, G., et al. (2011). Nitrate to silicate ratio variability and the composition of micro-phytoplankton blooms in the inner-fjord of Seno Ballena (Strait of Magellan, 54°S). *Cont. Shelf Res.* 31, 244–253. doi: 10.1016/j.csr.2010.07.014

Torres, R., Silva, N., Reid, B., and Frangopulos, M. (2014). Silicic acid enrichment of subantarctic surface water from continental inputs along the Patagonian archipelago interior sea (41–56 S). *Prog. Oceanogr.* 129, 50–61. doi: 10.1016/j.pocean.2014.09.008

Valdenegro, A., and Silva, N. (2003). Caracterización oceanográfica física y química de la zona de canales y fiordos australes de Chile entre el estrecho de Magallanes y cabo de Hornos (Cimar 3 Fiordos). *Rev. Cien. Tec. Mar.* 26, 19–60.

Valle-Levinson, A., Blanco, J., and Frangópulos, M. (2006). Hydrography and frontogenesis in a glacial fjord off the Strait of Magellan. *Ocean Dyn.* 56, 217–227. doi: 10.1007/s10236-005-0048-8

Vargas, C. A., Cuevas, L. A., Silva, N., González, H. E., De Pol-Holz, R., and Narváez, D. A. (2018). Influence of glacier melting and river discharges on the nutrient distribution and DIC recycling in the southern Chilean Patagonia. *J. Geophys. Res. Biogeosci.* 123, 256–270. doi: 10.1002/2017jg003907

Vergara-Jara, M. J., DeGrandpre, M. D., Torres, R., Beatty, C. M., Cuevas, L. A., Alarcón, E., et al. (2019). Seasonal changes in carbonate saturation state and air-sea CO2 fluxes during an annual cycle in a stratified-temperate fjord (Reloncaví Fjord, Chilean Patagonia). *J. Geophys. Res. Biogeosci.* 124, 2851–2865. doi: 10.1029/2019jg005028

Conflict of Interest: The authors declare that the research was conducted in the absence of any commercial or financial relationships that could be construed as a potential conflict of interest.

Publisher's Note: All claims expressed in this article are solely those of the authors and do not necessarily represent those of their affiliated organizations, or those of the publisher, the editors and the reviewers. Any product that may be evaluated in this article, or claim that may be made by its manufacturer, is not guaranteed or endorsed by the publisher.

frontiers in Marine Science

ORIGINAL RESEARCH
published: 24 January 2022
doi: 10.3389/fmars.2021.635756

Assessment of Exploitation Intensity of Commercial Species and Associated Benthic Communities, in Chilean Marine Management Areas of North Patagonia

Madeleine Hamame and Paula Ortiz*

Centro de Investigación en Ecosistemas de la Patagonia (CIEP) – Moraleda 16, Coyhaique, Chile

OPEN ACCESS

Edited by:
Eduardo Joel Quiroga Jamett, Pontificia Universidad Católica de Valparaíso, Chile

Reviewed by:
Carlos Rios, University of Magallanes, Chile
Michael Kriegl, Leibniz Centre for Tropical Marine Research (ZMT), Germany

****Correspondence:***
Madeleine Hamame
mhamame@ciep.cl

Specialty section:
This article was submitted to Marine Ecosystem Ecology, a section of the journal Frontiers in Marine Science

Received: *30 November 2020*
Accepted: *13 December 2021*
Published: *24 January 2022*

Citation:
Hamame M and Ortiz P (2022) Assessment of Exploitation Intensity of Commercial Species and Associated Benthic Communities, in Chilean Marine Management Areas of North Patagonia. Front. Mar. Sci. 8:635756. doi: 10.3389/fmars.2021.635756

The Aysén region of Chile (North Patagonia), has had limited studies on the effectiveness of management and exploitation areas of benthic resources, and performance relative to open access areas in this region has never been evaluated. We evaluated seven management areas (MAs) and five open access areas (OAAs) between 43.9°S and 45.2°S for exploitation intensity of three commercial species (*Concholepas concholepas, Loxechinus albus,* and *Ameghinomya antiqua*) together with characterization of the benthic community. Indicators based on size, density and weight were used to evaluate exploitation intensity of commercial species. Associated benthic communities were evaluated considering density, species composition, and community structure. We found a high species richness and a community structure with low variability between MAs and OAAs. Low densities and small sizes classes of *C. concholepas* in most of the areas indicated high exploitation intensity in both MAs and OAAs. In this context, a permanent ban to harvest *C. concholepas* within OAAs may need to be reevaluated since with no enforcement and monitoring, the exploitation status of this species remains unclear in these areas. *L. albus* in most areas were absent in the harvestable sizes, which could be indicating high exploitation intensity in both regimes. High densities and small sizes of *C. concholepas* and *L. albus* in some MAs, indicated a potential recruitment zones which bears further investigation. A. *antiqua*, showed better conditions than other commercial species evaluated, with no significant differences in densities and size-based indicators when comparing OAAs and MAs. Benthic communities were dominated numerically by the Echinoidea class in both MAs and OAAs, with *L. albus*, *Arbacia dufresnii* and *Pseudechinus magellanicus* being the dominant species. High densities of sea urchins co-occurring with low coverage of macroalgae found in MAs-Gala could indicate that a sea urchin barren was dominant during the study period. On the other hand, high densities of *Cosmasterias lurida*, a predatory sea star, in conjunction with low densities of *C. concholepas* in most of the studied areas suggested that a shift in predator roles is occurring. No differences were

estimated in terms of fisheries indicators and benthic community structure across the two management regimes, suggesting the poor performance of MAs in Aysén region. Our data also support the need to improve monitoring of MAs especially with respect to associated benthic community incorporating a broader spatial scale.

Keywords: North Patagonia, benthic community, exploitation intensity, management areas, *C. concholepas*, *L. albus*

INTRODUCTION

Management and exploitation areas of benthic resources (MAs) were established along the Chilean coast to contribute to the ecological sustainability of benthic resources; their establishment was driven by the biological collapse in the 80s of the muricid mollusk *Concholepas concholepas*, a previously profitable benthic fishery (Castilla, 1994; Stotz, 1997; Castilla et al., 1998; Gonzalez et al., 2006). This administrative system gives territorial user rights (TURFs) to artisanal fisheries organizations that are legally constituted for the co-management (with the state) of benthic resources within a limited geographic area (Zuñiga et al., 2008; Gelcich et al., 2010). After two decades of MAs functioning (Stotz, 1997; Gonzalez et al., 2006; Gelcich et al., 2016), the ecological effects of this management approach have been somewhat diverse. In Central Chile, higher densities, larger sizes, and lower mortality rates of commercial species (*C. concholepas*, *Loxechinus albus,* and *Fissurella* spp.) were found in MAs compared to Open-Access Areas (OAAs, i.e., no access restriction) (Castilla and Fernandez, 1998; Gelcich et al., 2010; Defeo et al., 2014; Andreu-Cazenave et al., 2017). Positive effects were also reported in the associated macroinvertebrate communities where higher species richness, biomass and densities were observed within MAs compared to OAAs (Gelcich et al., 2008, 2012, Biggs et al., 2016). In contrast, performances of MAs in northern Chile were classified as poorly sustainable, with few stocks showing stability in densities, sizes, and catches over time (Arias and Stotz, 2020). Moreover, to maintain productivity, studies showed that at least half of the catch was extracted from areas outside MAs (Gonzalez et al., 2006). The performance of MAs has been heterogeneous and appears to betoo complex to generalize for a country such as Chile, with an extensive coast that spans ∼38° of latitude, where a variety of environmental, social, geographical, and economical factors combine to produce different outcomes. In this context local research is needed to integrate site-specific particularity into the global analyses of benthic management.

The Aysén region of Chile (43°38′–49°16′S) harbors many small coves (fishers' villages) throughout islands, fjords and channels in which the subsistence primarily relies on artisanal fisheries. Their fishing grounds are situated within a marine ecosystem considered not only pristine compared to northern regions (Godoy et al., 2010; Navarrete et al., 2010), but also characterized by a high species richness (Fernandez et al., 2000; Häussermann and Försterra, 2009; Försterra et al., 2016; Betti et al., 2017; Bertolino et al., 2020). The presence of diverse and unique habitats not only support species richness but also host high abundances and biomass of important commercial species (Flores et al., 2020; Pardo et al., 2020). These highly productive ecosystems have been the target of illegal fishing, and regional fisheries authorities have needed to co-operate with local fishers to address the constant influx of fishers from neighboring regions. In this context, the introduction of MAs provided the potential for exclusive privileges in accessing benthic resources within a limited geographic area, and the interest and cooperation of local fishers has therefore increased in recent years. Currently in Aysén, there are 75 established MAs (data obtained from the Chile's Undersecretariat of Fisheries and aquaculture, Subpesca, 2020a), with 56% (43 total MAs) having resource management plans approved and 18 of which have extracted the estimated catch quota over the last years (2016–2019). Prior to this (2010–2015), only 7 MAs contributed to landings, showing that there is an increased interest from fishers to harvest under this management system. Moreover, there are now 210 MAs pending approval in Aysén. The remoteness and intricate geography of Aysén has limited studies on the effectiveness of MAs (Moreno and Revenga, 2014; Romero et al., 2019), and no studies have yet evaluated their performance relative to OAAs in this region. On the other hand, follow up studies that considered an annual stock assessment in the management area provide data on catch quotas for commercial species but neither explicitly evaluated the intensity of exploitation, nor assessed the ecological effects on the associated benthic community. Even though, several studies have indicated the potential degrading impact of harvests upon habitats and biodiversity (Perez-Matus et al., 2017; De Juan et al., 2018; Contreras et al., 2019), and therefore on resilience of communities and populations in continuing to provide an ecosystem service. The responses of communities to harvest can be highly variable and complex since many factors are involved, on one hand there is the magnitude, timing, and areal extent of fishing (often can be well documented), on the other, the productivity of the ecosystems and the biological, and ecological characteristics of harvestable species (often with a poor level of understanding) which determine different effects on ecosystem processes and functions (Levin et al., 2009; De Juan et al., 2015). The effects of harvest on the benthic community structure can be both direct and indirect (Jennings and Kaiser, 1998; Pinnegar et al., 2000). Decrease in the abundances and changes in size structures of commercial species had been described as direct effects while some examples of indirect effects are benthic habitat degradation and changes on trophic interactions (Pinnegar et al., 2000). The monitoring of these cascade-type effects, such as a decrease in macroalgae biomass due to grazing effects by strict herbivores (e.g., *L. albus*) (Dayton, 1985; Buschmann et al., 2004; Wright et al., 2005; Contreras et al., 2019) or the detection of changes in the roles of top predators (e.g., *C. concholepas*) and their concomitant effect on benthic communities structure

(Gaymer and Himmelman, 2008; Navarrete et al., 2010), are crucial to increase the knowledge related to responses of the ecosystem associated to impact of fishing.

The main objective of the present study was to evaluate MAs in the Aysén region by comparing their performance with OAAs in relation to: (i) exploitation intensity of three commercial species (*Concholepas concholepas, Loxechinus albus,* and *Ameghinomya antiqua*) and (ii) characterization of the overall benthic community structure associated with these commercial species. These results are discussed in the context of management of fisheries and benthic communities in Patagonian coastal waters.

MATERIALS AND METHODS

Study Area

The study was carried out in Northern Patagonia, in an area located between 43.9–45.2°S and 73.5–73.7°W (**Figure 1**), situated between southern Corcovado Gulf (Guaitecas Islands) and southern Moraleda Channel (Meninea constriction, 45.2°S–73.6°W). The Moraleda Channel is 90 miles long, has an approximate average depth of 250 m, and is the main channel that separates the archipelago to the west from the continental coast to the east.

Water masses and circulation in this region (Sievers and Silva, 2008) indicate that in the northern zone, Sub-Antarctic Water [SAAW: up to 150 m depth; Salinity between 32.5 and 34 psu; 1.2–1.6 μM PO_4^{-3}; 12–20 μM NO_3^-; 4–6 ml L^{-1} Dissolved Oxygen (DO)] flow on the surface through Boca del Guafo (Guaitecas Islands) mixing progressively toward the south with Estuarine Water (EW; 0–20 m depth, salinity between 2 and 25 psu; 1–8 μM NO_3^-; 0.1–0.8 μM PO_4^{-3}; 6–8 ml L^{-1} DO). As a result of this mixture, SAAW is modified creating a water mass with an intermediate salinity (MSAAW; ∼31 psu; 1.2–1.6 μM PO_4^{-3}; 12–16 μM NO_3^-; 5–6 ml L^{-1} DO), that flows toward the interior of the Moraleda Channel up to the Meninea constriction-sill (30–60 m depth) (Silva and Vargas, 2014). The vertical water characteristics creates a two-layer structure; a superficial layer that is warmer, more oxygenated, less saline and with lower nutrient concentrations that have greater seasonal variability (MASAAW or EW) compared to the deep layer (Silva and Guzman, 2006; Silva and Palma, 2008; Schneider et al., 2014; Silva and Vargas, 2014).

In the study area, seven MAs and five OAAs were sampled; two MAs (GUA1 and GUA2) localized northwest of Las Guaitecas archipelago near Melinka Cove (∼43.9°S) with more oceanic influence (i.e., SAAW) and with greater exposure to wave action compared to the other studied areas (Sievers and Silva, 2008). The main substrates (>80%) of these areas were hard bottom (i.e., boulder and rock slabs) in GUA1 and mixed bottom (hard and soft bottom) in GUA2 (i.e., sand, shells cover, boulder, and rock, **Table 1**). The other areas were localized in the so-called "inland sea" in the central-south zone of the Moraleda Channel where there is a greater influence of fresh waters (main water masses are represented by EW and MSAAW). In the central study zone, two MAs (GALA1 and GALA2) were located outside the Jacaf Channel near Puerto Gala Cove (∼44.2°S). Jacaf is a narrow and deep channel (>400 m) that connects with the Puyuhuapi Fjord, from which it receives freshwater influence (Schneider et al., 2014). The main substrate in these areas was hard bottom (rock slabs and rock) in Gala2 and soft bottom (sand) in Gala1. In the southern zone (Huichas), three MAs (HUIC1, HUIC2, and HUIC3) and five OAAs (OAAs1 to OAAs5) were located mainly in small, protected bays along the Moraleda Channel, close to Puerto Aguirre Cove (∼45.2°S). The main substrate in these MAs (HUIC1, 2, 3) was hard bottom (rock, rock slabs, and boulder). In most of OAAs (OAA3, 4, and 5), substrate was dominated by mixed (sand, gravel, rock slabs, rock, and boulder), being soft bottom (sand) the main substrate only in OAA2, and hard bottom in OAA1. In MAs, substrate type was obtained from baseline studies that considered characterization of the total surface of each area (**Table 1**). In the case of OAAs area, substrate type was characterized and quantified in each area. MAs were grouped considering their closeness to their coves since each of them has its socio-economic particularities that could influence their management, in this sense three zones were established: (1) Melinka (MAs-Guaitecas), (2) Gala (MAs-Gala), and (3) Aguirre (MAs-Huichas).

Open access areas were selected according to historical fishing grounds declared by local fishers of commercial species evaluated in the present study (*C. concholepas*, *L. albus,* and *A. antiqua*). In these areas, fishers who have registered commercial resources in the National Fishery Service can harvest them with the only restriction of following national regulations (e.g., minimum legal size of extraction, reproductive closure). Although only OAAs were studied around Huichas due to logistic problems, it is expected that these OAAs would allow for comparison among management regimes since these areas have a similar suitable substrate for the commercial species evaluated in MAs and its associated benthic communities.

Sampling

Commercial species were selected in MAs according to baseline studies (Subpesca, 2016) that described the species that constitutes the object of the management and exploitation plan according to their direct quantification (Subpesca, 1995). In this context, three species were considered; the red sea urchin *Loxechinus albus* (Molina, 1782) that principally inhabits kelp beds, rocky and mixed substrates (rock and sand), the gastropod mollusk *Concholepas concholepas* (Bruguiere, 1789) that is present in mixed/rocky habitats, and the bivalve mollusk *Ameghinomya antiqua* (King, 1832) which is mainly an inhabitant of soft substrates. All three species have a wide distribution along the Chilean coast (18°–56°S). These same species were evaluated in OAAs. Sampling was carried out during summer 2016 (9th of January till 14th of February) in most of the areas, except for three OAAs that were evaluated at the beginning of autumn 2016 (9th till 12th of April, **Table 2**).

In each area (MAs and OAAs), density of commercial species and mega-invertebrates were sampled by scuba diving surveys conducted from fishing boats. Five quadrats (0.25 m^2) were randomly placed within each transect (10 × 2 m) which were arranged parallel to the coast, at depths of up to 20 m (**Supplementary Table S1**). The total number of

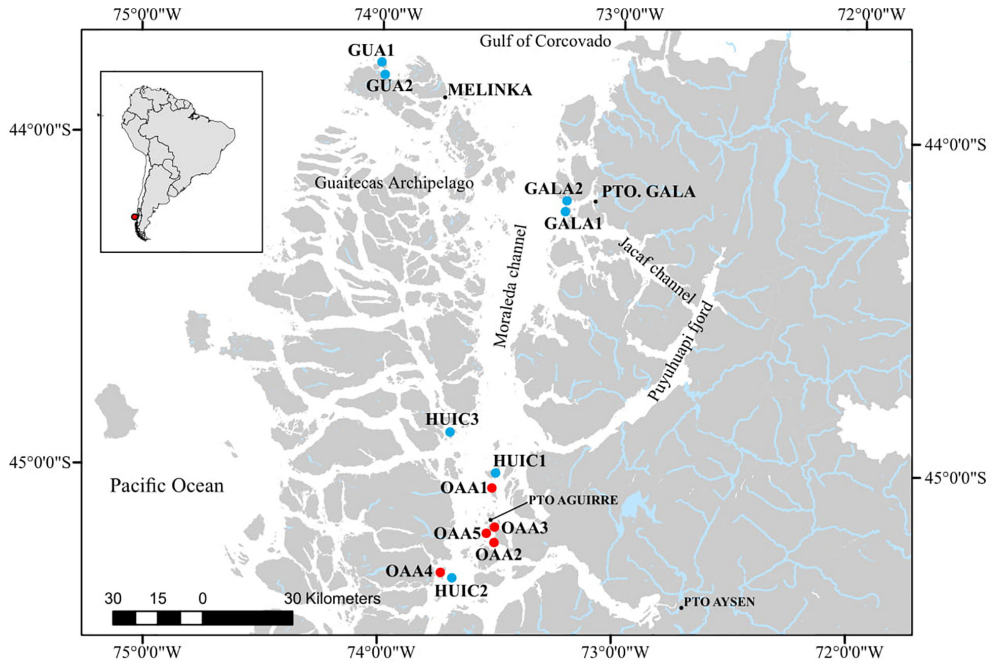

FIGURE 1 | Map of study area in the Aysén Region showing the MAs (blue circles) and OAAs (red circles) sampled between January and April 2016.

TABLE 1 | Substrate type (% of the total surface area) in each area studied.

SUBSTRATE	HUIC1	HUIC2	HUIC3	GALA1	GALA2	GUA1	GUA2	OAA1	OAA2	OAA3	OAA4	OAA5
Hard	98	90	65	20	83	88	0	45	8	37	0,3	20
Mixed	0	0	0	27	17	12	88	19	25	48	57	56
Soft	2	10	35	53	0	0	12	36	67	15	43	23

transects per area was established according to their surface area, fluctuating between 25 and 42 for the selected commercial species (*C. concholepas*, *L. albus,* and *A. antiqua*), and between 15 and 29 for analysis of benthic community structure (**Table 2**). On soft bottom benthic habitat, only the commercial species were evaluated with no analysis undertaken for the macroinfauna community. A total of 238 community transects were sampled, in which 19,818 individuals were identified to their lowest possible taxonomic level (Forcelli, 2000; Häussermann and Försterra, 2009); with the exception of a few taxa that could only be identified to higher taxonomic levels (e.g., Demospongiae, Actinaria, and Holothuroidea).

Biological sampling (measured and weighed) of primary target resources (*C. concholepas*, *L. albus* and *A. antiqua*) was performed in all areas, except in the ones with low densities and scarce presence of individuals along transects (<20% of the evaluated transects). Between 269 and 526 individuals per each primary target resource per area were collected by scuba diving, immediately after they were measured and weighed on shore (**Table 2**). For size of individuals test diameter was taken for *L. albus* and shell length for *C. concholepas* (peristome length: maximum length from the siphonal notch to the posterior edge of the shell) and *A. antiqua* (valvar length along the maximum axis). Size was measured using a Vernier caliper with a precision of 0.1 mm, and body wet weight (including the shell in mollusks) was measured using an electronic balance with a precision of 0.1 g.

Data Analysis

Commercial Species

Performances of MAs relative to OAAs were evaluated using three indicators as a proxy for exploitation intensity of commercial species (*C. concholepas, L. albus,* and *A. antiqua*). Fishing regulations have established a legal minimum size of extraction (MLS) and fishers clearly target larger individuals; therefore, the absence of the largest harvestable individuals can be assumed as a proxy for exploitation intensity of a given species (Blanchard et al., 2005; Miethe et al., 2016). In this context, two fisheries indicators were chosen based on size. The first indicator considered the average size of the largest 5% of the sample (Lmax5) and was selected as a measure that is less affected by environmental effects and recruitment variability (Miethe et al., 2016). The second indicator relates the number of individuals in a specific size class to the total number of individuals collected [proportional stock density (PSD)]. The limit sizes adopted were the MLS established by Subpesca by the time the studied was carried out (*C. concholepas* = 100 mm; *L. albus* = 70 mm, and *A. antiqua* = 55 mm), and PSD therefore estimates the percentage

of individuals whose size exceeds these MLS. A third indicator was not based on size, but instead considered average density of commercial species, estimated from the average number of individuals counted within each quadrat, divided by surface area (0.25 m^2). Average density of individuals for each area (ind.m^{-2}) was computed from replicate transects. As a measure of the nutritional condition of each species, a fourth indicator was estimated, the Medium Condition Factor (MCF; Arana, 2006). This indicator relates the average weight of the individuals in a specific size range in one area to the average weight of all individuals in that specific size range in all the areas. To compare the weight of a similar number of individuals between areas, size range was chosen considering the class intervals that had the highest but even number of individuals between areas. Values exceeding one, indicate that individuals in one area have a better nutritional condition (i.e., suggests adequate food supply) than in other areas. This indicator had been used previously to assess gonadal development in *L. albus* over a time series (Arana, 2006). Since our study examined only spatial variability, sampling was carried out trying to study the areas during the same period to find individuals in similar reproductive conditions. According to reproductive cycle of *L. albus*, *C. concholepas,* and *A. antiqua*, during our sampling, post-spawning individuals in a reproductive rest state were collected and therefore it would be reasonable to assume that the MCF indicators are comparable reflecting relative nutritional condition. In the case of *L. albus* reproductive cycle in the northern neighboring region (41°45′) and northern part of Aysén Region (Melinka, 43°53′) indicated that a higher proportion of mature individuals can be found between spring and beginning of summer (Bay-Schmith et al., 1981; Arias et al., 1995, Molinet et al., 2016) which coincides with the reproductive seasonal closure established between 15th of October till 15th of January (D. Ext. N°439, Subpesca, 2000). Studies of reproductive cycle of *C. concholepas* (41.8°S; Manriquez et al., 2009) indicated maximum gonadal development in December. Seasonal closure of this species is established between the 1st of September and 31th of January (D. Ext. 697, Subpesca, 2011). *A. antiqua*, has no seasonal closure; maximum reproductive months had been observed between July and August in northern part of Aysén Region (43.8°S), with spawning period occurring between spring and early summer (Canales et al., 2019).

The 12 areas studied were divided, according to their closeness to their coves and management regimes, into four groups: (1) MAs-Huichas (3 areas), (2) MAs-Gala (2 areas), (3) MAs-Guaitecas (2 areas), and (4) Open Access Areas (5 areas).

Since data was not normally distributed (Kolmogorov–Smirnov, $p < 0.01$) and data presented no homogeneity of variance (Levene's test $p < 0.05$), Kruskal–Wallis non-parametric test (Statistica software 7.0) was used to independently compare the different indicators between groups.

Benthic Communities

Benthic communities were characterized, considering the four sampling sites described previously, relative to: (i) average density (number of individuals in each quadrat divided by its surface area of 0.25 m^2 with data standardized to ind.m^{-2}) and (ii) dominance (% D, percentage of individuals of one species relative to the total number of individuals considering all species). Since density data was not normally distributed (Kolmogorov–Smirnov, $p < 0.01$), the Kruskal–Wallis non-parametric statistical test (Statistica software 7.0) was used to independently compare between the four groups. Additional measures of community structure were calculated, including total number of species (S), Shannon-Wiener diversity index (H′) and Evenness index (J′) (Pielou, 1977). The rarefaction method (ESn) was used to compare taxa richness in samples of unequal size for benthic macrofauna (Hurlbert, 1971). These measures were calculated using the software package PAST V4.03 (Hammer et al., 2001).

To determine which taxa contributed to the dissimilarity of the faunal assemblages between groups, an analysis of similarity was conducted (SIMPER, Clarke, 1993). Non-Metric Multidimensional Scaling (nMDS) and an analysis of similarity test (one-way ANOSIM) were used to evaluate similarities between groups, and for these analyses, species densities were transformed to the fourth root and the Bray-Curtis distance index was applied to estimate the degree of similarity between groups/species (Clarke, 1993). Transects were treated as replicates to provide an average density for each area. Differences between groups were evaluated using a one-way permutational multivariate variance analysis (PERMANOVA; Anderson, 2001). Since all OAAs were localized in Huichas, a more detailed statistical analyze was performed to compare them with MAs geographically closed. For this, nMDs and one-way ANOSIM analyses were performed using transects as replicas. SIMPER, nMDS, and ANOSIM analyses were completed using the software package PRIMER Version 6 (Clarke and Gorley, 2006).

RESULTS

Commercial Species

Concholepas concholepas was evaluated in all MAs studied since it is a primary target resource in all management plans. Suitable substrate in OAAs, indicated that four of the five areas studied should have had this resource, but it was present only in two of them. Mean densities varied between 0.4 and 3.8 ind.m^{-2} (**Figure 2A**) with significant differences (Kruskal–Wallis test, $p < 0.05$) in MAs (2.3 ± 5.6 ind.m^{-2}) compared to OAAs (0.4 ± 1.3 ind.m^{-2}). These differences were due to higher densities in MAs-Gala (2.6 ind.m^{-2}) and MAs-Huichas (2.6 ind.m^{-2}) compared to OAAs (Kruskal–Wallis test, $p < 0.05$). Within MAs-Huichas, the absence of this resource in MA-HUIC2 contrast with higher densities estimated in the other nearby areas (HUIC3 and HUIC1). In MAs-Gala high density was represented by small sized individuals (average 61 ± 11 mm) that resulted in Lmax5 of 84 (±15 mm) in comparison with MAs-Huichas where high densities were dominated by larger individuals (Lmax5 = 111 ± 11 mm) (**Figure 3A**). Densities between both groups of MAs (Huichas and Gala) were not significantly different (Kruskal–Wallis test, $p > 0.05$) but when comparing Lmax5, significant difference were estimated (Kruskal–Wallis test, $p < 0.05$). Due to low densities in most of the areas, fisheries indicators (Lmax and PSD) could only be estimated in one OAAs

preventing its statistical comparison with MAs. The percentage of individuals exceeding MLS (PSD) was 45% in MA-HUIC3, whereas in all other areas, PSD was <8%. MA-Gala1 represented an extreme example where none of the individuals sampled exceeded 100 mm (average size was 58 ± 9 mm). MCF, calculated over the size range of 70–89 mm, showed that individuals in MAs-Gala were also in poor nutritional condition compared to other areas (**Table 3**).

Loxechinus albus was the only commercial species present in almost all studied areas. Estimated densities varied between 4 and 26 ind.m^{-2}, significant differences (Kruskal–Wallis test, $p < 0.05$) were found for MAs (12 ± 8 ind.m^{-2}) compared to OAAs (6 ± 5 ind.m^{-2}). This difference resulted from MAs-Gala, where densities were significantly higher than the other areas (Kruskal–Wallis test, $p < 0.05$), with an average of 22 ± 13 ind.m^{-2} (**Figure 2B**). Other MAs (Huichas and Guaitecas) did not present significant differences in densities when comparing with OAAs (Kruskal–Wallis test, $p > 0.05$). High density in MAs-Gala was represented by small sized sea urchins (39 ± 10 mm) corresponding with Lmax5 of 62 mm (**Figure 3B**). Lmax5 varied between this minimum and a maximum estimated in MA-HUIC3 (Lmax5 = 91 mm). No significant differences (Kruskal–Wallis test, $p > 0.05$) were found for Lmax5 between MAs (77 ± 13 mm) and OAAs (84 ± 15 mm). When comparing Lmax5 between MAs closed to OAAs, i.e., MAs-Huichas with OAAs, significant difference where estimated (Kruskal–Wallis test, $p < 0.05$). Lmax5 was higher in MAs (86 ± 4 mm) compared to OAAs (83 ± 10 mm).

Proportional stock density which represented the percentage of individuals over the MLS (≥70 mm) showed high variability between areas (MAs; average 17 ± 15% and OAAs; average 10 ± 14%). In MAs, this indicator fluctuated between 0.3 and 55.7% (**Table 2**), with maximum values estimated in MA-HUIC3 and a minimum in MA-Gala2 (0.3%). In OAAs, PSD varied between 4.2 and 21.6%, with no significant differences between OAAs and MAs (Kruskal–Wallis test, $p > 0.05$). The Medium condition factor (MCF) considered size range between 40 and 59 mm showed that sea urchins in MAs-Gala had the lowest nutritional condition (MCF < 1, **Table 2**). No significant differences in MCF were found between MAs and OAAs (Kruskal–Wallis test, $p > 0.05$).

Ameghinomya antiqua was present in all OAAs and in four MAs (**Table 2**), with densities that varied between 1 and 11 ind.m^{-2} (**Figure 2C**). No significant differences in densities were found between OAAs (5 ± 4 ind.m^{-2}) and MAs (4 ± 3 ind.m^{-2}) (Kruskal–Wallis test, $p > 0.05$). Lmax5, was significantly higher (Kruskal–Wallis test, $p < 0.05$) in OAAs (84 ± 5 mm) compared to MAs (77 ± 10 mm). Within MAs, the lowest Lmax5 was estimated in Guaitecas (68 ± 3 mm) (**Figure 3C**) and was significantly different from areas localized in Huichas (MAs and OAAs, Kruskal–Wallis test, $p < 0.05$). No significant differences in Lmax5 were found between MAs-Huichas and OAAs (Kruskal–Wallis test, $p > 0.05$). PSD representing the percentage of individuals above 55 mm (MLS), fluctuated between 84% and 97% in OAAs, and between 44% and 92% in MAs, with no significant difference between both management regimes (Kruskal–Wallis test, $p > 0.05$). The MCF indicator was estimated considering the weight of individuals between sizes of 60 and 69 mm. Relatively lower values (MCF < 1) were found in MA-GUA1 which was consistent with the data of the other indicators (PSD and Lmax5). No significant differences were found between MAs and OAAs (Kruskal–Wallis test, $p > 0.05$).

Benthic Communities

A total of 102 taxa were recorded in the 12 areas studied, 84 taxa/species in MAs and 71 taxa/species in OAAs. The most significant Phyla in terms of species richness were Mollusca (MAs $n = 30$; OAAs $n = 24$), Echinodermata (MAs $n = 21$; OAAs $n = 16$) and Arthropoda (MAs $n = 12$; OAAs $n = 10$). Of the total taxa registered in the survey, 21 corresponded to species of commercial interest, and most of these were mollusks (**Figure 4A** and **Supplementary Table S2**).

The Echinoidea class represented mainly by *Loxechinus albus*, *Arbacia dufresnii,* and *Pseudechinus magellanicus* tended to dominate numerically (50–64% of total fauna density) in both MAs and OAAs. The bivalves *Ameghinomya antiqua* (11% of total fauna density) and *Aulacomya atra* (11% of total fauna density) also represented important numerical contributions to the overall density in MAs-Guaitecas and in OAAs, respectively (**Figure 4A** and **Supplementary Table S2**).

Average densities of benthic species (considering all the community) showed significant differences in MAs-Gala (Kruskal–Wallis test, $p < 0.05$) in comparison with other areas (**Table 4**). The Shannon-Wiener diversity index ranged between 2.09 and 2.33, indicating low variability between areas. Evenness index (J′) was ∼0.6 in all areas, indicating that the community was dominated by few species; no significant differences were estimated in either of the above indexes between the four groups (**Table 4**; Kruskal–Wallis test, $p > 0.05$). Rarefaction curves indicate equal values of $ES_{(100)} = 22$ both in MAs and OAAs (**Figure 4B**), although a trend of higher species richness was observed in MAs, with $ES_{(2000)} = 63$ compared to OAAs with $ES_{(2000)} = 58$. The shape of the curve for total-fauna, which considers all 102 taxa/species observed in MAs and OAAs, indicates that species richness was well represented by sampling effort in the studied areas (**Figure 4B**).

Analysis of data using nMDS highlighted three main groups: (i) MAs-Gala, (ii) MAs-Guaitecas, and (iii) another cluster grouping all OAAs with MAs-Huichas (**Figure 4C**). The one-way ANOSIM showed separation between groups (Global $R = 0.32$, $p < 0.05$) but only significant differences were found between MAs-Gala and OAAs (PERMANOVA test, $p < 0.05$). Results associated to the evaluation of the similarity between areas geographically closed (MAs-Huichas and OAAs) did not showed defined groups, associated to management regimes, in relation to the community composition and their abundances (one-way ANOSIM, Global $R = 0.33$, $p < 0.05$).

SIMPER similarity analysis was used to determine the species that contributed to the similarity (or dissimilarity) of the faunal assemblages within and between areas; high similarities within the areas (47–65%) were obtained, with group MAs-Gala having the highest percentage (65%). Dissimilarity between MAs and OAAs, showed MAs-Huichas as having

TABLE 2 | Primary target resource evaluated per area, number of transects for benthic community/commercial species and sampling dates.

Group	Name	No. transects	Sampling date	Primary target resource
OAAs	OAA1	20/25	3–4/02/2016	*L. albus*, ***A. antiqua*** (330), ***C. concholepas*** (256)
	OAA2	15/25	11-04-2016	***L. albus*** (330), ***A. antiqua*** (322)
	OAA3	15/29	12-04-2016	***L. albus*** (308), *A. antiqua, C. concholepas*
	OAA4	15/28	07-02-2016	*L. albus*, ***A. antiqua*** (327)
	OAA5	15/30	09-04-2016	***L. albus*** (343), ***A. antiqua*** (269)
MAs-GALA	GALA2	20/40	13–14/01/2016	***C. concholepas*** (359), ***L. albus*** (328)
	GALA1	20/40	12-13/01/2016	***L. albus*** (321), ***C. concholepas*** (526)
MAs-Huichas	HUIC1	25/35	08/01/2016 27/01/2016	***L. albus*** (330), ***C. concholepas*** (407)
	HUIC2	20/38	05/02/2016	***L. albus*** (330), ***A. antiqua*** (330), *C. concholepas*
	HUIC3	22/42	09–10/01/2016 01/02/2016	***L. albus*** (361), ***A. antiqua*** (312), ***C. concholepas*** (356)
MAs-Guaitecas	GUA1	22/40	11–12/02/2016	***L. albus*** (236), ***A. antiqua*** (291), *C. concholepas*
	GUA2	29/40	14/02/2016	***L. albus*** (287), ***A. antiqua*** (243), ***C. concholepas*** (204)

Biological sampling is represented by species written in bold; in parenthesis number of individuals measured and weighed.

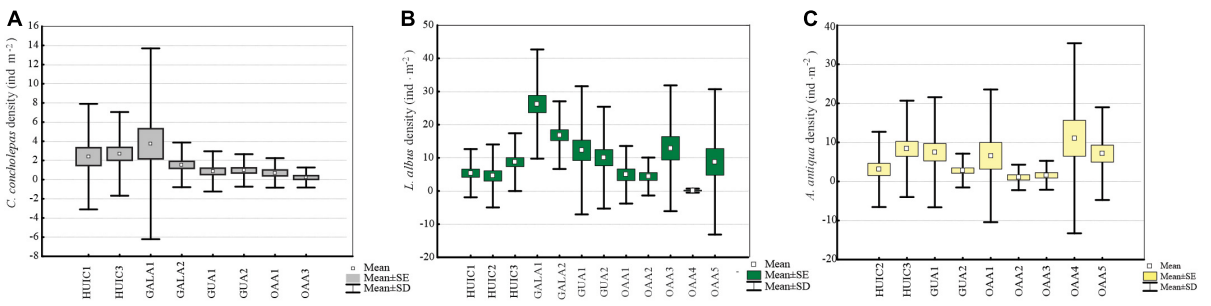

FIGURE 2 | Average densities (ind.m^{-2}) and standard deviation (SD) of commercial species in MAs and OAAs; **(A)** *C. concholepas,* **(B)** *L. albus,* and **(C)** *A. antiqua*.

lower dissimilarity (49%) compared to OAAs and MAs-Gala as having greater dissimilarity (63%) compared to OAAs. The main species that contributed to these dissimilarities (MAs-Gala and OAAs) were *Arbacia dufresnii*, *Loxechinus albus*, *Concholepas concholepas*, *Pentactella leonina*, *Tegula atra*, *Cosmasterias lurida, Argobuccinum pustulosum, Pseudechinus magellanicus, Ameghinomya antiqua*, *Actinaria unidentified*, *Aulacomya atra,* and *Metacarcinus edwardsii* (**Figure 4D**). However, only the first five of the above species showed significantly higher densities (Kruskal–Wallis test, $p < 0.05$) in MAs-Gala than in OAAs. In contrast to the other species, the sea star *Cosmasterias lurida,* showed significantly lower densities in MAs-Gala compared to MAs-Huichas and OAAs (Kruskal–Wallis test, $p < 0.05$).

DISCUSSION

Exploitation Intensity of Commercial Species

Concholepas concholepas is a species for which extraction has been banned from OAAs since 2002 (San Martin et al., 2010). Low densities in OAAs hinder the statistical comparison of fisheries indicators for *C. concholepas* between this regime and MAs. In most MAs, low densities combined with low values of the fisheries indicators could be indicative of a high exploitation intensity. To contribute to the discussion of these results, total allowable catch (TAC) for this resource and the others considered in this study, was estimated using the same methodology for MAs and OAAs (details of the methodology and quotas are given in **Supplementary Table S3**). In this context, only two areas obtained a quota for *C. concholepas* and only in one (MA-HUIC3), was high enough to be worth the extraction effort, suggesting that the exploitation intensity for this resource was high in most of the areas, despite their management regimes. Historical TACs for this resource in the studied MAs (obtained from Subpesca, 2020b) sustained this hypothesis since they had been decreasing since their first baseline study, except in HUIC3. Considering all MAs in Aysén, landings of *C. concholepas* have been decreasing since 2010, from 65,447 kg during the period 2010–2015, to 9,641 kg during the period 2016–2019, and in 2020 (up to October) only 1,180 kg has been harvested (data obtained from Servicio Nacional de Pesca, Sernapesca, 2020). OAAs were selected according to historical fishing grounds of the primary target resources, but no quotas were obtained suggesting illegal fishing activities. Data for illegal fishing shows that in the last 5 years, a total of 3,000 kg of *C. concholepas* has been confiscated (Sernapesca, 2020); although this is likely to be an underestimation of the true illegal harvest. In central Chile, a study of illegal extraction of this species concluded that fishers harvest illegally not only in OAAs, but also within their local MAs and within MAs of other organizations (Oyanedel et al., 2017). The same study estimated that official landings account for only

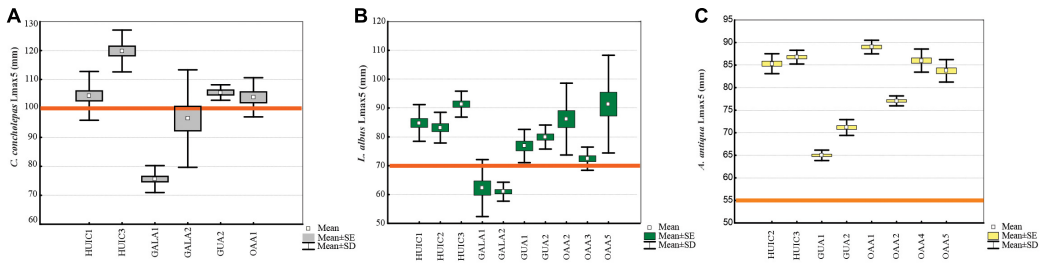

FIGURE 3 | Average size of the largest 5% (Lmax5, mm) and standard deviation (SD) of commercial species in MAs and OAAs; **(A)** *C. concholepas,* **(B)** *L. albus,* and **(C)** *A. antiqua*.

14–30% of the total *C. concholepas* catch. The massive extraction of this species within OAAs is not only of concern regarding total biomass, but also in the context of MLS; estimates suggest that up to 48% of this illegal catch is composed of undersized individuals, compared to only 8% in MAs (Fernandez et al., 2020). Our data therefore support the need to examine the effectiveness of the permanent ban on harvest of *C. concholepas* within OAAs (Bandin and Quiñones, 2014; Andreu-Cazenave et al., 2017).

In contrast to the *C. concholepas* fishery, *L. albus* can be extracted from OAAs, but is managed through an annual TAC. Higher densities estimated in MAs compared to OAAs were mainly driven by small sizes individuals in MAs-Gala. Low values of the fisheries indicators in both MAs and OAAs, could be indicating that harvest had been intense in most of the areas, except in some MAs in Huichas. Estimated TACs supports these findings, since on average, low quotas were estimated for MAs and OAAs (11 ton and ≤3 ton in MAs and OAAs, respectively). In Aysén, increased exploitation of this resource in MAs had been registered since 2010 (Sernapesca, 2020). Indeed, from 2016, this species has contributed to 99.5% of landings within MAs. It appears that MAs present an opportunity for fishers to extract and commercialize this resource at a higher price in MAs (USD 0.7 ± 0.2 in OAAs and USD 1.5 ± 0.1 in MAs; A. Lafon, personal communication, December 12, 2020), at a time when the regional TAC had been already harvested in OAAs.

MAs in Gala presented high densities of *C. concholepas* and *L. albus* but of small sizes individuals which could be indicating that this zone could be important in terms of recruitment. For both resources, the average sizes were in the lower limit of the first size at maturity; estimated between 70 and 90 mm for *C. concholepas* (41.8°S; Manriquez et al., 2009) and between 41 and 44 mm for *L. albus* (Arias et al., 1995). A regular sampling (at least annually) that includes habitat characteristics (e.g., food supply, water exchange) will allow to determine if this situation is permanent and the area has become important in terms of recruitment or small sizes are the result of the intense exploitation of harvestable individuals.

Ameghinomya antiqua is a species restricted to habitats with sandy-muddy bottoms. This clam has only been targeted as a primary resource in four MAs (Huichas and Guaitecas) and was present in all OAAs. Unlike other commercial species evaluated in the present study, there are no restrictions for fishers to extract this species in OAAs, since no TACs had been implemented. Our results showed no significant differences in densities between management regimes. In both MAs and OAAs, size-frequency distribution was skewed toward larger sizes showing that exploitation intensity was low both in OAAs and MAs. Since suitable substrate for this species was generally restricted within these areas, estimated quotas were not high (average TACs: MAs = 26 ton; OAAs = 13 ton). MAs-Guaitecas were the only areas with historical TACs. In both MAs, these first studies estimated higher quotas (∼ 113 ton) that the ones estimated in our study. After that, stable quotas of around 30–50 ton (Subpesca, 2020b) could be indicating and supporting our findings of low exploitation intensity.

TABLE 3 | Proportional stock density (PSD) and medium condition factor (MCF) calculated for the commercial species within MAs and OAAs.

Group	Name	*L. albus*		*A. antiqua*		*C. concholepas*	
		PSD (%)	MCF	PSD (%)	MCF	PSD (%)	MCF
MAs-Gala	GALA1	0.6	0.8	–	–	0.0	0.9
	GALA2	0.3	0.8	–	–	1.4	0.7
MAs-Guaitecas	GUA1	6.3	1.1	43.6	0.8	*	*
	GUA2	13.1	0.9	79.0	1.1	7.4	1.0
MAs- Huichas	HUIC1	10.3	0.9	–	–	4.4	1.0
	HUIC2	34.0	1.0	85.8	1.1	*	*
	HUIC3	55.7	1.1	92.3	0.9	44.7	1.1
OAAs	OAA1	*	*	97.0	0.9	3.1	1.1
	OAA2	6.7	1.1	83.5	1.0	–	–
	OAA3	4.2	1.0	*	*	*	*
	OAA4	*	*	93.6	1.2	–	–
	OAA5	21.6	1.1	92.6	1.0	–	–

**Indicate that although the species was present, densities were low hindering biological collection (measured and weighed).*
–Indicate that the species was not a primary target resource (in the case of MAs) or was not present (in the case of OAAs).

Benthic Community Structure

The benthic community was represented by a high number of species (102 taxa/species), dominated by Echinoidea (*Arbacia dufresnii*, *Pseudechinus magellanicus,* and *Loxechinus albus*). Diversity and evenness indexes did not show differences between areas with different management regimes. Only one group of

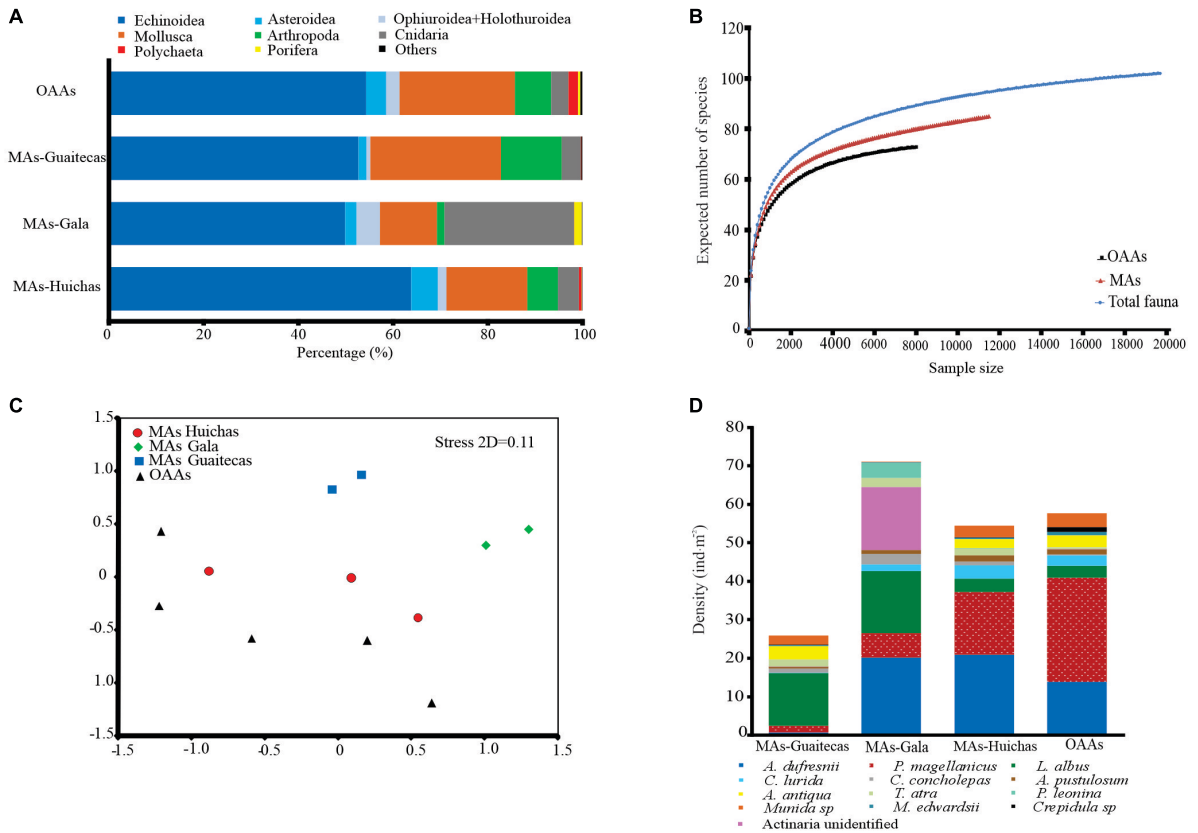

FIGURE 4 | (A) Benthic fauna contribution in terms of density in percentage (%) for main taxonomic groups. Others: Ascidiacea, Nemertea, Echiura, and Platyhelminthes. **(B)** rarefaction (ES) plot for the benthic fauna enumerated in MAs, OAAs and for total benthic fauna (MAs + OAAs). **(C)** Non-metric multidimensional scaling analysis (nMDS), showing OAAs (black triangles), MAs-Huichas (red circles), MAs-Guaitecas (blue squares), MAs-Gala (green diamonds). **(D)** Densities of the principal species contributing to dissimilarity between areas. The list is based on the species that contribute to >50% cumulative of the dissimilarity according to SIMPER analysis.

TABLE 4 | Benthic community parameters estimated for MAs and OAAs.

Groups	No. species/taxa	Av. density ± SD	Av. H′(±SD)	Av. J′(±SD)
MAs-Huichas	56	64 (±67)	2.09 (±0.27)	0.60 (±0.11)
MAs-Gala	49	86 (±59)	2.23 (±0.04)	0.62 (±0.002)
MAs-Guaitecas	44	31 (±27)	2.13 (±0.02)	0.61 (±0.007)
OAAs	71	81 (±150)	2.33 (±0.32)	0.69 (±0.14)
MAs	84	59 (±59)	2.14 (±0.16)	0.61 (±0.06)

Number of species/taxa; Average density (ind.m^{-2} ± standard deviation); Average diversity (H′ ± standard deviation; Average Evenness (J′ ± standard deviation).

MAs (Gala) showed significant differences with OAAs regarding the densities of commercial species (*L. albus* and *C. concholepas*) and other secondary species (*Arbacia dufresnii*, *Pentactella leonina,* and *Tegula atra*).

High densities of *L. albus* (10 ± 15 ind.m^{-2}) were comparable with those reported in northern Patagonia (11 ind.m^{-2}, Molinet et al., 2016; 29 ind.m^{-2}, Contreras et al., 2019). *L. albus* is a strict herbivore (Vasquez et al., 1984; Gonzalez et al., 2008) and therefore could have a controlling effect on macroalgae biomass and in surrounding communities, since macroalgae are three dimensional structures that favor settlement and serve as refuges for juveniles' stages (Dayton, 1985; Buschmann et al., 2004; Wright et al., 2005; Contreras et al., 2019). In MAs-Gala, high densities of sea urchins were observed, co-incident with low macroalgae abundance (<5%, **Supplementary Table S4**). These types of habitats dominated mainly by sea urchins and devoid of macroalgae, resemble the sea urchin barrens (Fillbee-Dexter and Schebling, 2014) that have been described in regions that support kelp beds as in Patagonia (Dayton, 1985; Fernandez et al., 2000). Sea urchin barrens can shift to a stage where kelp beds can recuperate or could maintain a stable state associated to long-term persistence of the parameters that drive and sustain high abundances of sea urchins (e.g., urchin grazing rate, kelp growth rate, recruitment rates, per capita predation rates) (Dayton, 1985; Fillbee-Dexter and Schebling, 2014). Threshold densities of sea urchins could determine these shifts: in fjords of the northern hemisphere, urchin densities of 45–75 ind.m^{-2} and 10–16 ind.m^{-2}, have been reported for barrens, and kelp beds, respectively (Fillbee-Dexter and Schebling, 2014). In northern and central Chile, barrens have been shown to alternate with kelps patches (Vasquez and Buschmann, 1997) and persistence

of barrens has been associated with unregulated extraction of macroalgae (Vasquez, 2008). In the fjords and channels of Patagonia (45°–54°S) barrens dominated by *L. albus* have been reported (with densities up to 100 ind.m^{-2}) (Dayton, 1985). In contrast, low densities of *L. albus* (<2 ind.m^{-2}) have been reported in dense kelp forest in parts of the Magellan region (Friedlander et al., 2018). In MAs-Gala, high densities of *L. albus* (22 ± 14 ind.m^{-2}, with a maximum of 78 ind.m^{-2}) and *A. dufresnii* (20 ± 14 ind.m^{-2} with a maximum of 51 ind.m^{-2}) coincided with relatively low coverage of macroalgae which could be indicating a sea urchin barren in these areas. This contention is supported by juveniles of *L. albus* (39 ± 9 mm) and *C. concholepas* (61 ± 11 mm) dominating the community in these areas. High settlement in barrens has been reported, probably due to the lower structural complexity, which could limit available habitats for predators (Fillbee-Dexter and Schebling, 2014). Further research is needed to evaluate the persistence of this sea urchin barren state in this zone.

An unexpected finding of the present study was related to *Cosmasterias lurida*, a predatory sea star that inhabits the subtidal environment. This species was present in high frequency of occurrence (64% of transects) and higher densities (2 ± 3 ind.m^{-2}) in the sampling sites compared to other studies in Patagonia (Vasquez and Castilla, 1984; Garrido, 2012). Recognized top predator such as *C. concholepas* (Navarrete et al., 2010) occurred infrequently and in low densities in our study, indicating that *C. lurida* would have no competitors being the highest-order predator. The intense harvesting of *C. concholepas* in the study area could be contributing to shifts on roles of predators that could have cascading effects on the structure of benthic communities (Fernandez et al., 2000; Pinnegar et al., 2000; Gaymer and Himmelman, 2008; Perez-Matus et al., 2017), and further evaluation of its effects is now a high priority.

Implications for Management of Fisheries and Benthic Environments in Patagonia

Our results indicate that MAs in the Aysén region are not fulfilling the objectives of sustainability regarding exploitation of benthic resources. Few of the MAs that were studied showed significantly lower exploitation intensities than OAAs, with most showing similar exploitation intensity. In both MAs and OAAs, benthic communities showed signs of disturbance characterized by the absence of the largest harvestable individuals (*L. albus* and *C. concholepas*). High densities of echinoderms (sea urchins and sea stars) were also indicative of changes in the community structure (e.g., trophic roles, competition, and dominances).

Currently, information provided by follow up studies is deficient in the sense that it does not permit evaluation of changes in benthic community structure associated to harvest. However, efforts have been made by the national fisheries institute (Spanish acronyms, IFOP) to evaluate MAs performance mainly in the northern regions. These results indicate that the community associated to *C. concholepas* presented two groups (north-central zone 28°–33°S and south zone 39°–41°S), with latitudinal differences in their abundances and composition of their functional groups. However, community indicators (e.g., density, diversity of functional groups, diversity, uniformity, and dominance indexes) resulted highly variable spatially and temporally (Ariz et al., 2017, 2018; Romero et al., 2019). Due to the high heterogeneity of these indicators, the use of a regional scale was recommended (Romero et al., 2019). A regional spatial scale will allow through environmental, biological and socioeconomic monitoring to identify more defined spatial patterns, and apply local management measures and policies (e.g., minimum extraction sizes). This monitoring should include integral spatial management since all commercial species considered in MAs management plans have long dispersive larval stages hence settlement, recruitment and growth are processes that probably greatly exceed the boundaries of MAs (Romero et al., 2019). In short, the productivity of one area is dependent on processes and management in other OAAs and MAs (Molinet et al., 2010; Arias and Stotz, 2020). It should be highlighted that our results are the first attempt to evaluate MAs' performance in comparison with OAAs regime on a regional scale with a community approach in Aysén (43.9°–45.2°S).

Illegal fishing has been recognized as a major impediment to marine conservation, and although MAs were designed to provide a disincentive, our data combined with regional statistics, highlight deficiencies in the existing system. The surveillance of fishers within MAs in the Aysén region has been almost impossible to implement because of long travel distances from fishing villages to their MAs (distances between coves and MAs in this study varied between ∼9 and ∼32 km and up to 180 km when considering all regional MAs). It should be highlighted that most fishers own small boats which resulted in 1 or 2 h sailing from their coves to their MAs. In this context, the only area (HUIC3) showing improved fisheries indicators for commercial species was one with year-round surveillance provided by the proximity of local fishers. In this case, fishermen asked for a land concession next to the area to diminish cost associated to surveillance. This surveillance system worked well because of social cohesion within their union, which highlighted the social capital as a key factor in the successful functioning of MAs (Marin and Gelcich, 2012). MAs-Gala were the only other management areas close to coves (∼9 km apart) but due to low social capital no vigilance has been implemented. Social capital is especially important in Aysén region because fishing coves are not only remote from MAs but also from markets. Clearly, the establishments of collaborative networks should be considered as a priority in the strengthening of this benthic management regime.

DATA AVAILABILITY STATEMENT

The original contributions presented in the study are included in the article/**Supplementary Material**, further inquiries can be directed to the corresponding author.

AUTHOR CONTRIBUTIONS

MH: conceptualization, methodology, writing – reviewing and editing, supervision, and visualization. PO: conceptualization, methodology, and writing – reviewing and editing. Both authors contributed to the article and approved the submitted version.

FUNDING

This study was financially supported by the Subpesca through grant CUI 2015-7-FAP "Asistencia para el desarrollo de Estudio de Situación Base de Área y Seguimiento en Áreas de Manejo de la Región de Aysén, Etapa 1". Regional Program ANID R17A10002 and R20F0002 partial funding.

ACKNOWLEDGMENTS

The authors would like to thank Ramiro Contreras for the discussion of the results and Subpesca for data handling. The authors would also like to thank Aldo Hernandez y Carlos Leal for methodology field support and estimation of catch quota, Eduardo Palma for diving during field trips, and David Crawford and Brian Reid for the English revision of the manuscript.

SUPPLEMENTARY MATERIAL

The Supplementary Material for this article can be found online at: https://www.frontiersin.org/articles/10.3389/fmars.2021.635756/full#supplementary-material

REFERENCES

Anderson, M. J. (2001). A new method for non-parametric multivariate analysis of variance. *Austral Ecol.* 26, 32–46. doi: 10.1111/j.1442-9993.2001.01070.pp.x

Andreu-Cazenave, M., Subida, M. D., and Fernandez, M. (2017). Exploitation rates of two benthic resources across management regimes in central Chile: evidence of illegal fishing in artisanal fisheries operating in open access areas. *PLoS One* 12:e0180012. doi: 10.1371/journal.pone.0180012

Arana, P. (2006). Demography and fishery of the sea urchin *Loxechinus albus* (Echinodermata: Echinidae) in south-austral Chile region. *Int. J. Trop. Biol.* 53, 367–382.

Arias, E., Barahona, E., Lozada, E., and Jerez, G. (1995). *Monitoreo Del Recurso Erizo En La X y XI Región*. Informe Final FIP 93-13. Valparaíso: Instituto de Fomento Pesquero.

Arias, N., and Stotz, W. (2020). Sustainability analysis of the benthic fisheries managed in the TURF system in Chile. *Int. J. Commons* 14, 344–365. doi: 10.5334/ijc.1011

Ariz, L., Arenas, G., Clavijo, L., Díaz, L., Figueroa, L., García, A., et al. (2018). *Programa de Seguimiento Pesquerías Bajo Régimen Áreas de Manejo, 2017. Convenio de Desempeño IFOP - Subsecretaría de Economía y Empresa de Menor Tamaño. Informe Final*. Valparaíso: Instituto de Fomento Pesquero (IFOP), 192.

Ariz, L., Clavijo, L., Carrasco, S., Díaz, L., Figueroa, L., Galleguillos, F., et al. (2017). *Programa De Seguimiento Pesquerías Bajo Régimen Áreas de Manejo, 2016*. Convenio de Desempeño IFOP – Subsecretaría de Economía y Empresa de Menor Tamaño. Informe Final. Valparaíso: Instituto de Fomento Pesquero (IFOP), 308 + Anexos.

Bandin, R. M., and Quiñones, R. A. (2014). Impacto de la captura ilegal en pesquerías artesanales bentónicas bajo el régimen de co-manejo: el caso de Isla Mocha, Chile. *Latin Am. J. Aquat. Res.* 42, 547–579. doi: 10.3856/vol42-issue3-fulltext-14

Bay-Schmith, E., Werlinger, C., and Silva, J. (1981). *Ciclo Anual de Reproducción Del Recurso Erizo Loxechinusalbus Entre la X y XII Región*. Concepción: Universidad de Concepción.

Bertolino, M., Costa, G., Bavestrello, G., Pansini, M., and Daneri, G. (2020). New sponge species from Seno Magdalena, Puyuhuapi Fjord and Jacaf Canal (Chile). *Eur. J. Taxon.* 715, 1–49.

Betti, F., Bavestrello, G., Bo, M., Enrichetti, F., Loi, A., Wanderlingh, A., et al. (2017). Benthic biodiversity and ecological gradients in the Seno Magdalena (Puyuhuapi Fjord, Chile). *Estuar. Coast. Shelf Sci.* 198, 269–278. doi: 10.1016/j.ecss.2017.09.018

Biggs, D., Amar, F., Valdebenito, A., and Gelcich, S. (2016). Potential synergies between nature-based tourism and sustanaible use of marine resources: insights from dive tourism in territorial user rights for fisheries in Chile. *PLoS One* 11:e0148862. doi: 10.1371/journal.pone.0148862

Blanchard, J. L., Dulvy, N. K., Jennings, S., Ellis, J. R., Pinnegar, J. K., Tidd, A., et al. (2005). Do climate and fishing influence size-based indicators of Celtic Sea fish community structure? *ICES J. Mar. Sci.* 62, 405–411. doi: 10.1016/j.icesjms.2005.01.006

Bruguiere, J. G. (1789). *Encycloped. Méth. (loe. tipo: Costas del Perú, por Designación Original) (Descripción Original)*. 252.

Buschmann, A. H., Garcia, C., Espinoza, R., Filun, L., and Vasquez, J. A. (2004). "Sea urchin (*Loxechinus albus*) and kelp (*Macrocystis pyrifera*) in protected areas in southern Chile," in *Sea Urchin Biology*, eds J. Lawrence and O. Guzmán (Harrisburg, PA: DEStech Publications), 120–130.

Canales, C., Adasme, N., Sanchez, N., Curiel, J., Mardones, M., Barahona, N., et al. (2019). *Estrategias de Manejo de la Pesquería de la Almeja Venus Antiqua en la Región de Los Lagos y la Región de Aysén Del General Carlos Ibáñez del Campo"*. Proyecto FIPA 2018-32. 244. Anexos. Subpesca, Valparaíso, Chile.

Castilla, J. C. (1994). The Chilean small-scale benthic shell fisheries and the institutionalization of new management practices. *Ecol. Inter. Bull.* 21, 47–63.

Castilla, J. C., and Fernandez, M. (1998). Small-scale benthic fisheries in Chile: on co-management and sustainable use of benthic invertebrates. *Ecol. Appl.* 8 (Suppl.), S124–S132.

Castilla, J. C., Manriquez, P., Alvarado, J., Rosson, A., Pino, C., and Espoz, C. (1998). Artisanal "Caletas" as units of production and co-managers of benthic invertebrates in Chile. *Can. Spec. Publ. Fish. Aquat. Sci.* 125, 407–413.

Clarke, K. R. (1993). Non-parametric multivariate analyses of changes in community structure. *Aust. J. Ecol.* 18, 117–143. doi: 10.1111/j.1442-9993.1993.tb00438.x

Clarke, K. R., and Gorley, R. N. (2006). *PRIMER v5: User Manual/Tutorial. PRIMER-E*. Plymouth: Plymouth Marine Laboratory.

Contreras, C., Niklitschek, N., Molinet, C., Díaz, P., and Díaz, M. (2019). Fishery-induced reductions in density and size truncation of sea urchin *Loxechinus albus* affects diversity and species composition in benthic communities. *Estuar. Coast. Shelf Sci.* 219, 409–419. doi: 10.1016/j.ecss.2019.02.030

Dayton, P. K. (1985). The structure and regulation of some South American kelp communities. *Ecol. Monogr.* 55, 447–468. doi: 10.2307/2937131

De Juan, S., Hewitt, J. E., Thrush, S. F., and Freeman, D. (2015). Standardizing the assessment of functional integrity in benthic ecosystems. *J. Sea Res.* 98, 33–41. doi: 10.1016/j.seares.2014.06.001

De Juan, S., Subida, M. D., Gelcich, S., and Fernandez, M. (2018). Ecosystem health in coastal areas targeted by small-scale artisanal fisheries: insights on monitoring and assessment. *Ecol. Indic.* 88, 361–371. doi: 10.1016/j.ecolind.2018.01.054

Defeo, O., Castrejon, M., Perez-Castaneda, R., Castilla, J. C., Gutierrez, N., Essington, T., et al. (2014). Co-management in Latin American small-scale shellfisheries: assessment from long-term case studies. *Fish Fish.* 17, 176–192. doi: 10.1111/faf.12101

Fernandez, M., Jaramillo, E., Marquet, P., Moreno, C., Navarrete, S., Ojeda, P., et al. (2000). Diversity, dynamics and biogeography of Chilean benthic nearshore ecosystems: an overview and guidelines for conservation. *Rev. Chil. Hist. Nat.* 73, 797–830. doi: 10.4067/S0716-078X2000000400021

Fernandez, M., Kriegl, M., Garmendia, V., Aguilar, A., and Subida, M. D. (2020). Evidence of illegal catch in the benthic artisanal fisheries of central Chile:

patterns across species and management regimes. *Latin Am. J. Aquat. Res.* 48, 287–303. doi: 10.3856/vol48-issue2-fulltext-2475

Fillbee-Dexter, K., and Schebling, R. (2014). Sea urchin barrens as alternative stable states of collapsed kelp ecosystems. *Mar. Ecol. Prog. Ser.* 495, 1–25. doi: 10.3354/meps10573

Flores, E., Parada, C., Castro, L., Narvaez, D., and Sepulveda, H. (2020). Connectivity in early life stages of the southern hake, *Merluccius australis*, in northern Chilean Patagonia. *J. Mar. Sci.* 212:103452. doi: 10.1016/j.jmarsys.2020.103452

Forcelli, D. (2000). *Moluscos Magallánicos: Guía de los Moluscos de la Patagonia y Del Sur de Chile*. Buenos Aires: Vásquez Mazzini Editores.

Försterra, G., Häussermann, V., and Laudien, J. (2016). "Animal forests in the Chilean fjords: discoveries, perspectives and threats in shallow and deep waters," in *Marine Animal Forests*, eds S. Rossi, L. Bramanti, A. Gori, and C. Orejas (New York, NY: Springer).

Friedlander, A. M., Ballesteros, E., Bell, T. W., Giddens, J., Henning, B., Hüne, M., et al. (2018). Marine biodiversity at the end of the world: cape Horn and Diego Ramirez islands. *PLoS One* 13:e0189930. doi: 10.1371/journal.pone.0189930

Garrido, I. (2012). *Ecologíatrófica del Asteroideocosmasteriaslurida (Phillipi, 1858) enelSeno del Reloncaví (Sur de Chile): Distribución, Abundancia, Alimentación y Movimiento*. Tesis de Grado Biológía Marina. Valdivia: Universidad Austral de Chile, 86.

Gaymer, C., and Himmelman, J. (2008). A keystone predatory sea star in the intertidal zone is controlled by a higher-order predatory sea star in the subtidal zone. *Mar. Ecol. Prog. Ser.* 370, 143–153. doi: 10.3354/meps07663

Gelcich, S., Cinner, J., Donlan, C. J., Tapia-Lewin, S., Godoy, N., and Castilla, J. C. (2016). Fishers' perceptions on the Chilean coastal TURF system after two decades: problems, benefits, and emerging needs. *Bull. Mar. Sci.* 93, 53–67. doi: 10.5343/bms.2015.1082

Gelcich, S., Fernández, M., Godoy, N., Canepa, A., Prado, L., and Castilla, J. C. (2012). Territorial user rights for fisheries as ancillary instruments for marine coastal conservation in Chile. *Conserv. Biol.* 26, 1005–1015. doi: 10.1111/j.1523-1739.2012.01928.x

Gelcich, S., Godoy, N., Prado, L., and Castilla, J. C. (2008). Add-on conservation benefits of marine territorial user rights fishery policies in central Chile. *Ecol. Appl.* 18, 273–281. doi: 10.1890/06-1896.1

Gelcich, S., Hughes, T. P., Olsson, P., Folke, C., Defeo, O., Fernández, M., et al. (2010). Navigating transformations in governance of Chilean marine coastal resources. *Proc. Natl. Acad. Sci. U.S.A.* 107, 16794–16799. doi: 10.1073/pnas.1012021107

Godoy, N., Gelcich, S., Vasquez, J., and Castilla, J. C. (2010). Spearfishing to depletion: evidence from temperate reef fishes in Chile. *Ecol. Appl.* 20, 1504–1511. doi: 10.1890/09-1806.1

Gonzalez, J., Stotz, W., Garrido, J., Orensanz, J. M., Parma, A. M., Tapia, C., et al. (2006). The Chilean TURF system: how is it performing in the case of the loco fishery? *Bull. Mar. Sci.* 78, 499–527.

Gonzalez, S. J., Caceres, C. W., and Ojeda, F. P. (2008). Feeding and nutritional ecology of the edible sea urchin *Loxechinus albus* in the northern Chilean coast. *Rev. Chil. Hist. Nat.* 81, 575–584.

Hammer, O., Harper, D., and Ryan, P. (2001). PAST: Palaeontological Statistics Software Package for Education and Data Analysis, Version 4.03. Palaeontol Electron 4: 9. Available online at: www.nhm.uio.no/english/research/infrastructure/past/ (accessed March 1, 2021).

Häussermann, V., and Försterra, G. (2009). *Marine Benthic Fauna of Chilean Patagonia*. Santiago: Nature in Focus, 1000.

Hurlbert, S. H. (1971). The nonconcept of species diversity: a critique and alternative parameters. *Ecology* 52, 577–586. doi: 10.2307/1934145

Jennings, S., and Kaiser, J. (1998). The effects of fishing on marine ecosystems. *Adv. Mar. Biol.* 34, 201–352. doi: 10.1016/S0065-2881(08)60212-6

King, P. P. (1832). Description of the Cirrhipeda, Conchifera and Mollusca, in a collection formed by the officers of H.M.S. Adventure and Beagle employed between the years 1826 and 1830 in surveying the southern coasts of South America, including the Straits of Magalhaens and the coast of Tierra del Fuego. *Zool. J.* 5, 332–349.

Levin, P. S., Murawski, S. A., and Fogarty, M. J. (2009). Integrated ecosystem assessments: developing the scientific basis for ecosystem-based management of the ocean. *PLoS Biol.* 7:e14. doi: 10.1371/journal.pbio.1000014

Manriquez, P., Alvarado, J., Huaquin, L., Carrillo, H., Rosson, A., Romero, C., et al. (2009). *Comportamiento y Parametros Reproductivos de C. Concholepas en la VIII y X Regiones*. Proyecto FIP N° 2006-24. 181. Anexos. Subpesca, Valparaíso, Chile.

Marin, A., and Gelcich, S. (2012). Gobernanza y capital social en el comanejo de recursos bentónicos en Chile: aportes del análisis de redes al estudio de la pesca artesanal de pequeña escala. *Cult. Hombre Soc.*22, 131–153. doi: 10.7770/cuhso-V22N1-art428

Miethe, T., Dobby, H., and McLay, A. (2016). *The Use of Indicators for Shellfish Stocks and Fisheries: A Literature Review*. Pitlochry: Scottish Marine and Freshwater Science.

Molina, J. I. (1782). *Saggiosullastorianaturale de Chili. Disponible en Biblioteca Digital – Real Jardín Botánico – CSIC (en Italiano)*. Boloña: Stamperia di S. Tomasod'Aquino, 367.

Molinet, C., Barahona, N., Díaz, M., Díaz, P. A., Millanao, M. O., Araya, P., et al. (2016). Using drift video transects and maximum likelihood geostatistics for quantifying and monitoring exploited subpopulations of *Loxechinus albus* at a mesoscale. *Mar. Coast. Fish.* 8, 70–80. doi: 10.1080/19425120.2015.1121939

Molinet, C., Niklitschek, E., Arevalo, A., and Matamala, M. (2010). Patch structure of benthic resources exploited in Chilean management areas: the shellfish bed concept under a territorial use rights for fisheries framework. *Bull. Mar. Sci.* 86, 555–569.

Moreno, A., and Revenga, C. (2014). *The System of Territorial Use Rights in Fisheries in Chile*. Arlington, TX: The Nature Conservancy.

Navarrete, S., Gelcich, S., and Castilla, J. C. (2010). Long-term monitoring of coastal ecosystems at Las Cruces, Chile: defining baselines to build ecological literacy in a world of change. *Rev. Chil. Hist. Nat.* 83, 143–157.

Oyanedel, R., Keim, A., Castilla, J. C., and Gelcich, S. (2017). Illegal fishing and territorial user rights in Chile. *Conserv. Biol.* 32, 619–627. doi: 10.1111/cobi.13048

Pardo, L. M., Rubilar, P., and Fuentes, J. P. (2020). North patagonian estuaries appear to function as nursery habitats for marble crab (*Metacarcinusedwardsii*). *Reg. Stud. Mar. Sci.* 36:101315. doi: 10.1016/j.rsma.2020.101315

Perez-Matus, A., Ospina-Alvarez, A., Camus, P. A., Carrasco, S. A., Fernandez, M., Gelcich, S., et al. (2017). Temperate rocky subtidal reef community reveals human impacts across the entire foodweb. *MEPS* 567, 1–16. doi: 10.3354/meps12057

Pielou, E. C. (1977). *Mathematical Ecology*. New York, NY: John Wiley & Sons.

Pinnegar, J. K., Polunin, N. V. C., Francour, P., Badalamenti, F., Chemello, R., Harmelin-Vivien, M. L., et al. (2000). Trophic cascades in benthic marine ecosystems: lessons for fisheries and protected-area management. *Environ. Conserv.* 27, 179–200. doi: 10.1017/s0376892900000205

Romero, P., Arenas, G., Velasco, E., Ariz, L., González, C., Manquehual, G., et al. (2019). *Programa de Seguimiento Pesquerías Bajo Régimen Áreas de Manejo, 2018-2019*. Convenio de Desempeño IFOP – Subsecretaría de Economía y Empresa de Menor Tamaño. Informe Final. Valparaíso: Instituto de Fomento Pesquero (IFOP), 347. pp + Anexos.

San Martin, G., Parma, A. M., and Orensanz, J. M. (2010). "The Chilean experience with territorial use rights in fisheries," in *Handbook of Marine Fisheries Conservation and Management*, eds R. Grafton, D. Squires, M. Tait, and M. Williams (New York, NY: Oxford University Press).

Schneider, W., Perez-Santos, I., Ross, L., Bravo, L., Seguel, R., and Hernandez, F. (2014). On the hydrography of puyuhuapi channel, Chilean Patagonia. *Prog. Oceanogr.* 128, 8–18. doi: 10.1016/j.pocean.2014.03.007

Sernapesca. (2020). *Anuario Estadístico de Pesca y Acuicultura. Desembarque Desde Áreas de Manejo Por Especie y Mes. Subsector pesquero Artesanal. Anuarios Estadísticos de Pesca y Acuicultura. Servicio Nacional de Pesca y Acuicultura*. Available online at: www.sernapesca.cl (accessed October 8, 2020).

Sievers, A. H., and Silva, N. (2008). "Water masses and circulation in austral Chilean channels and fjords," in *Progress in the Oceanographic Knowledge of Chilean Inner Waters, from Puerto Montt to Cape Horn*, eds N. Silva and S. Palma (Valparaíso: Pontificia Universidad Católica de Valparaíso), 53–58.

Silva, N., and Guzman, D. (2006). Condiciones oceanográficas fisicas y quimicas, entre la boca del Guafo y fiordo Aysén (crucero CIMAR 7 Fiordos). *Cienc. Technol. Mar.* 29, 25–44.

Silva, N., and Palma, S. (2008). *Progress in the Oceanographic Knowledge of Chilean Interior Waters, From Puerto Montt to Cap Horn*. Valparaíso: Comité Oceanográfico Nacional Pontificia Universidad Católica de Valparaíso, 161.

Silva, N., and Vargas, C. (2014). Hypoxia in Chilean patagonian fjords. *Prog. Oceanogr.* 129 (part A), 62–74. doi: 10.1016/j.pocean.2014.05.016

Stotz, W. (1997). Las areas de manejo en la Ley de Pesca y Acuicultura: primeras experiencias y evaluación de la utilidad de esta herramienta para el recurso loco. *Estud. Oceanol.* 16, 67–86.

Subpesca (1995). *D.S. N° 355-1995 Reglamento sobre Áreas de Manejo y Explotación de Recursos Bentónicos*. Available online at: http://www.subpesca.cl/portal/615/w3-article-11086.html (accessed February 5, 2020).

Subpesca (2000). *Establece Veda Biológica del Recurso Erizo en Área y Periodo que Indica*. Decreto Exento N°439. 27 de Diciembre 2000. Ministerio de Economía Fomento y Reconstrucción, Valparaíso, Chile.

Subpesca (2011). *D.EX. N° 697-2011, Mod. D.EX.N° 409-03 Veda Biológica VII-XI Reg. (F.D.O. 01/08/2011)*. Valparaíso: Ministerio de Economía, Fomento y Turismo.

Subpesca (2016). *XI Región - SUBPESCA Normativa*. Available online at: www.subpesca.cl (accessed February 5, 2020).

Subpesca. (2020a). *Aplicación de Visualización de Mapas de la Subsecretaría de Pesca y Acuicultura. Visualizador de Mapas*. Santiago.

Subpesca (2020b). *XI Región*. Available online at: https://www.subpesca.cl/portal/615/w3-propertyvalue-849.html (accessed December 10, 2020).

Vasquez, J. A. (2008). Production, use and fate of Chilean brown seaweeds: resources for a sustainable fishery. *J. Appl. Phycol.* 20, 457–467.

Vasquez, J. A., and Buschmann, A. H. (1997). Herbivore-kelp interactions in Chilean subtidal. *Rev. Chil. Hist. Nat.* 70, 41–52.

Vasquez, J. A., and Castilla, J. C. (1984). Some aspects of the biology and trophic range of *Cosmasteriaslurida* (ASTEROIDEA, ASTERIINAE) in belts of *Macrocystis pyrifera* at Puerto Toro, Chile. *Ambient. Acuat.* 7, 47–51.

Vasquez, J. A., Castilla, J. C., and Santelices, B. (1984). Distributional patterns and diet of four species of sea urchin giant kelp forest (Macrocystis pyrifera) of Puerto Toro, Navarino Island, Chile. *Mar. Ecol. Prog. Ser.* 19, 55–63. doi: 10.3354/meps019055

Wright, J. T., Dworjanyn, S. A., Rogers, C. N., Steinberg, P. D., Williamson, J. E., and Poore, A. G. B. (2005). Density-dependent sea urchin grazing: differential removal of species, changes in community composition and alternative community states. *Mar. Ecol. Prog. Ser.* 298, 143–156. doi: 10.3354/meps298143

Zuñiga, S., Ramírez, P., and Valdebenito, M. (2008). Situación socioeconómica de las áreas de manejo en la región de Coquimbo, Chile. *Lat. Am. J. Aquat. Res.* 36, 63–81. doi: 10.3856/vol36-issue1-fulltext-5

Conflict of Interest: The authors declare that the research was conducted in the absence of any commercial or financial relationships that could be construed as a potential conflict of interest.

frontiers | Frontiers in Marine Science

ORIGINAL RESEARCH
published: 01 April 2022
doi: 10.3389/fmars.2022.612021

Submarine Geomorphology and Glacimarine Sedimentary Processes Associated to Deglaciation in Europa Fjord, Chilean Patagonia

Cristián Rodrigo[1], Erick Cifuentes[2], Rodrigo Fernández[3], José Andrade[1], Lorena Rebolledo[4,5], Diego Muñoz[6] and Práxedes Muñoz[7,8]*

[1] Geologia, Facultad de Ingenieria, Universidad Andres Bello, Viña del Mar, Chile, [2] Departamento de Ciencias de la Tierra, Facultad de Quimica, Universidad de Concepción, Concepción, Chile, [3] Departamento de Geologia, Facultad de Ciencias Fisicas y Matematicas, Universidad de Chile, Santiago, Chile, [4] Departamento Cientifico, Instituto Antartico Chileno, Punta Arenas, Chile, [5] Centro de Investigacion Dinamica de Ecosistemas Marinos de Altas Latitudes (IDEAL), Punta Arenas, Chile, [6] Departamento de Hidrografia, Servicio Hidrografico y Oceanografico de la Armada, Valparaíso, Chile, [7] Departamento de Biología Marina, Universidad Católica del Norte, Coquimbo, Chile, [8] Centro de Estudios Avanzados en Zonas Áridas (CEAZA), La Serena, Chile

OPEN ACCESS

Edited by:
Giorgio Bavestrello, University of Genoa, Italy

Reviewed by:
Min Kyung Lee, Korea Polar Research Institute, South Korea
Giovanni Daneri, Patagonian Ecosystems Investigation Research Center (CIEP), Chile

****Correspondence:***
Cristián Rodrigo
cristian.rodrigo@unab.cl

Specialty section:
This article was submitted to Marine Biogeochemistry, a section of the journal Frontiers in Marine Science

Received: *16 November 2020*
Accepted: *25 February 2022*
Published: *01 April 2022*

Citation:
Rodrigo C, Cifuentes E, Fernández R, Andrade J, Rebolledo L, Muñoz D and Muñoz P (2022) Submarine Geomorphology and Glacimarine Sedimentary Processes Associated to Deglaciation in Europa Fjord, Chilean Patagonia. Front. Mar. Sci. 9:612021. doi: 10.3389/fmars.2022.612021

In a period of high rates of glacier retreat, increasing meltwater discharge from tidewater glaciers can influence marine fjord ecosystems due to increase sediment delivery and accumulation rates in the proglacial environment. Glacier variations and associated changes in glacimarine processes are recorded in the sedimentary record and submarine geomorphology of fjords. In October-November 2017, CIMAR23 Cruise surveyed several fjords adjacent to the Southern Patagonian Icefield (SPI). In this study, we show detailed results of the multibeam bathymetry, backscatter and sub-bottom seismic profiles, and sediment core samples from Europa Fjord, located west of the central SPI area, to improve the analysis of the fjord glacial and sedimentary evolution and to connect its behavior with the other fjords in the region. For the cores ^{210}Pb chronology, magnetic susceptibility, organic carbon, total nitrogen, and stable isotopes ($\delta^{13}C_{org}$, $\delta^{15}N$) were performed. The seafloor geomorphology showed that the most prominent submarine landforms are transverse morainal ridges, which indicate past stillstand glacier positions; these features formed during the deglaciation of the fjord (latest Pleistocene), and some, perhaps more recently during short episodic advance/retreat events. In the central and mouth fjord areas, erosional features such as lineations are found on the rocky bottom and interpreted as formed by past grounded glaciers. Several submarine moraines are generally well preserved, but some parts are crumbled by slope failures and erosion. Most of the seismic sections are interpreted as the expected subglacial-ice proximal-ice distal succession of facies, characteristic of single retreat environments. The sedimentary record includes bioturbed muds with muddy laminations and variable amounts of coarse sediments interpreted as ice rafted debris, suggesting a proglacial environment, punctuated by calving. From the beginning of the twentieth century there is a tendency to an increase in the terrigenous organic

material content, including an abrupt increase during the 80–90s, and a decline in the last decade. This behavior is indicating possibly a general increase of surface terrestrial runoff and, for the last decade, an increase of glacial meltwater input which would be caused by an accelerated deglaciation.

Keywords: acoustic data, seafloor, submarine landforms, sediments, tidewater glacier, fjord, climate change, Patagonia

INTRODUCTION

The sea floor geomorphology and glacimarine sedimentary processes of the fjords of western Patagonia are the result of a long history of glacial influence in the region. The last fully glacial conditions occurred associated with the Late Pleistocene Patagonian Ice Sheet (LPPIS), which was a large ice body that extended along the Southern Andes, between 30 and 56°S. The LPPIS covered ∼492,600 km^2 during glacial maxima conditions about 33–28 ka (Davies et al., 2020), which equals to more than 25 times the present-day glaciated area. After 18 ka, the relatively rapid shrinking of the LPPIS allowed the initiation of sedimentary glacimarine processes in the western fjords and the continental shelf of Patagonia. The LPPIS was separated in two ice bodies north and south of Canal Martinez-Baker at ∼13 ka (Turner et al., 2005); further shrinking of these ice masses would constitute the present-day Northern Patagonian Icefield (NPI) (46°35′S–47°35′S), and the Southern Patagonian Icefield (SPI) (48°20′S–51°30′S).

After the deglaciation of the Patagonian fjords, the Holocene extent of Patagonian glaciers, varied in a manner characterized by termini advance and retreat within at most, a few 10s of kilometers of the fjords' head, although studied areas are scarce and few (e.g., Harrison, 2004; Koppes et al., 2015). Available chronological and geomorphological data indicate that most SPI glaciers were near their maximum Late Holocene glacier extent state between the sixteenth and nineteenth centuries (Masiokas et al., 2009; Glasser et al., 2011), period that was followed by widespread glacier shrinkage during the twentieth century (Rivera et al., 2012). The twentieth century glacier retreat has been explained by regional increase in temperatures accompanied by decreasing precipitation, possibly associated to global climate changes resulting from the anthropogenic emission of greenhouse gases (Carrasco et al., 1998; Rignot et al., 2003; Gardner et al., 2013; IPCC, 2014; Marzeion et al., 2014). The shrinkage of SPI and increasing production of meltwater accounts for about 9% of the contribution from global mountain glaciers to the rate of sea level rise (Rignot et al., 2003), which highlights its importance for the present-day changing Earth System. Changes in sediment discharge associated with meltwater production, influence the biogeochemical cycles and ecosystems of fjords (e.g., Iriarte et al., 2010; Quiroga et al., 2013; Seifert et al., 2019), especially those most directly related to the seafloor such as benthic organisms (e.g., Quiroga et al., 2016). These environmental changes, includings changes in marine productivity, and geochemical characteristics, can be recorded in the fjord sediments, allowing the study of patterns of oceanographic and biological variables and their evolution (e.g., Rebolledo et al., 2008, 2011, 2019; Aracena et al., 2011; Silva et al., 2011).

The majority of SPI outlet glaciers are either fjord-calving tidewater glaciers or lake-calving glaciers, whose glacial and sedimentary dynamics are complex, especially in changing climate scenario (Moon et al., 2012; Schenk and Csatho, 2012). Numerous studies suggest that while climate may trigger changes in tidewater glacier mass balance and extent, the rate of retreat is mainly controlled by the unique geometry, shape, width and bathymetry of its channeling fjord, while stillstands and advance episodes are likely controlled by the capacity of construction of stabilizing grounding line moraines (Pfeffer, 2007; Briner et al., 2009; Post et al., 2011; Enderlin and Howat, 2013). In recent years, important steps forward to understand glacier behavior have been made in Patagonia (e.g., Koppes et al., 2009; Rivera et al., 2012), however, most of the studies focus on just a few case-study calving glaciers and are descriptive of recent changes, providing little information about the glacial and sedimentary processes at work and their influence on the glacimarine environment; nevertheless several studies demonstrate that the marine sedimentary record from the proglacial glacimarine environment can preserve a record of the spatial-temporal interactions between the glacier behavior, and climate and ocean changes (e.g., Boyd et al., 2008; Koppes et al., 2009, 2015; Fernández et al., 2012, 2017; Bertrand et al., 2017). On the other hand, the identification of submarine glacial morphologies has led to a better understanding of sub-glacial and proglacial processes and advance and retreat cycles (e.g., Rivera et al., 2012; Dowdeswell and Vásquez, 2013; Dowdeswell et al., 2016). In this work we present results from a marine geology study aimed at characterizing the recent and modern environmental and sedimentary conditions at Europa Fjord a 58 km long fjord located west of the central SPI area (∼50°10′S; **Figure 1**), that has the only one calving glacier, Europa Glacier, which is located at the fjord head. Like the majority of the SPI glaciers, Europa glacier has retreated over the last decades; however, relative to other SPI glaciers, its retreat rate is rather slow, not exceeding 300 m between 1984 and 2011 (Sakakibara and Sugiyama, 2014). Another particularity of Europa Glacier is that exhibits erosion rates of ∼0.14 mm yr^{-1} at millennial timescales, much lower than other Patagonian glaciers, and comparable to subpolar Antarctic sites (Fernández et al., 2016), which in principle, signify that it has a relatively low sediment production. Considering these particularities and the location of the Europa fjord in the SPI region, in this work we present detailed results on submarine geomorphology, seismic stratigraphy and characteristics of surface sedimentology, to specify the phenomena associated with glacial evolution and sedimentary processes of the Europa fjord, identifying its

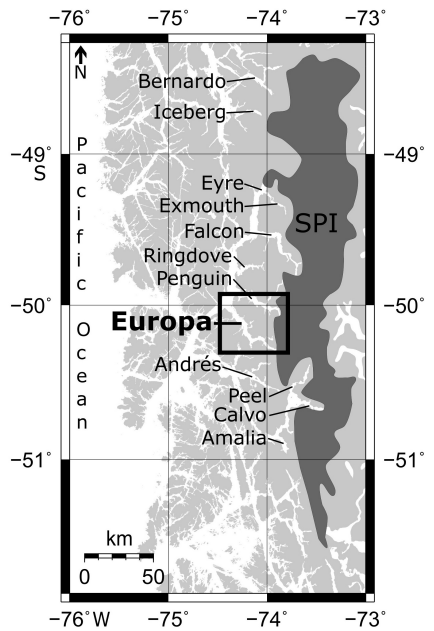

FIGURE 1 | Study area and Europa Fjord location. Approximate Southern Patagonian Icefield (SPI) coverage in the present time. Main fjords of the region are also identified.

behavior and providing background information to establish its connection with other fjords in the region, in order to contribute to a better understanding of the sensitive contact zone between glaciers and the marine environment.

MATERIALS AND METHODS

Study Area

The study area is in the Magallanes Region, Chilean Patagonia, between latitudes 49.95 and 50.33°S and longitudes 74.50 and 73.75°W (**Figure 1**), in which is located the Europa Fjord and its same name tidewater glacier, corresponding to an outlet glacier from the SPI, in the area of the Bernardo O'Higgins National Park.

The fjord has a length of ∼58 km, a maximum width of ∼6 km in its mouth, and a minimum width of 1 km in its head. It is oriented NW-SE and it is sinuous in its medial and proximal part with respect to the glacier front. Deeper areas are close to the fjord mouth (∼780 m) and the shallower are in the head (55 m) (**Figure 2**). The submarine profile is irregular with a pronounced topographic drop from its proximal zone up to its distal area (Araya-Vergara, 1999; Vieira and Simões, 2006). In the proximal area three morainal sills stand out, and other in the fjord mouth, which are forming, between them, several deep basins (Vieira and Simões, 2006; Dowdeswell and Vásquez, 2013).

The bedrock of Europa Fjord comprises rocks from the Southern Patagonian Batholith (SPB) and the Metamorphic Complex of the Eastern Andes (MCEA). The SPB crops out in the central part of the fjord and ice distal areas. On the northern coast, rocks correspond to the oldest set (Jurassic) of the SPB intrusives described by Hervé et al. (2007), while the southern coast includes some of the Jurassic units but it is comprised mostly by Cretaceous granites, granodiorites, and hornblende and biotite tonalites (Sernageomin, 1982). The ice proximal area of the fjord is composed by meta sandstones, phyllites and, to a lesser extent, marbles, cherts, metabasalts and metaconglomerates of the MCEA (Sernageomin, 1982), with ages between Lower Triassic to Upper Devonian (Hervé et al., 2003).

Geophysical Data and Processing

In October-November 2017, CIMAR23 Cruise surveyed several fjords adjacent to SPI to carry out studies on oceanography, biology and sedimentary fjord dynamics, with the science research vessel AGS "Cabo de Hornos." Multibeam bathymetry was obtained using a Kongsberg Simrad EM-122, 12 kHz frequency, whose data were georeferenced with DGPS, and corrected by geostationary satellite. During the cruise, sound velocity profiler (SVP) measurements were made *in situ* to calibrate the depth measurements respect to the sea water velocity of propagation of sound. The bathymetry processing consisted in the manual removal of anomalous beams using the workflow of the CARIS Hips and Sips software. A bathymetric digital grid was generated with a 10 ×10 m resolution, applying an algorithm that uses the "9 × 9 weighted swath angle" method, which aims to create a grid surface based on the intersection angle (CARIS, 2016). Similarly, backscatter data was also processed using the standard CARIS Sips workflow. Geomorphological interpretations were made with the Fledermaus software which allows improved 3D visualization of bathymetric grids. The Fledermaus FMGT module was used to perform a granulometric classification of the seabed sediments according to the program's acoustic library (model), after correcting the data for the angular response of the beams respect to the acoustic strength of the backscatter signal (ARA analysis). Only one superficial sediment sample was obtained in the Europa Fjord during the cruise which was used to verify the ARA analysis. For this sample, standard sieving granulometric analysis was carried out. The sample was classified texturally according to Folk (1974). Other granulometric sediment data served to verify the ARA analysis (Ahumada and Contreras, 1999; Aracena et al., 2011; Boldt et al., 2013). Finally, to build the maps, due to the variability of the acoustic data, the most dominant granulometric classification for specific areas was taken and re-classified texturally.

To improve the bathymetric model of Europa Fjord, we used previously acquired multibeam data from hydrographic cruises carried out by the Hydrographic and Oceanographic Service of the Chilean Navy (SHOA) between 2006 and 2008, which were acquired by the Atlas Fansweep and Hydrosweep MD systems aboard the PSH "Cabrales." These systems use frequencies of 200 and 50 kHz, respectively. The data were corrected by *in-situ* SVP and geo-referenced with real-time DGPS. They were processed in the same way as the data from the AGS "Cabo de Hornos," but the bathymetry was gridded at a resolution of 20 × 20 m. The bathymetric grids obtained from the two vessel data were blended

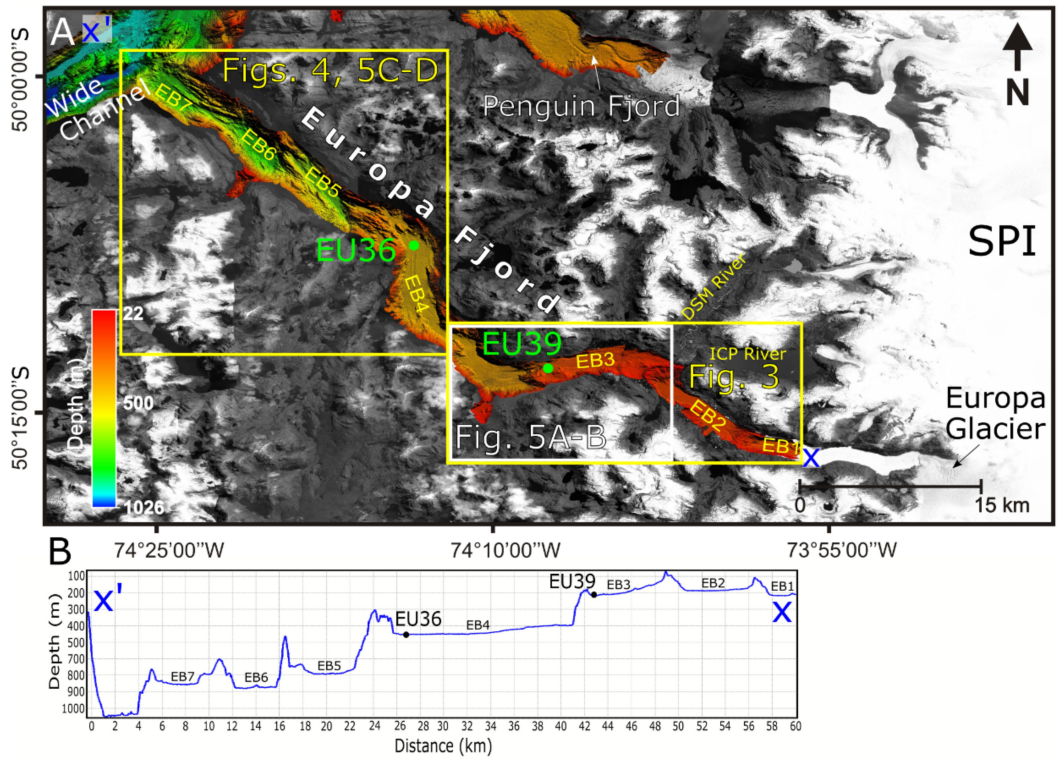

FIGURE 2 | (A) Shaded relief map that shows the coverage of the multibeam bathymetry from Cruise CIMAR 23 and SHOA data. Detailed submarine geomorphology and seafloor sediment distribution are showed in **Figures 3–5**, respectively (boxes). **(B)** Longitudinal bathymetric profile of the Europa Fjord. Europa Basins (EB) are showed.

with GMT software ("grdblend" command) (Wessel et al., 2013; **Figure 2**).

Sub-Bottom Profiler (SBP) data from Kongsberg's CHIRP SBP-120 system aboard the AGS "Cabo de Hornos" could not be obtained in Europa Fjord during CIMAR 23 Cruise. Instead, we used previously acquired SBP data from the NBP0505 Cruise onboard R/V "N.B. Palmer" in 2005 (not used before), which were obtained with a Knudsen 3.5 kHz CHIRP. Visualization of the NBP0505 data was achieved using the system manufacturer's program (Knudsen), adjusting the contrast appropriately (signal amplitude fit). Seismic facies were interpreted according to DaSilva et al. (1997).

Sediment Cores and Analysis

During CIMAR 23 Cruise, two ∼3 m long sediment cores were obtained with a standard gravity corer, in stations EU39 and EU36 (**Figure 2** and **Table 1**). Non-destructive analyses to sediment cores were performed before they were opened and included X-ray Computed Tomography (XT or CT) scanning and magnetic susceptibility measurement of cores. The XT scanning was performed at the Hospital Clinico de la Universidad de Chile (HCUCH) with a Somatom Definition Edge CT Siemens scanner using two X-ray energy levels (dual-energy mode), at 80 and 140 kV, and a spatial resolution that produced volumetric pixels (voxels) of 0.14 mm × 0.14 mm × 0.6 mm. The raw data were processed at HCUCH by a team of medical XT experts, resulting in high resolution and high signal to noise ratio images with cell values of X-rays attenuation in Hounsfield units (HU). Visualization and interpretation of XT processed images was done using the RadiAnt, which allows the 3D and 2D sectional visualization of reconstructed core 3D images. Since at energy values (above 100 kV), X-rays interact with matter mainly through Compton scattering, which is sensitive to the electron density and thus proportional to bulk density, high HU values were interpreted as high density materials. Thus, mapping of high attenuation elements (HAE) of sizes larger than 1 mm throughout the cores was used as a proxy for to the presence of pebbles or large calcareous (fossils?) elements, considering in their identification, the relative contrasting characteristics with the fine sediment matrix. This mapping was done using sectional XT images every 5 cm and manual counting of HAE elements for which HU > 1,400. Bulk magnetic susceptibility measurements (MS) were made using a MS2C Magnetic Susceptibility System

TABLE 1 | Locations of the sediment cores acquired during CIMAR 23 Cruise in 2017.

Core codes	Latitude (S)	Longitude (W)	Depth (m)	Length (m)	Distance from glacier (km)
EU36	50°07′33.6″	74°13′30.36″	447	2.54	20
EU39	50°12′59.54″	74°07′38.17″	222	2.72	13

(Bartington Instruments) which gives an along axis resolution of 2 cm at the Paleomagnetism Laboratory of Universidad de Chile.

Once the corers were opened, a visual description (VD) was performed, and samples were taken for several analyses. Color identification was based on Munsell Color Chart. Laser granulometry was made by a Mastersizer 2000 system, taking samples every 5 cm for each core section (at Geology Laboratory, Universidad de Chile). In addition, samples were taken every 2 cm for the top 30 cm from each core for dating and geochemical analysis. Sedimentation rates were estimated from the radioactive decay of $^{210}Pb_{xs}$ activities in excess (unsupported), considering that the ^{210}Pb flux and the sedimentation rate were constant according to CF-CS model (Goldberg, 1963). Supported activities were estimated from the last constant values (0.99 ± 0.03, 1.52 ± 0.12 dpm g^{-1}) in the range of those values reported by Boldt et al. (2013) in the same area (0.9 ± 0.2 dpm g^{-1}). These activities were assumed to be in equilibrium with ^{226}Ra. The total activities were corrected for the elapsed time between sampling and counting. Sedimentation rates were established from the best exponential fit model (r^2 = 0.82–0.63, p<0.01). Standard deviations (SD) of the ^{210}Pbxs and sedimentation rates estimations were estimated propagating the uncertainties of counting and the deviations of the supported activities estimations (Bevington and Robinson, 1992). Additionally, the activities were modeled according to the CRS model considering the inventories at every 2 cm (Turekian et al., 1980). The ages from both estimations only showed discrepancies in the last two estimations. Finally, to obtain ages at deeper core sections, they were estimated using the software CLAM 3.5.1 (Blaauw, 2010; Rebolledo et al., 2011). The activities were measured at the Chemical Oceanography Laboratory, Universidad de Concepción, using a Canberra QUAD alpha spectrometer, model 7404, obtaining an average error of 0.10 dpm g^{-1}. Geochemical analysis of Organic Carbon, Total Nitrogen, and Nitrogen and Carbon stable isotopes ($\delta^{13}C_{org}$, $\delta^{15}N$) were determined at the Biogeochemistry and Applied Stable Isotopes Laboratory of the Pontificia Universidad Católica de Chile, with an Isotope Ratio Mass Spectrometer (IRMS) Thermo Delta Advantage, coupled to an EA2000 Flash Elemental Analyzer. The associated isotopic error was 0.15 and 0.35 ‰ for Nitrogen and Carbon, respectively. In turn, the associated error in the elemental analysis was 0.002 mg and 0.017 mg for Nitrogen and Carbon, respectively, using a linear regression. The standard used for this calculation was Acetanilide, which contains 71.10% Carbon and 10.36% Nitrogen. For the calculation of the isotopic δ, 4 internal standards previously normalized were used: Acetanilide, Atropine, Caffeine, High Organic Sediment and Glutamic Acid. More methodology details can be found in Rebolledo et al. (2019).

RESULTS

Bathymetry and Geomorphology

The Europa Fjord has a complex seafloor morphology characterized by a series of esplanades or basins identifiable as flat areas separated by oblique or transverse ridges (**Figure 2**). Seven esplanades at different levels of depths are identifiable from SE to NW with: 215, 180, 200, 450, 690, 770, 750 m. Thus, these basins can be named as EB1 to EB7, respectively (**Figures 2–4**). Another basin is also observable outside the fjord in the Wide Channel with a 940 m of depth. Basin EB4 is further divided in two subbasins (EB4-A and EB4-B: **Figures 3**, **4**) based on its morphology. EB4-A has increasing depth toward the fjord's mouth (400–450 m) while EB4-B is mostly a large flat area of ∼450 m; these two sub-basins are connected through a narrow (∼400 m wide) flat bottom channel about 3 km in length. The bottom from EB1 to EB4 is noticeable smoother, flat areas are of lesser extent and more elongated than in basins from EB5 to EB7. The slopes from EB1 to EB7 are < 0.3° interpreted as damming esplanades of sediments (Araya-Vergara, 1997), except for EB3, which has an average slope of ∼1° in the direction of the fjord's mouth, interpreted as an outwash esplanade.

There are two distinct types of shallow areas separating the identified basins: arcuate asymmetrical ridges (AAR) and oblique streamlined sills (OSS). AARs separate EB1 from EB2, EB2 from EB3, and EB3 from EB4 (**Figure 3**), and EB7 from Wide Channel at Europa Fjord's mouth (**Figure 4**), and were interpreted by Dowdeswell and Vásquez (2013) as large moraine ridges generated during stillstand periods within general ice retreat from maximum glacial conditions. OSS define the boundaries between EB4, EB5, EB6 and EB7. They are characterized by streamlined monticules of 10–100s meter in length and irregular morphology and variable extent, often presenting deep narrow channels.

The AAR limiting basin EB1, the most proximal to Europa Glacier (**Figure 3**), has a relief of nearly 100 m and low curvature. It is identified by a series of relatively small ridges on its up-fjord slope (**Figure 3A**) that protrude 5 m from the 4.5° inclined seafloor and are 200, 250, and 400 m of distance from the axis of the main AAR, with the closer ridge (200 m) spatially associated with a long fjord ridge located near the northern coast. The down-fjord (western) side of the AAR has a much steeper slope (11°) and it is characterized by a couple of channels and their tributaries on the deeper part, and by a series of gullies in the upper part.

The AAR separating EB2 from EB3 (74°02′50″ W) has slightly greater relief than the previous one with an elevation difference of ∼115 m (**Figure 3B**) on its up-fjord side. This AAR has greater curvature and an average slope of 3.5° for the up-fjord side and 14° for the down-fjord flank. Small ridges and scour channelizations roughly perpendicular to the crest of the AAR have a relief varying from 5 to 10 m. A few narrow incisions, 300–400 m long and ∼10 m deep, appear near the foothill of the up-fjord flank resembling canyon heads. Gullies are present both sides of the ridge near the top but are more numerous on the down-fjord flank. The top of the AAR is irregular with the central part being deeper than the areas near the coast in both the northern and southern sides, and five depressions 6–10 m deep cut across the ridge.

There are other morphologies in the inner fjord area. On the southern side of the fjord, an underwater extension of the coastal mountain side is observable at ∼110 m depth, but it is flat, and it is surrounded by ridges with a height of ∼20 m respect to inner area. Also, toward the glacier, on the right-most side of the

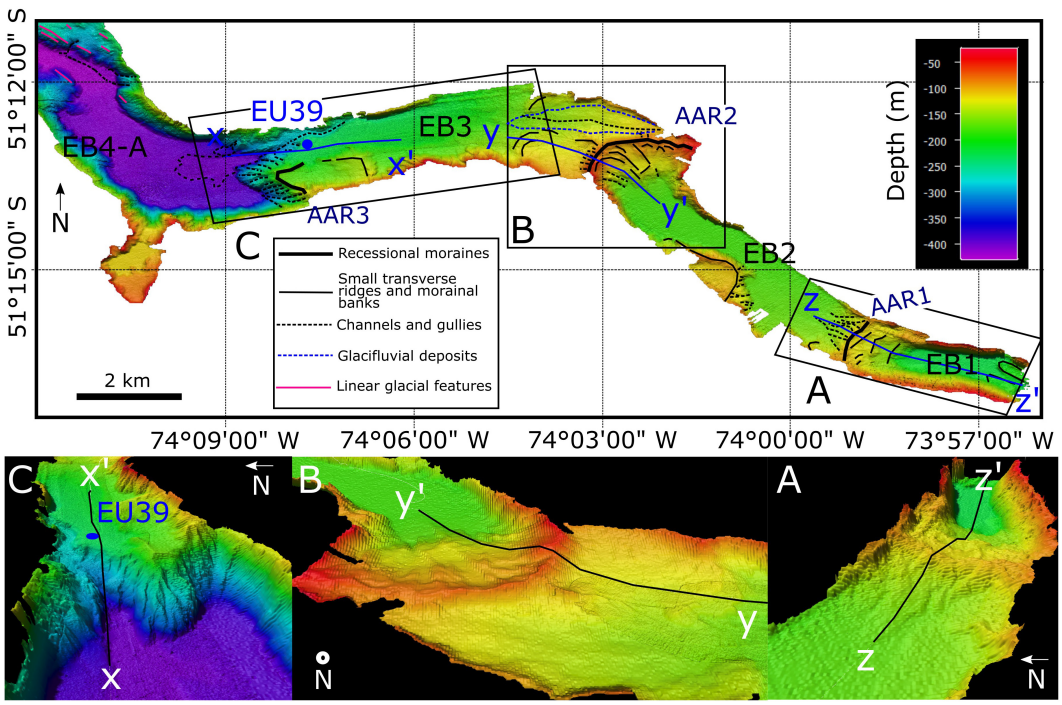

FIGURE 3 | Submarine geomorphology of the inner fjord area from multibeam bathymetry from Cruise CIMAR 23 and SHOA data. Interpretation of landforms are showed. Codes: EB, Europa Basin; AAR, Arcuate Asymmetrical Ridge. **(A)** Moraine proximal subarea and 3D model showing the SBP track for **Figure 6**. **(B)** Moraine medial subarea and 3D model showing the SBP track for **Figure 6**. **(C)** Moraine distal subarea and 3D model showing the SBP track for **Figure 6**, and location of the EU39 sediment core.

Figure 3A, two small arcuate ridges emerge from the flat seafloor on ∼210 m depth.

Basins EB3 and EB4 are separated by a couple of discontinuous and semi-arcuate transverse ridges that are seen only in the southern half of the fjord. The elevation difference between the deeper smooth seafloor of EB3 and the up-fjord areas of EB4 is 170–180 m, with the transition between the two being a cliff area of 15–30°. A large channel dominates the morphology of the northern part of the transition between EB3 and EB4 (**Figure 3C**). The mouth of the channel is 1.3 km wide and 185 m deep and narrows progressively up-fjord, being just 225 m wide at 1.5 km, and 150 m wide and 7 m deep 3 km from the channel mouth. The flanks of the channel have numerous gullies and a smaller side channel on the northern flank, and have steep flanks both sides, with maximum slopes reaching 20–30° in some areas.

The transition between EB4 and EB5 represents the largest depth drop (∼240 m) within Europa fjord, from the distal EB4 seafloor depth of ∼450 m to the proximal EB5 seafloor depth of 690 m (**Figure 4A**). The OSS1 marking the boundary between EB4 and EB5 is flanked by two small esplanades with a depth of ∼420 m located close to both sides of the fjord. The irregular shape of the OSS1 is interrupted by two channels on the down-fjord flank that connect directly to EB5. The OSS1 occurs following an abrupt change in the orientation of the fjord from azimuth 5 to 300°. Two sets of glacial lineations are found on OSS1. The most prominent is characterized by highly elongated monticules like glacial features such as roche moutonnées often observed in deglaciated land areas. These features are 300–1,000 m long and 100–300 m wide and with an azimuth of 310–315°, roughly parallel to the coastline. A smaller set of streamlines features occur partially overlapping or cutting the morphologies of the previous set. This set is characterized by elongated monticules 100–300 m long, mostly symmetrical in the axial direction although a few of them are noticeably asymmetrical, resembling drumlinoid features. Their orientation is ∼15° to the west of the set of larger features and are roughly parallel with the sides of the bottom of the fjord. A third set of streamlines features are observed in this area but east from OSS1 near the coast and are oriented ∼20° oblique to the coastline but roughly parallel to streamlined features observed on land.

The western border of OSS1 falls abruptly down to ∼680 m of depth to the esplanade that conforms EB5 (**Figure 4**). Both EB5 and EB6 are similarly oriented 15–20° oblique to the coastline (EB5 and EB6 azimuth: 330–335°; coastline azimuth: 315–320°), and are separated by OSS2, a 2.5 km long elongated ridge oriented with an azimuth of 335°. Several streamlined features in the area near OSS2 have similar orientation but a set of 300–500 m long elongated monticules overlapping OSS2, are oriented parallel to the coast (azimuth 315–320°). Several drumlinoid features are found in EB6, with some being as small as 150–200 m long and reaching up to ∼500 m in length. They are distributed both at the bottom and the sides of the basin and are spatially accompanied by symmetrical roche moutonnées.

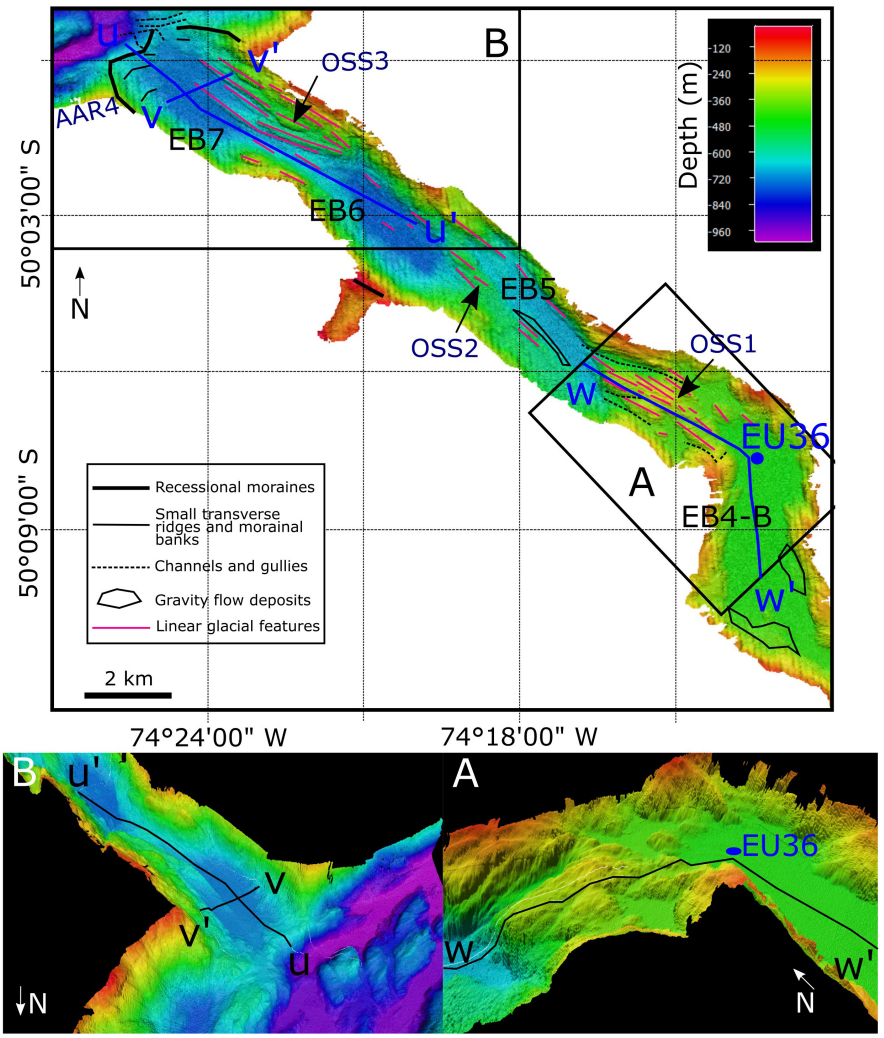

FIGURE 4 | Submarine geomorphology of the outer fjord area from multibeam bathymetry data. Interpretation of landforms are showed. Codes: EB, Europa Basin; AAR, Arcuate Asymmetrical Ridge; OSS, Oblique Streamlined Sills. **(A)** Eastern subarea and 3D model showing the SBP track for **Figure 7**, and location of the EU36 sediment core. **(B)** Western subarea and 3D model showing the SBP tracks for **Figure 7**.

The OSS that forms the transition from EB6 to EB7 (OSS3) has a different morphology than the previous boundary areas (**Figure 4B**). OSS3 is cut by a channel of 3,250 m long and 500 m wide that connects the down-fjord end of EB6 with the up-fjord end of EB7. OSS exhibits prominent 800–2,400 m long elongated features. Notably EB7 is oriented parallel to the southern coastline and is 25–30 m shallower than EB6, which breaks the tendency of down-fjord increasing basin depth. EB7 is characterized by large coastline parallel streamlined features, which reach more than 2–3 km in length and are located only in the northern flank of the fjord. The western limit of EB7 is given by an irregular and arcuate feature 665–685 m deep on its deeper part that marks the mouth of Europa Fjord and the connection to Wide Channel. On its northern part a depression 30 m deep and 700 wide is limited on its northern end by a highly asymmetrical 5 m high monticule perpendicular to the depression. On the up-fjord flank three small ridges form a stepwise morphology with steps occurring roughly every 25 m in depth.

Backscatter and Seafloor Sediments

The type of sediments and their distribution on the seafloor were determined through backscatter data from the AGS "Cabo de Hornos" (no other ship data included in the analysis), so the spatial coverage is less than for the bathymetry mapping. In general, the backscatter data show relatively low values toward the head of the fjord (**Figure 5A**). In EB3, low values of backscatter (< –8 dB) were obtained along the smooth part of the basin while high values are characteristic for AAR3 on its steep down-fjord flank. In EB4 intermediate backscatter values (–25 to –28 dB) predominate on the flat bottom of the basin while higher values are found in the middle of the basin and the narrow channel that connects EB4A and EB4B. High backscatter values dominate EB5, EB6

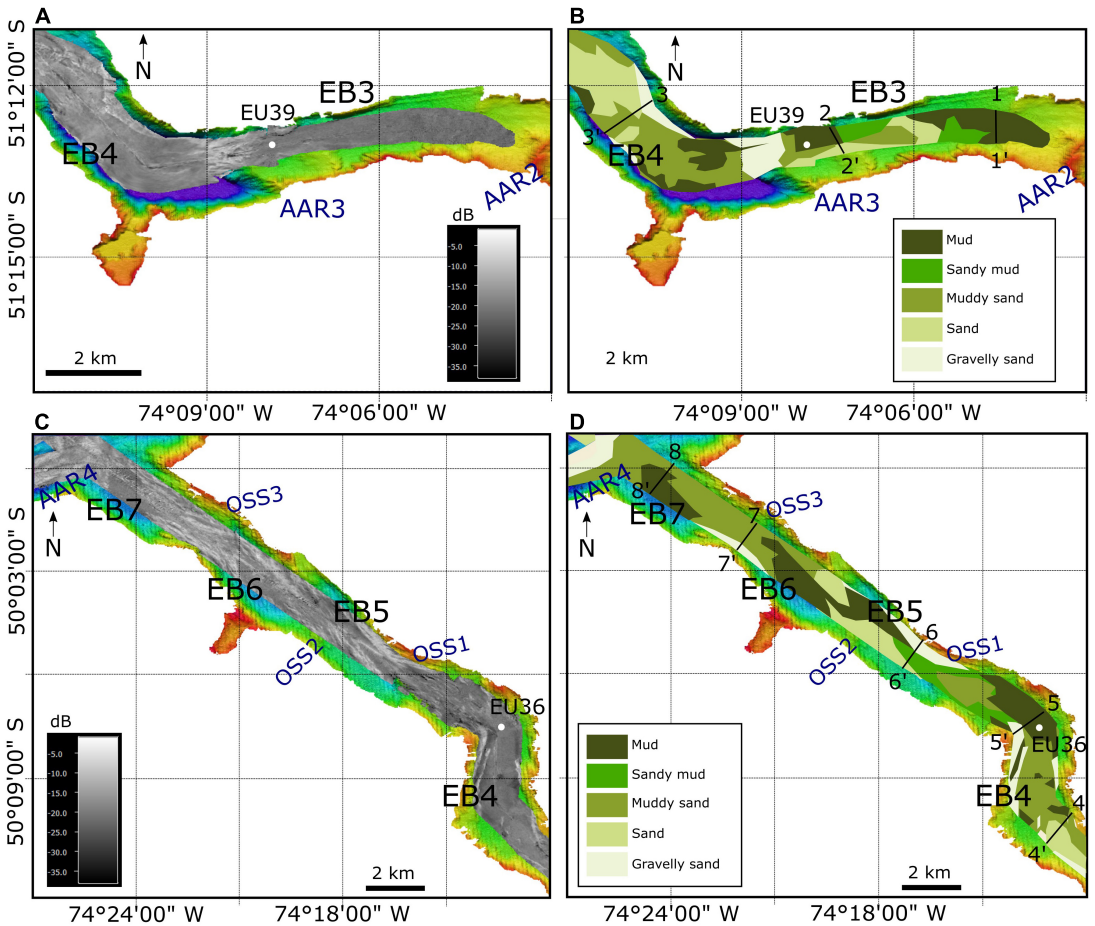

FIGURE 5 | Results from acoustic analysis from Cruise CIMAR 23 multibeam sonar data. **(A)** Backscatter image map for inner fjord area. **(B)** Seafloor sediment textural classification map for inner fjord area. **(C)** Backscatter image map for outer fjord area. **(D)** Seafloor sediment textural classification for outer fjord area. Location of the EU39 and EU36 sediment cores is shown, and example profile locations (e.g., 1–1') for ARA analysis original results are in the **Supplementary Material**.

and EB7 even in the flat parts of these basins. The results of the sediment classification showed that for the inner fjord area, mud is dominant toward the head sector (**Figure 5B**). Coarser material tends to be on the western side of the moraine face, in which its outer slope is composed of sand. For the outer fjord area (**Figure 5C**), intermediate backscatter values predominate, where, for the esplanades, there are low values, and for the structures that border them, higher values, including the moraine located at the fjord mouth. The elongated and pointed shapes of the structures are well defined in the backscatter image. Mud is the main sediment texture for the esplanades, but for that on the eastern side, only its northern part is mud, getting coarser to the south, coinciding in some parts with the identified deposits of gravity flows (sand and gravelly sand) (**Figure 5D**). The same tends to occur in the middle area (around 74°18′W). As was described for the moraine of **Figure 5A**, at the fjord mouth, the moraine is showing coarse material on the outer slope and finer inside. Examples of the original ARA analysis results for the ganulometric classification are available as **Supplementary Material**. The profiles shown in **Figure 5** indicate their position on the map.

Seismic Facies and Stratigraphy

Seismic records are described for the main landforms of the study along profiles shown in **Figures 3**, **4**. **Figure 6A** showed a profile across AAR1 that limits EB1 and EB2 (z'-z profile of **Figure 3A**). The up-fjord flank part of AAR1 showed a series of layers of variable thickness that onlap the acoustic basement and interfinger with layered sub-horizontal seismic facies of EB1. The layers observed in EB1 corresponded to two different seismic facies. Near the bottom and near the top of the sequence, layering was coarse and reflectors limiting them were irregular and discontinuous, while in the middle part of the section subparallel finely spaced reflectors dominated. The bottom facies were distributed filling the rugged acoustic basement resembling ponded sedimentation geometries and forming a smooth flat boundary with the finely layered middle part of the section. The down-fjord flank of AAR1 had a chaotic and coarsely layered seismic character, forming an inclined

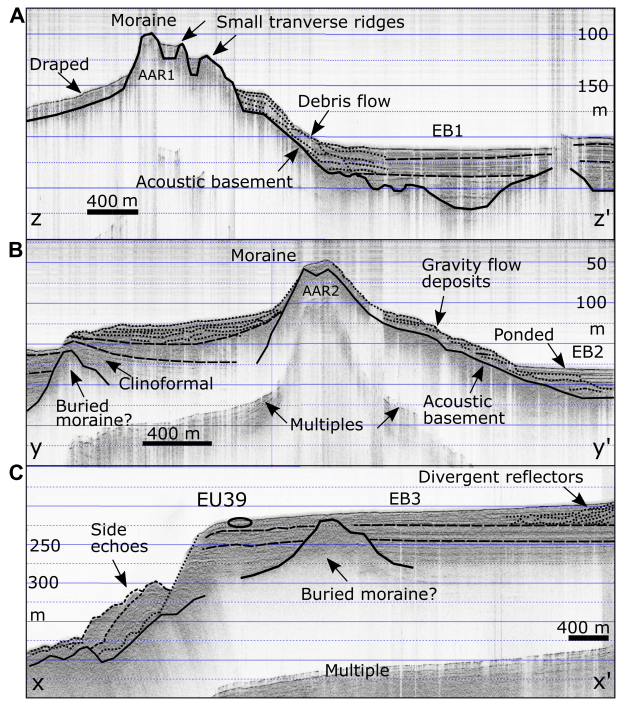

FIGURE 6 | Sub-bottom profile records from cruise NBP0505. Main seismic facies, seismic units (long segmented lines), side-echoes (short segmented lines), acoustic basements (solid lines), and other characters or processes (dotted lines) are showed. **(A)** Proximal subarea for the inner fjord area as showed in **Figure 3A** (z- z'). **(B)** Medial subarea for the inner fjord area as showed in **Figure 3B** (y-y'). **(C)** Distal subarea showed in **Figure 3C** (x-x'). Projected location of the EU39 sediment core is showed.

blanket that onlap onto the acoustic basement. Small transverse ridges appeared at AAR1's top, showing moderate seismic intensity and a chaotic internal reflection character. The third transverse ridge identified by bathymetry truly is a slope change of draped stratified semitransparent seismic facies, interpreted as glacimarine sediment which flow down the slope, forming gravity sediment deposits, who contacts the inner sedimentary basin. This basin showed three main seismic units. The upper had a thin transparent and weak surface layer, and then chaotic with some stratified seismic facies. The middle unit had moderate intensity, parallel ponded and stratified. The lower, was semi-transparent, chaotic and some stratified.

The seismic facies and general architecture of AAR2 are similar to AAR1's. **Figure 6B**, showed a profile across AAR2 (y'-y profile; **Figure 3B**). The up-fjord flank of AAR2 comprised partially chaotic and transparent seismic facies forming layers of irregular thickness that offlap onto each other. The bottom layers underlied sub-horizontal and finely stratified facies of EB2. Other layers of the up-fjord flank interfinger or have a grade with the subhorizontal layers of EB2 which in some cases onlap onto the flank layers. On the down-fjord flank, three main seismic units were present. The top unit had a thin acoustically transparent and forming a mounded seafloor surface. Underlying this unit, chaotic and layered seismic facies were present, with some of the lower ones downlapping onto the bottom unit, while others formed irregularly shaped layers that extend up to a mound that marks the down-fjord extent of the unit. The bottom unit had similar acoustic characteristics, but it thins its layering dips upfjord and is clinoformal with respect to a possible buried moraine due to its seismic facies and the identification of morainal banks nearby detected by the bathymetry.

The seismic section for the western side of EB3 is showed in **Figure 6C** (profile x'-x, **Figure 3C**). The main characteristics of EB3 were its gentle down-fjord slope, the stratified nature of the section, only interrupted by a chaotic or acoustically semi-transparent buried mound, and a series of mounds on the down-fjord end of the section. It was possible to identify three seismic facies that defined three distinguishable seismic units. The top unit was characterized by parallel reflectors that got thin out down-fjord. On the eastern side of the section this unit had several hummocky and subparallel layers that downlap onto the top of the middle unit. The middle unit is characterized by finely spaced layers interbedded with acoustically transparent intervals. The lower unit showed rhythmically layered facies that onlap a mound that extend up to the top of the section but does not crop out on the seafloor.

The seismic architecture of EB4 near the location of core EU36 is shown in **Figure 7A** (profile w'-w; **Figure 4A**). Three seismic units can be recognized in EB4. The top unit, the only one sampled by core EU36, is formed by subhorizontal parallel layers. Underlying the top unit, there was a unit with semi-transparent to chaotic facies and some reflectors of moderate amplitude that hint the presence of layering. The bottom unit had similar seismic facies than the middle one but with lower amplitude, however, layering is discernible. The prominent bathymetric high that forms the boundary between EB4 and EB5, OSS1, is characterized by chaotic and hummocky seismic facies and notable hyperbolic reflectors that indicate the presence of highly reflective or point features. On that bedrock, semi-transparent and hummocky facies are present which can be interpreted as sediment veneer.

The seismic architecture of EB7 is similar to EB4, with three seismic units being recognized in the flat areas of the basin (**Figures 7B,C**, profiles u'-u and v'-v shown in **Figure 4B**). The top unit showed clear layering, but reflectors are of less amplitude than in the top unit of EB4. Underlying the layered top unit, there was chaotic seismic facies with no evident layering that overly bottom facies of layered reflectors and acoustically semi-transparent intervals. The AAR located at the fjord mouth is characterized by high amplitude reflectors with chaotic and hummocky geometries (**Figure 7B**).

Sediment Cores Analysis

Visual Description

Visually, the EU39 core is mainly composed of silt (**Figure 8**). Sedimentary structures such as laminations and lenses were identified. The core can be divided in several visual units according to the general appearance, color and apparent grain size. The Unit 39-A (273–245 cm) composed by silt with mud lenses in smaller proportion than overlying unit, and quartz crystals of ∼ 2 mm size were found. At 74 cm, a rounded

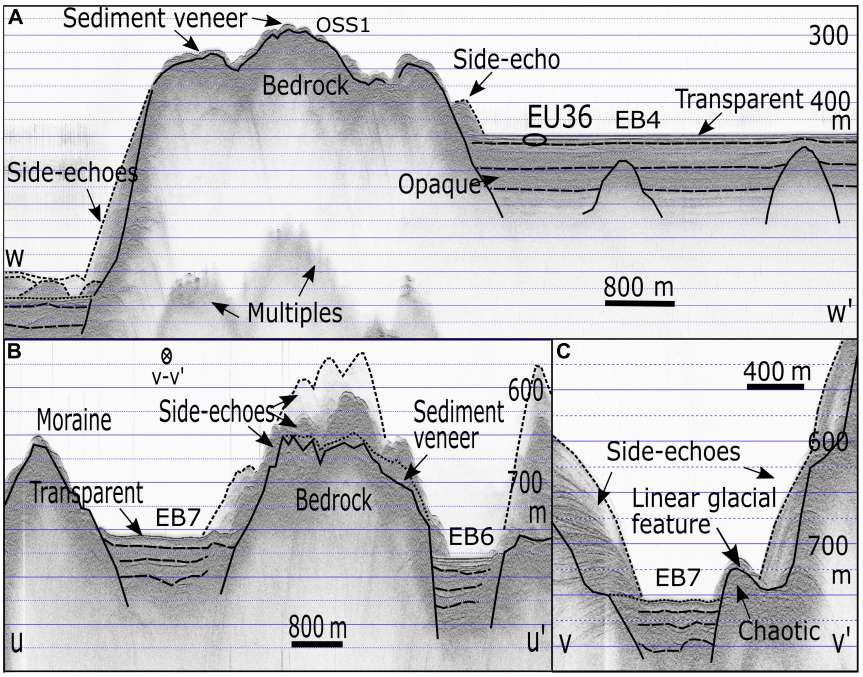

FIGURE 7 | Sub-bottom profile records from cruise NBP0505. Main seismic facies, seismic units (long segmented lines), side-echoes (short segmented lines), acoustic basements (solid lines), and other characters or processes (dotted lines) are showed. **(A)** Eastern subarea of the outer fjord area as showed in **Figure 4A** (w-w'). Projected location of the EU36 sediment core is showed. **(B)** Western subarea of the outer fjord area as showed in **Figure 4B** (u-u'). v-v'track crossing is indicated. **(C)** Crossing of the linear glacial feature and outer basin as showed in **Figure 4B** (v-v').

corneal rock fragment of size ∼1 cm was also found. The color of the unit was dark gray (10YR 4 4/1). The Unit 39-B (247–185 cm) is composed by silt with millimeter-thick mud lenses. Quartz fragments of size ∼ 2 mm were found, and a scaphopod fragment at 13 cm. It presented very thin banded sections of a material with a dark hue. The color of the unit was dark gray (10YR 4 4/1). Unit 39-C (185–143 cm) composed by silty clay, presented mud lens between 160 and 166 cm. Clay color was dark gray (10YR 4 4/1) and mud lens color was gray (10YR 5 5/1). The Unit 39-D (143–60cm) is composed by silty clay with stratifications and millimeter intercalations of fine sediments. At 99 cm there is a branch-like plant remnant no longer than 2 cm. The color of the unit was dark gray (10YR 4 4/1). The Unit 39-E (60–30 cm) is composed by massive silty clay. It presented a small quantity of mud lenses. Normal gradation is recognized in this unit. The color of the unit was gray (10YR 5 5/1). The top of the core (30–15 cm) is composed by massive mud with similar characteristic of the Unit 39-E including color.

Visually, the EU36 core is mainly composed of silt (**Figure 9**). The core can be divided in several visual units. The Unit 36-A (254–116 cm) is composed by massive silt, with a dark gray (5Y 4 4/1) color. The Unit 36-B (101–80 cm), composed by massive silt with a dark gray (5Y 4 4/1) color. This unit presented great loss of interstitial water; the sediment was dry and with low plasticity. The Unit 36-C (80–28 cm) is composed by clayey silt, with periodic intercalations of mud with 2–3 mm thick, and some mud lenses 5–6 mm thick. The color was greenish gray (5 GY 1/5). Unit 36-D (28–13 cm) is composed by massive mud. The section presented a noticeable loss of humidity.

X-Ray Computed Tomography

X-rays attenuation values (Hounsfield Units; HU) obtained through XT scanning allowed us to identify sedimentary structures and intervals of similar attenuation characteristics. Since HU values correlate with the atomic number and the density of the sediments, we used them as one to characterize changes in physical properties of the sediment cores defining XT units as intervals of similar HU values.

XT results for core EU39 are shown in **Figure 8**. Attenuation values vary throughout the core and indicate the existence of intervals of high (900–1,100 HU) and middle-low density materials (750–800 HU)EU39 showed relatively high attenuations at the top and bottom, and between ∼160 to 180 cm depth. The lowest attenuations were found between 245 and 200 cm depth, and between 150 and 158 cm, sections where the abundance of lenses and bioturbation is also greater. Traces of bioturbation were found practically throughout the entire core, this being of variable intensity. Although HAE are variable in quantity, they showed an increasing trend to the core bottom.

The XT results for core EU36 are shown in **Figure 9**. Attenuation values for EU36 also vary throughout the core including intervals of high (HU > 1,100) and low density (700–800 HU). The attenuations of the EU36 core indicate a decrease toward the top, only interrupted by a high attenuation section between 80 and 101 cm depth. We observed signs of intense

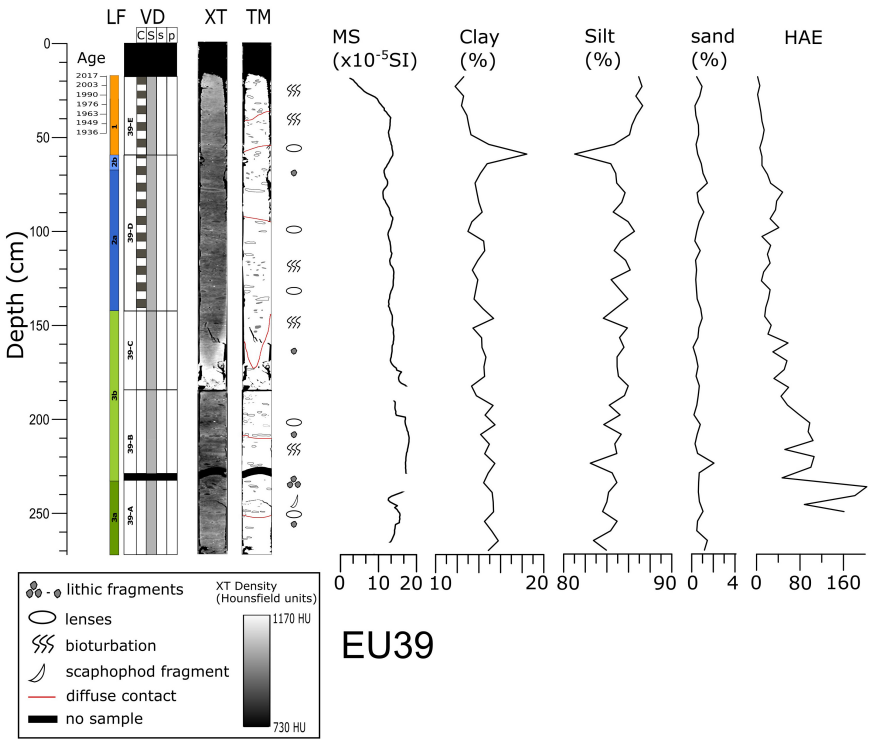

FIGURE 8 | EU39 sediment core with lithofacies identification (LF); Age (from ^{210}Pb dating); original granulometric visual description (VD), showing Clay (C), Silt (S), sand (s) and pebbles (p) contents; X-Ray tomographic image (XT), and interpreted mapping (TM); magnetic susceptibility (MS); laser granulometry showing clay, silt and sand contents; high attenuation elements from XT (HAE).

bioturbation between 146 and 115 cm and in the upper 45 cm of the core. The HAE count is higher in the 50–55 cm section, from which a decreasing trend is observed toward the top. It was not possible to observe HAE from 80 cm toward the bottom of the core.

Laser Granulometry and Magnetic Susceptibility

Laser granulometry and magnetic susceptibility (MS) results for core EU39 are shown in **Figure 8**. There was a slightly increase of MS with depth not exceeding 20 × 10^{-5} SI. Similar pattern is followed by the content of clay and sand, while silt content mirrors clay content and decreases with depth. Average content of clay was ∼15%, for silt ∼84% and for sand ∼1%, which corresponds to silt according to Folk's classification (Folk, 1974).

In core EU36 (**Figure 9**), MS increases with depth (not exceeding 20 × 10^{-5} SI) for the bottom part of the core (> 100 cm), but the top 100 cm shows a broad peak with variable values at the cm to tens of cm scale, indicating relatively high and variable relative proportion of siliciclastic sediments and organic matter, or changes in the quantity or composition of magnetic minerals. Clay and silt content were highly variable in the top 60 cm, while sand content, although variable as well, tended to decrease. Below 60 cm, clay and silt tended to vary around low/high values, respectively, compared with the top 60 cm. Average content of clay was ∼17%, for silt ∼82% and for sand ∼1%, which corresponded to silt according to Folk's classification (Folk, 1974).

Lithofacies

Based on the results from XT scanning, MS, and granulometry, as well as on the visual inspection of cores we defined three main lithofacies (LF1, LF2 and LF3; **Figures 8**, **9**). Lithofacies LF1 corresponded to highly bioturbed and homogeneous mud, including lenses of high and low attenuation (high/low HU values) and a scarce or absent HAE. This lithofacies characterized the top and bottom parts of cores EU39 and EU36. Lithofacies LF2 is composed of bioturbed mud with intercalations of a few millimeter in thickness, some lenses and a variable amount of HAE. Based on differences in the amount of HAE, we distinguished two subfacies: LF2a characterized by increasing amount of HAE with depth; and LF2b, characterized by decreasing amount of HAE with depth. This LF2 lithofacies was distinguished in both cores underlying the top LF1 lithofacies. Lithofacies LF3 is composed by homogeneous and bioturbed mud with the presence of lenses and variable amount of HAE. Like LF2, we defined subfacies LF3a and LF3b based on the relative abundance of HAE being LF3a characterized by noticeable higher presence of HAE relative to LF3b. LF3 was only distinguishable in core EU39.

^{210}Pb Dating and C, N Geochemistry

The ^{210}Pb activities for core EU39 fluctuated between 1.52 and 3.13 dpm g^{-1} and for EU36, between 0.92 and 1.50 dpm g^{-1} (**Figures 10A,G**). The curves lack an exponential decrease with depths, possibly due to the observed bioturbation that

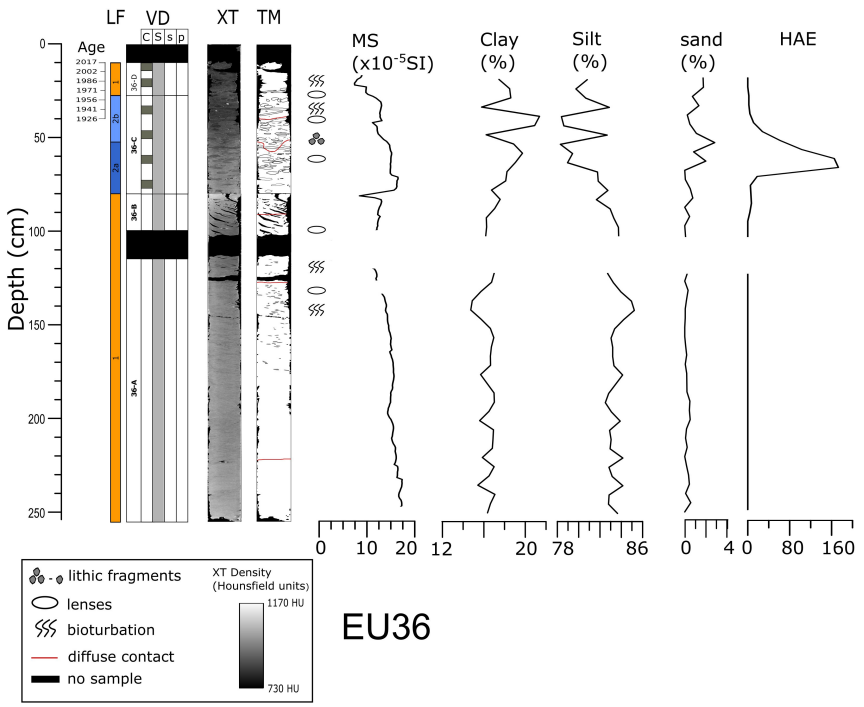

FIGURE 9 | EU36 sediment core with lithofacies identification (LF); Age (from ^{210}Pb dating); original granulometric visual description (VD), showing Clay (C), Silt (S), sand (s) and pebbles (p) contents; X-Ray tomographic image (XT), and interpreted mapping (TM); magnetic susceptibility (MS); laser granulometry showing clay, silt and sand contents; high attenuation elements from XT (HAE).

cause quite homogeneous layers or subsurface higher values on the first 15 cm, related with diffusive and non-local mixing, respectively. The supported activity for EU39 was found to be 1.52 ± 0.12 dpm g^{-1} and 0.97 ± 0.05 dpm g^{-1} for EU36. The sedimentation rates obtained from the best exponential fit model considering the entire core was 0.33 ± 0.05 cm yr^{-1} (r^2 = 0.83, $p < 0.1$) for EU39 and 0.37 ± 0.13 cm yr^{-1} (r^2 = 0.60, $p < 0.01$) for EU36. Estimations below the mixing layer resulted in lower sedimentation rates between 0.08 and 0.09 cm yr^{-1}. The assumption of constant sedimentation rates was based on that the bulk density distribution did not show changes in the depths intervals where ^{210}Pb activities were measured; there were no changes in grain size either, therefore no corrections were made for sediment compaction. The ages obtained with both models, CRS and CF-CS, showed few discrepancies except for the part where the CRS model showed older ages.

Results of C_{org} and N content showed that in each core they vary following the same pattern. A general trend of decreasing C_{org} and N content down-core is observed in core EU39, more prominently for the top ∼20 cm (**Figures 10B,C**). For core EU36 the both content of C_{org} and N were higher and showed greater variability than compared with EU39 (**Figures 10H,I**). The C/N ratio was highly variable throughout the cores (**Figures 10D,J**). In general, the C/N ratios were close to Redfield ratio (7–8), except at the surface in core EU36, reaching higher values (∼9).

The $\delta^{13}C_{org}$ and $\delta^{15}N$ results for EU39 and EU36 are shown in **Figures 10E,F,K,L**, respectively. Generally speaking $\delta^{13}C_{org}$ and $\delta^{15}N$ values were higher for EU36, reaching values close to −23.7‰ for $\delta^{13}C_{org}$ and up to ∼7.5‰ for $\delta^{15}N$. For EU39 both $\delta^{13}C_{org}$ and $\delta^{15}N$ data showed changes at similar depth than the C/N ratio. For EU36, the lower $\delta^{15}N$ data (5−6‰) are consistent with N increases. For EU39, this is observed in the first 5 cm; the increase of N toward recent times corresponded with slight decreases in the isotope but reaching lower values than core EU36. While $\delta^{13}C$ showed low variability in both cores; values were −26‰ for EU39 and ∼24‰ in core EU36, except at surface of this core, decreasing slightly to 25‰.

DISCUSSION

Submarine Landforms and Glacier Retreat

Models show that during the LGM most of the Patagonian fjords including the study area, were covered by glaciers, forming what is referred as the Pleistocene Patagonian Ice Sheet (PPIS) (Davies et al., 2020). In Europa Fjord we found a series of glacial features including glacial lineations, roche mountanee and drumlinoid morphologies indicating that relatively rapid ice flowed along the fjord from the cordillera to the west toward Wide Channel. Some of the features that we describe were recognized by Dowdeswell and Vásquez (2013) for around OSS1 and OSS3, near the middle and the end of the fjord (**Figure 4**). We found that streamlined features are also present in OSS2 and in the area connecting EB4-A and EB4-B, implying that past rapid ice-flow sculpted the sea floor for ∼30 km.

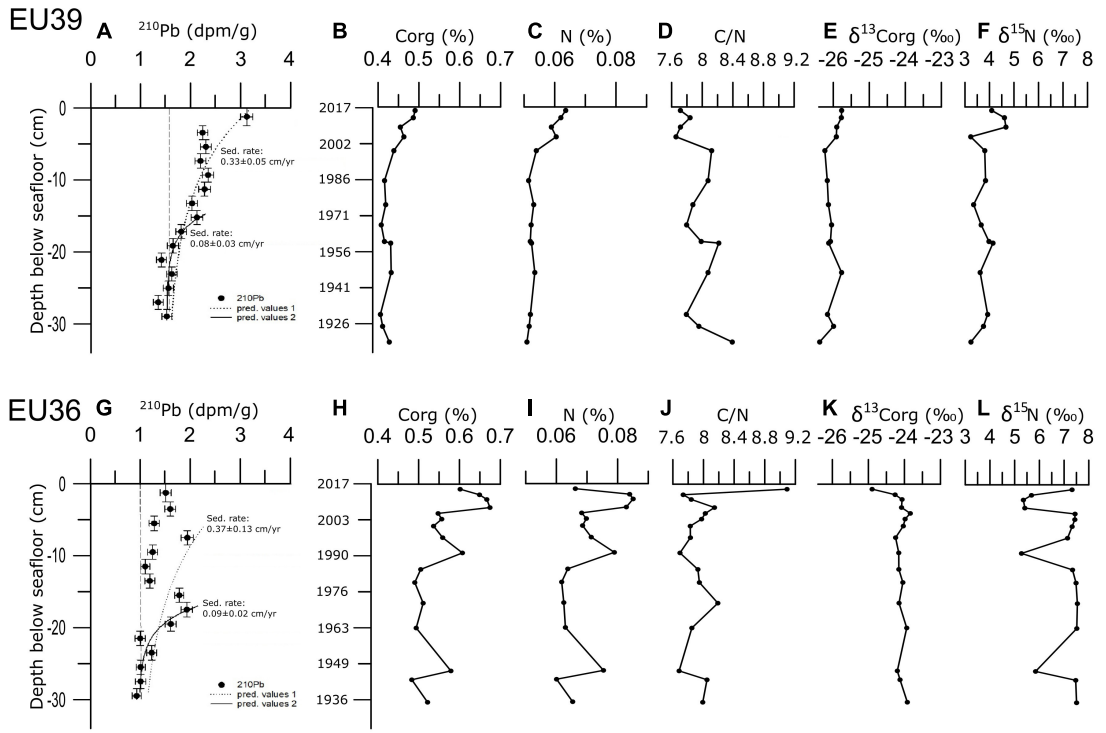

FIGURE 10 | Geochemical variables and sedimentation rates for EU39 **(A–F)** and EU36 **(G–L)** cores, plotted against depth below seafloor (cm) and AD years from 210Pb dating. **(A,G)** ^{210}Pb activity and sediment rates (two models). Vertical segmented lines are showing the supported activity (background). Error bars are indicated (2σ). **(B,H)** Total organic carbon content. **(C,I)** Total nitrogen. **(D,J)** C/N molar. **(E,K)** δ^{13}Corg stable isotope. **(F,L)**δ^{15}N stable isotope.

Evidence that the described streamlined features correspond to sculpted bedrock comes from the high seismic reflectivity, abundant diffraction hyperbolas and hummocky facies found in the seismic record (**Figure 7**). This interpretation is consistent with previous work by DaSilva et al. (1997) and Fernández et al. (2017) that described similar seismic facies in the Patagonian fjords. In some areas, our seismic records suggest that the bedrock is covered by stratified sediment veneers which we interpret as originated from post glacial processes such as hemipelagic sedimentation and mass wasting events. These post-glacial sediment veneers might explain why the backscatter data showed that the seafloor is composed of sediment instead of bare rock for those streamlined feature areas.

Several interpretations about the demise of the PPIS, indicate that rapid ice retreat from Last Glacial Maximum positions occurred probably around 17–15 ka (e.g., Harrison, 2004; McCulloch et al., 2005; Turner et al., 2005; Kilian et al., 2007; Boyd et al., 2008). After the initiation of the deglaciation, a phase of glacier stability occurred around 13.6–12.8 ka (Latest-Pleistocene) in the Magallanes Region, which has been associated with the cooling period registered in Antarctic ice core records known as the Antarctic Cold Reversal (ACR) (e.g., McCulloch et al., 2005; Moreno et al., 2009; García et al., 2012). North of our study area, east of the Northern Patagonia Icefield, a glacial advance occurring ∼11 and 12.8 ka has been associated with the European Younger Dryas (YD) (11–12.8 ka) (Glasser et al., 2012). In the case of the Patagonian fjords, data about the timing and mode of deglaciation is sparse or for some areas like Europa Fjord, non-existing. The few fjords with data are San Rafael Glacier, Gran Campo Nevado and Marinelli Glacier (Kilian et al., 2007; Boyd et al., 2008; Fernández et al., 2012; Bertrand et al., 2017), were radiocarbon dating of glacimarine post-glacial sediments indicate that the Patagonian fjords deglaciated after a period of stability that occurred ∼11 to 13 ka. Therefore, by correlation, we propose that the arcuate mound at the mouth of Europa Fjord, characterized by high amplitude reflectors and diffraction hyperbolas indicating point reflectors and a hard seafloor, represents a fjord-mouth moraine associated to glacier stillstand or readvance coeval with the period of glacier stability ∼11 to 13 ka reported from other areas. This interpretation is supported by the glacial implications of notable difference in depth and width observed at the fjord's mouth area where EB7 shows depths of ∼ 850 mbsl while Wide Channel reaches ∼1,050 mbsl; first, the fjord itself would act as a constriction and pinning point for the ice flowing into Wide Channel as part of the Late Pleistocene Europa Glacier, and second, the wider and deeper Wide channel requires a higher ice flux to maintain grounded flowing ice. It is also consistent with the existence of mouth fjord moraines in other areas of Patagonia (Rodrigo, 1996; Araya-Vergara, 1997, 1999; Vieira and Simões, 2006; Boyd et al., 2008) and other parts of the world (e.g., Shaw, 2016; Munoz and Wellner, 2016). This interpretation is also consistent with the finding

of a depression on the northern part of the Europa Fjord mouth moraine, which porbably represents the incision made by metwater outflow which would have delivered sediment to Wide Channel. In this context, three clearly identifiable bathymetric ridges that run parallel to the main morainal arc, as well as a ridge partially eroded, located 1.35 km up-fjord from the mouth moraine, would represent recessional ridges and moraine associated to the initial of glacier retreat from the outer fjord basins.

The absence of submarine features identifiable as moraines or morainal banks between the fjord mouth moraine until EB4, indicate that ice retreat proceeded rapidly with no stillstands or readvances for quite some time. This interpretation is also consistent with the abundance of streamlined features indicating fast ice flow parallel to the fjord axis. It has been documented from other works in Patagonia that glacial erosion rates scale with glacier retreat rates, which means that in a scenario of general glacier retreat and thinning, the capacity of glacier to sculpt the seafloor would have been enhanced when glaciers were retreating and being confined into the fjords. We note that the absence of land moraines along ∼35 km of fjord is remarkable given the existence of several possible pinning points produced by decreasing depths and constrictions.

The location of AAR2 and AAR3 occur at a major bend of the fjord and coincides with an area of geological contact between Devonian metamorphic rocks and Mesozoic granitoids. We also note that major lineations observed on land seem to continue across the fjord and are manifested in the seafloor as clear linear morphological features. Thus, it is possible that lithological changes and structural heterogeneities along the fjord, influenced the competence and morphology of the bedrock allowing the generation of constrictions that affected the flow of the ancient Europa Glacier, and determined the position of pinning points and moraines. This interpretation is supported by the important influence of morphological changes on glacier dynamics (e.g., Pelto and Warren, 1991; Benn et al., 2007; Barr and Lovell, 2014). We note, however, that AAR3 does not conform with the morphology of typical arcuate moraines such as those described by Dowdeswell and Vásquez (2013). Instead, we recognize two ridges that appear in the bathymetry only in the southern part of the fjord, and that run perpendicular to the fjord near the coast but parallel to the fjord axis near the central part. Our seismic data shows what can be interpreted as either a buried moraine or a subsurface prolongation of the coastal outcrops. It is possible that the origin of AAR3 is mixed, i.e., there was indeed the construction of a moraine at the location of a pinning point or constriction produced by the local bedrock morphology. In this case, the channel in the northern half of the fjord would be there due to the lack of a bedrock obstacle, which allowed the channelization of dense turbiditic flows originated from glacial melt water from Europa Glacier, as well as hyperpycnal fluvial flows from a side valley on the northern coast.

Other remarkable features in the AAR3 area are the high slopes (up to 30°) that limit this feature to the west, the great number of gullies, and the depression at the mouth of the turbidity channel. The origin of the high slopes that limit AAR3 is unclear to us, but we propose two hypotheses. One is that in the past, there was indeed an arcuate moraine built on a bedrock pinning point that was later eroded by flows going through the turbidity channel, and by mass wasting processes related to slope instability. The other possibility is that at some point during the general glacier retreat, a glacier coming from a lateral valley in the southern coast of the fjord, dammed the sediment laden melt waters coming from Europa Glacier resulting in high accumulation of glacial sediments and the formation of a now partially eroded kame terrace.

The arcuate asymmetrical ridge two (AAR2) which limits EB2 and EB3 constitutes a classic example of a submarine moraine. It was first described by Dowdeswell and Vásquez (2013) and interpreted as indicating a period of glacier stability during the overall period of glacier retreat (at the end of the Pleistocene?). We note that AAR2 is located at a major bend in the fjord, 600 m from a fluvial delta formed by rivers Domingo Santa Maria and Ignacio Carrera Pinto that drain two pro-glacial lakes of the same name. The good preservation of AAR2 and the fact that there is no indication of a breach related to fluvial erosion processes, indicates that the moraine is effectively acting as a gabion wall for discharge flows at depths below 70–80 m depth (homopycnal and hyperpycnal flows). We interpret that the channel identified on the seafloor near the northern coast of EB3 was formed by seafloor erosion by dense sediment-laden flows (turbidite flows) from these rivers. In the past, tributary glaciers coming from side valleys joined Europa Glacier and flowed down fjord. It is possible that some of the morphologies observed in EB3, that do not conform to typical cross-fjord arcuate moraine morphologies, where related to the complex glacial retreat history of the area, were side-valley glaciers retreated at a pace different from the main trunk glacier.

Another characteristic of AAR2 is that its flanks showed evidence of repeated gravity flows and slides (**Figure 3B**). On the steeper down fjord flank, facies showing some layering onlapping a curved acoustic basement, resemble the geometries of rotational slides. We noted that the acoustic basement, i.e., the strong seismic reflector below which little acoustic energy could penetrate, is interpreted as a submarine moraine, perhaps at least in part, having a bedrock core as suggested by the apparent continuation of surface bedrock morphologies on the moraine. Furthermore, gullies indicatives of active mass wasting processes are present on both sides of AAR2. On the up-fjord flank large indentations suggest that gullies coalesced to form larger ones whose heads increase the local slope further enhancing the influence of gravity erosional processes. Relatively small and discontinuous ridges on the up-fjord flank could represent the remnant of recessional moraines formed when the ancient Europa glacier started retreating from AAR2.

Closer to the present-day ice front, AAR1 constitutes the most proximal submarine moraine mapped in full so far in Europa Fjord. Both the up-fjord and the down-fjord flanks showed evidence of active mass wasting slope processes with gullies, and channels with steep headwalls, similarly to ARR2. Three small ridges on the up-fjord flank are interpreted as recessional

moraines formed when the glacier retreated from AAR1. We noted that EB1, the most glacier-proximal basin, is 35 m deeper than EB2 which can be interpreted as caused by the younger deglaciation age and consequent thinner sediment fill of the basin. However, it is also possible that the bedrock in EB1 is carved deeper than in EB2, a hypothesis that need future geophysical studies to be solved. On the easternmost area mapped we identified a 12 m high cross fjord asymmetrical feature that might represent another submarine moraine, but we lack seismic data to corroborate it. If so, it would mean that moraines are more closely spaced in the ice proximal basins and imply that glacial variations and associated advance or retreat events of morainal construction (stillstands) are more common for the glacier configuration in which ice is channelized within the fjord and the ice front is relatively close to the present day position, which suggest that the construction of AAR1 and AAR2 is at least in part, related to neoglaciations. Additional efforts to date the glacimarine sediments of EB1 and EB2 are necessary to test this hypothesis.

An important observation is that arcuate submarine moraines only exist at the mouth of Europa fjord and within ∼25 km from the present-day ice front. This suggests that the ice retreated relatively fast or at relatively constant rate, with only short lived stillstands for ∼32 km and from basins ∼750 to 800 m deep to the area of convergence of several ancient glaciers in EB3 which was at the moment ∼250–300 m depth considering a sediment infill of a few tens of meters. Such glacier retreat could be achieved by a sustained negative mass balance that produced a reduction in extent and thickness, which seems possible since the local topography is characterized by low elevations (average ∼200–300 masl for a strip 10 km wide each side from the fjord axis) for about 30 km from the fjord mouth and thus a modest rising of the equilibrium line altitude would have a major impact on the accumulation area.

Glacimarine Sedimentary Processes

From the sediments and seismic analysis, it is suggested that the main processes of sedimentation occurred in a glacimarine environment, whose intensities and properties depended on the glacier front location, the time period and climate variability that influence the retreat/advance velocity and stillstands, among other factors (Domack and McClennen, 1996; Powell and Domack, 2002). In the study area, can be identified the main following processes: subglacial flow, sediment plumes from the ice front and IRD linked by calving. On a second level are: debris flow, slope failure, river or fluviglacial input and non-glacial deposition (biogenic). Oceanographic factors in a glacimarine environment (e.g., Domack and Ishman, 1993) were not analyzed in this work in a direct way, but they could have a role too, considering the tide and wind currents, and turbulence on the moraines (sills) as possible forcing of sediment transport, remobilization and suspension, among others (e.g., Inall and Gillibrand, 2010) and the influence of warmer water masses on tidewater glaciers (e.g., Bendtsen et al., 2017; Holmes et al., 2019).

In general, we identified three main stratigraphic units for the flat seafloor areas characterizing the central part of the successive basins that form Europa Fjord (from EB1 to EB7). The top unit, with an estimated thickness of a few meters up to ∼10 m, showed parallel reflectors and transparent seismic facies, is interpreted as formed by sediments constituted by fine clastic and marine biogenic particles as well as organic matter from land areas. This was the only unit sampled by cores EU36 and EU39, which showed fine granulometry, which explain the internal acoustic transparency observed in the seismic section. In general, the total organic carbon within the top 30 cm is $< 1\%$, although showed an increasing trend from the 15 cm depth to top, which is in good agreement with the decreasing MS near the top of the cores. Similar seismic facies have been associated to ice distal environments (Araya-Vergara, 1997, 1998, 1999; Kilian et al., 2007; Fernández et al., 2017), and have been sampled in other fjords and channels of Patagonia (e.g., DaSilva et al., 1997; Boyd et al., 2008; Fernández et al., 2011; Aracena et al., 2015), where similar sedimentary facies were recognized.

Below the stratigraphic unit with sediment from the water column, seismic facies vary from basin to basin, from stratified facies to opaquer and more chaotic with discontinuous or low amplitude reflectors indicating little variation in acoustic properties (impedance contrast). As indicated before, these facies are found at least a few meters below the seafloor, beyond the reach of our sampling equipment (maximum possible core length was 3 m during the survey). The bottom unit had little internal organization and was mostly characterized by chaotic and semitransparent facies. Similar facies in other Patagonian fjords and channels are interpreted as subglacial till (e.g., DaSilva et al., 1997; Kilian et al., 2007; Boyd et al., 2008; Fernández et al., 2017). Thus, the most likely interpretation of seismic facies is that the bottom unit represents glacial till deposited subglacially, followed by predominantly glacimarine sedimentation represented by the middle unit, with the sequence being topped by stratified post-glacial sediments (e.g., biogenic water column) with glacial (e.g., IRDs) and non-glacial elements (e.g., biogenic, fluvial, mass wasting). The lack of buried moraine ridges suggests that the transition between the successive recessional depositional environments was relatively rapid with no indication of readvance stages.

The complex sedimentary processes taking place in the area are also reflected on the evidence of past and recent mass wasting events and slope erosional processes. The outcropping and buried dipping irregular reflectors and chaotic seismic facies, interpreted as gravity flow deposits in the area (Fernández et al., 2016), are associated with prominent arcuate submarine moraines, and occur on both the up-fjord and the down fjord flanks. This means that they were formed not by direct influence of the ancient Europa glacier but instead by the destabilization of the moraines after ice retreated from them. This interpretation is also supported by the interfingering and lateral transition geometries found in the seismic records and that directly relate several gravity flow units to the bottom and middle units of the respective basin (e.g., see the transition between EB2 and AAR2 in **Figures 6A,B**). On the other hand, sediment derived from fluvial or land mass wasting processes should enter the fjord basins at least at certain locations and be mixed with

marine sediments to form some of the described stratigraphic units. So far, the available data suggest that mass wasting or debris flow input from the coastal areas are not common in the Patagonian Fjords (Boyd et al., 2008; Dowdeswell and Vásquez, 2013; Lastras et al., 2016). An exception are the fjords of northern Patagonia located along the trace of the Liquiñe-Ofqui fault system (e.g., Vargas et al., 2013; Villalobos et al., 2020) where a large landslide related to a Mw 6.2 earthquake on the coastal areas of Aysen Fjord resulted in a major submarine deposit. In that case, the surficial seismic activity was key at generating sufficient energy to trigger the event; in the case of Europa Fjord, there is not known active faulting nor there is records of major surficial earthquakes.

Modern Variability of Glacimarine Sedimentary Processes

The sediments sampled with cores EU36 and EU39 correspond to mud, silt lenses, and variable amounts of lonestones and coarse materials interpreted as ice rafted debris (IRD), which indicate a depositional environment dominated by deposition from suspension processes, bottom flows or currents, and a variable contribution of glacial sediments. The mud and silt lenses are interpreted as the result of the erosion and reworking of bottom sediments either by tidal currents, dense turbiditic flows (hyperpycnal flows) from fluvial systems, or mass wasting processes on steep slope areas. These sedimentary environments and associated processes are well documented in other glacimarine settings such as in Greenland, the Svalbard Region and Antarctica (e.g., Cowan et al., 1997; Ó Cofaigh et al., 2001; Streuff et al., 2017).

Sedimentary processes in the Europa Fjord responded to the distance from glacier front to the deposition site. The passage from a weakly laminated sequence toward a sequence of massive and bioturbed muds, found in both cores, and developed more extensively in the interior of the fjord, is a reflection of the distance from the glacier front, also indicating a lesser influence of turbid plumes for distal areas. The absence of abrupt contacts, inside the cores, would indicate continuity and gradual change of these processes over time, ruling out rapid deposition processes such as turbidity currents on the esplanades where the cores were taken. Geochemical results and organic content in sediments showed the standard distance relation from the ice front, namely, in EU39 (proximal), C_{org}, N, $\delta^{13}C$ and $\delta^{13}N$ are lower than EU36, demonstrating more terrigenous influence from mainly glacimarine processes (Domack and McClennen, 1996; Rebolledo et al., 2011). Additionally, the low organic content at both cores with light $\delta^{13}C$ and $\delta^{15}N$ is also suggesting a higher impact of continental sources when are compared to other marine environments with higher isotopic values in zones of reduced freshwater influence and higher contribution of plankton in the organic sedimentation ($>$ 9; De Pol-Holz, Robinson et al., 2009; Vargas et al., 2011).

Otherwise, the trends observed for MS, in both cores showed an increase of values to older times, reflecting a greater gradual influence of the glacier in the past associated to its sediment yield. On the other hand, the lenses found in the sedimentary records, and the absence of other characteristic of fine-grained turbidite structures, such as erosion contacts, load-bearing structures, ripples, or convolute lamination (Stow and Shanmugam, 1980), allow the idea of the presence of low-energy bottom flows that remobilize surface sediments, especially for EU36 site, but whose energy is not sufficient to form turbidity current properly. Specifically, for EU39 site, there is a flow through channels on the northern part of the fjord, but is still far from it, not influencing this place with more intense energetic processes. Further, the Europa fjord presented much lower sedimentation rates compared to other glacimarine environments associated with temperate glaciers, such as the case of Alaska fjords (Boldt et al., 2013), so this characteristic also indicates low transport, possibly supported by the existence of several large sills that prevent the outwash of sediments and trap them inside individual basins in a ponded pattern (Araya-Vergara, 1997; Fernández et al., 2016), therefore, the sedimentary contributions from the different sources do not add up. Additionally, Europa fjord has lower values of SR compared with other Chilean fjords too (Boyd et al., 2008; Fernández et al., 2011; Boldt et al., 2013) evidencing a lower yield of glacimarine sediments, explained due to larger drainage glacier basin (Aniya et al., 1996) and higher glacier elevation (Fernández et al., 2016), that allows greater accumulation of precipitation.

In general, the values of ^{210}Pb activity are low and have a complex downcore pattern as Boldt et al. (2013) also found for the study area. Low values and same pattern have also been found in other sites of Patagonian fjords (Sepúlveda et al., 2005). The variability in ^{210}Pb activity might be due the effects of stratigraphic disruption produced by bioturbation. Therefore the sedimentation rates would be apparent due to the mixing of particles produce low exponential decay that imply high mass accumulation related with higher sedimentation rates. However, below the most intense mixing layer the values obtained (0.08–0.09 cm yr^{-1}) were in the range of that estimated by Boldt et al. (2013, 0.11 cm yr^{-1}) in one core that had better exponential decay below mixing layer. Other core reported indicated non-steady accumulation rates, probably caused by intense mixing or increased mass accumulation. Thus, the area could have a wider range in the sedimentation depending on the suspended matter loads, that could be underestimated when is only considered the activities below mixing layer. In general, the fjords are zones of higher sedimentation rates characterized by intense deposition of terrigenous material transported from the glaciers fronts being very high close to the glacier front decreasing exponentially toward outer fjord ($>$ 10–0.04 cm yr^{-1}, Zaborska et al., 2006). Our estimations allows establish the recent sedimentation rates in the last 100 years, in the range of the mass accumulation at fjords even if they could be overestimated. The Chilean fjords are dominated by sedimentation of fine-grained particles delivered from turbid meltwater that reach to the seawater from the glacier and glacifluvial systems (Dowdeswell and Vásquez, 2013), in this case, our estimations can account for active landforms that are still being developed today.

Higher percentage of rainfall respect to snow, and temperature-driven surface ice-melt, enhances infiltration of water to the subglacial system promoting sediment outflow through turbid plumes, which would increase the contribution of terrigenous sediments to the fjord system. The positive impact on biogeochemical cycles by the increasing sediment influx to the fjord system (e.g., Seifert et al., 2019), could explain the increase in N since the 1980 decade, found in cores EU36 and EU39. The increase in C_{org} and $\delta^{13}C_{org}$ and $\delta\ ^{15}N$ content for EU39 since the 1980s, is interpreted as due to an increase of influx of terrigenous organic matter from the rivers on the northern coast of the fjord (Ignacio Carrera Pinto and Domingo Santa Maria Rivers). A similar increase in continental organic matter influx since the 1980s was found by Sepúlveda et al. (2005) and Rebolledo et al. (2011) in the fjords of northern Patagonia.

The patterns of C and N variation for the top of core EU36 are more complex and not easily explained by terrestrial influx since the core is in an area with no major rivers nor mountain streams. However, major geochemical changes are also observed since the 1980s which might be partly explained by changes in the distal influx of glacial sediments to the marine environment from iceberg melting. The isotopic changes have been episodic, and the lower $\delta^{15}N$ values resemble the material composition at the core EU39. Notwithstanding, the lower values in $\delta^{15}N$ are concomitant with higher values of Corg and N that would not be related to different $\delta^{13}C$ sources since the profiles were almost constant. These lower values would correspond to the particulate organic matter (POM) and suspended sediment observed in zones influenced by rivers (−25 to −29‰ for ^{13}C, 2–5‰ for ^{15}N; Quiroga et al., 2016), in our case dragged from the glacier, containing organic matter from the continental source.

Regional climate changes over the last decades could also play a role in the isotopes distribution, such as rainfall changes associated to El Niño-Southern Oscillation (ENSO) variability (Ruttland and Fuenzalida, 1991). The Multivariate ENSO Oscillation Index (MEI) of Rebolledo et al. (2011) show fluctuating values for 1900–1940 AD, negative values for 1940–1980 AD, and positive values for the period 1980–2005 AD. The latter period correlates with the recent interval of increasing sedimentation rates and high variability of C and N content. The origin of the variability in C_{org} and N requires further studies, however, we noted that the observed changes are in the multi-annual timescales. We observed though, that the time-scale resolution of our data does not permit to infer the influence of annual or inter annual modes of climate variation. We cannot rule out at least the partial influence of non-climatic nor glacial factors in the variability of the geochemical proxies.

CONCLUSION

Our new high-resolution swath bathymetry and seismic data for Europa Fjord, allowed to improve the understanding of the submarine landforms that characterize the deglaciation of the fjord and subsequent development of sedimentary environments. Seven successive basins, separated by shallow promontories or arcuate submarine moraines, were recognized where sedimentary sequences of tens of meters in thickness exist. Although there is still lack of chronological control to assess the ancient glacial history of the fjord, we demonstrate that:

- The deglaciation of Europa fjord started after a period when the ancient Europa glacier stood still at the mouth fjord where a large arcuate submarine moraine was built. The retreat from the fjord's mouth started slowly as evidenced by recessional ridges on the up-fjord flank of the main moraine, but then proceeded rapidly and/or at constant rate for ∼32 km until the ice terminus grounded at a major fjord bend where several ancient glaciers once converged.
- Prominent submarine arcuate moraines in the inner fjord (∼25 km from present day glacier terminus), indicate that the deglaciation proceeded punctuated by long lived stillstands or periods of glacial advance during a general retreat and thinning stage.
- The coincidence in the location of the inner fjord arcuate moraines with changes in the sinuosity of the fjord, as well as with changes in depth and width, and the location of prominent side glacial valleys, suggest that the location of moraines was partially controlled by morphological factors, such as the existence of "pinning points," or the influence of the ratio between available cross sectional area and ice-flux. The magnitude of the influence of morphological factors on the retreat of other Patagonian Glaciers is a matter of future studies.
- The recognized submarine landforms show evidence of past and currently active erosional and sedimentary processes: slope erosion by mass wasting events (e.g., gullies, channel head-wall erosion, turbidity channels and associated sedimentary lobes). On the flanks of the most proximal arcuate moraines, seismic records show mass wasting deposits extending into the flat basin areas contributing to their sediment infill.

Respect to sedimentary processes acting since the deglaciation of Europa Fjord, we conclude that:

- The stratigraphy of the recognized basins is characterized (from bottom to top) by chaotic or acoustically semi-transparent deposits with or without recognizable layers, followed by several acoustically semi-transparent limited by relatively low amplitude but recognizable reflectors, overlaid by a well stratified units of a few meters to a few tens of meters in thickness. This sequence is characteristic of previously glaciated environments where the bottom units is interpreted as glacial till or diamictite, the middle unit is interpreted as glacimarine, and the stratified unit is interpreted as mostly sediment from water column with glacigenic influence. In case of Europa Fjord, the sequence grades to deposits from mass wasting processes and turbiditic flows, both near the base and near the top.
- Modern sedimentary environments and processes were deduced from two sediment cores (∼3 m long) characterized by highly biologically disturbed mud, fine sediment laminations, silt and mud lenses, and variable amounts of ice rafted debris (IRD). Modern sedimentary

environments are controlled by settling from suspension, deposition by turbid plumes, and calving on the glacier terminus. Lenses show that modern remobilization of sediments is active, probably linked to mass wasting processes.
- Values of ^{210}Pb activity are low and have a complex downcore pattern. From the ^{210}Pb dating, the sedimentation rate determined for the Europa fjord was 0.33 ± 0.05 cm yr^{-1} (EU39), and 0.37 ± 0.13 cm yr^{-1} (EU36), considering highest rates.
- The increase in C_{org} and $\delta^{13}C_{org}$ and $\delta^{15}N$ content for EU39 since the 1980s, indicate a decadal increase in the influx of terrigenous organic matter possibly from the rivers on the northern coast of the fjord. The increase in terrigenous materials is probably linked to the regional increase in temperature and the rainfall/snow ratio indicated by other authors, which should have as direct consequence, an increase in subglacial discharge from melt water and rainfall infiltration. Greater subglacial discharge would imply an increase in glacial sediment outflux with light $\delta^{15}N$.

DATA AVAILABILITY STATEMENT

The original contributions presented in the study are included in the article/**Supplementary Material**, further inquiries can be directed to the corresponding author/s.

AUTHOR CONTRIBUTIONS

CR designed the study, objectives, and fieldwork and wrote the manuscript with the critical contributions of EC and RF. CR, EC, RF, and JA analyzed and interpreted sediment cores. CR and DM processed multibeam bathymetry and backscatter data, which were interpreted by CR and RF. CR processed the seismic data. CR and RF interpreted the seismic data. LR and PM reviewed geochemical data and isotopes results and analyzed the 210Pb dating. All authors contributed to the final version.

FUNDING

This research was funded by CONA grant no. C23 F17-07 of the CIMAR CONA-SHOA Research Program.

ACKNOWLEDGMENTS

We thank the 2017 captain, officers and crew of the AGS "Cabo de Hornos" of the Chilean Navy, and the Hydrographic and Oceanographic Service of the Chilean Navy (SHOA) for the permission of the use of multibeam data obtained by the PSH "Cabrales." We would also like to thank Nicolás Philippi and Stefano Pontarelli for their assistance onboard the CIMAR 23 Cruise, also to Ximena Contardo and Ximena Toledo for field and laboratory management, and the UNAB Facultad de Ingeniería. We are grateful to the reviewers for improving the manuscript giving constructive comments.

SUPPLEMENTARY MATERIAL

The Supplementary Material for this article can be found online at: https://www.frontiersin.org/articles/10.3389/fmars.2022.612021/full#supplementary-material

REFERENCES

Ahumada, R., and Contreras, S. (1999). Contenido de metales (Ba, Cd, Co, Cr, Cu, Ni, Pb, Sr, V y Zn) en sedimentos de los fiordos y canales adyacentes a Campos de Hielo. *Sur. Cienc. Tecnol. Mar.* 22, 47–58.

Aniya, M., Sato, H., Nature, R., Skvarca, P., and Casassa, G. (1996). The use of satellite and airborne imagery to inventory outlet glaciers of the Southern Patagonia Icefield, South America. *Photogramm. Eng. &x Rem. S.* 62, 1361–1369.

Aracena, C., Kilian, R., Lange, C., Bertrand, S., Lamy, F., Arz, H. W., et al. (2015). Holocene variations in productivity associated with changes in glacier activity and freshwater flux in the central basin of the Strait of Magellan. *Palaeogeogr. Palaeoclimatol. Palaeoecol.* 436, 112–122. doi: 10.1016/j.palaeo.2015.06.023

Aracena, C., Lang, C., Iriarte, J., Rebolledo, L., and Pantoja, S. (2011). Latitudinal patterns of export production recorded in surface sediments of the Chilean Patagonian Fjords (41-55°S) as a response to water column productivity. *Cont. Shelf Res.* 31, 340–355. doi: 10.1016/j.csr.2010.08.008

Araya-Vergara, J. (1997). Perfiles geomorfológicos de los fiordos y depresión longitudinal de Norpatagonia. *Cienc. Tecnol. Mar.* 20, 3–22.

Araya-Vergara, J. (1998). El problema genético de los fondos de fiordo Norpatagónicos. *Invest. Mar.* 26, 71–81. doi: 10.4067/S0717-71781998002600007

Araya-Vergara, J. (1999). Perfiles longitudinales de fiordos de Patagonia central. *Cienc. Tecnol. Mar.* 22, 3–29.

Barr, I., and Lovell, H. (2014). A review of topographic controls on moraine distribution. *Geomorphology* 226, 44–64. doi: 10.1016/j.geomorph.2014.07.030

Bendtsen, J., Mortensen, J., Lennert, K., Ehn, J., Boone, W., Galindo, V., et al. (2017). Sea ice breakup and marine melt of a retreating tidewater outlet glacier in northeast Greenland (81°N). *Sci. Rep.* 7:4941. doi: 10.1038/s41598-017-05089-3

Benn, D., Warren, C., and Mottram, R. (2007). Calving processes and the dynamics of calving glaciers. *Earth Sci. Rev* 82, 143–179. doi: 10.1016/j.earscirev.2007.02.002

Bertrand, S., Lange, C., Pantoja, S., Hughen, K., Van Tornhout, E., and Wellner, J. (2017). Postglacial fluctuations of Cordillera Darwin glaciers (southernmost Patagonia) reconstructed from Almirantazgo fjord sediments. *Q. Sci. Rev.* 177, 265–275. doi: 10.1016/j.quascirev.2017.10.029

Bevington, P., and Robinson, K. (Eds) (1992). "Error analysis," in *Data Reduction and Error. Analysis for the Physical Sciences*, (New York, NY: WCB McGraw-Hill), 38–52.

Blaauw, M. (2010). Methods and code for "classical" age-modelling of radiocarbon sequences. *Quat. Geochronol.* 5, 512–518. doi: 10.1016/j.quageo.2010.01.002

Boldt, K., Nittrouer, C., Hallet, B., Koppes, M., Forrest, B., Wellner, J., et al. (2013). Modern rates of glacial sediment accumulation along a 15° S-N transect in fjords from the Antarctic Peninsula to southern Chile. *J. Geophys. Res.* 118, 2072–2088. doi: 10.1002/jgrf.20145

Boyd, B., Anderson, J., Wellner, J., and Fernández, R. (2008). The sedimentary record of glacial retreat, Marinelli Fjord, Patagonia: regional correlations and climate ties. *Mar. Geol.* 255, 165–178. doi: 10.1016/j.margeo.2008.09.001

Briner, J., Bini, A., and Anderson, R. (2009). Rapid early Holocene retreat of a Laurentide outlet glacier through an Arctic fjord. *Nat. Geosci.* 2, 496–499. doi: 10.1038/NGEO556

CARIS (2016). *CARIS HIPS and SIPS 9.1. User Guide*. Phoenix, AR: CARIS.

Carrasco, J., Casassa, G., and Rivera, A. (1998). Climatología actual del Campo de Hielo Sur y posibles cambios por el incremento del efecto invernadero. *Ann. Inst. Patagon. Ser. Cienc. Nat.* 26, 119–128.

Cowan, E., Cai, J., Powell, R., Clark, J., and Pitcher, J. (1997). Temperate glacimarine varves: an example from disenchantment bay, Southern Alaska. *J. Sediment. Res.* 67, 536–549. doi: 10.1306/D42685C7-2B26-11D7-8648000102C1865D

DaSilva, J., Anderson, J., and Stravers, J. (1997). Seismic facies changes a long a nearly continuous 24° latitudinal transect: the fjords of Chile and the northern Antarctic Peninsula. *Mar. Geol.* 143, 103–123. doi: 10.1016/S0025-3227(97)00092-3

Davies, B., Darvill, C., Lovell, H., Bendle, J., Dowdeswell, J., Fabel, D., et al. (2020). The evolution of the Patagonian Ice Sheet from 35 ka to the present day (PATICE). *Earth-Sci. Rev.* 204:103152. doi: 10.1016/j.earscirev.2020.103152

De Pol-Holz, Robinson, R., Hebbeln, D., Sigman, D., and Ulloa, O. (2009). Control son sedimentary nitrogen along the Chilean margin. *Deep Sea Res. II* 56, 1042–1054.

Domack, E., and McClennen, C. (1996). "Accumulation of Glacial Marine Sediments in Fjords of the Antarctic Peninsula and their use as Late Holocene Paleoenvironmental Indicators," in *Foundations for Ecological Research West of the Antarctic Peninsula*, ed. R. M. Ross (Washington DC: American Geophysical Union), 135–154. doi: 10.1029/AR070p0135

Domack, W., and Ishman, S. (1993). Oceanographic and physiographic controls on modern sedimentation within Antarctic fjords. *Geol. Soc. Am. Bull.* 105, 1175–1189.

Dowdeswell, J., Canals, M., Jakobsson, M., Todd, B., Dowdeswell, E., and Hogan, K. (2016). "The variety and distribution of submarine glacial landforms and implications for ice-sheet reconstruction," in *Atlas of Submarine Glacial Landforms: Modern, Quaternary and Ancient*, Vol. 46, eds J. A. Dowdeswell, M. Canals, M. Jakobsson, B. J. Todd, E. K. Dowdeswell, and K. A. Hogan (Burlington House: Geological Society London Memiors), 519–552. doi: 10.1144/M46.183

Dowdeswell, J., and Vásquez, M. (2013). Submarine landforms in the fjords of southern Chile: implications for glacimarine processes and sedimentation in a mild glacier-influenced environment. *Q. Sci. Rev.* 64, 1–19. doi: 10.1016/j.quascirev.2012.12.003

Enderlin, E., and Howat, I. (2013). Submarine melt rate estimates for floating termini of Greenland outlet glaciers (2000–2010). *J. Glaciol.* 59, 67–75. doi: 10.3189/2013JoG12J049

Fernández, R., Anderson, J., Bertrand, S., and Wellner, J. (2012). Gualas Glacier sedimentary record of climate and environmental change, Gold Elefantes, Western Patagonia (46.5°S). *Holocene* 22, 451–463. doi: 10.1177/0959683611425545

Fernández, R., Anderson, J., Wellner, J., and Haller, B. (2011). Timescale dependence of glacial erosion rates: a case study of Marinelli Glacier, Cordillera Darwin, southern Patagonia. *J. Geophys. Res.* 166:F01020. doi: 10.1029/2010JF001685

Fernández, R., Anderson, J., Wellner, J., Minzoni, R., Hallet, B., and Smith, T. (2016). Latitudinal variation in glacial erosion rates from Patagonia and the Antarctic Peninsula (46°S–65°S). *Geol. Soc. Am. Bull.* 128, 1000–1023. doi: 10.1130/B31321

Fernández, R., Gulich, S., Rodrigo, C., Domack, E., and Leventer, A. (2017). Seismic stratigraphy and glacial cycles in the inland passages of the Magallanes Region of Chile, southernmost South America. *Mar. Geol.* 386, 19–31. doi: 10.1016/j.margeo.2017.02.0061

Folk, R. L. (1974). *Petrology of Sedimentary Rocks*. Austin, TX: Hemphill Publishing Company.

García, J., Kaplan, M., Hall, B., Schaefer, J., Vega, M., Schwartz, R., et al. (2012). Glacier expansion in southern Patagonia throughout the Antarctic Cold Reversal. *Geology* 40, 859–862. doi: 10.1130/G33164.1

Gardner, A., Moholdt, G., Graham Cogley, J., Wouters, B., Arendt, A., Wahr, J., et al. (2013). A reconciled estimate of glacier contributions to sea level rise: 2003 to 2009. *Science* 340, 852–857. doi: 10.1126/science.1234532

Glasser, N., Harrison, S., Jansson, K., Anderson, K., and Cowley, A. (2011). Global sea-level contribution from the Patagonian Icefields since the Little Ice Age maximum. *Nat. Geosci.* 4, 303–307. doi: 10.1038/NGEO1122

Glasser, N., Harrison, S., Schnabel, C., Fabel, D., and Jansson, K. (2012). Younger dryas and early Holocene age glacier advances in Patagonia. *Q. Sci. Rev.* 58, 7–17. doi: 10.1016/j.quascirev.2012.10.011

Goldberg, E. D. (1963). "Geochronology with 210Pb, in radioactive dating," in *Radioactive Dating. Proceedings of the Symposium on Radioactive Dating Held by the International Atomic Energy Agency in Co-operation with the Joint Commission on Applied Radioactivity*, (Athens), 121–131.

Harrison, S. (2004). The Pleistocene glaciations of Chile. *Dev. Q. Sci.* 2, 89–103. doi: 10.1016/S1571-0866(04)80115-5

Hervé, F., Fanning, C., and Pankhurst, R. (2003). Detrital zircon age patterns and provenance of the metamorphic complexes of southern Chile. *J. South Am. Earth Sci.* 16, 103–123. doi: 10.1016/S0895-9811(03)00022-1

Hervé, F., Pankhurst, R., Fanning, C., Calderón, M., and Yaxley, G. (2007). The South Patagonian batholith: 150 my of granite magmatism on a plate margin. *Lithos* 97, 373–394. doi: 10.1016/j.lithos.2007.01.007

Holmes, F., Kirchner, N., Kuttenkeuler, J., Krützfeldt, J., and Noormets, R. (2019). Relating ocean temperatures to frontal ablation rates at Svalbard tidewater glaciers: insights from glacier proximal datasets. *Sci. Rep.* 9:9442. doi: 10.1038/s41598-019-45077-3

Inall, M., and Gillibrand, P. (2010). "The physics of mid-latitude fjords: a review," in *Fjord Systems and Archives*, Vol. 344, eds J. A. Howe, W. E. Austin, M. Forwick, and M. Paetzel (London: Geol. Soc. Lond. Spec. Publ), 17–33. doi: 10.1144/SP344.3

IPCC (2014). *Climate Change 2014: Synthesis Report (Fifth Assessment Report of the intergovernmental Panel on Climate Change)*. Available online at: https://archive.ipcc.ch/report/ar5/syr/ (accessed August 27, 2020).

Iriarte, J., Gonzalez, H., and Nahuelhual, L. (2010). Patagonian fjord ecosystems in Southern Chile as a highly vulnerable region: problems and needs. *Ambio* 39, 463–466. doi: 10.1007/s13280-010-0049-9

Kilian, R., Schneider, C., Koch, J., Fesq-Martin, M., Biester, H., Casassa, G., et al. (2007). Palaeoecological constraints on late Glacial and Holocene ice retreat in the Southern Andes (53°S). *Global Planet. Change* 59, 49–66. doi: 10.1016/j.gloplacha.2006.11.034

Koppes, M., Hallet, B., and Anderson, J. (2009). Synchronous acceleration of ice loss and glacial erosion, Glaciar Marinelli, Chilean Tierra del Fuego. *J. Glaciol.* 55, 207–220. doi: 10.3189/002214309788608796

Koppes, M., Hallet, B., Rignot, E., Mouginot, J., Smith Wellner, J., and Boldt, K. (2015). Observerd latitudinal variations in erosion as a function of glacier dynamics. *Nature* 526, 100–103. doi: 10.1038/nature15385

Lastras, G., Amblas, D., Canals, M., and Detsufa Shipboard Party. (2016). "Fjord-flank collapse and associated deformation in Aysén Fjord, Chile," in *Atlas of Submarine Glacial Landforms: Modern, Quaternary and Ancient*, Vol. 46, eds J. A. Dowdeswell, M. Canals, M. Jakobsson, B. J. Todd, E. K. Dowdeswell, and K. A. Hogan (Burlington House: Geological Society London Memiors), 107–108. doi: 10.1144/M46.15

Marzeion, B., Graham Cogley, J., Richter, K., and Parkes, D. (2014). Attribution of global glacier mass loss to anthropogenic and natural causes. *Science* 345, 919–921. doi: 10.1126/science.1254702

Masiokas, M., Rivera, A., Espizua, L., Villalba, R., Delgado, S., and Aravena, J. (2009). Glacier fluctuations in extratropical South America during the past 1000 years. *Palaeogeogr. Palaeoclimatol. Palaeoecol.* 281, 242–268. doi: 10.1016/j.palaeo.2009.08.006

McCulloch, R. D., Bentley, M. J., Tipping, R. M., and Clapperton, C. M. (2005). Evidence for lateglacial ice dammed lakes in the central Strait of Magellan and Bahía Inútil, southernmost South America. *Geogr. Ann. Ser. A Phys. Geogr.* 87, 335–362.

Moon, T., Joughin, I., Smith, B., and Howat, I. (2012). 21st-Century evolution of Greenland outlet glacier velocities. *Science* 336, 576–578. doi: 10.1126/science.1219985

Moreno, P., Kaplan, M., François, J., Villa-Martínez, R., Moy, C., Stern, C., et al. (2009). Renewed glacial activity during the Antarctic cold reversal and persistence of cold conditions until 11.5 ka in southwestern Patagonia. *Geology* 37, 375–387. doi: 10.1130/G25399A.1

Munoz, Y., and Wellner, J. (2016). Local controls on sediment accumulation and distribution in a fjord in the West Antarctic Peninsula: implications for palaeoenvironmental interpretations. *Polar Res.* 35:25284. doi: 10.3402/polar.v35.25284

Ó Cofaigh, C., Dowdeswell, J., and Grobe, H. (2001). Holocene glacimarine sedimentation, inner Scoresby Sund, East Greenland: the influence of fast-flowing ice-sheet outlet glaciers. *Mar. Geol.* 175, 103–129. doi: 10.1016/S0025-3227(01)00117-7

Pelto, M., and Warren, C. (1991). Relationship between tidewater glacier calving velocity and water depth at the calving front. *Ann. Glaciol.* 15, 115–118. doi: 10.3189/S0260305500009617

Pfeffer, W. (2007). A simple mechanism for irreversible tidewater glacier retreat. *J. Geophys. Res.* 112, F03S25. doi: 10.1029/2006JF000590

Post, A., O'Neel, S., Motyka, R., and Streveler, G. (2011). A complex relationship between calving glaciers and climate. *Eos* 93, 305–312. doi: 10.1029/2011EO370001

Powell, R., and Domack, G. (2002). "Modern glaciomarine environments," in *Modern and Past Glacial Environments*, ed. J. Menzies (Woburn, MA: Butterworth-Heinemann), 361–389. doi: 10.1016/B978-0-7506-4226-2.X5000-4

Quiroga, E., Ortiz, P., González-Saldías, R., Reid, B., Tapia, F., Pérez-Santos, I., et al. (2016). Seasonal benthic patterns in a glacial Patagonian fjord: the role of suspended sediment and terrestrial organic matter. *Mar. Ecol. Prog. Ser.* 561, 31–50.

Quiroga, E., Ortiz, P., Reid, B., and Gerdes, D. (2013). Classification of the ecological quality of the Aysen and Baker fjords (Patagonia, Chile) using biotic indices. *Mar. Pollut. Bull.* 68, 117–126. doi: 10.1016/j.marpolbul.2012.11.041

Rebolledo, L., Bertrand, S., Lange, C., Tapia, F., Quiroga, E., Troch, M., et al. (2019). Compositional and biogeochemical variations of sediments across the terrestrial-marine continuum of the Baker-Martínez fjord system (Chile, 48°S). *Prog. Oceanogr.* 174, 89–104. doi: 10.1016/j.pocean.2018.12.004

Rebolledo, L., González, H., Muñoz, P., Iriarte, J., Lange, C., Pantoja, S., et al. (2011). Siliceous productivity changes in Gulf of Ancud sediments (41°S, 72°W), southern Chile, over the last ˜150 years. *Cont. Shelf Res.* 31, 356–365. doi: 10.1016/j.csr.2010.06.015

Rebolledo, L., Sepúlveda, J., Lange, C., Pantoja, S., Bertrand, S., Hughen, K., et al. (2008). Late Holocene marine productivity changes in northern Patagonia-Chile inferred from a multi-proxy analysis of Jacaf channel sediments. *Estuar. Coast. Shelf Sci.* 80, 314–322. doi: 10.1016/j.ecss.2008.08.016

Rignot, E., Rivera, A., and Casassa, G. (2003). Contribution of the Patagonia Ice Fields of South America to sea level rise. *Science* 302, 434–437. doi: 10.1126/science.1087393

Rivera, A., Koppes, M., Bravo, C., and Aravena, C. (2012). Little Ice Age advance and retreat of Glaciar Jorge Montt, Chilean Patagonia. *Clim. Past* 8, 403–4014. doi: 10.5194/cp-8-403-2012

Rodrigo, C. (1996). "Morfología submarina de canales y fiordos: principales morrenas y umbrales. Resultados Crucero CIMAR-Fiordo 1," in *Resúmenes Ampliados CIMAR Fiordo 1*, ed. Comité Oceanográfico Nacional (Valparaíso: SHOA), 11–14.

Ruttland, J., and Fuenzalida, H. (1991). Synoptic aspects of the central chile rainfall variability associated with the southern oscillation. *Int. J. Climatol.* 11, 63–76. doi: 10.1002/joc.3370110105

Sakakibara, D., and Sugiyama, S. (2014). Ice-front variations and speed changes of calving glaciers in the Southern Patagonia Icefield from 1984 to 2011. *J. Geophys. Res* 119, 2541–2554. doi: 10.1002/2014JF003148

Schenk, T., and Csatho, B. (2012). A new methodology for detecting ice sheet surface elevation changes from laser altimetry data. *IEEE Trans. Geosci. Remote Sens.* 50, 3302–3316. doi: 10.1109/TGRS.2011.2182357

Seifert, M., Hoppema, M., Burau, C., Elmer, C., Friedrichs, A., Geuer, J., et al. (2019). Influence of glacial meltwater on summer biogeochemical cycles in Scoresby Sund. *East Greenland. Front. Mar. Sci.* 6:412. doi: 10.3389/fmars.2019.00412

Sepúlveda, J., Pantoja, S., Hughen, K., Lange, C., Gonzalez, F., Muñoz, P., et al. (2005). Fluctuations in export productivity over the last century from sediments of a southern Chilean fjord (44°S). *Estuar. Coast. Shelf Sci.* 65, 87–600. doi: 10.1016/j.ecss.2005.07.005

Sernageomin. (1982). *Mapa Geológico de Chile. Escala 1:1.000.000*. Santiago: Servicio Nacional de Geología y Minería.

Shaw, J. (2016). "Fjord-mouth submarine moraines, SW Newfoundland," in *Atlas of Submarine Glacial Landforms: Modern, Quaternary and Ancient*, Vol. 46, eds J. A. Dowdeswell, M. Canals, M. Jakobsson, B. J. Todd, E. K. Dowdeswell, and K. A. Hogan (Burlington House: Geological Society London Memiors), 79–80. doi: 10.1144/M46.65

Silva, N., Vargas, C., and Prego, R. (2011). Land-ocean distribution of allochthonous organic matter in surface sediments of the Chiloé and Aysén interior seas (Chilean Northern Patagonia). *Cont. Shelf Res.* 31, 330–339. doi: 10.1016/j.csr.2010.09.009

Stow, D., and Shanmugam, G. (1980). Sequence of structures in fine-grained turbidites: comparison of recent deep-sea and ancient flysch sediments. *Sediment. Geol.* 25, 24–42. doi: 10.1016/0037-0738(80)90052-4

Streuff, K., Ó Cofaigh, C., Noormets, R., and Lloyd, J. (2017). Submarine landforms and glacimarine sedimentary processes in Lomfjorden, East Spitsbergen. *Mar. Geol.* 390, 51–71. doi: 10.1016/j.margeo.2017.04.014

Turekian, K., Cochran, K., Benninger, L., and Aller, R. (1980). The sources and sinks of nuclides in Long Island Sound. *Adv. Geophys.* 22, 129–163. doi: 10.1016/s0065-2687(08)60065-5

Turner, K., Forwill, C., McCuloch, R., and Sugden, D. (2005). Deglaciation of the eastern flank of the North Patagonian Icefield and associated continental-scale lake diversions. *Geogr. Ann. A* 87, 363–374. doi: 10.1111/j.0435-3676.2005.00263.x

Vargas, C., Martínez, R., San Martin, V., Aguayo, M., Silva, N., and Torres, R. (2011). Allochthonous subsidies of organic matter across a lake–river–fjord landscape in the Chilean Patagonia: implications for marine zooplankton in inner fjord áreas. *Cont. Shelf Res.* 31, 187–201. doi: 10.1016/j.csr.2010.06.016

Vargas, G., Rebolledo, S., Sepúlveda, S. A., Lahsen, A., Thiele, R., Townley, B., et al. (2013). Submarine earthquake rupture, active faulting and volcanism along the major Liquiñe-Ofqui Fault Zone and implications for seismic hazard assessment in the Patagonian Andes. *Andean Geol.* 40, 141–171. doi: 10.5027/andgeoV40n1-a07

Vieira, R., and Simões, J. (2006). Coast of fjords in Central Patagonia, Chile, submarine morphology and acoustic facies. *Rev. Bras. Geof.* 24, 5–24. doi: 10.1590/S0102-261X2006000100001

Villalobos, A., Easton, G., Maksymowicz, A., Ruiz, S., Lastras, G., De Pascale, G. P., et al. (2020). Active faulting, submarine surface rupture, and seismic migration along the Liquiñe-Ofqui Fault System, Patagonian Andes. *J. Geophys. Res.* 125:e2020JB019946. doi: 10.1029/2020JB019946

Wessel, P., Smith, W., Scharroo, R., and Wobbe, F. (2013). Generic mapping tools: improved version released. *Eos* 94, 409–410. doi: 10.1002/2013EO450001

Zaborska, A., Pempkowiak, J., and Papucci, C. (2006). Some sediment characteristics and sedimentation rates in an Acrtic Fjord. *Ann. Environ. Prot.* 8, 79–96.

Conflict of Interest: The authors declare that the research was conducted in the absence of any commercial or financial relationships that could be construed as a potential conflict of interest.

frontiers | Frontiers in Marine Science

ORIGINAL RESEARCH
published: 23 June 2022
doi: 10.3389/fmars.2022.643811

Understanding the Implications of Hydrographic Processes on the Dynamics of the Carbonate System in a Sub-Antarctic Marine-Terminating Glacier-Fjord (53°S)

*Jurleys P. Vellojin[1,2,3], Gonzalo S. Saldías[2,4,5], Susan E. Allen[6], Rodrigo Torres[2,7], Maximiliano Vergara-Jara[1,2], Marcus Sobarzo[8,9], Michael D. DeGrandpre[10] and José Luis Iriarte[1,2,5]**

[1] Instituto de Acuicultura, Universidad Austral de Chile, Puerto Montt, Chile, [2] Centro de Investigación Dinámica de Ecosistemas Marinos de Altas Latitudes (IDEAL), Universidad Austral de Chile, Punta Arenas, Chile, [3] Instituto de Fomento Pesquero (IFOP), Centro Tecnológico para la Acuicultura Putemún (CTPA-Putemún), Castro, Chile, [4] Departamento de Física, Facultad de Ciencias, Universidad del Bío-Bío, Concepción, Chile, [5] Centro de Investigación Oceanográfica en el Pacífico COPAS Sur-Austral/COPAS Coastal, Universidad de Concepción, Concepción, Chile, [6] Department of Earth, Ocean and Atmospheric Sciences, University of British Columbia, Vancouver, BC, Canada, [7] Laboratorio de Química del Carbonato, Centro de Investigación en Ecosistemas de la Patagonia, Coyhaique, Chile, [8] Departamento de Oceanografía, Facultad de Ciencias Naturales y Oceanografía, Universidad de Concepción, Concepción, Chile, [9] Centro Interdisciplinario de Investigación en Acuicultura Sustentable (INCAR), Universidad de Concepción, Concepción, Chile, [10] Department of Chemistry and Biochemistry, University of Montana, Missoula, MT, United States

OPEN ACCESS

Edited by:
Eduardo Joel Quiroga Jamett, Facultad de Ciencias del Mar, Pontificia Universidad Católica de Valparaíso, Chile

Reviewed by:
Keyhong Park, Korea Polar Research Institute, South Korea
Bibiana Jara, Universidad de Magallanes, Chile

***Correspondence:**
José Luis Iriarte
jiriarte@uach.cl

Specialty section:
This article was submitted to Marine Biogeochemistry, a section of the journal Frontiers in Marine Science

Received: 18 December 2020
Accepted: 05 May 2022
Published: 23 June 2022

Citation:
Vellojin JP, Saldías GS, Allen SE, Torres R, Vergara-Jara M, Sobarzo M, DeGrandpre MD and Iriarte JL (2022) Understanding the Implications of Hydrographic Processes on the Dynamics of the Carbonate System in a Sub-Antarctic Marine-Terminating Glacier-Fjord (53°S). Front. Mar. Sci. 9:643811. doi: 10.3389/fmars.2022.643811

The biogeochemical dynamics of fjords in the southeastern Pacific Ocean are strongly influenced by hydrological and oceanographic processes occurring at a seasonal scale. In this study, we describe the role of hydrographic forcing on the seasonal variability of the carbonate system of the Sub-Antarctic glacial fjord, Seno Ballena, in the Strait of Magellan (53°S). Biogeochemical variables were measured in 2018 during three seasonal hydrographic cruises (fall, winter and spring) and from a high-frequency pCO_2-pH mooring for 10 months at 10 ± 1 m depth in the fjord. The hydrographic data showed that freshwater input from the glacier influenced the adjacent surface layer of the fjord and forced the development of undersaturated CO_2 (< 400 μatm) and low aragonite saturation state ($\Omega_{Ar} < 1$) water. During spring, the surface water had relatively low pCO_2 (mean = 365, range: 167 - 471 μatm), high pH (mean = 8.1 on the total proton concentration scale, range: 8.0 - 8.3), and high Ω_{Ar} (mean = 1.6, range: 1.3 - 4.0). Concurrent measurements of phytoplankton biomass and nutrient conditions during spring indicated that the periods of lower pCO_2 values corresponded to higher phytoplankton photosynthesis rates, resulting from autochthonous nutrient input and vertical mixing. In contrast, higher values of pCO_2 (range: 365 – 433 μatm) and relatively lower values of pH_T (range: 8.0 – 8.1) and Ω_{Ar} (range: 0.9 – 2.0) were recorded in cold surface waters during winter and fall. The naturally low freshwater carbonate ion concentrations diluted the carbonate ion concentrations in

seawater and decreased the calcium carbonate saturation of the fjord. In spring, at 10 m depth, higher primary productivity caused a relative increase in Ω_{Ar} and pH_T. Assuming global climate change will bring further glacier retreat and ocean acidification, this study represents important advances in our understanding of glacier meltwater processes on CO_2 dynamics in glacier–fjord systems.

Keywords: Patagonian fjord, glacial freshwater, water column stratification, Sub-Antarctic fjords, carbonate system, phytoplankton blooms

1 INTRODUCTION

As global climate change continues, there is increasing awareness of the influence of anthropogenic CO_2 on the melting of glaciers in polar and sub-polar marine ecosystems (Meredith et al., 2019). The input of glacial meltwater into fjords in these ecosystems strongly modulates their biogeochemistry with implications for sea-air CO_2 fluxes and ocean acidification (Fransson et al., 2011; Fransson et al., 2013). Seasonal ice-melting events change the water column's physical and optical properties, resulting in stratified, higher turbidity fjords. The suspended material decreases light availability for phytoplankton growth, causing a non-linear response of primary production rates (Hopwood et al., 2020) and potential feedback for the inorganic carbon cycle.

Northern Patagonian fjords (41°S) are typically CO_2 sinks during the warm and productive summer season and CO_2 sources in the cold and low productivity winter season (Torres et al., 2011b). While winter's high CO_2 levels, cold temperatures and low salinity surface waters result in strongly "corrosive conditions" for calcium carbonate (Feely et al., 2018), in the warm, less rainy and sunny season, primary productivity and high temperatures lead to higher levels of calcium carbonate saturation (Ω) (Alarcón et al., 2015).

High freshwater runoff of low alkalinity in Northern Hemisphere fjord systems during spring and summer produces low aragonite saturation state, low pH and favors the flux of CO_2 to the atmosphere. In some cases, the low aragonite saturation state and low pH are not compensated by the mixing of higher alkalinity water from depth, or by the uptake of carbon by primary productivity (Chierici and Fransson, 2009). Freshwater runoff in these fjords may also modulate the availability of organic matter (Dissolved Organic Carbon, DOC), macronutrients (N, P, Si), and micronutrients (Fe) in the euphotic zone, which are all important to phytoplankton and bacterial processes (Fransson et al., 2016). Under winter conditions, the coupling between physical (ice formation and physical mixing), chemical (increase in macronutrients and pCO_2, but decreasing availability of CO_3^{2-}), and biological processes (ratio of primary production to respiration <1) may decrease the $CaCO_3$ saturation state in surface waters (Chierici et al., 2011).

In the Sub-Antarctic region (50-55°S), glacier retreat (Bown et al., 2014) along with important atmosphere–ocean interactions (Garreaud, 2018), may profoundly influence biogeochemical processes. In this southernmost region (**Figure 1**), seasonal changes in glacier mass may simultaneously influence biogeochemical and physical oceanographic features. First, like Northern Hemisphere fjords, stratification and mixing processes impact nutrient fluxes. Second, melting glacier ice creates low temperature and low salinity surface water, generating large vertical and horizontal gradients in density. In fjords with a very shallow sill, tidal dynamics may produce Bernoulli aspiration (Kinder and Bryden, 1990), resulting in the injection at depth of nutrients to the inner portion of the fjord (Torres et al., 2011b). Reduced winter rates of glacier melting may result in longer residence times of deep water in the inner portion of the fjord, seasonally reducing the ventilation of deep waters. All of these factors may play a role in modulating the biological carbon pump, including the chemical speciation of the carbonate system in the fjord region.

Fjord-glacier systems are singular but diverse in their characteristics and thus likely also in their dynamics. Factors such as the hydrographic characteristics of the watershed, glacier dynamics, bathymetry, wind and sun orientation, latitude, location of the ice edge (e.g., glacier-terminating fjord, glacier edge on the coast or far from the shoreline) may be critical to understand the response of fjords to climate forcing. It has been suggested that the increase in air temperature and atmospheric pCO_2 in recent years may result in increased cold freshwater input from the glaciers (Bown et al., 2014), with a large potential to perturb the carbonate system speciation (Meire et al., 2015; Hopwood et al., 2020) and thus marine biota (Orr et al., 2005; Kurihara, 2008; Grear et al., 2017; Giesecke et al., 2019). Current projections of how changes in the ocean carbonate system may influence biological processes (i.e., photosynthesis and microbial respiration) in the future still remain speculative. Hydrological and biogeochemical information for Seno Ballena, a glacier-fjord system, will be relevant for explaining biological responses to coastal acidification interacting with other climate stressors (i.e., warming and reduced salinity due to increased freshwater flow). In this study, the main objective is to examine the carbonate system's seasonal dynamics due to the influence of glacier meltwater and oceanic waters on the upper surface layer along the fjord. This study specifically presents the seasonal hydrography and time series of pCO_2, pH_T, and O_2 in the Seno Ballena glacier Fjord from austral fall through spring (March to December, 2018).

2 MATERIALS AND METHODS

2.1 Study Area

Seno Ballena fjord is part of the Marine Protected Area Francisco Coloane, in the Strait of Magellan (53°42′S, 72°36′W;

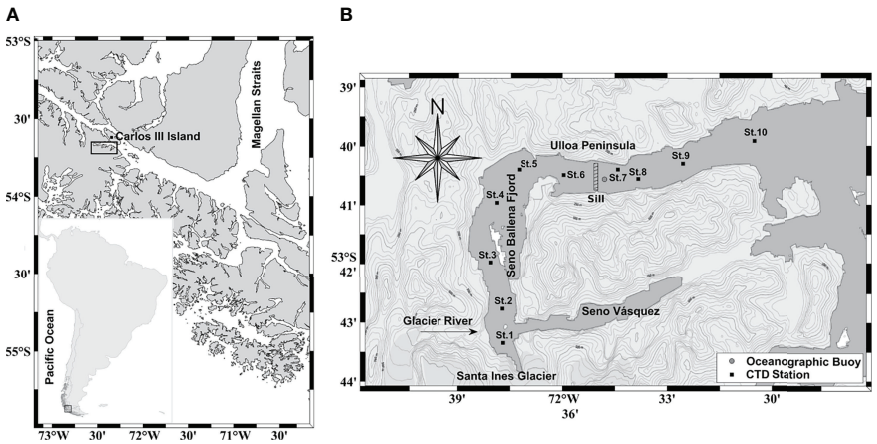

FIGURE 1 | Map of the fjord region in southernmost Patagonia **(A)**, showing Seno Ballena Fjord adjacent to Santa Inés glacier **(B)**. The mooring was anchored adjacent to the sill (circle, South Patagonia Buoy: http://portal.goa-on.org/Explorer?action=oiw:fixed_platform:M_653:observations). Squares indicate synoptic stations sampled during three seasons (fall, winter, and spring).

Frangópulos et al. (2007); **Figure 1**). It is 18 km long from the head, where the Santa Inés glacier is located, to the outside of the sill in the direction of Carlos III Island, Strait of Magellan (**Figure 1**). The lower (southwest) area of the fjord is approximately 9 km long and less than 1 km wide. A sill reaching a depth of 2–3 m from the surface during high tide is located 7 km from the glacier (Valle-Levinson et al., 2006). The bathymetry is highly variable from the inside to the outside of the fjord. Near the glacier depths are between 20 to 50 m, followed by a deeper area of 150 m up to the sill; past the sill depths of more than 200 m are found. This system is strongly influenced by freshwater input from (1) the melting of the glacial ice located at the head of the fjord; (2) a river of glacial origin; (3) melting snow of the adjacent mountains, that forms several small tributaries along the fjord (**Supplementary Figure 1**); and (4) high rainfall (4500–6000 mm y^{-1}; Meier et al., 2018). These hydrological processes are the primary controls of the stratification of the fjord, characterized by a thin (~10 m) surface layer of low-salinity water (24 - 28 S_p).

The fjord is within the Sub-Antarctic fjord and channel system of Patagonia (**Figure 1**), for which a strong influence of Modified Sub-Antarctic Waters mass (MSAAW) has been proposed (**Supplementary Figure 2**). This water mass occupies a significant fraction of the Strait of Magellan and Sub-Antarctic fjords, having practical salinity values (S_p) between 31 and 34 (Silva et al., 1998; Sievers et al., 2002; Valdenegro and Silva, 2003). When this water mass mixes with freshwater runoff from rivers and glaciers it forms estuarine waters, which are classified into three categories: the saline water of the estuary is more than 66% seawater (21-31 S_p); estuary-brackish water is 33-66% seawater (11-21 S_p); and freshwater in estuaries is less than 33% seawater (2-11 S_p) (Sievers and Silva, 2008). MSAAW has low dissolved silicate (DSi) compared to nitrate concentration. In contrast, given the geology of the drainage basin, the siliceous crystalline batholiths of Patagonia, the continental shelf waters of western Patagonia are characterized by high DSi, low nitrate, low alkalinity and low Ca^{2+} (Hervé et al., 2007; Torres et al., 2020).

2.2 Hydrographic Measurements

Three seasonal oceanographic cruises were conducted along the fjord in March (fall), August (winter), and December (spring), 2018. Five to ten stations along the main axis of the fjord were visited during each cruise (**Figure 1**). Hydrographic profiles (*in situ* temperature and salinity) were obtained using a CTD (SeaBird SBE model 19). The CTD salinity data in spring were not used due to CTD technical problems, and consequently salinity was determined from water samples taken at distinct depths (0, 5, 10, 25, and 50 m) and measured using a YSI-Pro30 probe at constant temperature previously calibrated with an IAPSO standard seawater (35 S_p); the nominal uncertainties on these measurements were ±1%. The water masses were identified by the mixing triangle method (Mamayev, 1975), using the information from the fall and winter campaigns to confirm the presence of MSAAW (Silva et al., 2009). Throughout practical salinity (PSS-78) is reported as S_p (UNESCO, I. 1981).

2.3 Water Samples and Analysis

Samples for the determination of carbonate chemistry parameters, inorganic nutrients and autotrophic biomass were taken at 5–8 stations, at 0, 5, 10, 25, and 50 m depths. Samples were also taken from glacier ice as well as river-glacier water and small freshwater tributaries along the fjord to determine freshwater end-members of salinity and alkalinity. Water samples were collected in 10 L Go-Flo bottles and stored in the dark at low temperature (< 7°C) in 250 mL gas-tight containers for the analysis of total alkalinity (A_T) and pH_T. Seawater samples for A_T analysis were poisoned with 50 µl of a saturated mercuric chloride solution ($HgCl_2$; Dickson et al., 2007). pH_T was analyzed soon after collection (<12 h), using purified *m*-cresol purple as an indicator at 25.0°C with an Ocean

Optics STS-Vis (350 – 800 nm) spectrophotometer (Byrne et al., 1988). When possible, pH_T was also measured with an aquatrode probe (Metrohm TM) with a single point calibration (pH Tris buffer pH=8.089 at 25.0°C and salinity 35) (Dickson and Goyet, 1994). Mean differences from three replicate samples between methods were 0.01 pH units in the 28 - 31 salinity range (spectrophotometer and electrode pH). Tris buffer was made for salinity 35 whereas the field salinities ranged from 27.4 to 31.2. Nevertheless, we have determined empirically (using buffers at salinity 35 and 25, and this electrode) that the uncertainties in pH due to differences in salinity between buffer and sample is lower than 0.01 pH units. The performance (i.e., Nernstian slope) of the electrode was better than 99.8% of the theoretical value.

A_T analysis was performed with the automatic open-cell potentiometric titration method (Haraldsson et al., 1997). This technique allows A_T to be obtained quickly and very precisely with a small sample volume (~ 40 ml) by adding hydrochloric acid (0.05 M HCl; Merck Titrisol®) in increasing volumes with a Dosimat 665. The reading was done with a combination Ross electrode (Orion 8102BN). The end-point was determined by the Gran method (Gran, 1952) according to Haraldsson et al. (1997). Each sample was analyzed twice and the average and standard deviation are reported. Seawater distributed by Dr. Andrew Dickson's laboratory was used to verify the A_T estimates.

Filtered (0.7 μm glass fiber filters; Whatman GF/F) samples were frozen (-20°C) for analysis of soluble reactive phosphate (SRP), NO_3^- and dissolved silicate (DSi), using the manual techniques recommended by Parsons et al. (1984). The inorganic nutrients and A_T were analyzed in the carbonate laboratory at the Centro de Investigación de Ecosistemas de la Patagonia (CIEP, Coyhaique). Chlorophyll-a concentration of seston larger than 0.7 μm was extracted with 90% acetone and measured using a fluorometer (Turner P700) following Parsons et al. (1984).

Estimates of *in situ* pH_T, pCO_2 and aragonite saturation state (Ω_{Ar}) were calculated using the chemical speciation model program CO_2SYS (Pierrot et al., 2006), using the dissociation constants (K_1 and K_2) estimated by Mehrbach et al. (1973), modified by Dickson and Millero (1987) for salinity = 20 - 40 and temperatures 2 - 35°C. Our values fit into these ranges of S_P and temperatures. We used the equilibrium constants for $KHSO_4$ determined by Dickson (1990) and those for Total Boron determined by Uppström (1974). The dissociation constants provided by Dickson and Millero (1987) have been shown to be consistent with results of previous studies carried out in the Chilean Patagonia fjords (Torres et al., 2011b; Alarcón et al., 2015; Vergara-Jara et al., 2019; Torres et al., 2020). Input data for CO_2SYS used T, S_P, A_T, pH_T@25°C and nutrients (SRP and DSi) (Kim and Lee, 2009). We measured only two parameters in discrete samples (pH_T and A_T) and two in the *in situ* sampling (pH_T and pCO_2, see section 2.5); therefore we cannot estimate the internal consistency of the measured carbonate system parameters. Organic matter (organic acids, fulvic and humic acids) could be a significant source of non-carbonate alkalinity, produced during decomposition of organic matter in sediments carried away by inland waters (Lukawska-Matuszewska, 2016). Therefore, care was taken to interpret calculated carbonate system parameters since they may result in overestimation of DIC and pCO_2. Organic alkalinity does not play an important role in this system, given the low average contribution to the total alkalinity of the freshwater end-members (5.8 ± 16.0 μmol kg^{-1}).

2.4 Water Mass Distribution Analysis

To quantify the relative contributions of freshwater from the Santa Ines glacier and adjacent river-glacier from the oceanic-type water mass (estuarine-brackish: MSAAW), an optimum multiparameter (OMP) analysis was performed, which uses a simple model of linear mixing to calculate the fraction of the source-water types. Two conditions are taken into account to apply the method: (1) all the calculated fractions are positive and (2) the sum of all the fractions is close to 100% (conservation of mass). In our analysis, we found that only two water masses were not sufficient to reproduce the properties of the samples. Thus, we assume mixing that involves 3 water masses: (1) near-surface and (2) deep inner fjord water masses, whose property definitions are determined from the average of a set of observations made during seasonal synoptic sampling, and (3) the oceanic water mass (MSSAW) that has traditionally been identified for this study area (Sievers and Silva, 2008; Silva et al., 2009).

To characterize the inner fjord water masses, property-property diagrams were made of the observations of salinity, temperature, A_T and nutrients to select values that represent the source water types. The observations used for the Inner Surface Source Water (ISSW) were from the surface sampling station closest to the glacier, to represent the properties of the freshwater from the glacier-ice and river-glacier. The observations used to characterize the Inner Bottom Source Water (IBSW) were from sampling stations 2 at 50 m depth (2 km from the glacier). The oceanic water mass that enters this Sub-Antarctic zone is the Sub-Antarctic water mass (SAAW), which is modified within the Strait of Magellan by mixing with continental freshwater (runoff from glaciers and rivers), forming MSAAW and is found from the surface to 150 m depth. The properties of the MSAAW were established based on reported information (Sarmiento et al., 2004; Sievers and Silva, 2008; Silva et al., 2009; Llanillo et al., 2012; Torres et al., 2014; Forcén-Vázquez et al., 2021). The strong salinity and alkalinity relationship reported for the Patagonian archipelago interior sea (41–56°S: Torres et al., 2011a; Torres et al., 2020) makes it possible to calculate alkalinity of the MSAAW using the equation: A_{Tsal} (μmol kg^{-1}) = 66.4 × Salinity + 1.1, (R^2 = 0.93, n=81; **Figure 2**; **Supplementary Table 1**). The regression is close to the equations reported for the Sub-Antarctic region A_T (μmol kg^{-1}) = 61.9 × Salinity + 151 and A_T (μmol kg^{-1}) = 61.8 × Salinity + 145; Torres et al. (2011b) (**Figure 2**). The intercept (1.1 μmol kg^{-1}) is a reasonable estimate of the freshwater end-members (glacier-ice and small tributaries along the fjord) with the value mean (A_T of 5.8 ± 16.0 μmol kg^{-1}; n = 7, salinity 0.0 ± 0.1 S_P).

The water masses proposed in this analysis have ranges of values, thus 5 source types of water (SWT) were used as described in **Table 1** ($ISSW_1$, $ISSW_2$, $ISBW_1$, $MSAAW_1$, and $MSAAW_2$). The weights for each variable were chosen taking into account the extent of their conservative behavior and their spatial and

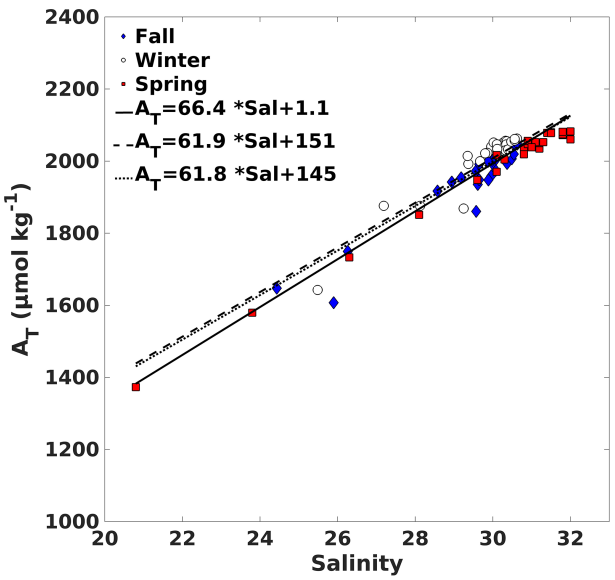

FIGURE 2 | Relationship between A_T and salinity from Seno Ballena Fjord transect data (fall-winter-spring austral, 2018). The line represents the regression obtained for Seno Ballena fjord in this study and the dashed lines are the regression obtained at the eastern portion of the Patagonia archipelago (from surface water) inner sea (50–53°S; Torres et al., 2011b).

temporal variability (S_p = 25, Temp = 25, DSi = 5, NO_3 = 5, A_T = 25). The salinity and A_T data were assigned relatively high weights, because they are conservative in the temporal and spatial scales considered here. Temperature and nutrients were assigned lower weights; temperature due to its high seasonal variability caused by heating and cooling and nutrients due to the changes caused by biological processes. The linear system of mixing equations, that were solved using the classic OMP analysis (MATLAB - version 1.2.0.0; Karstensen, 2013), are the following:

$$x_a T_a + x_b T_b + x_c T_c + x_d T_d + x_e T_e = T_{obs} + R_T \quad (1a)$$

$$x_a S_a + x_b S_b + x_c S_c + x_d S_d + x_e S_e = S_{obs} + R_S \quad (1b)$$

$$x_a A_{Ta} + x_b A_{Tb} + x_c A_{Tc} + x_d A_{Td} + x_e A_{Te} = A_{Tobs} + R_{A_T} \quad (1c)$$

$$x_a DSi_a + x_b DSi_b + x_c DSi_c + x_d DSi_d + x_e DSi_e = DSi_{obs} + R_{DSi} \quad (1d)$$

$$x_a NO_{3a} + x_b NO_{3b} + x_c NO_{3c} + x_d NO_{3d} + x_e NO_{3e} = NO_{obs} + R_{NO_3} \quad (1e)$$

$$x_a + x_b + x_c + x_d + x_e = 1 + R_\Sigma \quad (1f)$$

where T_{obs}, S_{obs}, A_{Tobs}, DSi_{obs} and NO_{3obs} are the values observed during the seasonal sampling and the R_Σ are their respective residuals. The values T_i, S_i, A_{Ti}, DSi_i and NO_i (i = a, b, c, d and e) define the fixed parameter values of the five source-water types, that define the three water masses (ISSW, IBSW and MSAAW). The five tracers plus conservation of mass leaves little redundancy for five water types (Karstensen and Tomczak, 1998), since we need to include the fifth water type (IBSW) as it is distinctly different than the other four. x_i is the fraction for each data point. Equation (1f) is the mass conservation constraint.

2.5 pH-pCO_2 Mooring Sensors

High-resolution measurements of pCO_2 and pH_T were recorded *in situ* using the autonomous submersible SAMI-CO_2 and SAMI-pH sensors (Sunburst Sensors, LLC) (DeGrandpre et al., 1995), temperature and conductivity using SBE37 sensors and dissolved oxygen (DO) using an Aanderaa 5331A sensor. SAMI-CO_2 measures the partial pressure of carbon dioxide (pCO_2) in water from 200 to 1000 µatm (precision <1 µatm, accuracy ~10 µatm), while SAMI-pH measures pH_T on total proton concentration scale in the marine pH range of 7 - 9 for salinity ranges 25 - 40 S_P (Clayton and Byrne, 1993). The two sensors use a high-precision colorimetric reagent method (http://www.sunburstsensors.com/).

The factory SAMI-CO_2 calibration, based on coincident measurements of pCO_2 using gas-equilibration with infrared detection, was used for this study. The SAMI-pH is not factory calibrated but was validated using a Tris buffer at 25°C (accuracy and precision ~ ± 0.003). All of the sensors were placed at 10 ± 1 m and mounted on one single steel frame with the sensors' water intakes in the same vertical position. The sensors were deployed in the lower part of the pycnocline on the outer side of the sill (**Figure 1**). Mooring measurements started early in austral fall (March, 2018) and ended in austral spring (December, 2018). All sensors recorded data every 4 hours. Discrete samples of the three seasonal oceanographic cruises (March, August, and December 2018) were used for data quality control.

TABLE 1 | Properties of ISSW (Inner Surface Source Water), IBSW (Inner Bottom Source Water), and MSAAW (Modified Sub-Antarctic Water) for the OMP and time-series water mass model.

SWT	S_p	Temp (°C)	DSi (µM)	NO_3 (µM)	A_T (µmol kg^{-1})	DIC (µmol kg^{-1})
SSW_1	20.80	4.45	0.30	4.72	1373	1308
$ISSW_2$	25.48	7.07	5.38	5.80	1647	1580
$IBSW_1$	31.00	7.41	4.52	14.14	2055	2020
$IBSW_2$	30.63	7.08	4.49	11.97	2047	1988
$MSAAM_1$	31.00	9.0	0.00	8.0	2059	2003*
$MSAAM_2$	33.00	11.00	5.00	14.80	2192	2003*

*DIC_{MSAAW} was calculated from: $DIC_{MSAAW} = \frac{DIC_{ST.10\text{-}10m} - (f_{ISSW} \times DIC_{ISSW})}{f_{MSAAW}}$, where $DIC_{ST.10\text{-}10m}$ is station 10 at 10 m that is near pure MSAAW water, f_{ISSW} is fraction of ISSW at station 10 to 10 m and f_{MSAAW} is fraction of MSAAW at station 10 to 10 m. Subscripts 1 and 2 in the water mass indicate slight variations in their physical-chemical characteristics.

The SAMI-pH and A_{Tsal} data were used to compute the additional carbonate system parameters because this pair was shown to yield good accuracy (Cullison Gray et al., 2011). The total alkalinity (A_{Tsal}) values derived from salinity carry an error of 42 µmol kg^{-1}. This error is estimated from the values of the A_{Tsal} time series for the days that coincide with the seasonal $A_{T\text{-}measured}$ samples measured in fall, winter, and spring. For this calculation, $A_{T\text{-}measured}$ data were collected from a sampling station near the mooring at a depth of 10 m.

All inorganic carbon parameters were calculated with CO_2SYS software (Pierrot et al., 2006) as described above (see item 2.3). Nutrient data were not included in the computations due to the lack of continuous measurements during the study. The calculated pCO_2 changed by ~ 1.0 µatm when the highest observed levels of SRP (1.76 µM) and DSi (5.47 µM) were included in CO_2SYS.

2.6 CO_2 Flux Determination

The air-sea CO_2 flux was determined using the diffusive boundary layer model, through the volumetric flux equation expressed in terms of CO_2 partial pressure:

$$F = K \times K_O(pCO_{2W} - pCO_{2a}) \quad (2)$$

where F is the air-sea flux in units of moles $area^{-1}$ $time^{-1}$, K is the gas transfer velocity in units of length $time^{-1}$ (Wanninkhof, 1992), K_O is the solubility coefficient of CO_2 (mol m^{-3} atm^{-1}), estimated from *in situ* salinity and temperature according to Weiss (1974) and the $pCO_{2W} - pCO_{2a}$ is the difference between the air and sea surface pCO_2 values in µatm. Results with positive values indicate that there is a flux from sea to atmosphere. The gas transfer velocity of CO_2 was calculated using the revised relationship recommended by Wanninkhof (2014):

$$K = 0.251 \langle U^2 \rangle \left(\frac{Sc}{660}\right)^{-0.5} \quad (3)$$

where $<U^2>$ is the mean squared wind speed (m s^{-1}). The wind speed data were obtained from a meteorological station near the study area (Chile Meteorological Directorate, Alberto Hurtado School station, coordinates: -53.16694°S, -70.94528°W).

The updated Wanninkhof (2014) parameterization was used in the study of the gas transfer rate estimation in Seno Ballena fjord because it considers the most recent advances in the quantification of the input parameters, improvements in the wind speed products and it provides good estimates for most insoluble gases in intermediate wind speed ranges (3 - 15 m s^1). The mean wind speed in Seno Ballena Fjord was 4.04 m s^{-1} during the study period (range of 3.73 to 6.04 m s^{-1}). Sc is the Schmidt number which accounts for the difference in molecular diffusivity between gases, with the leading coefficient updated for seawater (35 S_P) and freshwater (0 S_P) at temperatures ranging from -2 to 40°C by Wanninkhof (2014). *Sc* is calculated using:

$$Sc = A + B_t + C_t + D_t + E_t \quad (4)$$

where t is temperature (°C) and A, B, C, D, and E are fitting coefficients (Wanninkhof, 2014).

The formula described by Dickson et al., (2007) was used to calculate the atmospheric pCO_2 values in humid air and the water vapor pressure values:

$$pCO_{2a} = pCO_2(dry - air) \times (1 - P_W) \quad (5)$$

where pCO_2 (*dry - air*) is the air pressure at sea level taken from the Earth System Research Laboratory database (National Oceanic and Atmospheric Administration Marine Boundary Layer Reference 53.1 to 17.5°S; www.esrl.noaa.gov/gmd/ccgg/mbl/data.php), interpolated for the year 2018 and corrected with local barometric pressure. These values assume clean marine air, and therefore a possible error is created due to terrestrial effects on pCO_2, mainly of the export of organic and inorganic carbon from land runoff, rivers and glaciers (Lafon et al., 2014). The error is not readily quantifiable because no regional pCO_2 data are available. P_w is the equilibrium water vapor for the *in situ* temperature (°C) and salinity (S_P) (Forstner and Gnaiger, 1983).

2.7 Temperature Effect on pCO_2

Temperature changes affect the partial pressure of seawater due to its solubility. For this reason, the values of the pCO_2 time series were adjusted to a mean temperature, using the equation of Takahashi et al. (2009) (Eqn. 6). The temperature coefficient (0.0459) for cold (-1.8 to 10°C) and less saline ($30 < S_P < 35$) water (Ericson et al., 2018) was used, as these ranges match the observed salinity and temperature ranges of the Seno Ballena fjord.

$$npCO_2 = pCO_{2obs} \times exp[0.0459 \times (T_{ave} - T_{obs})] \quad (6)$$

where pCO_{2obs} are the values of the pCO_2 time series. The mean temperature during the study period (March to December 2018; T_{ave}) was 7.67°C, and T_{obs} is the measured temperature in degrees Celsius. This equation makes it possible to determine if changes in pCO_2 in spring are related to phytoplankton bloom events rather than just to temperature changes.

2.8 Apparent Oxygen Utilization

Apparent oxygen utilization is calculated to estimate the effect of biology on oxygen concentrations, eliminating the effect of temperature and solubility. It was calculated using the following equation:

$$AOU = DO_{sat} - DO \quad (7)$$

This equation represents the change in oxygen since a mass of water was last in contact with the atmosphere, assuming that the oxygen concentration at the surface was at equilibrium with the atmosphere (DO_{sat}). DO is the measured dissolved O_2. AOU estimates biological processes; positive values indicate aerobic remineralization processes, which consume DO, and negative values indicate photosynthetic processes, which produce DO (Pytkowicx, 1971; Ito et al., 2004; Jackson et al., 2021).

2.9 Mixing Model

We use a simplified mixing model to determine the effects of mixing versus photosynthesis/respiration in the time series.

Because we have no nutrient measurements at the mooring, we use only salinity and temperature and thus can only use three end-members. The choice of the end-members was based on a T-S diagram (**Supplementary Figure 3**). $ISSW_1$, $IBSW_2$, and $MSAAW_1$, define a triangle that best contains the mooring data and were selected to estimate the fractions of each type of water at the mooring at each moment. **Table 1** shows the values of end-members of temperature and salinity for each water type.

Equations (8a), (8b), and (8c) were used to determine the mixing ratios *f*. Equations (8d) and (8e) were used to calculate the DIC and A_T that would result from mixing these three water masses.

$$1 = f_{ISSW} + f_{IBSW} + f_{MSAAW} \tag{8a}$$

$$T_{mix} = f_{ISSW} \times T_{ISSW} + f_{IBSW} \times T_{IBSW} + f_{MSAAW} \times T_{MSAAW} \tag{8b}$$

$$S_{mix} = f_{ISSW} \times S_{ISSW} + f_{IBSW} \times S_{IBSW} + f_{MSAAW} \times S_{MSAAW} \tag{8c}$$

$$DIC_{mix} = f_{ISSW} \times DIC_{ISSW} + f_{IBSW} \times DIC_{IBSW} + f_{MSAAW} \times DIC_{MSAAW} \tag{8d}$$

$$A_{Tmix} = f_{ISSW} \times A_{TISSW} + f_{IBSW} \times A_{TIBSW} + f_{MSAAW} \times A_{TMSAAW} \tag{8e}$$

where *f* is the end-member mixing ratio. *T*°*C*, S_p, *DIC*, and A_T are temperature, salinity, dissolved inorganic carbonate, and total alkalinity for each end-member (**Table 1**).

The pCO_2 due to mixing was calculated from the following equation:

$$pCO_{2mix} = f(DIC_{mix}, A_{Tmix}, S_{mix}, T_{mix}) \tag{9}$$

where the term $f(DIC_{mix}, A_{Tmix}, S_{mix}, T_{mix})$ is the calculation of pCO_2 using DIC, A_T, S_p and T°C to the CO_2SYS program (Pierrot et al., 2006).

2.10 1-D Biochemical Mass Balance Model

A simple 1-D mass budget model determined the contribution of biological processes, physical mixing, air-sea CO_2 exchange, and thermodynamics to pCO_2 variability. The changes in pCO_2 due to dissolution/formation of $CaCO_3$ and salinity are omitted.

The daily changes in the pCO_2 were estimated as previously carried out by various authors (Chierici et al., 2006; Xue et al., 2016; Fransson et al., 2017; Li et al., 2018; Gac et al., 2021). Changes in pCO_2 (ΔpCO_2) are driven by changes in temperature (ΔpCO_{2tem}), air-sea CO_2 exchange (ΔpCO_{2gas}), mixing (ΔpCO_{2mix}), and biological activity (ΔpCO_{2bio}). ΔpCO_2 and ΔDIC are calculated using:

$$\Delta pCO_2 = (pCO_2)_{n+1} - (pCO_2)_n$$

$$= \Delta pCO_{2tem} + \Delta pCO_{2gas} + \Delta pCO_{2mix} + \Delta pCO_{2bio} \tag{10a}$$

$$\Delta DIC = (DIC)_{n+1} - (DIC)_n$$

$$= \Delta DIC_{gas} + \Delta DIC_{mix} + \Delta DIC_{bio} \tag{10b}$$

where Δ is the change in parameters between times (begin) t_n and t_{n+1} (end) are the difference between the daily value at t_{n+1} minus the daily value a t_n.

2.10.1 The Effect of Thermal Changes

Temperature changes affect the dynamics of the pCO_2 but not the DIC of the water. Therefore, the thermal effect on ΔpCO_{2tem} was determined according to the equation (similar to Eqn 6 above; Takahashi et al., 1993)

$$\Delta pCO_{2tem} = (pCO_2)_n \times exp(0.0459 \times \Delta T) - (pCO_2)_n \tag{11}$$

where $(pCO_2)_n$ is pCO_2 at time 1, ΔT is the temperature difference between time t_{n+1} and t_n.

2.10.2 The Effect of Air-Sea Gas Exchange

Air-sea CO_2 exchange affects the dynamics of DIC and pCO_2 but not the A_T. Therefore, the pCO_2 changes due to the air-sea CO_2 exchange (ΔpCO_{2gas}) are calculated using:

$$\Delta DIC_{gas} = F_{gas} \times (t_{n+1} - t_n) / (\rho \times d) \tag{12a}$$

where F_{gas} is the air-sea CO_2 flux (see Section "Air-sea CO_2 exchanges") $t_{n+1} - t_n$ is the number of days between two measurements, ρ is the seawater density (kg m^{-3}) calculated from the TEOS-10 calculations (McDougall et al., 2011), and *d* is the mixed layer depth taken to be 10 m, the depth of the mooring.

$$(DIC_{n+1})_{gas} = DIC_n + \Delta DIC_{gas} \tag{12b}$$

$$\Delta pCO_{2gas} = f((DIC_{n+1})_{gas}, A_{Tn}, S_n, T_n) - (pCO_2)_n \tag{12c}$$

where $(DIC_{n+1})_{gas}$ is DIC predicted for time t_{n+1} based solely on air-sea CO_2 exchange. The term $f((DIC_{n+1})_{gas}, A_{Tn}, S_n T_n)$ is the calculation of pCO_2 using DIC, A_T, S, and T to the CO_2SYS program (Pierrot et al., 2006).

2.10.3 The Effect of Water Mass Changes

To determine the changes in pCO_2 due to mixing the pCO_2 was calculated from DIC_{mix} and A_{Tmix} derived from the fraction of each water mass using equations:

$$\Delta DIC_{mix} = DIC_{mix(n+1)} - DIC_{mix(n)} \tag{13a}$$

$$\Delta A_{Tmix} = A_{Tmix(n+1)} - A_{Tmix(n)} \tag{13b}$$

where ΔDIC_{mix} and ΔA_{Tmix} are DIC and A_T of mixing (see Section "Mixing model") $t_{n+1} - t_n$ is the number of days between two measurements $DIC_{mix(n+1)}$ and $A_{Tmix(n+1)}$ are predicted DIC and A_T based solely on the mixing.

$$\Delta pCO_{2mix} = f((DIC_{n+1})_{mix},\ (A_{Tn+1})_{mix},\ S_{n+1},\ T_{n+1}) - (pCO_2)_n \quad (13e)$$

where $f((DIC_{n+1})_{mix}, (A_{Tn+1})_{mix}, S_{n+1}, T_{n+1})$ is the calculation of pCO_2 using DIC, A_T, S and T to the CO_2SYS program (Pierrot et al., 2006).

2.10.4 The Effect of Biological Processes

The biological effect on pCO_2 is estimated as the remainder in the change of DIC.

$$\Delta DIC_{bio} = \Delta DIC - \left(\Delta DIC_{gas} + \Delta DIC_{mix}\right) \quad (14a)$$

$$(DIC_{n+1})_{bio} = DIC_n + \Delta DIC_{bio} \quad (14b)$$

$$\Delta pCO_{2bio} = f((DIC_{n+1})_{bio},\ A_{Tn},\ S_n,\ T_n) - (pCO_2)_n \quad (14c)$$

where $(DIC_{n+1})_{bio}$ is the predicted DIC based solely on the biological factor. $f((DIC_{n+1})_{bio}, A_{Tn}, S_n, T_n)$ is the calculation of pCO_2 using DIC, A_T, S, and T in the CO_2SYS program (Pierrot et al., 2006).

3 RESULTS

3.1 Hydrography and Nutrients

The hydrography of the Seno Ballena fjord was modulated by the seasonal input of freshwater from glacier meltwater, the glacial river located at the head of the fjord, and the small tributaries along the fjord. The influence of the MSAAW was also evident given the range of salinities observed (24 - 31); the fjord water is estuarine-brackish (33 - 66% seawater). The contribution of freshwater from the Inner Surface Estuarine Water (ISSW) near the glacier is distributed from the head of the fjord towards the outside of the sill near the surface, with smaller fractions outside of the sill (**Figures 3A–C**). In fall and spring, the deep layer contained not only MSAAW, but also another type of water (IBSW) near the glacier, that is cold and nutrient-rich (**Figures 3D, F**). In fall the surface ISSW was mixed deep inside the fjord. Finally, the MSAAW dominated the deep layer of the inner fjord, which confirms that this estuarine-brackish water enters the fjord (**Figures 3G–I**). The MSAAW contribution was greater in winter (from 5 - 50 m depth). This mixed water mass was associated with a strong vertical density gradient (σ_t range from surface to depth: fall = 19.20 - 23.97; winter = 20.18 - 23.98; spring = 17.17 - 22.82).

We divided the fjord area into three zones (inner sill, outer sill, and off-shelf), based on stratification and mixing conditions. In the inner sill region, the 0 - 10 m surface layer showed low salinity, between S_P = 27.4 to 28.6, over a deeper layer with S_P ranging from 30.2 to 31.2 (**Figures 4A–C**). Salinity varied also with the season, showing high salinity in winter (range from surface to depth: S_P = 28.6 – 30.3) and low salinity in spring (range from surface to depth S_P = 27.4 – 31.2); the latter modulated by the input of glacier meltwater (**Figures 4–C**).

The water column had a thermal inversion and weak temperature variation in the inner sill region during fall and winter, with an increase of 0.7°C from the surface to the deep layer (**Figures 4D, E**). There were high temperature values in the fall (range from surface to depth 7.2 – 7.7°C) and low-temperature values in winter (range from surface to depth 6.4 – 7.3°C).

The stratification was much shallower in fall and spring and practically disappeared in winter in the outer sill section (**Figure 4**), coincident with a more significant influence of the oceanic water and lower influence of freshwater (S_P between 28.6 and 31.3 in the surface and deep layers, respectively; **Figures 3**, **4**). Mixed

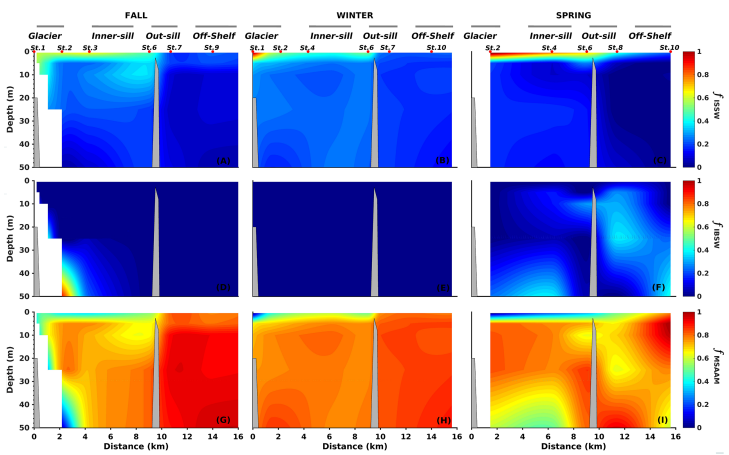

FIGURE 3 | Fraction (*f*) of Inner Surface Source Water (ISSW; **A–C**), Inner Bottom Source Water (IBSW; **D–F**), Modified Subantarctic Water (MSAAW; **G–I**) along Seno Ballena Fjord during the seasonal sampling. The fractions were estimated using OMP analysis (Optimum Multiparameter; MATLAB - version 1.2.0.0; Karstensen, 2013).

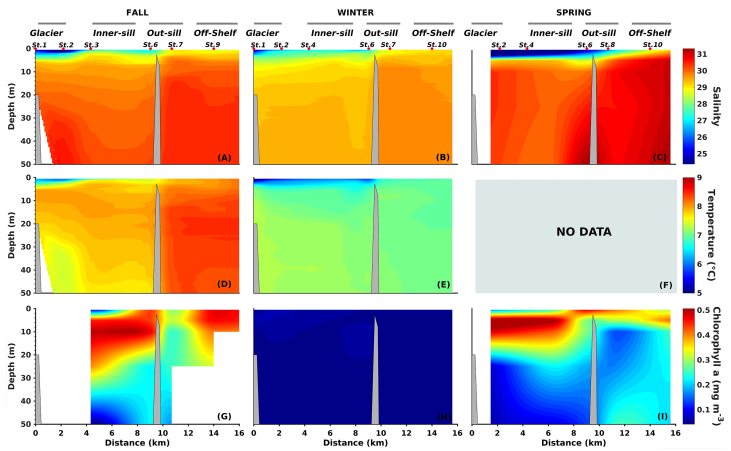

FIGURE 4 | Vertical distribution of Salinity **(A–C)**, Temperature **(D, E)**, and Vertical distribution of Chlorophyll-a **(G–I)** along the Seno Ballena Fjord transect, during austral fall, winter, and spring 2018. Red markers correspond to synoptic sampling stations and grey horizontal lines indicate the extent of each section of the fjord **(F)** The CTD temperature data in spring is not available.

conditions were observed in the off-shelf region, with a high S_P of 30.5 throughout the water column (**Figures 4A–C**). The fall and winter data showed a very stable surface layer (>10 m) in the water column of the inner section, with *Brunt-Väisälä* frequency squared values of 10 - 30x10^{-3} s^{-2} compared to outer sections (< 10x10^{-3} s^{-2}; **Supplementary Figure 4**).

Nutrient concentrations (SRP, NO_3^-, and DSi) had a clear spatial variability from the inner to the outer sections of the fjord (**Figure 5**; **Table 2**). Surface NO_3^- showed low to medium concentrations along the fjord, ranging from 5.7 – 7.4 µM (inner sill) to 9.3 µM (off-shelf), and in the deep layer NO_3^- concentrations ranged from 6.2 – 11.1 µM (inner sill) to 11.5 µM (off-shelf) (**Figure 5**). Most of the time DSi concentrations were below 5 µM throughout the water column along the fjord. DSi concentrations were very low in the surface water along the fjord in fall and spring, with a range from 0.2 µM (off-shelf) to 2.7 µM (inner sill), increasing up to 4.6 µM in the deep layer in the inner sill region. During winter, DSi values increased up to 5.5 µM, especially in the middle and inner sections of the fjord (**Figure 5**, **Table 2**). SRP concentrations were more homogeneously distributed throughout the water column with a range from 0.6 to 1.3 µM, with the highest concentrations in the inner section below 10 m during spring and fall (**Figure 5**; **Table 2**). NO_3^- was strongly correlated with SRP in fall (R^2 = 0.9; n=28; p< 0.001) and spring (R^2 = 0.6; n=25; p< 0.001). N:P fluctuated between 7.2 in fall and 6.9 in spring, with lower ratios than the expected Redfield N:P ratio (16:1). DSi:N ratios were low in fall (0.5), winter (0.1), and spring (0.2) during the hydrographic cruises. These values are consistent with the values of 0.2 - 0.5 recorded in this fjord during spring by Torres et al. (2011a).

3.2 Carbonate Parameters From Hydrography Cruises

Low pCO_2 values were observed in the upper 10 m layer during the fall and spring cruises (< 400 µatm) in the inner fjord section; whereas, higher mean values were seen during winter (**Table 2**). Below the 10 m surface layer, pCO_2 values were much higher close to the glacier, 500 to 589 µatm (**Figures 6A–C**; **Table 2**). Mean pH values of 8.0 and 7.9 were observed in the inner section

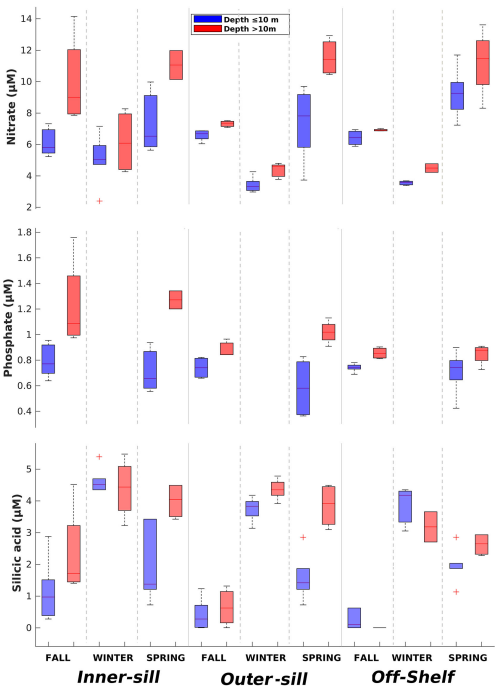

FIGURE 5 | Median concentrations of nitrate, orthophosphate (SRP), and silicic acid (DSi) along the Seno Ballena Fjord during austral fall, winter, and spring (seasonal cruises 2018). Box-plots show the 25th–75th quartiles of the data at each section; the lines show the maximum and minimum values; the red cross shows outlier values.

TABLE 2 | Statistical descriptors of physical, chemical, and biological variables along Seno Ballena Fjord obtained during March (fall), August (winter), and December (spring) 2018 during three hydrographic cruises (mean ± 1 SD).

Season	Depth (m)	Sal	Temp (°C)	NO_3^- (μM)	PO_4^{-3} (μM)	Si $(OH)_4$ (μM)	pCO_2 (μatm)	pH	A_T (μmol kg^{-1})	Ω_{Ar}	Chl a mg m^{-3}
						Inner sill					
Fall	≤ 10	27.5 ± 2.3	7.2 ± 09	6.2 ± 0.8	0.8 ± 0.1	1.1 ± 0.9	376 ± 36	8.0 ± 0.0	1736 ± 37	1.7 ± 0.4	0.5 ± 0.2
Fall	>10	30.2 ± 0.3	7.7 ± 0.2	10.0 ± 2.9	1.2 ± 0.4	2.3 ± 1.5	589 ± 22	7.9 ± 0.1	2000 ± 41	1.6 ± 0.4	0.2 ± 0.2
Winter	≤ 10	28.6 ± 1.8	6.4 ± 1.1	5.7 ± 1.3		4.6 ± 0.4	443 ± 42	7.9 ± 0.0	1936 ± 157	1.1 ± 0.2	0.1 ± 0.0
Winter	>10	30.3 ± 0.0	7.3 ± 0.1	6.2 ± 2.1		4.4 ± 0.9	500 ± 35	7.9 ± 0.0	2054 ± 2	1.2 ± 0.1	0.0 ± 0.0
Spring	≤ 10	27.4 ± 5.7		7.4 ± 2.3	0.7 ± 0.2	2.7 ± 1.3	335 ± 12	8.1 ± 0.2	1792 ± 365	1.2 ± 0.5	2.3 ± 1.3
Spring	>10	31.2 ± 0.1		11.1 ± 1.3	1.3 ± 0.1	4.0 ± 0.6	563 ± 6	7.9 ± 0.0	2051 ± 2	0.9 ± 0.0	0.2 ± 0.1
						Outer sill					
Fall	≤ 10	28.9 ± 1.5	7.9 ± 0.3	6.6 ± 0.3	0.7 ± 0.1	0.4 ± 0.5	422 ± 35	8.0 ± 0.0	1900 ± 98	1.9 ± 0.1	0.4 ± 0.1
Fall	>10	30.3 ± 0.3	8.2 ± 0.2	7.3 ± 0.2	0.9 ± 0.1	0.6 ± 0.7	443 ± 9	8.0 ± 0.0	2006 ± 12	2.0 ± 0.0	0.2 ± 0.0
Winter	≤ 10	29.8 ± 0.7	6.7 ± 0.4	3.4 ± 0.4		3.8 ± 0.3	461 ± 7	7.9 ± 0.0	1993 ± 71	1.1 ± 0.1	0.1 ± 0.0
Winter	>10	30.4 ± 0.2	7.1 ± 4.3	4.4 ± 0.4		4.4 ± 0.3	463 ± 20	7.9 ± 0.0	2041 ± 18	1.2 ± 0.1	0.0 ± 0.0
Spring	≤ 10	28.6 ± 2.9		7.3 ± 2.3	0.6 ± 0.2	1.6 ± 0.7	363 ± 50	8.0 ± 0.1	1886 ± 187	1.3 ± 0.2	2.1 ± 0.7
Spring	>10	31.3 ± 0.5		11.5 ± 1.2	1.0 ± 0.1	3.9 ± 0.7	479 ± 24	8.0 ± 0.0	2054 ± 6	1.2 ± 0.0	0.7 ± 0.4
						Off shelf					
Fall	≤ 10	29.6 ± 0.6	8.4 ± 0.3	6.4 ± 0.4	0.7 ± 0.0	0.2 ± 0.3	419 ± 11	8.0 ± 0.0	2081 ± 228	2.1 ± 0.1	0.4 ± 0.1
Fall	>10	30.5 ± 0.1	8.4 ± 01	6.9 ± 0.1	0.9 ± 0.0	0.0 ± 0.0	427 ± 22	8.0 ± 0.0	2013 ± 18	2.1 ± 0.1	0.3 ± 0.1
Winter	≤ 10	30.3 ± 0.2	7.0 ± 0.0	3.5 ± 0.2		3.9 ± 0.7	434 ± 6	8.0 ± 0.0	2040 ± 12	1.3 ± 0.0	0.0 ± 0.0
Winter	>10	30.6 ± 0.0	7.0 ± 0.0	4.5 ± 0.4		3.2 ± 0.7	450 ± 26	8.0 ± 0.0	2059 ± 3	1.3 ± 0.1	0.0 ± 0.0
Spring	≤ 10	30.7 ± 1.4		9.3 ± 1.5	0.7 ± 0.2	2.0 ± 0.5	433 ± 17	8.0 ± 0.0	2022 ± 87	1.3 ± 0.1	1.7 ± 0.7
Spring	>10	31.7 ± 0.3		11.2 ± 2.2	0.8 ± 0.1	2.6 ± 0.4	436 ± 25	8.0 ± 0.0	2080 ± 2	1.3 ± 0.1	1.1 ± 0.2

of the fjord in the upper 10 m layer and below 10 m depth, respectively, while pH for the outer sill was more homogeneous, with a mean value of 8.0 (SD=0.017) (**Figures 6D–F**; **Table 2**). The lowest pH values were observed below 10 m in the inner sections of the fjord and for most seasons were coincident with the highest pCO_2 values (**Figure 6**). High surface Chl-a was observed during spring in the upper layer in the whole transect, ranging from 2.3 (inner sill section) to 1.7 mg m^{-3} (outer sill section) (**Figure 4**). These high Chl-a biomass was associated with high pH values (R^2 = 0.48; n=7; p<0.001) (**Figures 4**, **6**, respectively).

The A_T was low in the surface layer (< 10 m), coincident with low-salinity waters in the inner section, with seasonal mean values of 1736 to 1993 μmol kg^{-1} (**Table 2**), associated with low values of Ω_{Ar} in the surface (R^2 = 0.42 n=50; p<0.001) (**Figures 6G–I**). Values of A_T were over 2000 μmol kg^{-1} in the inner section of the fjord below the 10 m layer. The maximum Ω_{Ar} and A_T values were recorded in the off-shelf sections (2.1 and 2081 μmol kg^{-1}, respectively). These results indicate that during all seasons, freshwater inputs from the melting glacier and the glacial river were low in alkalinity (5.82 μmol kg^{-1}), whereas MSAAW was high in alkalinity (2081 μmol kg^{-1}).

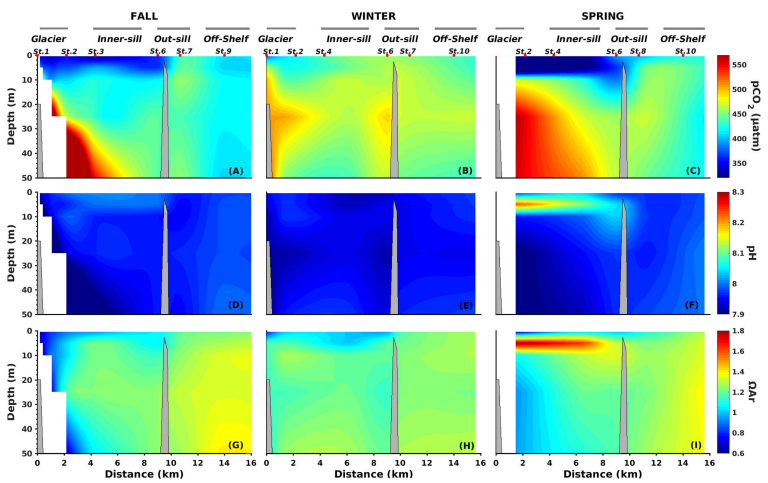

FIGURE 6 | Vertical distributions of the partial pressure of CO_2 (pCO_2) **(A–C)**, pH_T **(D–F),** and aragonite saturation state (Ω_{Ar}) **(G–I)** along the Seno Ballena Fjord transect, during austral fall, winter and spring, 2018. Red markers correspond to synoptic sampling stations and grey horizontal lines indicate the extent of each section of the fjord.

3.3 Parameters From Mooring Sensors

The sea surface temperature values (outer sill section) also showed low seasonal variability, with amplitude not greater than 2°C. High values were recorded in fall with a mean of 8.2 ± 0.32°C (range 7.8 – 8.6°C) and low values were recorded in spring with a mean of 7.2 ± 0.22°C (range 6.6 – 7.7°C) (**Figure 7**; **Supplementary Table 3**). The S_P values recorded at the mooring showed a range from 29.8 to 30.5 with high values occurring in fall; whereas, minimum S_P occurred in spring (**Figure 7**). The salinity was above 28 throughout most of the studied seasons but presented a clear low amplitude seasonality (S_P <1.5) (**Figure 7**). The seasonal variability of T and S_P is related to the variable contributions of the different water masses of the fjord, with minor contribution of ISSW (0.04 - 0.23) compared to IBSW (0.05- 0.97) and MSAAW (0.01 - 0.85) at the mooring (**Figure 8**). MSAAW dominated the water masses during the fall; whereas, IBSW dominated during the spring. During the spring season, we observed at the end of October, an event during which the contribution of MSAAW (0.51) and IBSW (0.45) was more similar coinciding with a noticeable change in T and S_P, with respect to the values observed when a larger fraction of IBSW or MSAAW is recorded.

The carbonate system showed clear seasonality in the upper 10 m layer, with the most noticeable changes during fall and spring (**Figure 7D**). During fall, pCO_2 values had a mean of 385 ± 26 µatm (range 240 – 431 µatm). pCO_2 values decreased in spring, with a mean of 365 ± 47 µatm (range 167 – 471 µatm) and were associated with an increase in dissolved oxygen (negative values of AOU) and a decrease in salinity (**Figure 7B**). An increase of pCO_2 was observed in winter, which reached a mean of 394 ± 10 µatm (range 365 – 433 µatm), coincident with a decrease in temperature as the system changed from warming to cooling. A negative relationship was observed between pCO_2 normalized to an average temperature

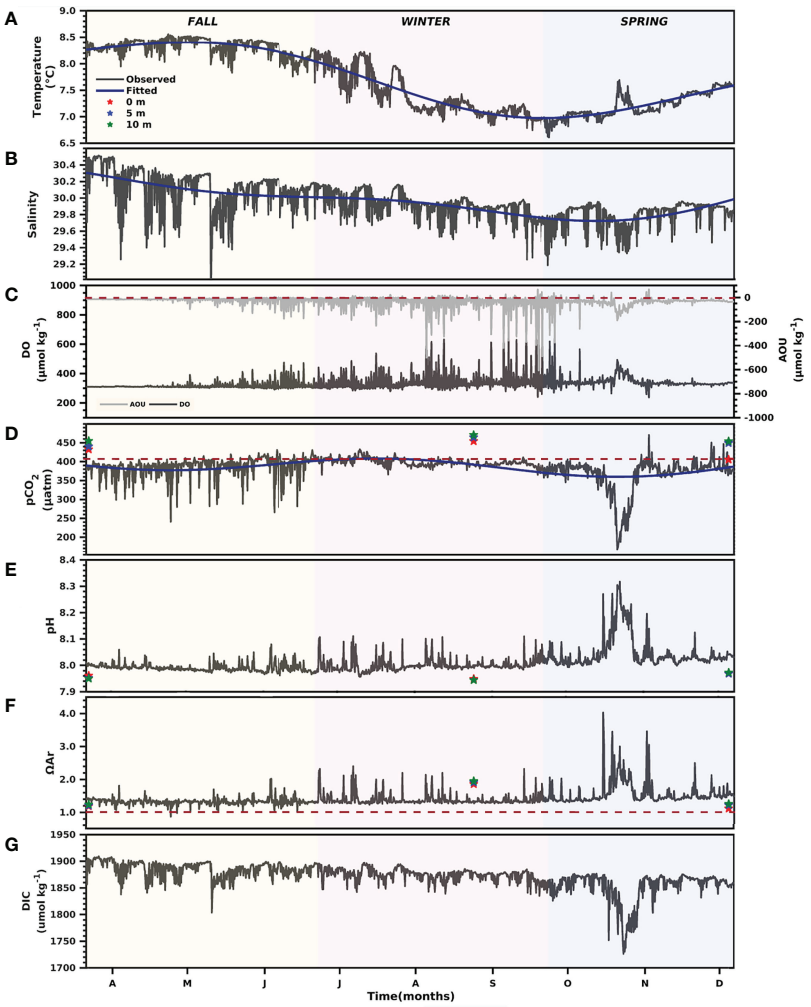

FIGURE 7 | Seasonal dynamics of the primary measured parameters at the Seno Ballena mooring (**Figures 1**). Time-series of Temperature **(A)**, Salinity **(B)**, Oxygen and AOU **(C)**, pCO_2 **(D)**, pH **(E)**, Aragonite saturation state **(F)** and dissolved in organic carbon (DIC) **(G)** from March to December 2018. The red dashed lines in **(C)** show the limit between positive values that indicate aerobic remineralization processes and negative values that indicate photosynthetic process, **(D)** shows the atmospheric value (mean 405 ± 1 uatm), **(F)** shows an aragonite saturation threshold of 1.

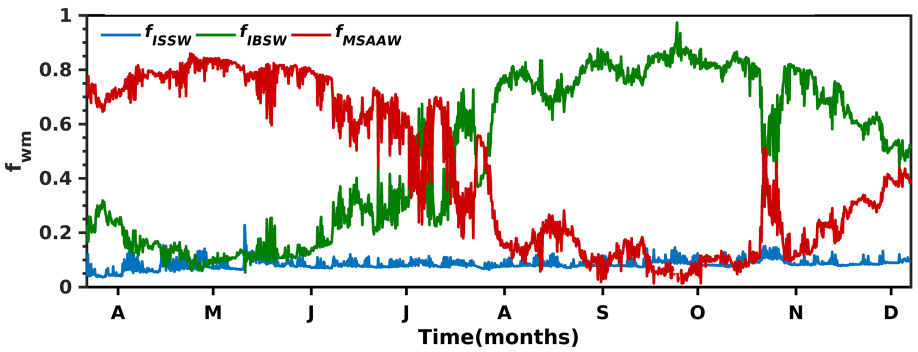

FIGURE 8 | The seasonal variability of ISSW (Inner Surface Source Water), IBSW (Inner Bottom Source Water), MSAAW (Modified Subantarctic Water) in the upper 10 ± 1 m of the water column in the Seno Ballena Fjord mooring.

($npCO_2$) and oxygen saturation percentage (%DO) (R^2 = 0.47, p<0.001; slope -3.7 µatm $\%DO^{-1}$; **Figure 9A**). Although the $npCO_2$–salinity relationship had high scatter (**Figure 9B**), it showed a significant positive relationship during spring (R^2 = 0.30, p<0.001). The pCO_2–temperature relationship (**Figure 9C**) also showed a significant positive relationship during winter (R^2 = 0.41, p<0.001; **Supplementary Table 2**).

Air-sea CO_2 fluxes varied from -3.08 mmol m^{-2} d^{-1} in spring to 0.29 mmol m^{-2} d^{-1} in winter (**Figure 10A**). CO_2 uptake in fall (March-May) fluctuated from -1.62 to -0.24 mmol m^{-2} d^{-1}, while in spring (September to December) it varied from -0.57 to -3.08 mmol m^{-2} d^{-1}. Degassing occurred only during the June-July winter months, with mean monthly fluxes of 0.09 and 0.26 mmol m^{-2} d^{-1}, respectively. The data show continuous CO_2 absorption over seasons, indicating that this fjord behaves as a net sink of atmospheric CO_2 (mean = -1.01 mmol m^{-2} d^{-1}). Water mass changes also played an important role in the change of DIC (range 41.39 - 180 µmol kg^{-1}) and therefore in pCO_2 (153 - 454 µatm). We observed large changes during the spring related to an influx of IBSW. The differences in DIC and pCO_2 at the mooring compared to a mixture of the water masses give the impact of the other factors: biology, air-sea gas exchange, and temperature (**Figures 10A–C**). The difference in DIC is always negative, which suggests that the mooring water mass always has more of a production signal, compared to a remineralization signal, than the underlying water types. These water masses are mainly subsurface water masses (ISBW and MSAAW) and have larger nutrient concentrations favoring primary productivity compared to the small contribution from the surface water mass (ISSW; **Figure 8**). The variability of pH_T was inversely correlated with pCO_2, showing maximum pH values during spring with a mean of 8.1 (range 8.0–8.3) and low values during winter and fall with a mean of 8.0 (range 8.0–8.1) (**Figure 7E**). The seasonal trend of pCO_2 and pH is followed by Ω_{Ar} (**Figures 7D–F**).

4 DISCUSSION

4.1 Hydrography and Nutrients

The results of our studies reveal the hydrographic control on the seasonal variability of the carbonate system, including the variability of the saturation state of seawater relative to calcium carbonate, pCO_2, and air-sea CO_2 fluxes (**Figures 7**, **10**). Within

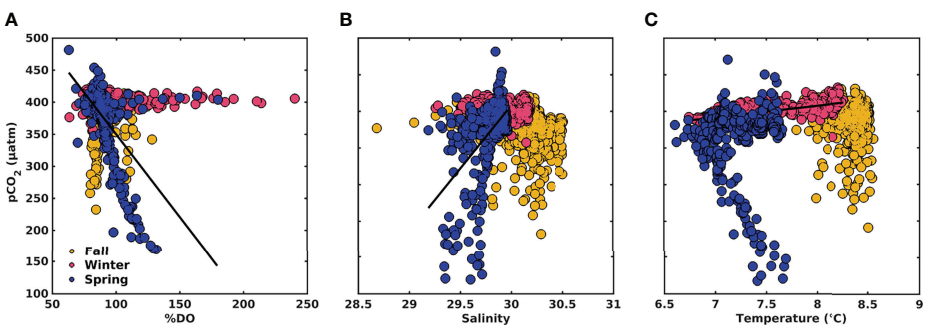

FIGURE 9 | Relationships between **(A)** surface $npCO_2$-%DO, **(B)** $npCO_2$-Salinity, and pCO_2-Temperature **(C)** of time-series data. The yellow, pink and blue markers correspond to fall, winter, and spring, respectively. Black lines correspond to significant relationships of $npCO_2$-%OD during spring (R^2 = 0.47; p < 0.0001), $npCO_2$-Salinity during spring (R^2 = 0.30; p < 0.0001), and pCO_2-Temperature during winter (R^2 = 0.41; p < 0.0001).

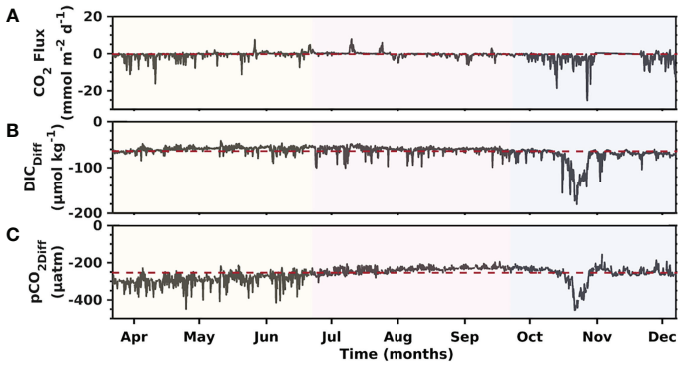

FIGURE 10 | CO_2 flux **(A)**, the difference between $DIC_{mooring}$ and DIC_{mix}; the red dashed line is DIC_{Diff} mean **(B)**, and the difference between $pCO_{2mooring}$ and pCO_{2mix}; the red dashed line is pCO_{2Diff} mean **(C)** recorded from March to December, 2018 at the Seno Ballena Fjord.

the marine fjord system of Patagonia, we find fjords that are: (1) simple, two-layer vertical structures, with an estuarine surface layer of low salinity and a subsurface layer of oceanic origin with higher salinity (Schneider et al., 2014; Saldías et al., 2019); and (2) more complex three-layer structures as found in the Seno Reloncaví Fjord (Valle-Levinson et al., 2007). The above is modulated by freshwater contributions of glacial origin, river discharge, and rainfall, which significantly influence the salinity gradient of the surface layer in the vast coastal ocean of western Patagonia (Acha et al., 2004; Saldías et al., 2019).

Our results indicate that the Seno Ballena Fjord has two layers; the salinity of the surface layer is modulated by the input of meltwater from the glacier, mainly through stratifying the inner sill region of the fjord. The freshwater stratification and surface water salinity varied seasonally, with a relatively deeper halocline in fall and spring due to higher freshwater input (**Figures 3**, **4**). The conditions were generally less stratified in winter, suggesting a limited supply of freshwater and strong ocean water contribution (**Figure 3**). As was observed in the water mass distribution analysis and the salinity gradients along the Seno Ballena Fjord, the influence of freshwater was higher on the inner-sill surface and reduced toward the outer-sill section. Only in spring does the freshwater plume spread past the sill (**Figure 3**), as has been observed in previous studies in this fjord during spring (Torres et al., 2011a). The observed seasonal variability of temperature and salinity was weaker (range Temp: 7.2 – 8.3°C/range S_P: 29.8 – 30.2) compared to other fjord systems of northern Patagonia (Seno Reloncaví (41°S); range Temp: 10.6 – 16.9°C/range S_P: 20.1 – 29.8) (Vergara-Jara et al., 2019) and western Canada (Strait of Georgia (49°N); S_P range: 5 – 29) (Moore-Maley et al., 2018), where strong seasonality in salinity is related to larger, seasonal river freshwater inputs (Puelo River: 713 to 4000 m^3 s^{-1} and Fraser River: 800 to 12.000 m^3 s^{-1}).

The deep layer with higher salinity was influenced by the inflow of MSAAW: S_P = 31–33, which is modified upon entry into the Strait of Magellan, mixing with freshwater from rivers and melting glaciers, forming estuarine water with salinity around 28 – 31 S_P (Sievers and Silva, 2008). During tidal flood, the acceleration of the flow forces aspiration (Bernoulli aspiration; Valle-Levinson et al., 2007), pumping denser deep water which sinks below the less salty buoyant water in the inner section (Valle-Levinson et al., 2007). The high salinity-deeper water that flows inward compensates for the surface layer of freshwater that flows toward the Strait of Magellan. This type of circulation also influences the temperature of the fjord, causing an inverted thermocline with low surface temperature, underlain by a deep homogeneous layer of higher temperature. The low temperature in the surface layer of the Seno Ballena Fjord was more pronounced in winter due to the formation of a thin, surface layer of ice near the glacier, ice that likely is derived from re-frozen subglacial discharges rather than sea ice.

Our results in the Seno Ballena Fjord show that the nutrient concentrations were modulated inside and outside by the sill and revealed the significant spatial variability of nutrients (N and DSi), consistent with previous reports (Frangópulos et al., 2007). The presence of the shallow sill dividing the fjord causes a thin plume of low salinity water to spread over the sill during ebb tide (Torres et al., 2011a), which is probably modulated by the wind. The deepwater aspiration, when the water flow accelerates during the flood tide, probably influences the nutrient concentration patterns in the inner fjord (**Figure 11**; Valle-Levinson et al., 2006; Torres et al., 2011a). There is a strong influence of MSAAW, which has low DSi compared to nitrate concentrations, which explains the higher nitrate concentration in the deep water. In contrast, the continental waters of western Patagonia are characterized by high DSi and low nitrate, which explains the higher concentration of DSi in surface waters and near the glacier (Hervé et al., 2007; Torres et al., 2020). Plumes, tides and wind stress have also been found to drive circulation and renewal of the water masses of Northern Hemisphere fjords with sills, demonstrating their importance in the physical, chemical, and biological processes that occur inside and outside the fjords (Mortensen et al., 2011).

The plume of low salinity is blocked to a greater extent by the sill, particularly during low tide (Valle-Levinson et al., 2006). This blockage was observed during fall and spring. Hence, we suggest that the inner fjord residence time seems to allow the

accumulation of local remineralization products such as nutrients and CO_2 in the inner fjord, allowing the IBSW to form near the glacier during fall and spring. IBSW represents the water mass observed near the glacier at subsurface levels (30 – 50 m), which has different properties (**Figures 3**, **5**, **6**) than those of the ISSW and MSAAW.

4.2 Carbonate Chemistry

The seasonal variability recorded in the Seno Ballena Fjord carbonate system can be assigned to several processes, including the input of freshwater from the melting of the Santa Inés glacier, the exchange with oceanic waters, biological production, seasonal variability in temperature, water column mixing and advection. The surface layer of the inner-sill region had undersaturated pCO_2 values with respect to the atmosphere during fall and spring, associated with the input of freshwater from the glacier (**Figures 3**, **4**, **6**). In this area, a higher fraction of ISSW is observed (range 1 to 0.3 of ISSB fraction, the surface to 10 m, respectively), which coincides with the lowest DIC_{mix} values (range 1489 - 1852 µmol kg^{-1} of DIC_{mix}, surface to 10 m, respectively; **Supplementary Figure 5**), this indicates that the DIC input of freshwater was low and contributes to the decrease of the DIC of the mixture and directly to the pCO_2. These observations are consistent with previous studies in fjords and channels of Patagonia in which low-salinity surface waters (e.g. salinity less than 28) are strongly undersaturated in CO_2 (Torres et al., 2011b). Subglacial environments have low pCO_2 due to the effect of temperature (cooling), photosynthesis, and dilution (Bates and Mathis, 2009; Meire et al., 2015).

Although the pCO_2 was low in surface waters in the inner section of the fjord region during fall and spring, it did not result in the increase of calcium carbonate saturation (Ω_{CaCO3}: Ω_{Ar} and Ω_{cal}) whose variation seems to be dominated by dilution (i.e. the reduction of CO_3^{-2} or Ca^{2+} ions by dilution with freshwater with very low levels of these ions). Our results were similar to conditions found in Alaska and Arctic fjords, where glacier fjords had low pCO_2 with respect to the atmosphere, and corrosive levels of aragonite (Ω_{Ar}) and calcite (Ω_{cal}) saturation near the surface (<50 m) due to the input of freshwater with low A_T and Ca^{2+} from glacier melting (Evans et al., 2014). The above finding suggests that the inner surface water of the Seno Ballena Fjord was under-saturated and corrosive to aragonite during the survey period, due to the intrusion of low A_T and Ca^{2+} (relationship Ω_{Ar}-A_T; R^2 = 0.42 n=50; p< 0.001) freshwater that drains the siliceous crystalline batholiths of Patagonia (Torres et al., 2011b; Torres et al., 2020). The above demonstrates the sensitivity of this Sub-Antarctic system to global stressors such as global warming and cooling, mainly for this Sub-Antarctic area where there has been a significant retreat of the glaciers in recent years (Bown et al., 2014).

The carbonate system presented clear seasonal variability in the outer sill region in March-December period, 2018 (**Figure 7**). A substantial reduction in pCO_2 and an increase in pH_T in spring months can be attributed to the dominance of photosynthesis (AOU: -191 µmol kg^{-1}) over respiration (%DO versus npCO_2, **Figure 9**; AOU **Figure 7C**). After the spring bloom, a signal of remineralization with higher values of pCO_2 (471 µatm) related to positive values of AOU (67 µmol kg^{-1}; **Figure 7C**) is observed, these results illustrate the key role that phytoplankton blooms and microbial respiration play in the variability of pCO_2, and therefore the change in pH and to a lesser extent the change in Ω_{Ar}, taking into account the signal that observed during the spring season that coincides in the three variables (pCO_2, pH_T, and Ω_{Ar}). In contrast, high pCO_2 values were recorded in winter, related to low pH_T and Ω_{Ar}, which could be attributed to subsurface water masses brought to the surface by increased water column mixing, which is more consistent between the months of July and August (IBSW and MSSAW; **Figure 8**) as well as the predominance of respiration over photosynthesis.

The variations recorded in the pCO_2 time-series seem to be driven by net primary productivity events due to the consistency of pCO_2 and dissolved oxygen variability (**Figure 7**). However, it should be borne in mind that the dynamics of coastal systems are also driven by other processes such as the mixing of different water masses; air-sea fluxes of CO_2, and variations in temperature. Therefore, in this study, these effects were also calculated (ΔpCO_{2mix}, ΔpCO_{2gas}, and ΔpCO_{2tem}, respectively). During spring, the biological processes (-4.72 to - 20.40 µatm day^{-1}), the changes in water mass (-5.42 to -17.2 µatm day^{-1}), and the sea-air CO_2 flux (-5.47 to - 21.81 µatm day^{-1}) contributed significantly to the decrease of pCO_2. The temperature effect is much smaller (-0.10 to 0.29 µatm day^{-1}). Similarly in fall, ΔpCO_{2bio} (22.68 to 30.13 µatm day^{-1}), ΔpCO_{2mix} (10.8 to 30.13 µatm day^{-1}), ΔpCO_{2gas} (11.25 to 30.72 µatm day^{-1}) dominate, which is why there are higher values of pCO_2 in fall compared to spring. The ΔpCO_{2tem} contribution is again small (**Supplementary Table 4**), as is observed in the linear regression of pCO_2/T (**Figure 9**). In contrast, in other studies, T is the most important factor in the variability of pCO_2, whereas in our studies it is the factor with the least importance in modulating the daily variability of pCO_2 (Xue et al., 2016).

The sea-air CO_2 flux varies seasonally, while low temperature and low haline stratification favors the positive sea-air CO_2 flux estimated in winter, the low wind speed limits those fluxes. In contrast, stronger winds during fall and spring contribute to the greater CO_2 uptake of Patagonian fjords. The mean wind speed was 4.04 m s^{-1} during the study period, with a maximum monthly average of 6.04 m s^{-1} (November) and a minimum of 3.73 m s^{-1} (July; see **Supplementary Figure 6**). The higher CO_2 uptake in spring is also related to the decrease of pCO_2 in surface water by photosynthesis. Previous studies have also suggested that the fjords of Patagonia in warm seasons behave as a sink for CO_2 in response to high productivity (Torres et al., 2011b; Vergara-Jara et al., 2019). This behavior is also observed in fjords of the Northern Hemisphere (Meire et al., 2015).

Variation in pCO_2 is also driven by water mass changes. In fall, MASSW dominates with high values of DIC, whereas in spring, ISBW dominates with much lower DIC values. When these subsurface water masses are mixed to the surface, they bring macronutrients, products of remineralization, to the surface layer and favor primary productivity (Jones et al., 2020). The nutrient ratios (Si:N<1 and N:P<15) may indicate

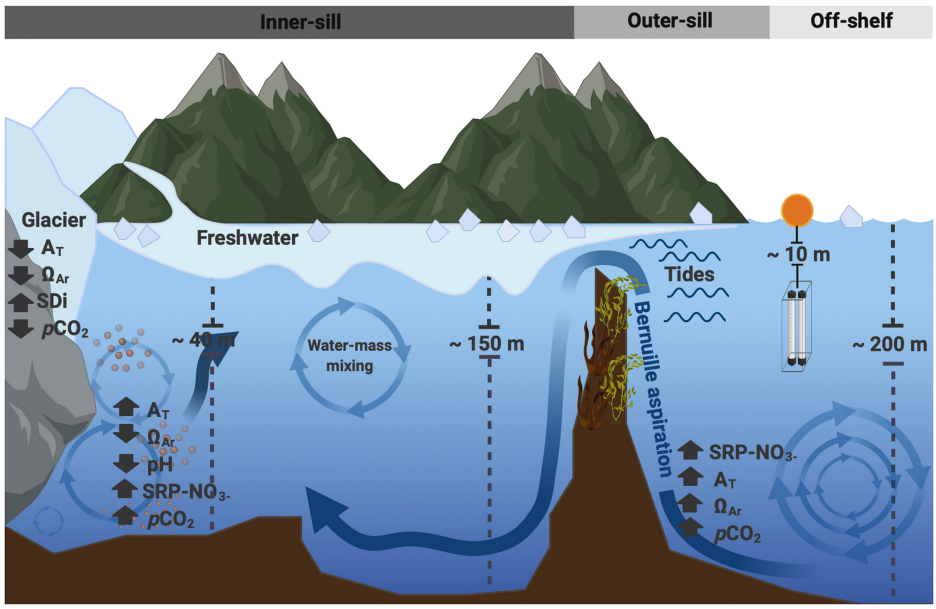

FIGURE 11 | Schematic of processes that occur inside and outside of the Seno Ballena glacial fjord: (1) The input of freshwater from the marine-terminating glacier and river glacier may change physical-chemical properties, such as the following: i) generate strong surface stratification in the inner fjord section, ii) bring low A_T, low Ω_{AR}, low nutrients (SPR and NO_3), and low pCO_2, and iii) bring sediment and dissolved organic carbon (DOC). (2) Advection of subsurface nutrient-rich waters near the glacier. (3) Bernoulli aspiration caused by the fast shallow flow into the inner fjord is capable of sucking deep water coming from the Strait of Magellan up and over the sill. The density of this water mass then causes it to sink.

that the availability of silicic acid and nitrate plays a critical role in determining the extent and/or the persistence of phytoplankton blooms and the effects on the variability of the carbonate chemistry of waters in the study area, mainly in the spring season.

5 CONCLUSION

Frequent pCO_2 and pH_T measurements allowed us to determine that the carbonate system's seasonal variability in the Seno Ballena Fjord was weaker compared to the northern Patagonia fjords. The most notable changes in pCO_2, pH_T, and Ω_{Ar} were driven by spring primary productivity, likely induced by the effect of seasonal increase of solar insolation in a recently stratified layer and local nutrient fertilization processes by the subsurface water mass ISBW (through aspiration and entrainment). In our results, we also found that the changes of the water masses play an important role in the daily variability of pCO_2 throughout the time series. In fall, MSAAW dominates with greater DIC contributing to the mixture and higher values of pCO_2 are recorded, whereas in spring the IBSW dominates with lower DIC compared to MSAAW, and lower pCO_2 values are recorded. The important role of mixing of the water masses ISSW, ISBW, and MSAAW and the air-sea exchange of CO_2 in the daily variability of pCO_2 was shown, which was generally just as important as biological processes. The very low freshwater-A_T end member means that meltwater significantly dilutes the concentration of A_T/DIC and calcium ions and plays a dominant role in driving low Ω_{Ar} values in estuarine waters (**Figure 11**). This study points out the importance of subglacial discharge from Santa Inés glacier in influencing the hydrography, nutrient, and carbonates system dynamics of the Seno Ballena Fjord, illustrating the sensitivity of this Sub-Antarctic system to global stressors such as global warming and freshening. The results highlight the important role of this high-latitude fjord as a CO_2 sink and the main processes driving this trend, including wind speed, low temperatures, and low salinity, these last two driven by surface freshwater runoff. These results suggest the importance of sustained high-resolution and long-term measurements of different physical and biogeochemical variables to understand the complex dynamics of the subantarctic fjords.

DATA AVAILABILITY STATEMENT

The data of the sensor SAMI-CO_2, SAMI-pH, SBE37, and Aanderaa 5331A used for this study are publicly available and can be accessed at https://figshare.com/articles/dataset/Buoy_Seno_Ballena/12888008

AUTHOR CONTRIBUTIONS

JV was responsible for data processing and analysis, designed the manuscript, and wrote the manuscript. GS and SA. Participated

in discussions on the data, review, and editing of the manuscript. MV-J Planning of the fieldwork methodology, installation, maintenance, and extraction of sensors data. MS and MD. Participated in part in the data analysis and review of the manuscript. RT. Participated in part in the data analysis. JI Participated in discussions on the data, review, editing, supervision of the manuscript, and funding acquisition. All authors approved the submitted version.

FUNDING

This project was supported by ANID-FONDECYT 1170174 (to J. L. Iriarte) and is part of the framework of Research Program 1 of the IDEAL Center (ANID-FONDAP 15150003).

ACKNOWLEDGMENTS

J.P Vellojin wishes to thank the School of Graduate Direction and the PhD program in Aquaculture Sciences at Universidad Austral de Chile, Campus Puerto Montt, and IDEAL Center for financial support during the 2017–2020 periods. Special thanks to Emerging Leaders of Americas (ELAP) Scholarships 2019 funded by Global Affairs Canada (GAC), managed by the Canadian Bureau for International Education (CBIE), for providing financial support to J.P Vellojin during the exchange program in the Department of Earth, Ocean and Atmospheric Sciences at the University of British Columbia, Canada. GSS thanks the partial funding from FONDECYT 1190805 and the Nucleus Center for the Study of Multiple-drivers on Marine Socio-Ecological Systems (MUSELS) funded by MINECON NC120086. Support at UBC was provided through NSERC Discovery Grant RGPIN-2016-03865 to SEA and Banting Post-doctoral Fellowship to GSS. MS was partially supported by INCAR (FONDAP-CONICYT No. 15110027). MD is supported by the U.S. National Science Foundation grant OPP-1723308. Special thanks to Marco Pinto for collaboration during the cruises carried out to Seno Ballena Fjord and Valeska Vasquez and Emilio Alarcón for collaboration in the sample analyses. The data presented are part of the Ph.D. thesis of Jurleys P. Vellojin at UACh. We thank the journal reviewers who made valuable suggestions and comments for improving the final version of the manuscript.

SUPPLEMENTARY MATERIAL

The Supplementary Material for this article can be found online at: https://www.frontiersin.org/articles/10.3389/fmars.2022.643811/full#supplementary-material

REFERENCES

Acha, E. M., Mianzan, H. W., Guerrero, R. A., Favero, M., and Bava, J. (2004). Marine Fronts at the Continental Shelves of Austral South America: Physical and Ecological Processes. *J. Mar. Syst.* 44, 83–105. doi: 10.1016/j.jmarsys.2003.09.005

Alarcón, E., Valdés, N., and Torres, R. (2015). Calcium Carbonate Saturation State in an Area of Mussels Culture in the Reloncaví Sound, Northern Patagonia, Chile. *Lat. Am. J. Aquat. Res.* 43, 277–281. doi: 10.3856/vol43-issue2-fulltext-1

Bates, N. R., and Mathis, J. T. (2009). The Arctic Ocean Marine Carbon Cycle: Evaluation of Air-Sea CO_2 Exchanges, Ocean Acidification Impacts and Potential Feedbacks. *Biogeosciences* 6, 2433–2459. doi: 10.5194/bg-6-2433-2009

Bown, F., Rivera, A., Zenteno, P., Bravo, C., Cawkwell, F., and Raup, (2014). "First Glacier Inventory and Recent Glacier Variation on Isla Grande De Tierra Del Fuego and Adjacent Islands in Southern Chile," in *Global Land Ice Measurements From Space Springer Praxis Books*. Eds. J. S. Kargel, G. J. Leonard, M. P. Bishop, A. Kääb and B. H. Raup (Berlin, Heidelberg: Springer), 661–674. doi: 10.1007/978-3-540-79818-7_28

Byrne, R. H., Robert-Baldo, G., Thompson, S. W., and Chen, C. T. A. (1988). Seawater pH Measurements: An at-Sea Comparison of Spectrophotometric and Potentiometric Methods. *Deep Sea Res.* 35, 1405–1410. doi: 10.1016/0198-0149(88)90091-X

Chierici, M., and Fransson, A. (2009). Calcium Carbonate Saturation in the Surface Water of the Arctic Ocean: Undersaturation in Freshwater Influenced Shelves. *Biogeosciences.* 6, 2421–2431. doi: 10.5194/bg-6-2421-2009

Chierici, M., Fransson, A., Lansard, B., Miller, L. A., Mucci, A., Shadwick, E., et al. (2011). Impact of Biogeochemical Processes and Environmental Factors on the Calcium Carbonate Saturation State in the Circumpolar Flaw Lead in the Amundsen Gulf, Arctic Ocean. *J. Geophys. Res. Oceans* 116, C00G09. doi: 10.1029/2011JC007184

Chierici, M., Fransson, A., and Nojiri, Y. (2006). Biogeochemical Processes as Drivers of Surface fCO_2 in Contrasting Provinces in the Subarctic North Pacific Ocean. *Glob. Biogeochem. Cycles* 20, BG1009. doi: 10.1029/2004GB002356

Clayton, T. D., and Byrne, R. H. (1993). Spectrophotometric Seawater pH Measurements: Total Hydrogen Ion Concentration Scale Calibration of M-Cresol Purple and at-Sea Results. *Deep Sea Res.* 40, 2115–2129. doi: 10.1016/0967-0637(93)90048-8

Cullison Gray, S. E., DeGrandpre, M. D., Moore, T. S., Martz, T. R., Friederich, G. E., and Johnson, K. S. (2011). Applications of *in Situ* pH Measurements for Inorganic Carbon Calculations. *Mar. Chem.* 125, 82–90. doi: 10.1016/j.marchem.2011.02.005

DeGrandpre, M. D., Hammar, T. R., Smith, S. P., and Sayles, F. L. (1995). *In Situ* Measurements of Seawater pCO_2. *Limnol. Oceanogr.* 40, 969–975. doi: 10.4319/lo.1995.40.5.0969

Dickson, A. G. (1990). Standard Potential of the Reaction: $AgCl(s) + 12H_2(G) = Ag(s) + HCl(aq)$, and the Standard Acidity Constant of the Ion HSO_4^- in Synthetic Sea Water From 273.15 to 318.15 K. *J. Chem. Thermodyn.* 22, 113–127. doi: 10.1016/0021-9614(90)90074-Z

Dickson, A. G., and Goyet, C. (1994). *Handbook of Methods for the Analysis of the Various Parameters of the Carbon Dioxide System in Sea Water; Version 2* (Tennessee, United States: ORNL/CDIAC-74), 187.

Dickson, A. G., and Millero, F. J. (1987). A Comparison of the Equilibrium Constants for the Dissociation of Carbonic Acid in Seawater Media. Deep Sea Res. *Part Oceanogr. Res. Pap.* 34, 1733–1743. doi: 10.1016/0198-0149(87)90021-5

Dickson, A. G., Sabine, C. L., and Christian, J. R. (2007). *Guide to Best Practices for Ocean CO_2 Measurements* Vol. 3 (Sidney, BC V8L 4B2 Canada: PICES Special Publication), 191.

Ericson, Y., Falck, E., Chierici, M., Fransson, A., Kristiansen, S., Platt, S. M., et al. (2018). Temporal Variability in Surface Water Pco_2 in Adventfjorden (West Spitsbergen) With Emphasis on Physical and Biogeochemical Drivers. *J. Geophys. Res. Ocean.* 123, 4888–4905. doi: 10.1029/2018JC014073

Evans, W., Mathis, J. T., and Cross, J. N. (2014). Calcium Carbonate Corrosivity in an Alaskan Inland Sea. *Biogeosciences* 11, 365–379. doi: 10.5194/bg-11-365-2014

Feely, R. A., Okazaki, R. R., Cai, W.-J., Bednaršek, N., Alin, S. R., Byrne, R. H., et al. (2018). The Combined Effects of Acidification and Hypoxia on pH and Aragonite Saturation in the Coastal Waters of the California Current

Ecosystem and the Northern Gulf of Mexico. *Cont. Shelf. Res.* 152, 50–60. doi: 10.1016/j.csr.2017.11.002

Forcén-Vázquez, A., Williams, M. J. M., Bowen, M., Carter, L., and Bostock, H. (2021). Frontal Dynamics and Water Mass Variability on the Campbell Plateau. *N. Z. J. Mar. Freshw. Res.* 55, 199–222. doi: 10.1080/00288330.2021.1875490

Forstner, H., and Gnaiger, E. (1983). "Calculation of Equilibrium Oxygen Concentration," in *Polarographic Oxygen Sensors*. Eds. E. Gnaiger and H. Forstner (Berlin, Heidelberg: Springer), 321–333. doi: 10.1007/978-3-642-81863-9_28

Frangópulos, M., Blanco, J., Hamamé, M., Rosales, S., Torres, R., and Valle-Levinson, A. (2007) *Análisis Y Diagnóstico De Las Principales Características Oceanográficas Del Área Marina Costera Protegida Francisco Coloane, Informe Proyecto Final GEF-PNUD "Conservación De La Biodiversidad De Importancia Mundial Al Largo De La Costa Chilena*. Available at: http://cpps.dyndns.info/cpps-docs-web/planaccion/biblioteca/pordinario/102.articles-47869_InformeFinal.pdf (Accessed May 15, 2021).

Fransson, A., Chierici, M., Hop, H., Findlay, H. S., Kristiansen, S., and Wold, A. (2016). Late Winter-to-Summer Change in Ocean Acidification State in Kongsfjorden, With Implications for Calcifying Organisms. *Polar. Biol.* 39, 1841–1857. doi: 10.1007/s00300-016-1955-5

Fransson, A., Chierici, M., Miller, L. A., Carnat, G., Shadwick, E., Thomas, H., et al. (2013). Impact of Sea-Ice Processes on the Carbonate System and Ocean Acidification at the Ice-Water Interface of the Amundsen Gulf, Arctic Ocean. *J. Geophys. Res. Ocean.* 118, 7001–7023. doi: 10.1002/2013JC009164

Fransson, A., Chierici, M., Skjelvan, I., Olsen, A., Assmy, P., Peterson, A. K., et al. (2017). Effects of Sea-Ice and Biogeochemical Processes and Storms on Under-Ice Water fCO_2 During the Winter-Spring Transition in the High Arctic Ocean: Implications for Sea-Air CO_2 Fluxes. *J. Geophys. Res. Ocean.* 122, 5566–5587. doi: 10.1002/2016JC012478

Fransson, A., Chierici, M., Yager, P. L., and Smith, W. O. (2011). Antarctic Sea Ice Carbon Dioxide System and Controls. *J. Geophys. Res. Oceans.* 116, C12035. doi: 10.1029/2010JC006844

Gac, J.-P., Marrec, P., Cariou, T., Grosstefan, E., Macé, É., Rimmelin-Maury, P., et al. (2021). Decadal Dynamics of the CO_2 System and Associated Ocean Acidification in Coastal Ecosystems of the North East Atlantic Ocean. *Front. Mar. Sci.* 8, 759.

Garreaud, R. D. (2018). Record-Breaking Climate Anomalies Lead to Severe Drought and Environmental Disruption in Western Patagonia in 2016. *Clim. Res.* 74, 217–229. doi: 10.3354/cr01505

Giesecke, R., Höfer, J., Vallejos, T., and González, H. E. (2019). Death in Southern Patagonian Fjords: Copepod Community Structure and Mortality in Land- and Marine-Terminating Glacier-Fjord Systems. *Prog. Oceanogr.* 174, 162–172. doi: 10.1016/j.pocean.2018.10.011

Gran, G. (1952). Determination of the Equivalence Point in Potentiometric Titrations. Part II. *Analyst* 77, 661–671. doi: 10.1039/AN9527700661

Grear, J. S., Rynearson, T. A., Montalbano, A. L., Govenar, B., and Menden-Deuer, S. (2017). pCO_2 Effects on Species Composition and Growth of an Estuarine Phytoplankton Community. *Estuar. Coast. Shelf. Sci.* 190, 40–49. doi: 10.1016/j.ecss.2017.03.016

Haraldsson, C., Anderson, L. G., Hassellöv, M., Hulth, S., and Olsson, K. (1997). Rapid, High-Precision Potentiometric Titration of Alkalinity in Ocean and Sediment Pore Waters. *Deep Sea Res.* 44, 2031–2044. doi: 10.1016/S0967-0637(97)00088-5

Hervé, F., Pankhurst, R. J., Fanning, C. M., Calderón, M., and Yaxley, G. M. (2007). The South Patagonian Batholith: 150 M Y of Granite Magmatism on a Plate Margin. *Lithos.* 97, 373–394. doi: 10.1016/j.lithos.2007.01.007

Hopwood, M. J., Carroll, D., Dunse, T., Hodson, A., Holding, J. M., Iriarte, J. L., et al. (2020). Review Article: How Does Glacier Discharge Affect Marine Biogeochemistry and Primary Production in the Arctic? *Cryosphere.* 14, 1347–1383. doi: 10.5194/tc-14-1347-2020

Ito, T., Follows, M. J., and Boyle, E. A. (2004). Is AOU a Good Measure of Respiration in the Oceans? *Geophys. Res. Lett.* 31, L17305. doi: 10.1029/2004GL020900

Jackson, J. M., Bianucci, L., Hannah, C. G., Carmack, E. C., and Barrette, J. (2021). Deep Waters in British Columbia Mainland Fjords Show Rapid Warming and Deoxygenation From 1951 to 2020. *Geophys. Res. Lett.* 48, e2020GL091094. doi: 10.1029/2020GL091094

Jones, E. M., Renner, A. H. H., Chierici, M., Wiedmann, I., Lødemel, H. H., and Biuw, M. (2020). Seasonal Dynamics of Carbonate Chemistry, Nutrients and CO_2 Uptake in a Sub-Arctic Fjord. *Elem. Sci. Anthr.* 8, 41. doi: 10.1525/elementa.438

Karstensen, J. (2013) *Análisis OMP (Optimum Multiparameter) - USER GROUP*. Available at: https://omp.geomar.de/ (Accessed May 17, 2021).

Karstensen, J., and Tomczak, M. (1998). Age Determination of Mixed Water Masses Using CFC and Oxygen Data. *J. Geophys. Res. Oceans.* 103 (C9), 18599–18609. doi: 10.1029/98JC00889

Kim, H.-C., and Lee, K. (2009). Significant Contribution of Dissolved Organic Matter to Seawater Alkalinity. *Geophys. Res. Lett.* 36, L20603. doi: 10.1029/2009GL040271

Kinder, T. H., and Bryden, H. L. (1990). "Aspiration of Deep Waters Through Straits," in *The Physical Oceanography of Sea Straits NATO ASI Series*. Ed. L. J. Pratt (Dordrecht: Springer Netherlands), 295–319. doi: 10.1007/978-94-009-0677-8_14

Kurihara, H. (2008). Effects of CO_2-Driven Ocean Acidification on the Early Developmental Stages of Invertebrates. *Mar. Ecol. Prog. Ser.* 373, 275–284. doi: 10.3354/meps07802

Lafon, A., Silva, N., and Vargas, C. A. (2014). Contribution of Allochthonous Organic Carbon Across the Serrano River Basin and the Adjacent Fjord System in Southern Chilean Patagonia: Insights From the Combined Use of Stable Isotope and Fatty Acid Biomarkers. *Prog. Oceanogr.* 129, 98–113. doi: 10.1016/j.pocean.2014.03.004

Li, D., Chen, J., Ni, X., Wang, K., Zeng, D., Wang, B., et al. (2018). Effects of Biological Production and Vertical Mixing on Sea Surface pCO_2 Variations in the Changjiang River Plume During Early Autumn: A Buoy-Based Time Series Study. *J. Geophys. Res. Ocean.* 123, 6156–6173. doi: 10.1029/2017JC013740

Llanillo, P. J., Pelegrí, J. L., Duarte, C. M., Emelianov, M., Gasser, M., Gourrion, J., et al. (2012). Meridional and Zonal Changes in Water Properties Along the Continental Slope Off Central and Northern Chile. *Cienc. Mar.* 38, 307–332. doi: 10.7773/cm.v38i1B.1814

Lukawska-Matuszewska, K. (2016). Contribution of non-Carbonate Inorganic and Organic Alkalinity to Total Measured Alkalinity in Pore Waters in Marine Sediments (Gulf of Gdansk, S-E Baltic Sea). *Mar. Chem.* 186, 211–220. doi: 10.1016/j.marchem.2016.10.002

Mamayev, O. I. (1975). *Temperature-Salinity Analysis of World Ocean Waters. 1st Edition* (Canada: Elsevier Science).

McDougall, T. J., and Barker, P. M. (2011). Getting Started With TEOS-10 and the Gibbs Seawater (GSW) Oceanographic Toolbox. Scor/Iapso WG, 127, 1–28.

Mehrbach, C., Culberson, C. H., Hawley, J. E., and Pytkowicx, R. M. (1973). Measurement of the Apparent Dissociation Constants of Carbonic Acid in Seawater at Atmospheric Pressure1. *Limnol. Oceanogr.* 18, 897–907. doi: 10.4319/lo.1973.18.6.0897

Meier, W. J.-H., Grießinger, J., Hochreuther, P., and Braun, M. H. (2018). An Updated Multi-Temporal Glacier Inventory for the Patagonian Andes With Changes Between the Little Ice Age and 2016. *Front. Earth Sci.* 6. doi: 10.3389/feart.2018.00062

Meire, L., Søgaard, D. H., Mortensen, J., Meysman, F. J. R., Soetaert, K., Arendt, K. E., et al. (2015). Glacial Meltwater and Primary Production are Drivers of Strong CO_2 Uptake in Fjord and Coastal Waters Adjacent to the Greenland Ice Sheet. *Biogeosciences.* 12, 2347–2363. doi: 10.5194/bg-12-2347-2015

Meredith, M., Sommerkorn, M., Cassotta, S., Derksen, C., Ekaykin, A., Hollowed, A., et al. (2019). "Chapter 3: Polar Regions. In: Polar Regions," in *IPCC Special Report on the Ocean and Cryosphere in a Changing Climate*. Eds. H.-O. Pörtner, D. C. Roberts, V. Masson-Delmotte, P. Zhai, M. Tignor, E. Poloczanska, K. Mintenbeck, A. Alegría, M. Nicolai, A. Okem, J. Petzold, B. Rama and N. M. Weyer(Ginebra), 203–320.

Moore-Maley, B. L., Ianson, D., and Allen, S. E. (2018). The Sensitivity of Estuarine Aragonite Saturation State and pH to the Carbonate Chemistry of a Freshet-Dominated River. *Biogeosciences.* 15, 3743–3760. doi: 10.5194/bg-15-3743-2018

Mortensen, J., Lennert, K., Bendtsen, J., and Rysgaard, S. (2011). Heat Sources for Glacial Melt in a Sub-Arctic Fjord (Godthåbsfjord) in Contact With the Greenland Ice Sheet. *J. Geophys. Res. Ocean.* 116, C01013. doi: 10.1029/2010JC006528

Orr, J. C., Fabry, V. J., Aumont, O., Bopp, L., Doney, S. C., Feely, R. A., et al. (2005). Anthropogenic Ocean Acidification Over the Twenty-First Centuryand

its Impact on Calcifying Organisms. *Nature*. 437, 681–686. doi: 10.1038/nature04095

Parsons, T. R., Maita, Y., and Lalli, C. M. (1984). *A Manual of Chemical& Biological Methods for Seawater Analysis* (Ox ford, UK: Pergamon Press).

Pierrot, D., Lewis, E., and Wallace, D. W. R. (2006). *MS Excel Program Developed for CO2 System Calculations. ORNL/CDIAC-105* (Washington, D.C: U.S. Department of Energy).

Pytkowicx, R. M. (1971). On the Apparent Oxygen Utilization and the Preformed Phosphate in the Oceans1. *Limnol. Oceanogr.* 16, 39–42. doi: 10.4319/lo.1971.16.1.0039

Saldías, G. S., Sobarzo, M., and Quiñones, R. (2019). Freshwater Structure and its Seasonal Variability Off Western Patagonia. *Prog. Oceanogr.* 174, 143–153. doi: 10.1016/j.pocean.2018.10.014

Sarmiento, J. L., Gruber, N., Brzezinski, M. A., and Dunne, J. P. (2004). High-Latitude Controls of Thermocline Nutrients and Low Latitude Biological Productivity. *Nature.* 427, 56–60. doi: 10.1038/nature02127

Schneider, W., Pérez-Santos, I., Ross, L., Bravo, L., Seguel, R., and Hernández, F. (2014). On the Hydrography of Puyuhuapi Channel, Chilean Patagonia. *Prog. Oceanogr.* 129, 8–18. doi: 10.1016/j.pocean.2014.03.007

Sievers, H. A., Calvete, C., and Silva, N. (2002). Distribución De Características Físicas, Masas De Agua Y Circulación General Para Algunos Canales Australes Entre El Golfo De Penas Y El Estrecho De Magallanes (Crucero CIMAR-2 Fiordos). *Rev. Cienc. Tecnol. Mar.* 25, 17–43.

Sievers, H. A., and Silva, N. (2008). "Water Masses and Circulation in Austral Chilean Channels," in *Progress in the Oceanographic Knowledge of Chilean Interior Waters, From Puerto Montt to Cape Horn*. Eds. N. Silva and S. Palma (Valparaíso, Chile: Comité Oceanográfico Nacional), 53–58.

Silva, N., Calvete, C., and Sievers, H. (1998). Masas De Agua Y Circulación General Para Algunos Canales Australes Entre Puerto Montt Y Laguna San Rafael, Chile (Crucero Cimar-Fiordo 1). *Cienc. Tecnol. Mar.* 21, 17–48.

Silva, N., Rojas, N., and Fedele, A. (2009). Water Masses in the Humboldt Current System: Properties, Distribution, and the Nitrate Deficit as a Chemical Water Mass Tracer for Equatorial Subsurface Water Off Chile. *Deep. Sea. Res. Part II. Top. Stud. Oceanogr.* 56, 1004–1020. doi: 10.1016/j.dsr2.2008.12.013

Takahashi, T., Sutherland, S. C., Wanninkhof, R., Sweeney, C., Feely, R. A., Chipman, D. W., et al. (2009). Climatological Mean and Decadal Change in Surface Ocean Pco_2, and Net Sea–Air CO_2 Flux Over the Global Oceans. *Deep. Sea. Res. Part II. Top. Stud. Oceanogr.* 56, 554–577. doi: 10.1016/j.dsr2.2008.12.009

Takahashi, T., Olafsson, J., Goddard, J. G., Chipman, D. W., and Sutherland, S. (1993). Seasonal Variation of CO_2 and Nutrients in the High-Latitude Surface Oceans: A Comparative Study. *Glob. Biogeochem. Cycles* 7 (4), 843–878.

Torres, R., Frangópulos, M., Hamamé, M., Montecino, V., Maureira, C., Pizarro, G., et al. (2011a). Nitrate to Silicate Ratio Variability and the Composition of Micro-Phytoplankton Blooms in the Inner-Fjord of Seno Ballena (Strait of Magellan, 54°s). *Cont. Shelf. Res.* 31, 244–253. doi: 10.1016/j.csr.2010.07.014

Torres, R., Pantoja, S., Harada, N., González, H. E., Daneri, G., Frangopulos, M., et al. (2011b). Air-Sea CO_2 Fluxes Along the Coast of Chile: From CO2 Outgassing in Central Northern Upwelling Waters to CO_2 Uptake in Southern Patagonian Fjords. *J. Geophys. Res. Ocean.* 116, C09006. doi: 10.1029/2010JC006344

Torres, R., Reid, B., Frangópulos, M., Alarcón, E., Márquez, M., Häussermann, V., et al. (2020). Freshwater Runoff Effects on the Production of Biogenic Silicate and Chlorophyll-a in Western Patagonia Archipelago (50–51°s). *Estuar. Coast. Shelf. Sci.* 241, 106597. doi: 10.1016/j.ecss.2020.106597

Torres, R., Silva, N., Reid, B., and Frangopulos, M. (2014). Silicic Acid Enrichment of Subantarctic Surface Water From Continental Inputs Along the Patagonian Archipelago Interior Sea (41–56°s). *Prog. Oceanogr.* 129, 50–61. doi: 10.1016/j.pocean.2014.09.008

UNESCO, I (1981). The Practical Salinity Scale 1978 and the International Equation of State of Seawater 1980. *Tenth. Rep. Jt. Panel. Oceanogr. Table. Stand. JPOTS.* 25, 36.

Uppström, L. R. (1974). The boron/chlorinity ratio of Deep-Sea Water From the Pacific Ocean. *Deep-Sea Res* 21, 161–162. doi: 110.1016/0011-7471(74)90074-6

Valdenegro, A., and Silva, N. (2003). Caracterización Oceanográfica Física Y Química De La Zona De Canales Y Fiordos Australes De Chile Entre El Estrecho De Magallanes Y Cabo De Hornos (Cimar 3 Fiordos). *Cienc. Tecnol. Mar.* 26, 16–60.

Valle-Levinson, A., Blanco, J. L., and Frangópulos, M. (2006). Hydrography and Frontogenesis in a Glacial Fjord Off the Strait of Magellan. *Ocean. Dyn.* 56, 217–227. doi: 10.1007/s10236-005-0048-8

Valle-Levinson, A., Sarkar, N., Sanay, R., Soto, D., and León, J. (2007). Spatial Structure of Hydrography and Flow in a Chilean Fjord, Estuario Reloncaví. *Estuar. Coast.* 30, 113–126. doi: 10.1007/BF02782972

Vergara-Jara, M. J., DeGrandpre, M. D., Torres, R., Beatty, C. M., Cuevas, L. A., Alarcón, E., et al. (2019). Seasonal Changes in Carbonate Saturation State and Air-Sea CO_2 Fluxes During an Annual Cycle in a Stratified-Temperate Fjord (Reloncaví Fjord, Chilean Patagonia). *J. Geophys. Res. Biogeosci.* 124, 2851–2865. doi: 10.1029/2019JG005028

Wanninkhof, R. (1992). Relationship Between Wind Speed and Gas Exchange Over the Ocean. *J. Geophys. Res. Ocean.* 97, 7373–7382. doi: 10.1029/92JC00188

Wanninkhof, R. (2014). Relationship Between Wind Speed and Gas Exchange Over the Ocean Revisited. *Limnol. Oceanogr. Methods* 12, 351–362. doi: 10.4319/lom.2014.12.351

Weiss, R. F. (1974). Carbon Dioxide in Water and Seawater: The Solubility of a non-Ideal Gas. *Mar. Chem.* 2, 203–215. doi: 10.1016/0304-4203(74)90015-2

Xue, L., Cai, W.-J., Hu, X., Sabine, C., Jones, S., Sutton, A. J., et al. (2016). Sea Surface Carbon Dioxide at the Georgia Time Series Site, (2006–2007): Air–sea Flux and Controlling Processes. *Prog. Oceanogr.* 140, 14–26. doi: 10.1016/j.pocean.2015.09.008

Conflict of Interest: The authors declare that the research was conducted in the absence of any commercial or financial relationships that could be construed as a potential conflict of interest.

Publisher's Note: All claims expressed in this article are solely those of the authors and do not necessarily represent those of their affiliated organizations, or those of the publisher, the editors and the reviewers. Any product that may be evaluated in this article, or claim that may be made by its manufacturer, is not guaranteed or endorsed by the publisher.

Advantages of publishing in Frontiers

OPEN ACCESS
Articles are free to read for greatest visibility and readership

FAST PUBLICATION
Around 90 days from submission to decision

HIGH QUALITY PEER-REVIEW
Rigorous, collaborative, and constructive peer-review

TRANSPARENT PEER-REVIEW
Editors and reviewers acknowledged by name on published articles

Frontiers
Avenue du Tribunal-Fédéral 34
1005 Lausanne | Switzerland

Visit us: www.frontiersin.org
Contact us: frontiersin.org/about/contact

REPRODUCIBILITY OF RESEARCH
Support open data and methods to enhance research reproducibility

DIGITAL PUBLISHING
Articles designed for optimal readership across devices

FOLLOW US
@frontiersin

IMPACT METRICS
Advanced article metrics track visibility across digital media

EXTENSIVE PROMOTION
Marketing and promotion of impactful research

LOOP RESEARCH NETWORK
Our network increases your article's readership